

# Lithium Ion Batteries

Fundamentals and Performance

Edited by  
M. Wakihara, O. Yamamoto



M. Wakihara, O. Yamamoto (Eds.)

**Lithium Ion  
Batteries**

**Fundamentals and  
Performance**



**KODANSHA**



**WILEY-VCH**

## **Further Reading from WILEY-VCH**

J. O. Besenhard (Ed.)  
**Handbook of Battery Materials**  
ISBN 3-527-29469-4

K. Kordesch, G. Simader  
**Fuel Cells  
and Their Applications**  
ISBN 3-527-28579-2

M. Wakihara, O. Yamamoto (Eds.)

# **Lithium Ion Batteries**

## **Fundamentals and Performance**



**KODANSHA**



**WILEY-VCH**

Weinheim • Berlin • New York • Chichester •  
Brisbane • Singapore • Toronto



Masataka Wakihara  
Professor  
Department of Chemical Engineering  
Tokyo Institute of Technology  
Tokyo 152  
Japan

Osamu Yamamoto  
Professor  
Department of Chemistry  
Mie University  
Tsu-shi, Mie 514  
Japan

This book was carefully produced. Nevertheless, authors, editors and publisher do not warrant the information contained therein to be free of errors. Readers are advised to keep in mind that statements, data, illustrations, procedural details or other items may inadvertently be inaccurate.

Published jointly by:  
Kodansha Ltd., Tokyo (Japan),  
WILEY-VCH Verlag GmbH, Weinheim (Federal Republic of Germany)

Library of Congress Card No. applied for.

A catalogue record for this book is available from the British Library.

Deutsche Bibliothek Cataloguing-in-Publication Data:  
**Lithium Ion Batteries**/eds. by M. Wakihara ; O. Yamamoto.-Weinheim  
; Berlin ; New York ; Chichester ; Brisbane ; Singapore ; Toronto :  
Wiley-VCH, 1998  
ISBN 3-527-29569-0 (WILEY-VCH)  
ISBN 4-06-208631-X (KODANSHA)

Copyright © Kodansha Ltd., Tokyo, 1998  
All rights reserved. No part of this book may be reproduced in any form, by photostat, microfilm, retrieval system, or any other means, without the written permission of Kodansha Ltd. (except in the case of brief quotation for criticism or review).

Printed in Japan

## List of Contributors

(Numbers in parentheses refer to the pages on which the contributor's paper begins.)

John B. Goodenough	Center for Materials Science and Engineering, ETC9.102, University of Texas at Austin, USA (1)
Masataka Wakihara	Department of Chemical Engineering, Tokyo Institute of Technology, Japan (26)
Guohua Li	Department of Chemical Engineering, Tokyo Institute of Technology, Japan (26)
Hiromasa Ikuta	Department of Chemical Engineering, Tokyo Institute of Technology, Japan (26)
M. Stanley Whittingham	Chemistry Department and Materials Research Center, State University of New York at Binghamton, USA (49)
Jun-ichi Yamaki	NTT, Nippon Telegraph and Telephone Corporation, Japan (67)
Nobuyuki Imanishi	Department of Chemistry, Mie University, Japan (98)
Yasuo Takeda	Department of Chemistry, Mie University, Japan (98)
Osamu Yamamoto	Department of Chemistry, Mie University, Japan (98)
Martin Winter	Institute of Chemical Technology of Inorganic Materials, Technical University Graz, Austria (127)
Jürgen O. Besenhard	Institute of Chemical Technology of Inorganic Materials, Technical University Graz, Austria (127)
Masayuki Morita	Department of Applied Chemistry and Chemical Engineering, Faculty of Engineering, Yamaguchi University, Japan (156)
Masashi Ishikawa	Department of Applied Chemistry and Chemical Engineering, Faculty of Engineering, Yamaguchi University, Japan (156)
Yoshiharu Matsuda	Department of Applied Chemistry, Faculty of Engineering, Kansai University, Japan (156)
Yoshio Nishi	Sony Corporation, Japan (181)
Shigeo Kondo	Technology Laboratory, Matsushita Battery Industrial Co., Ltd., Japan (199)
Bruno Scrosati	Dipartimento di Chimica, Università "La Sapienza", Italy (218)

# Contents

List of Contributors v

Preface xiii

<b>1</b>	<b>General Concepts</b>	<b>1</b>
1.1	Introduction	1
1.2	Design Considerations	1
1.2.1	Definitions	1
1.2.2	Design Considerations	3
1.2.3	Choosing an Electrode	8
1.2.4	Anodes	12
1.3	Insertion of Lithium into Structures Containing Polyanions	13
1.3.1	Close-Packed Oxide-Ion Arrays	15
1.3.2	NASICON Frameworks	18
1.3.3	Conclusion	24
	References	25
<b>2</b>	<b>Cathode Active Materials with a Three-dimensional Spinel Framework</b>	<b>26</b>
2.1	Introduction	26
2.2	Crystal Structure of Spinel Type Phases	27
2.3	Synthesis Technique	28
2.4	Relationship between Discharge Voltage and Thermodynamic Function of the Cathode Materials	30
2.5	Phase Transformation During Intercalation Processes	33
2.6	Doped Spinel Phases $\text{LiM}_y\text{Mn}_{2-y}\text{O}_4$ ( $\text{M} = \text{Co}, \text{Cr}, \text{Ni}$ ) as 4 V-Class Cathode Material	34
2.6.1	Doping Effect on Charge-Discharge Behavior of Manganese Spinel	34
2.6.2	OCV and Phase Transformation	36
2.6.3	Cycling Performance	38
2.6.4	Structure Aspects	40

2.6.5	The Chemical Diffusion Coefficients of Lithium Ions in $\text{Li}_x\text{M}_y\text{Mn}_{2-y}\text{O}_4$ ( $\text{M}=\text{Co}$ and $\text{Cr}$ ) .....	42
2.6.6	Low Temperature Behavior .....	44
2.7	Conclusions .....	46
	References .....	47
<b>3</b>	<b>The Relationship between Structure and Cell Properties of the Cathode for Lithium Batteries .....</b>	<b>49</b>
3.1	Introduction .....	49
3.2	Titanium Disulfide and Intercalation Chemistry .....	50
3.3	Vanadium Dichalcogenides .....	53
3.4	Layered Oxides .....	53
3.5	Manganese Oxides .....	55
3.6	Vanadium Oxides .....	58
3.7	The Future .....	63
	References .....	64
<b>4</b>	<b>Design of the Lithium Anode and Electrolytes in Lithium Secondary Batteries with a Long Cycle Life .....</b>	<b>67</b>
4.1	Introduction .....	67
4.2	Lithium Metal Anode .....	67
4.2.1	Protection Films on Lithium Metal Anode .....	67
4.2.2	Cycling Efficiency of Lithium Anode .....	69
4.2.3	Morphology of Deposited Lithium .....	72
4.2.4	Mechanism of Lithium Deposition and Dissolution .....	73
4.2.5	The Amount of Dead Lithium and Cell Performance .....	75
4.2.6	Improvement in the Cycling Efficiency of a Lithium Anode .....	77
4.3	Safety .....	83
4.3.1	Configuration of Prototype Cells .....	84
4.3.2	Cell Performance .....	84
4.3.3	Heat Generation in a Cell—General Considerations .....	86
4.3.4	Incidents During Normal Cycling .....	89
4.3.5	Safety Tests on AA-size $\text{Li/a-V}_2\text{O}_5(-\text{P}_2\text{O}_5)$ Cells .....	91
4.4	Conclusion .....	94
	References .....	94
<b>5</b>	<b>Development of the Carbon Anode in Lithium Ion Batteries .....</b>	<b>98</b>
5.1	Introduction .....	98
5.2	Structure of Carbon Materials .....	99
5.3	Development of the Carbon Anode .....	101
5.4	Intercalation Mechanism of Graphite .....	105
5.5	Electrochemistry of Soft Carbons .....	108
5.6	Electrochemistry of Hard Carbons .....	112

5.7	Irreversible Surface Reactions .....	114
5.8	Structural Modifications .....	116
5.9	Nitrides as New Anode Materials .....	120
5.9.1	$\text{Li}_7\text{MnN}_4$ and $\text{Li}_3\text{FeN}_2$ (Antifluorite Structure) .....	120
5.9.2	$\text{Li}_{3-x}\text{Co}_x\text{N}$ ( $\text{Li}_3\text{N}$ Structure) .....	122
5.10	Summary and Conclusions .....	124
	References .....	125
<b>6</b>	<b>Electrochemical Intercalation of Lithium into</b>	
	<b>Carbonaceous Materials .....</b>	<b>127</b>
6.1	Introduction .....	127
6.1.1	Negative Electrodes in Rechargeable Lithium Batteries .....	127
6.1.2	Lithium/Carbon Intercalation Compounds .....	128
6.1.3	Carbonaceous Host Materials .....	129
6.2	Graphitic Carbons as Host for Lithium Intercalation .....	131
6.2.1	Lithium/Graphite Intercalation Compounds .....	132
6.2.2	Effects of Electrolyte Composition .....	135
6.3	Non-graphitic Carbons as Lithium Intercalation Hosts .....	140
6.3.1	"Low Capacity" Non-graphitic Carbons .....	140
6.3.2	"High Capacity" Non-graphitic Carbons .....	140
6.4	Special Carbonaceous Materials as Hosts for Lithium Intercalation .....	144
6.4.1	Fullerenes .....	144
6.4.2	Carbonaceous Materials Containing Heteroatoms .....	144
6.5	Technical Aspects .....	145
6.6	Outlook .....	146
	References .....	147
<b>7</b>	<b>Organic Electrolytes for Rechargeable Lithium Ion Batteries .....</b>	<b>156</b>
7.1	Introduction .....	156
7.2	The Basic Concept for Designing Organic Electrolytes for Lithium Batteries .....	157
7.2.1	Organic Solvents .....	157
7.2.2	Lithium Salts .....	159
7.2.3	Ionic Conductivity .....	159
7.2.4	Recent Studies on Organic Electrolytes for Rechargeable Lithium Ion Batteries .....	161
7.3	Effects of the Electrolyte Composition on the Electrode Characteristics of Pitch-based Carbon Fiber with Graphite Structure .....	163
7.3.1	Voltammetric Behavior in PC- and EC-based Solutions .....	163
7.3.2	Charge/Discharge Characteristics of the Carbon Fiber Electrode in $\text{LiCF}_3\text{SO}_3$ Solutions .....	167
7.4	Effects of the Electrolyte Composition on the Electrode Characteristics of Graphitized Mesocarbon Microbeads (MCMB) .....	171

7.4.1	Charge/Discharge Performance of MCMB in Electrolyte Solutions of Lithium Imide Salt .....	171
7.4.2	Interfacial Characteristics between the MCMB Electrode and the Electrolyte Solutions Containing Lithium Imide Salt .....	173
7.5	Effects of Electrolyte Composition on the EQCM Response of Graphite during Cathodic Lithium Intercalation .....	174
7.5.1	Effects of Solvent Composition on the First Charging Process .....	175
7.5.2	Effects on the Structure Changes of Graphite during the Charge/Discharge Process .....	177
7.5.3	Effects of the Electrolytic Salt on the EQCM Response of Graphite .....	178
7.6	Concluding Remarks .....	179
	References .....	179
<b>8</b>	<b>Performance of the First Lithium Ion Battery and Its Process Technology .....</b>	<b>181</b>
8.1	Introduction .....	181
8.2	Anode Materials .....	182
8.3	Cathode Materials .....	191
8.4	Other Materials .....	194
8.4.1	Electrolyte .....	194
8.4.2	Separator .....	195
8.4.3	PTC Devices .....	195
8.5	Cell Structure .....	196
8.6	Performance of Lithium Ion Secondary Batteries .....	197
8.7	Possibility of Further Improvement .....	198
	References .....	198
<b>9</b>	<b>All Solid-State Lithium Secondary Battery with Highly Ion Conductive Glassy Electrolyte .....</b>	<b>199</b>
9.1	Introduction .....	199
9.2	Lithium Ion Conductive Solid Electrolytes .....	200
9.3	$\text{Li}_3\text{PO}_4\text{-Li}_2\text{S-SiS}_2$ Glassy Electrolyte .....	202
9.3.1	Synthesis and Glass-Forming Region .....	202
9.3.2	Ionic Conductivity and Structure of the Glass .....	203
9.3.3	Electrochemical Stability .....	206
9.4	Solid-State Lithium Batteries .....	208
9.4.1	Brief Review of Solid-State Lithium Batteries in Previous Studies .....	208
9.4.2	Application of $\text{Li}_3\text{PO}_4\text{-Li}_2\text{S-SiS}_2$ Glass to the Solid-State Battery .....	209
9.5	Prospects for Solid-State Lithium Batteries in the Future .....	214
9.6	Summary .....	216
	References .....	216

<b>10 Lithium Ion Plastic Batteries .....</b>	<b>218</b>
10.1 Introduction .....	218
10.2 Polymer Electrolyte Membranes .....	219
10.2.1 Types and Preparation Procedures .....	219
10.2.2 Ionic Conductivity .....	223
10.2.3 Electrochemical Stability Window .....	227
10.2.4 Lithium Ion Transference Number .....	230
10.3 Plasticized Electrodes .....	232
10.4 Practical PLI Batteries .....	235
10.5 New Types of PLI Batteries .....	236
10.5.1 PLI Batteries with $\text{TiS}_2$ Anodes .....	236
10.5.2 The Dion Plastic Battery .....	240
10.6 Conclusions .....	242
References .....	243
Index .....	245

## Preface

Recently, rechargeable batteries with high energy density are in great demand as energy sources for various purposes, *e.g.* handy electronic machines, zero emission electric vehicles, load leveling in electric power. Lithium secondary batteries are the most promising to fulfill such needs because of their intrinsic discharge voltage with relatively light weight.

In 1991, the first lithium secondary battery of high quality and revolutionary concept was put on the market by Sony. In the commercial battery, called the "lithium ion battery," lithium ions swing between the anode and the cathode through an organic liquid electrolyte dissolving an inorganic lithium salt, like a rocking chair rocking from side to side. The principal concept is based on the intercalation reaction and is rather different from conventional secondary batteries which are based on chemical reactions. The past excellent results of fundamental research and technology have been used to develop the lithium ion battery. The needs of the time, however, do not stop and require further quality and better cost-performance for this type of battery, and given this favorable environment excellent fundamental concepts, idea and technology regarding electrodes and electrolytes in the battery are being published in articles and proceedings. However, the description is not always sufficient for complete understanding due to limited space.

This volume has been conceived keeping in mind selected fundamental topics together with the characteristics of the lithium ion battery on the market. It is thus a comprehensive overview of the new challenges facing the further development of lithium ion batteries with higher quality from the standpoint of both materials science and technology. Fundamental aspects and ideas on the cathode are discussed in Chapters 1-3. Chapter 4 addresses safety aspects of the lithium ion battery. The various topics on the carbon anode are presented in Chapters 5 and 6. Also the organic electrolytes are discussed in Chapter 7. From the standpoint of application, the performance of the first lithium ion battery is presented in Chapter 8 by Sony and the performance of new all solid battery using inorganic solid electrolyte by Matsushita and a polymer battery based on a new concept is discussed in Chapters 9 and 10.

This volume will be useful for many researchers in chemical companies including battery companies and universities, and also for graduate students who are studying or are planning to start research on the lithium secondary batteries, since it covers important topics from both fundamental and application points of view.

Gratitude is expressed to all the contributors who are actively studying and working in the field of lithium secondary batteries. Our joint publishers, especially Kodansha, were particularly helpful at all stages of the project, and we are very grateful to them for their understanding attitude and support.

December, 1997

Masataka Wakihara  
Osamu Yamamoto



## 1

## General Concepts

J. B. Goodenough\*

## 1.1 Introduction

A reliable secondary (rechargeable) battery of high energy and power density is needed for a variety of new existing technologies. This introductory chapter is divided into two parts. Section 1.2 ("Design Considerations") introduces several definitions and the general considerations that make electrochemical cells using  $\text{Li}^+$  as the working ion the most promising elemental component for a secondary battery of high energy and power density. Section 1.3 ("Insertion of Lithium into Structures Containing Polyanions") illustrates structural and chemical considerations that may be useful for the design of (search for) a competitive cathode material. It compares lithium insertion into two types of transition-metal oxides: those having a close-packed oxide-ion array and those forming framework structures in which the oxide ions are replaced by the polyanions  $(\text{SO}_4)^{2-}$ ,  $(\text{PO}_4)^{3-}$ ,  $(\text{AsO}_4)^{3-}$  and  $(\text{P}_2\text{O}_7)^{4-}$ . Of particular interest are (1) tuning of the transition-metal redox energies through the inductive effect, (2) the trade-off between improved  $\text{Li}^+$  ion diffusion and polaronic electron conduction in open frameworks, (3) the use of mixed phases to buffer against over-discharging as exemplified by  $\text{LiTi}_2(\text{PO}_4)_3$  mixed with  $\text{Li}_x\text{Fe}_2(\text{SO}_4)_3$ , (4) the identification and explanation of a reversible capacity fade at higher current densities, and (5) the identification of new cathode materials operating on the  $\text{Fe}^{3+}/\text{Fe}^{2+}$  redox couple: the olivine  $\text{Li}_x\text{FePO}_4$  with a flat  $V_{\text{oc}} = 3.5 \text{ V}$  vs. lithium and an  $\text{Li}_{3+x}\text{Fe}_2(\text{PO}_4)_3$  having the rhombohedral NASICON structure with a closed-circuit voltage centered at  $V = 2.8 \text{ V}$  and a capacity of  $95 \text{ mAh} \cdot \text{g}^{-1}$  at a current density of  $1 \text{ mA} \cdot \text{cm}^{-2}$ .

## 1.2 Design Considerations

A battery consists of a group of interconnected electrochemical cells. How these are connected and packaged depends upon the specific application for which they are designed. Here we consider only the design of the elemental building block of a battery, viz., the electrochemical cell.

## 1.2.1 Definitions

An electrochemical cell interfaces the external world through two metallic posts: one

---

\* Center for Materials Science and Engineering, ETC 9.102, University of Texas at Austin, Austin, TX-78712-1063, USA

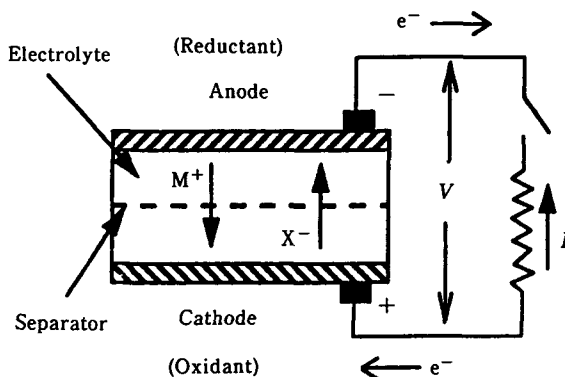


Fig. 1.1 Elements of an electrochemical cell; current flows shown occur during discharge.

contacts a negative electrode (the anode) and the other a positive electrode (the cathode) as illustrated schematically in Fig. 1.1. During cell discharge, electrons pass from the anode to the cathode through an external load of resistance  $R_L$  and ions flow inside the cell to convert chemical energy into electrical energy. The electronic current  $I$  delivered by the cell to the external circuit is matched by the ionic current within the cell. Any leakage of electrons from anode to cathode within the cell reduces the current  $I$  delivered by the cell.

During cell charge, electric current is forced in the opposite direction by an externally applied voltage to convert electrical energy back into chemical energy.

The ionic current within an electrochemical cell is carried between the electrodes by an electrolyte, which is ideally an electronic insulator and a good conductor of the working ion of the cell. One measure of the quality of an electrolyte is its transference (or transport) number

$$t_i \equiv \sigma_i / \sigma \quad (1.1)$$

where  $\sigma_i$  is the conductivity of the working ion and the total conductivity  $\sigma = \sum_j \sigma_j + \sigma_e$  is the sum of all the ionic conductivities and the electronic conductivity  $\sigma_e$  of the electrolyte under the working conditions of the cell. An ideal electrolyte has a  $t_i = 1$ .

If a liquid electrolyte is used, a separator is also needed to maintain an even spacing between the electrodes while blocking electronic current and passing the ionic current. A solid electrolyte can act as a separator; in this capacity it can allow the use of different liquid electrolytes at each electrode, a strategy that has yet to be explored. Common separators are porous electronic insulators permeated by a single liquid electrolyte.

The chemical at the anode that is consumed on discharge or produced on charge is the reductant of the chemical reaction; the chemical consumed on discharge or produced on charge at the cathode is the oxidant. The reductant and the oxidant are the two reactants of the cell; the energy of their reaction divided by the electronic charge passed in the reaction gives the maximum discharge voltage available between the positive and negative posts of the cells; it is the minimum voltage required to charge the cell.

A fuel cell operates in the discharge mode; the reductant is a convenient gaseous or liquid fuel that is fed from a reservoir (storage tank) to the anode, the oxidant is dioxygen,  $O_2$ , in

the air that is fed to the cathode, and the product of the reaction between the two reactants is the exhaust, which is vented at the cathode if the working ion is positive (a cation) and at the anode if the working ion is negative (an anion). An electrolysis cell operates in the charge mode; a product is separated into a reductant (a fuel or some other value-added chemical) that is extracted at the anode and an oxidant that is either vented or extracted at the cathode.

Present-day lithium batteries use a solid reductant as the anode and a solid oxidant as the cathode. On discharge, the metallic anode supplies  $\text{Li}^+$  ions to the  $\text{Li}^+$  ion electrolyte and electrons to the external circuit; the cathode is an electronically conducting host into which  $\text{Li}^+$  ions are inserted from the electrolyte as a guest species and charge-compensated by electrons from the external circuit. The chemical reactions at the anode and cathode of a lithium secondary battery must be reversible; on charge, removal of electrons from the cathode by an external field releases  $\text{Li}^+$  ions back to the electrolyte to restore the parent host structure and the addition of electrons to the anode by the external field attracts charge-compensating  $\text{Li}^+$  ions back into the anode to restore it to its original composition. In principle, the anode can be elemental lithium itself; in practice, it has been found necessary to use a reductant host for lithium. Where both the anode and cathode are hosts for the reversible insertion or removal of the working ion into/from the electrolyte, the electrochemical cell is commonly called a “rocking-chair” cell.

### 1.2.2 Design Considerations

The power output of a battery

$$P = IV \quad (1.2)$$

is the product of the electric current  $I$  delivered by the battery and the voltage  $V$  across the negative and positive posts. The voltage

$$V = V_{\text{oc}} - IR_{\text{b}} \quad (1.3)$$

is reduced from its open-circuit value ( $I=0$ )

$$V_{\text{oc}} = (\mu_{\text{A}} - \mu_{\text{C}})/(-nF) < 5 \text{ V} \quad (1.4)$$

by the voltage drop  $IR_{\text{b}}$  due to the internal resistance  $R_{\text{b}}$  of the battery. In Eq. (1.4),  $n$  is the number of electronic charges carried by the working ion and  $F$  is Faraday’s constant. The magnitude of the open-circuit voltage is constrained to  $V_{\text{oc}} < 5 \text{ V}$  not only by the attainable difference  $\mu_{\text{A}} - \mu_{\text{C}}$  of the electrochemical potentials of the anode reductant and the cathode oxidant, but also by the energy gap  $E_{\text{g}}$  between the HOMO (highest occupied molecular orbital) and the LUMO (lowest unoccupied molecular orbital) of a liquid electrolyte or by the gap  $E_{\text{g}}$  between the top of the valence band and the bottom of the conduction band of a solid electrolyte.

As illustrated in Fig. 1.2, the chemical potential  $\mu_{\text{A}}$ , which is the Fermi energy  $\varepsilon_{\text{F}}$  of a metallic reductant anode or the HOMO of a gaseous or liquid reductant, must lie below the LUMO of a liquid electrolyte or the conduction band of a solid electrolyte to achieve

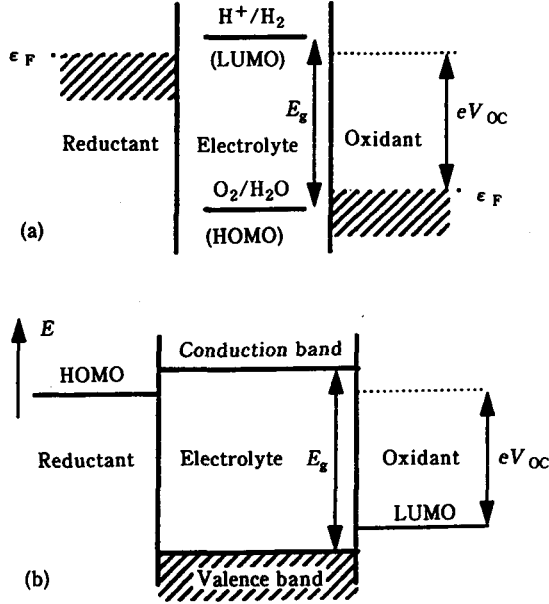


Fig. 1.2 Relative energies of the electrolyte window  $E_g$  and the electrode electrochemical potentials  $\mu_A = \epsilon_F$  or HOMO of reductant and  $\mu_C = \epsilon_F$  or LUMO of oxidant: (a) solid reactants liquid electrolyte; (b) liquid or gaseous reactants and solid electrolyte.

thermodynamic stability against reduction of the electrolyte by the reductant. Similarly, the chemical potential  $\mu_C$ , which is the LUMO of a gaseous or liquid oxidant or the Fermi energy of a metallic oxidant cathode, must lie above the HOMO of a liquid electrolyte or the valence band of a solid electrolyte to achieve thermodynamic stability against oxidation of the electrolyte by the oxidant. Thermodynamic stability thus introduces the constraint

$$\mu_A - \mu_C \leq E_g \quad (1.5)$$

as well as the need to match the “window”  $E_g$  of the electrolyte to the energies  $\mu_A$  and  $\mu_C$  of the reactants to maximize  $V_{oc}$ . Moreover, it follows then from Eqs. (1.2) and (1.3) that realization of a high maximum power

$$P_{\max} = I_{\max} V_{\max} \quad (1.6)$$

requires, in addition to as high a  $V_{oc}$  as possible, a low internal battery resistance

$$R_b = R_{el} + R_{in}(A) + R_{in}(C) + R_c(A) + R_c(C) \quad (1.7)$$

The electrolyte resistance

$$R_{el} = (L/\sigma_i A) \quad (1.8)$$

to the ionic current is proportional to the ratio of the effective thickness  $L$  to the geometrical area  $A$  of the interelectrode space that is filled with an electrolyte of ionic conductivity  $\sigma_i$ . Since ions move diffusively, *i.e.*, with a mobility  $\mu_i = qD/kT$  where the diffusion coefficient  $D = D_0 \exp(-\Delta G_m/kT)$  contains a motional free energy  $\Delta G_m$ , and  $\sigma_i = n_i q \mu_i$  is proportional to the density  $n_i$  of carriers of charge  $q$ ,

$$\sigma_i = (B/T) \exp(-E_a/kT) \quad (1.9)$$

increases with temperature  $T$ , and a  $\sigma_i \leq 0.1 \text{ S} \cdot \text{cm}^{-1}$  (the maximum  $\sigma_i$  represents the room temperature protonic conductivity  $\sigma_H$  in a strong acid) at an operating temperature  $T_{op}$  dictates the use of a membrane separator of large geometrical area  $A$  and small thickness  $L$ .

The resistance to transport of the working ion across the electrolyte-electrode interfaces is proportional to the ratio of the geometrical and interfacial areas at each electrode:

$$R_{in} \sim A/A_{in} \quad (1.10)$$

Where the chemical reaction of the cell involves ionic transport across an interface, relation Eq. (1.10) dictates construction of a porous, small-particle electrode as illustrated in Fig. 1.3. Achievement and retention of a high electrode capacity, *i.e.*, utilization of a high fraction of the electrode material in the reversible reaction, requires the achievement and retention of good electronic contact between particles over many discharge/charge cycles. If the reversible reaction involves a first-order phase change, the particles may fracture or lose contact with one another on cycling to break a continuous electronic pathway to the current collector.

Loss of interparticle electrical contact results in an irreversible loss of capacity. There may also be a reversible capacity fade. Where there is a two-phase process (or even a sharp guest-species gradient at a diffusion front) without fracture of the particles, the area of the interface (or diffusion front) decreases as the second phase penetrates the electrode particle; at a critical interface area, diffusion across the interface may not be fast enough to sustain the current  $I$ , so not all of the particle is accessible. The volume of inaccessible electrode increases with  $I$ , which leads to a diffusion-limited reversible capacity fade that increases with  $I$  as illustrated in Section 1.3.

Finally, current from the large-area electrodes must be collected to the negative and positive posts, and a clever geometrical design is needed to allow assembly of the cell into a small package that minimizes the current-collector resistance  $R_c$  of each electrode.

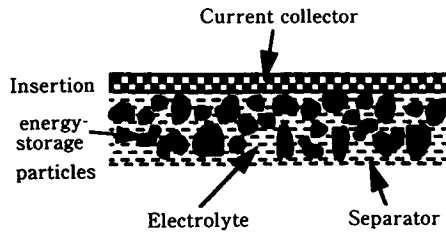


Fig. 1.3 Schematic of a porous electrode; not shown, individual electrode particles are in electronic contact with each other and the current collector.

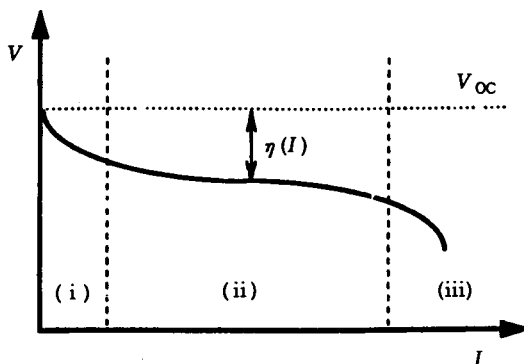


Fig. 1.4 Typical polarization curve.

$$R_c = (l/A\sigma_e) + (1/d\sigma_m) \quad (1.11)$$

In Eq. (1.11),  $l$  is the mean distance an electron (or hole) travels through the thickness of the electrode of electronic conductivity  $\sigma_e$  to reach the current-collector of conductivity  $\sigma_m$  and  $d$  is a geometrical parameter having units of length.

The battery voltage  $V$  vs. the current  $I$  delivered across a load is called the polarization curve. The voltage drop  $(V_{oc} - V) \equiv \eta(I)$  of a typical curve, Fig. 1.4, is a measure of the battery resistance

$$R_b(I) = \eta(I)/I \quad (1.12)$$

On charging,  $\eta(I) = (V_{app} - V_{oc})$  is referred to as an overvoltage. The interfacial voltage drops saturate in region (i) of Fig. 1.4; therefore in region (ii) the slope of the curve is

$$dV/dI \approx R_e + R_c(A) + R_c(C) \quad (1.13)$$

Region (iii) is diffusion-limited; at the higher currents  $I$ , normal processes do not bring ions to or remove them from the electrode/electrolyte interfaces rapidly enough to sustain an equilibrium reaction.

The battery voltage  $V$  vs. the state of charge, or the time during which a constant current  $I$  has been delivered, is called a discharge curve. Typical curves are shown in Fig. 1.5 for the solid solution reactions



In the first, illustrated schematically in Fig. 1.6, a complete solid solution  $0 \leq x \leq 1$  is obtained, and  $V(x)$  is described by the Nernst equation

$$V = V^\circ - \frac{RT}{F} \ln \frac{x}{1-x} \quad (1.15)$$

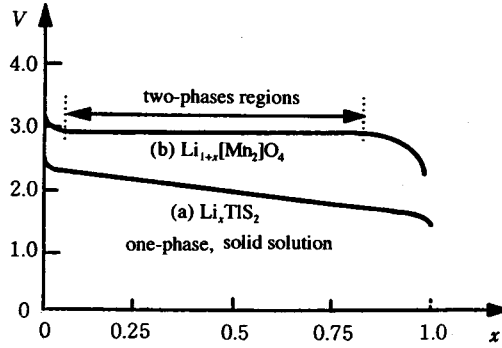


Fig. 1.5 Typical open-circuit discharge curves  $V_{oc}(x)$  with respect to a Li anode for two cathodes: (a)  $\text{Li}_x\text{TiS}_2$  and (b)  $\text{Li}_{1+x}[\text{Mn}_2]\text{O}_4$ .

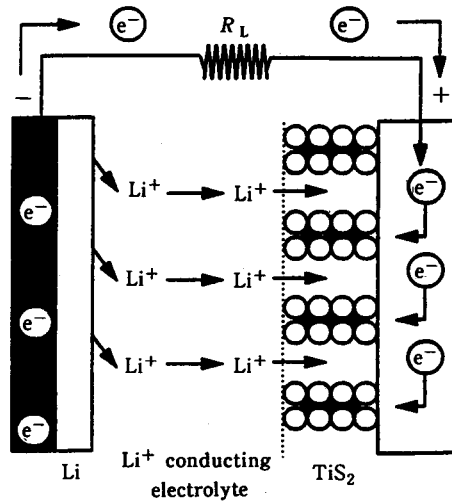


Fig. 1.6 Schematic of a  $\text{TiS}_2/\text{Li}^+$  electrolyte/Li battery. Current flows represent discharge.

where the standard potential  $V^\circ$  for the  $\text{Ti}^{4+}/\text{Ti}^{3+}$  redox couple is independent of  $x$  and corresponds to  $x=0.5$ . It is interesting that Eq. (1.15) is obeyed even though the electrons donated to the  $\text{TiS}_2$  array occupy a narrow Ti-3d band rather than a localized  $\text{Ti}^{3+}:^2\text{T}_{2g}$  configuration. In the second reaction (1.14b), the insertion of Li into the spinel  $\text{Li}[\text{Mn}_2]\text{O}_4$  induces a cooperative Jahn-Teller distortion from cubic to tetragonal symmetry that stabilizes the localized  $\text{Mn}^{3+}:^5\text{E}_g$  configuration of a cubic octahedral site. The solid solution within the tetragonal phase begins at  $x \approx 0.8$ ; and in accordance with the Gibbs phase rule, the voltage remains flat, independent of  $x$ , over the extended two-phase region  $0 < x < 0.8$ .

An implicit additional requirement of a secondary battery is maintenance of the electrode/electrolyte interfaces throughout repeated discharge/recharge cycles. Since the volumes of the electrodes change as a result of the transfer of atoms from one to another electrode in a reaction, this requirement normally excludes the use of a crystalline or glassy

electrolyte with a solid electrode. Liquid or elastomer electrolytes are used with solid electrodes; a solid electrolyte is preferred with liquid or gaseous reactants.

Traditional batteries use aqueous electrolytes. Protonic conductivity  $\sigma_H \leq 0.1 \text{ S} \cdot \text{cm}^{-1}$  can be achieved in aqueous solutions that are either strongly acidic, *e.g.*,  $\text{H}_2\text{SO}_4$ , or strongly alkaline, *e.g.*,  $\text{KOH}$ . An acidic solution provides protonic conduction at an  $\text{H}_3\text{O}^+/\text{H}_2\text{O}$  couple, an alkaline solution at an  $\text{H}_2\text{O}/\text{OH}^-$  couple.

The HOMO and LUMO for an aqueous solution are, respectively, the  $\text{O}_2/\text{H}_2\text{O}$  and the  $\text{H}^+/\text{H}_2$  couples; they are separated by an energy  $E_g = 1.23 \text{ eV}$ . Therefore thermodynamic stability limits the voltage of an aqueous system to 1.23 V. However, a kinetic energy barrier at an electrode/electrolyte interface may allow realization of an aqueous battery having a voltage  $V > 1.23 \text{ V}$ , as in the case of the lead-acid automobile battery with a  $V_{oc} \approx 2 \text{ V}$ . However, kinetic barriers are not compatible with a long shelf life.

The principal motivation for turning from the proton to  $\text{Li}^+$  as the working ion is the voltage limitation of a proton cell. Lithium is much more electropositive than hydrogen, which allows the realization of significantly higher voltages. However, to realize the higher voltages possible with a lithium battery, a non-aqueous electrolyte having a large energy-gap window between its HOMO and its LUMO must be used. Practical quantities of very ionic lithium salts such as  $\text{LiClO}_4$ ,  $\text{LiBF}_4$  and  $\text{LiPF}_6$  can be dissolved in empirically optimized mixtures of propylene carbonate (PC), ethylene carbonate (EC), or dimethyl carbonate (DMC), for example. Voltages approaching 4.5 V have been sustained in an electrolyte of  $\text{LiPF}_6$  in a 1 : 2 DMC : EC mixture. The  $(\text{ClO}_4)^-$  anion is explosive and not suitable for commercial applications. A commonly used electrolyte is  $\text{LiBF}_4$  in PC, but it is restricted to a  $V_{oc} < 4.2 \text{ V}$  vs. Li. An improved  $\text{Li}^+$  ion electrolyte would be welcome.

### 1.2.3 Choosing an Electrode

The working redox couples of a cathode host are commonly transition-metal  $3d^n$  energies as in  $\text{Li}_x\text{TiS}_2^{(1)}$ . Mixed-valent transition-metal oxides tend to be good electronic conductors, some are even metallic, and, with few exceptions, they are stable against disproportionation reactions like that occurring in  $\text{H}_{2x}\text{PbO}_2$ . Moreover, oxides allow realization of a higher  $V_{oc}$  for a given anode than do sulfides because higher cation valence states are accessible in an oxide than in a sulfide.

To illustrate this latter point, consider the  $\text{Mn}^{4+}/\text{Mn}^{3+}$  couple used with  $\gamma\text{-MnO}_2$  cathode in aqueous electrolytes and the spinel  $\text{Li}[\text{Mn}_2]\text{O}_4$  cathode used in lithium batteries. Whereas  $\text{Mn}^{4+}$  is accessible in  $\text{MnO}_2$ , the compound  $\text{MnS}_2$  contains  $\text{Mn}^{2+}$  and  $(\text{S}_2)^{2-}$  polyanions. The top of the  $\text{S}^{2-} : 3p^6$  valence band of a sulfide lies above the  $\text{Mn}^{4+}/\text{Mn}^{3+}$  couple; it also lies above the highest occupied molecular orbital of the electrolyte. The top of the  $\text{O}^{2-} : 2p^6$  valence band of an oxide, on the other hand, lies below both; it is possible to place the energy of the  $\text{Mn}^{4+}/\text{Mn}^{3+}$  redox couple above the highest occupied molecular orbital of the electrolyte with an oxide cathode, but it is not accessible with a sulfide cathode.

Figure 1.7 illustrates the situation by showing schematically the relevant electron energies for the  $\text{Mn}^{4+}/\text{Mn}^{3+}$  couple of the spinel  $\text{Li}[\text{Mn}_2]\text{O}_4$ . A 50 : 50 mixture of  $\text{Mn}^{4+}$  and  $\text{Mn}^{3+}$  ions on the octahedral sites of the close-packed oxygen array of an  $[\text{Mn}_2]\text{O}_4$  framework places the Fermi energy  $\varepsilon_F$  at the standard potential  $E^\circ = eV^\circ$  of the  $\text{Mn}^{4+}/\text{Mn}^{3+}$  couple, which lies above the top of the  $\text{O}^{2-} : 2p^6$  valence band. The empty  $\text{Mn}^{2+} : 3d^5$  level lies an



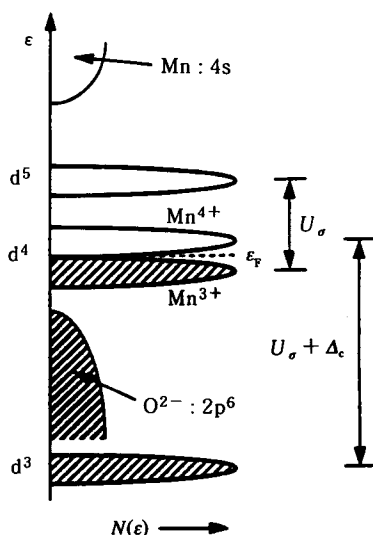


Fig. 1.7 Schematic energy diagram for the  $[\text{Mn}_2]\text{O}_4$  spinel framework of  $\text{Li}[\text{Mn}_2]\text{O}_4$ .

energy  $U_\sigma$  above the occupied  $\text{Mn}^{3+}:3d^4$  energies.  $U_\sigma$  is the energy required to add a fifth electron to the empty  $e$  orbital of the  $\text{Mn}^{3+}:t^3e^1$  majority-spin state of the high-spin configuration. The empty  $\text{Mn}^{4+}$  states of the  $3d^4$   $\text{Mn}^{4+}/\text{Mn}^{3+}$  couple are raised above the filled states by a reorganization, *i.e.*, small-polaron, energy because the time  $\tau_h$  for an electron to hop from a  $\text{Mn}^{3+}$  to a  $\text{Mn}^{4+}$  ion is long compared to the period  $\omega_R^{-1}$  of the optical-mode lattice vibration that traps it in a local deformation. If  $\tau_h$  were shorter than  $\omega_R^{-1}$ ,  $\varepsilon_F$  would lie in the middle of a narrow band of one-electron  $3d^4$  states. The occupied  $\text{Mn}^{4+}:3d^3$  states lie an energy  $U_\sigma + \Delta_c$  below the empty  $\text{Mn}^{4+}$  states of the  $3d^4$  couple because of the cubic-field splitting  $\Delta_c$  of the  $\pi$ -bonding  $t$  and  $\sigma$ -bonding  $e$  orbitals of the  $\text{Mn}$ - $3d$  manifold. In a sulfide, the top of the  $\text{S}^{2-}:3p^6$  valence band would overlap the  $\text{Mn}^{2+}:3d^5$  level to make inaccessible the  $\text{Mn}^{4+}/\text{Mn}^{3+}:3d^4$  redox couple; oxidation of the sulfide results in holes in the  $\text{S}^{2-}:3p^6$  band that become trapped in S-S disulfide bonds.

#### A. Layered Transition-Metal Oxides

Layered  $\text{TiS}_2$  consists of a close-packed-hexagonal sulfide-ion array with  $\text{Ti}^{4+}$  in alternate basal planes of octahedral sites; the empty planes of octahedral sites are between adjacent sulfide-ion planes held together by van der Waals bonding. In an oxide the Coulomb repulsion between oxide-ion planes is greater than any dipole-dipole bonding unless the cations of the "sandwich layer" are displaced from the center of their octahedral interstices to form permanent dipoles as in  $\text{V}_2\text{O}_5$ .

On the other hand, the cathode  $\text{NiOOH}$  of the nickel-cadmium battery is a layered oxide with  $\text{Ni}^{3+}$  ions occupying every other basal plane of octahedral sites of a close-packed-cubic array of oxide ions. In this oxide, protons provide a hydrogen bonding between O-Ni-O sandwich layers, and the hydrogen-bond network accommodates one hydrogen bond per oxygen atom in  $\text{Ni}(\text{OH})_2$ . Therefore protons may be inserted reversibly into the hydrogen-bond layers of  $\text{NiOOH}$  if charge-compensating electrons are introduced into the  $\text{Ni}^{3+}/\text{Ni}^{2+}$  couple indicated by the reaction

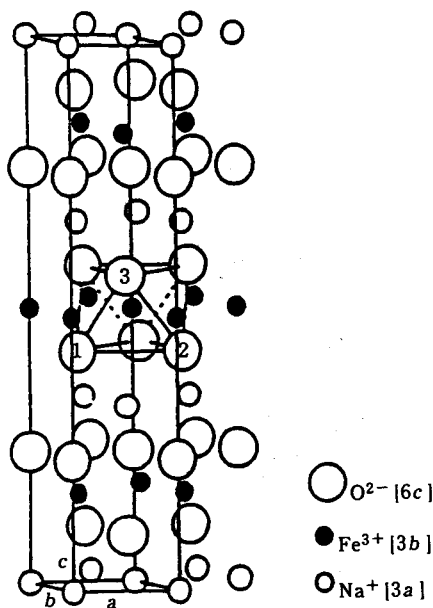


Fig. 1.8 The structure of layered  $\alpha$ - $NaFeO_2$ , prototype of  $LiCoO_2$  and  $LiNiO_2$ .

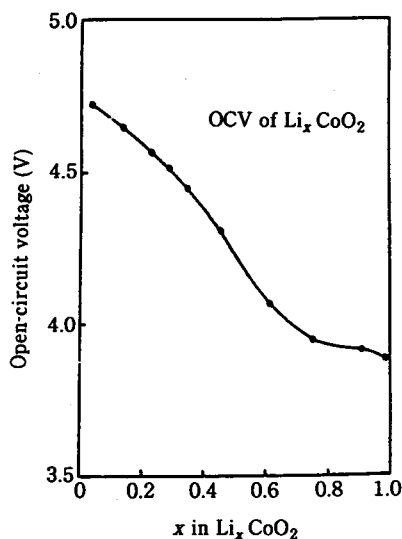
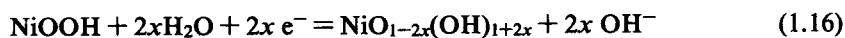


Fig. 1.9 Open-circuit voltage  $V_{oc}(x)$  vs. a Li anode for layered  $Li_xCoO_2$ ,  $0 < x \leq 1$ .<sup>2)</sup>  
 (Reproduced with permission by K. Mizushima *et al.*, *Mater. Res. Bull.*, 15, 783 (1980))



Replacement of the hydrogen of  $NiOOH$  by lithium gives the layered compound  $LiNiO_2$  with  $Li^+$  ions in the alternate basal planes of octahedral sites, Fig. 1.8, which invites

exploration of how much lithium can be extracted to give  $\text{Li}_{1-x}\text{NiO}_2$  before the layered structure becomes unstable. The largest solid solubility of Li in such a layered oxide has been found for  $\text{Li}_{1-x}\text{CoO}_2$ , and its open-circuit voltage  $V_{\text{oc}}(x)$  curve vs. a lithium anode is shown in Fig. 1.9; a  $V_{\text{oc}} \approx 4 \text{ V}$  is to be compared with the  $V_{\text{oc}} \approx 2.2 \text{ V}$  for  $\text{Li}_x\text{TiS}_2$ . A decrease in  $V_{\text{oc}}$  with increasing  $x$  that exceeds prediction from the Nernst equation (1.15) indicates a  $V_{\text{oc}}^0(x)$  for  $(1-x) < 0.7$ .

### B. Framework Transition-Metal Oxides

Removal of half the Li from  $\text{LiNiO}_2$  results in a metastable layered structure  $\text{Li}_{0.5}\text{NiO}_2$  that transforms, on heating to  $300^\circ\text{C}$ , to the cubic spinel  $\text{Li}[\text{Ni}_2]\text{O}_4$ .<sup>3)</sup> In the spinel structure, the oxide ions remain close-packed-cubic, but the Li atoms occupy  $8a$  tetrahedral sites forming a diamond-type subarray and the Ni atoms are rearranged into  $16d$  octahedral sites forming tetrahedral clusters in alternate quadrants of the cubic unit cell (Fig. 1.10). The empty  $16c$  octahedral sites form a similar three-dimensional (3D) configuration of edge-shared octahedral sites displaced by half the cubic lattice parameter, so the  $[\text{Ni}_2]\text{O}_4$  array may be considered a close-packed framework host with Li at tetrahedral sites of a 3D interstitial network of edge-shared octahedra sharing faces with the  $8a$  tetrahedral sites. Whereas the hexagonal layered structure has weak bonding between O–Ni–O sandwich layers and a variable  $c/a$  ratio that allows 2D  $\text{Li}^+$  ion transport, the 3D bonding of the  $[\text{Ni}_2]\text{O}_4$  framework allows 3D  $\text{Li}^+$  ion transport, but constrains the volume of the interstitial space. Although this constraint makes the spinel structure selective for insertion of  $\text{Li}^+$  ions, it reduces the  $\text{Li}^+$  ion mobility and hence the  $\text{Li}^+$  ion conductivity  $\sigma_{\text{Li}}$ . Nevertheless, the oxospinel  $\text{Li}_{1\pm x}[\text{Mn}_2]\text{O}_4$  with  $0 \leq x \leq 1$  have a sufficiently high  $\sigma_{\text{Li}}$  to be used commercially in low-power cells.<sup>4)</sup>

Extraction/insertion of Li from the tetrahedral sites of the  $\text{Li}_{1-x}[\text{Mn}_2]\text{O}_4$  spinel ( $0 \leq x \leq 1$ ) gives a  $V_{\text{oc}} \approx 4 \text{ V}$  vs. a Li anode with a small step in  $V_{\text{oc}}$  at  $x = 0.5$  presumably due to the onset of extraction/insertion of Li from the second face-centered-cubic subarray of the diamond-like array of  $8a$  tetrahedral sites. Insertion of Li into  $\text{Li}[\text{Mn}_2]\text{O}_4$  displaces the Li from the tetrahedral  $8a$  to the octahedral  $16c$  sites in  $\text{Li}_{1+x}[\text{Mn}_2]\text{O}_4$ , and the open-circuit

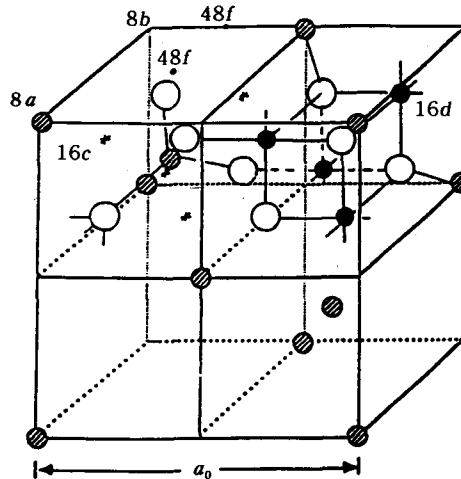


Fig. 1.10 The spinel structure.

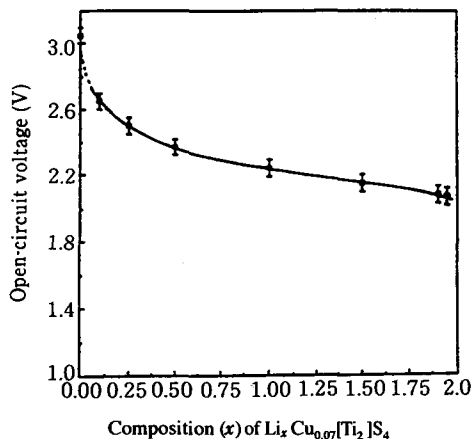


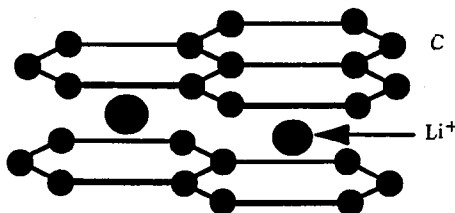
Fig. 1.11 Open-circuit voltage  $V_{oc}(x)$  vs. a Li anode for cubic  $\text{Li}_x\text{Cu}_{0.07}[\text{Ti}_2]\text{S}_4$ .

voltage drops to  $V_{oc} \approx 3\text{V}$ . Moreover, a cooperative Jahn-Teller deformation to tetragonal ( $c/a > 1$ ) symmetry sets in for a ratio  $\text{Mn}^{4+}/\text{Mn}^{3+} > 1$ , so the  $V_{oc}$  vs.  $x$  curve is flat over a two-phase cubic + tetragonal compositional range,  $0 < x < 0.8$  (see Fig. 1.5). The Jahn-Teller deformation tends to reduce the capacity of a practical  $\text{Li}_{1+x}[\text{Mn}_2]\text{O}_4$  cathode on repeated cycling, so it is preferable to reduce the  $\text{Mn}^{3+}$  ion concentration by introducing excess Li into the starting spinel up to a limiting composition  $\text{Li}[\text{Li}_{0.33}\text{Mn}_{0.67}]\text{O}_4$ .<sup>5)</sup>

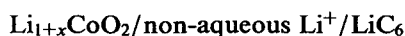
In sulfides, the  $\text{Li}^+$  ion has an important preference for octahedral sites, which favors stabilization of layered  $\text{Li}_{0.5}\text{TiS}_2$  over the spinel  $\text{Li}[\text{Ti}_2]\text{S}_4$ . However,  $\text{Cu}^+$  has a preference for tetrahedral sites, which stabilizes the sulfospinel  $\text{Cu}[\text{Ti}_2]\text{S}_4$ , and almost all the Cu atoms can be extracted chemically at room temperature to leave intact the metastable cubic spinel framework  $[\text{Ti}_2]\text{S}_4$ .<sup>6)</sup> Li atoms may be inserted into or extracted from this spinel framework to give  $\text{Li}_x[\text{Ti}_2]\text{S}_4$  over the entire compositional range  $0 \leq x \leq 2$ , and the  $V_{oc}(x)$  with respect to a Li anode (Fig. 1.11) may be nearly superimposed on that for  $\text{Li}_x\text{TiS}_2$  (Fig. 1.5) because the guest Li atoms occupy only octahedral sites. Moreover, the larger, more polarizable  $\text{S}^{2-}$  ions give a  $\sigma_{\text{Li}}$  in the sulfospinel that is comparable to that of the layered sulfide. In contrast,  $\sigma_{\text{Li}}$  in  $\text{Li}_{1-x}\text{CoO}_2$  is nearly an order of magnitude higher than in the sulfides whereas it is significantly lower in the oxospinel. These considerations suggest the use, in 3D framework structures, of oxopolyanions such as  $(\text{SO}_4)^{2-}$  and  $(\text{PO}_4)^{3-}$  in place of  $\text{O}^{2-}$  in order to obtain the high voltage realizable with an oxide and the larger free volume for cation motion associated with a larger anion. Tuning of the redox energies in framework structures containing polyanions are briefly reviewed in Section 1.3 of this chapter.

### 1.2.4 Anodes

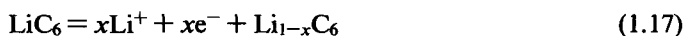
The electrochemical potential of Li metal lies above the LUMO of preferred electrolytes, and reaction with the electrolyte results in the formation of a passivating surface layer. Although  $\text{Li}^+$  ions pass through the layer on discharge, the Li redeposited on charge tends to form dendrites that traverse the electrolyte and separator to give electronic pathways that

Fig. 1.12 The structure of  $\text{LiC}_6$ .

short-circuit the cell. Lack of reliable reversibility of a Li-metal anode motivated development of oxide cathodes of high  $V_{\text{oc}}$  vs. a Li-metal anode so as to enable development of Li anodes having a lower electrochemical potential than metallic lithium. A candidate insertion host having a Fermi energy only about 0.5 eV below that of Li is carbon. Li can be inserted reversibly into graphite to  $\text{LiC}_6$  (Fig. 1.12). However, the bonding between graphite layers is too strong to give a high  $\sigma_{\text{Li}}$ , and a quasi-amorphous petroleum coke was developed<sup>7)</sup> to give the now commercial battery



having the anode reaction



### 1.3 Insertion of Lithium into Structures Containing Polyanions

The cathode of a secondary lithium battery consists of a host structure into which lithium can be inserted reversibly. The maximum power output,  $P_{\text{max}} = I_{\text{max}} V_{\text{max}}$ , that can be achieved by a cell depends on the open-circuit voltage  $V_{\text{oc}} = \Delta E/e$  and the overvoltage  $\eta(I)$  at the current  $I_{\text{max}}$  of maximum power

$$V_{\text{max}} = V_{\text{oc}} - \eta(I_{\text{max}})$$

$\Delta E$  is the energy difference between the work function of the anode (or the HOMO of the reductant) and that of the cathode (or the LUMO of the oxidant); HOMO and LUMO are, respectively, the highest occupied and the lowest unoccupied molecular orbitals. In order to obtain a high  $V_{\text{oc}}$ , it is necessary to use a cathode that is an oxide or a halide. To minimize  $\eta(I_{\text{max}})$ , the electrodes must be good electronic as well as ionic conductors and they must offer a low resistance to mass transfer across the electrode/electrolyte interface. To obtain a high  $I_{\text{max}}$ , it is necessary to have a large electrode/electrolyte surface area. In addition, where there is a two-phase interface within the electrode particle, the rate of mass transfer across this interface must remain large enough to sustain the current, a constraint that we shall see limits the electrode capacity more as the current increases. Since the electronic conductivity in halides is much poorer than in oxides, the cathode designers have looked to oxides for their host structures.

Oxide host structures with close-packed oxygen arrays may be layered, as in  $\text{Li}_{1-x}\text{CoO}_2$ ,

or strongly bonded in three dimensions (3D) as in the manganese spinels  $\text{Li}_{1-x}[\text{Mn}_2]\text{O}_4$ . Li intercalation into a gap between strongly bonded layers may be fast, but it can also be accompanied by unwanted species from a liquid electrolyte. On the other hand, strong 3D bonding within a close-packed oxygen array, as occurs in the spinel framework  $[\text{Mn}_2]\text{O}_4$ , offers too small a free volume for the guest  $\text{Li}^+$  ions to have a high mobility at room temperature, which limits  $I_{\text{max}}$ . Therefore, it is of interest to study oxides containing larger tetrahedral polyanions forming 3D framework host structures with octahedral-site transition-metal oxidant cations. In these framework hosts, the transition-metal ions are separated by the polyanions, so the electronic conductivity is polaronic rather than metallic. The following goals are of particular interest:

- Determination of oxidant redox couples (LUMO of cathode) for different transition-metal cations and how they vary with host structure, choice of polyanion, and degree of lithiation.
- Exploration of the advantage of a more open framework for  $\text{Li}^+$  ion diffusion vs. the disadvantage of a polaronic electronic conduction.
- The use of a second phase with higher redox energy (lower closed-circuit plateau) to act as a buffer against over-discharge.
- Identification of the cause of a reversible capacity fade with increasing current density.
- The design of new materials for secondary Li batteries.

Variation of the energy of a given cation redox couple from one compound to another depends on two factors: (a) the magnitude of the crystalline electric field at the cation, which may be calculated for a purely ionic model by a Madelung summation of the Coulomb fields from the other ions present, and (b) the covalent contribution to the bonding, which may be modulated by the strength of the covalent bonding at a nearest-neighbor cation. The stronger is the negative Madelung potential at a cation, the higher is a given redox energy of a cation. Similarly the stronger is the covalent bonding of the electrons at a transition-metal cation, the higher is a given redox energy of that cation.

The redox couples of interest for a cathode are associated with antibonding states of d orbital parentage at transition-metal cations M or 4f orbital parentage at rare-earth cations Ln in an oxide; therefore, the stronger is the cation–anion covalent mixing, the higher is the energy of a given LUMO/HOMO redox couple. Modulation of the strength of the cation–anion covalence at a given M or Ln cation by nearest-neighbor cations that compete for the same anion valence electrons is known by chemists as the inductive effect. Changes of structure alter primarily the Madelung energy as is illustrated by raising of the redox energy within a spinel  $[\text{M}_2]\text{O}_4$  framework by about 1 eV on transfer of  $\text{Li}^+$  ions from tetrahedral to octahedral interstitial sites. Changing the counter cation, but not the structure, alters primarily the inductive effect as is illustrated by a lowering of the  $\text{Fe}^{3+}/\text{Fe}^{2+}$  redox energy by 0.6 eV on changing  $(\text{MoO}_4)^{2-}$  or  $(\text{WO}_4)^{2-}$  to  $(\text{SO}_4)^{2-}$  polyanions in isostructural  $\text{Fe}_2(\text{XO}_4)_3$  compounds. Finally, it should be noted that raising the energy of a given redox couple in a cathode lowers the voltage obtained from cells utilizing a common anode. Conversely, raising the redox energy of an anode raises the cell voltage with respect to a common cathode.

### 1.3.1 Close-Packed Oxide-Ion Arrays

#### A. Spinel

The spinel systems  $\text{Li}_{1\pm x}[\text{Mn}_2]\text{O}_4$  and lithium insertion into  $\text{Li}_{1-x}[\text{Mn}_{2-y}\text{Li}_z]\text{O}_4$  ( $z \leq y$ ) have been studied extensively.<sup>5,8-11</sup> As originally emphasized<sup>12</sup>) in a study of  $\text{Li}_{1+x}[\text{Ti}_2]\text{O}_4$ , there is a remarkable change  $\Delta V_{\text{oc}} \approx -1.0$  V in the open-circuit voltage that accompanies a transfer of  $\text{Li}^+$  ions from tetrahedral to octahedral sites of the  $[\text{M}_2]\text{O}_4$  spinel framework; it is a measure of the stabilization of the spinel as against the cation-deficient rock-salt structure in the parent  $\text{Li}[\text{M}_2]\text{O}_4$  compound. On the other hand, where the  $\text{Li}^+$  ions occupy a set of crystallographically (hence energetically) equivalent sites, the variation in  $V_{\text{oc}}$  with site occupancy may, but generally does not, follow a Nernst law for the dependence of the chemical potential on lithium activity, as has been demonstrated<sup>13</sup>) for the layered system  $\text{Li}_x\text{TiS}_2$ . Comparisons of relative standard redox energies are appropriate for any

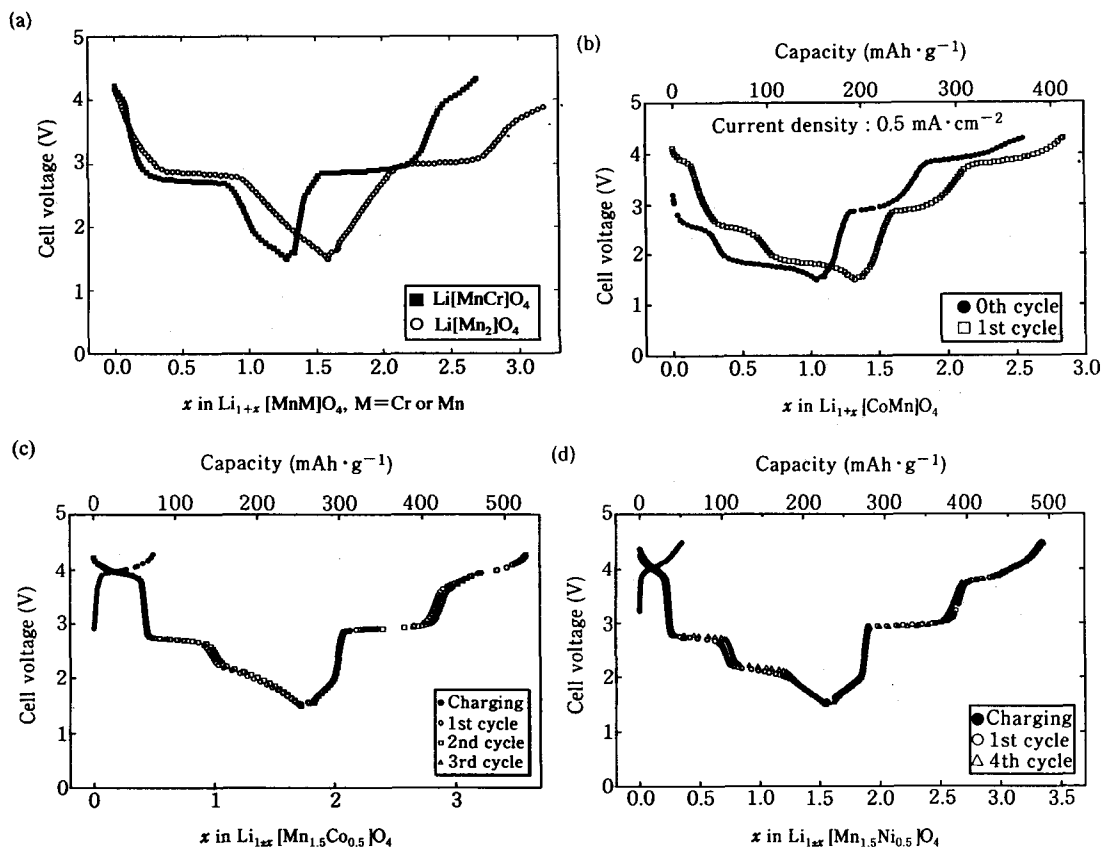
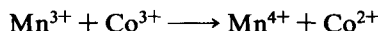


Fig. 1.13 Discharge/charge vs. lithium curves at  $0.05 \text{ mA} \cdot \text{cm}^{-2}$  for (a)  $\text{Li}_{1\pm x}[\text{MnM}]\text{O}_4$ , M = Co or Mn, (b)  $\text{Li}_{1\pm x}[\text{CoMn}]\text{O}_4$ , (c)  $\text{Li}_{1\pm x}[\text{Mn}_{1.5}\text{Co}_{0.5}]\text{O}_4$ , (d)  $\text{Li}_{1\pm x}[\text{Mn}_{1.5}\text{Ni}_{0.5}]\text{O}_4$  in which increasing  $x$  displaces Li from the tetrahedral 8a to the neighboring octahedral sites 16c of the spinel framework.

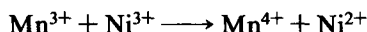
(Reproduced with permission by K.S. Najundaswamy *et al.*, *Proc. 37th Power Sources Conf.* (1996))

given family of isostructural compounds where lithium is inserted into energetically equivalent (or nearly so) interstitial sites of a host framework at low ( $0.05\text{--}0.1\text{ mA}\cdot\text{cm}^{-2}$ ) current densities provided there is a similar  $\text{Li}^+$  ion occupancy of these sites.

Figure 1.13 shows<sup>14)</sup> closed-circuit cell voltages  $V$  vs. lithium insertion  $x$  at  $0.05\text{ mA}\cdot\text{cm}^{-2}$  for the spinels  $\text{Li}_{1+x}[\text{MnM}]\text{O}_4$  with  $\text{M}=\text{Cr}, \text{Mn},$  or  $\text{Co}$  and  $\text{Li}_{1+x}[\text{Mn}_{1.5}\text{M}_{0.5}]\text{O}_4$  with  $\text{M}=\text{Co}$  or  $\text{Ni}$ . The initial drop from 4 V to a plateau at *ca.* 2.7 V for  $\text{Li}_{1+x}[\text{MnCr}]\text{O}_4$  is due to a change from tetrahedral site to octahedral site occupancy of the  $\text{Li}^+$  ions for the  $\text{Mn}^{4+}/\text{Mn}^{3+}$  redox couple. The octahedral sites are filled at  $x=1$ , and the fall-off to  $V\approx 1.7\text{ V}$  at higher  $x$  values is due to both a transition to the  $\text{Mn}^{3+}/\text{Mn}^{2+}$  couple and to an introduction of tetrahedral site  $\text{Li}^+$  ions in the presence of octahedral sites filled with  $\text{Li}^+$  ions. In  $\text{Li}_{1+x}[\text{MnCo}]\text{O}_4$ , the step at *ca.* 2.6 V near  $x=0.5$  is similarly due to the  $\text{Mn}^{4+}/\text{Mn}^{3+}$  couple, but a plateau at about 1.85 V at higher values of  $x$  indicates the  $\text{Co}^{3+}/\text{Co}^{2+}$  couple is overlapped by the  $\text{Mn}^{4+}/\text{Mn}^{3+}$  couple. A similar step at about  $x=0.5$  to a plateau near 2.0 V in  $\text{Li}_{1+x}[\text{Mn}_{1.5}\text{M}_{0.5}]\text{O}_4$  ( $\text{M}=\text{Co}$  or  $\text{Ni}$ ) indicates operation on the  $\text{Mn}^{4+}/\text{Mn}^{3+}$  couple with  $0\leq x\leq 0.5$  followed by reduction of  $\text{Mn}^{4+}$  destabilized by the equilibrium reactions



or



Another family of spinels,  $\text{V}[\text{LiM}]\text{O}_4$  with  $\text{M}=\text{Mn}, \text{Co}$  or  $\text{Ni}$ , contains  $\text{V}^{5+}$  ions on the tetrahedral sites with Li and M atoms randomly distributed over the octahedral sites. The  $\text{M}=\text{Mn}$  member of this family was obtained by a high-pressure (55 kbar) transformation of the ambient-pressure orthorhombic phase.<sup>15)</sup> A reversible lithium extraction from these spinels exposes the  $\text{Mn}^{3+}/\text{Mn}^{2+}$  redox couple; and at  $0.05\text{ mA}\cdot\text{cm}^{-2}$ , plateaus in the  $V$  vs.  $x$  curves for  $\text{V}[\text{Li}_{1-x}\text{M}]\text{O}_4$  give the redox energies for the  $\text{Mn}^{3+}/\text{Mn}^{2+}$ ,  $\text{Co}^{3+}/\text{Co}^{2+}$  and  $\text{Ni}^{3+}/\text{Ni}^{2+}$  couples at 3.8 eV, 4.2 eV and 4.8 eV<sup>16)</sup>, respectively, below the Fermi energy of a lithium anode. These values represent the stabilization of the redox energies by nearly 3 eV relative to their position with  $\text{Li}^+$  in the tetrahedral sites instead of the  $\text{V}^{5+}$  ion. This remarkable change indicates that the tetrahedral site vanadium may be considered to be a  $(\text{VO}_4)^{3-}$  polyanion. Strong covalent bonding within the polyanion polarizes the oxygen electrons away from the octahedral site cation towards the vanadium, which stabilizes the antibonding 3d electrons of the transition-metal M cation.

### B. Olivines<sup>17)</sup>

The olivine structure of  $\text{Mg}_2\text{SiO}_4$  consists of a slightly distorted array of oxygen atoms with  $\text{Mg}^{2+}$  ions occupying half the octahedral sites in two different ways: in alternate basal planes, they form zigzag chains of corner-shared octahedra running along the  $c$ -axis and in the other basal planes they form linear chains of edge-shared octahedra running also along the  $c$ -axis.

Replacement of  $\text{VO}_4$  by  $\text{PO}_4$  in the  $\text{V}[\text{LiM}]\text{O}_4$  compounds with  $\text{M}=\text{Mn}, \text{Fe}, \text{Co},$  or  $\text{Ni}$  yields an ordered  $\text{LiMPO}_4$  olivine structure in which the M atoms occupy the zigzag chains of octahedra and the Li atoms occupy the linear chains of the alternate planes of octahedral sites. Removal of all the lithium atoms leaves the layered  $\text{FePO}_4$ -type structure, which has the same  $Pbnm$  orthorhombic space group. These phases may be prepared from either end, *e.g.*,  $\text{LiFePO}_4$  (triphylite) or  $\text{FePO}_4$  (heterosite); each parent compound supports the



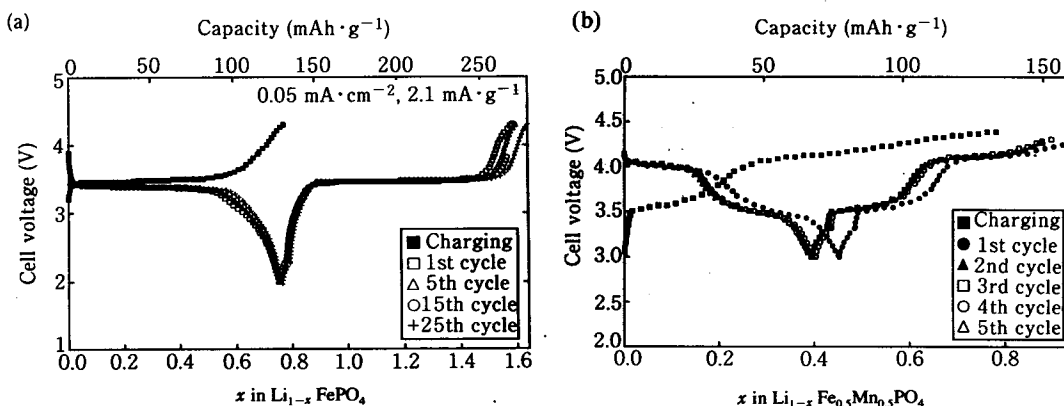


Fig. 1.14 Discharge/charge curves vs. lithium at  $0.05 \text{ mA} \cdot \text{cm}^{-2}$  for the olivines (a)  $\text{Li}_{1-x}\text{FePO}_4$  and (b)  $\text{Li}_{1-x}\text{Fe}_{0.5}\text{Mn}_{0.5}\text{PO}_4$ .

(Reproduced with permission by A.K. Padhi *et al.*, *Proc. 189th ECS Meeting* (1996))

reversible extraction or insertion of lithium.

Figure 1.14 shows discharge/charge curves at  $0.05 \text{ mA} \cdot \text{cm}^{-2}$  ( $0.95 \text{ mA} \cdot \text{g}^{-1}$  and  $1.13 \text{ mA} \cdot \text{g}^{-1}$ , respectively) for  $\text{Li}_{1-x}\text{FePO}_4$  and  $\text{Li}_{1-x}\text{Fe}_{0.5}\text{Mn}_{0.5}\text{PO}_4$ . A plateau at 3.4 V corresponds to the  $\text{Fe}^{3+}/\text{Fe}^{2+}$  redox couple; a plateau at 4.1 V to the  $\text{Mn}^{3+}/\text{Mn}^{2+}$  couple. It was not possible to extract lithium from  $\text{LiMnPO}_4$ ,  $\text{LiCoPO}_4$  and  $\text{LiNiPO}_4$  while charging up to 4.3 V, *i.e.*, with the electrolyte  $\text{LiClO}_4$  in PC and DME, due to the stability of the  $\text{Mn}^{3+}/\text{Mn}^{2+}$ ,  $\text{Co}^{3+}/\text{Co}^{2+}$  and  $\text{Ni}^{3+}/\text{Ni}^{2+}$  couples in the presence of the polyanion  $(\text{PO}_4)^{3-}$ . It appears that the greater covalence of the  $\text{PO}_4$  tetrahedron relative to that of the  $\text{VO}_4$  tetrahedron not only favors the olivine as against the spinel structure; it also stabilizes the redox couples at the octahedral sites by about 0.3 eV, lowering the  $\text{Mn}^{3+}/\text{Mn}^{2+}$  couple from 3.8 eV below the lithium anode Fermi energy in  $\text{V}[\text{LiMn}]\text{O}_4$  to 4.1 eV in  $\text{LiFe}_{0.5}\text{Mn}_{0.5}\text{PO}_4$ . Apparently the initial removal of lithium to oxidize  $\text{Mn}^{2+}$  requires more than 4.3 V vs. lithium in  $\text{LiMnPO}_4$ . However, the substitution of Fe for Mn in  $\text{LiMn}_{1-x}\text{Fe}_x\text{PO}_4$  allows the initial removal of lithium to oxidize  $\text{Fe}^{2+}$ , which is 0.6 eV above the  $\text{Mn}^{2+}$  level, and the  $\text{Mn}^{3+}/\text{Mn}^{2+}$  couple becomes accessible in the presence of  $\text{Fe}^{3+}$  and some lithium vacancies.

Insertion of lithium into  $\text{FePO}_4$  was reversible over the several cycles investigated.  $\text{Li}_x\text{FePO}_4$  represents a cathode of good capacity and it contains inexpensive, environmentally benign elements. However, a nearly close-packed-hexagonal oxide-ion array provides a relatively small free volume for  $\text{Li}^+$  ion motion, so the electrode supports only relatively small current densities at room temperature. Nevertheless, increasing the current density does not lower the closed-circuit voltage  $V$ ; rather it decreases, reversibly, the cell capacity. Reducing the current restores the capacity.

As is illustrated schematically in Fig. 1.15, lithium insertion proceeds from the surface of the particle moving inwards behind a two-phase interface, a  $\text{Li}_x\text{FePO}_4/\text{Li}_{1-x}\text{FePO}_4$  interface in this system. As the lithiation proceeds, the surface area of the interface shrinks. For a constant rate of lithium transport per unit area across the interface, a critical surface area is reached where the rate of total lithium transported across the interface is no longer able to sustain the current; the cell performance becomes diffusion-limited. The higher the current, the greater is the total critical interface area and, hence,

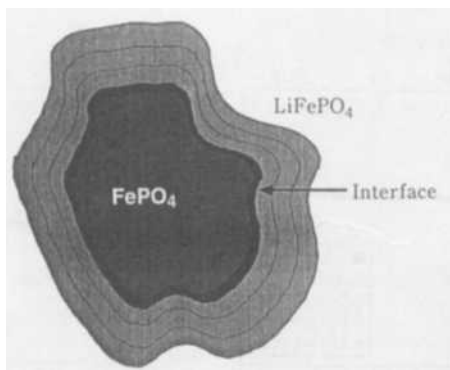


Fig. 1.15 Schematic representation of the motion of  $\text{LiFePO}_4/\text{FePO}_4$  interface on lithium insertion into a particle of  $\text{FePO}_4$ .

the smaller the concentration  $x$  of inserted lithium before the cell performance becomes diffusion-limited. On extraction of lithium, the parent phase at the core of the particle grows back towards the particle surface, which is why the parent phase is retained on repeated cycling and the loss in capacity is reversible on lowering the current density delivered by the cell. This loss of capacity is not due to a breaking of the electrical contact between particles as a result of volume changes, a process that is normally irreversible.

### 1.3.2 NASICON Frameworks

The compound  $\text{Fe}_2(\text{SO}_4)_3$  has two forms, the rhombohedral NASICON structure<sup>18)</sup> of Fig. 1.16(a) and the related monoclinic form of Fig. 1.16(b).<sup>19)</sup> Each structure contains units of two  $\text{FeO}_6$  octahedra bridged by three corner-sharing  $\text{SO}_4$  tetrahedra. These units form 3D frameworks by the bridging  $\text{SO}_4$  tetrahedra of one unit sharing corners with  $\text{FeO}_6$  octahedra of neighboring  $\text{Fe}_2(\text{SO}_4)_3$  elementary building blocks so that each tetrahedron shares corners with only octahedra and each octahedron with only tetrahedra. In the

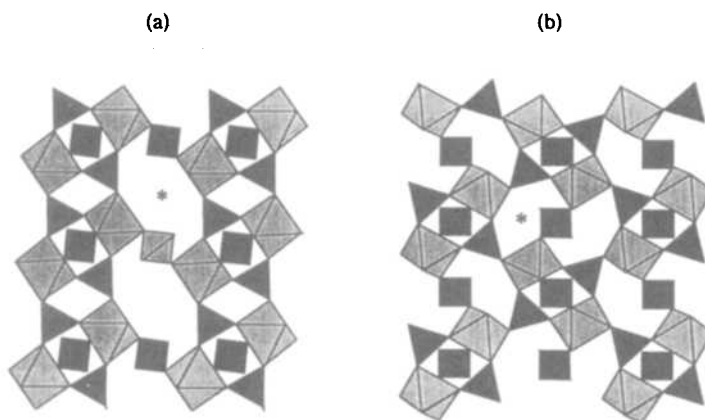


Fig. 1.16 The framework structures of  $\text{Fe}_2(\text{SO}_4)_3$ : (a) rhombohedral  $R\bar{3}c$  and (b) monoclinic  $P2_1/n$ .

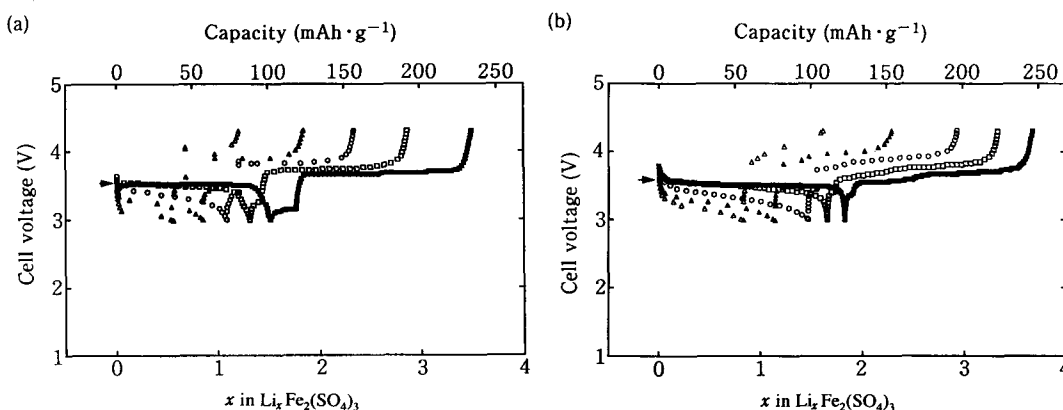


Fig. 1.17 Discharge/charge curves vs. lithium for current densities  $0.05\text{--}2.0\text{ mA}\cdot\text{cm}^{-2}$  for (a) monoclinic  $\text{Fe}_2(\text{SO}_4)_3\text{--Li}_2\text{Fe}_2(\text{SO}_4)_3$ , (b) rhombohedral/orthorhombic  $\text{Fe}_2(\text{SO}_4)_3\text{--Li}_2\text{Fe}_2(\text{SO}_4)_3$ . (Reproduced with permission by S. Okada *et al.*, *Proc. 36th Power Sources Conf.* (1994))

rhombohedral form, the building blocks are aligned parallel; in the monoclinic phase they are aligned nearly perpendicular to one another. The collapsed monoclinic form has a smaller free volume for  $\text{Li}^+$ -ion motion. Large-scale production of rhombohedral  $\text{Fe}_2(\text{SO}_4)_3$  can be readily achieved by oxidative thermal decomposition of the ferrous salt  $(\text{NH}_4)_2\text{Fe}(\text{SO}_4)_2\cdot 6\text{H}_2\text{O}$  at  $500^\circ\text{C}$ .<sup>20)</sup>

In these structures, the  $\text{FeO}_6$  octahedra do not make direct contact, so electron transfer from an  $\text{Fe}^{2+}$  to an  $\text{Fe}^{3+}$  ion is polaronic and therefore activated. The question to be resolved experimentally is whether the reduction in the activation energy for  $\text{Li}^+$  ion motion in the open framework is more important than the introduction of an electronic activation energy and a two-phase interface for determining the limiting current density of the cathode.

The reversible lithium insertion into both rhombohedral and monoclinic  $\text{Fe}_2(\text{SO}_4)_3$ <sup>21–23)</sup> gives a flat closed-circuit voltage vs. a lithium anode of 3.6 V, which is to be compared with 3.0 V for isostructural  $\text{Fe}_2(\text{MoO}_4)_3$  and  $\text{Fe}_2(\text{WO}_4)_3$  and 3.4 V for the ordered olivine  $\text{LiFePO}_4$ . Neither parent phase has any significant solid solution with the orthorhombic lithiated phase  $\text{Li}_2\text{Fe}_2(\text{SO}_4)_3$ , which is derived from the rhombohedral form of  $\text{Fe}_2(\text{SO}_4)_3$  by a displacive transition that leaves the framework intact. Powder X-ray diffraction verified that lithiation occurs via a two-phase process.<sup>23)</sup> Fig. 1.17 shows that increasing the current density does not change significantly the closed-circuit voltage  $V$ , but it does reduce reversibly the capacity. The reduction in capacity for a given current density is greater for the monoclinic parent than for rhombohedral  $\text{Fe}_2(\text{SO}_4)_3$  as anticipated for a dynamic limit to the motion of the lithiated interface. The interstitial space of the framework allows fast  $\text{Li}^+$  ion motion; but the movement of lithium across the orthorhombic/monoclinic interface is slower than that across the orthorhombic/rhombohedral interface, which makes the reversible loss of capacity with increasing current density greater for the monoclinic than for the rhombohedral parent phase. On recharge, the parent phase at the core grows back, so the particles retain the form of the initial parent phase on repeated cycling. If the discharging voltage is restricted, reduction of  $\text{Fe}^{2+}$  to  $\text{Fe}^0$  at the surface can be suppressed; we found that the rhombohedral  $\text{Fe}_2(\text{SO}_4)_3$  starting material retains good capacity at lower current densities even after 80 cycles.

Table 1.1 Redox energies in eV below the Fermi energy of lithium for different polyanions and structures.

	NASICON-type						Close-packed	
	SO <sub>4</sub>	MoO <sub>4</sub>	PO <sub>4</sub>	AsO <sub>4</sub>	P <sub>2</sub> O <sub>7</sub>	II-AsO <sub>4</sub>	V[Li <sub>1-x</sub> M]O <sub>4</sub>	Li <sub>1-x</sub> MPO <sub>4</sub>
Ti <sup>4+</sup> /Ti <sup>3+</sup>	3.4		2.5–2.7					
Ti <sup>3+</sup> /Ti <sup>2+</sup>								
V <sup>4+</sup> /V <sup>3+</sup>			3.7–3.8					
V <sup>3+</sup> /V <sup>2+</sup>	2.5		1.7					
Mn <sup>3+</sup> /Mn <sup>2+</sup>								
Fe <sup>3+</sup> /Fe <sup>2+</sup>	3.6	3.0	2.7–3.0	2.6–2.9	2.9–3.1	3.1 Fe(1) 2.4 Fe(2)	3.8	4.1 3.4
Co <sup>3+</sup> /Co <sup>2+</sup>							4.2[10]	>4.3
Ni <sup>3+</sup> /Ni <sup>2+</sup>							4.8[10]	>4.3
Nb <sup>5+</sup> /Nb <sup>4+</sup>			2.2–2.5					
Nb <sup>4+</sup> /Nb <sup>3+</sup>			1.7–1.8					

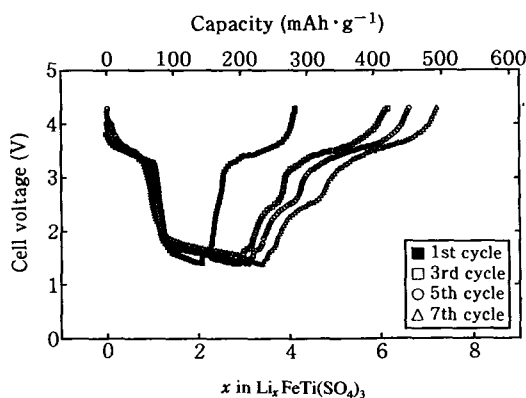


Fig. 1.18 Discharge/charge curves vs. lithium at  $0.05 \text{ mA} \cdot \text{cm}^{-2}$  for monoclinic  $\text{Li}_x\text{FeTi}(\text{SO}_4)_3$ .  
(Reproduced with permission by S. Okada *et al.*, *Proc. 36th Power Sources Conf.* (1994))

The abrupt voltage drop occurring for  $x > 2$  in  $\text{Li}_x\text{Fe}_2(\text{SO}_4)_3$  can be held in check by the addition of buffer phases such as  $\text{Li}_3\text{Fe}_2(\text{PO}_4)_3$ , and  $\text{FeV}(\text{SO}_4)_3$  or  $\text{LiTi}_2(\text{PO}_4)_3$ , which have closed-circuit voltages  $V$  vs. lithium of 2.8 V, 2.5 V and 2.5 V, respectively, for the  $\text{Fe}^{3+}/\text{Fe}^{2+}$ ,  $\text{V}^{3+}/\text{V}^{2+}$  and  $\text{Ti}^{4+}/\text{Ti}^{3+}$  couples. Tailoring an appropriate buffer relies on a knowledge of the relative positions of the redox couples for a given polyanion and of how these positions shift with a change of the polyanion. These data are given in Table 1.1. We illustrate how these data were generated with some examples.

Attempts to make the solid solution  $\text{Fe}_{2-x}\text{Ti}_x(\text{SO}_4)_3$  were not successful; only  $\text{FeTi}(\text{SO}_4)_3$  could be made, and that only in the monoclinic form. Fig. 1.18 shows<sup>23)</sup> the discharge/charge curves for Li insertion into monoclinic  $\text{FeTi}(\text{SO}_4)_3$  at  $0.05 \text{ mA} \cdot \text{cm}^{-2}$ . With cut-off voltages of 4.2 V and 1.5 V vs. lithium, two Li atoms per formula unit were inserted in the first cycle, but three in subsequent cycles. On discharge, an initial redox process occurring from 3.5 V to 3.2 V vs. lithium is not flat, indicative of retention of the monoclinic framework. It extends for approximately one Li atom per formula unit before a sharp drop to a process occurring at 1.7 V to 1.5 V. Identification of this second redox process

is not attempted. On recharge, a short  $\Delta x$  step at 2.5 V is followed by a longer  $\Delta x$  step over the range 3.2 V to 3.6 V. These results indicate that the  $\text{Fe}^{3+}/\text{Fe}^{2+}$  redox couple is located at about 3.4 V below the Fermi energy of lithium and that the  $\text{Ti}^{4+}/\text{Ti}^{3+}$  couple lies only a little above it, the two redox couples having some overlap. Mössbauer data<sup>24)</sup> have shown independent evidence for the presence of mixed  $\text{Fe}^{3+}/\text{Fe}^{2+}$  and  $\text{Ti}^{4+}/\text{Ti}^{3+}$  states in  $\text{FeTi}(\text{SO}_4)_3$ . This overlap makes the  $\text{Ti}^{4+}/\text{Ti}^{3+}$  couple unsuitable as a buffer for  $\text{Fe}_2(\text{SO}_4)_3$ . The step at 2.5 V in the charging curves is tentatively assigned to the  $\text{Ti}^{3+}/\text{Ti}^{2+}$  couple.

$\text{V}_2(\text{SO}_4)_3$  and  $\text{Cr}_2(\text{SO}_4)_3$  crystallize in the rhombohedral form<sup>25,26)</sup>. Insertion of Li into  $\text{V}_2(\text{SO}_4)_3$  gives a flat  $V_{\text{oc}} = 2.6$  V vs. lithium indicating a two-phase insertion process and a  $\text{V}^{3+}/\text{V}^{2+}$  redox couple 2.5 eV below the Fermi energy of the lithium anode<sup>23)</sup>. This voltage is excellent to serve as a buffer against an over-discharge of  $\text{Fe}_2(\text{SO}_4)_3$ . We were unable to insert Li into  $\text{Cr}_2(\text{SO}_4)_3$ ; the  $\text{Cr}^{3+}/\text{Cr}^{2+}$  redox couple is at too high an energy for initiation of the lithiation.

Comparison of the redox energies in isostructural sulfates and phosphates was undertaken to obtain the magnitude of the change due to the different inductive effects of sulfur and phosphorus. Rhombohedral  $\text{LiTi}_2(\text{PO}_4)_3$  shows<sup>22)</sup> a flat open-circuit voltage  $V_{\text{oc}} = 2.5$  V vs. lithium, which is roughly 0.8 V below the  $\text{Ti}^{4+}/\text{Ti}^{3+}$  level found for  $\text{FeTi}(\text{SO}_4)_3$  in Fig. 1.18. The flat voltage  $V(x)$  for  $\text{Li}_{1+x}\text{Ti}_2(\text{PO}_4)_3$  is indicative of a two-phase process, and a coexistence of rhombohedral and orthorhombic phases was found for  $x = 0.5$ .<sup>27,28)</sup>

All three phosphates  $\text{Li}_3\text{M}_2(\text{PO}_4)_3$  with  $\text{M} = \text{Fe}, \text{Fe/V}, \text{ or V}$  have the monoclinic  $\text{Fe}_2(\text{SO}_4)_3$  structure if prepared by solid-state reaction. Insertion of Li atoms into monoclinic  $\text{Li}_{3+x}\text{Fe}_2(\text{PO}_4)_3$  occurs in two steps,<sup>22)</sup> at 2.85 V for  $0 < x < 1$  and 2.70 V for  $1 < x < 1.8$ ; the two plateaus apparently correspond to different  $\text{Li}^+$ -ion distributions in the interstitial space. We take the average value  $V_{\text{oc}} = 2.8$  V vs. lithium as the location of the  $\text{Fe}^{3+}/\text{Fe}^{2+}$  redox couple in this structure in the presence of  $\text{PO}_4$  tetrahedra; this assignment locates the  $\text{Fe}^{3+}/\text{Fe}^{2+}$  couple 0.8 eV above its value in  $\text{Li}_x\text{Fe}_2(\text{SO}_4)_3$ , which has a  $V_{\text{oc}} = 3.6$  V. The change of about 0.8 eV between isostructural sulfates and phosphates for both the  $\text{Ti}^{4+}/\text{Ti}^{3+}$  and  $\text{Fe}^{3+}/\text{Fe}^{2+}$  couples is significant and demonstrates primarily the inductive-effect influence of a substitution of  $\text{PO}_4$  for  $\text{SO}_4$  groups; additional charge-compensating Li atoms appears to have only a minor influence in this structure. This and similar results for other cations indicate that the relative positions of the redox couples remains constant but their absolute positions change with structural or counter-cation changes. Fig. 1.19 shows the discharge curves for a mixture of rhombohedral  $\text{Fe}_2(\text{SO}_4)_3$  cation with a  $\text{LiTi}_2(\text{PO}_4)_3$  buffer to protect against overdischarge and  $\text{Fe}^0$  extrusion.<sup>23)</sup>

Monoclinic  $\text{Li}_3\text{FeV}(\text{PO}_4)_3$  takes 1.5 Li per formula unit reversibly in the range 4.2 V to 1.5 V (Fig. 1.20).<sup>23)</sup> Plateau A of the first discharge corresponds to the  $\text{Fe}^{3+}/\text{Fe}^{2+}$  redox couple at 2.8 V vs. lithium; plateau B to the  $\text{V}^{3+}/\text{V}^{2+}$  redox couple at 1.7 V. Plateau C in the second discharge, which corresponds to  $\text{Li}_{2+x}\text{FeV}(\text{PO}_4)_3$ , locates the  $\text{V}^{4+}/\text{V}^{3+}$  couple at 3.8 eV below the Fermi energy of lithium. These relative assignments are consistent with  $\text{Fe}^{3+}$  and  $\text{V}^{3+}$  coexisting in the disordered corundum structure of  $\text{FeVO}_3$  as against  $\text{Fe}^{2+}$  and  $\text{Ti}^{4+}$  in the ordered ilmenite structure. Moreover, a splitting of 2.0 V between the  $\text{V}^{4+}/\text{V}^{3+}$  and  $\text{V}^{3+}/\text{V}^{2+}$  couples is compatible with the stabilization of octahedral-site valence states  $\text{V}^{2+}$  to  $\text{V}^{5+}$  in the vanadium oxides.

Rhombohedral  $\text{TiNb}(\text{PO}_4)_3$  can be prepared by solid-state reaction at 1200 °C; up to three Li atoms per formula unit can be inserted, which allows access to the  $\text{Nb}^{4+}/\text{Nb}^{3+}$  couple at

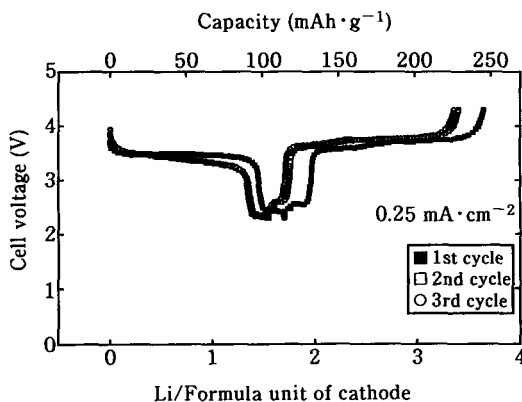


Fig. 1.19 Discharge/charge curves vs. lithium at  $0.05 \text{ mA} \cdot \text{cm}^{-2}$  for rhombohedral  $\text{Fe}_2(\text{SO}_4)_3$  mixed in 4 : 1 ratio with rhombohedral  $\text{LiTi}_2(\text{PO}_4)_3$ .  
(Reproduced with permission by S. Okada *et al.*, *Proc. 36th Power Sources Conf.* (1994))

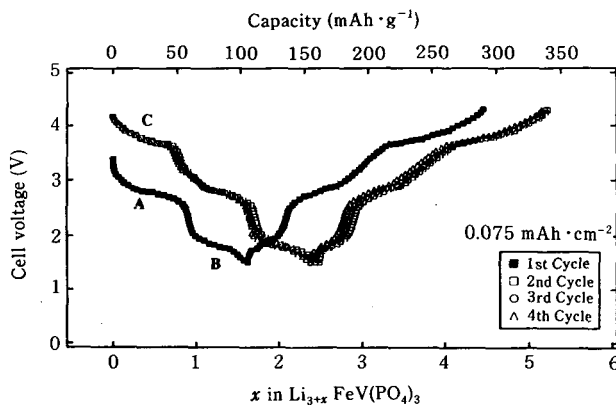


Fig. 1.20 Discharge/charge curves vs. lithium at  $0.075 \text{ mA} \cdot \text{cm}^{-2}$  for monoclinic  $\text{Li}_{3+x}\text{FeV}(\text{PO}_4)_3$  (first cycle) and  $\text{Li}_{2+x}\text{FeV}(\text{PO}_4)_3$  (subsequent cycles).  
(Reproduced with permission by K.S. Najundaswamy *et al.*, *Solid State Ionics*, **92**, 1 (1996))

1.8 V vs. lithium for  $x > 2$  in  $\text{Li}_x\text{TiNb}(\text{PO}_4)_3$ .<sup>29)</sup> Two steps are perhaps discernible in the compositional range  $0 < x < 2$ ; one in the range  $0 < x < 1$  corresponds to the  $\text{Ti}^{4+}/\text{Ti}^{3+}$  couple in the voltage range  $2.5 \text{ V} < V < 2.7 \text{ V}$  and the other for  $1 < x < 2$  to the  $\text{Nb}^{5+}/\text{Nb}^{4+}$  couple in the range  $2.2 \text{ V} < V < 2.5 \text{ V}$ . However, it appears that these redox energies overlap. This assignment is based on the fact that the  $\text{Ti}^{4+}/\text{Ti}^{3+}$  couple in  $\text{Li}_{1+x}\text{Ti}_2(\text{PO}_4)_3$  gives a flat plateau at 2.5 V due to the presence of two-phases, rhombohedral  $\text{LiTi}_2(\text{PO}_4)_3$  and orthorhombic  $\text{Li}_3\text{Ti}_2(\text{PO}_4)_3$ . The presence of Nb in the structure suppresses the formation of the second phase in the range  $0 < x < 2$ . A plateau at 1.8 V in the range  $2 < x < 3$  reflects the  $\text{Nb}^{4+}/\text{Nb}^{3+}$  couple, as is confirmed by the following experiments.

Rhombohedral  $\text{LiFeNb}(\text{PO}_4)_3$  and  $\text{Li}_2\text{FeTi}(\text{PO}_4)_3$  can be prepared by ion exchange with molten  $\text{LiNO}_3$  at  $300^\circ\text{C}$  from  $\text{NaFeNb}(\text{PO}_4)_3$  and  $\text{Na}_2\text{FeTi}(\text{PO}_4)_3$ , respectively.<sup>30)</sup> The discharge/charge curves for  $\text{Li}_{2+x}\text{FeTi}(\text{PO}_4)_3$  show that two Li atoms per formula unit can

be inserted reversibly, with a little loss of capacity at  $0.5 \text{ mA} \cdot \text{cm}^{-2}$ . Insertion of the first Li atom in the range  $2.7 \text{ V} < V < 3.0 \text{ V}$  corresponds to the  $\text{Fe}^{3+}/\text{Fe}^{2+}$  redox couple and of the second Li atom in the range of  $2.5 \text{ V} < V < 2.7 \text{ V}$  to an overlapping  $\text{Ti}^{4+}/\text{Ti}^{3+}$  redox couple. The insertion of lithium into  $\text{Li}_{1+x}\text{FeNb}(\text{PO}_4)_3$  gives a  $V$  vs.  $x$  curve that further verifies our location of the relative positions of the  $\text{Fe}^{3+}/\text{Fe}^{2+}$ ,  $\text{Nb}^{5+}/\text{Nb}^{4+}$  and  $\text{Nb}^{4+}/\text{Nb}^{3+}$  redox energies in phosphates with NASICON-related structures. It is possible to insert three lithium atoms into the structure; and there are three distinct plateaus corresponding to  $\text{Fe}^{3+}/\text{Fe}^{2+}$  at 2.8 V,  $\text{Nb}^{5+}/\text{Nb}^{4+}$  at 2.2 V and  $\text{Nb}^{4+}/\text{Nb}^{3+}$  at 1.7 V vs. lithium in the discharge curve. Whereas the  $\text{Ti}^{4+}/\text{Ti}^{3+}$  couple overlaps both the  $\text{Fe}^{3+}/\text{Fe}^{2+}$  and  $\text{Nb}^{5+}/\text{Nb}^{4+}$  couples, the  $\text{Fe}^{3+}/\text{Fe}^{2+}$  and  $\text{Nb}^{5+}/\text{Nb}^{4+}$  couples are separated by 0.4 eV.

A rhombohedral polymorph of  $\text{Li}_3\text{Fe}_2(\text{PO}_4)_3$  can be prepared by ion exchange in  $\text{LiNO}_3$  at  $300^\circ\text{C}$  from the sodium analog  $\text{Na}_3\text{Fe}_2(\text{PO}_4)_3$ .<sup>31)</sup> The shape of the discharge/charge curve of Fig. 1.21(a) for lithium insertion into rhombohedral  $\text{Li}_{3+x}\text{Fe}_2(\text{PO}_4)_3$ <sup>32)</sup> is quite

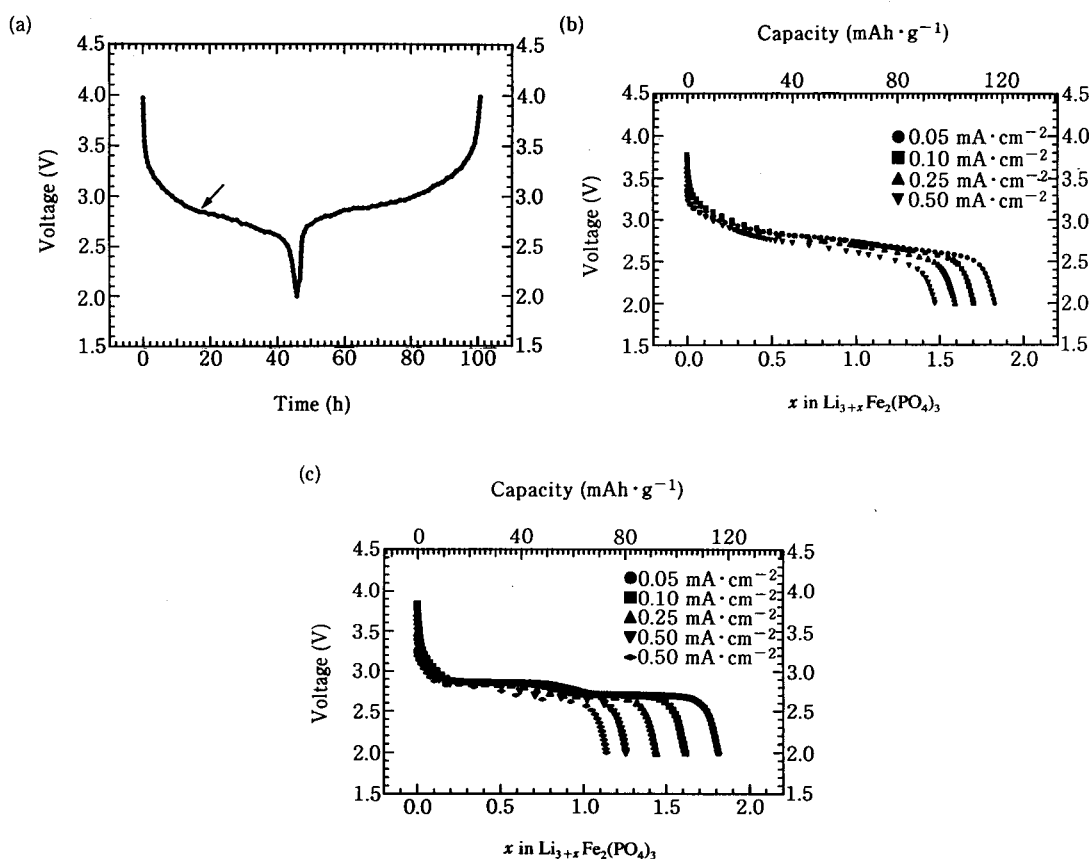


Fig. 1.21 (a) Discharge/charge curves vs. lithium at  $0.1 \text{ mA} \cdot \text{cm}^{-2}$  for rhombohedral  $\text{Li}_{3+x}\text{Fe}_2(\text{PO}_4)_3$  and discharge curves at different current densities ( $0.05$ – $0.5 \text{ mA} \cdot \text{cm}^{-2}$ ) for (b) rhombohedral and (c) monoclinic  $\text{Li}_{3+x}\text{Fe}_2(\text{PO}_4)_3$ .

(Reproduced with permission by C. Masquelier *et al.*, *Proc. 37th Power Sources Conf.* (1996))

different from that for the monoclinic form; however, the average  $V_{oc}$  at 2.8 V remains the same. Up to two lithiums per formula unit can be inserted into  $\text{Li}_3\text{Fe}_2(\text{PO}_4)_3$ , leading to  $\text{Li}_{3+x}\text{Fe}_2(\text{PO}_4)_3$ . The  $\text{Li}^+$  ion distribution in the interstitial space of  $\text{Li}_{3+x}\text{Fe}_2(\text{PO}_4)_3$ ,  $0 < x < 2$ , appears to vary continuously with  $x$  with a high degree of disorder. Fig. 1.21(b) shows a reversible capacity loss on increasing the current density from 0.05 to 0.5  $\text{mA} \cdot \text{cm}^{-2}$ ; this loss is much reduced compared to what is encountered with the monoclinic system  $\text{Li}_{3+x}\text{Fe}_2(\text{PO}_4)_3$  (Fig. 1.21(c)). A reversible discharge capacity of 95  $\text{mAh} \cdot \text{g}^{-1}$  is still observed for rhombohedral  $\text{Li}_{3+x}\text{Fe}_2(\text{PO}_4)_3$  at a current density of 20  $\text{mA} \cdot \text{g}^{-1}$ . With a current density of 23  $\text{mA} \cdot \text{g}^{-1}$  (or 1  $\text{mA} \cdot \text{cm}^{-2}$ ), the initial capacity of 95  $\text{mAh} \cdot \text{g}^{-1}$  was maintained in a coin cell up to the 40th cycle. A sharp irreversible capacity fade occurred after the 40th cycle; this failure does not appear to be an intrinsic property of this promising, although metastable cathode material.

A monoclinic  $\text{Li}_3\text{Fe}_2(\text{AsO}_4)_3$  isotypic with monoclinic  $\text{Li}_3\text{Fe}_2(\text{PO}_4)_3$  can be prepared by direct decomposition and solid-state reaction at 860 °C of intimately mixed  $\text{LiOH} \cdot \text{H}_2\text{O}$ ,  $\text{Fe}_2\text{O}_3$  and  $\text{NH}_4\text{H}_2\text{AsO}_4$  powders.<sup>31)</sup> The discharge/charge curves obtained at 0.1  $\text{mA} \cdot \text{cm}^{-2}$  for  $\text{Li}_{3+x}\text{Fe}_2(\text{AsO}_4)_3$  show two plateaus, one at 2.90 V for  $0 < x < 1$  and the other at 2.65 V for  $1 < x < 1.8$ , which are to be compared with plateaus at 2.85 and 2.70 V for  $\text{Li}_{3+x}\text{Fe}_2(\text{PO}_4)_3$ .<sup>32)</sup> P and As have the same electronegativity, and the change in the polyanion from  $\text{PO}_4$  to  $\text{AsO}_4$  appears to have little influence on the average  $\text{Fe}^{3+}/\text{Fe}^{2+}$  redox energy; however, changes in  $\text{Li}^+$  ion distribution and the fact that the two iron atoms are crystallographically different have more influence in  $\text{Li}_3\text{Fe}_2(\text{AsO}_4)_3$ .

### 1.3.3 Conclusion

The redox energies summarized in Table 1.1 show a sensitivity to the charge and bonding of the counter cation. In the case of  $\text{Li}_{1+x}[\text{Mn}_{1-y}\text{M}_y]\text{O}_4$  spinels with  $\text{M} = \text{Co Ni}$ , conversion of  $\text{M}^{3+}$  to  $\text{M}^{2+}$  in the equilibrium reaction  $\text{Mn}^{3+} + \text{M}^{3+} \rightarrow \text{Mn}^{4+} + \text{M}^{2+}$  was found to raise the  $\text{Mn}^{4+}/\text{Mn}^{3+}$  redox energy neighboring the M atom by 0.6 V to 0.8 eV. In isostructural systems, shifts in the energy of the redox energies reflect the inductive effect, *i.e.*, the competition for covalent mixing with bridging oxygen. The stronger the covalent mixing at the given transition-metal cation, the higher are the energies of its HOMO and LUMO. Changing the structure may change the Madelung potential at a redox site.

At 3.6 V and 3.5 V vs. a lithium anode, respectively, the  $\text{Fe}^{3+}/\text{Fe}^{2+}$  redox couple was found to be at an attractive energy for the cathode of a Li secondary battery in  $\text{Fe}_2(\text{SO}_4)_3$  and  $\text{LiFePO}_4$ . A capacity fade at higher current densities was found to be reversible, indicating a kinetic barrier associated with diffusion-limited charge transfer across a two-phase interface. The  $\text{Li}_3\text{Fe}_2(\text{PO}_4)_3$  phase having the rhombohedral NASICON framework can be prepared from  $\text{Na}_3\text{Fe}_2(\text{PO}_4)_3$ ; it shows a continuous solid solution over the range  $0 < x < 2$  with a closed-circuit voltage at 1  $\text{mA} \cdot \text{cm}^{-2}$  (23  $\text{mA} \cdot \text{g}^{-1}$ ) centered at 2.8 V vs. lithium with a capacity of 95  $\text{mAh} \cdot \text{g}^{-1}$ .  $\text{Li}_2\text{FeTi}(\text{PO}_4)_3$  having the NASICON framework also looks promising as a cathode material with a voltage ranging from 3.0 V to 2.5 V. A small concentration of  $\text{LiTi}_2(\text{PO})_3$  mixed with  $\text{Fe}_2(\text{SO}_4)_3$  was demonstrated to serve as a suitable buffer against over-discharge and extrusion of  $\text{Fe}^0$ .



## Acknowledgments

The Robert A. Welch Foundation (Houston, Texas), the Institute for Advanced Technology (IAT), University of Texas at Austin, federated with the U.S. Army Research Laboratory, and the Texas Advanced Research Program (TARP) are gratefully acknowledged for financial support.

## REFERENCES

- 1) M.S. Whittingham, *J. Electrochem. Soc.*, **123**, 315 (1976).
- 2) K. Mizushima, P.C. Jones, P.J. Wiseman and J.B. Goodenough, *Mater. Res. Bull.*, **15**, 783 (1980).
- 3) M.G.S.R. Thomas, W.I.F. David and J.B. Goodenough, *Mater. Res. Bull.*, **20**, 1137 (1985).
- 4) M.M. Thackeray, W.I.F. David, J.B. Goodenough and P. Groves, *Mater. Res. Bull.*, **20**, 1137 (1983).
- 5) M.M. Thackeray, *J. Electrochem. Soc.*, **142**, 2568 (1995).
- 6) R. Schöllhorn and A. Payer, *Angew. Chem. Int. Ed. Engl.*, **24**, 67 (1985); S. Sinha and D.W. Murphy, *Solid State Ionics*, **20**, 81 (1986).
- 7) Y. Nishi, H. Azuma and A. Omaru, U.S. Patent 4959281, September 25, 1990.
- 8) M.M. Thackeray, W.I.F. David, P.G. Bruce and J.B. Goodenough, *Mater. Res. Bull.*, **18**, 461 (1983).
- 9) M.M. Thackeray, P. J. Johnson, L.A. de Piciotto, P.G. Bruce and J.B. Goodenough, *Mater. Res. Bull.*, **19**, 179 (1984).
- 10) D. Guyomard and J.M. Tarascon, *J. Electrochem. Soc.*, **139**, 937 (1992).
- 11) C. Masquelier, M. Tabuchi, K. Ado, R. Kanno, Y. Kobayashi, Y. Maki, O. Nakamura and J.B. Goodenough, *J. Solid State Chem.*, **123**, 255 (1996), and references therein.
- 12) J.B. Goodenough, A. Manthiram and B. Wnietrzewski, *J. Power Sources*, **43-44**, 269 (1993).
- 13) M.S. Whittingham, *Progr. Solid State Chemistry*, **12**, 41 (1976).
- 14) K.S. Nanjundaswamy, A.K. Padhi, C. Masquelier, S. Okada and J.B. Goodenough, Proc. 37th Power Sources Conf., Cherry Hill, NJ, USA, p. 184 (1996).
- 15) A.K. Padhi, W.B. Archibald, K.S. Nanjundaswamy and J.B. Goodenough, *J. Solid State Chem.*, **128**, 267 (1996).
- 16) G.T.K. Fey, W. Li and J.R. Dahn, *J. Electrochem. Soc.*, **141**, 2279 (1994).
- 17) A.K. Padhi, K.S. Nanjundaswamy and J.B. Goodenough, *J. Electrochem. Soc.*, **144**, 1188 (1997).
- 18) J.B. Goodenough, H.Y.P. Hong and J.A. Kafalas, *Mater. Res. Bull.*, **11**, 203 (1976).
- 19) G. J. Long, G. Longworth, P. Battle, A.K. Cheetham, R.V. Thundathil and D. Beveridge, *Inorg. Chem.*, **18**, 624 (1979).
- 20) JCPDS X-ray powder diffraction No. 33-0679 and #42-0229.
- 21) A. Manthiram and J.B. Goodenough, *J. Power Sources*, **26**, 403 (1989).
- 22) S. Okada, K.S. Nanjundaswamy, A. Manthiram, H. Ohtsuka, J.B. Goodenough, H. Arai and J. Yamaki, Proc. 36th Power Sources Conf., Cherry Hill, NJ, USA, p. 110 (1994).
- 23) K.S. Nanjundaswamy, A.K. Padhi, S. Okada, J.B. Goodenough, *Solid State Ionics*, **92**, 1 (1996).
- 24) T.C. Gibb, N.N. Greenwood, A. Tetlow and W. Twist, *J. Chem. Soc. A*, 2955 (1968).
- 25) JCPDS X-ray powder diffraction No. 42-0231.
- 26) JCPDS X-ray powder diffraction No. 42-0232.
- 27) C. Delmas and A. Nadiri, *Mater. Res. Bull.*, **23**, 63 (1988).
- 28) S. Wang and S. J. Hwu, *Chem. Mater.*, **4**, 589 (1992).
- 29) Geeta Ahuja, Ph. D. dissertation, Univ. of Texas, Austin (1991).
- 30) A.K. Padhi, K.S. Nanjundaswamy, C. Masquelier and J.B. Goodenough, Proc. 37th Power Sources Conf., Cherry Hill, NJ, USA, p. 180 (1996).
- 31) F. d'Yvoire, M. Pintard-Scrépel, E. Bretey and M. de la Rochère, *Solid State Ionics*, **9 & 10**, 851 (1983).
- 32) C. Masquelier, A.K. Padhi, K.S. Nanjundaswamy, S. Okada and J.B. Goodenough, Proc. 37th Power Sources Conf., Cherry Hill, NJ, USA, p. 188 (1996).

## 2

## Cathode Active Materials with a Three-dimensional Spinel Framework

M. Wakihara\*, Guohua Li\* and H. Ikuta\*

## 2.1 Introduction

Lithium secondary batteries using intercalation compounds as the cathode and lithium metal as the anode have been intensively studied during the past decade. However, it has been recognized that this type of battery will unlikely reach commercialization because of safety problems. To overcome this problem, a safer approach to rechargeable lithium batteries is to replace lithium metal with a lithium intercalation compound, usually a carbon, leading to the so-called “rocking-chair” or “lithium ion” batteries,<sup>1,2)</sup> first commercialized in 1990 by Sony Energetic Inc.<sup>3)</sup> The energy density of lithium ion battery with high discharge voltage (3.6 V) is nearly twice as high as the Ni–Cd battery. Excellent cycle life and a higher level of intrinsic safety have been demonstrated.<sup>4,5)</sup> Compared to lithium metal batteries, the cathode materials suitable for lithium ion batteries are very highly oxidizing compounds in order to compensate the loss in cell potential at the anode. Candidate cathode materials include layered compounds such as  $\text{LiCoO}_2$ ,<sup>3,6)</sup>  $\text{LiNiO}_2$ ,<sup>7,8)</sup>  $\text{LiNi}_{1-y}\text{Co}_y\text{O}_2$ <sup>9,10)</sup> and three-dimensional  $\text{LiMn}_2\text{O}_4$  spinel phase.<sup>11-17)</sup> For practical application, considering the high cost of cobalt or nickel,  $\text{LiMn}_2\text{O}_4$  spinel is a more desirable cathode candidate for Li ion batteries. Manganese-based materials offer following advantages: low cost resulting from natural abundance of manganese, lower toxicity and well-known recycling problems.

Recent developments of lithium secondary batteries have shown that some three-dimensional compounds are one of the most promising cathode materials for secondary lithium batteries. Generally, compounds with a three-dimensional framework are more stable than the two-dimensional compounds. Lithium ion diffusion is clearly easier in three-dimensional framework than in two-dimensional structure, because in the former structure the number of contact points of the diffusion paths for lithium ions is larger than that in the latter. For instance, the three-dimensional  $\text{V}_2\text{O}_5$ ,<sup>18-20)</sup>  $\text{V}_6\text{O}_{13}$ <sup>21)</sup> (shear structure);  $\text{MnO}_2$  (rutile structure);  $\text{LiM}_2\text{O}_4$ <sup>22,23)</sup> ( $\text{M} = \text{Ti}, \text{V}, \text{Mn}$ , spinel structure); and Chevrel phase sulfides,  $\text{M}_x\text{Mo}_6\text{S}_8$ <sup>24-28)</sup> (cluster compound,  $\text{M} = \text{metal}$ ) exhibit very interesting lithium intercalation properties. Among them, spinel phase compounds are of extreme interest as the cathode active materials for high energy density rechargeable lithium batteries.

A general discussion about all the requirements necessary for a suitable intercalation

\* Department of Chemical Engineering, Tokyo Institute of Technology, Ookayama, Meguro-ku, Tokyo 152, Japan

electrode material is not the subject of this chapter. In this chapter the fundamental aspects of the cathode materials with a three-dimensional framework will be discussed, with special focus on spinel phases. Here we will draw the cathode properties mainly from examples taken from our own work. However, references to other scientists will be made when necessary.

## 2.2 Crystal Structure of Spinel Type Phases

In the ideal spinel oxide  $AB_2O_4$  structure, oxygen atoms form a face-centered cubic packing and occupy  $32e$  sites of space group  $Fd\bar{3}m$ . The A cations are located in the tetrahedral  $8a$  sites, while the B cations occupy the octahedral  $16d$  sites. The octahedral  $16c$  sites remain empty. The spinel structure is illustrated in Fig. 2.1. Generally, lithium spinel oxides  $LiM_2O_4$  (M: transition metals) suitable for the cathode are limited to those with a normal spinel in which the lithium ions occupy the tetrahedral ( $8a$ ) sites and the transition-metal ions reside at the octahedral ( $16d$ ) sites. The  $8a$  and  $16c$  sites form a three-dimensional pathway for lithium diffusion. Each angle formed by consecutive straight spokes,  $8a-16c-8a$ , is about  $107^\circ$ . In an inverse spinel, however, a part or half of the M ions in the  $16d$  sites displace the lithium ions in the  $8a$  sites and prevent easier diffusion of lithium ions from  $8a$  to other  $8a$  sites *via* vacant octahedral  $16c$  sites. The lithium intercalation has previously been demonstrated for  $LiM_2O_4$  (M = Ti, V, Mn) with a capacity of one additional Li per formula unit at room temperature.<sup>22,29-33</sup> Besides these, some studies were carried out on more complex spinel type phases such as  $Li_2Mn_4O_9$ ,  $Li_4Mn_5O_{12}$ ,  $Li_4Ti_5O_{12}$ ,  $LiFe_5O_8$ , etc.<sup>34-37</sup>

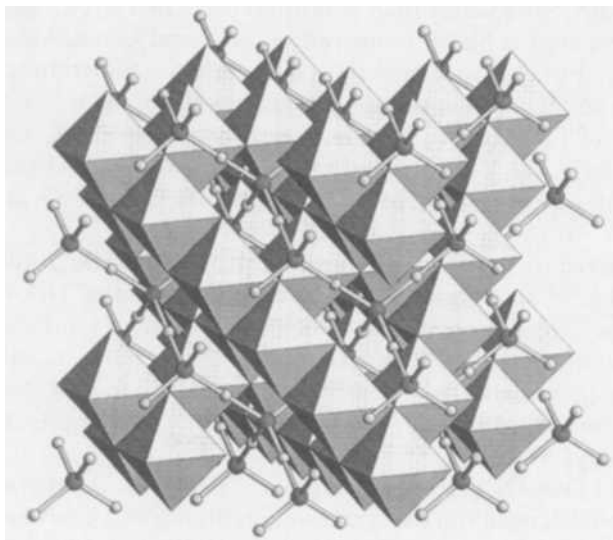


Fig. 2.1 Crystal structure of spinel type phases.

### 2.3 Synthesis Technique

Besides  $\text{LiMn}_2\text{O}_4$  that can be prepared by heating the mixture of  $\text{Li}_2\text{CO}_3$  and manganese oxides in air,<sup>38)</sup> other  $\text{LiM}_2\text{O}_4$  spinels are difficult to be obtained by a conventional high temperature solid-state reaction.

Preparation of the spinel  $\text{LiV}_2\text{O}_4$  by conventional technique proved to be quite difficult.<sup>39,40)</sup> Zachau-Christiansen *et al.* reported that  $\text{LiV}_2\text{O}_4$  was prepared by reacting equimolar amounts of  $\text{LiVO}_2$  and  $\text{VO}_2$  in an evacuated silica tube at  $750^\circ\text{C}$  for three days. The product contained an impurity of  $\text{V}_4\text{O}_7$ , probably due to Li loss because of the formation of lithium silicate.<sup>23)</sup> According to Picciotto *et al.*, spinel  $\text{LiV}_2\text{O}_4$  was previously prepared by heating  $\text{Li}_{0.5}\text{VO}_2$  which was obtained by chemical extraction of lithium from a layered  $\text{LiVO}_2$  ( $R\bar{3}m$ ) with bromine, to  $300^\circ\text{C}$  under vacuum.<sup>41,42)</sup> Similarly, the spinels  $\text{LiNi}_2\text{O}_4$  and  $\text{LiCo}_2\text{O}_4$  have been prepared by thermal treatment of partially delithiated layered oxides  $\text{Li}_{0.5}\text{NiO}_2$  and  $\text{Li}_{0.5}\text{CoO}_2$ , respectively.<sup>43,44)</sup>

In our laboratory,  $\text{LiV}_2\text{O}_4$  was prepared by a conventional direct solid-state reaction of the stoichiometric mixture of  $\text{Li}_2\text{CO}_3$  and  $\text{V}_2\text{O}_3$  powders under controlled partial pressure of oxygen.<sup>45)</sup>  $\text{V}_2\text{O}_3$  was preliminarily prepared by reacting  $\text{V}_2\text{O}_5$  under hydrogen atmosphere at  $600^\circ\text{C}$ . The reactants were ground, pelletized under a pressure of ca. 20 MPa, then heated at  $650\text{--}950^\circ\text{C}$  for 4 h–one week in  $\text{CO}_2$  or  $\text{CO}_2\text{--H}_2$  atmosphere.<sup>46,47)</sup> Although a spinel single phase was obtained at different temperatures, only the samples prepared at lower temperatures ( $650\text{--}680^\circ\text{C}$ ) showed good properties as the cathode active material for lithium secondary batteries. The scanning electron microscope (SEM) micrographs showed that the average particle size of samples obtained at  $950^\circ\text{C}$  was about  $5\text{--}7\text{ }\mu\text{m}$ , which was obviously larger than that obtained at  $680^\circ\text{C}$  ( $< 1\text{ }\mu\text{m}$ ). This suggests that the products prepared at higher temperatures delivered less usable surface area as the cathode material.<sup>45)</sup> For electrode materials, the synthesis temperature should not be too high. However, at  $650^\circ\text{C}$ , it took too long (one week) to prepare  $\text{LiV}_2\text{O}_4$ . The suitable synthesis condition of  $\text{LiV}_2\text{O}_4$  is to heat reactant mixture at  $680^\circ\text{C}$  for 20 h under  $\text{CO}_2$  atmosphere. Similarly, the V-substituted spinel  $\text{LiMn}_{0.2}\text{V}_{1.8}\text{O}_4$  was prepared by heating the stoichiometric mixture of  $\text{Li}_2\text{CO}_3$ ,  $\text{Mn}(\text{CH}_3\text{COO})_2 \cdot 4\text{H}_2\text{O}$  and  $\text{V}_2\text{O}_3$  at  $700^\circ\text{C}$  under  $\text{CO}_2$  atmosphere for 40 h.<sup>47)</sup>

$\text{LiTi}_2\text{O}_4$  was prepared by heating a mixture of  $\text{Li}_2\text{CO}_3$  and  $\text{TiO}_2$  (rutile) at  $850^\circ\text{C}$  under  $\text{H}_2$  atmosphere for 2 h.<sup>47,48)</sup> A small amount of unreacted residual  $\text{TiO}_2$  (rutile) was always mixed in the product, rendering it unsatisfactory. Another synthetic route to obtain  $\text{LiTi}_2\text{O}_4$  according to Murphy *et al.*<sup>49)</sup> is first to prepare  $\text{Li}_{0.5}\text{TiO}_2$  by reacting  $\text{TiO}_2$  (anatase) with *n*-butyl-lithium (*n*-BuLi) at room temperature, and then to heat the product at  $850^\circ\text{C}$  for one week. By contrast,  $\text{Li}_4\text{Ti}_5\text{O}_{12}$  can be prepared by heating  $\text{Li}_2\text{CO}_3$  and  $\text{TiO}_2$  in air to  $800^\circ\text{C}$  for three days.<sup>23)</sup>

The synthesis of  $\text{LiMn}_2\text{O}_4$  is relatively simple. However, its characterization as the cathode active material depends on the synthesis conditions, especially heating temperature and cooling rate. As pointed by Tarascon *et al.*<sup>11,14)</sup> and Momchilov *et al.*,<sup>50)</sup> the appropriate synthesis temperature for  $\text{LiMn}_2\text{O}_4$  is from  $650^\circ\text{C}$  to  $800^\circ\text{C}$ . In our experience, even for the doped manganese spinel phases  $\text{LiM}_y\text{Mn}_{2-y}\text{O}_4$  ( $\text{M} = \text{Co}, \text{Cr}$  and  $\text{Ni}$ ), the optimum heating temperature is  $750^\circ\text{C}$ .<sup>51,52)</sup> The cooling rate strongly affects the properties of the product as the cathode material. The quenched samples showed smaller

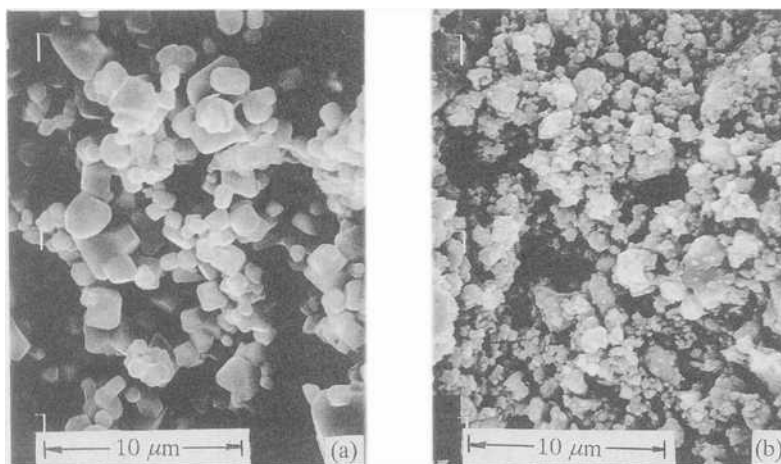


Fig. 2.2 SEM micrographs of  $\text{LiCr}_{1/6}\text{Mn}_{11/6}\text{O}_4$  samples prepared at different cooling rates: (a) quenching, (b) slow cooling.

initial capacity and shorter cycle life than samples obtained by slow cooling. Fig. 2.2 shows the SEM micrographs of  $\text{LiCr}_{1/6}\text{Mn}_{11/6}\text{O}_4$  samples prepared at the same heating temperature and time but followed by quench and slow cooling, respectively. As can be seen, the particles of the sample obtained by slow cooling are finer and have larger surface area than those of quenched sample. And the intermittent grinds are also beneficial to the improvement of the properties of the product as electrode materials. Studies on the structural aspects (especially oxygen stoichiometry) have also been conducted by many research groups. The phase transformation of  $\text{LiMn}_2\text{O}_4$  from a cubic to a tetragonal at  $T > 840^\circ\text{C}$  in air was identified by Tarascon *et al.*<sup>14,15)</sup> and Yamada *et al.*<sup>53)</sup> The oxygen stoichiometry,  $\delta$ , in  $\text{LiMn}_2\text{O}_{4-\delta}$  spinel is an important problem of scientific interest. In our laboratory, the oxygen deficiency in  $\text{LiMn}_2\text{O}_{4-\delta}$  and its dependence on the partial pressure of oxygen were investigated using thermogravimetry (TG). At  $750^\circ\text{C}$ , when the partial pressure of oxygen  $P_{\text{O}_2}$  is higher than 0.16 atm, no oxygen defect was found in the  $\text{LiMn}_2\text{O}_4$  sample.<sup>54)</sup> Similar results were achieved by Yamada *et al.*<sup>53)</sup> Thus,  $\text{LiMn}_2\text{O}_4$  and  $\text{LiM}_y\text{Mn}_{2-y}\text{O}_4$  ( $\text{M} = \text{Co}, \text{Cr}$  and  $\text{Ni}$ ) samples prepared at  $750^\circ\text{C}$  in air followed by slow cooling had no oxygen defect. On the other hand,  $\text{LiMn}_2\text{O}_{4-\delta}$  with oxygen deficiency showed poor cathode properties compared with standard  $\text{LiMn}_2\text{O}_4$  spinel.

The typical established synthesis method of  $\text{Li}_4\text{Mn}_5\text{O}_{12}(\text{Li}_{4/3}\text{Mn}_{5/3}\text{O}_4)$  is as follows. A mixture of  $\text{Li}_2\text{CO}_3$  and  $\text{Mn}(\text{CH}_3\text{COO})_2 \cdot 4\text{H}_2\text{O}$  was heated at  $400^\circ\text{C}$  under oxygen atmosphere for 3 h. To improve the crystallinity of the sample, the intermediate product was ground, pelletized, sealed in an evacuated silica tube, then heated at  $400^\circ\text{C}$  for one week.<sup>55)</sup> The oxygen deficiency was examined by both thermal analysis and composition analysis using inductively coupled plasma method (ICP) (SPS 1500VR Plasma Spectrometer, SEIKO Instrument Inc.).

## 2.4 Relationship between Discharge Voltage and Thermodynamic Function of the Cathode Materials

Since the energy density of the cathode of a lithium secondary battery is the product of its capacity density and discharge voltage, the open-circuit voltage (OCV) of a lithium cell, corresponding to the cell voltage without polarization, is important for estimating the energy density of the cathode. In this section, the relationship between OCV and thermodynamic functions for some normal spinel compounds are discussed.

The procedures for the fabrication and measurement of lithium rechargeable cells are almost the same as those described previously.<sup>27,56)</sup> A composite cathode was made by mixing the active material, acetylene black, and polytetrafluoroethylene (PTFE) and then pressing into a film. A disk 5 mm in diameter was cut from the film and used as the cathode. To evaluate the cathode properties, an excess amount of lithium foil was used as the anode. The electrolyte was 1 M  $\text{LiClO}_4$  dissolved in propylene carbonate (PC) obtained from Tomiyama Pure Chemical Co., Ltd. The electrolyte had a water content of less than 20 ppm.

The quasi-OCV's of the  $\text{Li}/\text{Li}_{1+x}\text{M}_2\text{O}_4$  cell for  $0 \leq x \leq 1$  as a function of  $x$  were measured as follows. The cell was first discharged or charged galvanostatically to a desired  $x$  at a current density of  $0.1 \text{ mA} \cdot \text{cm}^{-2}$ , and then the cell was left on an open circuit for two days. The final cell voltage was recorded as the OCV value for that composition.

Figure 2.3 shows the OCV data of the  $\text{Li}/\text{Li}_{1+x}\text{M}_2\text{O}_4$  cells obtained at 298 K vs. lithium composition  $x$  for three spinels. The OCV's of the  $\text{Li}/\text{Li}_{1+x}\text{Mn}_2\text{O}_4$  and  $\text{Li}/\text{Li}_{1+x}\text{V}_2\text{O}_4$  cells agreed well with those reported in the literatures.<sup>11,12,32)</sup> The OCV curves are flat over the wide range of  $x$  except for  $\text{Li}_{1+x}\text{Ti}_2\text{O}_4$ , because the phase transformation from cubic spinel structure to atacamite structure occurs along with the lithium intercalation. The general equation can be written as follows:

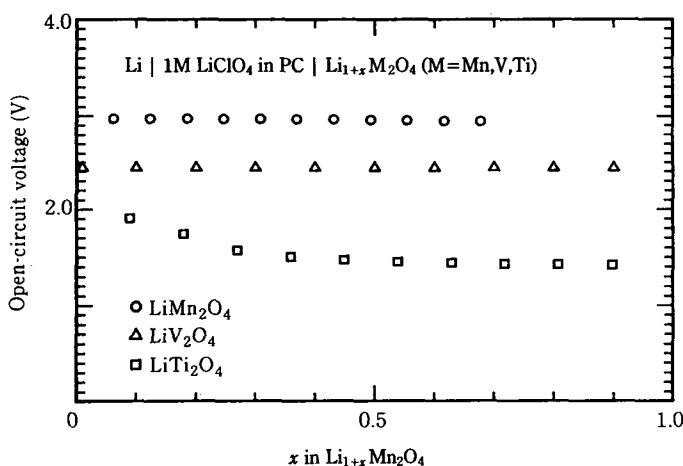


Fig. 2.3 Plot of  $\text{Li}/\text{Li}_x\text{M}_2\text{O}_4$  cells vs. lithium content  $x$  at 298 K.

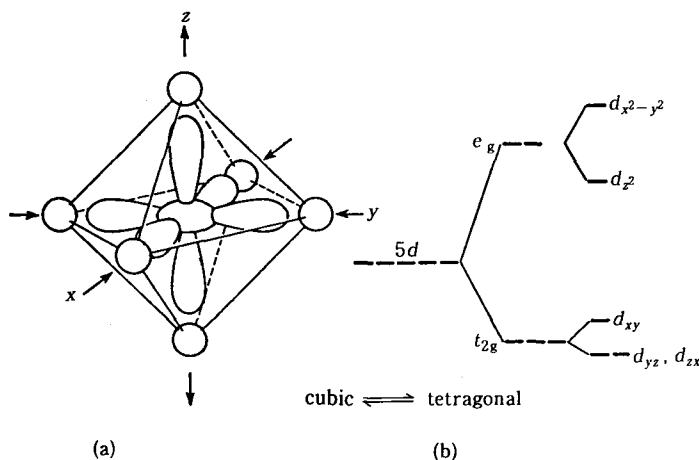
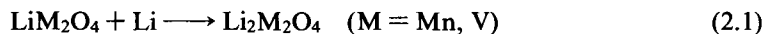


Fig. 2.4 Jahn-Teller distortion of the octahedron coordination. (a) distortion of an octahedron; (b) splitting of the d orbital.



Although a very pure single phase of the  $\text{LiTi}_2\text{O}_4$  could not be synthesized directly, the profile of the OCV decreased gradually with increasing  $x$  and then became flat after  $x > 0.4$ . This suggests that when the lithium ions enter the vacant 16c sites of the  $\text{Li}_{1+x}\text{Ti}_2\text{O}_4$ , lithium ions in the 8a sites remain at the original positions when  $x < 0.4$ , and then a phase transformation from a spinel cubic to an ordered rock salt (atacamite) occurs. In this study, a horizontal potential was chosen as the OCV value on the two-phase region.

It has already been pointed out that lithiation into vacancies of the  $\text{Li}_{1+x}\text{M}_2\text{O}_4$  causes a cooperative displacement of the lithium ions, which reside in the 8a sites, to neighboring vacant 16c sites and a simultaneous reduction of the host transition metal ions; this process results, in most cases, in an atacamite structure  $(\text{LiLi})_{16c}[\text{MM}]_{16d}\text{O}_4$  as described briefly above.<sup>29,32)</sup> Actually, the structural integrity of the  $[\text{M}]_2\text{O}_4$  spinel framework was maintained for  $\text{Li}_{1+x}\text{V}_2\text{O}_4$ , and  $\text{Li}_{1+x}\text{Ti}_2\text{O}_4$  during lithiation in this study. However, as pointed out in the literatures,<sup>12,33)</sup> for the lithium insertion into  $\text{Li}_{1+x}\text{Mn}_2\text{O}_4$ , a phase transformation from a cubic to a tetragonal symmetry due to Jahn-Teller distortion<sup>57,58)</sup> of a  $\text{Mn}^{3+}\text{O}_6$  octahedron occurred. The Jahn-Teller distortion can occur for unequal occupancy of the  $e_g$  or  $t_{2g}$  orbital. However, the distortion for unequal occupancy of the  $e_g$  orbital (in the situation for  $d^4$ ,  $d^9$ ) is expected to be greater than that for the  $t_{2g}$  orbital. As shown in Fig. 2.4, distortion of the octahedron along the  $z$ -axis results in the splitting of the  $e_g$  orbital.  $\text{Mn}^{4+} \rightarrow \text{Mn}^{3+}$  reduction occurs during the lithium insertion into  $\text{Li}_{1+x}\text{Mn}_2\text{O}_4$ . The Jahn-Teller distortion is expected because of the  $d^4$  configuration of  $\text{Mn}^{3+}$ .

In Table 2.1, the OCV values for the reaction,  $\text{LiM}_2\text{O}_4 + \text{Li} \rightarrow \text{Li}_2\text{M}_2\text{O}_4$ , at 298 K are summarized for the related spinel compounds. The standard Gibbs energy of this phase transition reaction ( $\Delta G_{p,t}^\circ$ ) for the spinel compounds is expressed as follows:

Table 2.1 Observed OCV and the Gibbs energy of the phase transition at 298 K.

$\text{LiM}_2\text{O}_4 + \text{Li} \longrightarrow \text{Li}_2\text{M}_2\text{O}_4 \quad \Delta G_{\text{p.t.}}^\circ = -FE^\circ$		
	OCV (V)	$\Delta G_{\text{p.t.}}^\circ (\text{kJ} \cdot \text{mol}^{-1})$
$\text{LiMn}_2\text{O}_4$	2.97	-287
$\text{LiV}_2\text{O}_4$	2.44	-235
$\text{LiTi}_2\text{O}_4$	1.44	-139

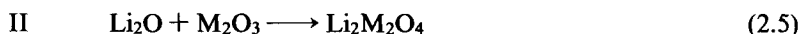
$$\Delta G_{\text{p.t.}}^\circ = \Delta G_{\text{f}}^\circ(\text{Li}_2\text{M}_2\text{O}_4) - \Delta G_{\text{f}}^\circ(\text{LiM}_2\text{O}_4) - \Delta G_{\text{f}}^\circ(\text{Li}) \quad (2.2)$$

where  $\Delta G_{\text{f}}^\circ(\text{Li}_2\text{M}_2\text{O}_4)$ ,  $\Delta G_{\text{f}}^\circ(\text{LiM}_2\text{O}_4)$  and  $\Delta G_{\text{f}}^\circ(\text{Li})$  are the standard Gibbs energies of formation for  $\text{Li}_2\text{M}_2\text{O}_4$ ,  $\text{LiM}_2\text{O}_4$  and  $\text{Li}$ , respectively. Since lithium metal is pure,  $\Delta G_{\text{f}}^\circ(\text{Li})$  becomes zero. The Gibbs energy of the phase transition is directly derived from the OCV using following equation:

$$\Delta G_{\text{p.t.}}^\circ = -FE^\circ \quad (2.3)$$

$\Delta G_{\text{p.t.}}^\circ$  for several spinel compounds at 298 K is also summarized in Table 2.1.  $\text{LiM}_2\text{O}_4$  with a larger negative Gibbs energy of formation for the constituent  $\text{MO}_2$  reveals a higher OCV.

On the other hand, the formation reactions of  $\text{LiM}_2\text{O}_4$  and  $\text{Li}_2\text{M}_2\text{O}_4$  from  $\text{Li}_2\text{O}$ ,  $\text{M}_2\text{O}_3$  and  $\text{MO}_2$  are written as follows:



The Gibbs energy of the reaction ( $\Delta G_{\text{r}}$ ) is expressed using the Gibbs energy of formation for each oxide as follows:

$$\Delta G_{\text{r}}(\text{I}) = \Delta G_{\text{f}}(\text{LiM}_2\text{O}_4) - \{1/2\Delta G_{\text{f}}(\text{Li}_2\text{O}) + 1/2\Delta G_{\text{f}}(\text{M}_2\text{O}_3) + \Delta G_{\text{f}}(\text{MO}_2)\} \quad (2.6)$$

$$\Delta G_{\text{r}}(\text{II}) = \Delta G_{\text{f}}(\text{Li}_2\text{M}_2\text{O}_4) - \{\Delta G_{\text{f}}(\text{Li}_2\text{O}) + \Delta G_{\text{f}}(\text{M}_2\text{O}_3)\} \quad (2.7)$$

If the reactions of both (I) and (II) are equilibrated at standard condition, the Gibbs energies of formation  $\Delta G_{\text{f}}^\circ(\text{LiM}_2\text{O}_4)$  and  $\Delta G_{\text{f}}^\circ(\text{Li}_2\text{M}_2\text{O}_4)$  are expressed as follows:

$$\Delta G_{\text{f}}^\circ(\text{LiM}_2\text{O}_4) = 1/2\Delta G_{\text{f}}^\circ(\text{Li}_2\text{O}) + 1/2\Delta G_{\text{f}}^\circ(\text{M}_2\text{O}_3) + \Delta G_{\text{f}}^\circ(\text{MO}_2) \quad (2.8)$$

$$\Delta G_{\text{f}}^\circ(\text{Li}_2\text{M}_2\text{O}_4) = \Delta G_{\text{f}}^\circ(\text{Li}_2\text{O}) + \Delta G_{\text{f}}^\circ(\text{M}_2\text{O}_3) \quad (2.9)$$

These two equations are substituted in Eq. (2.2).



Table 2.2 Calculated Gibbs energy of the phase transition at 298 K.

$$\Delta G_{p.t.}^{\circ} = 1/2\Delta G_f^{\circ}(\text{Li}_2\text{O}) + 1/2\Delta G_f^{\circ}(\text{M}_2\text{O}_3) - \Delta G_f^{\circ}(\text{MO}_2)$$

$$\Delta G_f^{\circ}(\text{Li}_2\text{O}) = -562 \text{ (kJ} \cdot \text{mol}^{-1}) \text{ (298 K)}$$

M	$\Delta G_f^{\circ}(\text{M}_2\text{O}_3) \text{ (kJ} \cdot \text{mol}^{-1})$	$\Delta G_f^{\circ}(\text{MO}_2) \text{ (kJ} \cdot \text{mol}^{-1})$	$\Delta G_{p.t., \text{calc}}^{\circ} \text{ (kJ} \cdot \text{mol}^{-1})$	$E_{\text{calc}}^{\circ} \text{ (V)}$
Mn	-881	-465	-257	2.66
V	-1139	-659	-192	1.99
Ti	-1433	-889	-109	1.13

Ref. Thermodynamic Data of Pure Substances, I. Barin.

$$\begin{aligned} \Delta G_{p.t.}^{\circ} &= \{\Delta G_f^{\circ}(\text{Li}_2\text{O}) + \Delta G_f^{\circ}(\text{M}_2\text{O}_3)\} - \{1/2\Delta G_f^{\circ}(\text{Li}_2\text{O}) + 1/2\Delta G_f^{\circ}(\text{M}_2\text{O}_3) + \Delta G_f^{\circ}(\text{MO}_2)\} \\ &= 1/2\Delta G_f^{\circ}(\text{Li}_2\text{O}) + 1/2\Delta G_f^{\circ}(\text{M}_2\text{O}_3) - \Delta G_f^{\circ}(\text{MO}_2) \end{aligned} \quad (2.10)$$

The calculated standard Gibbs energy of the phase transition and calculated OCV are listed in Table 2.2. The difference between observed (Table 2.1) and calculated (Table 2.2) values of  $\Delta G_{p.t.}^{\circ}$  would be caused by the difference in the slight individual structural configuration of the spinel and the atacamite.

Accordingly, the precise observed  $\Delta G_{p.t.}^{\circ}$  is more reliable than the calculated  $\Delta G_{p.t.}^{\circ}$ .

## 2.5 Phase Transformation During Intercalation Processes

The intercalation reactions may be divided mainly into two categories, *i.e.*, a homogeneous solid phase reaction and a two-phase reaction. Correspondingly, the discharge curve for an intercalation electrode can be classified as (a) an S-shaped curve when a solid solution is formed along with intercalation, (b) an L-shaped curve when a second phase is formed, and (c) a step-shaped curve when multiple phases are formed.

Lithium insertion-extraction in  $\text{Li}_x\text{M}_2\text{O}_4$  spinels in the different range of  $x$  exhibit different phase transformation behavior. For  $\text{Li}_x\text{Ti}_2\text{O}_4$ , the lithium insertion-extraction reaction,  $\text{LiTi}_2\text{O}_4 + y\text{Li} \rightarrow \text{Li}_{1+y}\text{Ti}_2\text{O}_4$ , occurs in the range of  $0 \leq y < 1$ . For  $\text{Li}_x\text{V}_2\text{O}_4$ , the lithium insertion-extraction reaction,  $\text{LiV}_2\text{O}_4 + y\text{Li} \rightarrow \text{Li}_{1+y}\text{V}_2\text{O}_4$  ( $0 \leq y \leq 1$ ), exhibits a two-phase coexistence and gives rise to an extremely flat potential plateau with average discharge voltage of 2.44 V. The potential difference between the plateaus of the discharge and charge curves was very small (only 0.15 V), suggesting that the reaction is reversible. The  $\text{Li}/\text{Li}_{1+y}\text{V}_2\text{O}_4$  cell has a rather long cycle life, more than 70% of the initial capacity was maintained over 700 cycles.<sup>47)</sup> On the other hand, removing lithium ions from  $\text{LiV}_2\text{O}_4$  has been proved to be possible but poorly reversible. For instance, the  $\text{Li}/\text{Li}_{1-y}\text{V}_2\text{O}_4$  cell can only be charged to  $y \approx 0.15$  when charged to 4.2 V, and only a very small capacity can be delivered at the first discharge. According to Pistoia *et al.*, the  $[\text{V}_2]\text{O}_4$  spinel framework remains intact only to  $y \approx 0.3$  in  $\text{Li}_{1-y}\text{V}_2\text{O}_4$ .<sup>32)</sup> The lithium extraction reaction,  $\text{LiV}_2\text{O}_4 - y\text{Li} \rightarrow \text{Li}_{1-y}\text{V}_2\text{O}_4$  ( $0 \leq y < 1$ ), is rather irreversible.

The X-ray diffraction (XRD) pattern of the  $\text{Li}_{1+x}\text{V}_2\text{O}_4$  cathode after 880 cycles at charged state was identical with that of the fresh cathode. It suggests that the spinel skeleton structure  $[\text{V}_2]\text{O}_4$  is very stable. The cubic lattice parameter of the  $\text{Li}_2\text{V}_2\text{O}_4$  formed electrochemically was  $8.292 \pm 0.001 \text{ \AA}$  ( $8.291 \text{ \AA}$  by Pistoia *et al.*<sup>32)</sup>). The volume change from  $\text{LiV}_2\text{O}_4$  (cubic spinel,  $a = 8.243 \pm 0.001 \text{ \AA}$ ,  $V = 560.1 \pm 0.002 \text{ \AA}^3$ ) to  $\text{Li}_2\text{V}_2\text{O}_4$  (ordered

NaCl type cubic,  $a = 8.292 \pm 0.001 \text{ \AA}$ ,  $V = 570.1 \pm 0.002 \text{ \AA}^3$ ) was only 1.8 vol%. This small volume change would contribute such a long cycle life.

Reversible lithium insertion-extraction occurs in  $\text{Li}_x\text{Mn}_2\text{O}_4$  spinel phase for two compositional ranges,  $0.1 \leq x \leq 1$  and  $1 \leq x \leq 2$ , and gives rise to two voltage plateaus located at 4 V and 3 V, respectively.<sup>11,12)</sup> However, in the 3 V range, a fast capacity fading occurs because of the phase transformation from spinel to atacamite during the lithium insertion. The cycle life for the  $\text{Li}/\text{Li}_{1+x}\text{Mn}_2\text{O}_4$  cell (3 V range) has been reported to be rather short by Tarascon and Guyomard.<sup>59)</sup> A rather large volume change (6%) from the cubic spinel  $\text{LiMn}_2\text{O}_4$  ( $a = 8.244 \text{ \AA}$ ,  $V = 560.3 \text{ \AA}^3$ ) to the tetragonal  $\text{Li}_2\text{Mn}_2\text{O}_4$  ( $a = 8.007 \text{ \AA}$  ( $=\sqrt{2}a_T$ ),  $c = 9.274 \text{ \AA}$ ,  $V = 594.6 \text{ \AA}^3$ , atacamite-like structure) accompanying the Jahn-Teller distortion may have affected the limited cycles. Even for Cr-doped manganese spinel phases, the cycle life of the  $\text{Li}/\text{Li}_{1+x}\text{Cr}_y\text{Mn}_{2-y}\text{O}_4$  cell was also not satisfactory in the 3 V range.<sup>60)</sup> Kanno *et al.* found that Jahn-Teller distortion also occurs in  $\text{LiCrMnO}_4$  spinel.<sup>61)</sup>

Although the  $\text{Li}_x\text{Mn}_2\text{O}_4$  electrode in the 4 V range is significantly more tolerant to cycling than in the 3 V range, a slow capacity fading is encountered in the 4 V range.<sup>14,16)</sup> In order to improve the cycle performance of  $\text{Li}_x\text{Mn}_2\text{O}_4$  as the 4 V class cathode material for lithium secondary batteries, a considerable amount of work has been carried out by Tarascon *et al.*<sup>59)</sup> that to optimize the synthesis conditions and other relating parameters. On the other hand, several investigations have been made for the performance of manganese-substituted spinels  $\text{LiM}_y\text{Mn}_{2-y}\text{O}_4$  ( $M = \text{Co, Fe, Mg, Ti, Ge, Ni, Zn}$ ).<sup>11,17)</sup> Bittihn *et al.* have reported that the cobalt-doped  $\text{LiCo}_x\text{Mn}_{2-x}\text{O}_4$  improved cycling behavior.<sup>62)</sup> The doping effect on the  $\text{LiM}_y\text{Mn}_{2-y}\text{O}_4$  ( $M = \text{Co, Cr, Ni}$ ) spinel phases is discussed in detail below.

## 2.6 Doped Spinel Phases $\text{LiM}_y\text{Mn}_{2-y}\text{O}_4$ ( $M = \text{Co, Cr, Ni}$ ) as 4 V-Class Cathode Material

### 2.6.1 Doping Effect on Charge-Discharge Behavior of Manganese Spinel

The quaternary spinel phases  $\text{LiM}_y\text{Mn}_{2-y}\text{O}_4$  ( $y = 0; y = 1/9, 1/6, 1/3$  for  $M = \text{Co}$  and  $\text{Cr}$ ;  $y = 1/12, 1/9, 1/6$  for  $M = \text{Ni}$ ) were prepared by reacting a stoichiometric mixture of  $\text{Li}_2\text{CO}_3$  and  $\text{Mn}(\text{CH}_3\text{COO})_2 \cdot 4\text{H}_2\text{O}$  or  $\text{MnCO}_3$ , by adding  $\text{Cr}_2\text{O}_3$ ,  $\text{CoC}_2\text{O}_4 \cdot 2\text{H}_2\text{O}$  and  $\text{NiC}_2\text{O}_4 \cdot 2\text{H}_2\text{O}$ , respectively. The mixtures were preheated at  $600^\circ\text{C}$  for 6 h, then heated at  $750^\circ\text{C}$  for 3 days in air with intermittent grinding, followed by slow cooling. All samples were identified as a single-phase spinel. The cathode properties were evaluated by using the  $\text{Li}/1 \text{ M LiClO}_4$  in  $\text{PC}/\text{LiM}_y\text{Mn}_{2-y}\text{O}_4$  cells.

Figure 2.5 shows the galvanostatic charge-discharge curves of the  $\text{Li}/\text{Li}_x\text{M}_{1/6}\text{Mn}_{11/6}\text{O}_4$  cells for  $M = \text{Cr, Co}$  and  $\text{Ni}$ , together with that of the parent  $\text{Li}/\text{Li}_x\text{Mn}_2\text{O}_4$  cell. The initial capacity of the cells was reduced by doping. Among them, the nickel-doped cathode showed the lowest initial capacity at the same dopant content. This suggests that even for the substituted spinel phases, only the amount of  $\text{Mn}^{3+}$  contributes to the charge capacity, because the extraction of  $\text{Li}^+$  from the host structure must be electrically compensated by the oxidation of  $\text{Mn}^{3+}$  to  $\text{Mn}^{4+}$ . So the initial capacity of the cathode is limited by the amount of  $\text{Mn}^{3+}$  in the spinel phase in its synthesized state. At the present synthesis condition, the stable oxidation state of the dopant cations are  $\text{Cr}^{3+}$  and  $\text{Ni}^{2+}$ . It is reasonable to assume that the oxidation state of cobalt is  $\text{Co}^{3+}$  because  $\text{Li}_x\text{Co}_{1/6}\text{Mn}_{11/6}\text{O}_4$

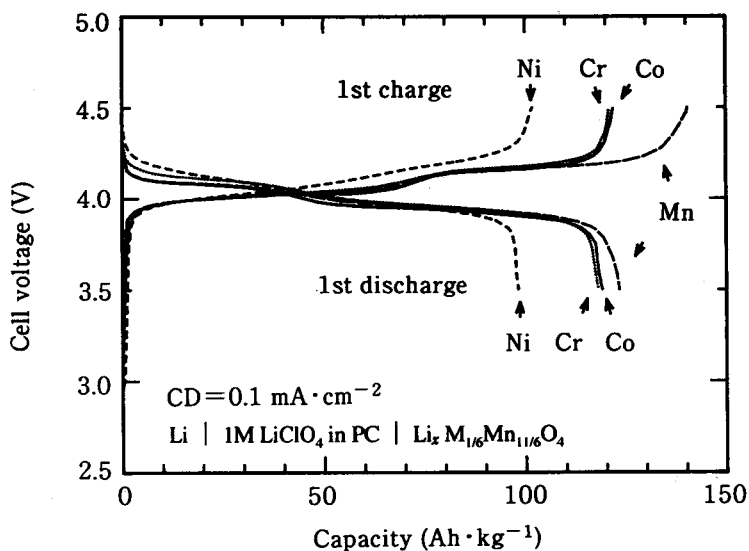


Fig. 2.5 Galvanostatic charge-discharge curves of the  $\text{Li}/\text{Li}_x\text{M}_y\text{Mn}_{2-y}\text{O}_4$  cells for  $M = \text{Cr}, \text{Co}$  and  $\text{Ni}$ , compared with the  $\text{Li}/\text{Li}_x\text{Mn}_2\text{O}_4$  cell.

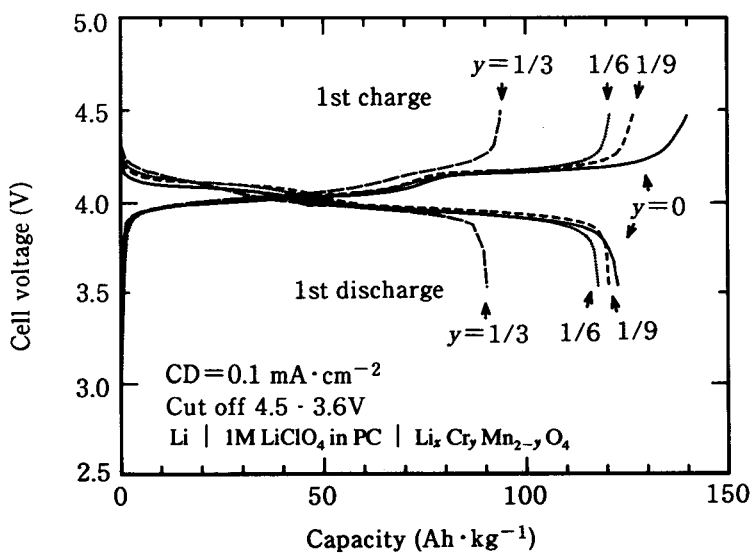


Fig. 2.6 Galvanostatic charge-discharge curves of the  $\text{Li}/\text{Li}_x\text{Cr}_y\text{Mn}_{2-y}\text{O}_4$  cells with  $y = 0, 1/9, 1/6$  and  $1/3$ .

offers almost the same initial capacity as that of  $\text{Li}_x\text{Cr}_{1/6}\text{Mn}_{11/6}\text{O}_4$  (see Fig. 2.5). At the same doping content (in atomic ratio), the average manganese oxidation state in a nickel-doped spinel phase is higher than that of a chromium- or cobalt-doped one, so that nickel-doped spinel phase delivers lower initial capacity. In other words, the initial capacity of the cathode is determined by the average manganese oxidation state instead of the nature of the doping cations.

Figure 2.6 shows the galvanostatic charge-discharge curves at the first cycle for the  $\text{Li}/\text{Li}_x\text{Cr}_y\text{Mn}_{2-y}\text{O}_4$  cells with  $y=0, 1/9, 1/6$  and  $1/3$ . The initial capacity of the cell was reduced by increasing the dopant content. In terms of the capacity, the dopant content should not be too large, especially for the divalent doping cations. For example, the initial discharge capacity of the  $\text{Li}/\text{Li}_x\text{Ni}_{1/9}\text{Mn}_{17/9}\text{O}_4$  cell was  $115 \text{ Ah} \cdot \text{kg}^{-1}$ , which was close to that of the  $\text{Li}/\text{Li}_x\text{Cr}_{1/6}\text{Mn}_{11/6}\text{O}_4$  cell,  $117 \text{ Ah} \cdot \text{kg}^{-1}$  (cutoff voltage 4.45 to 3.60 V,  $\text{CD}=0.1 \text{ mA} \cdot \text{cm}^{-2}$ ).

### 2.6.2 OCV and Phase Transformation

Figure 2.7 shows the variation of the quasi-OCV vs. lithium compositions  $x$  of the  $\text{Li}/\text{Li}_x\text{M}_{1/6}\text{Mn}_{11/6}\text{O}_4$  cells for  $\text{M}=\text{Co}, \text{Cr}$  and  $\text{Ni}$ . The OCV curve of the  $\text{Li}/\text{Li}_x\text{Mn}_2\text{O}_4$  cell is also shown for comparison. In the present cutoff voltage range of 4.45 V to 3.60 V, the maximum amount of lithium which can be removed from  $\text{Li}_x\text{Mn}_2\text{O}_4$  was  $\Delta x_{\text{max}} \approx 0.94$ . For cobalt- and chromium-doped spinel phases with  $y=1/6$ ,  $\Delta x_{\text{max}} \approx 0.83$ , which is approximately equal to the stoichiometric number of  $\text{Mn}^{3+}$  of these compounds in their initial state ( $5/6=0.833$ ).

The anomaly in the OCV curves implies that a phase transformation occurs in doped spinel phases. There is almost no inflection in the OCV curve of  $\text{Li}_x\text{Ni}_{1/6}\text{Mn}_{11/6}\text{O}_4$ , which is different from the other three in Fig. 2.7. However, at least, no clear phase

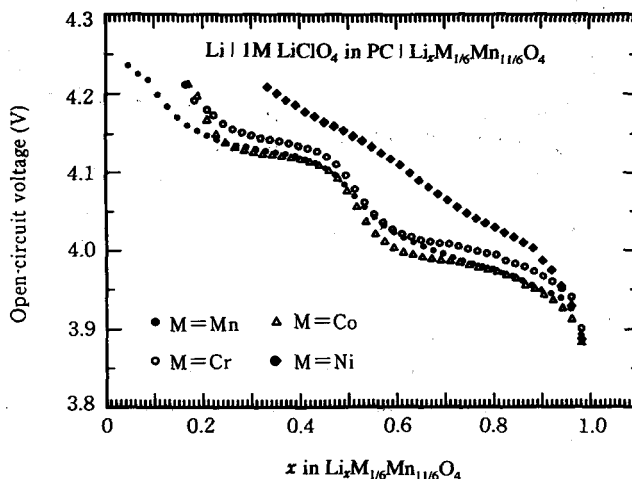


Fig. 2.7 Open-circuit voltages vs. lithium compositions  $x$  of the  $\text{Li}/\text{Li}_x\text{M}_{1/6}\text{Mn}_{11/6}\text{O}_4$  ( $\text{M}=\text{Cr}, \text{Co}, \text{Ni}$  and  $\text{Mn}$ ) cells.

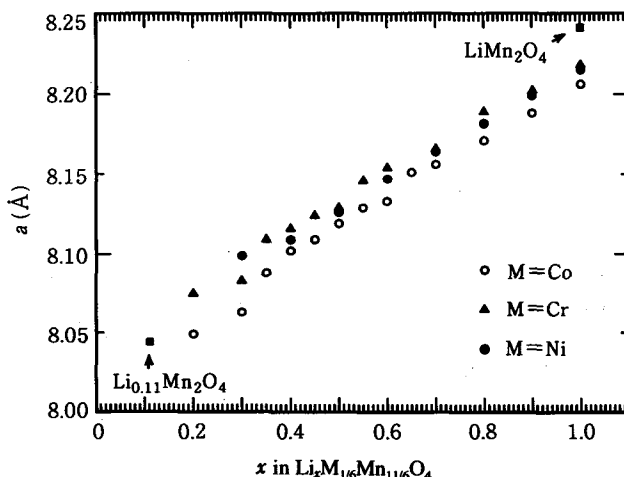


Fig. 2.8 Variations of the cubic lattice constants as a function of  $x$  for  $\text{Li}_x\text{M}_{1/6}\text{Mn}_{11/6}\text{O}_4$  ( $\text{M} = \text{Cr}, \text{Co}$  and  $\text{Ni}$ ).

transformation of the first order was observed from the XRD profiles of the charged  $\text{Li}_x\text{M}_y\text{Mn}_{2-y}\text{O}_4$  ( $0 < x \leq 1$ ) samples.<sup>51)</sup> All the peaks of the  $\text{Li}_x\text{M}_y\text{Mn}_{2-y}\text{O}_4$  samples were identical to those of the corresponding  $\text{LiM}_y\text{Mn}_{2-y}\text{O}_4$  phases. It seems that the cubic symmetry of the spinel structure is maintained during the deintercalation of lithium from these doped spinel phases, just like that pointed out by Gummow *et al.*<sup>17)</sup> for  $\text{Li}_{1+\delta}\text{Mn}_{2-\delta}\text{O}_4$  and  $\text{LiM}_{\delta/2}\text{Mn}_{2-\delta}\text{O}_4$  ( $\text{M} = \text{Mg}$  and  $\text{Zn}$ ) phases. It also agreed with the results of Pistoia and Wang that  $\text{Li}_x\text{Mn}_2\text{O}_4$  synthesized at  $750^\circ\text{C}$  maintains a single phase on electrochemical full delithiation.<sup>63)</sup> Probably, a lithium ordering-disordering process occurs during the lithium deintercalation-intercalation across  $x = 0.5$ , which causes a phase transformation of second or higher order. Fig. 2.8 shows the variations of the cubic lattice constant  $a$  as a function of  $x$  for the  $\text{Li}_x\text{M}_{1/6}\text{Mn}_{11/6}\text{O}_4$  formed electrochemically. The lattice constant  $a$  values decreased along with the deintercalation. The variations of the cubic lattice constant of the  $\text{Li}_x\text{Ni}_{1/6}\text{Mn}_{11/6}\text{O}_4$  was almost linear just like the OCV profiles. At the same doping content, the phase transformation in the nickel-doped phase occurred to the least extent among these phases. Similarly, the OCV curve of  $\text{Li}/\text{Li}_x[\text{Li}_{1/3}\text{Mn}_{5/3}]\text{O}_{4-\delta}$  cell (the cathode is  $\text{Li}_4\text{Mn}_5\text{O}_{12}$  with a defect composition,  $\delta = 0.2 \pm 0.002$ ) was also almost linear in the range of  $0.4 < x < 0.9$ , and the lattice constant  $a$  of  $\text{Li}_x[\text{Li}_{1/3}\text{Mn}_{5/3}]\text{O}_{4-\delta}$  increased almost linearly with the increase in  $x$ .<sup>48)</sup> The average manganese oxidation state in  $\text{Li}_{4/3}\text{Mn}_{5/3}\text{O}_{4-\delta}$  is 3.76 for  $\delta = 0.2$ , which is higher than that in  $\text{LiNi}_{1/6}\text{Mn}_{11/6}\text{O}_4$  (3.64), while the average manganese oxidation state in  $\text{Li}_x\text{Cr}_{1/6}\text{Mn}_{11/6}\text{O}_4$  is 3.55. This suggests that the phase transformation may be also related to the Jahn-Teller distortion caused by the  $\text{Mn}^{3+}$ . In addition, unlike  $\text{LiM}_y\text{Mn}_{2-y}\text{O}_4$ , the oxygen defect in  $\text{Li}_{4/3}\text{Mn}_{5/3}\text{O}_{4-\delta}$  is necessary when it is used as 4 V class cathode material. When  $\delta$  increases, the oxidation state of manganese decreases and substantial Li can then be deintercalated.

The electrochemical behavior of doped  $\text{LiM}_y\text{Mn}_{2-y}\text{O}_4$  was also studied by cyclic voltammetry using the three-electrode cell. For instance, the voltammograms of  $\text{Li}_x\text{Co}_{1/6}\text{Mn}_{11/6}\text{O}_4$  in 1 M  $\text{LiClO}_4$  in PC show two peaks in oxidation sweep and two peaks in

reduction sweep, when the electrode is cycled between 4.5 V and 3.0 V vs.  $\text{Li}/\text{Li}^+$  at the sweep rate of  $0.01 \text{ mV} \cdot \text{s}^{-1}$ . The potential corresponding to the valley between two peaks just corresponds to  $x=0.5$ . These findings suggest that the reversible transformation occurs in two steps across  $x=0.5$ . This agreed with the result by Guyomard and Tarascon for  $\text{LiMn}_2\text{O}_4$ .<sup>64)</sup>

### 2.6.3 Cycling Performance

Figure 2.9 shows the cycling behavior of the  $\text{Li}/\text{LiCr}_y\text{Mn}_{2-y}\text{O}_4$  cells over subsequent cycles for (a)  $y=0$ ; (b)  $y=1/6$ , and (c)  $y=1/3$ , respectively. Obviously, the doped phases were more tolerant to repeated lithium extraction and insertion than the parent  $\text{LiMn}_2\text{O}_4$  spinel phase with the expense of the initial capacity, and the capacity fading was suppressed by increasing the dopant content. At higher dopant content, for example,  $1/3$  atomic

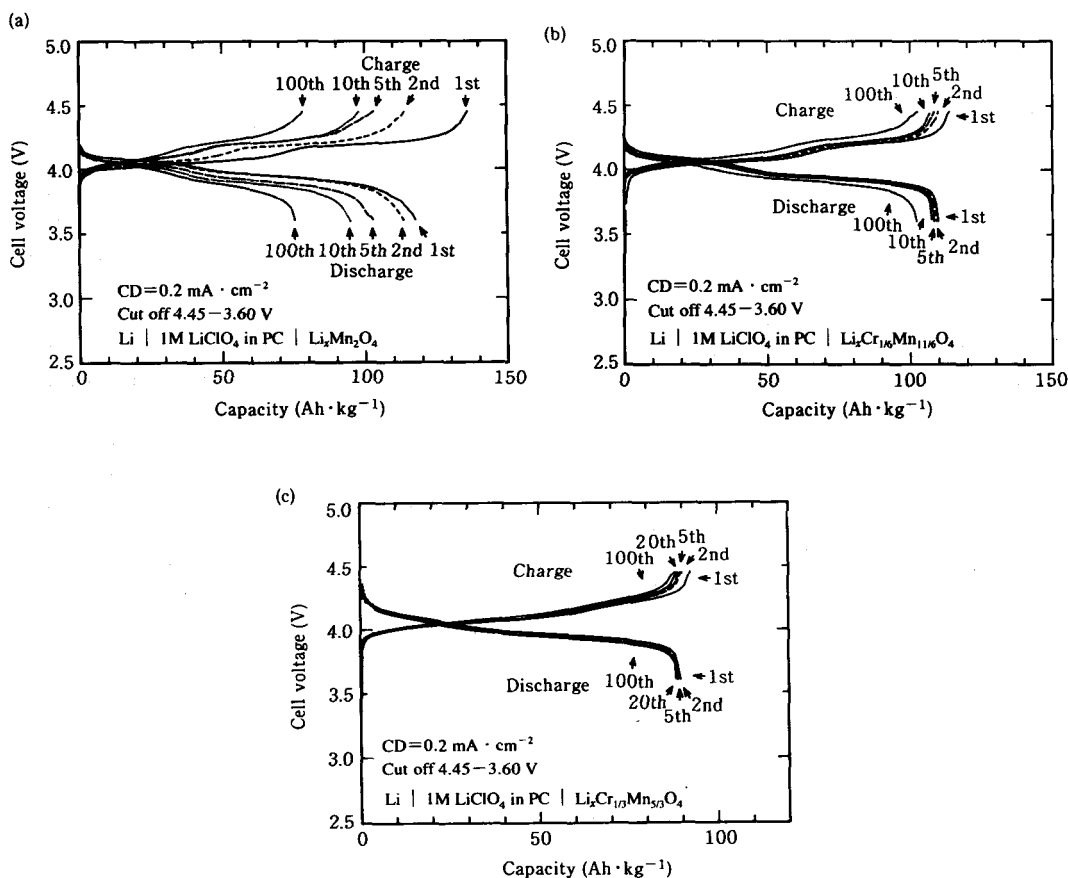


Fig. 2.9 Cycling behavior of the  $\text{Li}/\text{LiCr}_y\text{Mn}_{2-y}\text{O}_4$  cells over subsequent cycles. (a)  $\text{Li}_x\text{Mn}_2\text{O}_4$ , (b)  $\text{Li}_x\text{Cr}_{1/6}\text{Mn}_{11/6}\text{O}_4$  and (c)  $\text{Li}_x\text{Cr}_{1/3}\text{Mn}_{5/3}\text{O}_4$ .

fraction of Cr as shown in Fig. 2.9(c), the discharge curves hardly changed from the second to the 100th cycle. For other doping cations, the effect of dopant content on the cycling behavior were similar to that shown in Fig. 2.9. The cycle performance was evaluated galvanostatically at current densities of 0.2 and 0.5  $\text{mA} \cdot \text{cm}^{-2}$ , between 4.45 V and 3.60 V. The relationships between the discharge capacity density of the cathode (only the net weight of the cathode material was considered for calculation) and the cycle number of the  $\text{Li}/\text{Li}_x\text{M}_y\text{Mn}_{2-y}\text{O}_4$  cells are shown in Figs. 2.10a–2.10c. As can be seen, the capacity fading of the  $\text{Li}/\text{Li}_x\text{Mn}_2\text{O}_4$  cell was the most severe among these cells in spite of the largest initial capacity. In terms of cycle life, the spinel phases with higher dopant content are beneficial as seen for  $\text{M}_y = \text{Cr}_{1/3}$ ,  $\text{Co}_{1/3}$ , or  $\text{Ni}_{1/6}$ . In the cases of  $\text{Cr}_{1/9}$ ,  $\text{Co}_{1/9}$  and  $\text{Ni}_{1/6}$  (data not shown in Fig. 2.10), the dopant content are not enough to suppress the capacity fading. Among these cathode materials,  $\text{LiCo}_{1/6}\text{Mn}_{11/6}\text{O}_4$  showed the best cycle performance in terms of the capacity and cycle life. When cycled at 0.2  $\text{mA} \cdot \text{cm}^{-2}$  between 4.45 V and

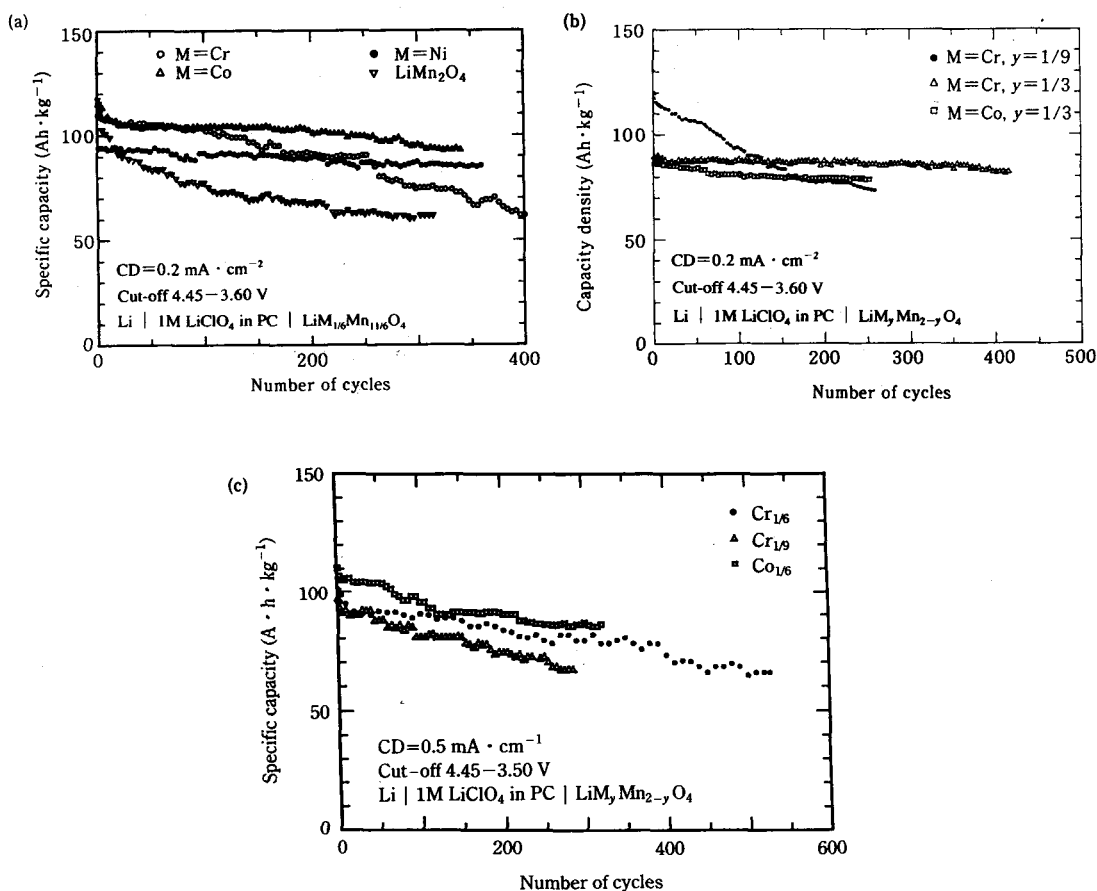


Fig. 2.10 Relationships between the capacity density and the cycle number of the  $\text{Li}/\text{Li}_x\text{M}_y\text{Mn}_{2-y}\text{O}_4$  cells. (a)  $\text{M} = \text{Cr}, \text{Co}, \text{Ni}$ ;  $y = 0, 1/6$ ,  $\text{CD} = 0.2 \text{ mA} \cdot \text{cm}^{-2}$ ; (b)  $\text{M} = \text{Cr}$ ,  $y = 1/9, 1/3$ ;  $\text{M} = \text{Co}$ ,  $y = 1/3$ ;  $\text{CD} = 0.2 \text{ mA} \cdot \text{cm}^{-2}$ ; and (c)  $\text{M} = \text{Cr}$ ,  $y = 1/9, 1/6$ ;  $\text{M} = \text{Co}$ ,  $y = 1/6$ ;  $\text{CD} = 0.5 \text{ mA} \cdot \text{cm}^{-2}$ .

3.6 V, the  $\text{Li}/1\text{ M LiClO}_4 + \text{PC}/\text{Li}_x\text{Co}_{1/6}\text{Mn}_{11/6}\text{O}_4$  cell deliver a calculated specific capacity of  $96\text{ Ah}\cdot\text{kg}^{-1}$  of active cathode material with an average discharge voltage of 3.85 V, resulting in a calculated energy density of *ca.*  $370\text{ Wh}\cdot\text{kg}^{-1}$  of active cathode material at the 300th cycle.  $\text{LiNi}_{1/9}\text{Mn}_{17/9}\text{O}_4$  is expected to be another promising cathode material from our present results, and its long cycle performance will be evaluated in further work.

Moreover, the  $\text{Li}/\text{Li}_{4/3}\text{Mn}_{5/3}\text{O}_{4-\delta}$  cell delivered a discharge capacity of  $78\text{ Ah}\cdot\text{kg}^{-1}$  of cathode active material at first discharge (cutoff voltage 4.5 to 3.5 V,  $\text{CD}=0.5\text{ mA}\cdot\text{cm}^{-2}$ ). A discharge capacity of  $74\text{ Ah}\cdot\text{kg}^{-1}$  was maintained even at 80th cycle.<sup>65)</sup>

## 2.6.4 Structure Aspects

Now let us consider the changes in the structural parameters. Fig. 2.11 shows the variations of (a) the lattice constant  $a$  and (b) the bond length as a function of  $y$  for the  $\text{LiCr}_y\text{Mn}_{2-y}\text{O}_4$  phases based on the Rietveld analysis.<sup>66)</sup> As can be seen, the lattice constant decreased with increase in dopant content. In other words, doping cations draw the crystal lattice tighter. In Fig. 2.11(b), the bond length of the  $16d-32e$  refers to the average bond length of M–O bonds (includes both Cr–O and Mn–O bond for Cr-doped spinel phases). Both the Li–O bond ( $8a-32e$ ) and the M–O bond became shorter with increasing dopant content. A schematic structure of Cr-doped manganese spinel phase is shown in Fig. 2.12. M atoms in the  $\text{MO}_6$  octahedron include Mn and Cr atoms.

It has been demonstrated that doped manganese spinel phases showed better cycling performance than  $\text{LiMn}_2\text{O}_4$  at the expense of initial capacity. The improvement in cycle performance by substitution can be explained by considering the fact that the doping metal cations enhance the stability of the octahedral sites in the spinel skeleton structure. It is useful to compare the binding energy for the M–O bond in the spinel structure, because the  $\text{MO}_2$  with a stronger binding energy results in a weaker interaction between guest Li and host O atoms, leading to the appearance of a lower OCV, and *vice versa*, an  $\text{MO}_2$  with weaker binding energy follows a higher OCV. The reaction model is given as follows;

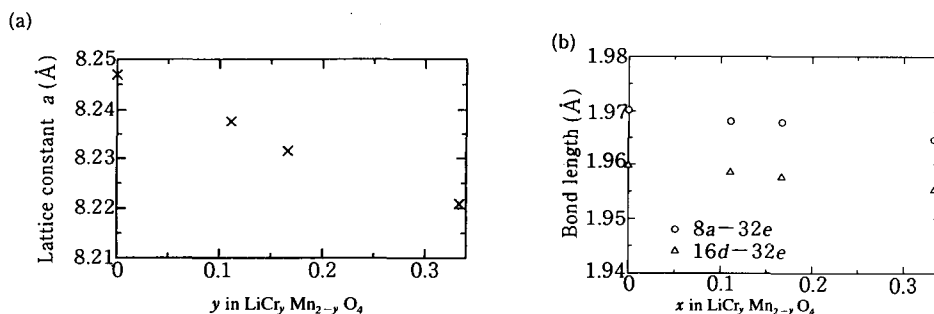
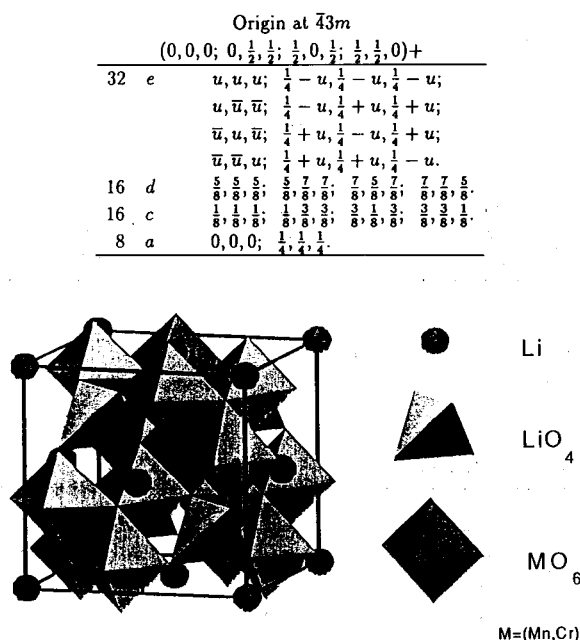
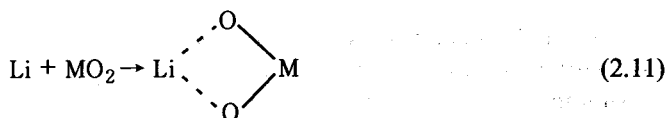


Fig. 2.11 Variations of (a) the cubic lattice constant and (b) bond length as a function of  $y$  for  $\text{LiCr}_y\text{Mn}_{2-y}\text{O}_4$ .



Fig. 2.12 Schematic illustration of framework of Cr-doped manganese spinel phases  $\text{LiCr}_y\text{Mn}_{2-y}\text{O}_4$ .

The binding energy  $E_{\text{B.E.}}$  can be evaluated by relating the thermodynamic functions of  $\text{MO}_2$  (the enthalpy of formation of  $\text{MO}_2$ , the enthalpy of vaporization of  $M$  and the enthalpy of dissociation of  $\text{O}_2$ ) with a part of simple Born-Harber's cycle process ( $E_{\text{B.E.}} = -\Delta H_f^\circ + \Delta H_{\text{vap}}^\circ + \Delta H_{\text{diss}}^\circ$ ) (see Table 2.3) if  $\text{MO}_2$  forms complete ionic bonding.

For example, the binding energy of  $\text{MnO}_2$  ( $\alpha$ -type),  $\text{VO}_2$  (rutile-like), and  $\text{TiO}_2$  (rutile) can be calculated to be 1296, 1727 and 1912  $\text{kJ} \cdot \text{mol}^{-1}$ , respectively. Thus, the order of the OCV can be explained qualitatively by association with the binding energy. Also, the binding energy of  $\text{MnO}_2$  ( $\alpha$ -type),  $\text{CrO}_2$ ,  $\text{CoO}_2$  and  $\text{NiO}_2$  could be estimated as 1296, 1492, 1418 and 1380  $\text{kJ} \cdot \text{mol}^{-1}$ , respectively. It is reasonable to assume that the  $M\text{-O}$  bonds for  $M = \text{Cr}, \text{Co}$  and  $\text{Ni}$  are stronger than the  $\text{Mn-O}$  bond, so that the dopants enhance the stability of the spinel structure.

In order to estimate the binding energy of the  $M\text{-O}$  bond for the lithium spinels,  $\text{LiM}_2\text{O}_4$ , it will be more useful to compare the binding energy of  $\text{M}_2\text{O}_{3.5}$  ( $\text{MO}_2 + 1/2\text{M}_2\text{O}_3$ :  $M$  in octahedral site), because the average oxidation number of the transition metal ion is +3.5 on each lithium spinel. This binding energy can be evaluated as listed in Table 2.4. This

Table 2.3 Thermodynamic functions at 298 K.  
 $\Delta H_{\text{diss}}^{\circ} = 497 \text{ (kJ} \cdot \text{mol}^{-1} \text{ at 298 K)}$ 

	$\Delta G_f^{\circ} \text{ (kJ} \cdot \text{mol}^{-1})$	$\Delta H_f^{\circ} \text{ (kJ} \cdot \text{mol}^{-1})$	$\Delta H_{\text{vap}}^{\circ} \text{ (kJ} \cdot \text{mol}^{-1})$	$E_{\text{B.E.}} \text{ (kJ} \cdot \text{mol}^{-1})$
TiO <sub>2</sub> (anatase)	-883	-941	469	1907
TiO <sub>2</sub> (rutile)	-891	-946	469	1912
VO <sub>2</sub> <sup>1)</sup>	-661	-715	515	1727
CrO <sub>2</sub> <sup>1)</sup>	-544	-598	397	1492
MoO <sub>2</sub> <sup>2)</sup>	-531	-590	665	1752
MnO <sub>2</sub> <sup>1)</sup>	-464	-519	280	1296
CoO <sub>2</sub>	-444*	(-494)**	427	(1418)**
NiO <sub>2</sub>	-406*	(-452)**	431	(1380)**

\* evaluated from OCV data.

\*\* assumed value.

<sup>1)</sup> Thermodynamic Data of Pure Substances, I. Barin.<sup>2)</sup> JANAF Thermochemical Tables.Table 2.4 Binding energy for MO<sub>1.5</sub>, MO<sub>2</sub> and MO<sub>1.75</sub> at 298 K.

	$E_{\text{B.E.}} \text{ (kJ} \cdot \text{mol}^{-1})$		
	MO <sub>1.5</sub>	MO <sub>2</sub>	MO <sub>1.75</sub> (1/2M <sub>2</sub> O <sub>3.5</sub> )
Ti	1602	1912	1757
V	1497	1727	1612
Cr	1340	1492	1416
Mn	1133	1296	1215

estimation also demonstrates that the order of the OCV can be explained qualitatively by association with the binding energy.

An important parameter expressing the structural stability is the lattice volume change during the extraction-insertion process. For the Li/Li<sub>x</sub>Co<sub>1/6</sub>Mn<sub>11/6</sub>O<sub>4</sub> cell, the volume change during cycling (from  $x \approx 0.95$ ,  $a \approx 8.20 \text{ \AA}$ ,  $V \approx 551 \text{ \AA}^3$  to  $x \approx 0.20$ ,  $a \approx 8.05 \text{ \AA}$ ,  $V \approx 522 \text{ \AA}^3$ ) was *ca.* 5%, while for the Li/Li<sub>x</sub>Co<sub>1/3</sub>Mn<sub>5/3</sub>O<sub>4</sub> cell, the volume change during cycling (from  $x \approx 0.95$ ,  $a \approx 8.17 \text{ \AA}$ ,  $V \approx 545 \text{ \AA}^3$  to  $x \approx 0.40$ ,  $a \approx 8.05 \text{ \AA}$ ,  $V \approx 522 \text{ \AA}^3$ ) was *ca.* 4%. The smaller the volume change is, the more stable is the structure. The Li/Li<sub>x</sub>M<sub>1/3</sub>Mn<sub>5/3</sub>O<sub>4</sub> (M = Co and Cr) cells were stable over long cycles at the expense of capacity.

While almost all the Li<sup>+</sup> can be removed electrochemically from the LiMn<sub>2</sub>O<sub>4</sub> structure leading to  $\lambda$ -MnO<sub>2</sub> at full charge,<sup>12,34,67)</sup> it is difficult to remove all the Li<sup>+</sup> from the doped spinel phases; this keeps the structural framework intact even at overcharge.

### 2.6.5 The Chemical Diffusion Coefficients of Lithium Ions in Li<sub>x</sub>M<sub>y</sub>Mn<sub>2-y</sub>O<sub>4</sub> (M = Co and Cr)

In order to further understand the doping effect on the spinel phases, the chemical diffusion coefficients of lithium ions in Li<sub>x</sub>M<sub>y</sub>Mn<sub>2-y</sub>O<sub>4</sub> (M = Co and Cr) cathodes were measured using the current pulse relaxation technique (CPR)<sup>68)</sup> in the following two-electrode electrochemical cells:

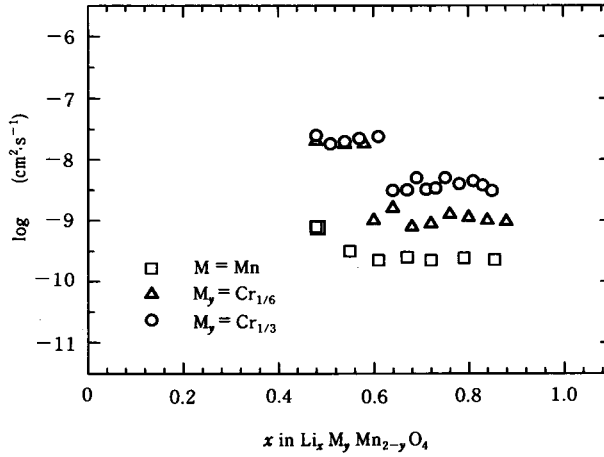


Fig. 2.13 The chemical diffusion coefficients of lithium in  $\text{Li}_x\text{Cr}_y\text{Mn}_{2-y}\text{O}_4$  ( $y = 0, 1/6$  and  $1/3$ ) at various lithium compositions.

$\text{Li} | 1 \text{ M LiClO}_4 \text{ in PC} | \text{Li}_x\text{M}_y\text{Mn}_{2-y}\text{O}_4$  ( $\text{M} = \text{Co}$  and  $\text{Cr}$ )

The cell was first galvanostatically charged to 4.50 V (vs.  $\text{Li}/\text{Li}^+$ ), then discharged galvanostatically to a given lithium composition  $x$  at a current density of  $0.1 \text{ mA} \cdot \text{cm}^{-2}$  (Charge-Discharge Unit HJ-201B, Hokuto Denko). After the cell was equilibrated at each lithium composition, lithium was injected into the cathode by a constant current pulse ( $0.5 \text{ mA} \cdot \text{cm}^{-2}$ ) for a short time (10 s). The chemical diffusion coefficients of lithium ions ( $\bar{D}$ ) was calculated from the decay rate of the transient voltage using the following equation.

$$\bar{D} = \left[ \frac{V_M (dE/dx)}{nFa} \frac{i\tau}{\Delta E / \Delta(t^{-1/2})} \right]^2 \quad (2.12)$$

where  $V_M$  is molar volume,  $dE/dx$  the slope of the equilibrium potential-composition curve,  $F$  is Faraday's constant,  $a$  the surface area,  $i$  the intensity of current pulse,  $\tau$  pulse duration, and  $\Delta E / \Delta(t^{-1/2})$  the slope of the straight line obtained from the plot of the relaxation potential vs.  $t^{-1/2}$  after the current pulse is stopped.

The quasi open-circuit voltage (OCV) curves of the cells were measured by the galvanostatic intermittent charge-discharge method mentioned above.

Figure 2.13 shows the variation of the  $\bar{D}$  values, the chemical diffusion coefficients of lithium ions in  $\text{Li}_x\text{Cr}_y\text{Mn}_{2-y}\text{O}_4$  for  $y = 0, 1/6$  and  $1/3$  as a function of composition  $x$ . The  $\bar{D}$  values in the  $\text{LiMn}_2\text{O}_4$  electrode ( $y = 0$ ) were between  $10^{-9}$  and  $10^{-10} \text{ cm}^2 \cdot \text{s}^{-1}$  in the range of  $0.2 \leq x \leq 0.85$ . The  $\bar{D}$  values in the Cr-doped  $\text{Li}_x\text{Cr}_y\text{Mn}_{2-y}\text{O}_4$  electrodes were larger than those in the  $\text{LiMn}_2\text{O}_4$  electrode, and the  $\bar{D}$  values suddenly increased one or one and a half order of magnitude near  $x = 0.5$ . For  $y = 1/3$ , the  $\bar{D}$  values were at least one order of magnitude larger than those in the  $\text{LiMn}_2\text{O}_4$  electrode. The  $\bar{D}$  values in the  $\text{LiMn}_2\text{O}_4$  electrode measured using the potentiostatic intermittent titration technique (PITT) by Guyomard and Tarascon<sup>64)</sup> were in the order of  $10^{-9} \text{ cm}^2 \cdot \text{s}^{-1}$ . The variations of the  $\bar{D}$  values in  $\text{Li}_x\text{Co}_{1/6}\text{Mn}_{11/6}\text{O}_4$  cathode are almost the same as that in the  $\text{Li}_x\text{Cr}_{1/6}\text{Mn}_{11/6}\text{O}_4$

cathode. At the same doping concentration for Co and Cr, the  $\tilde{D}$  values were almost the same as a value on the order of  $10^{-9} \text{ cm}^2 \cdot \text{s}^{-1}$  except for the range in compositions near  $x=0.5$ .<sup>69)</sup> Since lithium ions occupy half the tetrahedral  $8a$  sites at  $x=0.5$ , ordered arrangement of lithium ions may be formed and this would contribute to the one order higher  $\tilde{D}$  values. An order-disorder phase transformation near  $x=0.5$  for  $\text{Li}_x\text{Cr}_y\text{Mn}_{2-y}\text{O}_4$  seems to accelerate the diffusion of lithium ions in the spinel structure. These results confirm a reasonable mobility of lithium ions in doped spinel electrodes.

The fact that the increase of the chemical diffusion coefficients of lithium ions in the cathodes by the doping can be explained by considering the changes in metal–oxygen bonding in the spinel structure. As mentioned above, it is reasonable to assume that the Co–O and Cr–O bonds are stronger than the Mn–O bond. Therefore, in the doped spinel phases, the total metal–oxygen bonding is stronger than that in the parent  $\text{LiMn}_2\text{O}_4$  phase. This results in weaker lithium–oxygen bonding and leads to easier lithium diffusion in the cathode. Obviously, the increase in the chemical diffusivity of lithium also contributes to the improvement in the cycling performance of doped manganese spinel cathodes.

### 2.6.6 Low Temperature Behavior

For practical application, the electrode performance at low temperature is an important aspect of the batteries because the batteries may need to work over a wide temperature range, for example, from  $-20^\circ\text{C}$  to  $40^\circ\text{C}$ . Comparison of Cr-doped spinel phase  $\text{LiCr}_y\text{Mn}_{2-y}\text{O}_4$  ( $y=1/9$  and  $1/6$ ) and  $\text{LiMn}_2\text{O}_4$  will be given here on the basis of thermal analysis and XRD experiments at low temperature.

Figure 2.14 shows the curves of the differential scanning calorimetry (DSC) for  $\text{LiCr}_y\text{Mn}_{2-y}\text{O}_4$  ( $y=0, 1/9$  and  $1/6$ ) phases. For  $\text{LiMn}_2\text{O}_4$  sample, an exothermic process occurred in a wide temperature range ( $\sim 601 \text{ J} \cdot \text{mol}^{-1}$ ), from *ca.* 280 K to 240 K, when the sample was cooled from room temperature to 100 K. For the doped phase, when dopant content is not high enough, for example, an exothermic process was also detected in  $\text{LiCr}_{1/9}\text{Mn}_{17/9}\text{O}_4$  sample ( $\sim 60 \text{ J} \cdot \text{mol}^{-1}$ ), but the thermal process occurred in a narrower

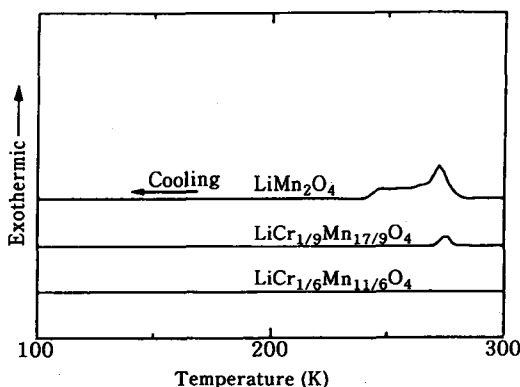


Fig. 2.14 DSC curves for  $\text{Li}_x\text{Cr}_y\text{Mn}_{2-y}\text{O}_4$  ( $y=0, 1/9$  and  $1/6$ ) phases.

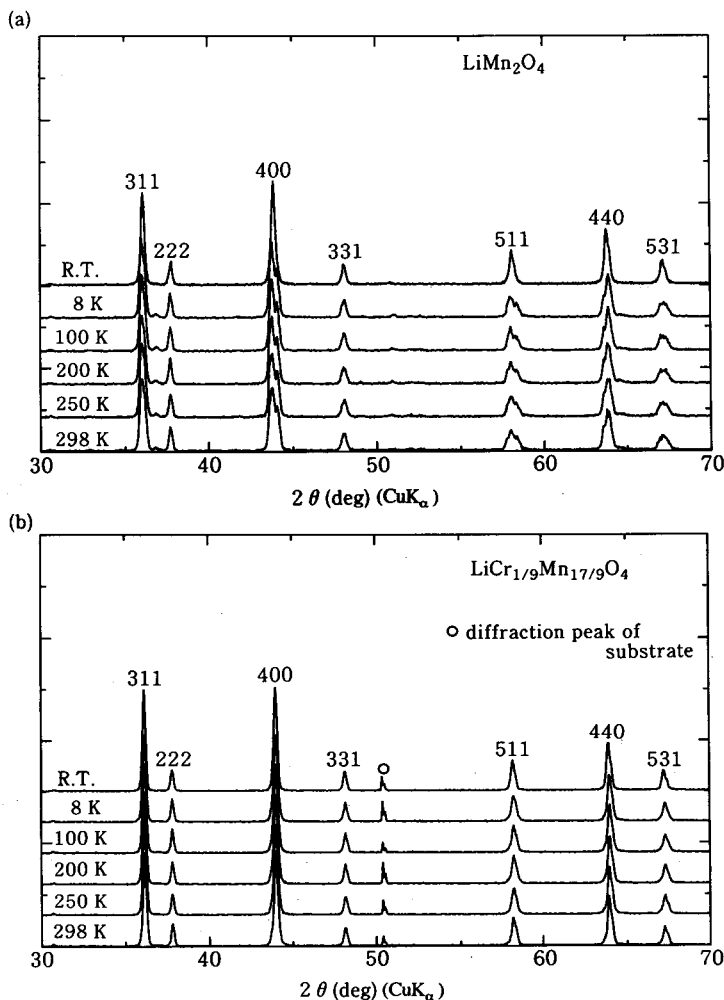


Fig. 2.15 Powder XRD patterns at different temperatures of (a)  $\text{LiMn}_2\text{O}_4$  and (b)  $\text{LiCr}_{1/9}\text{Mn}_{17/9}\text{O}_4$ .

temperature range (from 280 K to 270 K) with smaller heat emission. When dopant content was increased, as for the situation for  $\text{LiCr}_{1/6}\text{Mn}_{11/6}\text{O}_4$ , no thermal emission occurred in the whole temperature range of 300–100 K. Obviously, the doping atoms suppressed the processes which result in the thermal event. Generally, exothermic processes are related to oxidation or solid-solid phase transition.

In order to understand the process further, XRD measurements were carried out at low temperatures. Fig. 2.15 shows powder XRD patterns of  $\text{LiMn}_2\text{O}_4$  and  $\text{LiCr}_{1/9}\text{Mn}_{17/9}\text{O}_4$  at different temperatures. The XRD data were collected by the following procedure. The XRD data were first measured at room temperature (the curve labeled R.T. in both Figs. 2.15a and 15b), then temperature was lowered to an extremely low temperature, 8 K, and the XRD data were collected at different rising temperatures. Clearly, at room temperature, the XRD pattern of  $\text{LiMn}_2\text{O}_4$  was identical to that of  $\text{LiCr}_{1/9}\text{Mn}_{17/9}\text{O}_4$ , which

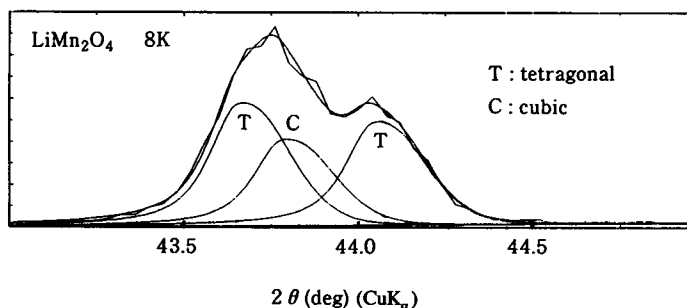


Fig. 2.16 Scattering peak near 44 degrees ( $2\theta$ ) of  $\text{LiMn}_2\text{O}_4$  at 8 K and peak separation by the Rietveld method.

can be identified as a single phase of cubic spinel. All the scattering peaks were sharp without splitting. At low temperatures, the XRD patterns of  $\text{LiCr}_{1/9}\text{Mn}_{17/9}\text{O}_4$  changed little, *i.e.*, the cubic symmetry was maintained at low temperatures even as low as 8 K. By contrast, peak splitting of several Bragg peaks such as [400], [511], [440] and [531] could be observed from the XRD patterns of  $\text{LiMn}_2\text{O}_4$  at low temperatures.

In order to understand the change in the structure further, structure refinement was carried out by Rietveld method using RIETAN.<sup>70)</sup> As an example, the result of peak separation for the peaks between 43.5 and 44.5 degrees is shown in Fig. 2.16. These peaks can be considered as a combination of two peaks belonging to a tetragonal lattice and a cubic lattice. Therefore, a phase transition from cubic to tetragonal spinel occurs when the temperature is lowered. Once the phase transition occurs in  $\text{LiMn}_2\text{O}_4$ , reversible recovery of tetragonal phase to cubic cannot be achieved even though the temperature is increased to 298 K. The XRD pattern of  $\text{LiCr}_{1/9}\text{Mn}_{17/9}\text{O}_4$  at 8 K was almost the same as that at room temperature except for a little decrease in diffraction intensity. Such excellent structure stability at such low temperatures offers low temperature cycling properties for the doped spinel cathode. Thus the conclusion is that the doped spinel phases were more tolerant to changes in temperature than  $\text{LiMn}_2\text{O}_4$ .

The doping cations affect not only cycle performance at ambient temperature but also low temperature properties.

## 2.7 Conclusions

Cathode materials such as spinel oxides with a three-dimensional framework exhibit very interesting lithium intercalation properties. Three-dimensional compounds have advantages over two-dimensional layered compounds, most notably in structural stability, easier lithium diffusion, and cycle life. Improved cycle life in rechargeable  $\text{Li}/\text{Li}_x\text{M}_y\text{Mn}_{2-y}\text{O}_4$  ( $\text{M} = \text{Co}, \text{Cr}$  and  $\text{Ni}$ ) cells has been demonstrated at the expense of capacity at room temperature. This improvement is attributed to the enhancement in the stability in the spinel structure and increase in lithium diffusivity by doping. Moreover, phase transition occurring at low temperature was also suppressed by doping. This results in an improvement on low temperature performance of batteries. Among these doped phases,

the cobalt-doped manganese spinel phase  $\text{LiCo}_{1/6}\text{Mn}_{11/6}\text{O}_4$  is the most promising candidate to replace  $\text{LiCoO}_2$  as the cathode material for lithium ion batteries.

The volume change during intercalation-deintercalation processes is an important parameter for predicting cycle life. Electrode materials (both cathode and anode) with a smaller volume change are favorable to a long cycle life. For doped manganese spinel phases, the volume change during the lithium insertion-extraction was less than 5%.

Further development of lithium ion batteries will require cooperative research on cathode materials, anode materials, electrolytes and technical design. Such comprehensive researches will lead to a new field in materials science for advanced batteries.

#### REFERENCES

- 1) D.W. Murphy and J.N. Carides, *J. Electrochem. Soc.*, **126**, 349 (1979).
- 2) M. Lazzari and B. Scrosati, *J. Electrochem. Soc.*, **127**, 773 (1980).
- 3) T. Nagaura and K. Tazawa, *Progr. Batteries Solar Cells*, **9**, 20 (1990).
- 4) Y. Nishi, Proc. 3rd Sony Res. Forum, Tokyo, p. 333, November, 1993.
- 5) K. Hoshino, T. Murakami, A. Ohtsuka, Y. Ozaki, S. Watanabe and Y. Takahashi, *National Technical Report*, **40**, 455 (1994).
- 6) K. Ozawa, *Solid State Ionics*, **69**, 212 (1994).
- 7) J.R. Dahn, U. von Sacken, M.R. Jukow and H. Al-Janaby, *J. Electrochem. Soc.*, **138**, 2207 (1991).
- 8) W. Ebner, D. Fouchard and L. Xie, *Solid State Ionics*, **69**, 238 (1994).
- 9) C. Delmas, I. Saadoun and A. Rougier, *J. Power Sources*, **43-44**, 595 (1993).
- 10) R. J. Gummow and M.M. Thackeray, *J. Electrochem. Soc.*, **140**, 3365 (1993).
- 11) J.M. Tarascon, E. Wang, F.K. Shokoohi, W.R. McKinnon and S. Colson, *J. Electrochem. Soc.*, **138**, 2859 (1991).
- 12) T. Ohzuku, M. Kitagawa and T. Hirai, *J. Electrochem. Soc.*, **137**, 769 (1990).
- 13) J.M. Tarascon and D. Guyomard, *Electrochim. Acta*, **38**, 1221 (1991).
- 14) J.M. Tarascon, W.R. McKinnon, F. Coowar, T.N. Boowmer, G. Amatucci and D. Guyomard, *J. Electrochem. Soc.*, **141**, 1421 (1994).
- 15) D. Guyomard and J.M. Tarascon, *Solid State Ionics*, **69**, 222 (1994).
- 16) J.M. Tarascon and D. Guyomard, *Solid State Ionics*, **69**, 293 (1994).
- 17) R. J. Gummow, A. de Kock and M.M. Thackeray, *Solid State Ionics*, **69**, 59 (1994).
- 18) D.W. Murphy, P.A. Christian, F. J. Disalvo and J.V. Waszczak, *Inorg. Chem.*, **18**, 2800 (1979).
- 19) P.G. Dickens, S.J. French, A.T. Hight and M.F. Pye, *Mater. Res. Bull.*, **14**, 1295 (1979).
- 20) C. Delmas, S. Br  thes and M. M  n  trier, *J. Power Sources*, **34**, 113 (1991).
- 21) K.M. Abraham, *J. Power Sources*, **7**, 1 (1981/82).
- 22) J.B. Goodenough, A. Manthiram and A.C.W. James, *Mater. Res. Soc. Symp. Proc.*, **135**, 391 (1989).
- 23) B. Zachau-Christiansen, K. West, T. Jacobsen and S. Atlung, *Solid State Ionics*, **40/41**, 580 (1990).
- 24) Li Guohua, H. Ikuta, T. Uchida and M. Wakihara, *J. Power Sources*, **54**, 519 (1995).
- 25) M. Wakihara, H. Ikuta and T. Uchida, *J. Power Sources*, **43-44**, 651 (1993).
- 26) S. Yamaguchi, T. Uchida and M. Wakihara, *J. Electrochem. Soc.*, **138**, 687 (1991).
- 27) M. Wakihara, T. Uchida, K. Suzuki and M. Taniguchi, *Electrochim. Acta*, **34**, 867 (1989).
- 28) P. J. Mulhern and R.R. Hareing, *Can. J. Phys.*, **62**, 527 (1984).
- 29) D.W. Murphy, R. J. Cava, S.M. Zahurak and A. Santoro, *Solid State Ionics*, **9/10**, 413 (1983).
- 30) L. A. de Picciotto and M.M. Thackeray, *Mater. Res. Bull.*, **20**, 1409 (1985).
- 31) L. A. de Picciotto and M.M. Thackeray, *Solid State Ionics*, **18/19**, 773 (1986).
- 32) G. Pistoia, M. Pasquali, L.A. de Picciotto and M.M. Thackeray, *Solid State Ionics*, **28**, 879 (1988).
- 33) M.M. Thackeray, W.I.F. David, P.G. Bruce and J.B. Goodenough, *Mater. Res. Bull.*, **18**, 461 (1983).
- 34) M.H. Rossouw, A. de Kock, L. A. de Picciotto, M.M. Thackeray, W.I.F. David and R.M. Ibberson, *Mater. Res. Bull.*, **25**, 173 (1990).
- 35) F. Lubin, A. Lecerf, M. Broussely and J. Labat, *J. Power Sources*, **34**, 161 (1991).
- 36) K.M. Colbow, J.R. Dahn and R.R. Haering, *J. Power Sources*, **26**, 397 (1989).
- 37) L.A. de Picciotto and M.M. Thackeray, *Mater. Res. Bull.*, **21**, 583 (1986).
- 38) D.G. Wickham and W. J. Croft, *J. Phys. Chem. Solids*, **7**, 351 (1958).
- 39) D.B. Rogers, J.B. Goodenough and A. Wold, *J. Appl. Phys.*, **35**, 1069 (1964).

- 40) D.B. Rogers, J.L. Gillson and I.E. Gier, *Solid State Commun.*, **5**, 263 (1967).
- 41) L.A. de Picciotto and M.M. Thackeray, *Mater. Res. Bull.*, **20**, 187 (1985).
- 42) A. Manthiram and J.B. Goodenough, *Can. J. Phys.*, **65**, 1309 (1987).
- 43) M.G.S.R. Thomas, W.I.F. David and J.B. Goodenough, *Mater. Res. Bull.*, **20**, 1137 (1985).
- 44) R. J. Gummow, D.C. Liles and M.M. Thackeray, *Mater. Res. Bull.*, **28**, 235 (1993).
- 45) Li Guohua, K. Sakuma, H. Ikuta, T. Uchida, M. Wakihara and Guo Hetong, *Denki Kagaku*, **64**, 202 (1996).
- 46) Li Guohua, H. Ikuta, T. Uchida and M. Wakihara, 35th Battery Symp. Japan, Nagoya, Japan, November 1977, Ext. Abstr., p. 171.
- 47) M. Wakihara, Li Guohua, K. Sakuma, H. Ikuta and T. Uchida, Proc. Symp. Rechargeable Lithium and Lithium-Ion Batteries, (Eds. by S. Megahed, B. M. Barnett and L. Xie), Pennington, NJ, USA, **PV94-28**, p. 53 (1995).
- 48) M. Wakihara, Li Guohua, H. Ikuta and T. Uchida, Proc. Int. Workshop Advan. Batteries, Osaka, Japan, p. 47, February (1995).
- 49) D.W. Murphy, M. Greenblatt, S.M. Zahurak, R.J. Cava, J.V. Waszczak, G.W. Hull, Jr. and R.S. Hutton, *Rev. Chim. Miner.*, **19**, 441 (1982).
- 50) A. Momchilov, V. Manev and A. Nassalevska, *J. Power Sources*, **41**, 305 (1993).
- 51) Li Guohua, H. Ikuta, T. Uchida and M. Wakihara, *J. Electrochem. Soc.*, **143**, 178 (1996).
- 52) Li Guohua, H. Ikuta, T. Uchida and M. Wakihara, 36th Battery Symp. Japan, Kyoto, Japan, September, 1995, Ext. Abstr., p. 181.
- 53) A. Yamada, K. Miura, K. Hinokuma and M. Tanaka, *J. Electrochem. Soc.*, **142**, 2149 (1995).
- 54) H. Hosoya, H. Ikuta, T. Uchida and M. Wakihara, 36th Battery Symp. Japan, Kyoto, Japan, September 1995, Ext. Abstr., p. 69.
- 55) H. Ikuta, T. Uchida and M. Wakihara, 36th Battery Symp. Japan, Kyoto, Japan, September 1995, Ext. Abstr., p. 31.
- 56) T. Uchida, Y. Tanjo, M. Wakihara and M. Taniguchi, *J. Electrochem. Soc.*, **137**, 7 (1990).
- 57) B.E. Douglas and C.A. Hollingworth, *Symmetry in Bonding and Spectra*, p. 226, Academic Press (1985).
- 58) P.A. Cox, *The Electronic Structure and Chemistry of Solids*, Chapter 5, Oxford Univ. Press (1987).
- 59) J.M. Tarascon and D. Guyomard, *J. Electrochem. Soc.*, **138**, 2864 (1991).
- 60) Wang Baochen, Xia Yongyao, Feng Li and Zhao Dongjing, *J. Power Sources*, **43-44**, 539 (1993).
- 61) S. Kanno and M. Sato, *Solid State Ionics*, **79**, 215 (1995).
- 62) R. Bittihn, R. Herr and D. Hoge, *J. Power Sources*, **43-44**, 223 (1993).
- 63) G. Pistoia and G. Wang, *Solid State Ionics*, **66**, 135 (1993).
- 64) D. Guyomard and J.M. Tarascon, *J. Electrochem. Soc.*, **139**, 937 (1992).
- 65) H. Ikuta, T. Uchida and M. Wakihara, 35th Battery Symp. Japan, Nagoya, Japan, November 1994, Ext. Abstr., p. 155.
- 66) H. Ikuta, D. Nakazato, T. Uchida and M. Wakihara, *J. Solid State Chem.*, submitted.
- 67) M.M. Thackeray, P.J. Johnson, L.A. de Picciotto, P.G. Bruce and J.B. Goodenough, *Mater. Res. Bull.*, **19**, 179 (1984).
- 68) S. Basu and W.L. Worrell, *Fast Ion Transport in Solids* (Eds. by P. Vashishta, J.N. Mundy and G.K. Shenoy), p. 149, Elsevier North-Holland (1979).
- 69) M. Wakihara, Li Guohua, H. Ikuta and T. Uchida, *Solid State Ionics*, **86-88**, 907 (1996).
- 70) F. Izumi, *The Rietveld Method* (Ed. by R. A. Young), Chapter 13, Oxford Univ. Press (1993).



## 3

## The Relationship between Structure and Cell Properties of the Cathode for Lithium Batteries

M. Stanley Whittingham\*

## 3.1 Introduction

Only a quarter of a century ago was the critical role that crystal structure plays in the electrochemical behavior of solids recognized. It is the crystal structure that controls the kinetics of reaction within the solid, and more specifically allows for insertion and specifically intercalation reactions that are now routinely assumed to dominate in electrochemical redox reactions.<sup>1-3)</sup> Not only were the observed emfs not consistent with the reactions proposed then, *e.g.*,



but such reactions would require the complete destruction and reconstruction of the crystalline lattice, an unlikely situation. Cell emfs and structural considerations were more consistent with the reaction<sup>4)</sup>:



In historical perspective non-stoichiometric transition metal oxides/chalcogenides such as the tungsten bronzes,  $\text{Na}_x\text{WO}_3$ , were first used as the electrodes for measuring the ionic transport properties of the electrolyte beta-alumina.<sup>5,6)</sup> This first use of mixed conducting oxides for measuring ion transport in electrolytes was found to be critically dependent on the structure of the oxide. The tungsten bronzes take up a variety of structures depending on the size of the alkali (or other) ion found in the tunnels of the tungsten oxide matrix; the tunnels may be surrounded by 3, 4, 5 or 6 corner sharing  $\text{WO}_6$  octahedra. For measuring the ionic conductivity of sodium beta-alumina, the diffusion of the sodium ions in the simple cubic phase was not found to be sufficiently high to allow the structure to act as a sodium reversible electrode. However, the tetragonal phase was found to be suitable<sup>5)</sup> as was the sodium vanadium bronze.<sup>3)</sup> For potassium, high ionic mobility is found in the hexagonal structure. Hydrogen and lithium show high mobility in the cubic phase, and extensive studies have been made of these insertion reactions because of the color changes that occur that lead to their potential use in electrochromic displays.

---

\* Chemistry Department and Materials Research Center, State University of New York at Binghamton, Binghamton, NY 13902, USA

At about the same time, much interest was expressed in the behavior of graphite as the container of anode and cathode active materials.  $\text{CF}_x$  was the cathode of the Matsushita lithium primary cell, transition metal oxides were "inserted" into graphite and studied as the cathode of lithium cells by Armand,<sup>7,8)</sup> and the all-graphite cell:  $\text{C}_8\text{K}(\text{anode})//\text{C}_8\text{Br}(\text{cathode})$  was proposed as an all-intercalation battery.<sup>1)</sup>

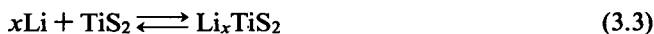
The tungsten bronzes showed the promise of insertion reactions as the basis for solid electrodes of high energy density batteries. However, lower equivalent weight materials were needed. Thus, intercalation electrodes, whose structure remains essentially unchanged over wide composition ranges and best exemplified by the layered dichalcogenides such as  $\text{Li}_x\text{TiS}_2$ , for  $0 \leq x \leq 1$ , were extensively studied as the cathode for high energy density lithium batteries.<sup>4,9,10)</sup> The structurally identical oxides, such as  $\text{Li}_x\text{CoO}_2$ , were found to behave similarly,<sup>11)</sup> and have since been commercialized by Sony and other Japanese companies for small reversible lithium batteries. These batteries also rely on an intercalation anode, such as lithium intercalated graphite/coke. Sodium intercalation reactions with  $\text{TiS}_2$  have also been proposed for battery use,<sup>2)</sup> but their poor capacity/reversibility due to changes of structure, overall low energy density, and safety concerns have essentially eliminated them from further consideration.<sup>12,13)</sup>

The role of structure in the above layered sulfide and oxide materials will be examined, as it indicates what will be required for commercial applications even though both have limitations that may prevent their use in large scale consumer devices, such as electric vehicles. The  $\text{Li}/\text{TiS}_2$  couple has too low a voltage, 1.7–2.5 V, for use with carbon-containing anodes. Cobalt-containing cathodes are much too expensive to be used in any but the most specialized, or very small cells where the active material costs are minimal. Moreover, the  $\text{Li}/\text{Li}_x\text{CoO}_2$  couple cycles less than one lithium per cobalt and thus has no higher an energy density than  $\text{Li}/\text{TiS}_2$ .<sup>14)</sup> The key attributes that any successful cathode material needs are:

- (1) A high free energy of reaction with lithium; this equates to  $\geq 1$  Li reacting per transition metal, and a cell voltage of 3.0–3.5 V. The last dictates that the anion be oxygen (or possibly a halide).
- (2) Rapid reaction with lithium ions to give a high power density. Electrochemically this equates to a rate of  $10 \text{ mA} \cdot \text{cm}^{-2}$ ,<sup>15)</sup> and such a rate would cause a solution of *n*-butyl lithium to boil on reaction with the oxide.
- (3) Complete chemical reversibility, which is most easily attained if the crystalline structure does not change during reaction with lithium.
- (4) Low cost and low toxicity.

### 3.2 Titanium Disulfide and Intercalation Chemistry

The now classical intercalation electrode is titanium disulfide, which readily and reversibly reacts with lithium either electrochemically or chemically according to the equation:



The lamellar lattice, exemplified in Fig. 3.1, simply expands perpendicular to the  $\text{TiS}_2$  sheets from 5.7 in  $\text{TiS}_2$  itself to 6.2 Å in  $\text{LiTiS}_2$ . This is a single phase over the entire composition

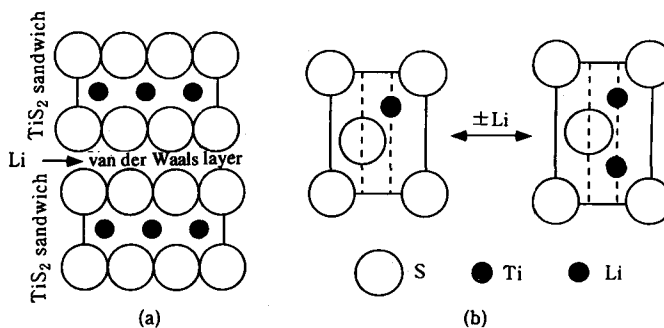


Fig. 3.1 (a) Schematic structure of  $\text{TiS}_2$ , showing the  $\text{TiS}_2$  sandwiches between which lithium ions can be inserted, and (b) 110 projection of structure of  $\text{TiS}_2$  and  $\text{LiTiS}_2$ . It should be noted that the lithium and titanium atoms reside directly above one another.

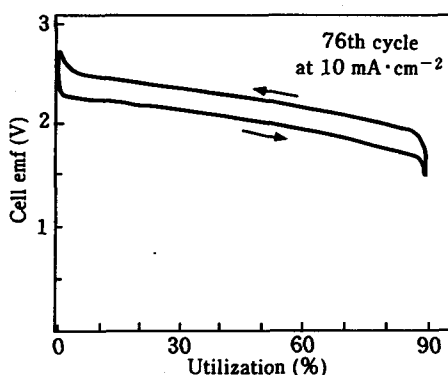


Fig. 3.2 Cycling of  $\text{TiS}_2$  at  $10 \text{ mA} \cdot \text{cm}^{-2}$ , after Ref. 13.

range, so no energy need be expended in nucleating a new phase. This single phase behavior is noted in the continuous variation of the  $c$  lattice parameter from  $5.7 \text{ \AA}$  to  $6.2 \text{ \AA}$ , and in the emf of a  $\text{Li}/\text{Li}_x\text{TiS}_2$  cell from around  $2.5 \text{ V}$  to  $1.87 \text{ V}$ . The free energy of formation of  $\text{LiTiS}_2$  from  $\text{Li}$  and  $\text{TiS}_2$  is  $-206 \text{ kJ} \cdot \text{mol}^{-1}$ , which corresponds to a theoretical energy storage of  $473 \text{ Wh} \cdot \text{kg}^{-1}$ . The high electrical conductivity of titanium disulfide<sup>16)</sup> removes the need for the addition of conductive diluents such as carbon black, so that practical electrodes can approach more closely the theoretical capacity.

The soft nature of the  $\text{TiS}_2$  lattice enhances the diffusion of lithium ions, so that very high rates of reaction can be obtained. Thus, addition of  $\text{TiS}_2$  to  $n$ -butyl lithium solutions causes them to boil, and rates of  $10 \text{ mA} \cdot \text{cm}^{-2}$  can be readily achieved with complete reversibility in electrochemical cells.<sup>13)</sup> A typical cell cycling curve at  $10 \text{ mA} \cdot \text{cm}^{-2}$  is shown in Fig. 3.2; the electrolyte resistance accounts for the difference in the discharge and charge curves, there is essentially no electrode polarization. Few other electrodes have shown this rate capability in lithium cells; surprisingly vanadium diselenide may be almost as rapid even though it is a two-phase reaction.<sup>13)</sup> This high rate results from the high values of the lithium chemical and self diffusion coefficients in  $\text{Li}_x\text{TiS}_2$ , which are  $10^{-8} \text{ cm}^2 \cdot \text{s}^{-1}$  and  $10^{-9} \text{ cm}^2 \cdot \text{s}^{-1}$ , respectively.  $\text{TiS}_2$  cells have been cycled for more than 500 cycles

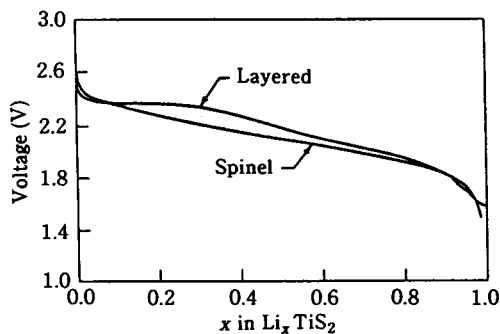


Fig. 3.3 The emf of lithium intercalation into layered and cubic  $\text{TiS}_2$ .  
(Reproduced with permission by S. Shinha and D.W. Murphy, *Solid State Ionics*, **20**, 81 (1986))

at rates up to  $10 \text{ mA} \cdot \text{cm}^{-2}$ , with capacity loss of around 30%. Even today,  $\text{TiS}_2$  is of interest for thin film batteries to be used in microelectronic applications, where long life is critical.<sup>17)</sup>

The phase  $\text{Li}_x\text{TiS}_2$  is the thermodynamically stable compound over the entire range of lithium composition, so that there is no tendency to disproportionate for example to  $\text{Li}_2\text{S}$  and  $\text{Ti}_2\text{S}_3$ . Nor does there appear to be any tendency for the lithium and titanium to disorder in the lattice, and only at high temperatures is there any tendency for the titanium atoms to migrate into the van der Waals layer. Thus, there is no degradation of the electrode's properties by disordering of the transition metal as apparently occurs in nickel and manganese oxides. However, titanium disulfide can be formed with excess titanium,  $\text{Ti}_{1+y}\text{S}_2$ , and this excess resides in the same layer where the lithium intercalation occurs. This results in a pinning of the lattice so that the lithium diffusion rate is reduced, leading to lower discharge rates; in addition, the overall capacity is reduced because the titanium occupies some of the sites normally occupied by lithium. However, a very little excess titanium is desired as it reduces the sulfur thermodynamic activity and thereby the corrosion rate of the container and the possible solubility of excess sulfur in the electrolyte.

A cubic form of  $\text{TiS}_2$  has been formed by the deintercalation of copper from the spinel  $\text{CuTi}_2\text{S}_4$ .<sup>18,19)</sup> A slight excess of titanium had to be present to remove all the copper. Surprisingly, the volumes of the unit cells of  $\text{Li}_x\text{TiS}_2$  and cubic  $\text{Li}_x\text{TiS}_2$  are almost identical, and both show a volume change of 10.7% between  $x=0$  and  $x=1$ . This suggests that the volume is controlled by close packed sulfurs, with their effective size increasing with electron donation from lithium. For cubic  $\text{Li}_x\text{TiS}_2$  the volume change is isotropic and the lattice parameter changes linearly with lithium content,  $a = 9.74 + 0.34x \text{ \AA}$ .<sup>19)</sup> This linear behavior is consistent with all the lithium ions residing on a single type of site, and neutron diffraction confirmed that they reside on octahedral sites.<sup>20)</sup> Thus, just as in layered  $\text{LiTiS}_2$ , all the octahedral sites are occupied and the tetrahedral sites remain vacant.

The cell emf data, Fig. 3.3, are almost identical for the two forms of  $\text{Li}_x\text{TiS}_2$ , with the layered material showing a slight plateau at around  $x=0.25$  due to partial ordering of the lithium.<sup>21)</sup> That the thermodynamic curve of the cubic form shows no break is another clear indication that all the lithium resides on the same group of sites. The Gibbs energy of formation from  $\text{TiS}_2$  of the two forms of  $\text{LiTiS}_2$  are very similar; however, cubic  $\text{TiS}_2$  converts to the layered form on heating to  $400^\circ\text{C}$ ,<sup>19)</sup> suggesting that the cubic form has a lower free energy of formation than the layered form. The lithium chemical diffusion

coefficient in the cubic phase varies from  $10^{-9} \text{ cm}^2 \cdot \text{s}^{-1}$  to  $10^{-10} \text{ cm}^2 \cdot \text{s}^{-1}$  depending on  $x$  in  $\text{Li}_x\text{Cu}_{0.07}\text{TiS}_2$ ,<sup>20)</sup> about one order of magnitude lower than in layered  $\text{TiS}_2$ .<sup>13)</sup> This indicates that diffusion in spinel lattices may be more difficult than in layered lattices. The cubic form can also be cycled,<sup>22)</sup> but little work has been reported on it.

### 3.3 Vanadium Dichalcogenides

Vanadium diselenide is another high-rate cathode like titanium disulfide. However, in this case the reactions occurring are not single phase. As shown in Fig. 3.4, the discharge curve shows at least three plateaus, indicative of two-phase behavior. In the discharge of the first lithium, two-phases are formed  $\text{LiVSe}_2$  and  $\text{Li}_x\text{VSe}_2$  where  $x$  is around 0.2.<sup>23)</sup> A second lithium ion may be intercalated. The rate characteristics of  $\text{VSe}_2$  are almost as good as  $\text{TiS}_2$ , despite the two-phase reaction mechanism.

Vanadium sulfides have also been investigated,<sup>24)</sup> but a number of distortions in the sulfide matrix restrict the cycling to around half a lithium per vanadium. Substitution of part of the vanadium by iron or chromium significantly increased the cycling capacity to around 0.8 Li.<sup>24)</sup> However, effort on the sulfides diminished because of a desire for a cell with a higher voltage that could be used with safer lithium intercalation anodes, and could power a computer CPU with a single cell. Vanadium oxides, such as  $\text{V}_6\text{O}_{13}$ ,<sup>25)</sup> and  $\text{LiCoO}_2$ <sup>11)</sup> were extensively studied and that experience can be of great help in determining the optimum structure for cathodes.

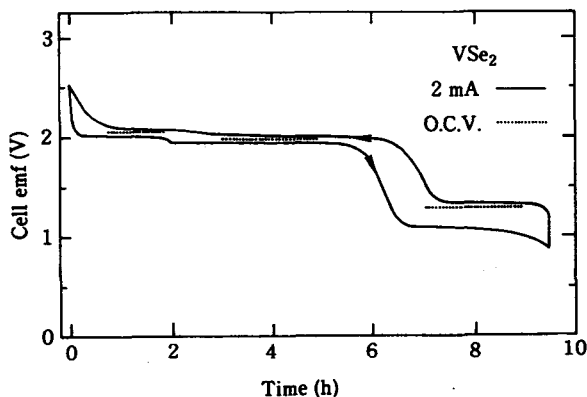


Fig. 3.4 The discharge curve of vanadium diselenide,<sup>23)</sup> showing the multiphase behavior.

### 3.4 Layered Oxides

It was found<sup>11)</sup> that  $\text{LiCoO}_2$  which can be formed at high temperatures can have its lithium removed electrochemically. It has the same structure (Fig. 3.5) as  $\text{LiZrS}_2$ ,<sup>13,26)</sup> and only differs from that of  $\text{LiTiS}_2$  in that the oxide layers are cubic close-packed, rather than hexagonal close-packed as in  $\text{LiTiS}_2$ .

The electrochemical behavior of lithium cobalt oxide is shown in Fig. 3.6,<sup>27)</sup> the very small polarization is notable and less than that in  $\text{LiNiO}_2$  or  $\text{LiMn}_2\text{O}_4$ . This cell has been cycled more than 500 times with 80–90% capacity retention, depending on discharge rate. The

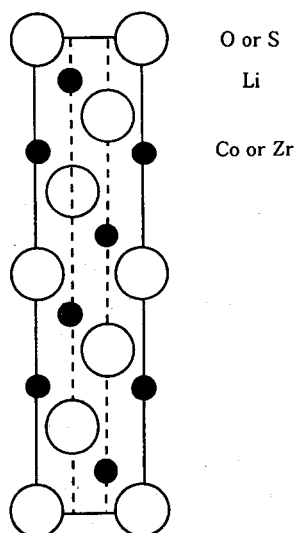


Fig. 3.5 110 projection of structure of  $\text{LiZrS}_2$  and  $\text{LiCoO}_2$ . (Note that the lithium and transition metal atoms do not reside above one another.)

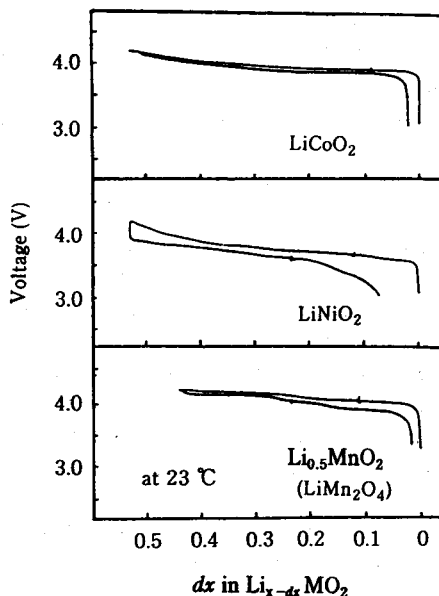


Fig. 3.6 The cycling behavior of  $\text{LiCoO}_2$ ,  $\text{LiNiO}_2$  and  $\text{LiMn}_2\text{O}_4$  at  $0.5 \text{ mA} \cdot \text{cm}^{-2}$  between 4.2 and 3.3 V. (Reproduced with permission by K. Ozawa, *Solid State Ionics*, **69**, 212 (1994))

capacity maintenance is critically dependent on the electrolyte used; this is probably associated with the very high potentials which can cause electrolyte decomposition. Energy densities of  $110 \text{ Wh} \cdot \text{kg}^{-1}$  have been achieved.  $\text{CoO}_2$  itself does exist<sup>28)</sup> and has the same 1T structure as  $\text{TiS}_2$  with  $a = 2.82 \text{ \AA}$  and  $c = 4.29 \text{ \AA}$ , but just a little lithium causes the structure to switch to 3R, which suggests there must be a two-phase region at low lithium concentrations just as in  $\text{Li}_x\text{ZrS}_2$ , where the lower limit of  $x$  is 0.25.<sup>29)</sup> Capacity loss on cycling is partially due to cobalt dissolution above 4.2 V, which restricts the charging regime<sup>28)</sup> and hence the capacity to around 0.5 Li/Co.

Sony has fully developed this very successful cell,<sup>27)</sup> and it is available for many electronic applications from several sources; it uses a lithium carbon anode in which the lithium intercalates an amorphous/graphitic carbon structure.

Cobalt oxide is, however, very expensive so substitutes must be found for larger scale applications. A number of other oxides, such as  $\text{LiNiO}_2$ , form the same layered structure but the nickel atoms tend to migrate at low lithium levels to the lithium sites, degrading the capacity and rate capability. However, this is much less marked in the case of cobalt, and in fact substitution of 20% of the nickel by cobalt in  $\text{LiNiO}_2$  appears to stabilize the structure at low lithium contents<sup>30)</sup>; 2% gallium substitution is also reported to improve the recharge characteristics.<sup>31)</sup>  $\text{LiNiO}_2$  is a very interesting cathode as close to 100 cycles at  $2 \text{ mA} \cdot \text{cm}^{-2}$  have been achieved; discharge rates of around  $5 \text{ mA} \cdot \text{cm}^{-2}$  can be sustained.<sup>32)</sup> However, nickel is also almost certainly too expensive. Thus much effort has been placed on

vanadium and manganese oxides<sup>33-37</sup>); iron oxides have also provoked interest but little success has been had with cycling iron-based materials.

Attempts to form ternary lithium iron oxides appear to result in a mixture of phases including layer and spinel structures.<sup>38</sup> The sodium compound  $\alpha$ -NaFeO<sub>2</sub> can be formed by hydrothermal treatment of FeOOH with a large excess of NaOH (Na:Fe = 250) at 220 °C; this sodium compound can then be partially converted to the lithium compound by ion exchange under hydrothermal conditions<sup>39</sup> with 80% conversion in 4 h at 140 °C. Recently, layered LiFeO<sub>2</sub> has been partially prepared by ion-exchange of NaFeO<sub>2</sub>.<sup>39</sup> If the ion-exchange is performed at 380 °C in a LiCl/KCl molten salt LiFeO<sub>2</sub> is formed but the lithium cannot be de-intercalated; however, if the ion-exchange is carried out at 80–300 °C a corrugated form of LiFeO<sub>2</sub> is formed and around 0.3 Li can be cycled above 2.0 V.<sup>40,41</sup>

### 3.5 Manganese Oxides

Although layered manganese oxides, M<sub>y</sub>MnO<sub>2</sub>, are well known for the heavier alkali metals,<sup>42,43</sup> just like the iron compounds the lithium analog cannot be prepared at high temperatures. The stable LiMn<sub>2</sub>O<sub>4</sub> spinel is formed instead. However, a number of layered manganates have been formed by low temperature methods<sup>35,44-47</sup> and have generally been of rather low crystallinity. Recently, Chen *et al.*<sup>48</sup> have shown that the simple hydrothermal decomposition of potassium permanganate leads to the layered K<sub>y</sub>MnO<sub>2</sub>·*n*H<sub>2</sub>O. A summary of the different methods of making layered manganese oxides is shown in Fig. 3.7.<sup>49</sup> The chemistry of these manganese oxides is complicated by the existence of manganese vacancies within the manganese layer, as well as by diffusion of the manganese into the van der Waals layer.

Figure 3.8 shows the electrochemical cycling of K<sub>y</sub>MnO<sub>2</sub> in a lithium cell.<sup>50</sup> The capacity is essentially constant although more charge is removed on charging than is available in the subsequent discharge. This is believed to be associated with removal of some of the potassium ions. The analogous sodium compound can be similarly formed.<sup>49</sup> However, the formation of the lithium equivalent is a little more complex, but has been successfully accomplished by the following steps: ion exchange in a column of KMnO<sub>4</sub> to HMnO<sub>4</sub> followed by an acid base exchange using LiOH giving LiMnO<sub>4</sub> which was then hydrothermally decomposed. All these manganates prepared from aqueous solutions contain water, which can be removed under mild heating. The initial lattice spacing for the hydrates, 7.220 Å for the potassium, 7.294 Å for the sodium and 7.082 Å for the lithium, reduce to 6.385 Å, 5.620 Å and 4.869 Å, respectively, for the dehydrated compounds.

Recently, the fully lithiated manganese oxide, LiMnO<sub>2</sub>, has been synthesized by two groups<sup>51,52</sup> by ion exchange from NaMnO<sub>2</sub>, a similar method as attempted for the iron compounds. In this case complete exchange was accomplished, with maintenance of high crystallinity; *a* = 5.439 Å, *b* = 2.809 Å, *c* = 5.391 Å and β = 116.0°. The MnO<sub>6</sub> octahedra are significantly distorted with two long Mn–O bonds, 2.27 Å, and four shorter ones, 1.92 Å.<sup>51</sup> Some initial electrochemical cycling has been reported, but a fairly high fade rate was noted. But more critically the electrochemical cycling clearly indicates<sup>51</sup> that the lattice is converting over to the spinel structure. The open circuit cell data for this layered lithium manganate is compared to that of the spinel in Fig. 3.9; data from Ref. 53). This data may be compared with that for the two forms of TiS<sub>2</sub> in Fig. 3.3, where the emf is continuous indicative of a single phase and probably of a single site for the lithium ions.

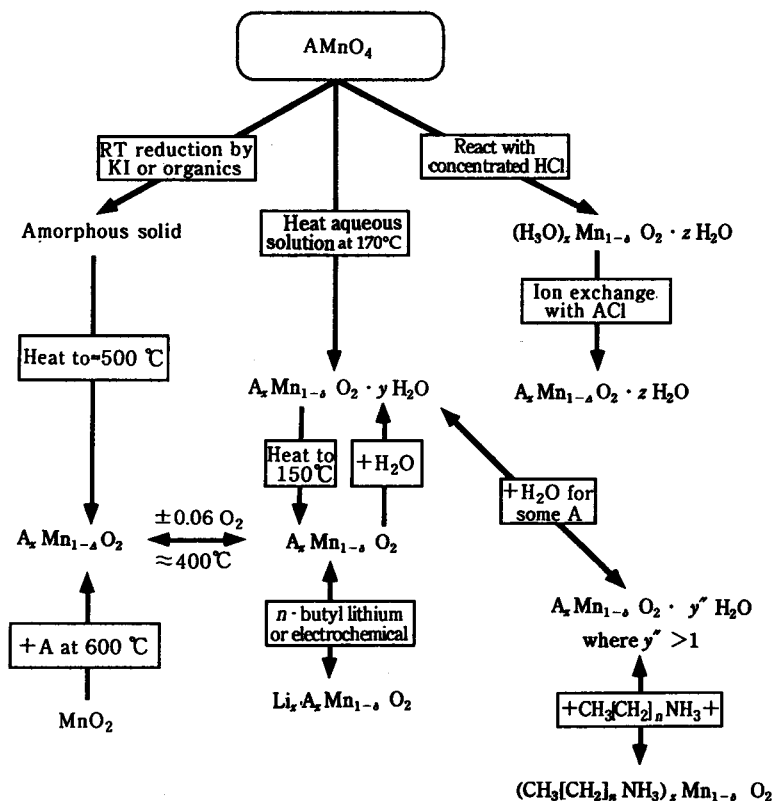


Fig. 3.7 Summary of various preparative routes for layered manganates.  
(Reproduced with permission by R. Chen *et al.*, *Proc. 10th Int. Symp. Solid State Ionics*, **86-88**, 1 (1996))

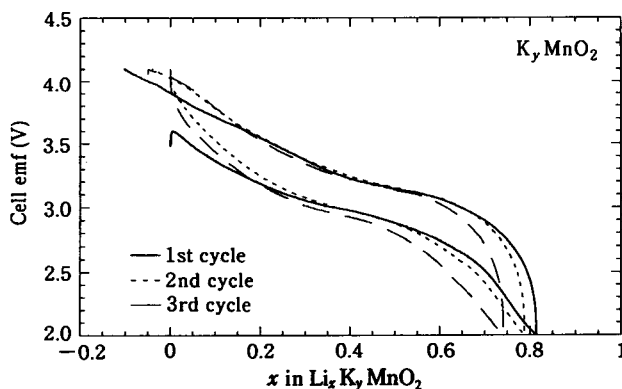


Fig. 3.8 The electrochemical cycling of  $K_x MnO_2$ .  
(Reproduced with permission by M.S. Whittingham *et al.*, *Solid State Ionics*, **44**, 227 (1997))



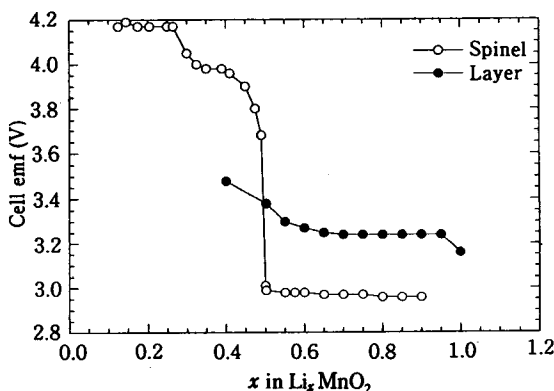


Fig. 3.9 Comparison of the open circuit emfs of the layered manganate  $\text{Li}_x\text{MnO}_2$  and the spinel  $\text{Li}_{2x}\text{Mn}_2\text{O}_4$ .

Three-phases are formed on discharge of the spinel  $\text{Li}_x\text{Mn}_2\text{O}_4$  and at least two for the discharge of layered  $\text{Li}_x\text{MnO}_2$ .

A problem with the layered manganates is that they are almost certainly thermodynamically metastable relative to the spinel  $\text{LiMn}_2\text{O}_4$  so that on cycling lithium in and out there will be a tendency for the manganese to migrate into the lithium layers until the spinel distribution of manganese is obtained, as noted by Delmas and Capitané.<sup>51)</sup> The oxygen layers are already cubic close-packed so no layer rearrangement is necessary in going from the layered to the spinel structure (see Fig. 3.10). This is opposite to the case of titanium disulfide where the layered compound  $\text{Li}_{0.5}\text{TiS}_2$  is thermodynamically more stable than the spinel  $\text{LiTi}_2\text{S}_4$ , and moreover, the sulfide layers would have to rearrange from hexagonal to cubic close-packing. These differences can almost certainly be related to the ionicity of the lattices. The more covalent the lattice the more stable the layered structure, and in

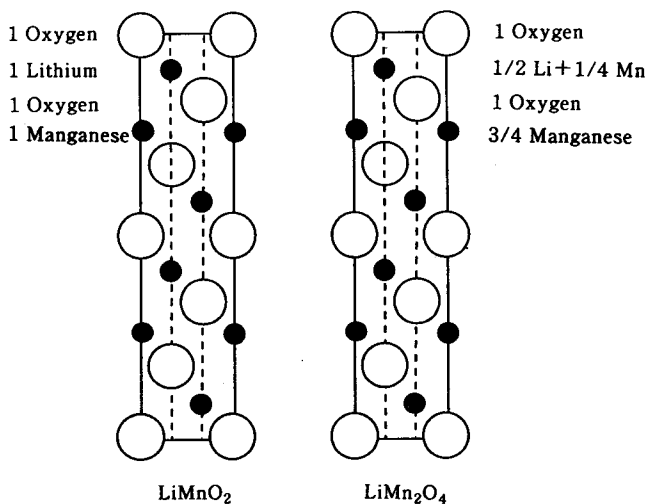


Fig. 3.10 The 110 representation of  $\text{LiMnO}_2$  and  $\text{LiMn}_2\text{O}_4$ .

particular the 1T hexagonal close-packing observed in  $\text{LiTiS}_2$  and  $\text{LiVSe}_2$ . In contrast  $\text{LiZrS}_2$  is cubic close-packed, just as are  $\text{LiCoO}_2$ ,  $\text{LiNiO}_2$  and the spinels,  $\text{LiMn}_2\text{O}_4$ . The more ionic the bonding the further apart the transition metal cations; hence the behavior observed in going from  $\text{LiTiS}_2$  to  $\text{LiZrS}_2$ , but note that  $\text{ZrS}_2$  itself exhibits hexagonal close-packing. The softer diselenides of Ti, Zr, Hf and V all show hexagonal close-packing, just as do their lithium discharge products. The highest reaction rates are observed in the hexagonal close-packed lattices of  $\text{Li}_x\text{TiS}_2$  and  $\text{Li}_x\text{VSe}_2$ , where sustained discharge rates of  $5\text{--}10\text{ mA}\cdot\text{cm}^{-2}$  are obtainable. Can the layered oxides be stabilized in hexagonal close-packing, which should help prevent the migration of the transition metal cations toward a spinel structure?

The spinel  $\text{LiMn}_2\text{O}_4$  has been extensively investigated<sup>34,54)</sup> in lithium cells. It shows good reversibility and may be cycled in the high voltage regime,  $0 \leq x \leq 1$ , in  $\text{Li}_x\text{Mn}_2\text{O}_4$  or in the low voltage regime,  $1 \leq x \leq 2$ . In the high voltage regime, Tarascon's group<sup>54)</sup> found that around 0.8–0.9 Li per  $\text{Mn}_2\text{O}_4$  can be cycled more than 2000 times with the capacity only dropping from  $100\text{ mAh}\cdot\text{g}^{-1}$  to  $60\text{ mAh}\cdot\text{g}^{-1}$  in a coke anode cell. They also noted that the high open circuit potentials cause self discharge on standing, and that also some irreversible charging was related to electrolyte oxidation. The rate of the latter was proportional to the amount of carbon black added as conductive diluent to the cathode. AA-size prototype cells provide comparable excellent behavior to  $\text{LiCoO}_2$  cells and possibly at a lower cost. However, the maximum practical cycling of 0.5 Li per transition metal is insufficient for high energy density cells, and added effort is needed to find cathode materials that ideally have carbon cell emfs of over 3 V and can cycle at least 1 Li per transition metal.

Can a layered  $\text{LiMnO}_2$  be formed and stabilized, over thousands of cycles at full depth, so that it does not revert to the spinel form? This is the challenge facing the synthetic chemist. Alternatively, can a vanadium or iron oxide be formed that will readily intercalate lithium? If successful, this goal will likely be achieved by using a mixed metal oxide, with one metal component providing primarily structural stability and the other primarily the redox properties.

### 3.6 Vanadium Oxides

Vanadium pentoxide has been investigated for over 20 years as the cathode of secondary lithium cells<sup>4,55)</sup>; the structural behavior is fairly complex with the initial lithium merely intercalating the structure first forming the  $\alpha$ -phase ( $x < 0.01$ ) and then the  $\varepsilon$ -phase ( $0.35 < x < 0.7$ ) where the layers are more puckered. At  $x = 1$  shifting of one layer out of two leads to the  $\delta$ -phase. However, if more than one lithium is discharged then significant permanent structural changes occur, giving the  $\gamma$ -phase, which can be cycled in the range  $0 \leq x \leq 2$ . In the  $\alpha$ -,  $\varepsilon$ - and  $\delta$ -phases the  $\text{VO}_5$  square pyramids that make up the structure of  $\text{V}_2\text{O}_5$  are arranged in rows which have their apices ordered up, up, down, down, as shown in Fig. 3.11. In contrast in the highly puckered  $\gamma$ -phase these are organized up, down, up, down. When still more lithium is added, a rock salt-like structure is formed, which is named the  $\omega$ - $\text{Li}_3\text{V}_2\text{O}_5$  phase. This last phase cycles in a single continuous solid solution with the last lithium coming out at over 4 V, clearly showing the difference between this vanadium oxide and the initial  $\text{V}_2\text{O}_5$ , which has an OCV of 3.5 V. The change in cell behavior is clearly shown in Fig. 3.12.  $\text{Li}_3\text{V}_2\text{O}_5$  has a tetragonal structure,  $a = 9.2\text{ \AA}$ ,

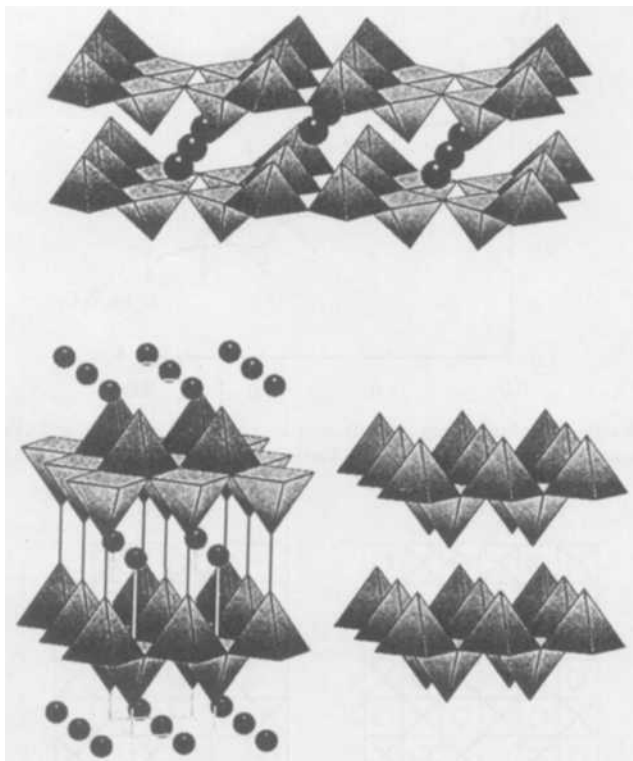


Fig. 3.11 Side view of sheets showing arrangements of  $\text{VO}_5$  square pyramids in (top)  $\text{V}_2\text{O}_5$  and (bottom) hydrated and anhydrous  $\text{VO}_2$ .

$c = 4.1 \text{ \AA}$ , according to electron diffraction studies. On extended cycling the structure appears to become simple rock salt-structure with  $a = 4.1 \text{ \AA}$ , which then has the formula  $\text{Li}_{0.6}\text{V}_{0.4}\text{O}$ . Delmas attributes the high OCV at low  $x$  to the metastability of the highly defect rock salt lattice which contains up to 60% vacancies on the cation sublattice. These structural modifications have been recently reviewed by Delmas *et al.*<sup>56)</sup>

It is interesting at this stage to discuss a new vanadium dioxide,  $\text{VO}_2$ , which has a structure almost identical to that of  $\text{V}_2\text{O}_5$ . Their structures are compared in Figs. 3.11 and 3.13. “ $\text{VO}_2$ ” has a simple tetragonal structure with  $a = 3.70 \text{ \AA}$  and  $c = 15.81 \text{ \AA}$ <sup>14)</sup> as the hydrate  $\text{Li}_x\text{VO}_2 \cdot \text{H}_2\text{O}$  and  $a = 3.687 \text{ \AA}$  and  $c = 6.794 \text{ \AA}$  for  $\text{Li}_x\text{VO}_2$  itself and is constructed by sharing of the edges around the base of the  $\text{VO}_5$  square pyramids.<sup>57,58)</sup>  $\text{V}_2\text{O}_5$  has the same structure but with 33% of the square pyramids missing in an ordered manner, as shown in Fig. 3.13. This tetragonal  $\text{VO}_2$  phase is made hydrothermally,<sup>57)</sup> and can be readily cycled in a lithium cell as shown in Fig. 3.14.<sup>58)</sup> A number of other layered vanadium oxides can be readily prepared hydrothermally; they include the structure types  $\text{N}(\text{CH}_3)_4\text{V}_4\text{O}_{10}$ ,<sup>14,59)</sup>  $\text{N}(\text{CH}_3)_4\text{V}_3\text{O}_7$ ,<sup>60)</sup>  $[\text{DABCO}]\text{V}_6\text{O}_{14}$ ,<sup>61)</sup>  $\text{C}_3\text{N}_2\text{H}_{12}\text{V}_4\text{O}_{10}$ <sup>62)</sup> and  $\text{CH}_3\text{NH}_2\text{V}_2\text{O}_5$ .<sup>63)</sup> Electrochemical evaluation of them is just beginning, with the DABCO compound reacting with 0.15 Li/V. However, after heating to drive out the organic DABCO, the cell cycled about 1.1 Li/V in a manner reminiscent of the  $\omega\text{-V}_2\text{O}_5$  phase.<sup>61)</sup>

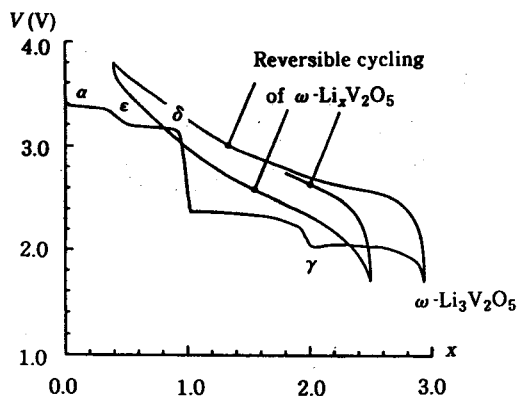


Fig. 3.12 Discharge of  $V_2O_5$  showing formation of  $\alpha$ -,  $\epsilon$ -,  $\gamma$ - and  $\delta$ -phases, and cycling of  $\omega$ -phase. (Reproduced with permission by C. Delmas *et al.*, *Solid State Ionics*, **69**, 257 (1994))

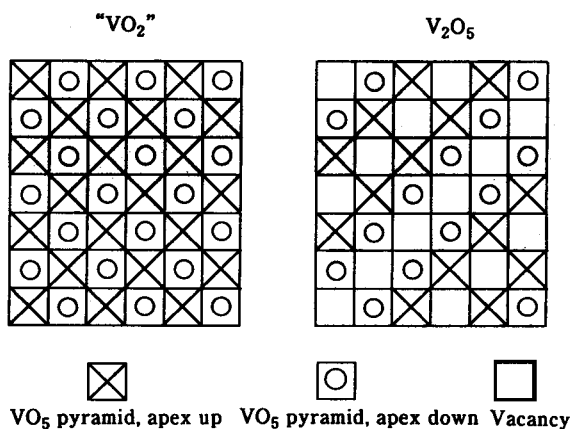


Fig. 3.13 Schematic view of basal plane of  $V_2O_5$  and  $VO_2$ ; the latter may be converted into the former by removal of 33% of the  $V=O$  groups.

(Reproduced with permission by T. Chirayil *et al.*, *J. Electrochem. Soc.*, **143**, L193 (1996))

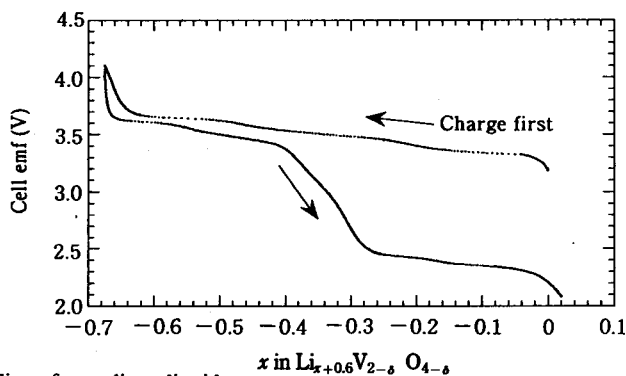


Fig. 3.14 Cycling of vanadium dioxide.

(Reproduced with permission by T. Chirayil *et al.*, *J. Electrochem. Soc.*, **143**, L193 (1996))

Similar behavior is observed on an ethylenediamine vanadium oxide,<sup>64)</sup> but the methylamine complex itself readily reacts with lithium.<sup>63)</sup>

There has been much interest recently in xerogel vanadium pentoxides made by a sol-gel process.<sup>65,66)</sup> Typically, acidification of a sodium vanadate solution is accomplished by passing it through an ion exchange column; a viscous gel results, which on drying leads to the compound  $V_2O_5 \cdot 1.8H_2O$ . About 1.1 water may be removed under vacuum or on mild heating. The resulting product is believed to be  $H_{\sim 0.3}V_2O_5 \cdot \approx 0.5H_2O$ , based on its high ion exchange capacity, and comprises fragments of the  $V_2O_5$  crystalline lattice around 1000 Å long. The interlayer spacing is around 8.8 Å for the dried material and 11.5 Å for that containing 1.8 water. Livage<sup>65)</sup> also reports that aqueous surface reactions lead to hydrated  $VO^+$  intercalated between the  $V_2O_5$  sheets with a 14.3 Å repeat distance. The protons and water can be readily exchanged for  $Li^+$  and organic solvents such as propylene carbonate, thus making the material useful in lithium batteries; however, it is suggested that the high lithium diffusion coefficients observed at low lithium contents is due to the organic solvent being intercalated. As the lithium content increases, the propylene carbonate is expelled causing the diffusion coefficient to drop two orders of magnitude.<sup>47)</sup> Previous work on titanium disulfide showed that solvent co-intercalation caused degradation of the cathode.<sup>13)</sup> Recently, it has been claimed<sup>67)</sup> that making the  $V_2O_5$  through an aerogel process with supercritical drying in  $CO_2$ /acetone gives a much more active product,  $H_yV_2O_5 \cdot 0.4H_2O \cdot \text{carbon}$ ; the amount of carbon was 3.9 wt%, the value of  $y$  was not specified. The dried material, which has a 12.5 Å-spacing (much larger than the xerogel  $V_2O_5$ ), reacts with lithium in a single continuous discharge curve with a midpoint emf of around 3.1 V thus giving a much higher capacity than crystalline  $V_2O_5$ . The reported end-point for 4 Li is around 2.8 V as high as the initial value for  $V_6O_{13}$ , a compound with an apparent higher vanadium oxidation state of 4.17 vs. the 3.0 for  $Li_4V_2O_5$ . If these data hold up in cycling tests, the material's structure can be expected to undergo rigorous characterization.

Murphy *et al.*<sup>25)</sup> made an extensive study of several vanadium oxides and found that  $V_6O_{13}$  had some very good characteristics reacting with up to 1 Li/V. They also recognized that the method of preparation, which determines the V : O ratio, critically determined the capacity for lithium. The structure consists of alternating double and single zigzag chains of distorted  $VO_6$  octahedra, and may be looked at as a rather open perovskite-like lattice as shown in Fig. 3.15.<sup>25)</sup> A variety of sites are available for lithium intercalation, which if sequentially filled would lead to the various steps seen in the discharge curve. There is some disagreement about the exact phases formed and recent careful diffraction work is helping resolve the picture. There is a 7.6% expansion along the  $c$ -axis during the first discharge step and single crystals of this electrochemically formed phase  $Li_2V_6O_{13}$  have been fully characterized: monoclinic  $C2/m$ ,  $a = 11.857$  Å,  $b = 3.660$  Å,  $c = 10.909$  Å and  $\beta = 100.436^\circ$ .<sup>68)</sup> This compares with the data reported by Murphy *et al.*<sup>25)</sup> for  $V_6O_{13}$  and  $Li_4V_6O_{13}$  of  $a = 11.92$  Å,  $b = 3.68$  Å,  $c = 10.14$  Å and  $\beta = 100.87^\circ$ , and  $a = 11.89$  Å,  $b = 3.98$  Å,  $c = 10.24$  Å and  $\beta = 100.4^\circ$ , respectively. Thus, lithium intercalation first expands the  $c$ -axis predominantly, and then the  $b$ -axis.

$Li_{1+x}V_3O_8$  has a layer structure composed of octahedral and trigonal bipyramidal ribbons, as shown in Fig. 3.16, which can be swelled just like the alkali titanium disulfides and clays, and can intercalate lithium.<sup>69,70)</sup> Another extensively studied vanadium oxide, it was recognized early that the method of preparation was important to its electrochemical

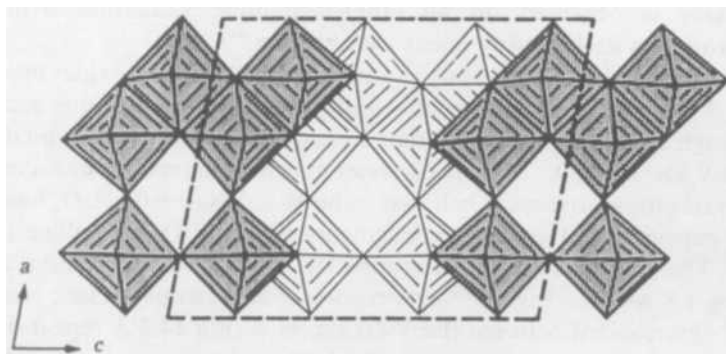


Fig. 3.15 Structure of  $V_6O_{13}$ .  
(Reproduced with permission by D.W. Murphy *et al.*, *J. Electrochem. Soc.*, 126, 497 (1979))

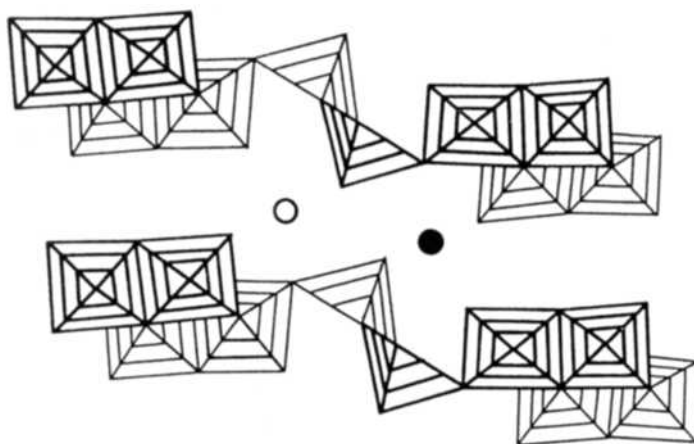


Fig. 3.16 Structure of  $Li_{1+x}V_3O_8$ .

characteristics.<sup>71)</sup> West *et al.*<sup>72)</sup> have made a systematic study of synthesis technique on capacity and cycling, and showed that amorphous material increased the capacity above 2.0 V from 3 to 4 lithium per mole of  $Li_{1+x}V_3O_8$  at low current drains,  $6\text{--}200\ \mu\text{A}\cdot\text{cm}^{-2}$ .

The tendency of vanadium to form layer compounds and not close-packed structures resulting from the stability of the vanadyl bond,  $V=O$ , makes it a rich hunting ground for new cathode materials. A number of the vanadium oxides discussed above show remarkably large uptakes of lithium and a wide cycling regime. Schematics of the discharge curves are shown in Fig. 3.17, which suggest a concern. In contrast to  $Li_xTiS_2$  and  $Li_xCoO_2$ , where the change in voltage is no more than 0.5 V, many of these vanadium oxides change from 3.5 V initially to 2.0 V. This will make electronic conditioning of a full battery system difficult. However, the remarkable open circuit behavior of the aerogel  $V_2O_5$  where the potential drop is only 0.7 V for the insertion of two lithium per vanadium merits further study; no data is available on discharge-charge rates or cycling.

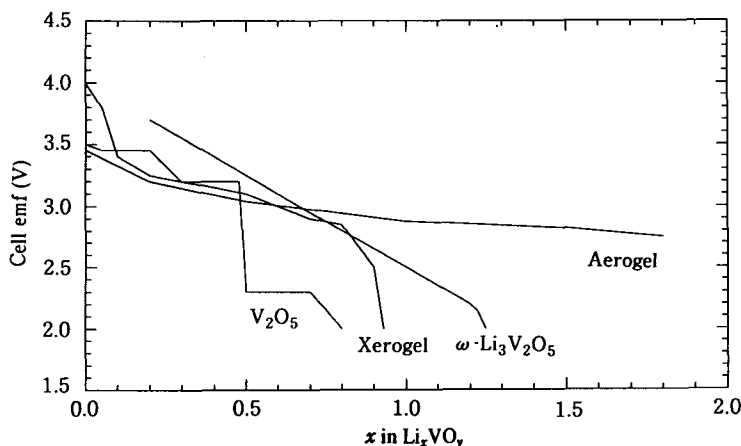


Fig. 3.17 Schematic of the emf curves for several vanadium oxides: crystalline  $\text{V}_2\text{O}_5$ ,<sup>47)</sup> xerogel  $\text{V}_2\text{O}_5$ ,<sup>47)</sup>  $\omega\text{-Li}_3\text{V}_2\text{O}_5$ ,<sup>56)</sup> and aerogel  $\text{V}_2\text{O}_5$ .<sup>67)</sup> Where open circuit data was not available, the mean of the discharge and curves were used. Straight lines have been used even where there are small changes from linearity.

### 3.7 The Future

The desire for fast chemical reactions and complete chemical reversibility dictates that the reaction be of the intercalation type, *i.e.*, where the lithium can be inserted reversibly into a crystalline lattice without significant changes to that lattice on extended cycling (reorganization may occur on the first cycle). Such lattices need to have an open or openable, *e.g.*, a tunnel or layered structure, and as a result may not be either closed-packed or convert to the thermodynamically stable phase. Examples include layered  $\text{Li}_x\text{MnO}_2$  and  $\text{TiS}_2$  where the former is metastable relative to the spinel  $\text{Li}_x\text{Mn}_2\text{O}_4$ , but layered  $\text{TiS}_2$  is stable relative to cubic spinel  $\text{Li}_x\text{TiS}_2$ . Thus, potential structures commonly have to be synthesized under conditions of kinetic rather than thermodynamic control. This in turn tends to lead to the use of lower temperatures than traditional in solid state chemistry. However, as appears to be the case with the layered  $\text{Li}_x\text{MnO}_2$ , the structure can re-organize itself to form the more stable case, in this case  $\text{LiMn}_2\text{O}_4$ . To stabilize the layered structure which appears to have a flatter discharge curve over a wider lithium range might require the incorporation of bridging or pinning groups between the  $\text{MnO}_2$  layers. More difficult might be the stabilization of these layered oxides into a hexagonal packing of the oxygen layers, rather than the cubic close-packing found now in both layered lithium oxides and in the spinel phases. The flatter discharge observed for layered  $\text{LiMnO}_2$  begins to approach the ideal, that would probably look like Fig. 3.18, which is very similar to that of  $\text{Li}_x\text{TiS}_2$ , but one volt higher in potential.

Structure building or phase modification might be best accomplished using low temperature mild techniques, commonly known as "soft chemistry." These include precipitation, intercalation-deintercalation accomplished either chemically or electrochemically as in the formation of  $\text{Li}_x\text{CoO}_2$ , ion exchange as in the formation of  $\text{LiFeO}_2$  and  $\text{LiMnO}_2$ , hydrothermal, redox and combinations of the above reactions.

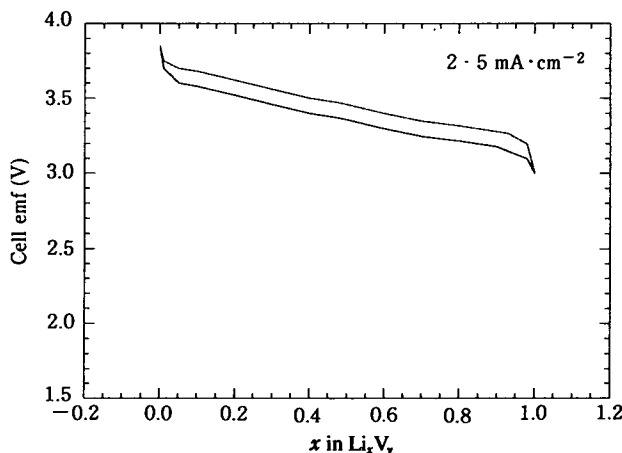


Fig. 3.18 The ideal cycling curve: charges below 4.0 V and discharges above 3.0 V for 1 lithium per transition metal and at a rate of 2 to 5 mA·cm<sup>-2</sup>.

They might involve modification of an existing crystalline lattice as in the electro-intercalation of oxygen into oxide lattices,<sup>73)</sup> or the construction of a new crystalline lattice from solution species.<sup>74)</sup> Hydrothermal synthesis is one soft chemistry approach to prepare new oxides with open crystalline lattices. In its most basic form, oxides are dissolved in water and heated to between 100° and 200°C for a few days. Thus, for example, the hexagonal and pyrochlore tunnel structures of tungsten oxide are formed by heating acidified sodium tungstate, Na<sub>2</sub>WO<sub>4</sub>,<sup>75,76)</sup> and at least five different compounds may be formed by the reaction of V<sub>2</sub>O<sub>5</sub>, N(CH<sub>3</sub>)<sub>4</sub><sup>+</sup> ions and Li<sup>+</sup> ions, the particular product being determined by the pH of the solution.<sup>60)</sup>

There is much need for thermodynamic data to elucidate the relative stabilities of different structures, of for example LiMnO<sub>2</sub> and LiMn<sub>2</sub>O<sub>4</sub> and the gel V<sub>2</sub>O<sub>5</sub>'s.

#### REFERENCES

- 1) M.S. Whittingham, *Layered Compounds*, Asilomar, Monterey, California (1972).
- 2) B.C.H. Steele, *Fast Ion Transport in Solids* (Ed. by W. van Gool), p. 103, North-Holland (1973).
- 3) M.S. Whittingham and R.A. Huggins, *Fast Ion Transport in Solids* (Ed. by W. van Gool), p. 645, North-Holland (1973).
- 4) M.S. Whittingham, *J. Electrochem. Soc.*, **123**, 315 (1976).
- 5) M.S. Whittingham and R.A. Huggins, *J. Chem. Phys.*, **54**, 414 (1971).
- 6) M.S. Whittingham and R.A. Huggins, *NBS Special Publications*, **364**, 139 (1972).
- 7) M.S. Armand, *Fast Ion Transport in Solids* (W. van Gool), p. 665, North-Holland (1973).
- 8) M. Armand and P. Touzan, *Mater. Sci. Eng.*, **31**, 319 (1977).
- 9) M.S. Whittingham, U.S. Patent 4009052 and U.K. Patent 1468416 (1973).
- 10) M.S. Whittingham, *Science*, **192**, 1126 (1976).
- 11) K. Mitzushima, P.C. Jones, P.J. Wiseman and J.B. Goodenough, *Mater. Res. Bull.*, **17**, 785 (1980).
- 12) G.H. Newman and L.P. Klemann, *J. Electrochem. Soc.*, **127**, 2097 (1980).
- 13) M.S. Whittingham, *Progr. Solid State Chem.*, **12**, 41 (1978).
- 14) M.S. Whittingham, J. Guo, R. Chen, T. Chirayil, G. Janauer and P. Zavalij, *Solid State Ionics*, **75**, 257 (1995).
- 15) L.H. Gaines, R.W. Francis, G.H. Newman and B.M.L. Rao, 11th Intersociety Energy Conversion



- Conference, Stateline, Nevada (1976).
- 16) A.H. Thompson, *Phys. Rev. Letters*, **35**, 1786 (1975).
  - 17) S.D. Jones, J.R. Ackridge and F.K. Shokoohi, *Solid State Ionics*, **69**, 357 (1994).
  - 18) R. Schöllhorn and A. Payer, *Angew. Chem. Int. Ed. Engl.*, **24**, 67 (1985).
  - 19) S. Sinha and D.W. Murphy, *Solid State Ionics*, **20**, 81 (1986).
  - 20) A.C.W.P. James and J.B. Goodenough, *Solid State Ionics*, **27**, 37 (1988).
  - 21) A.H. Thompson, *Phys. Rev. Letters*, **40**, 1511 (1978).
  - 22) J.B. Goodenough, A. Manthiram and B. Wnetrzewski, *J. Power Sources*, **43–44**, 269 (1993).
  - 23) M.S. Whittingham, *Mater. Res. Bull.*, **13**, 959 (1978).
  - 24) D.W. Murphy, J.N. Carides, F.J. DiSalvo, C. Cros and J.V. Waszczak, *Mater. Res. Bull.*, **12**, 825 (1977).
  - 25) D.W. Murphy, P.A. Christian, F.J. DiSalvo and J.N. Carides, *J. Electrochem. Soc.*, **126**, 497 (1979).
  - 26) M.S. Whittingham and F.R. Gamble, *Mater. Res. Bull.*, **10**, 363 (1975).
  - 27) K. Ozawa, *Solid State Ionics*, **69**, 212 (1994).
  - 28) G.G. Amatucci, J.-M. Tarascon, and L.C. Klein, Abstracts of the 8th Int. Meeting Lithium Battery, **8**, p. 406 (1996).
  - 29) A. LeBlanc, M. Danot, L. Trichet and J. Rouxel, *Mater. Res. Bull.*, **9**, 191 (1974).
  - 30) C. Delmas and I. Saadonne, *Solid State Ionics*, **53–56**, 370 (1992).
  - 31) Y. Nishida, K. Nakane and T. Satoh, Abstracts of the 8th Int. Meeting Lithium Battery, **8**, p. 440 (1996).
  - 32) W. Ebner, D. Fouchard and L. Xie, *Solid State Ionics*, **69**, 238 (1994).
  - 33) J.-M. Tarascon, *Solid State Ionics*, **69**, 173–368 (1994).
  - 34) D. Guyomard and J.M. Tarascon, *J. Electrochem. Soc.*, **139**, 937 (1992).
  - 35) F. Leroux, D. Guyomard and Y. Piffard, *Solid State Ionics*, **80**, 307 (1995).
  - 36) J.M. Tarascon, E. Wang, F.K. Shokoohi, W.R. McKinnon and S. Colson, *J. Electrochem. Soc.*, **138**, 2859 (1991).
  - 37) G. Pistoia, Lithium Batteries, *Industrial Chemistry Library*, Vol. 5, Elsevier (1994).
  - 38) M. Tabuchi, K. Ado, H. Sakaebe, C. Masquelier, H. Kageyama and O. Nakamura, *Solid State Ionics*, **79**, 220 (1995).
  - 39) M. Tabuchi, C. Masquelier, T. Takeuchi, K. Ado, I. Matsubara, T. Shirane, R. Kanno, S. Nasu, H. Sakaebe, H. Okuyama and O. Nakamura, 10th Int. Conf. Solid State Ionics, Singapore, December 1995, Abstr., p. 197.
  - 40) R. Kanno, T. Shirane and Y. Kawamoto, 8th Int. Meet. Lithium Batteries, Nagoya, Japan, June 1996, Abstr. p. 133.
  - 41) R. Kanno, T. Shirane, Y. Kawamoto, Y. Takeda, M. Takano, M. Ohashi and Y. Yamaguchi, *J. Electrochem. Soc.*, **143**, 2435 (1996).
  - 42) C. Delmas and C. Fouassier, *Z. Anorg. Allgem. Chem.*, **420**, 184 (1976).
  - 43) C. Delmas, C. Fouassier and P. Hagenmuller, *J. Solid State Chem.*, **13**, 165 (1975).
  - 44) F. Leroux, D. Guyomard and Y. Piffard, *Solid State Ionics*, **80**, 299 (1995).
  - 45) Q. Feng, H. Kanoh, Y. Miyai and K. Ooi, *Chem. Mater.*, **7**, 1226 (1995).
  - 46) F.L. Cras, S. Rohs, M. Anne and P. Strobel, *J. Power Sources*, **54**, 319 (1995).
  - 47) J.P. Pereira-Ramos, N. Baffier and G. Pistoia, *Lithium Batteries*, (Ed. by G. Pistoia), p. 281, Elsevier (1994).
  - 48) R. Chen, P. Zavalij and M.S. Whittingham, *Chem. Mater.*, **8**, 1275 (1996).
  - 49) R. Chen, T. Chirayil and M.S. Whittingham, Proc. 10th Int. Symp. Solid State Ionics, Singapore, December 1995; *Solid State Ionics*, **86–88**, 1 (1996).
  - 50) M.S. Whittingham, R. Chen, T. Chirayil and P. Zavalij, *Solid State Ionics*, **94**, 227 (1997).
  - 51) C. Delmas and F. Capitaine, 8th Int. Meet. Lithium Batteries, Nagoya, Japan, 1996, Ext. Abstr., p. 470.
  - 52) A.R. Armstrong and P.G. Bruce, *Nature*, **381**, 499 (1996).
  - 53) P.G. Bruce, Personal communication.
  - 54) D. Guyomard and J.M. Tarascon, *Solid State Ionics*, **69**, 222 (1994).
  - 55) C.R. Walk and J.S. Gore, *J. Electrochem. Soc.*, **122**, 68 (1975).
  - 56) C. Delmas, H. Cognac-Auradou, J.M. Cocciantelli, M. Ménétrier and J.P. Doumerc, *Solid State Ionics*, **69**, 257 (1994).
  - 57) T. Chirayil, P. Zavalij and M.S. Whittingham, *Solid State Ionics*, **84**, 163 (1996).
  - 58) T. Chirayil, P. Zavalij and M.S. Whittingham, *J. Electrochem.*, **143**, L193 (1996).
  - 59) P. Zavalij, M.S. Whittingham, E.A. Boylan, V.K. Pecharsky and R.A. Jacobson, *Z. Kryst.*, **211**, 464 (1996).
  - 60) E. A. Boylan, T. Chirayil, J. Hinz, P. Zavalij and M.S. Whittingham, *Solid State Ionics*, **86**, 1 (1996); T. Chirayil, E. A. Boylan, M. Mamak, P.Y. Zavalij and M.S. Whittingham, *J. Chem. Soc. Chem. Commun.*, **33** (1997).
  - 61) L.F. Nazar, B.E. Koene and J.F. Britten, *Chem. Mater.*, **8**, 327 (1996).
  - 62) D. Riou and G. Férey, *J. Solid State Chem.*, **120**, 137 (1995).
  - 63) R. Chen, P.Y. Zavalij and M.S. Whittingham, Mater. Res. Soc. Fall, Abstracts, p. 538 (1997).
  - 64) T. Chirayil, Personal communication; results on samples provided by A. J. Jacobson (1996).

- 65) J. Livage, *Mater. Res. Bull.*, **26**, 1173 (1991).
- 66) J. Livage, *Chem. Mater.*, **3**, 578 (1991).
- 67) D.B. Le, S. Passerini, J. Guo, J. Ressler, B.B. Owens and W.H. Smyrl, *J. Electrochem. Soc.*, **143**, 2099 (1996).
- 68) Ö. Bergström, T. Gustafsson and J. Thomas, Abstracts of the XVII Int. Union of Crystallography Congress, Seattle, WA (1996).
- 69) J.O. Besenhard and R. Schöllhorn, *J. Power Sources*, **1**, 267 (1976).
- 70) R. Schöllhorn, F. Klein-Reesink and R. Reimold, *J. Chem. Soc. Chem. Commun.*, 398 (1979).
- 71) K. Nassau and D.W. Murphy, *J. Non-Cryst. Solids*, **44**, 297 (1981).
- 72) K. West, B. Zachau-Christiansen, S. Skaarup, Y. Saidi, J. Barker, I.I. Olsen, R. Pynenburg and R. Koksang, *J. Electrochem. Soc.*, **143**, 820 (1996).
- 73) J.-C. Grenier, M. Pouchard and A. Wettiaux, *Current Opinion in Solid State & Materials Science*, **1**, 233 (1996).
- 74) M.S. Whittingham, *Current Opinion in Solid State and Materials Science*, **1**, 227 (1996).
- 75) J.R. Günter, M. Amberg and H. Schmalte, *Mater. Res. Bull.*, **24**, 289 (1989).
- 76) K.P. Reis, A. Ramanan and M.S. Whittingham, *Chem. Mater.*, **2**, 219 (1990).

## 4

Design of the Lithium Anode and Electrolytes in  
Lithium Secondary Batteries with a Long Cycle Life

Jun-ichi Yamaki\*

## 4.1 Introduction

Lithium rechargeable cells with lithium metal anodes have a very high energy density. This section provides a detailed description of an AA-size lithium metal anode cell<sup>1)</sup> with amorphous  $V_2O_5$  cathodes fabricated in the author's laboratory. The energy of this cell is 2 Wh, which is higher than the value of 1.8 Wh for a lithium ion cell with a  $LiCoO_2$  cathode (The estimated value for an AA-size lithium metal cell with a  $LiCoO_2$  cathode is about 3 Wh). However, the metal anode cell has a cycle life of 150 times and its thermal stability is 130 °C at a high rate discharge cycle. At a low discharge rate cycle, its cycling life is 50 cycles and its thermal stability 125 °C. These values are not good compared with lithium ion cells, whose corresponding values are 500 cycles and more than 130 °C. This poor performance is mainly explained by the characteristics of the lithium metal anode, specifically its low cycling efficiency. The lithium metal anode has a very large theoretical capacity of  $3860 \text{ mAh} \cdot \text{g}^{-1}$ , in contrast to the value of  $372 \text{ mAh} \cdot \text{g}^{-1}$  for a  $LiC_6$  carbon anode. This high capacity encouraged us to improve the lithium metal anode.

Many studies have been undertaken with a view to improving lithium anode performance for the practical use of the cell. The following section (Section 4.2) describes studies on lithium metal anode protection films, methods for measuring cycling efficiency, the morphology of deposited lithium, the mechanism of lithium deposition and dissolution, the amount of dead lithium and cell performance and improvement of cycling efficiency. Section 4.3 focuses on safety aspects related to the exothermic reaction in a cell and compares the results with those for lithium ion cells.

## 4.2 Lithium Metal Anode

## 4.2.1 Protection Films on Lithium Metal Anode

Lithium metal is very active and reacts with any organic electrolyte. However, in practice, lithium metal can be dissolved and deposited electrochemically in some organic electrolyte.<sup>2)</sup> It is generally believed that a protection film is formed on the lithium anode

---

\* NTT, Nippon Telegraph and Telephone Corporation, Tokai-mura, Naka-gun, Ibaraki Pref., 319-11 Japan

Present address: Institute of Advanced Material Study, Kyushu University, 6-1, Kasuga-koen, Kasuga-shi, Fukuoka Pref., 816 Japan

Table 4.1 Protection films on lithium metal.

Electrolyte	Protection film	Reference
PC/LiClO <sub>4</sub>	LiClO <sub>4</sub>	6
	Li <sub>2</sub> CO <sub>3</sub> , LiCl, partially chlorized hydrocarbons and their lithium compounds (LiCHClCHCl, LiCH <sub>2</sub> CHClCH <sub>2</sub> Cl, etc.)	7
	Li <sub>2</sub> CO <sub>3</sub> , LiCl, RCO <sub>2</sub> Li, [(CH <sub>2</sub> CHCH <sub>2</sub> OCO <sub>2</sub> Li, CH <sub>3</sub> CHCHOCO <sub>2</sub> Li, LiOCH <sub>2</sub> (CH <sub>3</sub> )CHOCO <sub>2</sub> Li]	8
DEC mixture	CH <sub>3</sub> CH <sub>2</sub> OCO <sub>2</sub> Li, CH <sub>3</sub> CH <sub>2</sub> OLi	8
SO <sub>2</sub> /LiAlCl <sub>4</sub>	Li <sub>2</sub> S <sub>2</sub> O <sub>4</sub> , Li <sub>2</sub> SO <sub>3</sub> , LiS <sub>n</sub> O <sub>6</sub> , Li <sub>2</sub> S <sub>2</sub> O <sub>5</sub>	9
THF/LiAsF <sub>6</sub>	BuOLi, CH <sub>3</sub> (CH <sub>2</sub> ) <sub>n</sub> Li, -As-O-As-	10
	BuOLi, LiOCH <sub>2</sub> CH <sub>2</sub> CH <sub>2</sub> CH <sub>3</sub>	11
	-O(CH <sub>2</sub> ) <sub>4</sub> -THF <sup>+</sup> , F <sub>2</sub> -As-O-As-F <sub>2</sub>	12
2Me-THF/LiAsF <sub>6</sub>	(-As-O-) <sub>n</sub> , LiAs(OR) <sub>x</sub> F <sub>6-x</sub> , AsO <sub>x</sub> F <sub>5-x</sub> , As(OR) <sub>x</sub> F <sub>3-x</sub>	13
DME/LiAsF <sub>6</sub>	CH <sub>3</sub> OLi, LiF	11
γ-BL mixture	CH <sub>3</sub> CH <sub>2</sub> CH <sub>2</sub> OCO <sub>2</sub> Li derivatives, β-ketoester-anion-derivatives	14
DOL/LiClO <sub>4</sub>	CH <sub>3</sub> OLi, CH <sub>3</sub> CH <sub>2</sub> OLi,	
	LiOCH <sub>2</sub> CH <sub>2</sub> (OCH <sub>2</sub> ) <sub>n</sub> OX (X = OLi, H, OR)	15
MF mixture	LiOCH <sub>3</sub> , LiOOCH	16

PC: Propylene carbonate	DME: Dimethoxyethane
DEC: Diethylcarbonate	γ-BL: γ-Butyrolacton
THF: Tetrahydrofuran	DOL: Dioxilane
2Me-THF: 2-Methyl-tetrahydrofuran	MF: Methylformate

which prevents further reaction.<sup>3,4)</sup> In 1979, the Solid Electrolyte Interphase (SEI) model was presented by Peled to explain this phenomenon.<sup>5)</sup> According to this model, the reaction products of the lithium and the electrolyte form a thin protection film on a lithium anode. This film is a lithium ion conductor and an electronic insulator with characteristics preventing further chemical reaction. Aurbach *et al.* and many other researchers tried to identify the chemical products composing the protection film<sup>6-17)</sup> using Fourier transform infrared spectroscopy (FTIR), X-ray photoelectron spectroscopy (XPS) and Raman spectroscopy. The results are summarized in Table 4.1. The protection films differ depending on the kind of electrolyte and consist mainly of Li<sub>2</sub>CO<sub>3</sub>, LiX (X: halogen), ROLi and ROCOOLi (R: hydrocarbon). LiAsF<sub>6</sub> solute forms some As-compounds as protection films.

Irish *et al.* studied the reactivity of electrolytes using an *in situ* cutting technique to expose bare lithium.<sup>18,19)</sup> Using mixed potential theory, they showed that for very carefully purified LiAsF<sub>6</sub>/tetrahydrofuran (THF) and 2-methyl-tetrahydrofuran (2Me-THF) the exchange current density and corrosion potential are primarily determined by two reactions: the anodic dissolution of lithium and the cathodic reduction of AsF<sub>6</sub><sup>-</sup> by bare lithium metal. Extending this study, they examined the effects of impurities in electrolytes. The solvents they used were THF, 2Me-THF and propylene carbonate (PC). The solutes were LiAsF<sub>6</sub>, LiPF<sub>6</sub>, LiBF<sub>4</sub>, LiClO<sub>4</sub> and Li(CF<sub>3</sub>SO<sub>2</sub>)<sub>2</sub>N. The corrosion potential did not increase by impurity of water when the solvent of electrolytes was not THF. Anion reduction is one of the major reactions determining the behavior of bare lithium metal. The result suggests that the protection film is very strong against water present as an impurity in electrolyte without THF. Indeed, they found that during anodic cycling with LiAsF<sub>6</sub>/THF, the presence of water leads to the breakdown of the surface film.

Layer structures of Li<sub>2</sub>O, LiOH, hydrocarbon, LiF and Li<sub>2</sub>CO<sub>3</sub> are proposed<sup>20)</sup> by XPS

measurements. Impurities of  $\text{H}_2\text{O}$ ,  $\text{O}_2$  and  $\text{CO}_2$  in an electrolyte react with organic lithium compounds in protection film to form  $\text{Li}_2\text{CO}_3$ ,  $\text{Li}_2\text{O}_2$ ,  $\text{Li}_2\text{O}$  and  $\text{LiOH}$ .<sup>21,22)</sup> Following this result, the protection film is similar to the native film which is on the lithium surface before immersion in electrolytes. These studies identified the chemical composition of the protection film. However, regarding the ionic conductivity of these lithium compounds, the mechanism by which the protection films act as lithium ion conductors must be taken into consideration.

Takehara *et al.* have proposed a model explaining why the protection layer is a lithium ion conductor.<sup>23)</sup> Their model is that the protection layer has narrow paths or pores which fill with electrolyte. An equivalent circuit based on this model could explain the AC impedance behavior on a lithium electrode. From their model, they assume that an electrolyte for a rechargeable lithium battery must have higher viscosity and higher surface tension than THF (THF is very reactive with lithium) in order to avoid direct reaction between electrolyte and lithium metal. A similar model has been proposed by Fletcher *et al.*<sup>24)</sup> Their model is based on the idea that surface film is porous and electrolyte can move through sites where the  $\text{Li}/\text{Li}^+$  couple is rapid. They believe that the film structure can be markedly different during charge, rest and discharge periods.

#### 4.2.2 Cycling Efficiency of Lithium Anode

Since the lithium anode is consumed during cycling, in a practical lithium secondary cell, excess lithium is included to compensate for the consumed lithium. The cycling efficiency of a lithium anode (*Eff*) is defined by the following equation, where  $Q_p$  is the amount of electricity to plate lithium and  $Q_s$  is the amount of electricity needed to strip all the plated lithium.

$$\text{Eff} = 100 \times Q_s / Q_p \quad (\%) \quad (4.1)$$

From an early work on the rechargeability of lithium by Selim and Bro<sup>25)</sup>, all the  $Q_p$  is used for lithium plating and the plating efficiency is 100% at a higher deposition current. Bro estimated the plating efficiency from the amount of gas generated when the deposited product (lithium and protection film) was mixed with water. Thus, in the opinion of the present author, a lower deposition efficiency at a low current density may be caused by reactions between the deposited lithium and the water contained in the electrolyte as an impurity. In this case, some organic products composing the protection film may react with water to generate  $\text{H}_2$ . This means that the surface of the deposited lithium has already reacted with the electrolyte. However, this reaction occurs after deposition, so the deposition efficiency is 100%. In other words, lithium may be consumed after deposition and during the stripping process (discharge).

The figure of merit for lithium cycling efficiency (FOM)<sup>26)</sup> is also often used to evaluate performance. FOM is also referred to as lithium turnover.<sup>27)</sup> The definition of FOM is the number of cycles completed by one atom of lithium before it becomes electrochemically inactive. The following equation is derived from the above definition.

$$\text{FOM} = \frac{\text{(summation of each discharge capacity to the end of cycle life)}}{\text{(capacity of lithium anode in a cell)}} \quad (4.2)$$

If the cycling is continued with a constant capacity ( $C_0$ ), Eq. (4.2) becomes Eq. (4.3).

$$FOM = [(the\ cycle\ life) \times C_0] / (\text{capacity of a lithium anode in a cell}) \quad (4.3)$$

Equation (4.3) is very useful for roughly approximating cycle life when the  $FOM$  is known.

We can calculate the  $FOM$  from  $Eff$ , using the following equation.<sup>28)</sup>

$$FOM = 1 / (1 - Eff/100) \quad (4.4)$$

Although this equation is true for any cycling condition,<sup>28)</sup> Eq. (4.4) is derived from Eq. (4.3) and the following Eq. (4.5) when the cell is cycled at a constant capacity.

$$(\text{capacity of lithium anode in a cell}) = (\text{the cycling life}) \times (1 - Eff/100) C_0 \quad (4.5)$$

Several methods for evaluating the cycling efficiency are described below. Care must be paid in selecting the method to be used, because the value depends very strongly on the method.

#### A. Li on Ni

Reported by Rauh,<sup>4)</sup> this is the simplest method. Lithium is deposited on a Ni electrode for a given  $Q_p$  from a counter electrode of lithium, then all the deposited lithium is stripped to measure  $Q_s$ .  $Eff$  is then evaluated using Eq. (4.1). The name of this method varies depending on the type of working electrode that is used. If lithium is deposited on a working electrode made of stainless steel, the name is "Li on stainless steel." Sazhin *et al.*<sup>63)</sup> measured the cycling efficiency using the Li on stainless steel method, and also examined the effect of using different substrate materials.

#### B. Li on Li

This was also reported by Rauh.<sup>29)</sup> An excess amount of lithium ( $Q_{ex}$ ) is plated on a Ni electrode from a counter electrode of lithium, and the constant capacity cycling ( $Q_{ps}$ ;  $Q_{ps}$  is smaller than  $Q_{ex}$ ) is continued until all the excess lithium is consumed. During this process, the cell voltage is monitored to determine the end of the cycle. From Eq. (4.3),  $FOM$  can be evaluated as shown in Eq. (4.6).

$$FOM = [(the\ cycling\ life) \times Q_{ps}] / (Q_{ex}) \quad (4.6)$$

#### C. Conventional Full Cell

A cell is made with a lithium anode (the total capacity is  $Q_{li}$ ) and a cathode. The cell is cycled with a given cycling capacity ( $Q_{cy}$ ) for a given number of cycles, then all the lithium on the anode is plated on the cathode to measure the amount of electrochemically active lithium ( $Q_{ac}$ ).<sup>30)</sup> From Eq. (4.3),  $FOM$  can be determined as shown in Eq. (4.7).

$$FOM = [(the\ cycle\ number) \times Q_{cy}] / (Q_{li} - Q_{ac}) \quad (4.7)$$

#### D. Full Cell

A cell is made with a lithium anode (the total capacity is  $Q_{li}$ ) and a cathode. The cell is cycled with a certain cycling capacity ( $Q_{cy}$ ) to the end of cycle.<sup>31)</sup> By using Eq. (4.3),  $FOM$  can be evaluated as shown in Eq. (4.8).

$$FOM = [(the\ cycling\ number\ to\ the\ end\ of\ cycle) \times Q_{cy}] / (Q_i) \quad (4.8)$$

Among these methods, the most reliable is the full cell method, even though this method requires more time. The difference in the *Eff* or *FOM* values with different measuring methods is mainly due to the difference in the working electrode. In the case of the Li on Ni method, lithium is plated on Ni, and some of the deposited lithium may be disconnected easily from the Ni electrode. With the Li on Li method, lithium is already plated on the working electrode, so some of the lithium may be deposited on lithium. However, lithium does not cover the whole electrode, and some lithium may be deposited on the Ni electrode. For the conventional full cell and full cell methods, the working electrode is lithium, so very reliable data can be obtained. Another factor is oxidation of electrolytes on a cathode. The first two methods described above cannot have a high potential cathode, therefore, sometimes an electrolyte which has a high *Eff* as determined by one of these methods is not a good electrolyte for an actual cell because of oxidation of the electrolyte. The last two methods described above are superior in terms of evaluating the practical performance of electrolytes.

The best *Eff* data reported is about 99%. To express this another way, *FOM* is 100. This seems to be a very high value. However, it is not high enough for practical cells, because their cycle life is only 300, even if three times lithium for the nominal capacity is contained in a cell (Eq. (4.3) is used to calculate the cycle life).

The reasons for low cycling efficiency are considered to be as follows.

(i) The consumption of lithium by reaction with electrolyte, forming a protection film<sup>3)</sup>

During the deposition and stripping of lithium, the surface shape is changed to make a fresh lithium surface. New protection film is formed on the new surface, consuming lithium.

(ii) Lithium isolation in a protection film<sup>5)</sup>

During the deposition of lithium, the protection film may be heated locally by the ion transport in the protection film. As a result of this local heating, some part of the protection film (SEI) becomes an electronic conductor, so lithium metal is deposited in the protection film. If local heating does not occur during stripping, the isolated lithium becomes electrochemically inactive.

(iii) Isolation of deposited lithium from base anode<sup>32,33)</sup>

When a cell is charged, lithium is deposited on the lithium substrate of the anode. Sometimes, the plated lithium is not flat but fiber-like. When the cell is discharged, the lithium anode dissolves, and sometimes the fiber-like lithium is cut and becomes isolated from the anode substrate.<sup>33)</sup> This isolated lithium is called “dead lithium,” and it is electrochemically inactive but chemically active. During cycling, this dead lithium accumulates on the anode.

The present author believes that (iii) is the main reason for the low cycling efficiency. As the lithium metal cells decrease in thermal stability with cycling,<sup>34–36)</sup> the dead lithium may decrease the thermal stability. Thus, the cycling efficiency is strongly affected by the morphology of the lithium surface.

### 4.2.3 Morphology of Deposited Lithium

There are many reports on the morphology of the lithium electrochemically deposited in various kinds of organic electrolytes.<sup>37–44)</sup> Koshina and other researchers reported<sup>45)</sup> that there are three kinds of morphology: dendritic, granular and mossy. They used  $\text{LiPF}_6/\text{PC}$ -ethylene carbonate (EC) electrolyte and found that mossy lithium is formed when the deposition current is small and the salt concentration is high. The mossy lithium provided a high cycling efficiency.

A very basic theoretical study on electrolytes was undertaken by Matsui and Takeyama.<sup>46)</sup> They calculated how close lithium ions can approach a metal electrode in EC, PC, THF and 2Me-THF. From their calculation using a Monte Carlo simulation, lithium ions can approach the electrode more closely in EC or PC than in THF or 2Me-THF. They also studied the morphology of electro-deposition and dissolution process by the Monte Carlo technique under a two-dimensional lattice scheme.<sup>47)</sup> When the charge of electrode particles is small, the morphology of the deposition is thin and sparse. The shape is moss-, needle- or rod-like. This is because the deposition occurs at the tip of the deposited product. When the charge of electrode particles and the sticking probability are small, the shape is leaf-like or flat because of activated ion diffusion on the electrode surface. If only a small part of the electrode is active, the deposition shape is like a temple bell. During the stripping, needle-like or rod-like deposition products are separated from the electrode, and much of the deposition product cannot be stripped. Deposition products which are flat or temple bell-shaped can be stripped without isolation. Such a theoretical approach is useful for a better understanding of lithium deposition.

Uchida *et al.*<sup>48)</sup> used a microelectrode to study lithium deposition in order to minimize the effect of solution resistance. They used a Pt electrode 10–30  $\mu\text{m}$  in diameter to measure the lithium ion diffusion coefficient in 1 mM  $\text{LiClO}_4/\text{PC}$  electrolyte. The diffusion coefficient was  $4.7 \times 10^{-6} \text{ cm}^2 \cdot \text{s}^{-1}$  at 25 °C.

The lithium morphology at the beginning of the deposition was measured by Morigaki *et al.*<sup>49)</sup> using *in situ* atomic force microscopy (AFM). There were grains of 1–2  $\mu\text{m}$ , and in the grains there were thin lines of 100–300 nm and flat parts on native lithium surface. The flat part was composed of small elliptical particles of about 60 nm in size. When lithium was deposited for  $0.6 \text{ C} \cdot \text{cm}^{-2}$ , small particles 200–1000 nm in size were deposited on the thin lines and grain boundaries in  $\text{LiClO}_4/\text{PC}$ . Lump-like growth was observed in  $\text{LiAsF}_6/\text{PC}$  along the line.

An electrochemical quartz crystal microbalance (EQCM or QCM) can be used to estimate the surface roughness of deposited lithium. Naoi *et al.*<sup>50)</sup> reported that a  $\text{LiPF}_6/\text{PC}$  electrolyte displayed the highest cycling efficiency and the resistance parameter from QCM did not increase upon deposition, whereas the resistance parameter for  $\text{LiClO}_4/\text{PC}$  did increase because of the surface roughness.

The author<sup>51)</sup> and Arakawa<sup>52)</sup> have observed lithium deposition on a stainless steel (SS) substrate in 2Me-THF-EC/ $\text{LiAsF}_6$  electrolyte at a deposition current of  $0.5 \text{ mA} \cdot \text{cm}^{-2}$ . A scanning electron microscope (SEM) was used for the observation. After 1 min of deposition (Fig. 4.1a), small particles about 0.1  $\mu\text{m}$  in diameter were deposited. Fiber-like lithium with a diameter of about 0.1  $\mu\text{m}$  and 1  $\mu\text{m}$  in length was also deposited. After deposition for 3 min (Fig. 4.1b), no particle-like lithium could be observed, and only the



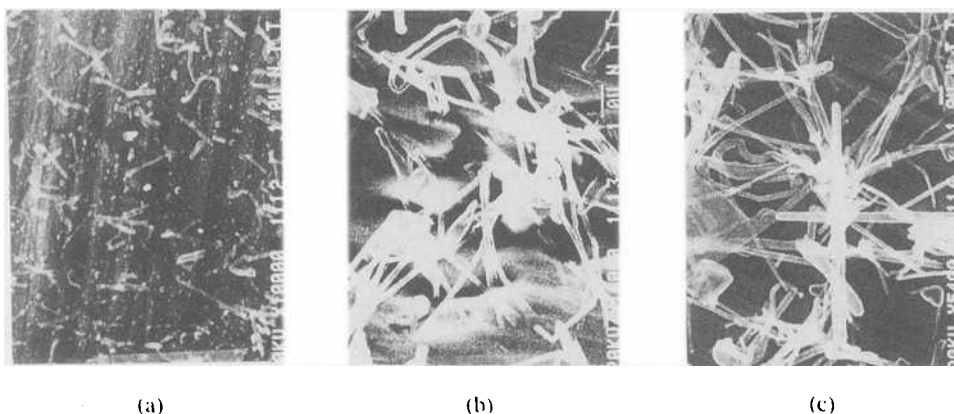


Fig. 4.1 SEM images of lithium deposited on a stainless steel substrate in 2Me-THF-EC/LiAsF<sub>6</sub> electrolyte at deposition current of  $0.5 \text{ mA} \cdot \text{cm}^{-2}$ . (a) after 1 min deposition, (b) after 3 min, (c) after 10 min.

fiber-like lithium was present, some fiber-like lithium of which had a thicker diameter of  $0.5 \mu\text{m}$ . The particle-like lithium grew and became fiber-like. When the deposition was continued for 10 min (Fig. 4.1c), particle-like or amorphous lithium (diameter: about  $1 \mu\text{m}$ ) was deposited among the fiber-like pieces of lithium (some of which were  $1 \mu\text{m}$  in diameter). When the deposition current was changed, the fiber-like lithium showed a tendency to become thinner with increasing current. When the deposition current was small (less than  $1.5 \text{ mA} \cdot \text{cm}^{-2}$ ), much amorphous or particle-like lithium was observed. The temperature dependence was also examined and it was found the diameter of deposited lithium was very small (about  $0.3 \mu\text{m}$ ) at  $-10^\circ\text{C}$ , even after 5 min of deposition at  $0.5 \text{ mA} \cdot \text{cm}^{-2}$ . Electrode stack pressure also changes the lithium morphology.<sup>43)</sup> In a practical cell, stack pressure is usually applied on the lithium anode. This makes it interesting to study the effects of pressure on lithium morphology. As lithium is a soft metal, fiber-like lithium deforms and becomes a flat surface. Surface observation reveals that lithium deposited under pressure is metallic silver while that deposited without pressure is gray or dark brown. This is explained in more detail in Section 4.2.6.(D).

#### 4.2.4 Mechanism of Lithium Deposition and Dissolution

As shown in SEM photos, the shape of the deposited lithium is rod-like with kinks, and the deposited lithium is often called dendrites. However, as there are no branches on the fiber-like lithium, the author believes that lithium whisker<sup>53)</sup> is a better appellation.

From the many studies on whiskers that have been undertaken,<sup>54)</sup> it is clear that there are two kinds of growth mechanism. The earlier proposed mechanisms called for growth from the tip. The other possibility is growth from the base. As regards lithium deposition, the growth process still remains unclear. However, I would like to suggest one possible explanation<sup>53)</sup> based on the supposition that the fiber-like lithium is a whisker.

It has been reported that tin whiskers grow from the base and not from the tip.<sup>55)</sup> As lithium is a soft metal like tin, I believe that lithium whiskers also grow *via* the same mechanism as tin, namely growth from the base. The difference is that tin whiskers are

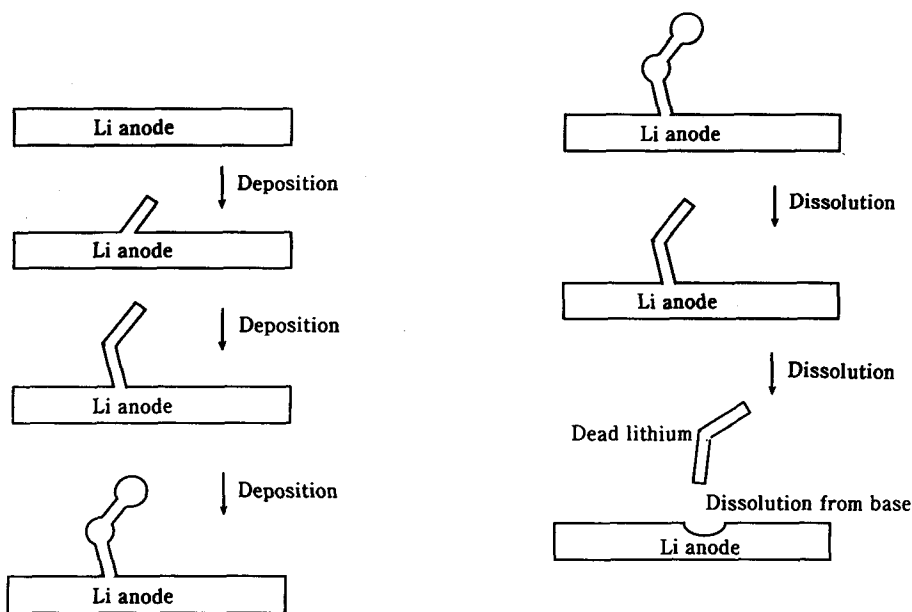


Fig. 4.2 A possible mechanism for lithium deposition based on lithium morphology observation in EC/2Me-THF//LiAsF<sub>6</sub> electrolyte.

created by stress in a tin substrate while lithium whiskers are formed by electrochemical deposition. I believe that lithium, deposited on a lithium substrate, causes stress in the substrate. *In situ* observations of lithium deposition showed a lithium whisker growing without change in the shape of its tip,<sup>53)</sup> although attempts to observe directly the situation at the base have been unsuccessful.<sup>56)</sup>

A possible mechanism for lithium deposition based on observations of lithium morphology in EC/2Me-THF//LiAsF<sub>6</sub> electrolyte is described below. Fig. 4.2 is a diagram of the mechanism.

- (1) Lithium is deposited on lithium anode under the protection film without serious damage to the film.
- (2) The deposition points on the lithium electrode are the points at which the protection film has a higher lithium ion conductivity. One example of these deposition points are the pits on the lithium anode caused by discharge. Crystalline defects and grain boundaries in lithium may also initiate deposition.
- (3) As lithium is not deposited uniformly for the reason mentioned above, mechanical stress is created in the lithium electrode under the protection film.
- (4) The stress causes lithium atom transport, which means deformation of the lithium, to release the stress in lithium. The lithium transport is not free but conditioned by a force created by lithium surface tension (including the surface tension caused by protection films) at a curved surface. In addition to this effect, the lithium transport may be affected by crystalline defects and grain boundaries.
- (5) The protection film is broken at certain places on the lithium surface by the stress. (*cf.* Ref. 57. Whiskers grow from weaker spots on the Sn surface where the surface oxide

has been broken.) Lithium whiskers grow, as extrusions of lithium, through these broken holes in the film. If the deposition current is small enough and the stress is therefore small, the protection film will probably not break. In this case, the deposited lithium may be particle-like or amorphous.

- (6) After lithium whiskers have grown, lithium is still deposited on the lithium substrate but not on the tip of the lithium whisker. If the deposition continues for a long time, the lithium electrode becomes covered with long lithium whiskers. In this situation, lithium ion transport in the electrolyte to the lithium electrode surface is hindered by the whiskers. Then, lithium begins to be deposited on the tip and on the kinks of the whiskers, where there are crystalline defects. The morphology of the deposited lithium is particle-like or amorphous. As there are many kinks, the current density of the lithium deposition becomes very low. This low current density may create particle-like lithium, rather than whiskers. So, the morphology of the lithium as a whole becomes mushroom-like.<sup>33)</sup>

The dissolution process of plated lithium may be the reverse of the plating process. First, the particle-like lithium on the kinks is dissolved. Then, the whiskers at the base are dissolved. If the dissolution current is larger than the deposition current, dissolution is not exactly the reverse of deposition. In this case, the amount of lithium dissolved at the kinks is larger. This situation is determined by the ease with which lithium ions are transported to the base lithium. When the dissolution current is smaller than the deposition current, the amount of lithium dissolved is smaller. During this process, whiskers are sometimes cut from the lithium substrate and become dead lithium. The amount of dead lithium is large when the whisker diameter is small under conditions of high rate deposition and/or low temperature deposition, because the whiskers are easily cut.

Experimental evidence to support this mechanism is as follows.

- (1) Lithium deposition was observed with an optical microscope in a dry room.<sup>53)</sup> The shape of the lithium whisker tip appears to remain the same during whisker growth.
- (2) The lithium whiskers begin to grow after some induction time and then suddenly stop growing. The whisker growing area on a lithium electrode moves from time to time. These phenomena are in good agreement with those of a proper whisker induced by stress in the base.
- (3) Kinks are also observed on the whisker as with a proper whisker growing from the base.<sup>56)</sup> The kinks of a whisker are created by crystalline defects in the base.
- (4) The diameter of the whisker appears to remain the same throughout the growth. This evidence supports the idea of lithium extrusion through a hole in the protection film.
- (5) Lithium deposition at kinks has been observed experimentally.<sup>56)</sup>

I have outlined the whisker theory concerning deposited lithium. This theory must be discussed and further experiments undertaken to confirm its validity. At the present time there exists no better explanation for the fiber-like and particle-like appearance of deposited lithium. A more detailed study should be undertaken in the future.

#### 4.2.5 The Amount of Dead Lithium and Cell Performance

This section describes the cycling life of lithium metal/a-V<sub>2</sub>O<sub>5</sub> AA-type cells<sup>1)</sup> with 2Me-THF-EC/LiAsF<sub>6</sub> electrolyte. FOMs are calculated using Eq. (4.8) based on cycling tests performed on the cells. The results are shown in Fig. 4.3. It is clear that FOM at a

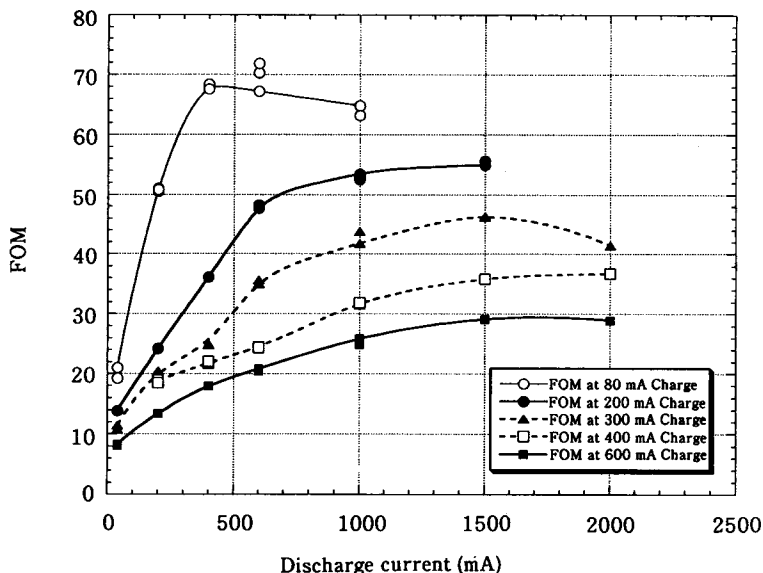


Fig. 4.3 FOMs calculated from cycling lives of lithium metal/a- $\text{V}_2\text{O}_5$  AA-type cells<sup>1)</sup> with 2Me-THF-EC/LiAsF<sub>6</sub> electrolyte.

low discharge rate is considerably smaller than that at a high discharge rate.

A heating test in an incubator is effective for evaluating the thermal limit at and below which the cell does not catch fire. In the thermal stability test, the temperature is increased by  $5^\circ\text{C}\cdot\text{min}^{-1}$  from room temperature and is held there once the hot box temperature reaches the target temperature. The thermal limit is the maximum temperature at which the cell does not ignite or smoke. From the experiment, the thermal limits are  $130^\circ\text{C}$ ,  $150^\circ\text{C}$  and  $125^\circ\text{C}$  for cells without cycling, cycled at a  $1000\text{ mA}$  (about  $5\text{ mA}\cdot\text{cm}^{-2}$ ) discharge for 150 cycles and cycled at  $100\text{ mA}$  (about  $0.5\text{ mA}\cdot\text{cm}^{-2}$ ) for 50 cycles. The thermal limit became higher as the current density increased. It is clear that lithium secondary battery safety is related to the discharge current density and that a lithium secondary battery cycled at a low discharge rate has poor thermal stability.

The influence of the discharge rate on the specific surface area of a lithium anode was examined<sup>58)</sup> using the Brunauer-Emmett-Teller (BET) equation. The cells were cycled at a high discharge rate  $3\text{ mA}\cdot\text{cm}^{-2}$  and at a low discharge rate of  $0.2\text{ mA}\cdot\text{cm}^{-2}$  for 6 cycles. The charge rate was  $1.0\text{ mA}\cdot\text{cm}^{-2}$  for all cells. The specific surface area was  $26\text{ m}^2\cdot\text{g}^{-1}$  for a low rate discharge of  $0.2\text{ mA}\cdot\text{cm}^{-2}$ , and  $13\text{ m}^2\cdot\text{g}^{-1}$  for a high rate discharge of  $3.0\text{ mA}\cdot\text{cm}^{-2}$ . It is clear that the surface area for low-rate discharge cycles is double that for high-rate discharge cycles. In addition the surface area increases with increase in cycle number. The surface area after the 6th discharge at a low discharge rate was 30 times larger than that before cycling ( $1\text{ m}^2\cdot\text{g}^{-1}$ ). The main reason for the increase in the lithium surface area is considered to be the accumulation of dead lithium on the anode surface. More dead lithium is accumulated during low-rate discharge cycles than during high-rate discharge cycles.

There are four reasons<sup>59)</sup> to explain why a higher current discharge creates a smaller

amount of dead lithium.

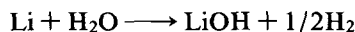
- (1) When the stripping current is high, delocalized pits (small in size but large in number) are formed on a native lithium anode. However, at low current, the pits are localized (large in size but few in number). As lithium is deposited on these pits, the local charge current density becomes high when the discharge current is low. The high charge current produces thinner lithium whiskers, which are easily cut off to form dead lithium.
- (2) When the stripping current is large, delocalized pits are formed on a native lithium anode, as mentioned above. The pits are shallow, so the deposited lithium whiskers can easily come out of the pits and stack pressure can be applied to them. When the stack pressure of the electrodes is high, the lithium whiskers are not cut easily during discharge, because the whiskers are compressed on base lithium anode. This compression effect is described in detail in a separate section.
- (3) Isolated lithium near the anode becomes a local cell because of stray current when the cell is discharged. Lithium deposition occurs at the side facing the anode, and stripping occurs at the other side. If the local deposition continues, the isolated lithium recombines with the base of the anode. Because the stray current is high when the cell discharge current is high, the lithium recombination occurs easily at a high discharge current.<sup>56)</sup>
- (4) As mentioned earlier, the ease with which the lithium is transported through deposited whiskers determines the stripping location. If the transport is easy, the stripping occurs from the base lithium. If the transport is difficult, the stripping occurs from the particle-like lithium on the tip and on the kinks of the whiskers. When the stripping (discharge) current is large, the transport becomes difficult, and this reduces the possibility of stripping from the base. In this case, the lithium whiskers rarely break off and the efficiency increases.

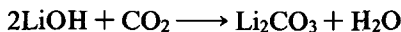
#### 4.2.6 Improvement in the Cycling Efficiency of a Lithium Anode

There have been many attempts to improve the cycling efficiency. Some of these, including native film on lithium, electrolyte, additive in electrolyte, stack pressure on electrode, composite anode and basic considerations are discussed below.

##### A. Native Film on Lithium

Commercially available lithium film is made by extruding a lithium ingot through a slit. The atmosphere in which the extrusion takes place affects the kind of native film produced. Hirayama *et al.*<sup>59)</sup> studied the discoloration of lithium foil during storage. They extruded lithium in dry air with different dew points, and observed the color after storage for 7 days at 60 °C. Extrusion at a dew point of −20 °C resulted in a blackish color. The native film of this sample was found to be LiOH rich by electron spectroscopy for chemical analysis (ESCA). This is caused by the reaction with H<sub>2</sub>O, and the sample showed high impedance. When the dew point is −40 °C, the lithium surface remains silver. Under drier conditions with a dew point of −60 °C, the surface changed to a yellowish color. The authors suggest that this yellowish discoloration is caused by a reaction with N<sub>2</sub>. This reaction is limited by the surface layer of stable Li<sub>2</sub>CO<sub>3</sub>, which is formed by the reaction with H<sub>2</sub>O, following the reaction





The sample does not exhibit a high impedance. However, the authors recommend the commercial production of silver lithium foil. Such foil can be produced by controlling the dew point during extrusion and by storing the lithium foil in an Ar + 0.10% CO<sub>2</sub> atmosphere. Similar results have also been reported<sup>60)</sup> for an Ar + CO<sub>2</sub> gas. By adding CO<sub>2</sub> atmosphere, impedance of the lithium does not become larger by storage. This result is also attributed to the formation of a stable Li<sub>2</sub>CO<sub>3</sub> film.

Higuchi *et al.*<sup>61)</sup> studied the dissolution of a lithium anode prepared in Ar + CO<sub>2</sub> gas. The lithium anode had clear boundaries after the dissolution. In contrast, a lithium anode prepared in Ar gas was partially dissolved and most of the surface was passivated.

### B. Electrolytes

Lithium cycling efficiency is strongly influenced by impurities in electrolytes. This relationship was studied in EC-2Me-THF/LiAsF<sub>6</sub> by Arakawa *et al.*<sup>62)</sup> When the electrolyte contains 130 ppm of water, 6200 ppm of 2-methylfuran (2MeF) and 6500 ppm of organic compounds, its FOM is 15 (Eff is 93%). The electrolyte was purified to an impurity level of 14 ppm water, 10 ppm 2MeF and 10 ppm organic compounds, and as a result the FOM was improved to 35.6 (Eff is 97%). Further 2MeF addition had no effect.

It was suggested by Pletcher *et al.*<sup>24)</sup> that PC will decompose when it comes in contact with lithium. This can occur indirectly *via* the formation of bases and/or nucleophiles, which include the lithium superoxide/peroxide/hydroxide layers formed by the reduction of O<sub>2</sub> and H<sub>2</sub>O existing as impurities in electrolytes.

Hayashi *et al.*<sup>31)</sup> investigated electrolytes using various carbonates and ethers as solvents and two solutes, in relation to the cycling efficiency of a lithium metal anode, using cells with a LiMn<sub>1.9</sub>Co<sub>0.1</sub>O<sub>4</sub> cathode. The cells were charged to 4.3 V at 1 mA·cm<sup>-2</sup> and discharged to 3.3 V at 3 mA·cm<sup>-2</sup> to the end of cycle. The end of cycle is the time when the capacity has fallen to 80% of its initial value. As electrolyte solvents, four carbonates were used: PC, EC, dimethylcarbonate (DMC), diethylcarbonate (DEC) and two ethers; 1,2-dimethoxyethane (DME) and 1,2-diethoxyethane (DEE). The electrolyte solutes were LiClO<sub>4</sub> and LiPF<sub>6</sub>. The lithium cycling efficiencies and figure of merit (FOM) are listed in Table 4.2. The EC-mixed electrolytes provided a higher FOM than the PC-mixed electrolytes. Of the electrolytes used, 1.0 M LiPF<sub>6</sub>-EC/DMC provided a high FOM of more than 40. A long cycle life of about 680 cycles was obtained using 1.0 M LiPF<sub>6</sub>-EC/DMC.

Table 4.2 Lithium cycling efficiency for EC and PC mixed electrolytes.<sup>31)</sup>

Electrolyte	FOM	Cycling efficiency (%)	Electrolyte	FOM	Cycling efficiency (%)
PC-DME/LiPF <sub>6</sub>	4.2	76	PC-DME/LiClO <sub>4</sub>	5.1	81
PC-DEE//LiPF <sub>6</sub>	2.1	53	PC-DEE/LiClO <sub>4</sub>	1.8	44
PC-DMC//LiPF <sub>6</sub>	29.9	97	PC-DMCLiClO <sub>4</sub>	13.2	92
PC-DEC/LiPF <sub>6</sub>	0	0	PC-DEC/LiClO <sub>4</sub>	0.2	0
EC-DME/LiPF <sub>6</sub>	14.2	93	EC-DME/LiClO <sub>4</sub>	7.8	87
EC-DEE//LiPF <sub>6</sub>	10.2	90	EC-DEE/LiClO <sub>4</sub>	12.2	92
EC-DMC//LiPF <sub>6</sub>	43.5	98	EC-DMC/LiClO <sub>4</sub>	23.3	96
EC-DEC//LiPF <sub>6</sub>	5.5	82	EC-DEC/LiClO <sub>4</sub>	4.3	77

Yokoyama *et al.*<sup>64)</sup> studied solvent stability toward metallic lithium. DMC and DME were stable; however, DEC reacted with lithium and produced ethanol, ethylene, acetylene and lithiummethoxide. The authors proposed a reaction mechanism on the basis of those products. Takehara *et al.*<sup>65)</sup> showed that lithium metal does not react with  $\text{LiPF}_6/\text{DEC}$ . They concluded that HF, included in the electrolyte as an impurity, is effective in suppressing the direct reaction between lithium and solvent.

3-Propylsydonone (3-PSD) was proposed as a new solvent by Sasaki *et al.*<sup>66)</sup> They studied mixed binary solutions of 3-PSD, 2Me-THF and 2,5-dimethyl-tetrahydrofuran with  $\text{LiPF}_6$ . The cycling efficiency of lithium on a Ni electrode was about 60% and it was stable with cycling.

### C. Additives in Electrolytes

There have been many studies with the goal of improving the lithium cycling efficiency by the use of additives in electrolytes. These additives can be classified into the following three types: (1) stable additives which cover the lithium to limit any chemical reaction between the electrolyte and lithium; (2) additives which modify the state of solvation on lithium ions; and (3) reactive additives used to make a better protection film.

Some of the studies on additives based on this classification are described below.

- (1) Stable additives which cover the lithium to limit any chemical reaction between the electrolyte and lithium.

Besenhard *et al.*<sup>67)</sup> studied corrosion protection of lithium anodes by adding saturated hydrocarbons to electrolytes. They considered saturated hydrocarbons to be chemically stable, thus able to delay the irreversible reduction of organic electrolytes by these highly active negatives. They found that the deposited lithium was particle-shape when *cis*- or *trans*-decalin was added to  $\text{LiClO}_4/\text{PC}$  electrolyte. Although there was no change in the cycling efficiency, the long-term storage characteristics were found to have improved.

Hirai *et al.*<sup>68)</sup> examined tetraalkylammonium chlorides with a long *n*-alkyl chain  $[\text{C}_n\text{H}_{2n+1}\text{N}(\text{CH}_3)_3]^+\text{Cl}^-$  ( $n = 1, 10, 12, 14, 16$  or  $18$ ) for use as additives in EC-2Me-THF/ $\text{LiAsF}_6$  electrolyte. The largest FOM was obtained by adding cetyltrimethylammonium chloride (CTAC;  $n = 16$ ). However, the stack pressure effect was suppressed by the addition.

Yoshio *et al.*<sup>69)</sup> tried benzene and toluene as additives and found them to be effective.

Later, Saito *et al.*<sup>70)</sup> studied anodes with a layered structure consisting of /Li/protection film/additive/protection film/Li/protection film/additive/—. They made the anode by dropping the additive on a lithium sheet, folding the lithium sheet and then compressing the folded lithium with an oil press. They repeated this process more than ten times. The FOMs in EC-2Me-THF/ $\text{LiAsF}_6$  electrolyte were 7.41, 13.5 and 37.0 for a lithium anode without additives, a lithium anode with toluene in the electrolyte and the layered structure lithium anode containing toluene, respectively. The layered structure lithium anode without additives also improved FOM. Thus, it appears that lithium incorporating protection layers is effective in increasing FOM.

- (2) Additives which modify the state of solvation on lithium ions

Tetramethylethylenediamine (TMEDA), cryptand [2,1,1] and tetraglyme were studied by Tobishima *et al.*<sup>71)</sup> The cycling efficiency was improved by adding TMEDA; however the other two additives proved ineffective.

Yoshio *et al.*<sup>72)</sup> studied the addition of organic compounds containing nitrogen atom to EC-PC-DME/ $\text{LiPF}_6$ . They used a thin lithium sheet to avoid the adverse effects of using

a substrate (full cell method). Their idea for selecting additives was to choose compounds with a high donor number, which solvate very strongly to lithium ions resulting a high over potential of deposition. This high over potential may result in a flat deposition because nonuniform activity on the lithium surface may not contribute to the total over potential. They found that the cycle life triples when 2-methylpyridine or *N,N*-dimethyl-*p*-toluigine is used.

### (3) Reactive additives used to make a better protection film

In the present author's opinion, the most exciting invention regarding an electrolyte for a lithium anode is 2Me-THF/LiAsF<sub>6</sub> by Koch.<sup>73)</sup> This electrolyte has good cycling efficiency. Abraham *et al.*<sup>74)</sup> showed that the high cycling efficiency is caused by 2MeF, which is naturally contained in 2Me-THF as an impurity. Tobishima and Okada<sup>75)</sup> showed that 2MeF is also a good additive for ester-based-electrolytes. Barthel *et al.*<sup>76)</sup> examined the cycling efficiency in 2Me-THF-based electrolytes, using Li on stainless steel method. They measured the dependence of LiClO<sub>4</sub> concentration (from 0.5 mol·kg<sup>-1</sup> to 2.8 mol·kg<sup>-1</sup>) and cycling capacity (from 10 mC·cm<sup>-2</sup> to 500 mC·cm<sup>-2</sup>) in LiClO<sub>4</sub>/2Me-THF electrolyte and found that there is no dependence on the cycling efficiency or cycling depth. An increase in the cycling efficiency was observed by the addition of a small amount of LiAsF<sub>6</sub>.

Quinoneimine dyes, aromatic-NO<sub>2</sub> compounds and triphenylmethane compounds were studied by Tobishima and Okada.<sup>77)</sup> The cycling efficiency was improved by adding quinoneimine dyes. However, the other two additives were ineffective.

Carbon dioxide has been proposed as an additive to improve the performance of lithium batteries.<sup>78)</sup> Osaka *et al.*<sup>79)</sup> made a detailed study of the effects of H<sub>2</sub>O and CO<sub>2</sub> in PC/LiClO<sub>4</sub> electrolyte. They deposited lithium on a Ni electrode and measured the AC-impedance. When the H<sub>2</sub>O concentration increases, the charge transfer resistance obtained from Cole-Cole plots becomes larger and the lithium cycling efficiency decreases. By adding CO<sub>2</sub>, the resistance becomes smaller and the cycling efficiency becomes larger. Protection against H<sub>2</sub>O impurity was also confirmed. These enhancements are only observed when the lithium is electrodeposited in the presence of CO<sub>2</sub> on Ni substrate. There is no enhancement when lithium is deposited without CO<sub>2</sub> and is cycled with CO<sub>2</sub>. They believe that this enhancement is due to products formed by the reaction of lithium with CO<sub>2</sub> on the electrodeposited lithium surface. Aurbach and Chusid<sup>80)</sup> studied the film formed on lithium in electrolytes saturated with CO<sub>2</sub>, and using *in situ* FTIR, found Li<sub>2</sub>CO<sub>3</sub> to be a major surface species. This means that the formation of stable Li<sub>2</sub>CO<sub>3</sub> film on lithium surface may improve cyclability.<sup>81)</sup> Osaka *et al.*<sup>82)</sup> also studied the dependence of the efficiency on the substrate using the Li on Ni method. The addition of CO<sub>2</sub> resulted in an increase in the efficiency when the substrate was Ni or Ti. However, no effect was observed with Ag or Cu substrates.

Takehara *et al.*<sup>83)</sup> tried to modify the lithium native film by acid-base reaction. HF, HI, H<sub>3</sub>PO<sub>4</sub> and HCl were selected as acids because of their possibility to react with Li<sub>2</sub>CO<sub>3</sub>, LiOH and Li<sub>2</sub>O, which compose the lithium native film, resulting in the formation of LiA (HA: Acid). By XPS, LiF was observed in the film treated with HF, and there was Li<sub>3</sub>PO<sub>4</sub> in the film treated with H<sub>3</sub>PO<sub>4</sub>. All acid-treated lithium exhibited dendritic (fiber-like) deposition in LiClO<sub>4</sub>/PC electrolyte. In contrast, HF treatment changed the deposition morphology from dendritic to particle-like in LiPF<sub>6</sub>/PC electrolyte. They suggest that the particle-like deposition is caused by the use of LiPF<sub>6</sub> solute and thin native film. XPS



showed that after HF treatment the lithium surface was composed of two layers (LiF and  $\text{Li}_2\text{O}$ ), whereas the native surface was composed of three layers ( $\text{Li}_2\text{CO}_3$ , LiOH and  $\text{Li}_2\text{O}$ ). The impedance of the lithium was reduced by this treatment. The morphology of lithium electrodeposited on the modified lithium was spherical even after the charge and discharge cycles. The cycling efficiencies<sup>84)</sup> in  $\text{LiPF}_6/\text{PC}$  were 57% and 70% for as-received and HF-treated lithium, respectively. Modification similar to that achieved with HF-treatment can be accomplished by immersing lithium in  $\text{LiPF}_6/\gamma\text{-BL}$  or  $\text{LiPF}_6/\text{PC}$  for three days.<sup>85)</sup> The lithium modified in  $\text{LiPF}_6$  solution showed particle-like lithium deposition. However, dendritic lithium was deposited from a lithium anode treated in  $\text{LiBF}_4$  solution. The authors consider this difference to be due to the morphological difference in the LiF layer. The lithium surface was identified by XPS analysis. The layers, starting from the top are: /LiOH and  $\text{Li}_2\text{CO}_3$ -major species, LiF or LiCl-minor species/ $\text{Li}_2\text{O}/\text{Li}/$ , /LiF-major species, LiOH and  $\text{Li}_2\text{CO}_3$ -minor species/LiF-major species,  $\text{Li}_2\text{O}$ -minor species/Li/ and /LiF-major species, organic compounds, LiOH and  $\text{Li}_2\text{CO}_3$ -minor species/LiF and  $\text{Li}_2\text{O}/\text{Li}/$  for the lithium immersed in  $\text{LiClO}_4$  or  $\text{LiAsF}_6/\gamma\text{-BL}$ ,  $\text{LiBF}_4/\gamma\text{-BL}$  and  $\text{LiPF}_6/\gamma\text{-BL}$ . They reported that  $\text{LiClO}_4/\text{PC}$  containing a small amount of HF also improved the morphology of lithium deposited on Ni to a particle-like shape.<sup>86)</sup>

Matsuda *et al.*<sup>87)</sup> examined LiI,  $\text{SnI}_2$ ,  $\text{AlI}_3$  and 2Me-F (2-methylfuran) as additives in  $\text{LiClO}_4/\text{PC}$  electrolyte. They measured the cycling efficiency of lithium on a Ni electrode. All the additives increased the efficiency. The best additive was a combination of  $\text{AlI}_3$  and 2Me-F. They considered that the formation of Li-Al alloy on the surface by  $\text{AlI}_3$  or a better protection film formed by 2Me-F was the reason for the improvement.

As described above, much research is currently being undertaken and the cycling efficiency of practical cells is certain to be improved in the near future. However, it will be useful to consider the following three points when studying additives.

- (1) Some additives are decomposed by reduction on the anode and/or oxidation on the cathode with long cycling.
- (2) Actual cycling efficiency is different from that obtained by the Li on Ni or Li on Li method. The substrate where lithium is deposited is not Ni but lithium.
- (3) In practical cells, the electrodes are pressurized as a result of the limited volume of the can. As described in the following section, this stack pressure increases the cycling efficiency. Some additives suppress the effect of the improvement caused by the pressure.

#### D. Stack Pressure on Electrodes

One very useful method for improving the cycling efficiency is to pressurize the electrode stack. The 1985 patent for this method (by Moli Energy Limited)<sup>88)</sup> mentions that lithium deposited under stack pressure is nonporous, and the load enhances the lithium cycling efficiency. A more detailed study was undertaken by Wilkinson *et al.*<sup>89)</sup> and Hirai *et al.*<sup>43)</sup>

Wilkinson *et al.*<sup>89)</sup> examined the effect of stack pressure on the lithium turnover (FOM for lithium cycling efficiency) in Li/ $\text{MoS}_2$  prismatic cells containing 1 M  $\text{LiAsF}_6/\text{PC}$ . The lithium turnover was only about 2 without pressure. The value increased to about 9 when the pressure was 60 psi–170 psi. They believe that the effect is the result of lithium deformation because the creep strength of lithium is 60 psi for 2.2 h and tensile strength is 84 psi at room temperature. The cycle life for spirally wound AA-size Li/ $\text{MoS}_2$  cells showed that when the electrode assembly is housed tightly in the cell the cycle life is longer than with loosely housed cells.

FOMs were also measured<sup>43)</sup> by full cells with an amorphous  $V_2O_5(-P_2O_5)$  cathode and a very thin lithium anode. EC-2Me-THF/LiAsF<sub>6</sub> electrolyte showed FOM of 80 at 125 kgf·cm<sup>-2</sup> ( $1.23 \times 10^3$  Ncm<sup>-2</sup>), which was almost four times the value without compression. The SEM image of the lithium deposited under stack pressure shows that the deposition is densely packed. The lithium whiskers and particles were deformed by the small space available for deposition. They contacted each other and the substrate anode. This morphology suggests that the lithium deposited under stack pressure was not isolated from the anode substrate resulting in a high cycling efficiency.

In practical cells, the volume of some cathode active materials increases with cycling because of the transition from the crystalline state to the amorphous state. And lithium anode becomes porous with cycling. However, because here the space for the deposition is limited, the lithium does not become very porous. For this reason, high stack pressure should be employed for the anode in a practical cell.

### E. Composite Lithium Anode

Desjardins and MacLean<sup>90)</sup> studied a composite of lithium and Li<sub>3</sub>N named "Linode." Their research cell showed improved cycle life, shelf life and electrode morphology after cycling. A lithium alloy with a very small amount of Al (0.1–2.0 wt%) or Sn (0.3 wt%) was studied by Matsuda *et al.*<sup>91)</sup> They found that their Li–Al electrode showed low impedance even after long immersion in electrolyte, and the charge–discharge current did not decay during repeated cycling voltammetry.

A lithium anode mixed with conductive particles of Cu or Ni was studied by Saito *et al.* with the goal of improving the cycling efficiency.<sup>92)</sup> Their idea is based on a recombination of dead lithium and the formation of many active sites for deposition. The cycling efficiency was measured using the conventional full cell method with an amorphous  $V_2O_5(-P_2O_5)$  cathode in EC-2Me-THF/LiAsF<sub>6</sub>. At a low rate discharge cycle (discharge current: 0.2 mA·cm<sup>-2</sup>, charge current: 0.4 mA·cm<sup>-2</sup>), the efficiencies were 92.0%, 97.2%, 94.9% and 98.3%, respectively, for pure lithium, lithium with Cu particles, lithium with Ni particles and lithium with carbon particles.

The advantage of these composite anodes is that they result in uniform lithium deposition at the boundaries of two components, and this uniform deposition may improve the cycling efficiency.

### F. Basic Considerations Regarding Efficiency Improvement

Dendritic structures are observed at the interface between two immiscible fluids with different viscosities, confined between two parallel closely separated plates, when pressure is applied to the less viscous fluid.<sup>93)</sup> The structure of the pattern changes depending on the strength of the applied pressure. The mathematical model describing the dynamics of the interface is fluid dynamics with a boundary condition of pressure induced by surface tension at the interface of the two fluids. Basically, the morphology of the deposited lithium can be explained with this model.

First, we introduce a very simple model.<sup>53)</sup> If we assume that lithium is deformed as the result of a pressure difference on the lithium surface ( $\Delta P$ ) caused by surface tension and that deformation occurs even by a very low  $\Delta P$  (like water), the following equation is applied:

$$\Delta P = \gamma(1/R_1 + 1/R_2) \quad (4.9)$$

where  $\gamma$  is the surface tension on the lithium surface (or surface energy), and  $1/R_1$  and  $1/R_2$

$R_2$  are normal curvatures of the lithium surface whose curves on the surface are perpendicular to each other.

Supposing that the lithium surface is symmetrical around the  $x$ -axis, we can describe the lithium surface by the distance between the surface and the  $x$ -axis;  $y=f(x)$ . In this case, Eq. (4.10) is derived from Eq. (4.9).<sup>94)</sup>

$$d^2y/dx^2 = -\Delta P/\gamma[1 + (dy/dx)^2]^{3/2} + [1 + (dy/dx)^2]/y \quad (4.10)$$

Numerical calculation was performed from Eq. (4.10) using the calculation program Mathematica (Wolfram Research, Inc.). From Eq. (4.9), a solution is a sphere with a radius of  $2\gamma/\Delta P$ . Another way to calculate the radius is from Eq. (4.10). The shape is spherical when  $\Delta P/\gamma$  is  $2/\{y(0)[1 + y'(0)^2]^{1/2}$ . If  $2\gamma/\Delta P$  is larger than  $2/\{y(0)[1 + y'(0)^2]^{1/2}$ , the surface does not have a solution near  $y=0$ . The boundary condition for this solution is that the lithium is on a plate with corn. If  $\Delta P/\gamma$  is smaller than  $2/\{y(0)[1 + y'(0)^2]^{1/2}$ , the surface also has no solution near  $y=0$ . This solution appears when the lithium is between two plates. There is a numerical solution for  $\Delta P/\gamma=0$ ;  $y=A \cosh[(x+B)/A]$ , where  $A$  and  $B$  are constants.<sup>95)</sup>

At the beginning of lithium deposition, lithium morphology corresponding to  $\Delta P/\gamma < 2/\{y(0)[1 + y'(0)^2]^{1/2}$  or  $\Delta P/\gamma > 2/\{y(0)[1 + y'(0)^2]^{1/2}$  may not appear because they do not have a value at  $y=0$ . As the plating continues, the radius of the sphere becomes larger and  $\Delta P$  decreases. As a result, the lithium cannot become deformed because  $\Delta P$  is low. The shape will no longer be a sphere, but probably a deformed sphere. With further plating, the lithium may break a weak spot in the protection film and be extruded through the hole to form a whisker. If we want to continue the sphere deposition,  $\Delta P$  must be large even if  $R$  is large. From the relation  $\Delta P=2\gamma/R$  derived by Eq. (4.9),  $\Delta P$  is large when the surface tension is high. If we use an additive to create a very high surface tension, sphere lithium may be deposited.

### 4.3 Safety

Lithium metal secondary battery systems were formerly extensively investigated.<sup>96)</sup> With regard to large capacity lithium secondary cells such as AA-size or larger, many prototype cells with different cell chemistries were constructed and evaluated worldwide.<sup>97)</sup> However, AA-size Li/MoS<sub>2</sub> cells were recalled because of an unfortunate incident in 1989. Since then the development of the lithium metal cells has almost completely stopped because of safety problems. Just after the incident, a safer lithium cell called a lithium ion cell was developed and is now commercially available.

However, the high energy density of the lithium metal cell is still very attractive, if the safety problem can be resolved. Now, Tadiran (Tadiran Battery Division, Israel) and NTT (Nippon Telegraph and Telephone Corporation, Japan) are working independently on prototype cells with metal lithium anodes. Tadiran has reported making an AA-size cell (TLT-7301) with a metal lithium anode and a lithiated MnO<sub>2</sub> cathode.<sup>98)</sup> The separator is a polypropylene porous film and the electrolyte is an organic electrolyte. The cell possesses an energy density of 125 to 140 Wh·kg<sup>-1</sup> and 280 to 315 Wh·l<sup>-1</sup>. The cell is cycled between 3.4 and 2 V at a discharge current of 250 mA and a charge current of 60 mA. The initial capacity is about 800 mAh. After 250 cycles, its capacity is about 550 mAh. The

*FOM* of lithium cycling efficiency is 70–80. There is no undesirable event by short circuit, overcharge, forced discharge, crush and nail penetration tests. The cell appears to be excellent in many respects. However, the available information is limited, and so I would like to introduce the performance of the NTT cell,<sup>1)</sup> in detail in this section.

#### 4.3.1 Configuration of Prototype Cells<sup>1)</sup>

The conductivity of the nonaqueous electrolyte used in the AA-size lithium metal anode prototype cells is one order of magnitude lower than that of an aqueous system. Thus thin electrodes are wound in a “jelly roll” configuration in order to increase the electrode area and thereby provide the cell with a high rate capability.

Amorphous- $\text{V}_2\text{O}_5(-\text{P}_2\text{O}_5)(\text{a-V}_2\text{O}_5(-\text{P}_2\text{O}_5))$  was used as the cathode active material. To make amorphous state  $\text{V}_2\text{O}_5$  easily, a small amount of  $\text{P}_2\text{O}_5$  was mixed with it.<sup>99)</sup> Fig. 4.4 shows the long term cyclability of a- $\text{V}_2\text{O}_5(-\text{P}_2\text{O}_5)$  in a laboratory coin-type cell with a large excess of lithium. Amorphous- $\text{V}_2\text{O}_5(-\text{P}_2\text{O}_5)$  could be cycled more than 4000 cycles with a minimal capacity fading rate. An a- $\text{V}_2\text{O}_5(-\text{P}_2\text{O}_5)$  cathode, comprising a- $\text{V}_2\text{O}_5(-\text{P}_2\text{O}_5)$ , carbon and polymer binder, was coated and pressed on aluminum foil by the conventional slurry coating method.  $\text{LiAsF}_6/\text{EC}-2\text{Me}-\text{THF}/\text{LiAsF}_6$  electrolyte<sup>100)</sup> was used as the electrolyte because of its high lithium cycling efficiency as well as its high lithium ion conductive nature. A microporous polyethylene film was used as the separator.

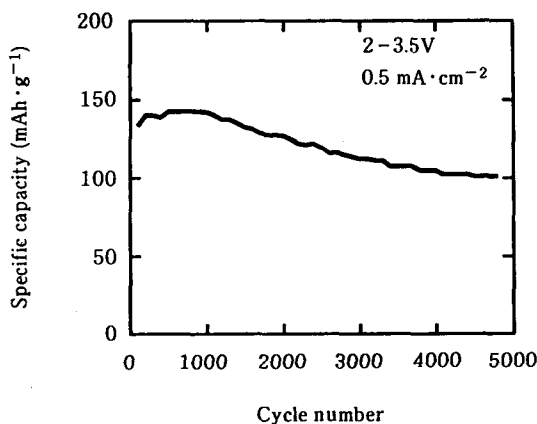


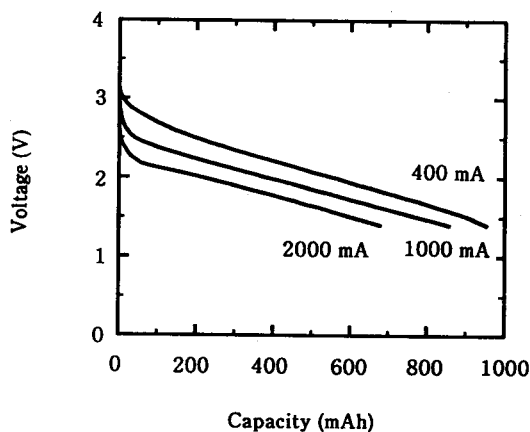
Fig. 4.4 The long-term cyclability of a- $\text{V}_2\text{O}_5(-\text{P}_2\text{O}_5)$  in a laboratory coin-type cell with a large excess of lithium.

#### 4.3.2 Cell Performance<sup>1)</sup>

The characteristics of the prototype AA-cell are shown in Table 4.3. A 2WH-class AA-size rechargeable  $\text{Li}/\text{a-V}_2\text{O}_5(-\text{P}_2\text{O}_5)$  cell has been developed. It weighs 18 g and delivers a nominal capacity of 900 mAh at 600 mA for 150–300 cycles, resulting in a high energy density of  $110 \text{ Wh}\cdot\text{kg}^{-1}$  or  $250 \text{ Wh}\cdot\text{l}^{-1}$ . Moreover, it can be discharged up to about a 2C

Table 4.3 Characteristics of AA-size Li/a- $\text{V}_2\text{O}_5$ (- $\text{P}_2\text{O}_5$ ) cell.

Volume	8 cm <sup>3</sup>
Weight	18 g
Current range	discharge: 400–2000 mA charge: not larger than 200 mA
Voltage range	3.3–1.5 V
Capacity	900 mAh
Energy	2 Wh
Energy density	weight: 110 Wh·kg <sup>-1</sup> volume: 250 Wh·l <sup>-1</sup>
Cycle life	150–300 cycle
Self-discharge rate	1%/month at 21 °C

Fig. 4.5 Rate capability of AA-size Li/a- $\text{V}_2\text{O}_5$ (- $\text{P}_2\text{O}_5$ ) cell.Table 4.4 Safety test results for AA-size Li/amorphous  $\text{V}_2\text{O}_5$ (- $\text{P}_2\text{O}_5$ ) cells (Precycling conditions; charge current; 200 mA, discharge current; shown in the table, cycling number; shown in the table).

Abuse test	Test conditions	Fresh cell	Results (○; no fire)			
			Discharge current; 1000 mA		Discharge current; 400 mA	
			Cycled 75 times	Cycled 150 times	Cycled 60 times	Cycled 120 times
External short	Room temp. (RT)	○	○	○	○	○
	40 °C	○	○	○	○	○
Forced discharge*	RT	○	○	○	○	○
	40 °C	○	○	○	○	○
Overcharge	Charge; { RT	○	○	○	○	○
	200 mA { 40 °C	○	○	○	○	○
	Charge; { RT	○	○	○	○	○
	600 mA { 40 °C	○	○	○	○	○
Crush	RT, round bar	○	○	○	○	○
	RT, flat plate	○	○	○	○	○
Nail penetration	RT	○	○	○	○	○
Thermal stability (Max. safe temp.)	5 °C/min, held at a certain temp.	130 °C	150 °C	150 °C	140 °C	130 °C

\* Forced discharge; Short test of 4 cell pack with series connection. 3 cells are fully charged. 1 cell is discharged to 1.5 V.

rate. These are very attractive features for high rate discharge applications. A low self-discharge rate of 1%/month is also a beneficial characteristic of this cell.

The maximum discharge current is 2 A, which value is limited by a polyswitch (thermal and current fuse) in the cell. The rate capability is shown in Fig. 4.5. The cycle life depends on both the charge and discharge currents as with other lithium metal anode cells. The cycle life tends to decrease with increasing discharge current. As regards charging, the life decreased with increasing charge current. The standard charge current is 200 mA. This is because a too long charge time is not good for practical use.

The results of safety tests are summarized in Table 4.4. I will describe the technology used to improve the safety in the following section.

### 4.3.3 Heat Generation in a Cell—General Considerations

This section is a basic discussion of safety issues. The discussion is not restricted to the cells studied by NTT, but is intended to be useful for all kinds of lithium metal and lithium ion cells. For this reason, both metal lithium and carbon anodes are discussed in this section.

The temperature of a cell is determined by the heat balance between the amount of heat generated in the cell and heat dissipated outside the cell. Heat is generated in a cell by the thermal decomposition and/or reaction of the materials in the cell. The different causes are listed below.

- (1) A reaction between an electrolyte and an anode
- (2) The thermal decomposition of an electrolyte
- (3) A reaction between an electrolyte and a cathode
- (4) The thermal decomposition of an anode
- (5) The thermal decomposition of a cathode
- (6) An entropy change in a cathode active material (and an anode active material)
- (7) Current passing through a cell with electric resistance

When a cell is heated by some trigger (for example, internal short, high current application and overcharge), heat will be generated as mentioned above, if the cell temperature is high enough to cause decomposition and/or a reaction. This situation leads to the thermal run-away of the cell. The problem is that the electrolyte used in the cell is flammable. In the worst case, the cell ignites. If the additional heat generation is small, the cell temperature does not rise too high, and the cell is safer. The causes of internal heat generation are described below.

- (1) A reaction between an electrolyte and an anode

Although the reaction between an electrolyte and lithium metal (or lithiated carbon) is limited by a protection film on the surface of the lithium anode, the two react when the temperature increases, because the thickness of the protection film is insufficient to prevent the reaction at an elevated temperature. The reaction continues until the protection film reaches a given thickness. This reaction is exothermic, so it increases the cell temperature. For example, this situation appears at a cell heating test. A cell is placed in an incubator, and the air temperature is increased to a certain temperature. The cell temperature

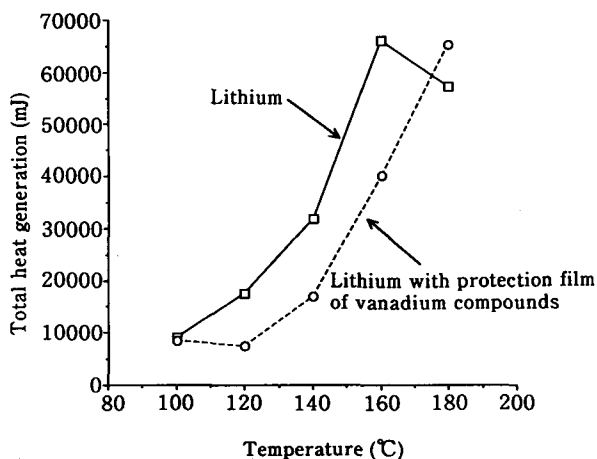


Fig. 4.6 The amount of heat generation for 10 h by mixing lithium metal deposited on stainless steel and EC-PC/LiAsF<sub>6</sub>. Open squares: usual protection film on lithium. Open circles: vanadium compounds covering the lithium surface.

becomes higher than the ambient air temperature. The higher temperature is caused mainly by the reaction between the electrolyte and the lithium metal, because the cell temperature finally decreases to the air temperature.

Arakawa *et al.*<sup>101)</sup> measured the amount of generated heat. Lithium metal was deposited on stainless steel in EC-2Me-THF/LiAsF<sub>6</sub>, and the deposited lithium was removed from the electrolyte. The deposited lithium and EC-PC/LiAsF<sub>6</sub> electrolyte were suddenly mixed at a certain temperature. As shown by the squares in Fig. 4.6, the amount of heat generated in 10 h increased as the mixing temperature increased, because a thicker protection film is formed at a higher temperature. It appears that all the lithium reacts at a temperature above 160 °C. If a cell has an a-V<sub>2</sub>O<sub>5</sub>(-P<sub>2</sub>O<sub>5</sub>) cathode, a small amount of vanadium compound dissolves in the EC-2Me-THF/LiAsF<sub>6</sub> electrolyte and some vanadium compounds cover the lithium surface forming a protection film. This type of lithium anode, with a protection layer formed of vanadium compounds, showed less reactivity than the normal lithium anode, as shown by the circles in Fig. 4.6.

## (2) The thermal decomposition of an electrolyte

When an electrolyte is heated, it decomposes at a certain temperature with heat generation. The decomposition temperatures of electrolytes are measured using an accelerating-rate calorimeter.<sup>102)</sup> For EC-PC/LiAsF<sub>6</sub> electrolyte, the onset temperature of the decomposition is 190 °C. When 2Me-THF is added to the electrolyte, the decomposition temperature becomes lower. The decomposition temperatures are 145 °C and 155 °C for EC-2Me-THF(50:50)/LiAsF<sub>6</sub> and PC-EC-2Me-THF(70:15:15)/LiAsF<sub>6</sub>, respectively. When LiCF<sub>3</sub>SO<sub>3</sub> is used instead of LiAsF<sub>6</sub>, the thermal stability is greatly improved. PC-EC-2Me-THF(70:15:15)/LiCF<sub>3</sub>SO<sub>3</sub> has a decomposition temperature of 260 °C. The thermal stability of the electrolytes decreased after anodic oxidation for one day.

2Me-THF cannot be used for 4 V cells because of its low oxidation potential. The decomposition temperatures of electrolytes with EC-DME solvent were observed by

Table 4.5 Decomposition onset temperature of PC/DME.<sup>103,104)</sup>

Solvent	Salt	Others	Decomposition onset temperature (°C)
PC/DME	{ none	none	265
	{ LiClO <sub>4</sub>	none	217
	{ LiCF <sub>3</sub> SO <sub>3</sub>	none	268
	{ LiPF <sub>6</sub>	none	156
	{ none	Lithium metal	185
	{ LiClO <sub>4</sub>	Lithium metal	149
	{ LiCF <sub>3</sub> SO <sub>3</sub>	Lithium metal	155
	{ none	MnO <sub>2</sub>	132
	{ LiClO <sub>4</sub>	MnO <sub>2</sub>	138
	{ LiCF <sub>3</sub> SO <sub>3</sub>	MnO <sub>2</sub>	144
	{ none	Lithium metal and MnO <sub>2</sub>	187
	{ LiClO <sub>4</sub>	Lithium metal and MnO <sub>2</sub>	173
	{ LiCF <sub>3</sub> SO <sub>3</sub>	Lithium metal and MnO <sub>2</sub>	171

Hasegawa and Arakawa.<sup>103)</sup> Their results are shown in Table 4.5. LiCF<sub>3</sub>SO<sub>3</sub> salt was found to be the most stable solute. They also examined other electrolytes for 4 V cathodes and found that the onset temperatures are 151 °C [PC–DME(50 : 50)/LiPF<sub>6</sub>], 175 °C [PC–DEC(50 : 50)/LiPF<sub>6</sub>], 175 °C [EC–DEC(50 : 50)/LiPF<sub>6</sub>], 181 °C [EC–DMC(50 : 50)/LiPF<sub>6</sub>] and 161 °C [EC–PC(50 : 50)/LiPF<sub>6</sub>].<sup>104)</sup>

(3) A reaction between an electrolyte and a cathode

An electrolyte whose decomposition voltage is higher than the cathode voltage is usually selected for a cell. So this reaction seldom occurs. One example is overcharge, where the electrolyte is oxidized with heat generation. Laman *et al.*<sup>105)</sup> measured the temperature during the overcharge of a Li/a-V<sub>2</sub>O<sub>5</sub>(-P<sub>2</sub>O<sub>5</sub>) cell with 2Me–THF–EC/LiAsF<sub>6</sub>. They calculated the amount of heat generated by the electrolyte decomposition and found that the amount is double that caused by  $I^2R$  ( $I$ : current,  $R$ : cell resistance).

(4) The thermal decomposition of an anode

Lithium metal melts at 180 °C (endothermic). When a cell with a lithium anode is heated to higher than 180 °C, the cell temperature stops rising at around 180 °C because of melting lithium. There is no problem for the lithium metal cell. However, one must be careful about the melted lithium in terms of its reactivity and the fact that when it flows it may cause an internal short.

Carbon anodes are used in lithium ion cells. Fouchard *et al.*<sup>106)</sup> reported that lithium inserted graphite (Li<sub>0.86</sub>C<sub>6</sub>) decomposes at 180 °C with heat generation. Tukamoto *et al.*<sup>107)</sup> examined the lithium content in a graphite and nail penetration test. If it is assumed that 100% lithium insertion is LiC<sub>6</sub>, the safety limit of lithium insertion is 60%, because too much insertion causes exothermic decomposition from a lower temperature.

(5) The thermal decomposition of a cathode

A 4 V cathode (LiCoO<sub>2</sub>, LiNiO<sub>2</sub> and LiMn<sub>2</sub>O<sub>4</sub>) is unstable, especially when in the charged state.<sup>9)</sup> Some decompose even at 180 °C. The V<sub>2</sub>O<sub>5</sub> cathode is safer because it melts at 690 °C consuming heat (endothermic) and decomposes at a high temperature of 1750 °C (exothermic).

Fouchard *et al.*<sup>106)</sup> examined the heat generation of a cell with 4 V cathodes in the charged state, and they found that the decomposition temperature decreased in the order of



$\text{LiMn}_2\text{O}_4$ ,  $\text{LiCoO}_2$  and  $\text{LiNiO}_2$ . Dahn *et al.*<sup>108)</sup> reported similar results. Ohzuku *et al.*<sup>109)</sup> were successful in improving the thermal stability of  $\text{LiNiO}_2$  by replacing Ni with Al. Replacement with Co or Mn was also reported to be effective.  $\text{LiNiO}_2$  is a very attractive material in terms of its high rechargeable capacity compared with the other two materials. However, its stability seems to be reduced when too much lithium is extracted from it.

(6) Entropy change of a cathode active material (and an anode active material)

Kanari *et al.*<sup>110)</sup> showed that when a lithium ion cell (AA-size) with  $\text{LiCoO}_2$  cathode is charged, it is endothermic, and during discharge, the cell is exothermic. This is because of the change in entropy caused by the insertion to the cathode active material. The amount of heat output and input at 36 mA current appears to be less than 10 mW. This value is small but cannot be ignored. All chemical cells exhibit this effect.

(7) Current passing through a cell with electric resistance

A cell has electrical resistance ( $R_c$ ), and when a current ( $I$ ) is passed through the cell, the amount of heat generated by the cell resistance is  $I^2 R_c$ . This is sometimes called heat generation from polarization. When a cell is externally shorted, the heat generated by the cell resistance is dominant. However, this effect is also observed for all other types of cells including NiCd and NiMH cells.

If we reduce the amount of heat generation and increase the heat generation temperature of the above factors, the cell becomes safer. Another approach is to use a non-flammable or non-burning electrolyte. Some very interesting basic studies have been reported on the possibility of the use of room temperature molten salt by Koura *et al.*,<sup>111)</sup> Carlin<sup>112)</sup> and Fuller.<sup>113)</sup> At present, lithium cannot be cycled in a molten salt electrolyte because of the reduction of the electrolyte. A higher voltage anode such as Li-Al alloy can be cycled. This approach is very interesting as a way of improving cell safety.

#### 4.3.4 Incidents During Normal Cycling

The author has been undertaking cycling tests on lithium metal anode AA-size cells since 1985. Unfortunately, in early stages of this work, there were incidents during normal cycling tests. The incidents occurred at a probability of around 1%. These incidents are believed to have occurred for the following reasons.

(1) A lithium anode cut at the end of a cathode

Lithium is not consumed uniformly on an anode during cycling. When a cell is disassembled after cycling, more lithium is consumed along the line where the anode lithium is facing the winding end of the cathode sheet. This is caused by the "edge effect." A larger current passes through the edge of an electrode than through any other part, because ions in the electrolyte can move outside the electrode to reach the end. When the anode is cut by the edge effect during cycling, the surface area of anode decreases to about one tenth. Then a very large current density appears on the anode, and this heats up the cell. To confirm this theory, a cell with its anode deliberately cut at the place was made. The separator in the cell was burned after discharge.

To avoid cutting the anode, a lithium sheet with a copper substrate is used. However, the cycle life is reduced to 75%. The cycle life of this cell with a pure lithium anode (not using a copper substrate) is shown in Fig. 4.7.

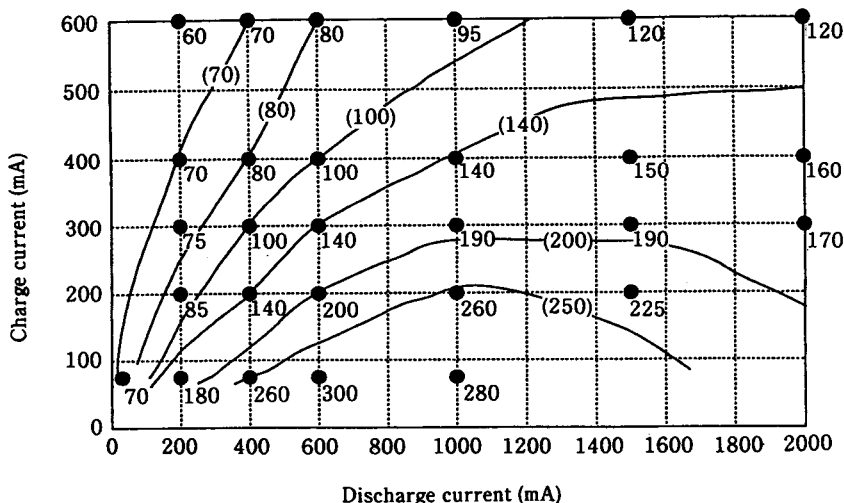


Fig. 4.7 The cycling life of AA-size Li/a- $\text{V}_2\text{O}_5(-\text{P}_2\text{O}_5)$  cell with pure lithium anode (not using copper substrate).

### (2) An anode tab disconnection during cycling

The disconnection of an anode tab by the edge effect is another possible reason for the incidents. If the anode tab is welded to the lithium and the welded part is facing the cathode, the lithium surface next to the tab is consumed rapidly by the edge effect. Then, after a long period of cycling, the tab may become disconnected from the lithium. In this case, the surface area of the anode is reduced to just the anode tab, and as a result, the high current density on the anode generates heat. In our cell, the anode tab does not face the cathode.

### (3) An internal short

There is also the possibility that an internal short may lead to an incident. A nail penetration test is an effective way of insuring against such an occurrence. If a cell smokes, fires or explodes as a result of the test, the cell is deemed unsuitable for commercial use. However, an internal short will raise the cell temperature above  $100^\circ\text{C}$  even if the cell has passed the nail penetration test. So it is recommended to try to reduce the probability of the internal short itself.

An internal short may be caused by a manufacturing defect such as a small conductive particle wound in a jelly roll, a wrinkle in a separator or poor alignment. In addition to the above, a lithium dendrite short may occur in a lithium metal anode cell. From our AA-cell data, a dendrite short should not occur if the discharge current is higher than 200 mA ( $1\text{ mA}\cdot\text{cm}^{-2}$ ). Unfortunately, we experienced a short at a discharge of 100 mA. If it is accepted that the lithium whisker grows from the base during deposition, the current dependence of the dendrite short can be explained. When the lithium grows from the base, no lithium whisker can pass through the holes in the separator because the whiskers are soft and the holes are not straight. Growth from the base may be terminated by the accumulation of the dead lithium, which suppresses lithium ion transport to the base. Then, at a low-rate discharge, lithium may be deposited on the surface of the deposited lithium (tip or kink) resulting in lithium deposition in the holes of the separator. In this

case, a lithium dendrite short will occur. Of course, a very high stack pressure is another factor that can induce a dendrite short caused by separator damage.

#### 4.3.5 Safety Tests on AA-size Li/a-V<sub>2</sub>O<sub>5</sub>(-P<sub>2</sub>O<sub>5</sub>) Cells

The results are summarized in Table 4.4. These results suggest that if the cells are made very carefully and do not differ from the intended design, they will be safe. At a low rate discharge (less than 400 mA), the cycle life is very short. Therefore, if the application is limited to high rate use, the cell is almost as safe as a lithium ion cell.

A brief description of each test is given below.

##### (1) External short

The old type of cell had a polypropylene separator and no polyswitch (thermal and current fuse). Some of these old type cells became unsafe after a long low rate discharge cycle (40 mA discharge). A polyethylene separator was used to overcome this problem. In the final version of the cell, a polyswitch is also used to make an even safer cell.

##### (2) Overcharge

We tried a very deep overcharge. In every case, if we continued charging, the cell suddenly exhibited a very high impedance. With a high charging current, the high impedance is caused by the separator melting. At a lower charge current, it is as the result of the electrolyte drying up by electrolyte oxidation. If a lithium dendrite short occurs during the overcharge, the cell may be heated up, because a high current passes at the point of the dendrite short when the cell impedance becomes high as a result of the separator melting or the electrolyte drying up. The situation is very similar to that of lithium ion cells. When a lithium ion cell with LiCoO<sub>2</sub> cathode is overcharged, lithium is deposited on the carbon anode, because only about half the lithium in LiCoO<sub>2</sub> is used under standard cycling conditions. The lithium remaining on the cathode is deposited on the carbon anode. In other words, the carbon anode becomes a lithium metal anode. If a crush test is performed on the overcharged lithium ion cell, the cell fires violently. And even if lithium is not deposited on the carbon, too much lithium in the carbon makes the cell smoke when the cell is crushed. This shows that ion cells are very sensitive to overcharge. They have a good protection circuit against overcharge. Lithium metal cells will probably require a similar type of protection.

##### (3) Forced discharge

If forced discharge occurs, the lithium anode will be cut and the cell becomes unsafe. Since our cell employs lithium with a copper substrate, it is safer. The experimental results are shown in Table 4.6. The probability of firing by the forced discharge was reduced by the use of an anode with a copper substrate. When a cell is forced to discharge, excess lithium in the anode is deposited on the cathode. In contrast to this, lithium ion cells do

Table 4.6 Results of forced discharge tests on AA-size Li/a-V<sub>2</sub>O<sub>5</sub>(-P<sub>2</sub>O<sub>5</sub>) cells

Precycling before the forced discharge test (discharge current; 40 mA, charge current; 80 mA)	Ratio of venting for cells with pure lithium anodes	Ratio of venting for cells with lithium/Cu/lithium anodes
10 cycles ( 0 °C)	1/4	0/11
25 cycles (21 °C)	9/9	5/12

forced discharge current = 3 A, maximum applied voltage = -10 V, duration of forced discharge = 1 h

not deposit lithium but probably Cu on the anode. It is fair to say that lithium ion cells are safer than lithium metal cells in this situation. Therefore, some type of protection circuit is needed to protect against a forced discharge, if we use lithium metal cells.

However, the cell itself must be resistant to forced discharge to some extent. An example of an actual situation of forced discharge is the external short of a battery composed of cells connected in a series with one low voltage cell. When the battery is shorted, the low voltage cell is in a forced discharge situation with minus voltage. Therefore we tried a short circuit test on a battery where four cells were connected in a series and three of them were cells charged to 3.3 V and one was a cell discharged to 1.5 V. No incident occurred in this test.

When ion cells are used in a series connection, it is recommended that each cell voltage be monitored to avoid overcharge. If the lithium metal cells are connected in this way, the voltage monitoring of each cell is also recommended to avoid overcharge and forced discharge.

#### (4) Crush

This test is done to check the damage caused by external mechanical stress. There are two types of crush tests. One is crush with plate and the other is with bar. We use crush with bar because crush it is the more difficult test to pass. If a cell fires, it occurs within 3 s after the bar touches the cell. The trigger of the firing is not clear but possible reasons are: (i) The separator is broken at some point by the crush, causing an internal short. A very high current passes for a short time from the capacitance of the cell. This high current heats the cell locally and initiates an unsafe situation. (ii) The separator is broken at some point by the crush, and a cathode active material and an anode active material are mixed directly. The direct mixing causes some exothermic reaction. (iii) The separator is broken at some point by the crush, and an electric spark is generated. This spark ignites the organic solvent in the electrolyte.

Our cells satisfactorily passed this test even after cycling.

#### (5) Nail penetration

A nail 3 mm in diameter is used. As mentioned above, this test is very useful for estimating the situation when an internal short occurs. Our cells also passed this test even after cycling. If a cell fires, it occurs within 3 s. The reasons for this are probably similar to those for the crush test.

However, there is still some questions as to whether the nail test is a good model of an internal short or not. The test tends to become easier to pass as the diameter of the nail decreases. Then, is a diameter of 3 mm suitable? There is no particular reason for the selection of 3 mm. Sometimes the author recommends a diameter of 2.5 mm according to the method determined for the UL test. A detailed study is needed on the internal short.

#### (6) Thermal stability

This test is very useful for evaluating the thermal stability after cycling. If the thermal stability decreases after cycling, care must be taken to evaluate the safety of the cell after the cycle. The thermal stability of our cell is 130 °C before cycling. Even after cycling, the thermal stability temperature is higher than 130 °C.

Various aspects of cell safety have been described. However, it is not easy to decide which cell is safe simply from cell characteristics. To better understand this, the safety of lithium ion cells will be described. Having discussed the safety of lithium ion cells with battery makers before the use in portable telephones and PHS, the following aspects

regarding safety are explained below.

- (i) Safety depends on the cell, the battery pack (with a protection circuit), the charger and portable telephone (or PHS). The combined performance of the above must be considered. If a new portable telephone is made, it must be tested again in combination with a different portable telephone or charger even if the cell has already been checked for safety.
- (ii) The cell must meet the following minimum requirements;
  - ① external short—no smoke and no fire
  - ② crush with bar—no smoke and no fire
  - ③ nail penetration—no smoke and no fire
  - ④ thermal stability test—survive at around 150 °C

The following types of cell should be tested:

- ① fresh cells,
- ② cycled cells at the charge current of the charger and at the discharge current of waiting mode to the end of cycle (EOC) and to 50% of EOC.
- ③ cycled cells at the charge current of the charger and at the discharge current of talking mode to the end of cycle (EOC) and 50% of EOC.

The kinds of battery pack to be tested are:

- ① fresh packs
- ② cycled packs at the charge current of the charger and at the discharge current of waiting mode to the end of cycle (EOC) and to 50% of EOC.
- ③ cycled packs at the charge current of the charger and at the discharge current of talking mode to the end of cycle (EOC) and to 50% of EOC.
- (iii) Even if one electrical component is broken, a cell or a pack damaged by the incident must pass the tests listed in (2): external short, crush with bar, nail penetration and thermal stability test.

For example, if the constant charge voltage of the charger (*e.g.*, 4.1 V) is out of order, a cell is overcharged. If the overcharge protection is in the battery pack and the charging is stopped at 4.3 V, the cell charged to 4.3 V must pass the above tests.

This is only one example. All possible cases must be considered very carefully before suitable protection circuits are selected for practical use. Other factors which must be considered are as follows:

- (iv) No leakage of electrolyte during storage
- (v) Safety vent opens without exploding
- (vi) Safety at high temperatures where customers may use cellular phones
- (vii) Safety when the customer drops the telephone many times
- (viii) Quality control and reliability of cells, packs and chargers

At present, lithium metal cells are not commercially available. However, their safety is not bad compared with that of lithium ion cells. Some undesirable situations can be avoided by employing suitable designs for the battery pack and charger. However, there must be guarantees that no cell incident will occur during cycling under normal conditions. So far, there does not seem to be an appropriate cell, such issues as the possibility of a lithium dendrite shorts, the stability of lithium anodes during long time storage, the possibility of accumulation of lithium dendrite (dead lithium) on some part as the result of manufacturing defects, etc. must be carefully considered. The author believes that a better lithium cell will be produced in the not-too-distant future.

## 4.4 Conclusion

The state of lithium metal anode cells from basic studies to prototype cells has been presented. There remains much to be clarified. How does the protection film conduct lithium ions and protect against the reduction of electrolytes? How can the morphology of deposited lithium and that after a long cycle be explained? Why does a high-rate discharge reduce the accumulation of dead lithium? What is the actual mechanism of firing of lithium metal cells? Other questions must be dealt with regarding lithium metal anode cells. Some answers and approaches to answering the questions have been described in this chapter.

Electrolytes and cathode materials have not been discussed in detail. Electrolytes are described in Chapter 7, and cathodes in Chapters 2 and 3. Common cathodes are used in both lithium metal cells and lithium ion cells. As regards safety, both lithium metal cells and lithium ion cells have been discussed to help the reader understand the actual level of safety for lithium metal cells.

The author believes that good lithium cells will soon be realized.

## REFERENCES

- 1) Y. Sakurai, S. Sugihara, M. Shibata and J. Yamaki, *NTT Review*, **7**, 60 (1995).
- 2) W.R. Harris, Ph.D. Dissertation, University of California, Berkeley (1958).
- 3) A.N. Dey, ECS Meet., Atlantic City, NJ, USA, October 1970, Abstr. p. 62.
- 4) R.D. Rauh and S.B. Brummer, *Electrochim. Acta*, **22**, 75 (1977).
- 5) E. Peled, *J. Electrochem. Soc.*, **126**, 2047 (1979).
- 6) A.N. Dey, *Thin Solid Films*, **43**, 131 (1977).
- 7) G. Nazri and R.H. Muller, *J. Electrochem. Soc.*, **132**, 2050 (1985).
- 8) D. Aurbach, M.L. Daroux, P.W. Faguy and E. Yeager, *J. Electrochem. Soc.*, **134**, 1611 (1987).
- 9) K.M. Abraham and S.M. Chaudhri, *J. Electrochem. Soc.*, **133**, 1307 (1986).
- 10) J.L. Goldman, R.M. Mank, J.H. Young and V.R. Koch, *J. Electrochem. Soc.*, **127**, 1461 (1980).
- 11) D. Aurbach, M.L. Daroux, P.W. Faguy and E. Yeager, *J. Electrochem. Soc.*, **135**, 1307 (1986).
- 12) M. Odziemkowski, M. Krell and D.E. Irish, *J. Electrochem. Soc.*, **139**, 3052 (1992).
- 13) S.P.S. Yen, D. Shen, R.P. Vasquez, F.J. Grunthaner and R. Samoano, *J. Electrochem. Soc.*, **128**, 1434 (1981).
- 14) D. Aurbach, *J. Electrochem. Soc.*, **136**, 1606 (1989).
- 15) D. Aurbach, O. Youngman, Y. Gofer and A. Meitav, *Electrochim. Acta*, **35**, 625 (1990).
- 16) Y.E. Ely and D. Aurbach, Proc. Symp. High Power Ambient Temp. Lithium Batteries (Eds. by W. Clark and G. Halpaert), p. 157 (1992).
- 17) T. Itoh, T. Nishina, T. Matsue and I. Uchida, 36th Battery Symp. Japan, Kyoto, September 1995, Ext. Abstr., p. 171.
- 18) M. Odziemkowski and D.E. Irish, *J. Electrochem. Soc.*, **139**, 3063 (1992).
- 19) M. Odziemkowski and D.E. Irish, *J. Electrochem. Soc.*, **140**, 1546 (1993).
- 20) K. Kanamura, S. Shiraishi, H. Tamura and Z. Takehara, *J. Electrochem. Soc.*, **141**, 2379 (1994).
- 21) D. Aurbach, Y. Ein-Ely and A. Zaban, *J. Electrochem. Soc.*, **141**, L1 (1994).
- 22) D. Aurbach, A. Zaban, Y. Ein-Ely, I. Weissman, O. Chusid and O. Abramson, *J. Power Sources*, **54**, 76 (1995).
- 23) K. Kanamura, H. Tamura, S. Shiraishi and Z. Takehara, *J. Electrochem. Soc.*, **142**, 340 (1995).
- 24) D. Pletcher, J.F. Rohan and A.G. Ritchie, *Electrochim. Acta*, **34**, 1369 (1994).
- 25) R. Selim and P. Bro, *J. Electrochem. Soc.*, **121**, 1457 (1974).
- 26) L.P. Klemann and G.H. Newman, Proc. Symp. Lithium Batteries, Battery Div. (Ed. by H. V. Venkatesetty), **81-4**, p. 189 (1981); K.M. Abraham, J.L. Goldman and D.L. Natwig, *J. Electrochem. Soc.*, **129**, 2404 (1982).
- 27) D.P. Wilkinson, H. Blom and K. Brandt, Proc. 5th Int. Meet. Lithium Batteries, Beijing, China, p. 145, May 27-June 1 (1990).

- 28) J. Yamaki, M. Arakawa, S. Tobishima and T. Hirai, Proc. Symp. Lithium Batteries, Battery Div. (Ed. by A.N. Dey), **87-1**, p. 166 (1987).
- 29) R.D. Rauh, T.F. Reise and S.B. Brummer, *J. Electrochem. Soc.*, **130**, 101 (1983).
- 30) K. Saito, S. Tobishima and J. Yamaki, 35th Battery Symp. Japan, Nagoya, Japan, November 1994, Ext. Abstr., p. 103.
- 31) K. Hayashi, S. Tobishima and J. Yamaki, '95 Asian Conf. Electrochem., Osaka, Japan, May 1995, Ext. Abstr., **3A-6**, p. 140.
- 32) F.C. Laman and K. Brandt, *J. Power Sources*, **24**, 195 (1988).
- 33) I. Yoshimatsu, T. Hirai and J. Yamaki, *J. Electrochem. Soc.*, **135**, 2422 (1988).
- 34) D.P. Wilkinson, J.R. Dahn, U. von Sacken and D.T. Fouchard, 178th Electrochem. Soc. Meet., Seattle, WA, USA, October 1990, Ext. Abstr., p. 85.
- 35) U. von Sacken and J.R. Dahn, 178th Electrochem. Soc. Meet., Seattle, WA, USA, October 1990, Ext. Abstr., p. 87.
- 36) J. Yamaki, Proc. 1st Korea-Japan Joint Seminar, Advan. Batteries, Seoul, Korea, p. 63 (1996).
- 37) K. Kanamura, S. Shiraishi and Z. Takehara, *J. Electrochem. Soc.*, **141**, L108 (1994).
- 38) J.O. Besenhard and G. Eichinger, *J. Electroanal. Chem.*, **68**, 1 (1976).
- 39) S. Tobishima, J. Yamaki, A. Yamaji and T. Okada, *J. Power Sources*, **13**, 261 (1984).
- 40) S. Tobishima and T. Okada, *Electrochim. Acta*, **30**, 1715 (1985).
- 41) S. Tobishima and T. Okada, *J. Appl. Electrochem.*, **15**, 317 (1985).
- 42) S. Tobishima, J. Yamaki and T. Okada, *Denki Kagaku*, **53**, 173 (1985).
- 43) T. Hirai, I. Yoshimatsu and J. Yamaki, *J. Electrochem. Soc.*, **141**, 611 (1994).
- 44) C. Fringant, A. Tranchant and R. Messina, *Electrochim. Acta*, **40**, 513 (1995).
- 45) H. Koshina, N. Eda and A. Morita, 40th ISE Meet., Kyoto, Japan, September 1989, Ext. Abstr., 19-02-14-G, p. 520.
- 46) T. Matsui and K. Takeyama, 34th Battery Symp. Japan, Hiroshima, Japan, November 1993, Ext. Abstr., p. 29.
- 47) T. Matsui and K. Takeyama, 35th Battery Symp. Japan, Nagoya, Japan, November 1994, Ext. Abstr., p. 95.
- 48) I. Uchida, X. Wang and T. Nishina, 35th Battery Symp. Japan, Nagoya, Japan, November 1994, Ext. Abstr., p. 73.
- 49) K. Morigaki, N. Kabuto, K. Yoshino and A. Ohta, 35th Battery Symp. Japan, Nagoya, Japan, November 1994, Ext. Abstr., p. 83.
- 50) M. Mori, Y. Shinagawa, T. Suzuki and K. Naoi, 36th Battery Symp. Japan, Kyoto, Japan, September 1995, Ext. Abstr., p. 169.
- 51) J. Yamaki, IBA LA Meet., Los Angeles, LA, USA, May 1989, Ext. Abstr., p. 31.
- 52) M. Arakawa, Ph.D. Dissertation, Tohoku University, Sendai, Japan (1958).
- 53) J. Yamaki, K. Hayashi, K. Saito, T. Shodai, M. Arakawa and S. Tobishima, 188th Electrochem. Soc. Meet., Chicago, IL, USA, October 1995, Ext. Abstr., no. 84.
- 54) R.H. Doremus, B.W. Roberts and D. Turnbull (Eds.), Proc. Int. Conf. Crystal Growth, Cooperstown, NY, USA, August (1958).
- 55) J. Franks, *Acta Met.*, **6**, 103 (1958).
- 56) M. Arakawa, S. Tobishima, Y. Nemoto, M. Ichimura and J. Yamaki, *J. Power Sources*, **43-44**, 27 (1993).
- 57) K.N. Tu, *Phys. Rev. B*, **49**, 2030 (1994).
- 58) K. Saito, M. Arakawa, S. Tobishima and J. Yamaki, *Denki Kagaku*, **62**, 888 (1994).
- 59) S. Hirayama, H. Hiraga, K. Otsuka, N. Ikeda and M. Sasaki, 34th Battery Symp. Japan, Hiroshima, Japan, November 1993, Ext. Abstr., p. 13.
- 60) N. Yamamoto, K. Saito, T. Ishibashi, M. Honjo, T. Fujieda and S. Higuchi, 34th Battery Symp. Japan, Hiroshima, Japan, November 1993, Ext. Abstr., p. 15.
- 61) T. Fujieda, N. Yamamoto, K. Saito, T. Ishibashi, M. Honjo, S. Koike, N. Wakabayashi and S. Higuchi, *J. Power Sources*, **52**, 197 (1994).
- 62) M. Arakawa, S. Tobishima, T. Hirai and J. Yamaki, Electrochem. Soc. Japan, Spring Meet., Tokyo, Japan, April 1986, Ext. Abstr., **A-203**, p. 17.
- 63) S.V. Sazhin, A.V. Gorodyskii and M. Yu. Khimchenko, *J. Power Sources*, **47**, 57 (1994).
- 64) K. Yokoyama, M. Toriida and A. Hiwara, 36th Battery Symp. Japan, Kyoto, Japan, September 1995, Ext. Abstr., p. 161.
- 65) H. Takehara, S. Shiraishi, K. Kanamura and Z. Takehara, 36th Battery Symp. Japan, Kyoto, Japan, September 1995, Ext. Abstr., p. 165.
- 66) Y. Sasaki, H. Kaido, H. Ohashi, T. Minato, M. Handa and N. Chiba, 34th Battery Symp. Japan, Hiroshima, Japan, November 1993, Ext. Abstr., p. 305.
- 67) J.O. Besenhard, J. Guertler and P. Komenda, *J. Power Sources*, **20**, 253 (1987).
- 68) T. Hirai, I. Yoshimatsu and J. Yamaki, *J. Electrochem. Soc.*, **141**, 2300 (1994).

- 69) M. Yoshio, H. Nakamura, K. Isono, S. Itoh and K. Holzleithner, *Progr. Batteries Solar Cells*, **7**, 271 (1988).
- 70) K. Saito, Y. Nemoto, S. Tobishima and J. Yamaki, 36th Battery Symp. Japan, Kyoto, Japan, September 1995, Ext. Abstr., p. 151.
- 71) S. Tobishima, M. Arakawa, K. Hayashi and J. Yamaki, 34th Battery Symp. Japan, Hiroshima, Japan, November 1993, Ext. Abstr., p. 307.
- 72) H. Nakamura, E. Mitani and M. Yoshio, 36th Battery Symp. Japan, September 1995, Ext. Abstr., p. 159.
- 73) V.R. Koch, *J. Power Sources*, **6**, 357 (1981).
- 74) K.M. Abraham, J.S. Foos and J.L. Goldman, *J. Electrochem. Soc.*, **131**, 2197 (1984).
- 75) S. Tobishima and T. Okada, *Denki Kagaku*, **53**, 742 (1985).
- 76) J. Barthel, M. Wuehr, W. Sauerer and B. Hefer, *J. Electrochem. Soc.*, **140**, 6 (1993).
- 77) S. Tobishima and T. Okada, *J. Appl. Electrochem.*, **15**, 901 (1985).
- 78) M. Salomon, *J. Power Sources*, **26**, 9 (1989).
- 79) T. Osaka, T. Momma, T. Tajima and Y. Matsumoto, *J. Electrochem. Soc.*, **142**, 1057 (1995).
- 80) D. Aurbach and O. Chusid (Youngman), *J. Electrochem. Soc.*, **140**, L155 (1993).
- 81) T. Osaka, T. Momma, T. Tajima and Y. Matsumoto, *Denki Kagaku*, **62**, 451 (1994).
- 82) Y. Matsumoto, Y. Uchida, T. Momma and T. Osaka, 36th Battery Symp. Japan, Kyoto, Japan, September 1995, Ext. Abstr., p. 157.
- 83) S. Shiraishi, K. Kanamura and Z. Takehara, 34th Battery Symp. Japan, Hiroshima, Japan, November 1993, Ext. Abstr., p. 25.
- 84) S. Shiraishi, K. Kanamura and Z. Takehara, 35th Battery Symp. Japan, Nagoya, Japan, November 1994, Ext. Abstr., p. 93.
- 85) K. Kanamura, S. Shiraishi and Z. Takehara, *Electrochim. Acta*, **40**, 913 (1995).
- 86) K. Kanamura, H. Tamura, S. Shiraishi and Z. Takehara, *J. Electrochem. Soc.*, **141**, L108 (1994).
- 87) M. Ishikawa, S. Yoshitake, M. Morita and Y. Matsuda, *J. Electrochem. Soc.*, **141**, L159 (1994).
- 88) J.A.R. Stiles and K. Brandt, Canada Patent 1190279 (1985).
- 89) D.P. Wilkinson, H. Blom, K. Brandt and D. Wainwright, *J. Power Sources*, **36**, 517 (1991).
- 90) C.D. Desjardins and G.K. MacLean, Electrochem. Soc. Meet., Hollywood, FL, USA, October 1989, Ext. Abstr., no. 52.
- 91) Y. Matsuda, K. Otani, M. Ishikawa and M. Morita, 35th Battery Symp. Japan, Nagoya, Japan, November 1994, Ext. Abstr., p. 99.
- 92) K. Saito, M. Arakawa, S. Tobishima and J. Yamaki, Electrochem. Soc. Meet., Reno, NV, USA, May 1995, Ext. Abstr., no. 14.
- 93) E. Ben-Jacob, R. Godbey, N.D. Goldenfeld, J. Koplik, H. Levine, T. Mueller and L.M. Sander, *Phys. Rev. Letters*, **55**, 1315 (1985).
- 94) J. Yamaki and Y. Katayama, *J. Appl. Polymer Sci.*, **19**, 2897 (1975).
- 95) H. Margenau and G.M. Murphy, *The Mathematics of Physics and Chemistry*, D. van Nostrand Co., Inc. (1943).
- 96) Z. Takehara, Proc. Int. Workshop Advan. Batteries, p. 1, Osaka, Japan, Feb. 22–24 (1995).
- 97) T.C. Murphy, D.M. Cason-Smith, S.D. James and P.H. Smith, Proc. 34th Int. Power Sources Symp., Cherry Hill, NJ, USA, p. 176 (1990).
- 98) P. Dan, E. Mengeritski, Y. Geronov, D. Aurbach and I. Weisman, *J. Power Sources*, **54**, 143 (1995).
- 99) Y. Sakurai and J. Yamaki, *J. Electrochem. Soc.*, **135**, 791 (1988).
- 100) M. Arakawa, S. Tobishima, T. Hirai and J. Yamaki, *Electrochem. Soc.*, **133**, 1527 (1986).
- 101) M. Arakawa, Y. Nemoto, S. Tobishima, M. Ichimura and J. Yamaki, *J. Power Sources*, **43–44**, 517 (1993).
- 102) M. A. Gee and F.C. Laman, *J. Electrochem. Soc.*, **140**, L53 (1993).
- 103) K. Hasegawa and Y. Arakawa, *J. Power Sources*, **43–44**, 523 (1993).
- 104) K. Hasegawa, S. Okawa and Y. Arakawa, 35th Battery Symp. Japan, Nagoya, Japan, November 1994, Ext. Abstr., p. 69.
- 105) F.C. Lama, Y. Sakurai, T. Hirai, J. Yamaki and S. Tobishima, 6th Int. Meet. Lithium Batteries, Muenster, Germany, May 1992, Ext. Abstr., III-A-01, p. 298.
- 106) D. Fouchard, L. Xie, W. Ebner and S. Megahed, Electrochem. Soc. Proc., 94–28, p. 348 (1995).
- 107) H. Tukamoto, S. Komatsu, M. Mizutani and M. Yamachi, Technical Report of IEICE, **PE94-57, CPM94-100**, p. 7 (1995).
- 108) J. R. Dahn, E. W. Fuller, M. Obrovac and U. von Sacken, *Solid State Ionics*, **69**, 265 (1994).
- 109) T. Ohzuku, A. Ueda and M. Kouguchi, *J. Electrochem. Soc.*, **142**, 4033 (1995).
- 110) T. Saito, K. Takano, K. Kanari and T. Masuda, Proc. Int. Workshop Advan. Batteries, p. 283, 1A-18, Osaka, Japan, February 22–24 (1995).
- 111) K. Takeishi, N. Koura and Y. Idemoto, Chem. Soc. Japan, Spring Meeting, Kyoto, Japan, March 1995, Ext. Abstr., 3C443, p. 222; K. Ui, N. Koura and Y. Idemoto, 36th Battery Symp. Japan, Kyoto, Japan, September 1993, Ext. Abstr., 1A19, p. 41.



- 112) R.T. Carlin, Proc. First Sci. Workshop Electrochem. Mater., p. 123, IV-1, Osaka, Japan, January 18-19 (1996).
- 113) J. Fuller, Proc. First Sci. Workshop Electrochem. Mater., p. 142, IV-3, Osaka, Japan, January 18-19 (1996).

## 5

## Development of the Carbon Anode in Lithium Ion Batteries

Nobuyuki Imanishi\*, Yasuo Takeda\* and Osamu Yamamoto\*

## 5.1 Introduction

This chapter describes the recent development of various carbon anodes with emphasis on electrochemical performance and intercalation mechanism. Throughout the chapter, with respect to carbon anodes, “charge” means intercalation and “discharge” means deintercalation of lithium.

A crucial problem of the lithium metal anode is high reactivity with an organic electrolyte solvent which results in nonuniform formation of a passivation film on the anode surface.<sup>1-5)</sup> This film cannot prevent further reaction with the electrolyte and causes dendritic growth of lithium metal which can result in short-circuit and ignition. The use of lithium metal is the ultimate goal in the battery research field, but many efforts have also been made to find a competitive anode with more stability and safety. In the late 1980's, electrochemical lithium intercalation which showed much negative potential close to lithium metal, less reactivity and good reversibility was found in carbon materials. Carbon anodes became a break through in realizing the lithium “rocking chair” battery and has solved the safety problem of the lithium metal anode.<sup>6)</sup> The system was first commercialized in 1991 and gave rise to today's theoretical and commercial development of the lithium rechargeable battery. The choice of carbon anode also matches the current trend toward high performance cathodes, such as  $\text{LiCoO}_2$ ,  $\text{LiNiO}_2$  and  $\text{LiMn}_2\text{O}_4$ . These cathodes need to be charged initially prior to use, because they are only prepared as a discharged form which is thermodynamically stable. The application of the carbon anode is not possible with lithium-free cathodes such as  $\text{TiS}_2$ .

From the viewpoint of materials science as well as battery applications, carbons attract much interest because of their diverse characteristics. This diversity can be attributed to the variety of structures, and it is the structure which plays the most important role in electrochemical performance. The preparation history influences the construction of each carbon structure, and the starting materials also strongly control the structure of the final product. Materials prepared from solid phase such as organic polymers and resins are highly disordered; examples include glassy carbons and some kinds of carbon fibers. Materials synthesized from liquid phase such as petroleum pitch can be highly oriented and crystallized petroleum cokes and artificial graphites. A third group comprises products from gas phase, *e.g.*, vapor grown carbon fibers and pyrolytic carbons.

---

\* Department of Chemistry, Mie University, 1515, Kamihama-cho, Tsu-shi, Mie Pref. 514, Japan

Research on the intercalation of carbon materials dates back to the 1950's when Herold first reported the chemical intercalation of lithium into graphite.<sup>7)</sup> Much research has concentrated on the study of graphite intercalation compounds (GIC) for a long time.<sup>8-10)</sup> On the other hand, major advances in fundamental aspects of electrochemical lithium intercalation into carbon materials other than graphite have been made since the lithium ion battery was first commercialized. We have faced the difficulties in correlating electrochemical performances and structure because of the many different types of structural parameters that must be characterized in a single material. Therefore, the first task is to understand the structure correctly in order to discuss the intercalation mechanism, then improvement of the carbon anode can be achieved by structural designing. In the following part of the chapter carbon materials are sorted into several types with respect to structure, and charge-discharge mechanisms are explained in association with each specific type.

In section 5.2, detailed explanations of different scales of structures which characterize carbon materials are given. A brief history of carbon anodes in the early period of the research is presented in section 5.3. As the standard for all carbon materials, we will discuss the intercalation mechanism of graphite in section 5.4. Carbon materials can be roughly divided into two groups which show remarkably different physical and chemical natures. One is called soft carbon represented by graphitic carbons in which every graphene layer can easily align at relatively low temperatures. The other is hard carbon represented by glassy carbons whose transition from a random state to a two-dimensional structure is extremely slow even at high temperatures. Their electrochemical performance and intercalation mechanism are discussed in sections 5.5. and 5.6, respectively. The surface chemistry concerning irreversible reaction of electrolyte is discussed in section 5.7. The carbon materials are known to form solid solutions with other elements such as B, N, O, *etc.* In section 5.8, several structural modifications including doping with these elements in order to improve carbon's performance are discussed. The effect of texture in bulk material is also discussed. In section 5.9, discussion of lithium nitrides as a novel anode including results obtained in our own laboratory is presented. Section 5.10 is a summary of this chapter. Apart from section 5.9, most of the data and figures are taken from the published works of other battery research groups.

## 5.2 Structure of Carbon Materials

In this section, we consider several important types of structures ranging from nano to millimeter order, all of which are necessary to describe carbons correctly. The smallest level of structure is a bonding form between carbon atoms. Carbons bind themselves together by  $sp^3$ ,  $sp^2$  and  $sp$  hybrid orbitals, forming many kinds of organic compounds. The carbon materials discussed here are built up mainly by  $sp^2$  bonding, although there are some reports suggesting the existence of  $sp^3$  bonding.<sup>11)</sup> However, three-dimensional fraction, if any, is negligible, so normally does not need to be taken into consideration. The  $sp^2$  bonding is the smallest structural unit and the effect of  $sp^3$  bonding will not be discussed in this chapter except with reference to hydrogen-containing carbon anodes. Repeating  $sp^2$  bonding results in a large network of 6-ring structures leading to a two-dimensional graphene sheet.

The stacking order of these graphene sheets, is important. Van der Waals force binds the sheets together to form layered structures called crystallites. The ideal stacking order

of graphite has two patterns; the carbon positions of these patterns are described as ABAB... and ABCABC.... The former has hexagonal symmetry with space group  $P6_3/mmc$  and the latter has rhombohedral symmetry with  $R\bar{3}m$ .<sup>12)</sup> Natural graphite usually comprises these two crystal structures, but the rhombohedral ratio is below 3 to 4 percent. The consecutive stacking of two-dimensional sheets results in the anisotropic property of carbon materials.

In the case of graphite, the weak van der Waals force between layers enables the planes to slide easily. However, most of the artificial carbon materials generally have varying degrees of stacking faults caused by relative rotating or sliding sheets. As a consequence, carbon atoms deviate from the regular position and periodic stacking is no longer maintained. It is difficult to completely eliminate these misfits even by high temperature annealing because these disordered graphene layers are pinned to each other. This type of structure is called turbostratic structure and their X-ray diffraction (XRD) patterns only show (00 $l$ ) and asymmetric ( $hk$ ) diffraction peaks.<sup>13)</sup> This is because the three-dimensional regularity is poor and parallel but random stacking of layers is detectable. In the turbostratic structure, interlayer distances are somewhat diffused and on average larger than graphite. With increase in pyrolyzing temperature, the distance decreases towards that of graphite. However, high pressure as well as high temperature is normally necessary to reach the value. In the turbostratic structure no stage compounds occur and reversible lithium intercalation is significantly limited. This phenomenon is discussed later in the chapter.

The third type of structure involves texture, depending on how crystallites are conjoined. This type is grouped by the degree of orientation from random to systematic orientation. If the crystallite size is small enough and there is no specific orientation, the material appears to be amorphous. Examples of this type are thermal decomposition products of furan resin, phenol resin and polyfurfuryl alcohol resin. They do not give clear XRD peaks, but transmission electron microscope (TEM) observation reveals that the basic structure is principally two-dimensional graphite layers. "Hard carbon" is the general term given to this kind of material which has the common character by which random orientation is barely improved by high temperature treatment. Direct pyrolysis from solid phase leads to the severe restriction of the motion of intermediate graphitic units, in contrast to the case of liquid or gas phase. On the other hand, in highly oriented materials, there are three types of textures called plane orientation, axis orientation and point orientation. "Soft carbon" usually has one or more of the above three types of orientation throughout the material. Examples are seen in most of the cokes (plane), vapor grown carbon fibers (axis) and mesophase pitch-based carbons (axis, point).

An aggregation of different types of textures can be considered as the largest scale of a structure and results in more variety of characteristics. Application examples of this form are the artificial graphite electrode for steel manufacture and building materials for nuclear reactors. In the battery research field, this corresponds to a composite electrode such as graphite + acetylene black. In some carbon fibers used for the anode, two different textures coexist within a single fiber. Electrochemical properties depend partially on microporosity of anode matrix, which is also controlled by the state of aggregation. An example of composite electrodes is discussed briefly at the end of section 5.3.

Four different types of bulk structures have been described:  $sp^2$  bonding, stacking order, texture and aggregation form. The fifth structure is surface structure. There are two

different types of surface in graphitic carbons due to the two-dimensional anisotropic structure. One is the basal plane of graphene layers. Its chemical inertness excludes itself from partaking in most electrochemical reactions. The other is the edge surface located at the end of each graphene sheet. Contrary to the basal plane, the edge surface is chemically quite radical. On the surface there are many functional groups such as OH, COOH, and C=O which can play a role in acid-base reactions and organic reactions. Radicals are also found on the surface by ESR measurement. Catalytic reactions, adsorption reaction of molecules, hydrogen spill-over reaction are all specific to the edge surface. In an electrochemical cell, a big problem is the irreversible electrolyte decomposition on the carbon anode surface. This reaction is strongly related to the structure of the edge surface. Several studies to reduce the decomposition associated with these surface structures are discussed below.

### 5.3 Development of the Carbon Anode

The electrochemical reduction of graphite in an aprotic solvent of alkali salts was studied by Besenhard *et al.* in the 1970's.<sup>14,15)</sup> They observed that a cyclic voltammetry of a graphite foil in LiClO<sub>4</sub>/1,2-dimethoxyethane (DME) showed a reversible reduction peak at potentials more positive than that of lithium metal. This reduction of graphite was accompanied by swelling and macroscopic disintegration. As a consequence of several electrochemical tests, it was concluded that electrochemical intercalation of alkali metals into a graphite had occurred in addition to decomposition of solvent.

The first two papers reporting the performance of a practical carbon anode for lithium rechargeable battery appeared in a journal in 1989. Kanno *et al.* examined the thermal decomposition products of polymers and commercial carbon fibers.<sup>16)</sup> In the paper the surface area dependence of the lithium storage capacity was discussed in detail. The storage capacity of the first cycle increases with surface area, but at the fifth cycle there is

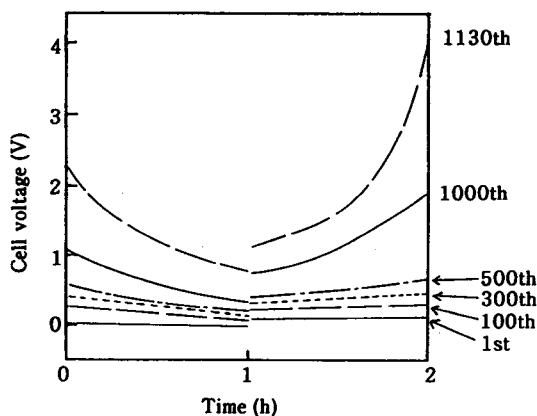


Fig. 5.1 Cycling behavior of a Li/M46 cell at a lithium storage level of 0.1125Li/C (250 mAh·g<sup>-1</sup>). [R. Kanno *et al.*, *J. Power Sources*, 26, 535 (1989)]

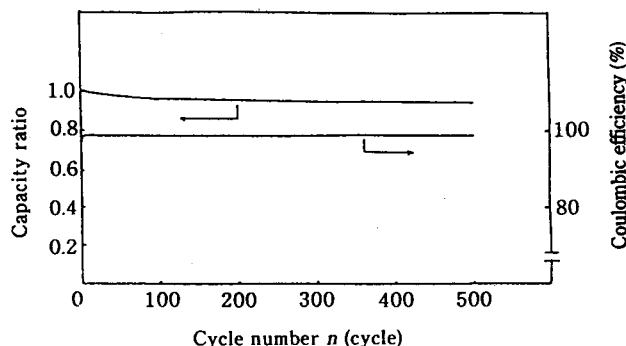


Fig. 5.2 Capacity and coulombic efficiency dependencies of the carbon electrode on cycle number. [M. Mohri *et al.*, *J. Power Sources*, 26, 549 (1989)]

no correlation between capacity and surface area, indicating that irreversible capacity related with the carbon surface exists in the first cycle and the reversible lithium storage does not proceed via surface reaction. Fig. 5.1 presents the cycling performance of a PAN-based carbon fiber M46 (Toray) showing the largest storage capacity. This work revealed that normal carbon products as well as graphite can work as the anode and show good reversibility at high current density.

In the same journal, there was another report on a different carbon anode by Mohri *et al.*,<sup>17)</sup> who tested a pyrolytic carbon which showed small irreversible capacity and high coulombic efficiency. A lithium ion cell with a metal oxide cathode and a pyrolytic carbon anode were constructed and cycled. Fig. 5.2 shows the plot of the cycle efficiency vs. cycle number of the cell. During the first 100 cycles, there is gradual capacity fading, but thereafter the efficiency remains around 80% until the 500th cycle. This work also indicated the potential possibility of carbon materials as the anode and promoted battery researchers to search for better carbons.

The number of researches on the carbon anode increased when Sony Energytec Inc. first marketed the lithium ion battery in 1991.<sup>18)</sup> In this battery, thermal decomposition product of polyfurfuryl alcohol resin (PFA) was used as the carbon anode. This is a typical "hard carbon" material prepared from solid phase. Open circuit voltages and intermittent charge-discharge curves of the pyrolyzed PFA anode are shown in Fig. 5.3.<sup>19)</sup> Although there are some irreversible capacities as for other carbons, a long discharge plateau appears near the lithium metal potential. The obtained reversible capacity is about  $350 \text{ mAh} \cdot \text{g}^{-1}$ , which almost equals the theoretical capacity of a graphite,  $372 \text{ mAh} \cdot \text{g}^{-1}$ . In a parallel work, the enhancement of the capacity by doping with phosphorus atoms was reported.<sup>20)</sup> The capacity almost linearly increases with the amount of phosphorus but starts decreasing beyond the optimal composition. According to this work, a maximum capacity of  $460 \text{ mAh} \cdot \text{g}^{-1}$  was achieved, which implies that the capacity of hard carbon is not confined by the theoretical limit of graphite. The effect of other dopants is also described in section 5.8.

Figure 5.4 shows a comparison of anode performances between thermal decomposition products of polymers including PFA.<sup>19)</sup> Each carbon material was cycled within various charge-discharge depths and the possible cycle numbers are plotted against cycling

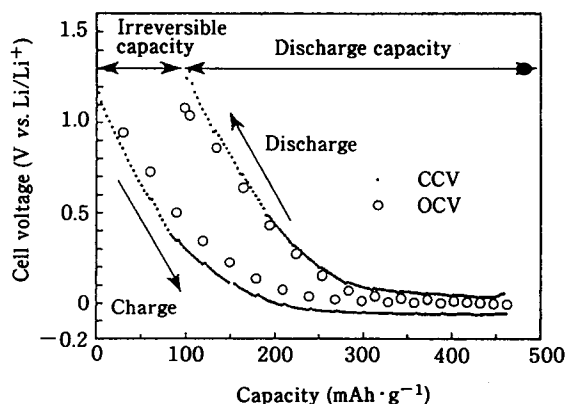


Fig. 5.3 Potential profile of intermittent cycling of pyrolyzed PFA resin.

[M. Nagamine *et al.*, *Extended Abstracts Spring Meeting of Electrochemical Society of Japan*, p. 167 (1993)]

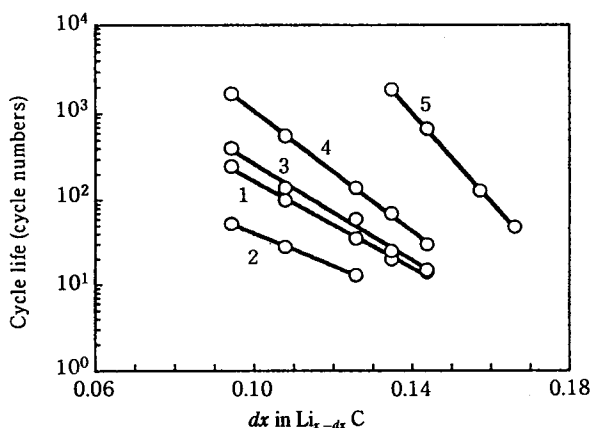


Fig. 5.4 Cycle life vs. lithium content of various carbon materials. 1: coke, 2–5: thermal decomposition products of PVC, PAN, PVA, PFA and resins, respectively.

[M. Nagamine *et al.*, *Extended Abstracts Spring Meeting of Electrochemical Society of Japan*, p. 167 (1993)]

capacities. The cycle numbers of all the materials monotonically decrease with capacity. PFA shows a longer cycle life than other carbon materials, especially under deep charge-discharging conditions. These data demonstrate that not only soft carbons, but hard carbons in addition to pyrolyzed PFA also have the capability to operate as the anode.

As the last topic of this section, the anodic behavior of a graphite electrode is discussed. Recently graphite has become a more promising material and studies on graphite are increasing.<sup>21–23)</sup> Nishio *et al.* compared natural graphite to other carbon materials, acetylene black, petroleum coke (1400 °C), pitch coke (1200 °C), artificial graphites (1200–2800 °C).<sup>23)</sup> For these samples the discharge capacities were found to be inversely proportional to  $d_{002}$  values. This rule has been separately confirmed by other research groups as valid for soft carbons heat-treated at relatively high temperatures ( $> ca.$  1500 °C).

Natural graphite showed the largest capacity, being more than  $330 \text{ mAh} \cdot \text{g}^{-1}$ , which nearly equals the theoretical value of  $372 \text{ mAh} \cdot \text{g}^{-1}$  calculated for  $\text{LiC}_6$ . This theoretical upper limit in capacity seems rather small when compared to high capacity hard carbons, but its

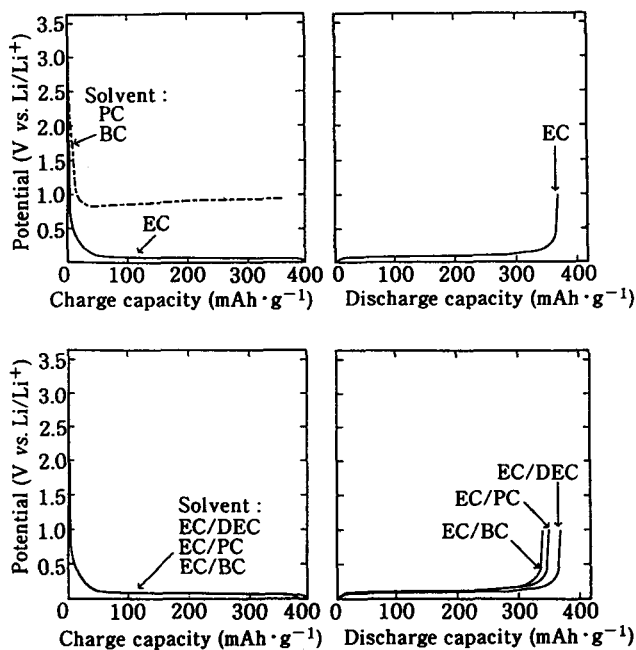


Fig. 5.5 Charge-discharge curves of natural graphite in various electrolytes. [K. Nishio *et al.*, *Extended Abstracts IMLB-8*, pp. 95, 96 (1996)]

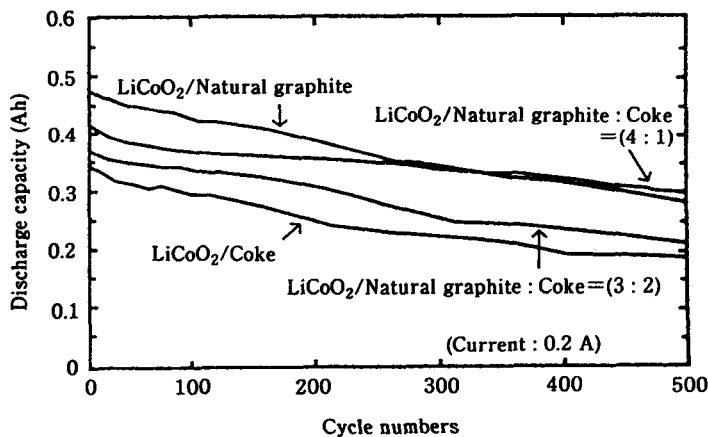


Fig. 5.6 The charge-discharge cycle performance of AA-type test cells using natural graphite, coke and a mixture of the two.

[H. Kurokawa *et al.*, *Extended Abstracts IMLB-8*, p. 223 (1996)]



long potential plateau over almost the entire charge-discharge curve is a big advantage which does not exist for other carbons. The redox potential of the lithium intercalation lies close to that of lithium metal, contributing to the high energy density of the cell. Fig. 5.5 shows the first cycle of the natural graphite electrode in various electrolyte systems. In propylene carbonate (PC), butylene carbonate (BC) and mixed solvents containing PC or BC, natural graphite cannot be charged because gas evolution occurs at 1.0 V. This is the greatest drawback of the graphite electrode, but in electrolyte systems using ethylene carbonate (EC), EC/PC, EC/BC and EC/diethyl carbonate (DEC) solvent, it can be cycled with the side reaction significantly suppressed.

The behavior in EC solution seems satisfactory and the long-term stability will be a key problem of graphite anodes. Some attempts have been made to reduce electrolyte decomposition on graphite by making a composite with other carbon materials. Fig. 5.6 shows the battery performance of a cylindrical AA-size cell using a graphite-coke composite anode.<sup>24)</sup> One test cell with a certain mixing ratio shows a good cycle performance up to 500 cycles with a small capacity fading (0.057% per cycle). Ten-Wh class cylindrical test cells were prepared using  $\text{LiCo}_{0.3}\text{Ni}_{0.7}\text{O}_2$  cathode and the composite anode with the best composition, which showed a energy density of  $101 \text{ Wh} \cdot \text{kg}^{-1}$  and  $235 \text{ Wh} \cdot \text{l}^{-1}$ .

## 5.4 Intercalation Mechanism of Graphite

The potential profile of the natural graphite has a step-wise shape due to the occurrence of different stages and its transitions. Dahn determined these stage occurrence and transitions in  $\text{Li}_x\text{C}_6$ .<sup>25)</sup> He used a specially designed cell for *in situ* X-ray diffraction measurements enabling structural changes to be detected during charge-discharging. At the same time, another cell was galvanostatically cycled to derive a  $-dx/dV$  plot, whose

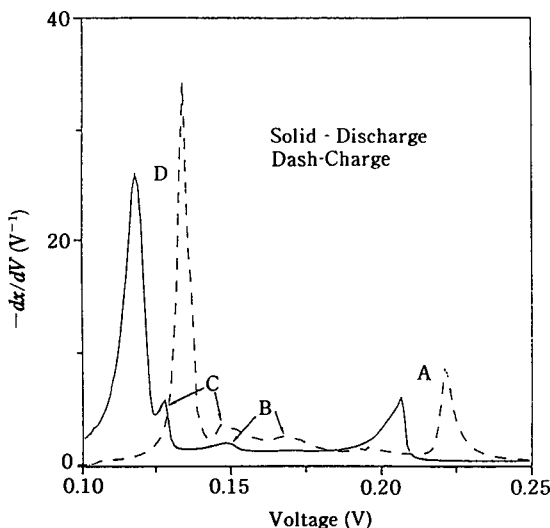


Fig. 5.7  $-(dx/dV)_T$  vs.  $V$  for the voltage profile of a Li/graphite cell. [J.R. Dahn, *Phys. Rev. B*, **44**, 9172 (1991)]

data were used to determine at which voltage stage transitions occurred. All these experiments were conducted under carefully controlled temperatures within  $\pm 0.1^\circ\text{C}$  accuracy in order to construct a phase diagram of the lithium-graphite system. Fig. 5.7 shows the  $-dx/dV$  plot at one temperature. Four peaks labeled A, B, C and D are denoted to show the coexistence of two stages, and the following staging mechanism was proposed.

peak A diluted stage-1' to stage-4

peak C stage-3 to stage-2L

peak D stage-2L to stage-2

Here the stage-2L indicates a "liquid-like" stage-2 phase. Their results of *in situ* XRD measurements scanned in a voltage region from 0.257 to 0.2 V, which corresponds to the vicinity of peak A, clearly indicate coexistence of a (002) peak of diluted stage-1' and a (004) peak of stage-4. The coexistence of the two stages during first-order transition appears as a potential plateau in the charge curve. They also observed a (005) super lattice peak for stage-4. The occurrence of a super lattice peak was explained as the result of staging in GIC. The above mechanism concerning peaks C and D was also confirmed by *in situ* XRD data. However, in the region between A and C where transition from stage-4 to -3 was expected, they observed only one diffraction peak corresponding to the average spacing. The stage-4 to -3 transition may be different from others and its mechanism has not been clarified in detail. At the position of peak B corresponding to the 100% stage-3 phase, they considered the possibility of lithium in-plane ordering is taking place.

Figure 5.8 shows Dahn's phase diagram of lithium-graphite system derived from the work cited above. There is the temperature dependence of stage-2L which disappears below  $10^\circ\text{C}$ . This diagram provided important information that the dilute stage-1' phase appears from  $x=0$  to 0.04 in  $\text{Li}_x\text{C}_6$  and the highest stage is stage-4. With respect to the problem of the stage-4 to -3 transition, they suspected the effect of kinetics and

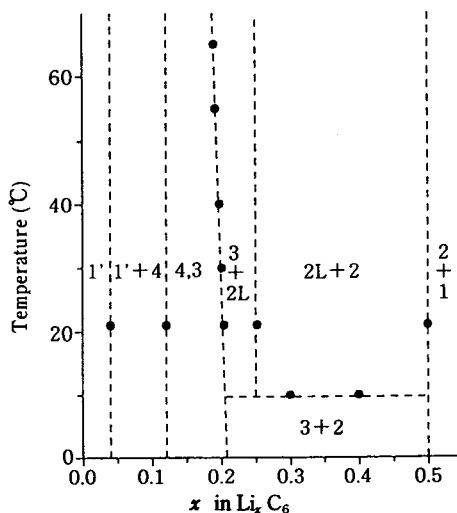


Fig. 5.8 Phase diagram of  $\text{Li}_x\text{C}_6$  in the range  $0^\circ\text{C} < T < 70^\circ\text{C}$ .  
[J.R. Dahn, *Phys. Rev. B*, **44**, 9172 (1991)]

recommended measurement at higher temperatures using a solid polymer electrolyte.

Ohzuku *et al.* also discussed the intercalation mechanism and tried to identify each stage by measuring XRD and open circuit voltages of a lithium/natural graphite cell.<sup>26)</sup> They prepared intercalation compounds by electrochemical charge-discharging in 1 M LiClO<sub>4</sub> ethylene carbonate (EC) + 1,2-dimethoxyethane (DME) at 30 °C. Table 5.1 summarizes the XRD data collected at several degrees of intercalation with the calculated average interlayer distance  $d_n$  for the  $n$ th-stage compound using the relation  $d_n = c_L + (n-1)c_0$ . Here  $c_L$  denotes the thickness of one lithiated layer of LiC<sub>6</sub>, 3.703 Å and  $c_0$  means vacant interlayer distance of the natural graphite, 3.355 Å. Although this is a rough estimation, the experimental data show fairly good agreement with the calculated values. Consequently, Ohzuku assumed the existence of 1, 2, 3, 4 and 8th-stages for the obtained XRD patterns. Coexistence of two-phases was observed by XRD in the first/second,

Table 5.1 Fitness in the repeated distance ( $d_n$ ) of the  $n$ th-stage compound between the calculated and observed values for the lithium-graphite intercalation compounds.

Stage	Repeated distance $d_n$ (Å) observed		Calculated <sup>a)</sup> (Å)	Difference (Å)	
	Reduction	Oxidation		Reduction	Oxidation
1	3.703	3.703	3.703	—	—
2	7.043	7.072	7.06	0.02	−0.01
3	10.401	10.473	10.41	0.01	−0.06
4	13.76 <sup>b)</sup>	13.900	13.77	0.01	−0.13
8	27.186	27.22 <sup>b)</sup>	27.19	0.00	−0.03
Graphite	3.355	3.358	3.355	—	0.00

<sup>a)</sup> Calculation was made using  $d_n = 3.703 + (n-1) \times 3.355$ .

<sup>b)</sup> Single-stage compound was not obtained.

[T. Ohzuku *et al.*, *J. Electrochem. Soc.*, **140**, 2492 (1993)]

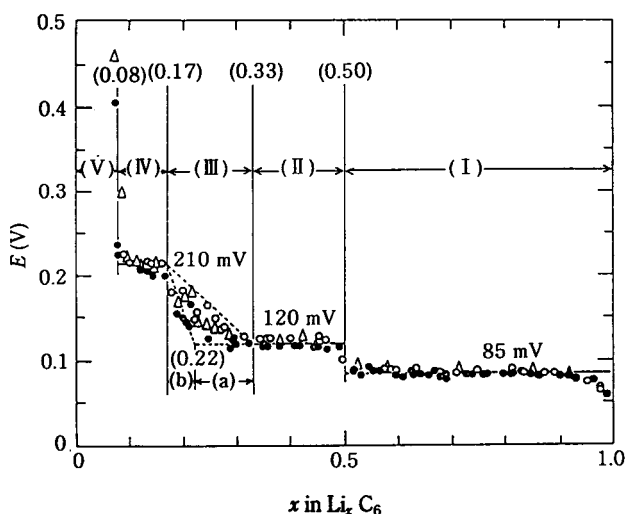
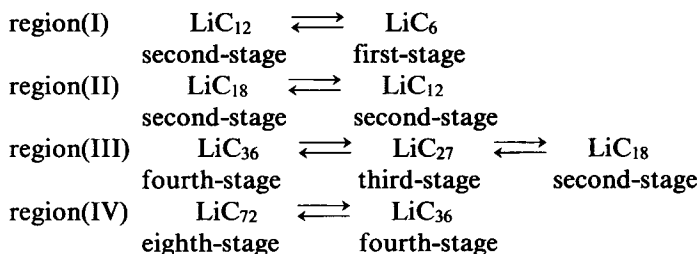


Fig. 5.9 Reversible potential of the lithium-graphite intercalation compounds vs. composition  $x$  in Li <sub>$x$</sub> C<sub>6</sub> plots. [T. Ohzuku *et al.*, *J. Electrochem. Soc.*, **140**, 2496 (1993)]

second/third and fourth/eighth-stages. The coexistence of the third and fourth-stages could not be detected; this is not found in Dahn's work either. The appearance of a series of (00 $l$ ) peaks in the pattern of the second-stage indicates the existence of a super lattice.

Figure 5.9 shows their open-circuit voltage (OCV) profiles recorded against  $x$  in  $\text{Li}_x\text{C}_6$ . Three distinct regions at about 85, 120 and 210 mV appears with little hysteresis between charge and discharge processes. Each potential plateau is explained as corresponding to the coexistence of two-phases. Ohzuku's group tried to interpret the change of OCVs so as to coincide with the obtained XRD data. Li-graphite system was considered to undergo transitions of each stage according to the following scheme.



They proposed six discrete phases resulting in two types of in-plane lithium density, that is,  $\text{LiC}_6$ -type for  $\text{LiC}_6$  and  $\text{LiC}_{12}$  phase and  $\text{LiC}_9$ -type for  $\text{LiC}_{18}$  and higher phases. The existence of  $\text{LiC}_6$  and  $\text{LiC}_{12}$  phase had already been known for the chemically prepared Li-GIC for a long time. On the other hand, the existence of  $\text{LiC}_{18}$  is now under investigation. There are several reports insisting on its existence and as having a remarkably different character from  $\text{LiC}_{12}$  phase.<sup>27,28)</sup> Other higher stages than  $\text{LiC}_{27}$  were originally proposed in this work.

There are some discrepancies between the two staging models presented here. In particular, stories of higher stages do not coincide well. For example, the super lattice peaks obtained in Dahn's work are only recognized in the second-stage compound in Ohzuku's report. Due to the narrow compositional range of the higher stages, identification of stages becomes difficult. The effect of a surface passivation layer and solvent cointercalation discussed later on may affect the following intercalation mechanism. The type of graphite is also an important factor. Further work is necessary to reconcile all the models.

## 5.5 Electrochemistry of Soft Carbons

In this section, soft carbons with less crystallinity than graphite are discussed. Mesocarbon microbeads (MCMB) have been studied by Mabuchi *et al.*<sup>29-31)</sup> This material is considered to have a turbostratic structure to some extent. The material was prepared from coal-tar pitch. The crude material was first carbonized under nitrogen then graphitized at temperatures ranging from 1200 to 2800 °C. Electrochemical performance of MCMBs in various electrolytes is shown in Fig. 5.10. The left figure shows the behavior of MCMB heat-treated at 1000 °C and the right one shows that of the 2800 °C-sample. The 1000 °C-sample does not show clear dependence on the type of electrolyte. The voltage increases and decreases continuously, which is generally seen for low temperature-

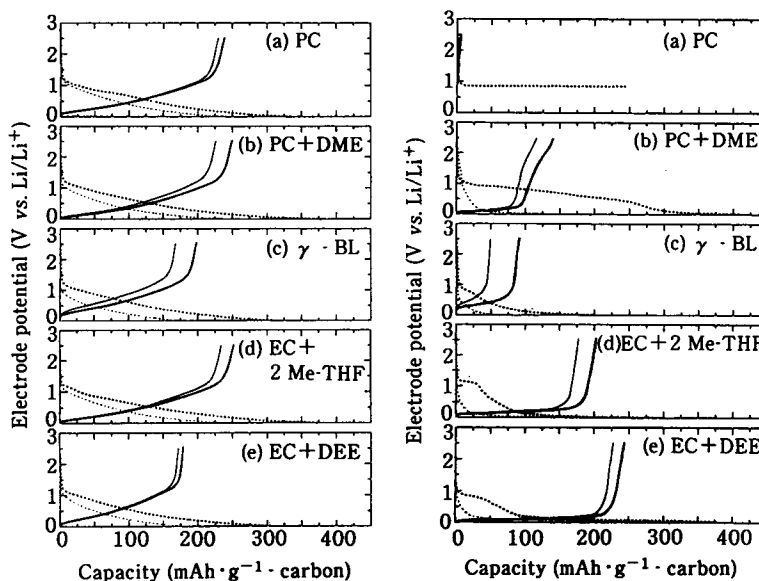


Fig. 5.10 Potential change during the charge (solid line) and discharge (dashed line) examination of MCMB heat-treated at 1000 °C (left) and 2800 °C (right).

[K. Tatsumi *et al.*, *J. Electrochem. Soc.*, **142**, 718 (1995)]

synthesized soft carbons. On the other hand, MCMB prepared at 2800 °C shows strong dependence on the electrolyte. In PC solution, it did not deliver any discharge capacity, exactly like the natural graphite charged in PC or BC mentioned above. The irreversible reaction that occurs is considered to be the electrolyte decomposition. In EC-based electrolyte, the cycle performance was improved leading to a charge capacity of 240 mAh · g<sup>-1</sup>.

This work provides a good example for the discussion of two interesting problems regarding all carbons. One problem is which factor determines the amount of reversible capacity. Samples heat-treated at different temperatures show different shapes of polarization curves and reversible capacities. The other problem concerns which factor controls the gas-evolutional reaction occurring at 0.8 V vs. lithium metal. In this work, the 2800 °C-sample cannot be cycled in PC, while gas-evolution barely occurs in the 1000 °C-sample.

For the first question, Tatsumi and Dahn's groups have shown almost same interpretation.<sup>31,32)</sup> Tatsumi used the  $P_1$  value, an index of fractional ratio of perfect graphite stacking in a carbon material,<sup>33)</sup> while Dahn used the  $P$  value indicating the probability of random stacking between adjacent two layers. The following is Tatsumi's proposed mechanism. First, the charge potential region of the MCMBs in EC + DEE was divided into three parts (I, II and III) according to the threshold voltages of 0.25 and 1.3 V. The voltage of 0.25 V was determined to be the final potential of the deintercalation process of 2800 °C-MCMB and the voltage of 1.3 V is the end point of deintercalation of the 1000 °C-sample. Fig. 5.11 shows the plot of charge capacities of region (I) against  $P_1$  values of MCMBs heat-treated from 1000 to 2800 °C. The charge reaction of MCMBs below

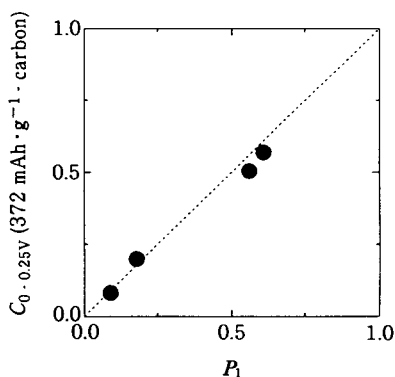


Fig. 5.11 Relation between the first charge capacity in the potential range 0 to 0.25 V and the  $P_1$  value.  $C_{0-0.25V}$  is normalized by the capacity of  $\text{LiC}_6$ . [K. Tatsumi *et al.*, *J. Electrochem. Soc.*, **142**, 720 (1995)]

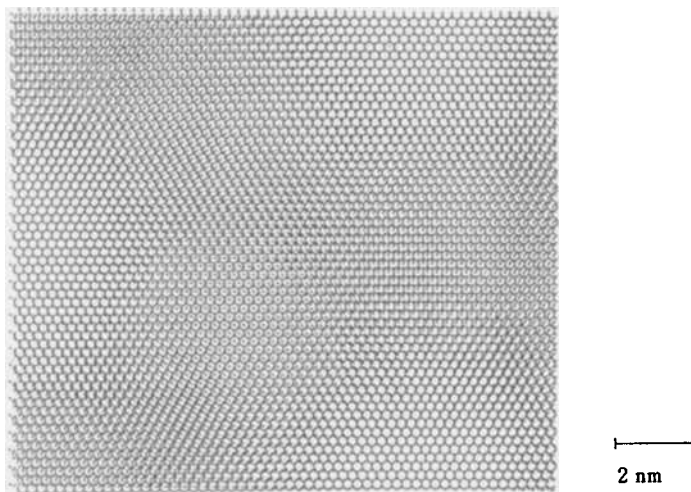


Fig. 5.12 Simulation for the turbostratic structure where the upper carbon plane is twisted by 1.14 degree against the lower plane. [T. Kasuh *et al.*, *Extended Abstracts IMLB-8*, p. 99 (1996)]

0.25 V is considered to be the intercalation of lithium into the graphitic structure with the AA-stacking order. This linear relation is maintained up to  $P_1 = 1.0$  (graphite), so this rule may be applicable to other soft carbon materials having some turbostratic structure.

In contrast to region (I), the mechanism of region (II) is more complicated. Tatsumi *et al.* explained the capacity delivered in the region by considering the  $(1 - P_1)$  value, which is a fractional ratio of the turbostratic structure. In the turbostratic structure, graphite sheets are randomly stacked and pinned to each other. Therefore, the rearrangement of the graphite planes into A/Li layer/A requires much energy and cannot be achieved by lithium intercalation. Kasuh *et al.* calculated the projected probability function and measured ( $hk$ ) XRD peaks of MCMBs to simulate turbostratic structure in adjacent to parallel two graphite layers.<sup>34)</sup> The calculated pattern of angularly displaced layers is

illustrated in Fig. 5.12. In this pattern the variety of stacking order ranging from perfect AA to perfect AB can be seen at the same time. Lithium intercalation can occur in AA-stacking but lithium cannot enter the AB-stacking portion for the reason stated above.

The capacity of the samples heat-treated at 2000, 2300 and 2800 °C is proportional to  $(1 - P_1)$  values. The maximum capacity of fully intercalated turbostratic structure can be estimated as  $\text{Li}_{0.2}\text{C}_6$  by extrapolation in Tatsumi's study. However, the capacity of 1000 °C-sample in region (II) is significantly larger than the value expected from the proportional line in the figure. A drastic increase in capacity of carbons heat-treated around 1000 °C can be also observed for other soft carbons.<sup>22)</sup> For example, vapor grown carbon fibers heat-treated from 1000 to 2800 °C show a tendency similar to that of MCMBs. To explain the capacity increase of materials synthesized at low temperature, Tatsumi proposed two mechanisms. One is intercalation into the turbostratic structure whose spacing is significantly larger than that of graphitized carbons. Therefore, the planes slide relatively easily by lithium intercalation. The other explanation assumes a new mechanism for storing lithium. Nongraphitized carbon materials have many crystal defects and lithium can be doped into the space.

In summarizing this work on soft carbons, it was concluded that soft carbons always have at least two mechanisms to accommodate lithium. In the potential range from 0 to 0.25 V, lithium is intercalated into a graphitic part and the capacity can be described as  $372 \times P_1 \text{ mAh} \cdot \text{g}^{-1}$ . The maximum capacity is  $372 \text{ mAh} \cdot \text{g}^{-1}$  when  $P_1 = 1$  for graphite. In the potential region above 0.25 V, the intercalation mechanism changes according to heat-treatment temperature. In a highly crystallized sample, intercalation of the turbostratic part is dominant, although the capacity is limited to within quite a small amount of about  $50 \text{ mAh} \cdot \text{g}^{-1}$ . A low crystalline sample synthesized at 1000 °C show large capacity but its mechanism is not clear. Tatsumi suggested the existence of additional sites for lithium storage. This point is discussed in detail below.

Mabuchi *et al.* considered these sites as micropores, which they called "cavities" formed between crystallites.<sup>30,35)</sup> They estimated the total amount of cavities in carbons per unit volume. For samples heat-treated from 700 to 1000 °C, they found a linear correlation between the discharge capacity of the region between 0.9 and 2 V and the amount of cavities. It was assumed that lithium ions in the cavities are stored in the form of clusters, because the repulsion between ionic species becomes significantly large if amounts of lithium are packed in small spaces. From XRD results and hysteresis of the charge-discharge curve the mechanism illustrated in Fig. 5.13 was proposed. Lithium intercalates into the graphite layers and the cavities at the same time during charge. In discharge, lithium is first deintercalated from the layers, then extracted from cavities. This mechanism can be described as a two-step reaction.

There is another way to explain a large capacity of higher than  $372 \text{ mAh} \cdot \text{g}^{-1}$  of carbons synthesized below 1000 °C. Dahn *et al.* set importance on the interpretation of the hysteresis of charge-discharge curves which disappear in carbons pyrolyzed above 1000 °C. They doubted the possibility of lithium clusters in cavities for the reason that the potential must be much closer to lithium metal if clusters are formed. They introduced a new mechanism in which hydrogen atoms contained in carbons play a significant role during charge-discharging.<sup>36,37)</sup> In their work, the correlation between reversible capacity and H/C atomic ratio of materials synthesized below 1000 °C were examined and the capacity was found to be proportional to the hydrogen content. These data indicate that hydrogen

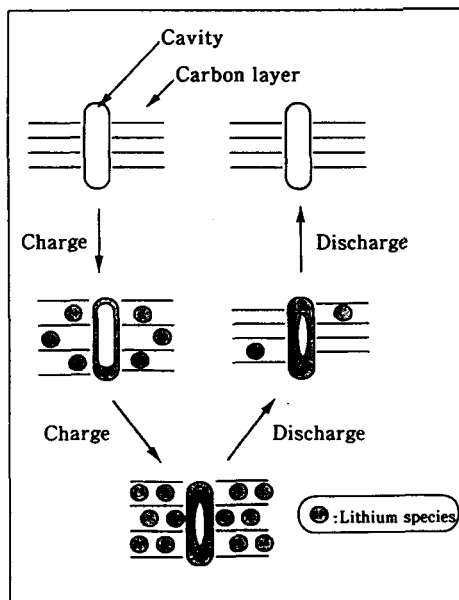


Fig. 5.13 Schematic illustration of the charge-discharge mechanism involving cavities.  
[A. Mabuchi *et al.*, *J. Electrochem. Soc.*, **142**, 1045 (1995)]

atoms participate in the intercalation mechanism and the amount determines the reversible capacity. Dahn *et al.* assumed that lithium atoms preferentially attack  $\text{-CH}$  bonding situated at the edge surface. This results in change in carbon-carbon surface bonding from  $\text{sp}^2$  to  $\text{sp}^3$ . The origin of the hysteresis is explained by this change in the host structure.

According to their model, the sites next to hydrogen atoms are named "bonding sites." Lithium atoms first occupy sites between layers, then occupy the bonding sites. However, intercalated lithium can enter these bonding sites only by passing the activation state, which means there is some energy barrier between these sites. The transfer of lithium from intercalated sites to bonding sites begins after the chemical potential of intercalated lithium atoms becomes high enough. In discharge, lithium in intercalated sites is first removed without passing the bonding sites, then atoms in bonding sites transfer to intercalated sites. This work gives a good model which can rationally explain the occurrence of the hysteresis. Theoretical details are given in the original literature.

## 5.6 Electrochemistry of Hard Carbons

The number of studies on hard carbon is relatively small compared to studies on soft carbons, but hard carbons usually deliver large capacity beyond the theoretical one of  $\text{LiC}_6$ . In this sense, hard carbons can be a powerful candidate for a practical anode. Thermal decomposition product of PFA and products from petroleum pitch by Ishikawa *et al.*<sup>38)</sup> are examples of actively studied hard carbons. Ishikawa *et al.* pointed out the importance of open micropores in hard carbon matrix as a lithium reservoir. These pores become more closed with increasing heat-treating temperature. Dahn *et al.* have also investigated many



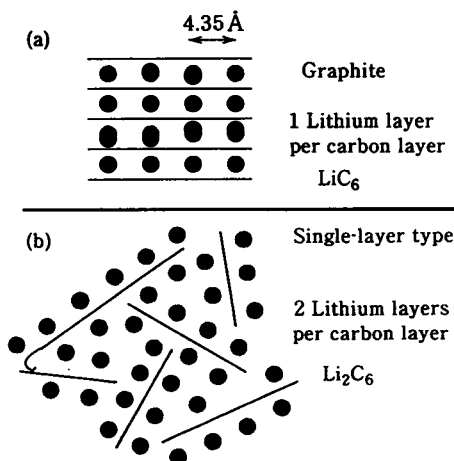


Fig. 5.14 Schematic presentation of (a) lithium intercalation in graphite and (b) lithium insertion in a single-layer carbon.

[J.S. Xue *et al.*, *J. Electrochem. Soc.*, **142**, 3669 (1995)]

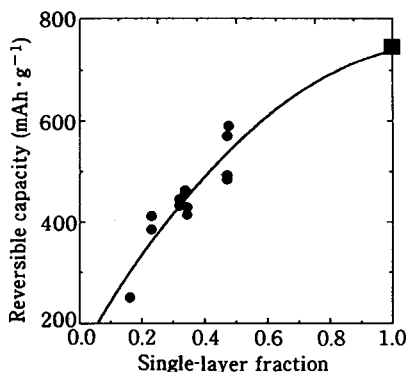


Fig. 5.15 Capacity vs. single-layer fraction for carbons prepared by pyrolyzed epoxy novolac resin at 1000 °C. [J.R. Dahn *et al.*, *Extended Abstracts of Society Meeting*, 95-2, p. 129 (1996)]

kinds of hard carbons prepared from epoxy resins and phenolic resins.<sup>39,40)</sup> According to their work, hard carbons are made up of single graphene sheets which are arranged like a “house of cards.” On charging, intercalated lithium adsorbs onto the both sides of each graphene sheet, leading to high lithium storage capability. The illustration of the model is shown in Fig. 5.14, which shows two lithium layers for each graphene sheet corresponding to  $\text{Li}_2\text{C}_6$ . This is confirmed by the experimental result that the reversible capacity increases almost linearly with the single-layer fraction as shown in Fig. 5.15.<sup>36)</sup> Dahn *et al.* also pointed out the importance of the structure of nanopores whose internal surfaces are adsorbed by lithium atoms. Thermal oxidation under air atmosphere changes the pore structure and significantly affects electrochemical behavior. They did a careful estimation

of the average pore volume and surface area at different oxidation levels. Consequently, it was found that the pores do not grow much in size by oxidation but their openings become larger. Once the size of the openings becomes large enough for the electrolyte to penetrate, electrolyte decomposition occurs inside the pores. The decomposition products cover the graphene surface, leading to a drastic decrease in reversible capacity.

### 5.7 Irreversible Surface Reactions

One of the major problems regarding the carbon anode is the irreversible decomposition of organic solvents. A paper published by Dey and Sullivan in 1970 reported a cathodic decomposition of PC on a graphite electrode.<sup>41)</sup> The production of  $\text{Li}_2\text{CO}_3$  and propene gas at potentials from 0.6 to 1.0 V vs. lithium metal was already referred to in this work. These side reactions not only decrease cycle efficiency, but disintegrate the carbon anode. To prevent this, much research has focused on the elucidation of the mechanism, and there are many opinions regarding exfoliation of graphene sheets and occurrence of passivation film. As a result of intensive research to seek a more stable solvent, ethylene carbonate and its mixture with other solvents were found to be practically stable during cathodic polarization down to 0 V. However, the involvement of electrolyte in the intercalation is not fully understood yet because there are many parameters concerning the surface structure which could influence the decomposition.<sup>42–44)</sup> Recently, Aurbach and Ein-Eli reported the behavior of graphite electrode in various electrolyte systems by using *in situ* XRD method.<sup>45)</sup> In this work electrolytes are divided into three major groups according to the surface situation after decomposition starts. A graphite anode in PC solution shows voltage plateau at about 0.8 V vs. lithium metal. During the plateau region, PC is reduced to form a surface layer which is primarily made of  $\text{CH}_3\text{CH}(\text{OCO}_2\text{Li})\text{CH}_2\text{OCO}_2\text{Li}$  as identified by Fourier transform infrared spectroscopy (FT-IR).<sup>46)</sup> The *in situ* XRD results show a broad peak at  $20^\circ$ , the intensity of which becomes larger with charging potential down to 0.7 V. Hence, this peak was interpreted as fragments of destroyed graphite embedded in the surface passivation layer. On the other hand, (002) peak corresponding to the interlayer distance barely shifted during the charge process, but its intensity decreased significantly. To explain these changes, the following model was proposed. Prior to lithium intercalation which occurs below 500 mV, charge current was consumed for the formation of surface passivation film. This film appears to be quite porous by nature and cannot cover the surface well. Therefore, lithium ions easily intercalate with solvent molecules from the uncovered part at potentials above 500 mV, leading to exfoliation of graphite sheets and preventing the formation of lithium-GIC.

Next group comprises EC and EC-based electrolytes. In these electrolytes, a surface film mainly made of  $(\text{CH}_2\text{OCO}_2\text{Li})_2$  and  $\text{Li}_2\text{CO}_3$  is formed. In contrast to the case of PC the film is formed uniformly over the surface. As it completely screens the graphite from the electrolyte, further decomposition is prevented and the capacity of decomposition is limited to a negligible level. In addition, this surface film is a good lithium conductor and lithium ions can migrate through it without solvent molecules. This results in no exfoliation of graphene sheets and stable reversible behavior of the anode. The third group shows intermediate behavior of the above two groups. A surface film partly protects the active materials, but it is not effective enough to prevent the destruction of the graphite. Although some degree of intercalation compounds can form in early cycles, the

destruction occurring with the solvent cointercalation leads to a gradual decreases in reversible capacity with cycling. An example of this type is dried dimethylcarbonate (DMC).

This model, in which a passivation layer is always formed in any electrolyte system and the characteristics of the formed film greatly affect subsequent electrode behavior, is based on the following assumptions. The intercalation of solvated lithium ions causes exfoliation and occurs at more positive potentials than that of bare lithium. With respect to the potential of solvent cointercalation, the model appears correct because the interaction between guest and host species becomes much weaker by solvent molecules lying in between. From XRD data of the PC case, the solvent seems to cointercalate at 1.0 V, because the peak of decomposed graphite already appears. For further understanding of the irreversible solvent decomposition, study of solvent cointercalation is necessary. Solvent cointercalation has been known for a long time, but there are no electrochemical data such as the redox potential of solvated lithium intercalation. Concerning this point recent research work is discussed below.

The work done by Inaba *et al.* investigated the surface morphology of a highly oriented pyrolytic graphite (HOPG) anode using electrochemical scanning tunneling microscopy (STM) in EC–DEC mixed electrolyte.<sup>47)</sup> This enables *in situ* observation of the basal plane during charge-discharging. When the sample potential was potentiostatically stepped to 1.1 V vs. lithium metal, nucleation of a flat hill-like structure and its planar growth with time were observed near the edge. A similar island-like structure was also observed by Lang *et al.* for stage-1 GIC prepared in liquid phase.<sup>48)</sup> The height of the hill observed was about 10 Å. If lithium ions intercalate into graphite, expansion of 0.36 Å for each layer can be expected from the difference in *d*-values of pristine graphite (3.35 Å) and LiC<sub>6</sub> (3.71 Å). The sample studied is an exfoliated fragment containing 9–10 graphene sheets. Therefore, the total increment along the *c*-axis must be around 3.6 Å at most by unsolvated lithium intercalation. However, the experimental value of 10 Å is more than twice this calculated value and lithim intercalation is not supposed to occur at such a high potential. It was concluded from these results that the hill was formed as a result of solvated lithium intercalation at 1.1 V.

Besenhard *et al.* also studied the expansion of HOPG intercalated in various organic solvents by dilatometry.<sup>49)</sup> In this work, the drastic expansion was observed at potentials more negative than 1.0 V. They also attributed this expansion to solvent cointercalation. The reason for the potential difference is not specified, but Inaba *et al.* noted that the hill formation at the atomic level started at 1.1 V. Apart from this point they reached the same conclusion that the decomposition of intercalated solvent results in products remaining between layers which prevent further insertion of solvent and exfoliation of layers.

In summarizing these works, it is possible to say that the stability of the cointercalated solvent determines the electrochemical behavior of a graphite anode. These phenomena can only be observed in highly crystallized carbons, because in less graphitized carbons large solvent molecules cannot enter the interlayer space. However, this information is quite important because the long-term stability of the anode clearly depends on the property of the surface film and natural graphite has recently become a more promising candidate for the anode.

## 5.8 Structural Modifications

To improve anode performance of carbon materials, it is important to reduce the irreversible decomposition of electrolytes and enhance the reversible capacity. In this section, works aiming at such improvement by structural modification are presented.

As explained in section 5.2, the texture of carbon materials is one type of structure involving crystallite size and its orientation. Texture control cannot change the properties of individual crystallites but can change the properties of the electrode as an agglomerate of crystallites. Electrochemical performance depends on macroscopic factors such as

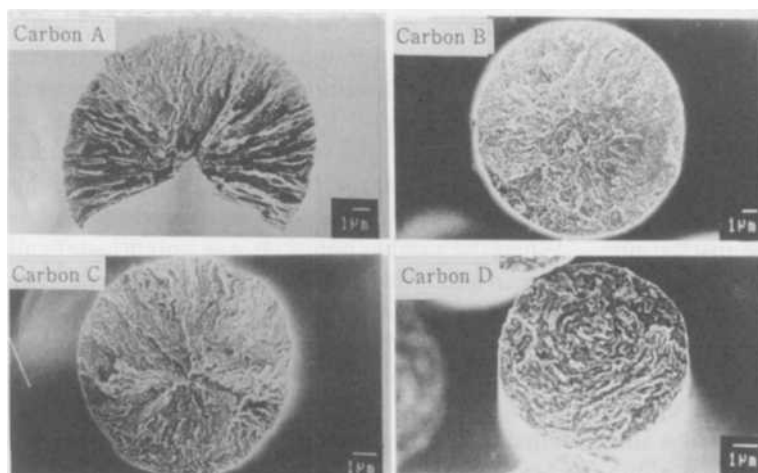


Fig. 5.16 SEM photos of cross sections of four types of carbon fibers A,B, C and D. [N. Imanishi *et al.*, *J. Electrochem. Soc.*, **140**, 315 (1993)]

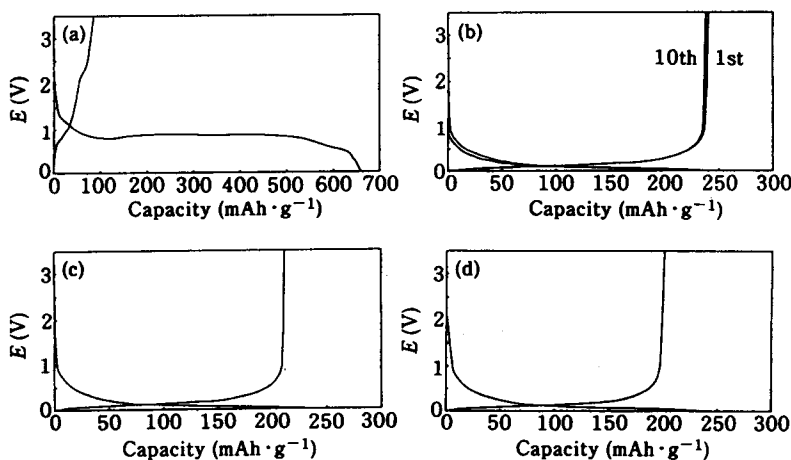


Fig. 5.17 The charge-discharge behavior of carbon fibers A, B, C and D in PC-THF electrolyte. [N. Imanishi *et al.*, *J. Electrochem. Soc.*, **140**, 317 (1993)]

electrical conductivity of electrode, active surface area, porosity and structure of interface between electrode and electrolyte. These are changeable to some extent by texture control. It is important to arrange the texture appropriately to derive as much potential capability from each crystallite as possible. Fig. 5.16 shows the cross sectional views of four types of carbon fibers with different textures.<sup>50)</sup> These fibers were heat-treated at 2800°C (A) and 2600°C (B, C, D), so that they have quite similar crystal parameters. Their textures can be expressed as radial with wedge (A), radial with zigzag layers (B), double core-shell texture (C) and concentric texture (D). The electrochemical behaviors in PC–THF solution are shown in Fig. 5.17. Carbon fiber (A) shows no reversibility due to the decomposition of the solvent, as indicated by a plateau at 0.8 V. This texture exposes an edge surface to the solvent so that solvated lithium intercalates easily followed by decomposition between layers. Scanning electron microscope (SEM) observations of fiber (A) after charging show disintegration of the original structure because of exfoliation of layers. On the other hand, the other three types of textures can be cycled even in PC–THF solution. The outermost shell of the fibers observed looks very smooth and very different from the texture of fiber (A). SEM observation implies that these fibers are surfaced with basal planes and there are no large openings for solvent to permeate. Most solvent molecules were probably blocked out at the surface, a fact which leads to stable cycling even in PC–THF solution. This example shows that adjusting the texture is effective in optimizing electrode property. On the other hand, the polarization behaviors are not very different among (B), (C) and (D). These internal textures were expected to influence the lithium diffusion in bulk electrode, but the results showed that the texture difference was not large enough to demonstrate noticeable effect.

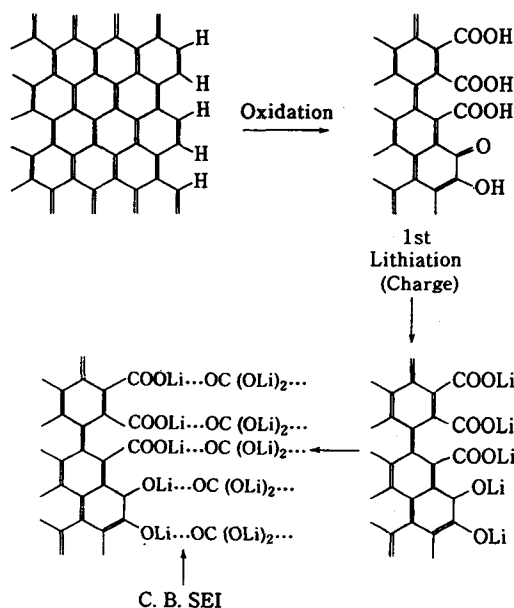


Fig. 5.18 The formation of C. B. SEI (chemically-bonded SEI) at the edge surface of graphite.  
[E. Peled *et al.*, *J. Electrochem. Soc.*, 143, L5 (1996)]

The surface modification of graphite by mild oxidation was investigated by Peled *et al.*<sup>51)</sup> They found that appropriate oxidation below 1000 °C leads to prevention of solvent cointercalation and better cycle performance. It should be noted that this is a different case from the oxidation effect on hard carbons mentioned above. According to Peled's model, the oxidation occurs mainly at the edge plane and surface CH bonding is transferred to COOH groups, as shown in Fig. 5.18. Electrochemical lithiation in an organic solvent results in the formation of a compact solid electrolyte interface (SEI) chemically bonded to these surface functional groups. Cycling behaviors show different tendencies according to the degree of oxidation. However, in all cases mild oxidation increases the reversible capacity by 10–30% of the original. Peled *et al.* deduced the reasons for the improvement to the following: (1) the formation of surface functional groups prevented cointercalation of solvent molecules prior to intercalation; (2) the surface functional groups provided a good affinity to the electrolyte, leading to increase of active surface area; (3) the extra lithium may be stored in the vicinity of these groups. The increase in capacity by oxidation is in contrast to the case of hard carbons showing capacity decrease by burn-off. In highly graphitized carbons, there are intrinsically few pores between crystallites for solvent to penetrate. The mild oxidation of the surface produces the same solvent-blocking effect as seen in texture control technique.

Next, the effect of doping with other elements is discussed. For example, phosphorus doping effect of pyrolyzed PFA has been shown in section 5.3. There are some studies on nitrogen and boron doping effect on lithium intercalation.<sup>52,53)</sup> Dahn's group investigated carbonaceous materials containing silicon and oxygen atoms which were synthesized by thermal decomposition of epoxy-silane composites.<sup>54)</sup> They controlled Si/C atomic ratio in products by adjusting the amount of starting nonsilicon polymers (epoxy novolac resins) and silicon-containing polymers (epoxy-functional silane). XRD study of these pyrolyzed products revealed that two types of compounds were formed. When the starting silane contained more than 50% by weight, a single glassy  $C_{1-y-z}Si_zO_y$  phase was obtained. If it was below 50%, coexistence of the glassy phase and single-layer carbon phase appeared. The highest reversible capacity as high as  $770 \text{ mAh} \cdot \text{g}^{-1}$  was observed for the glassy product corresponding to  $C_{0.50}Si_{0.19}O_{0.31}$  from 100% epoxy-functional silane. In a parallel work, hard carbons synthesized from phenolic resins delivered reversible capacity of about

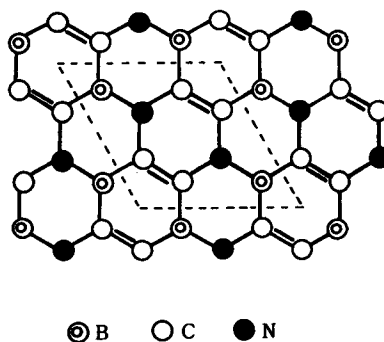


Fig. 5.19 A possible configuration of atoms in the basal plane of  $BC_2N$ .  
[M. Morita *et al.*, *J. Electrochem. Soc.*, **139**, 1228 (1992)]

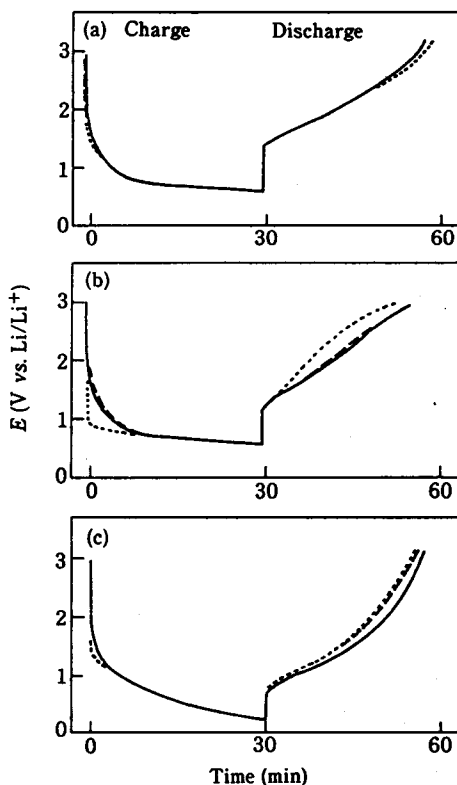


Fig. 5.20 Charge-discharge curves of  $\text{BC}_2\text{N}$  electrode in various electrolytes. [M. Morita *et al.*, *J. Electrochem. Soc.*, 139, 1229 (1992)]

$600 \text{ mAh} \cdot \text{g}^{-1}$ . This result shows that the capacity can be enhanced by silicon doping, although there are some disadvantages, such as occurrence of large irreversible capacity.

Morita *et al.* investigated  $\text{BC}_2\text{N}$ , which has a structure identical to that of graphite.<sup>55)</sup> A possible arrangement of atoms in a basal plane is illustrated in Fig. 5.19. This material was prepared from  $\text{CH}_3\text{CN}$  and  $\text{BCl}_3$  source gasses by CVD method at  $1000^\circ\text{C}$ . XRD pattern of the products showed two peaks, assigned as (002) and (10) diffractions. These peaks are quite broad due to poor crystallinity. By analogy to carbon materials, synthesized  $\text{BC}_2\text{N}$  is considered to have a turbostratic structure. Fig. 5.20 shows typical charge-discharge curves of the  $\text{BC}_2\text{N}$  electrode at a constant current of  $1 \text{ mA} \cdot \text{cm}^{-2}$ . The electrolytes used were PC and PC-DME mixed solution in which  $\text{LiClO}_4$  or  $\text{LiPF}_6$  was dissolved. Interestingly, there is no potential plateau of electrolyte decomposition in spite of using PC solution. Chemical analysis of the products charged at different degrees showed that the side reactions occurred mainly at potentials more negative than 0.8 V. Cointercalation of solvent molecules into  $\text{BC}_2\text{N}$  may not occur because the two-dimensional layered structure did not develop enough at  $1000^\circ\text{C}$ , or slower decomposition speed on the surface of  $\text{BC}_2\text{N}$  electrode reduced the irreversible capacity. There are some similar features between the electrochemical behavior of  $\text{BC}_2\text{N}$  and that of turbostratic soft carbons.

The maximum experimental capacity was  $x = 0.58$  in  $\text{Li}_x\text{BC}_2\text{N}$  obtained in PC solution at quite low current density ( $25 \mu\text{A} \cdot \text{cm}^{-2}$ ). This value is comparable to the theoretical capacity of  $\text{LiC}_6$ . More than 90% of coulombic efficiency could be obtained and no degradation was observed during repeated cycles. On the other hand, the discharge potential is too high for use as the anode. The high-rate character and its cost are inferior to other carbon materials currently under study. These drawbacks must be overcome to compete with other carbon anodes. This work not only shows a novel anode material, but implies nitrides or borides also have the possibility for use as the anode.

## 5.9 Nitrides as New Anode Materials

In this section, the lithium-metal-nitrogen ternary system is discussed as a new candidate for the reversible anode. Although lithiated carbon is a promising anode because of good rechargeability, small volume changes with lithium intercalation and safety, it still suffers from various problems. The most important issue is its small specific capacity due to the limitation of lithium content shown as  $\text{LiC}_6$  ( $372 \text{ mA} \cdot \text{g}^{-1}$ ) and capacity fading due to the disintegration of carbon matrix. The research works presented in the other sections mainly involve structural adjustment for better performance. This new work aims at finding a completely new anode material to solve the problems stemming from the original character of carbon materials. The nitride system has no direct relation to carbon materials, but its novelty as an intercalation system and good anode performance is worth studying. The data presented here were obtained in the authors' laboratory.

The nitride system belongs to the group of compounds having antifluorite or  $\text{Li}_3\text{N}$  structure. Both structures are known to be good ionic conductors, so high lithium ion mobility and reversibility can be expected for the system. In addition, they show a negative potential close to that of lithium metal, indicating that the nitrides may be a good anode candidate.

### 5.9.1 $\text{Li}_7\text{MnN}_4$ and $\text{Li}_3\text{FeN}_2$ (Antifluorite Structure)<sup>56,57)</sup>

Li-M-N compounds with antifluorite structure, where M stands for a transition metal, have been known for a long time, *e.g.*,  $\text{Li}_5\text{TiN}_3$ ,  $\text{Li}_7\text{VN}_4$ ,  $\text{Li}_{15}\text{CrN}_9$ ,  $\text{Li}_7\text{MnN}_4$ ,  $\text{Li}_3\text{FeN}_2$ , *etc.* We found that  $\text{Li}_3\text{FeN}_2$  and  $\text{Li}_7\text{MnN}_4$  could be easily synthesized using traditional ceramic methods by reacting the transition metal nitride  $\text{M}_x\text{N}_y$  and lithium nitride  $\text{Li}_3\text{N}$  in a 1% $\text{H}_2$ -99% $\text{N}_2$  stream. The crystal structure of  $\text{Li}_7\text{MnN}_4$  and  $\text{Li}_3\text{FeN}_2$  by Rietveld refinement using the space group  $P3n$  are illustrated in Fig. 5.21.  $\text{Li}_7\text{MnN}_4$  has isolated  $\text{MnN}_4$  tetrahedra. The nitrogen atoms are arranged in a distorted cubic close-packed array and the tetrahedra in which Li and Mn atoms are located form an anionic three-dimensional network.  $\text{Li}_3\text{FeN}_2$  also crystallizes in a distorted antifluorite structure, in which, in contrast to  $\text{Li}_7\text{MnN}_4$ ,  $\text{FeN}_4$  tetrahedra sharing edges form one-dimensional chains along the *c*-axis.

Figure 5.22 shows the charge and discharge curves of the  $\text{Li}/\text{Li}_{3-x}\text{FeN}_2$  and  $\text{Li}/\text{Li}_{7-x}\text{MnN}_4$  cell at a current density of  $0.3 \text{ mA} \cdot \text{cm}^{-2}$ . Both  $\text{Li}_3\text{FeN}_2$  and  $\text{Li}_7\text{MnN}_4$  have good reversibility and high specific capacities of  $150 \text{ mAh} \cdot \text{g}^{-1}$  and  $210 \text{ mAh} \cdot \text{g}^{-1}$ , respectively. The lithium ions were electrochemically deintercalated up to about  $x = 1$  in  $\text{Li}_{3-x}\text{FeN}_2$ , and  $x = 1.25$  in  $\text{Li}_{7-x}\text{MnN}_4$  with terminating potential of 1.5 V. A completely



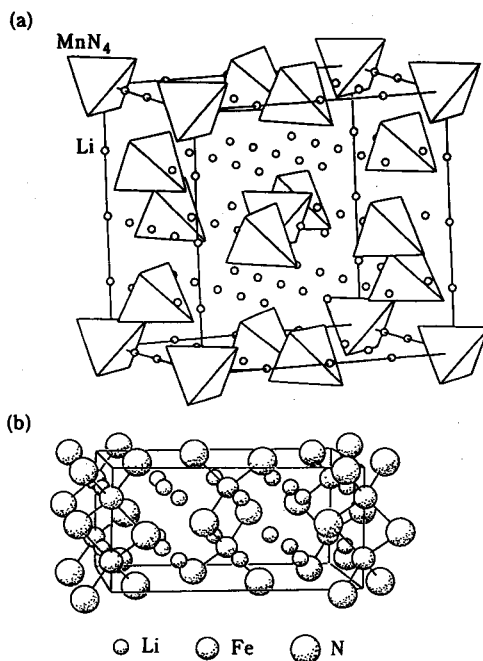


Fig. 5.21 The crystal structures of (a)  $\text{Li}_7\text{MnN}_4$  and (b)  $\text{Li}_3\text{FeN}_2$ . [(a) M. Nishijima *et al.*, *J. Electrochem. Soc.*, **141**, 2968 (1994); (b) M. Nishijima, *J. Solid State Chem.*, **113**, 207 (1994)]

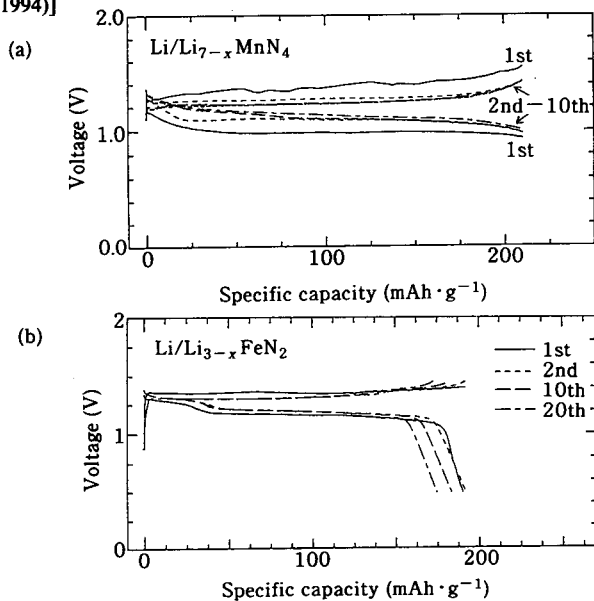


Fig. 5.22 Charge and discharge curves for the  $\text{Li}/\text{Li}_{7-x}\text{MnN}_4$  and  $\text{Li}/\text{Li}_{3-x}\text{FeN}_2$  cell. The current density was  $0.3 \text{ mA} \cdot \text{cm}^{-2}$ . [(a) M. Nishijima *et al.*, *J. Electrochem. Soc.*, **141**, 2970 (1994); (b) M. Nishijima, *J. Solid State Chem.*, **113**, 208 (1994)]

reversible reaction occurs over the range of  $0 \leq x \leq 0.75$  in  $\text{Li}_{3-x}\text{FeN}_2$  and  $0 \leq x \leq 1.25$  in  $\text{Li}_{7-x}\text{MnN}_4$ . Throughout these ranges, lithium deintercalation occurs by a two-phase reaction. The newly occurring phase has the same symmetry as the original one but slightly different lattice parameters. This results in the charge and discharge potential curves of these nitrides appearing as a plateau. The potentials around 1.2 V for  $\text{Li}_3\text{FeN}_2$  and 1.1 V for  $\text{Li}_7\text{MnN}_4$  are more negative than ordinary lithium intercalation potentials of oxide electrodes. The chemical diffusion coefficients by galvanostatic intermittent titration technique method are in the range of  $5 \times 10^{-12} - 1 \times 10^{-10} \text{ cm}^2 \cdot \text{s}^{-1}$ .

### 5.9.2 $\text{Li}_{3-x}\text{Co}_x\text{N}$ ( $\text{Li}_3\text{N}$ Structure)<sup>58,59)</sup>

Another ternary lithium transition metal nitride system,  $\text{Li}_{3-x}\text{M}_x\text{N}$  ( $\text{M} = \text{Co}, \text{Ni}$  and  $\text{Cu}$ ), is isostructural to  $\text{Li}_3\text{N}$ , which is composed of  $\text{Li}^+_2\text{N}^{3-}$  layers with  $\text{Li}^+$  between them as described in Fig. 5.23. Metal ions, Co, Ni and Cu can be substituted for lithium between the  $\text{Li}_2\text{N}$  layers. The solid solution region of  $\text{Li}_{3-x}\text{M}_x\text{N}$  prepared under flow of  $\text{N}_2$  gas are in the range of  $0 \leq x \leq 0.5$ ,  $0 \leq x \leq 0.6$  and  $0 \leq x \leq 0.3$  for  $\text{M} = \text{Co}, \text{Ni}$  and  $\text{Cu}$ , respectively. As the  $\text{M}^{2+}$  (especially  $\text{Co}^{2+}$  and  $\text{Ni}^{2+}$ ) and  $\text{M}^+$  states coexist in  $\text{Li}_{3-x}\text{M}_x\text{N}$ , the same number of lithium defects are created. The system is correctly represented as  $\text{Li}_{3-x-y}(\text{M}_{x-y}^+\text{M}_{2+y}^{2+})\text{N}$  where  $y$  indicates number of lithium vacancies. In stoichiometric  $\text{Li}_{3-x}\text{M}_x\text{N}$ , the doped metals exist as  $\text{M}^+$  ion in the structure. When a lithium ion is deintercalated, an  $\text{M}^+$  ion will be oxidized to  $\text{M}^{2+}$ .

$\text{Li}/\text{Li}_{3-x-z}\text{M}_x\text{N}$  cells were cycled in the range of  $0 \leq z \leq 1.0$  and showed a high capacity of  $480 \text{ mAh} \cdot \text{g}^{-1}$  in  $\text{Li}_{2.6-z}\text{Co}_{0.4}\text{N}$ , and  $460 \text{ mAh} \cdot \text{g}^{-1}$  in  $\text{Li}_{2.6-z}\text{Cu}_{0.4}\text{N}$ , while it is only  $200 \text{ mAh} \cdot \text{g}^{-1}$  in  $\text{Li}_{2.5-z}\text{Ni}_{0.5}\text{N}$ . The cycle behavior of the  $\text{Li}/\text{Li}_{2.6}\text{Co}_{0.4}\text{N}$  cell in 1 M  $\text{LiClO}_4/$

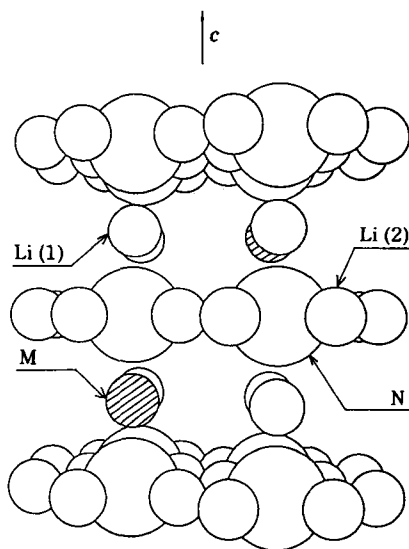


Fig. 5.23 The crystal structure of  $\text{Li}_{3-x}\text{M}_x\text{N}$ .  
[M. Nishijima *et al.*, *Extended Abstracts IMLB-8*, p. 403 (1996)]

PC + DMC electrolyte is shown in Fig. 5.24. The small capacity of the first discharge ( $z \sim 0.3$ ,  $150 \text{ mAh} \cdot \text{g}^{-1}$ ) corresponds to the lithium intercalation into the vacancy formed in order to compensate the charge of the  $\text{Co}^{2+}$  state. The characteristic feature of the behavior is the big difference between the first discharge profile and those of subsequent cycles. XRD study shows that the amorphous phase is formed during the first discharge process, causing the hysteresis. Contrary to our expectation, the initial crystalline

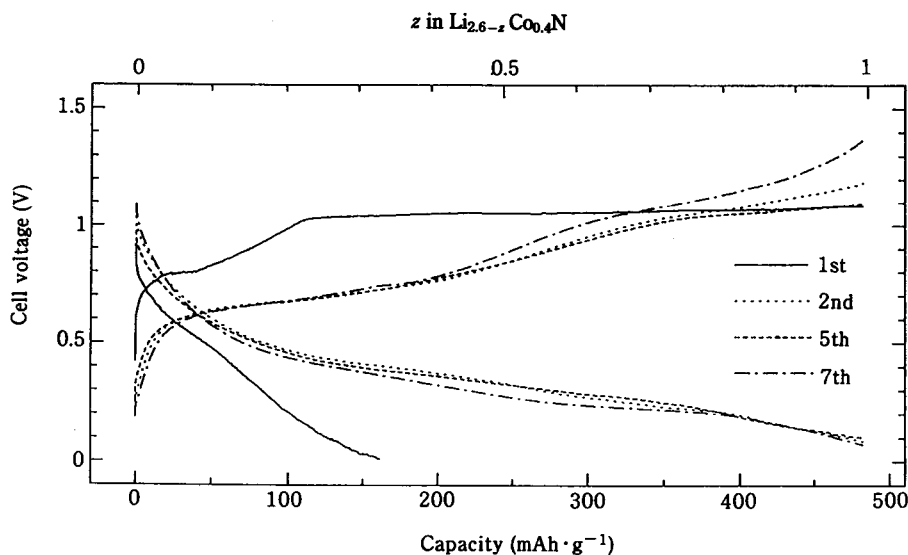


Fig. 5.24 Discharge and charge curves for the  $\text{Li}/\text{Li}_{2.6}\text{Co}_{0.4}\text{N}$  cell ( $0.3 \text{ mA} \cdot \text{cm}^{-2}$ ).  
[M. Nishijima *et al.*, *Extended Abstracts IMLB-8*, p. 403 (1996)]

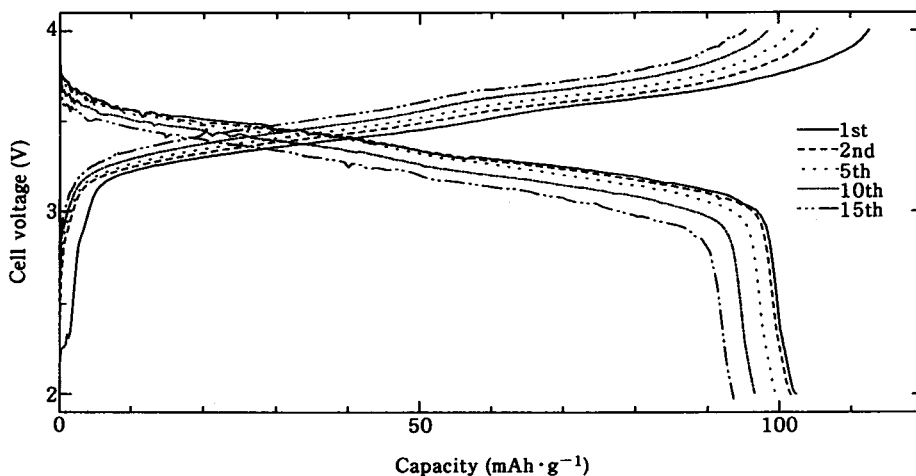


Fig. 5.25 Charge and discharge curves for  $\text{Li}_{2.6}\text{Co}_{0.4}\text{N}/\text{LiMn}_2\text{O}_4$  cell ( $0.3 \text{ mA} \cdot \text{cm}^{-2}$ ).

$\text{Li}_{3-x-z}\text{M}_x\text{N}$  phase can only deintercalate and intercalate limited amounts of lithium ions (the region where the voltage gradually increases in Fig. 5.24). The high capacity of  $\text{Li}_{3-x}\text{M}_x\text{N}$  is due to the amorphous phase, which shows good reversibility and negative discharge potential (0.5 V in average) after the second cycle. An NTT group recently reported the improved capacity of these systems.<sup>60,61)</sup> For example, in  $\text{Li}_{2.6}\text{Co}_{0.4}\text{N}$  the capacity reported is  $760 \text{ mAh} \cdot \text{g}^{-1}$  in the 0.0–1.4 V potential range. The reason is not clarified but the electrolyte may play a role in the amorphous process. The NTT group uses EC + 1,2-diethoxyethane solution, while we use PC + DME solution. The results sufficiently prove that  $\text{Li}_{3-x}\text{M}_x\text{N}$  can be a good candidate as an anode in a lithium ion battery for good reversibility, enough negative and flat potential and large reversible capacity.

Finally, the cyclic performance of  $\text{Li}_{2.6}\text{Co}_{0.4}\text{N}/\text{LiMn}_2\text{O}_4$  cell is shown in Fig. 5.25. The charge and discharge cut-off voltages were set at 4.0 V and 2.0 V, respectively. As  $\text{Li}_{2.6}\text{Co}_{0.4}\text{N}$  has some lithium vacancies ( $y \sim 0.3$  in  $\text{Li}_{2.6-y}\text{Co}_{0.4}\text{N}$ ), the cathodes such as  $\text{LiMn}_2\text{O}_4$  or  $\text{LiCoO}_2$  which starts from lithium deintercalation are applicable. The amount of the starting materials are determined so that  $\text{Li}_{2.6-y}\text{Co}_{0.4}\text{N}$  ( $y \sim 0.3$ ) anode is reduced to  $\text{Li}_{2.6}\text{Co}_{0.4}\text{N}$  while  $\text{LiMn}_2\text{O}_4$  cathode is oxidized to  $\text{Li}_{0.2}\text{Mn}_2\text{O}_4$ . The good cycling efficiency and large capacity was obtained for this “rocking-chair” cell. Although carbon anodes operate at lower potentials, the nitride anode can eliminate the irreversible capacity sometimes observed in carbon materials and can be used with lithium-free cathodes.

## 5.10 Summary and Conclusions

Practical carbon anodes, first appearing in 1989, have changed the direction of lithium battery researches, and a commercial rechargeable battery has been realized within quite a short period of time. With intensive researches worldwide, remarkable progress in understanding the fundamental aspects of carbon anodes has been made. Soft carbons having a graphitic structure show dependence of specific capacities on the index of graphite stacking fraction. The role of hydrogen atoms is emphasized in low crystalline soft carbons synthesized below  $1000^\circ\text{C}$ . The hard carbons are considered to have random stacking of single layers on which lithium ions can be adsorbed. Surface reactions of HOPG are being investigated by new methods such as STM, giving rise to the possibility of solvated lithium intercalation at high potentials.

Along with these fundamental researches, application technologies have also recorded great progress as symbolized by the widespread commercialization of portable electronic equipment such as mobile telephones and notebook computers. For operation under heavier loads, further improvement of carbon anodes is essential. Hard carbons are promising but the large irreversible capacity must be solved. Doping with other element is an effective method of improvement, but the chemistry of these materials is not well understood and their stability and the cost must be taken into a consideration.

Recently, the graphite anode has become increasingly popular as a practical anode, because its capacity,  $372 \text{ mAh} \cdot \text{g}^{-1}$  is acceptable for the current levels of application. There are statistics which indicate that the ratio of the graphite materials used in rechargeable lithium ion cells exceeds 50% in 1996, from below 20% in 1994. In the development of a graphite anode, control of the macroscopic structure will gain in

importance.

A continuous effort to understand the fundamental aspects of carbon materials will lead to lithium ion batteries for larger scale applications such as load leveling and electric vehicles.

#### REFERENCES

- 1) E. Peled, *J. Electrochem. Soc.*, **126**, 2047 (1979).
- 2) V.R. Koch, J.L. Goldman, C. J. Mattos and M. Mulvaney, *J. Electrochem. Soc.*, **129**, 1 (1982).
- 3) D. Aurbach, Y. Gofer and J. Langzam, *J. Electrochem. Soc.*, **136**, 3198 (1989).
- 4) M. Arakawa, S. Tobishima, Y. Nemoto and M. Ichimura, *J. Power Sources*, **43-44**, 27 (1993).
- 5) T. Hirai, I. Yoshimatsu and J. Yamaki, *J. Electrochem. Soc.*, **141**, 2300 (1994).
- 6) S. Megahed and B. Scrosati, *J. Power Sources*, **51**, 79 (1994).
- 7) A. Herold, *Bull. Soc. Chim. France*, **187**, 999 (1955).
- 8) L.B. Ebert, *Ann. Rev. Mater. Sci.*, **6**, 181 (1976).
- 9) M. Inagaki, *Tanso*, **94**, 106 (1978).
- 10) J.E. Fischer and T.E. Thompson, *Phys. Today*, **31**, 36 (1978).
- 11) S. Iijima, *J. Crystal Growth*, **50**, 675 (1980).
- 12) M. Inagaki, *Tanso*, **59**, 286 (1969).
- 13) B.E. Warren, *J. Chem. Phys.*, **2**, 551 (1934).
- 14) J.O. Besenhard and H.P. Fritz, *J. Electroanal. Chem.*, **53**, 329 (1974).
- 15) J.O. Besenhard and G. Eichinger, *J. Electroanal. Chem.*, **68**, 1 (1976).
- 16) R. Kanno, Y. Takeda, T. Ichikawa, K. Nakanishi and O. Yamamoto, *J. Power Sources*, **26**, 535 (1989).
- 17) M. Mohri, N. Yanagisawa, Y. Tajima, H. Tanaka, T. Mitate, S. Nakajima, M. Yoshida, Y. Yoshimoto, T. Suzuki and H. Wada, *J. Power Sources*, **26**, 545 (1989).
- 18) T. Nagaura and K. Tozawa, *Progr. Batteries and Solar Cells*, **9**, 209 (1990).
- 19) M. Nagamine, Electrochem. Soc. Japan, Spring Meet., Tokyo, Japan, 1993, Ext. Abstr., p. 167.
- 20) H. Azuma, A. Omaru and Y. Nishi, Electrochem. Soc. Japan, Fall Meet., Nagoya, Japan 1991, Ext. Abstr., p. 132.
- 21) Z. Jiang, M. Alamgir and K.M. Abraham, *J. Electrochem. Soc.*, **142**, 333 (1995).
- 22) A. Satoh, N. Takami and T. Ohsaki, *Solid State Ionics*, **80**, 291 (1995).
- 23) K. Nishio, M. Fujimoto, Y. Shoji, R. Ohshita, T. Nohma, K. Moriwaki, S. Narukawa and T. Saito, 8th Int. Meet. Lithium Batteries, Nagoya, Japan, 1996, Ext. Abstr., p. 93.
- 24) H. Kurokawa, T. Maeda, N. Nakanishi, T. Nohma and K. Nishio, 8th Int. Meet. Lithium Batteries, Nagoya, Japan, Ext. Abstr., p. 222.
- 25) J.R. Dahn, *Phys. Rev. B*, **44**, 9170 (1991).
- 26) T. Ohzuku, Y. Iwakoshi and K. Sawai, *J. Electrochem. Soc.*, **140**, 240 (1993).
- 27) K.C. Woo, W. A. Kamitakahara, D.P. DiVincenzo, D.S. Robinson, H. Mettway, J.W. Milliken and J.E. Fischer, *Phys. Rev. Letters*, **50**, 182 (1983).
- 28) S.B. DiCenzo, S. Basu and G.K. Wertheim, *Syn. Metals*, **3**, 139 (1981).
- 29) A. Mabuchi, H. Fujimoto, K. Tokumitsu and T. Kasuh, *J. Electrochem. Soc.*, **142**, 3049 (1995).
- 30) A. Mabuchi, K. Tokumitsu, H. Fujimoto and T. Kasuh, *J. Electrochem. Soc.*, **142**, 1041 (1995).
- 31) K. Tatsumi, N. Iwashita, H. Sakaebe, H. Shioyama, S. Higuchi, A. Mabuchi and H. Fujimoto, *J. Electrochem. Soc.*, **142**, 716 (1995).
- 32) T. Zheng, J.N. Reimers and J.R. Dahn, *Phys. Rev. B*, **51**, 734 (1995).
- 33) C.R. Honska and B.E. Warren, *J. Appl. Phys.*, **25**, 2503 (1954).
- 34) T. Kasuh, A. Mabuchi, K. Tokumitsu and H. Fujimoto, 8th Int. Meet. Lithium Batteries, Nagoya, Japan, 1996, Ext. Abstr., p. 97.
- 35) H. Fujimoto, K. Tokumitsu, A. Mabuchi and T. Kasuh, *Carbon*, **32**, 1249 (1994).
- 36) J.R. Dahn, T. Zheng, Y. Liu and J.S. Xue, *Science*, **270**, 590 (1995).
- 37) T. Zheng, W.R. Mckinnon and J.R. Dahn, *J. Electrochem. Soc.*, **143**, 2137 (1996).
- 38) M. Ishikawa, N. Sonobe, H. Chuman and T. Iwasaki, 35th Battery Symp. Japan, Nagoya 1994, Ext. Abstr., p. 49.
- 39) T. Zheng, Q. Zhong and J.R. Dahn, *J. Electrochem. Soc.*, **142**, L211 (1995).
- 40) J.S. Xue and J.R. Dahn, *J. Electrochem. Soc.*, **142**, 3668 (1995).
- 41) A.N. Dey and B.P. Sullivan, *J. Electrochem. Soc.*, **117**, 222 (1970).
- 42) M. Arakawa and J. Yamaki, *J. Electroanal. Chem.*, **219**, 273 (1987).

- 43) Z.X. Shu, R.S. Mcmillan and J. J. Murray, *J. Electrochem. Soc.*, **140**, 922 (1993).
- 44) O. Chusid, Y. Ein-Eli, M. Babai, Y. Carmeli and D. Aurbach, *J. Power Sources*, **43-44**, 47 (1993).
- 45) D. Aurbach and Y. Ein-Eli, *J. Electrochem.*, **142**, 1746 (1995).
- 46) D. Aurbach, Y. Ein-Eli, O. Chusid, M. Babai, Y. Carmeli and H. Yamin, *J. Electrochem. Soc.*, **141**, 603 (1994).
- 47) M. Inaba, Z. Siroma, A. Funabiki and Z. Ogumi, *Langmuir*, **12**, 1535 (1996).
- 48) H.P. Lang, R. Wisendanger, V.-T. Gaise and H.-J. Guntherodt, *Phys. Rev. B*, **45**, 1829 (1992).
- 49) J.O. Besenhard, M. Winter, J. Yang and W. Biberacher, *J. Power Sources*, **54**, 228 (1995).
- 50) N. Imanishi, H. Kashiwagi, T. Ichikawa, Y. Takeda, O. Yamamoto and M. Inagaki, *J. Electrochem. Soc.*, **140**, 315 (1993).
- 51) E. Peled, C. Menachem, D. Bar-Tow and A. Melman, *J. Electrochem. Soc.*, **143**, L4 (1996).
- 52) W. J. Weydanz, B.M. Way, T. van Buuren and J.R. Dahn, *J. Electrochem. Soc.*, **141**, 900 (1994).
- 53) B.M. Way and J.R. Dahn, *J. Electrochem. Soc.*, **141**, 907 (1994).
- 54) J.S. Xue, K. Myrtle and J.R. Dahn, *J. Electrochem. Soc.*, **142**, 2927 (1995).
- 55) M. Morita, T. Hanada, H. Tsutsumi and Y. Matsuda, *J. Electrochem. Soc.*, **139**, 1227 (1992).
- 56) M. Nishijima, Y. Takeda, N. Imanishi, O. Yamamoto and M. Takano, *J. Solid State Chem.*, **113**, 205 (1994).
- 57) M. Nishijima, N. Tadokoro, Y. Takeda, N. Imanishi and O. Yamamoto, *J. Electrochem. Soc.*, **141**, 2966 (1994).
- 58) M. Nishijima, T. Kagohashi, N. Imanishi, Y. Takeda, O. Yamamoto and S. Kondo, *Solid State Ionics*, **83**, 107 (1996).
- 59) M. Nishijima, T. Kagohashi, Y. Takeda, N. Imanishi and O. Yamamoto, 8th Int. Meet. Lithium Batteries, Nagoya, Japan, 1996, Ext. Abstr., p.402.
- 60) T. Shodai, S. Okada, S. Tobishima and J. Yamaki, *Solid State Ionics*, **86-88**, 785 (1996).
- 61) T. Shodai, S. Okada, S. Tobishima and J. Yamaki, 8th Int. Meet. Lithium Batteries, Nagoya, Japan, 1996, Ext. Abstr., p.404.

## 6

## Electrochemical Intercalation of Lithium into Carbonaceous Materials

Martin Winter\* and Jürgen Otto Besenhard\*

## 6.1 Introduction

## 6.1.1 Negative Electrodes in Rechargeable Lithium Batteries

Metallic lithium is a highly attractive material for the negative electrode of high energy density batteries as it combines an extremely negative standard redox potential with a low equivalent weight. Indeed, the commercialization of primary batteries with a metallic lithium negative electrode was very successful (*e.g.*, review papers<sup>1-20</sup>). However, apart from TADIRAN's Li/MnO<sub>2</sub> cell,<sup>21-23</sup> which has only found special applications, the commercial breakthrough of secondary (rechargeable) batteries with a metallic lithium negative electrode failed. This is due to the limited cycle life and safety problems of lithium metal electrodes in liquid electrolytes, *i.e.*, lithium corrosion and passivation, lithium dendrite formation and filament growth (*e.g.*, selected papers<sup>24-41</sup> and book<sup>42</sup>), and above all the safety problems associated with the low melting point of Li (*ca.* 180 °C) in the event of a thermal runaway.<sup>43,44</sup> On the other hand, the lithium insertion materials used for positive electrode exhibited sufficient cyclability and safety. Thus, in the early 1980's Armand, Scrosati and others<sup>45-50</sup> suggested replacing the metallic lithium by a lithium insertion material (see review papers<sup>1,24,25,39,51-58</sup>) having a lower standard redox potential than the positive insertion electrode, resulting in a "Li ion"-<sup>59-64</sup> or "rocking chair"-cell<sup>46-50,57,58</sup> with both negative and positive electrodes capable of reversible lithium insertion.

Various insertion materials have been proposed, including carbons, Li-alloys,<sup>24,25,54,65-70</sup> transition metal oxides and chalcogenides (*e.g.*, MoO<sub>2</sub>,<sup>71,72</sup> WO<sub>2</sub>,<sup>47,48,50,72,73</sup> and TiS<sub>2</sub>,<sup>54,72,74-76</sup>), and some polymers.<sup>77,78</sup> Table 6.1 illustrates the generally lower theoretical capacities of the lithium insertion materials compared with those of metallic lithium. However, the practical (reversible) capacity of a metallic lithium negative electrode in a rechargeable cell differs greatly from the theoretical capacity. Considering the maximum cycling efficiency of lithium of ~99%, one has to employ a manifold excess of Li<sup>1,79-81</sup>) to reach a reasonable cycle number (see Table 6.1, considering a threefold excess of Li). Therefore, the practical gravimetric capacities of some alternative lithium compounds, listed in Table 6.1, are comparable to metallic Li and their volumetric capacities are even higher.

\* Institute of Chemical Technology of Inorganic Materials, Technical University Graz, Stremayrgasse 16/III, A-8010 Graz, Austria

Table 6.1 Selected physical and electrochemical properties of some negative electrode materials for lithium batteries with respect to the fully lithiated host material. The values in parentheses are given with respect to the lithium-free host material (in order to reach a reasonable cycle number, for some host materials only a partial lithiation or delithiation is practical, see *e.g.*, Ref. 1). Li<sup>#</sup> denotes a threefold lithium excess which is necessary for a sufficient cycle life in a rechargeable cell. Reported values are calculated using Refs. 66, 72, 82, 83.

Negative electrode material	Molecular weight	Density (g·cm <sup>-3</sup> )	Theoretical gravimetric capacity (mAh·g <sup>-1</sup> )	Theoretical volumetric capacity (mAh·cm <sup>-3</sup> )
Li (primary)	6.94	0.53	3862	2047
Li <sup>#</sup> (secondary)	6.94	0.53	966	512
LiC <sub>6</sub> (graphite)	79.00 (72.06)	2.24 (2.25)	339 (372)	759 (837)
LiAl	33.92 (26.98)	1.75 (2.70)	790 (993)	1383 (2681)
Li <sub>21</sub> Sn <sub>5</sub>	739.19 (539.19)	2.55 (7.28)	761 (948)	1941 (6901)
LiWO <sub>2</sub>	222.79 (215.85)	11.30 (12.11)	120 (124)	1356 (1502)
LiMoO <sub>2</sub>	134.88 (127.94)	6.06 (6.47)	199 (210)	1206 (1359)
LiTiS <sub>2</sub>	118.94 (112.0)	3.06 (3.22)	225 (239)	689 (770)

Among the negative lithium insertion materials, carbonaceous materials are at present considered to be most promising. Carbonaceous materials exhibit higher capacities and potentials against the positive electrode than the polymers, metal oxides and chalcogenides and show better cycling performance than Li-alloys.<sup>24,25,54,68,70</sup> Furthermore, most carbons are cheap and abundant comparing to the other materials. In addition, lithium insertion into carbon leads to binary phases LiC<sub>n</sub>, which are close to equilibrium, whereas ambient temperature lithium insertion into metal oxide host matrices yields in many cases ternary non-equilibrium phases Li<sub>x</sub>MO<sub>n</sub>, which in the long run may decompose to yield electrochemically inactive phases.

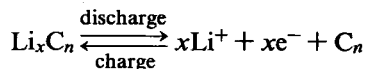
The safety of the negative electrode material is an important point to be kept in mind. The redox potential of lithium-rich LiC<sub>n</sub> compounds is close to that of metallic lithium (see sections 6.2 and 6.3). The chemical reactivity of lithium-rich compounds LiC<sub>n</sub> does not differ much from that of metallic lithium. In particular, the particle size of LiC<sub>n</sub> in batteries is only the order of 10 μm, *i.e.*, the reactive surface area is large. Moreover, recent investigations show that cycling of graphite-based LiC<sub>n</sub> electrodes produces an increase of the surface area by a factor of five.<sup>84</sup> However, the reaction rate of lithium located at the surface of the carbon particle is limited by the rather low (*e.g.*, Refs. 19, 57, 58) transport kinetics of lithium from the interior to the surface of the carbon particle.<sup>43</sup> An even more important reason for using LiC<sub>n</sub> is the fact that the melting point of LiC<sub>n</sub> is very much higher than that of metallic lithium (180 °C), *i.e.*, there is no risk of a hazardous breakdown of the protective solid electrolyte interface layer (see section 6.2.2) which happens at the melting of metallic lithium electrodes.

### 6.1.2 Lithium/Carbon Intercalation Compounds

The reversible insertion of mobile lithium guests into the structure of a solid carbon host is commonly referred to as "intercalation." In general, the designation of an insertion reaction by the term "intercalation" involves the condition that the host matrix units mostly retain their integrity with respect to composition and structure during the intercalation and



deintercalation process (see also Refs. 72, 85–90). Electrochemical intercalation reactions are confined to coupled electron/ion transfer (“mixed conduction”) reactions.<sup>72,86–89,91</sup> For the lithium intercalation into a carbon electrode from an appropriate  $\text{Li}^+$ -containing electrolyte,\* this means that due to the cathodic reduction of the carbon the lithium guest ions penetrate into the carbon host, forming a lithium/carbon intercalation compound. The corresponding negative charges are accepted into the carbon host lattice. The reversibility of the intercalation reaction can be checked by subsequent anodic oxidation of  $\text{LiC}_n$ , *i.e.*, by removal or deintercalation of  $\text{Li}^+$ :



The host/guest charge transfer, although not complete, usually leads to an increased electron density in the conductivity band of carbon and thus to an increase of the in-plane electronic conductivity of several orders of magnitude. Therefore, carbon intercalation compounds are occasionally named “synthetic metals.”

### 6.1.3 Carbonaceous Host Materials

The electrochemical lithium intercalation depends in a complex manner on the crystallinity and morphology of the carbonaceous host material,<sup>24,112–114</sup> which has been investigated by many groups (*e.g.*, review papers<sup>54,67,81,105,113,114</sup>) and Refs. 115–126). For instance, the parent carbonaceous material determines both the potential and current characteristics of the intercalation reaction and also the tendency for the solvation of  $\text{LiC}_n$  compounds and therefore the suitability and compatibility of an electrolyte system (see sections 6.2, 6.3 and 6.4 below).

Carbonaceous materials suitable for lithium intercalation are commercially available in hundreds of types and qualities, *e.g.*, Refs. 81, 114, 127, 128. Several tailored varieties have been synthesized for the purpose of lithium intercalation, *e.g.*, carbons with a remarkable high lithium storage capacity (see section 6.3.2) or tailored carbons prepared by the use of inorganic templates.<sup>129,130</sup> Most carbons capable of lithium intercalation can roughly be separated into graphitic carbons and non-graphitic (disordered) carbons. Some special carbons are treated separately in section 6.4.

Graphitic carbons are carbonaceous materials with a layered structure but with a number of structural defects. From a strictly crystallographic point of view, the term “graphite” is only applicable to carbon materials having a layered lattice structure with a perfect stacking order of graphene layers, either the more prevalent AB (hexagonal graphite, Fig. 6.1) or the less common ABC (rhombohedral graphite). Due to the small energy required for the transformation of an AB- into an ABC-stacking (and *vice versa*), perfectly stacked graphite crystals are practically not available. Therefore, the term “graphite” is commonly used regardless of the stacking order.

As most carbonaceous materials deviate more or less from the graphite structure, even materials which consist of aggregates of graphite crystallites are named graphites, *e.g.*, the terms natural graphite, artificial or synthetic graphite and pyrolytic graphite are commonly

\* The electrolytes comprise (i) liquid aprotic organic electrolytes (*e.g.*, reviews<sup>39,92,93</sup>), (ii) but also polymeric electrolytes, *e.g.*, Refs. 39, 67, 78, 94–105, solid electrolytes<sup>106,107</sup>) and even (iii) liquid inorganic electrolytes<sup>108,109</sup>) and molten salts.<sup>110,111</sup>

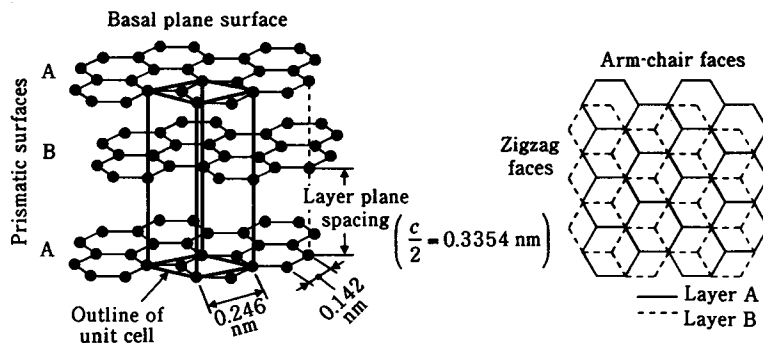


Fig. 6.1 Left: schematic drawing of the crystal structure of hexagonal graphite showing AB-layer stacking sequence and unit cell. Right: view perpendicular to the basal plane of hexagonal graphite.

used, although the materials are polycrystalline.<sup>131)</sup> The crystallites may vary considerably in size. In some carbons, the aggregates are large and relatively free of defects, *e.g.*, in highly oriented pyrolytic graphite (HOPG). In addition to graphitic crystallites, some carbons may also include crystallites which contain carbon layers or packages of stacked carbon layers characterized by significant misfits and misorientation angles of the stacked segments to each other (= turbostratic orientation or turbostratic disorder<sup>132)</sup>), leading to higher average layer plane spacing.<sup>131,133)</sup>

When the turbostatically disordered structure becomes more distinct and dominates among the crystallites, the carbonaceous material is no longer graphitic and can be considered as a non-graphitic carbon. In general, there is no strict boundary between graphitic and non-graphitic carbonaceous materials for carbon types that contain characteristic graphitic and non-graphitic structure units. Thus, the differentiation is in many cases somehow arbitrary and only made for the sake of convenience.

Non-graphitic carbonaceous materials consist of carbon atoms with most of them arranged in a planar hexagonal network but without the crystallographic order in the *c*-direction of the graphite structure. The structure of those carbons is characterized by amorphous areas embedding and crosslinking more graphitic ones<sup>134–136)</sup> (*e.g.*, Fig. 6.2). The respective area number and their size vary, depending on the precursor material and the manufacturing temperature.

Non-graphitic carbons are mostly prepared by pyrolysis of organic polymer or hydrocarbon precursors at temperatures below  $\sim 1500^\circ\text{C}$ . Further heating of most non-graphitic (disordered) carbons to temperatures between  $\sim 1500$ – $\sim 3000^\circ\text{C}$  allows division into two distinctly different carbon types. Graphitizing carbons develop the graphite structure continuously during the heating process since crosslinking between the carbon layers is weak and the layers therefore mobile enough to form graphite-like crystallites. The ability for graphitization is also dependent on the preordering of the respective material. For example, the graphitization ability is higher (i) if the precursor material comprises highly condensed aromatic hydrocarbons, which can be considered to have a graphene-like structure and (ii) if neighboring graphene layers or graphitic crystallites are suitably oriented to each other. Non-graphitizing carbons exhibit no true development of

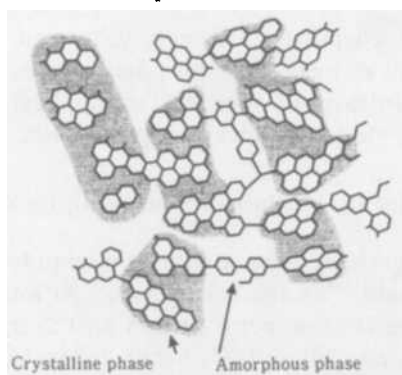


Fig. 6.2 Sketch of a non-graphitic (disordered) carbonaceous material ("linear graphite hybrid") for the negative electrode. Modified and redrawn from Ref. 136).

the graphite structure even at high temperatures (2500–3000 °C) since the carbon layers are immobilized by crosslinking.

The mobility of the carbon structure units, which determines the degree of microstructural ordering of the carbonaceous material, is dependent on the state of aggregation of the intermediate phase of the material during pyrolysis, which can be solid, liquid or gaseous.<sup>137)</sup> Therefore, non-graphitizing carbons are usually products of the solid-phase pyrolysis whereas graphitizing carbons are commonly produced by liquid- or gas-phase pyrolysis. Examples of products of the solid-phase pyrolysis are carbonaceous materials like chars and glassy (vitreous) carbon, which are produced by pyrolysis of crosslinked polymers. Because of the small crystal size and high structural disorder of the polymers, the ability of these carbons to graphitize is low. Pyrolysis of thermally stabilized polyacrylonitrile or pitch, which are the precursors for carbon fibers, yields also solid intermediate phases, but stretching of the fibrous material during the manufacturing process produces an ordered microstructure.<sup>137)</sup> The synthesis of petroleum coke, which is the most important raw material for the manufacture of carbons and graphites, is an example of liquid-phase pyrolysis. Petroleum coke is produced by the pyrolysis of petroleum pitch, which is the residue from the distillation of petroleum fractions. Cokes are also products of pyrolyzed coal-tar pitch and pyrolyzed aromatic hydrocarbons at 300–500 °C. Carbon black, pyrocarbon and carbon films are examples of gas-phase pyrolysis products, *i.e.*, products of thermal cracking of gaseous hydrocarbon compounds which are deposited as carbon on a substrate.<sup>131,137)</sup> For more details on pyrolysis, carbonization and graphitization processes, see Refs. 131, 134, 137, 138.

It is also common to divide the non-graphitic carbons into "soft" and "hard" carbons according to their hardness. Non-graphitizing carbons are hard carbons with a large fine-structure porosity (nanoporosity). By contrast, graphitizing carbons are softer and less porous.<sup>134)</sup>

## 6.2 Graphitic Carbons as Host for Lithium Intercalation

The intercalation into graphitic carbons yielding graphite intercalation compounds (GIC) has been reviewed by several authors<sup>91,139–153)</sup> since graphites have a long tradition as

host materials in solid state chemistry. Seventy years ago, in 1926, Fredenhagen and Cadenbach<sup>154)</sup> synthesized alkali metal GICs of potassium, rubidium and caesium and as early as 1938, Rüdorff and Hofmann<sup>155)</sup> suggested the application of graphite intercalation compounds for rechargeable electrochemical energy sources.

### 6.2.1 Lithium/Graphite Intercalation Compounds

The synthesis of lithium-graphite intercalation compounds ( $\text{Li}_x\text{C}_n$ ) is well known since the pioneering work of Hérolde<sup>156)</sup> in the mid 1950's. At ambient pressure a maximum lithium acceptance of 1 Li guest atom per 6 carbon host atoms can be reached in highly crystalline graphitic carbon, *i.e.*, " $n$ " in  $\text{LiC}_n=6$  or " $x$ " in  $\text{Li}_x\text{C}_6=1$ . The intercalation reaction proceeds *via* the prismatic surfaces (arm-chair faces and zigzag faces) of the host carbon, intercalation through the basal plane can occur only at defect sites.<sup>157)</sup> During the intercalation reaction the stacking order of the graphene layers in graphite shifts to AA, *i.e.*, the intercalated Li guests in  $\text{LiC}_6$  are held between two carbon layers directly facing each other (see Fig. 6.3a). Due to intercalation of lithium the interlayer distance between the graphene layers is moderately increased (10.3% calculated for  $\text{LiC}_6$ ).<sup>83,158)</sup> The lithium intercalate interlayer stacking order is  $\alpha\alpha$  leading to a  $\text{Li}-\text{C}_6-\text{Li}-\text{C}_6-\text{Li}$  chain along the  $c$ -axis.<sup>150,159)</sup> Strictly speaking, the term "topotactic intercalation," which is commonly applied to an intercalation reaction, in which the lattice dimension of the host varies only in one direction, is not applicable to the formation of  $\text{LiC}_6$ , as the lattice dimensions vary

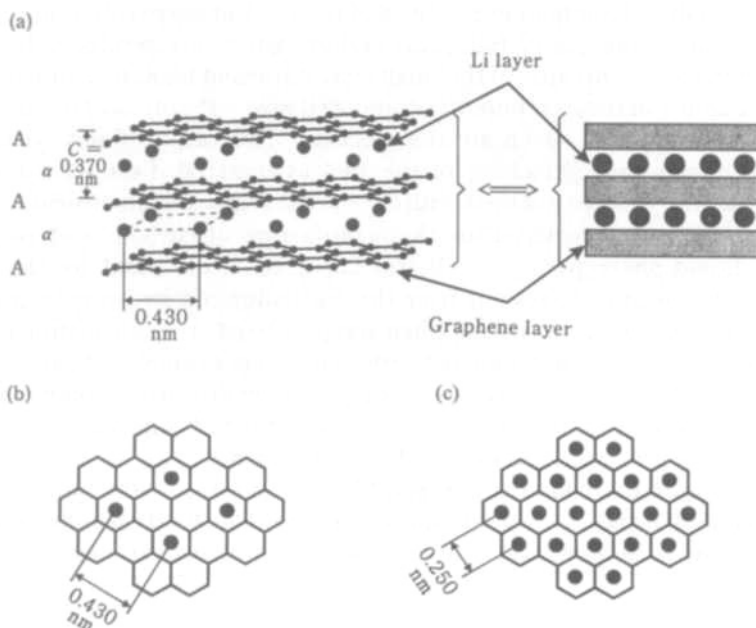


Fig. 6.3 Structure of  $\text{LiC}_6$ . (a) Left: schematic showing graphite AA-layer stacking and lithium intercalate  $\alpha\alpha$  interlayer ordering. Right: showing simplified schematic representation.<sup>164)</sup> (b) In-layer ordering model of  $\text{LiC}_6$ . (c) In-layer ordering model of  $\text{LiC}_2$ .

parallel and perpendicular to the basal planes.

In  $\text{LiC}_6$  the lithium is distributed in-plane in such a manner that it avoids the occupation of nearest neighbor sites (Fig. 6.3b). A higher lithium in-plane density by occupation of nearest neighbor sites is obtained in the phases  $\text{LiC}_2$ – $\text{LiC}_4$ , *i.e.*, “ $x$ ” in  $\text{Li}_x\text{C}_6 = 2$ –3, which are prepared chemically from graphitic carbon under high pressure ( $\sim 60$  kbar) and temperature ( $\sim 300^\circ\text{C}$ ) conditions.<sup>105,160–163</sup> The close Li–Li distance in  $\text{LiC}_2$  (see Fig. 6.3c) results in a higher chemical activity of lithium than that of lithium metal (Li–Li bond length ( $20^\circ\text{C}$ ) =  $0.304\text{ nm}^{82}$ ). Under ambient conditions  $\text{LiC}_2$  decomposes slowly *via* different metastable intermediate Li/C phases to  $\text{LiC}_6$  and metallic lithium.<sup>105,162</sup> A preliminary study of the electrochemical behavior of  $\text{LiC}_2$  can be found in Ref. 105.

A general feature of intercalation into graphite is the formation of a periodic array of unoccupied layer gaps when a low concentration of guest species is present (= stage formation).<sup>155,156,165,166</sup> The graphite intercalation process can be described by the stage index “ $s$ ”, which is equal to the number of graphene layers between two guest layers. Staging is a thermodynamic phenomenon caused by the considerable quantity of energy required to “open” the van der Waals gap between two graphene layers (*e.g.*, Refs. 68). The repulsive coulombic interactions between the guests, which would bring about a more uniform guest distribution, are less effective.

The staging phenomenon—and more generally, the degree of intercalation—can be easily monitored and controlled by the electrochemical reduction of carbons in  $\text{Li}^+$ -containing electrolytes. Two basic methods have proved to be particularly useful, galvanostatic (controlled constant current) and potentiodynamic (controlled continuously changing potential = linear sweep voltammetry) intercalations.<sup>91</sup> Fig. 6.4 (left-hand side) shows a

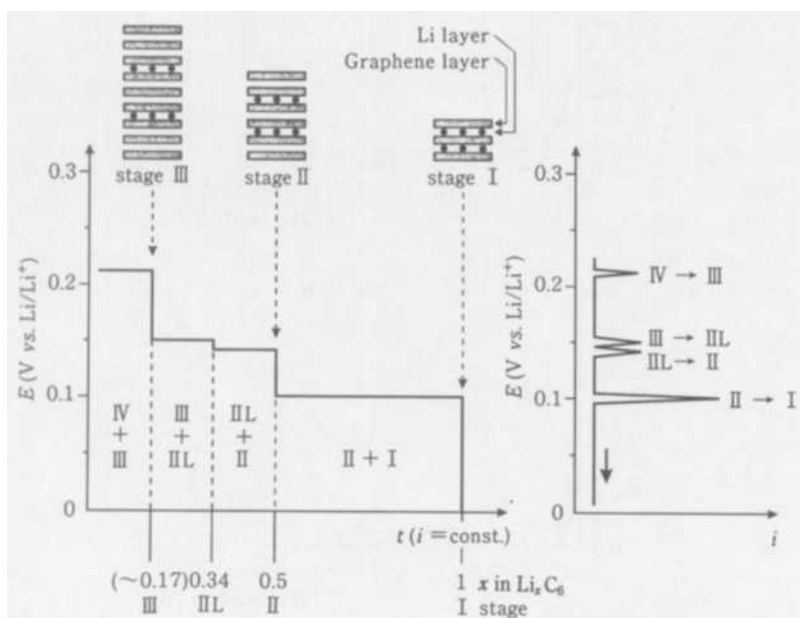


Fig. 6.4 Electrochemical lithium intercalation with stage formation. Left: schematic constant current  $E/x$  in  $\text{Li}_x\text{C}_6$  curve. Right: voltammetric  $i/E$  curve ( $\Delta E/\Delta t = \text{constant}$ ). Modified and redrawn from Ref. 91.

schematic potential/composition curve for the galvanostatic reduction of graphite to  $\text{Li}_x\text{C}_6$ . The distinguishable plateau on the potential curve indicate two-phase regions in the lithium/graphite phase diagram.<sup>167,168</sup> Under potentiodynamic control (Fig. 6.4, right-hand side), current peaks indicate the two-phase regions. Assuming that the current yield is 100%, one can analyze phases and determine the stoichiometric factor “ $x$ ” for the individual stages  $\text{Li}_x\text{C}_6$ . Apart from stage  $s=\text{I}$ , four other binary phases  $\text{Li}_x\text{C}_6$  corresponding to the stages  $s=\text{IV}$ ,  $\text{III}$ ,  $\text{IIL}$  and  $\text{II}$  (which can also be obtained by chemical synthesis<sup>112,165–167,169,170</sup>) were characterized by these methods. X-ray<sup>83,167–172</sup> and Raman measurements<sup>173</sup> confirm the results. The occurrence of two second stages  $s=\text{II}$  ( $x$  in  $\text{Li}_x\text{C}_6=0.5$ ) and  $s=\text{IIL}$  ( $x$  in  $\text{Li}_x\text{C}_6=0.33$ ) is due to different lithium packing densities. The reversibility of the intercalation reaction (= charge recovery) can be inspected by the reversal of current or direction of potential change (= cyclic voltammetry), resulting in deintercalation of  $\text{Li}^+$ .

Figure 6.5 illustrates experimental potential/composition curves for the  $\text{Li}^+$ -intercalation in graphite. A distinct border between the two-phase regions cannot be observed because (i) the packing density varies within certain limits, *i.e.*, a phase width exists and (ii) various types of overpotentials (*e.g.*, textbooks on electrochemistry<sup>174–176</sup>) lead to peak broadening during voltammetry or to plateau sloping in galvanostatic measurements. The charge

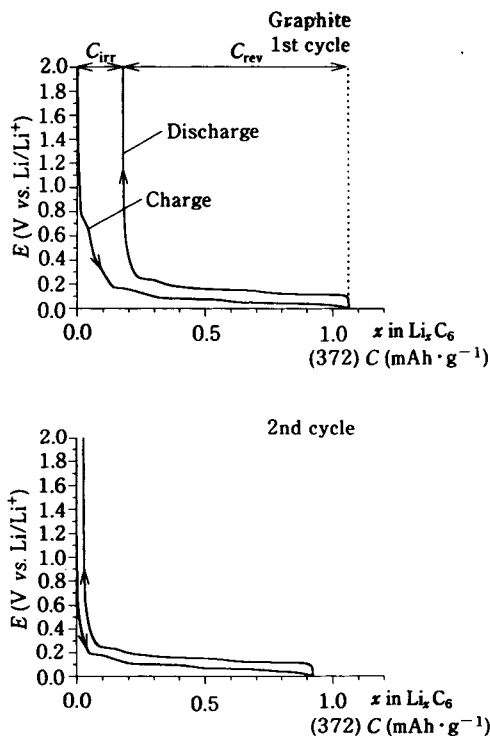


Fig. 6.5 Constant current charge/discharge of graphite (TIMREX® KS 44) using  $\text{LiN}(\text{SO}_2\text{CF}_3)_2$  in ethylene carbonate/dimethyl carbonate as electrolyte.<sup>164</sup>  $C_{\text{irr}}$  denotes the irreversible capacity,  $C_{\text{rev}}$  the reversible capacity.

consumed in the first cycle usually exceeds the theoretical capacity of  $372 \text{ mAh} \cdot \text{g}^{-1}$  for first stage  $\text{LiC}_6$  (Fig. 6.5 and Table 6.1). Subsequent deintercalation exhibits a charge recovery of only  $\sim 80\%$ . In the second cycle the charge recovery is close to  $100\%$ . This is also true for the later cycles.

The extra charge in the first cycle is generally ascribed to corrosion reactions of lithium/carbon intercalation compounds with electrolyte components (Fong *et al.*<sup>177</sup>) and *e.g.*, Refs. 81, 178, 179)\*. Like metallic lithium, lithium-carbon intercalation compounds are thermodynamically unstable in battery electrolytes so their surfaces must be protected by SEI- (solid electrolyte interface-) films. The composition and properties of the films on carbon electrodes have been subject to many investigations (*e.g.*, Refs. 189–194). In contrast to the spontaneous film formation on metallic Li upon contact with electrolyte, film formation on  $\text{LiC}_n$  surfaces proceeds as a charge-consuming side reaction in the first few  $\text{Li}^+$ -intercalation/deintercalation cycles. Because of the irreversible consumption of material (lithium and electrolyte), the corresponding charge loss is called “irreversible capacity” (by contrast, the reversible lithium intercalation is called “reversible capacity”). Even after film formation, the self-discharge of  $\text{LiC}_n$  electrodes associated with their reactivity with the organic electrolyte is considerable (see section 6.2.2). Since the positive electrode is the only lithium source in the Li ion cell, these losses are detrimental to the capacity of the whole cell.<sup>24,25,68</sup>

### 6.2.2 Effects of Electrolyte Composition

The irreversible losses are strongly affected by the composition of the electrolyte, in particular by their tendency for co-intercalation in the graphite matrix.<sup>195</sup> In 1970, Dey and Sullivan<sup>196</sup> reported the electrochemical decomposition of propylene carbonate (PC) on graphite at potentials positive to lithium deposition ( $\sim 0.8 \text{ V}$  vs.  $\text{Li}/\text{Li}^+$ ). In 1974, Besenhard and Fritz,<sup>197</sup> who investigated the electrochemical reduction of graphitic carbons in aprotic organic electrolytes in detail, found that the reaction at these potentials is a partly reversible electrochemical intercalation of solvated  $\text{Li}^+(\text{Li}^+(\text{solv})_n)$  into the carbon host. Since then, it has become well known that the intercalation of  $\text{Li}^+$  (and other alkali metal ions) from organic donor solvent electrolytes into fairly crystalline graphitic carbons quite often leads to solvated (ternary) graphite intercalation compounds (*e.g.*,  $\text{Li}(\text{solv})_n\text{C}_n$ , Fig. 6.6).<sup>24,25,68,91,198–204</sup> The solvated intercalation is associated with a drastic swelling of the graphite matrix (typically  $\sim 150\%$ ), usually leading to a deterioration (exfoliation) of the graphite matrix and drastically decreased available capacities. The solvated compounds are thermodynamically favored over the binary compounds  $\text{LiC}_n/\text{Li}_x\text{C}_6$  (Fig. 6.6), *i.e.*, the electrochemical potentials are more positive than those of the corresponding binary GICs, as long as the content of lithium is very low ( $x$  in  $\text{Li}_x\text{C}_6 \leq \sim 0.33$ ). At this state of  $\text{Li}^+$  uptake, coulombic interaction between the lithium guest layer ( $\text{Li}^+$ ) and the balancing negative charge distributed over the graphene layers ( $\text{C}_n^-$ ) is weak, resulting in high mobility of the intercalants and therefore incommensurable

\* The contribution of other effects to the additional charge is discussed by many authors,<sup>58,180–188</sup> *e.g.*, the irreversible lithium incorporation in the carbon matrix (=formation of residue compounds<sup>181–184</sup>), the irreversible reduction of impurities on the carbon surface, or the irreversible reduction of “surface group”<sup>185–188</sup> like “surface oxides” at the prismatic surfaces of the carbon (it should be noted, that carbonaceous materials, *e.g.*, polycrystalline carbons, also have “interior” prismatic surfaces that may contain surface groups).

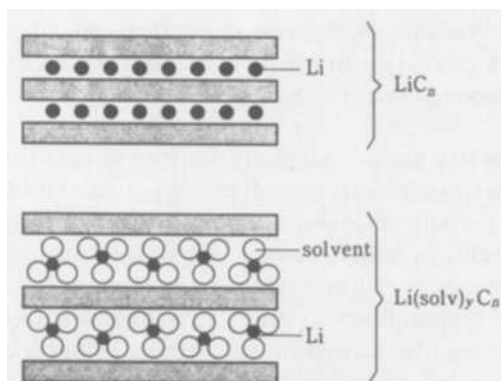


Fig. 6.6 Schematic drawing of binary ( $\text{LiC}_n$ ) and ternary ( $\text{Li(solv)}_y\text{C}_n$ ) lithium-GICs.  
[Reproduced with permission by M. Winter *et al.*, *GDCh-Monographie*, 3, 438, 1996]

guest distribution\*. Moreover, space to accommodate large solvent molecules is still available.<sup>24,68,205,206)</sup>

Solvated alkali metal GICs are always thermodynamically unstable with respect to reduction of the intercalated polar solvents. The solvent reduction is mostly kinetically controlled. It is slow *e.g.*, in dimethyl sulfoxide (DMSO), where even staging of solvated GICs can be observed,<sup>199,207)</sup> but very much faster *e.g.*, in PC,<sup>197,208–213)</sup> where the electrochemical intercalation and fast subsequent decomposition of the intercalated  $\text{Li}^+(\text{solv})_y$  can be misunderstood as simple electrolyte decomposition. By contrast, alkali metal transfer in hydrocarbon solution yields binary, *i.e.*, unsolvated, alkali metal GICs.<sup>204,205)</sup>

The solvation of intercalated lithium in carbon electrodes and the decomposition of solvates with subsequent film formation are serious problems which contribute to a large extent to the self-discharge of  $\text{LiC}_n$  electrodes in organic electrolytes. Particularly in the first charge/discharge cycles when the film formation on  $\text{LiC}_n$  electrodes is insufficient, the tendency for solvent co-intercalation and subsequent lithium corrosion is high. However, recent measurements of the self-discharge of sufficiently filmed and lithium intercalated carbon electrodes show a linear lithium loss with storage time during  $\sim 40$  d of storage. Thereafter, the reaction rate decreases, but self-discharge still exists after  $\sim 170$  d.<sup>214,215)</sup> Moreover, the film formation on the carbon electrode, which is associated with the self-discharge of  $\text{LiC}_n$ , causes an extra “film” resistance for the lithium ion transfer, which—particularly at higher cycle numbers when the films have become thicker—decreases the rate capability of the electrode.

As parts of the self-discharge capacity at higher cycle numbers are reversible, a generally satisfactory explanation for these self-discharge processes is missing. The breaking of the films due to expansion/contraction during lithium intercalation/deintercalation might be responsible for the self-discharge phenomenon, see also Refs. 216. Other authors assume that the film components are soluble and can migrate between the negative and positive electrodes.<sup>217)</sup>

\* The guest distribution among the interlayer spaces can lead to either commensurable or incommensurable structures, *e.g.*, Refs. 91, 139. Only in a commensurable structure, which can be found *e.g.*, in the binary phase  $\text{LiC}_6$ , the guests are organized according to the “raster” of the graphene layers.



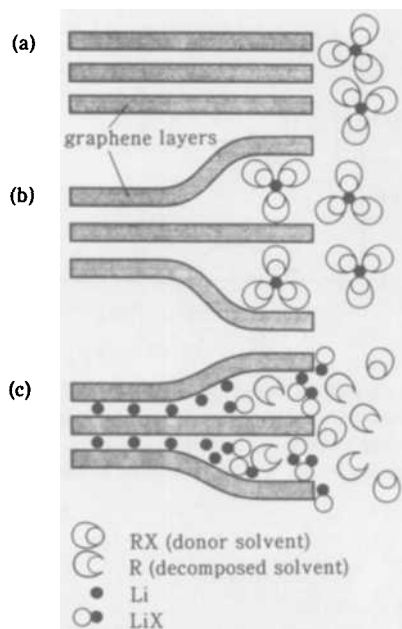


Fig. 6.7 Schematic model of the film forming mechanism on graphite: (a) before reaction, (b) formation of ternary solvated lithium/graphite intercalation compound  $\text{Li(solv)}_y\text{C}_n$ , (c) film formation due to decomposition of  $\text{Li(solv)}_y\text{C}_n$ .<sup>195)</sup>  
[Reproduced with permission by J.O. Besenhard *et al.*, *J. Power Sources*, **54**, 228, 1995]

Since 1990, electrolytes based on ethylene carbonate (EC) have been used to retard the formation of ternary graphite intercalation compounds  $\text{Li(solv)}_y\text{C}_n$ .<sup>177)</sup> As the viscosity of pure EC electrolytes is too high for battery applications, mixtures of EC with low viscosity solvents such as ethers, *e.g.*, 1,2-dimethoxyethane (DME)<sup>81,108,114,183,218)</sup> and 1,2-diethoxyethane (DEE)<sup>219–221)</sup> or organic carbonates, *e.g.*, dimethyl carbonate (DMC)<sup>220–225)</sup> and diethyl carbonate (DEC)<sup>191,221,224–226)</sup> are widely used. A comparison of the performance of electrolyte blends can be found in Refs. 227–229.

Although binary lithium/graphite compounds are eventually formed in EC-based electrolytes, solvated lithium/graphite compounds participate in the intercalation reaction. Film formation due to electrolyte decomposition at potentials of  $\sim 0.8$  V *vs.*  $\text{Li/Li}^+$  (Fig. 6.5a) during the first reduction of the host material is not merely a simple surface reaction but a rather complex three-dimensional process. Reactions leading to irreversible capacity losses take part also on surfaces between the graphene layers *via* a secondary (chemical) reduction of electrochemically formed solvated GICs and this leads to the formation of a film penetrating into the bulk of the graphite host (Fig. 6.7)<sup>108)</sup> and Refs. 194, 230 and 231.

The exceptional compatibility of the solvent EC with graphite-based  $\text{LiC}_n$  is related to the properties of the formed protective films,<sup>108)</sup> which prevent excessive solvent co-intercalation in the early stages of the first reduction of the host.<sup>108,192,195)\*</sup> Many research

\* The tendency for solvent co-intercalation is also dependent on the crystallinity and morphology of the parent carbonaceous material (see section 6.3.1).

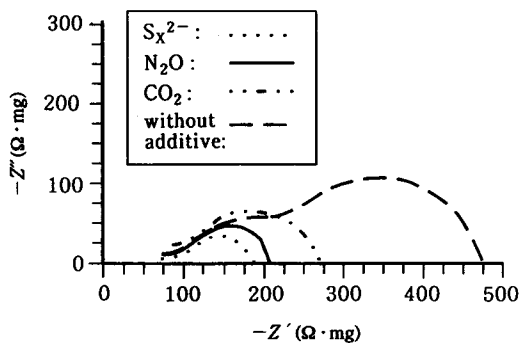


Fig. 6.8 Schematic impedance spectra of  $\text{LiC}_8$ -electrodes (highly oriented turbostratic mesophase pitch carbon fiber P 100, FMI Composites-Union Carbide) during the first constant current charge using  $\text{LiClO}_4$  in PC (in absence and presence of various electrolyte additives) as electrolyte.<sup>195)</sup>  
[Reproduced with permission by M. Winter *et al.*, *GDCh-Monographie*, 3, 438, 1996]

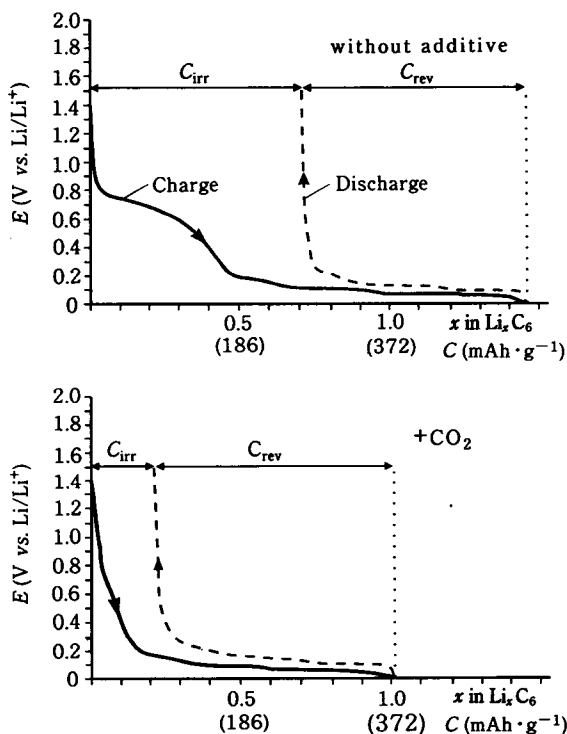


Fig. 6.9 Constant current charge/discharge of graphite (TIMREX® KS 44) using  $\text{LiN}(\text{SO}_2\text{CF}_3)_2$  in DMC (in absence and presence of  $\text{CO}_2$ ) as electrolyte.<sup>195)</sup>  $C_{\text{irr}}$  denotes the irreversible capacity,  $C_{\text{rev}}$  the reversible capacity.

[Reproduced with permission by M. Winter *et al.*, *GDCh-Monographie*, 3, 438, 1996]

activities focus on the improvement of these films by the proper choice of new electrolyte components (*e.g.*, Refs. 232–234).<sup>\*</sup> Some progress has been made with inorganic additives such as  $\text{CO}_2$ ,<sup>189,191,192,242–245</sup>  $\text{N}_2\text{O}$ <sup>246</sup> and  $\text{S}_x^{2-}$ <sup>246,247</sup> to promote the formation of more compact and presumably thinner inorganic films (Fig. 6.8) that are more selective for unsolvated  $\text{Li}^+$ -cations than organic film components which are supposed to be penetrated more easily—by also organic—solvent molecules. This is consistent with the potential plateau at  $\sim 0.8$  V vs.  $\text{Li}/\text{Li}^+$ , which indicates solvent co-intercalation, being suppressed upon addition of the inorganic additive  $\text{CO}_2$  to the base electrolyte (Fig. 6.9). The protective effect of inorganic solid electrolyte membranes is further demonstrated by Fig. 6.10, which displays the successful operation of lithium/carbon negative electrodes in inorganic electrolytes.<sup>108)</sup>

The tendency for solvent co-intercalation is also dependent on the size of the  $\text{Li}^+$ -solvating solvents. Crown ethers<sup>81,211–213,218</sup> and other bulky electrolyte additives<sup>218)</sup>

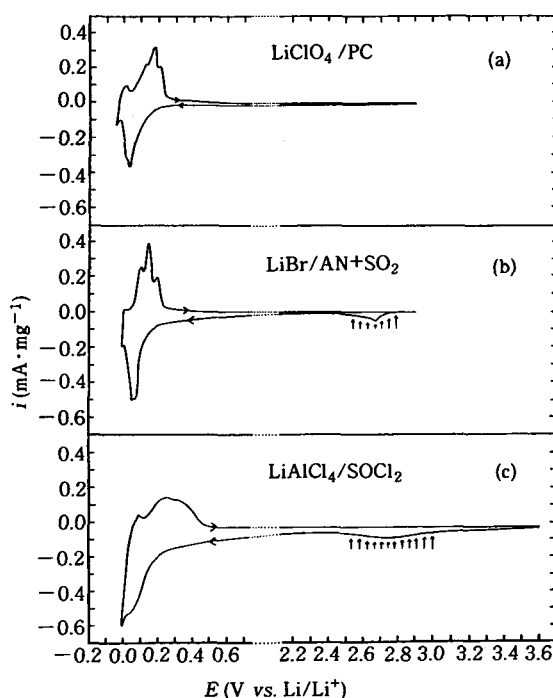


Fig. 6.10 Voltammograms of carbon fiber electrodes (highly oriented turbostratic mesophase pitch carbon fiber P 100, FMI Composites-Union Carbide) in organic (PC) and inorganic solvent-based electrolytes ( $\text{SO}_2/\text{AN}$ ,  $\text{SOCl}_2$ ). AN = acetonitrile.<sup>108)</sup>  
(Reproduced with permission by J.O. Besenhard *et al.*, *J. Power Sources*, **54**, 228, 1995)

\* Since the film formation on the surfaces of  $\text{LiC}_n$  always leads to irreversible capacity losses, the use of pretreated carbonaceous materials is being evaluated as a means of overcoming this problem. The main methods under investigation are as follows: (i) electrochemical<sup>108,189,235)</sup> and chemical<sup>123,211,236,237)</sup> “pre-filming” prior to the actual energy storage application, (ii) “surface-conditioning” by low temperature heat-treatment or mild burn-up<sup>185–188,238–240)</sup> and (iii) coating with  $\text{Li}^+$  permeable solids.<sup>241)</sup>

coordinate  $\text{Li}^+$ -ions in solution in such a way that solvent co-intercalation is suppressed.<sup>108,192</sup> The electrochemical synthesis of binary  $\text{Li}_x\text{C}_6$  was also reported for the reduction of graphite in electrolytes containing higher molecular polymers as the electrolyte solvent, although the noted stage formation proceeds in a potential region where usually solvated Li-GICs are formed<sup>67,103,105,248</sup> (for comparison, see Refs. 104).

### 6.3 Non-graphitic Carbons as Lithium Intercalation Hosts

From the point of view of electrochemical lithium intercalation, non-graphitic carbons can be classified with respect to their capability for (reversible) lithium storage. “High capacity” carbons can store more lithium per mass unit than graphite, *i.e.*, more than one lithium per six carbons. In contrast, carbonaceous materials that incorporate a considerably lower lithium amount than graphite are called “low capacity” carbons.

#### 6.3.1 “Low Capacity” Non-graphitic Carbons

For graphitizing (soft) carbons like turbostratic carbons<sup>114,117,178,249–251</sup> and more disordered carbons like cokes<sup>114,178,252–255</sup> and carbon blacks,<sup>236,255,256</sup> the maximum stoichiometric factor “ $x$ ” in  $\text{Li}_x\text{C}_6$  is typically  $\sim 0.5$ – $\sim 0.8$  (“ $x$ ” in  $\text{Li}_x\text{C}_6 = 1$  for graphite). In case of turbostratic carbons, this is partly due to the lower number of available lithium sites in “wrinkled” and “buckled” structure segments.<sup>24,25</sup> In addition, crosslinking of carbon sheets in turbostratically disordered carbons hampers the shift to AA-stacking, which is necessary for the accommodation of a higher lithium amount into graphitic sites.<sup>249–251</sup> Turbostratic carbons and cokes have found considerable interest as lithium host material because the crosslinking of the graphene layers mechanically suppresses the excessive formation of  $\text{Li}(\text{solv})_x\text{C}_n$ .<sup>68,81,108,177</sup>\* The use of composite carbons comprising a “core” of graphite and a protective “shell” of disordered carbon successively retards solvent co-intercalation in graphite.<sup>257,258</sup>

Figure 6.11 illustrates the first  $\text{Li}^+$ -intercalation/deintercalation cycle of a coke electrode. The voltage profile differs greatly from that of graphite, as the reversible intercalation of Li begins at *ca.* 1.5 V vs.  $\text{Li}/\text{Li}^+$  and the potential curve slopes without distinguishable plateau (see also section 6.4). This behavior is consequence of the disordered structure providing electronically and geometrically non-equivalent sites, whereas for a particular intercalation stage in highly crystalline graphite the sites are equivalent.<sup>81,108</sup>

#### 6.3.2 “High Capacity” Non-graphitic Carbons

Presently, much enthusiasm and effort is concentrated on the development of high capacity carbonaceous materials that are synthesized at “low” temperatures ( $\sim 500$ – $\sim 900^\circ\text{C}$ ) and show reversible capacities between *ca.* 200–2000  $\text{mAh}\cdot\text{g}^{-1}$  (“ $x$ ” in  $\text{Li}_x\text{C}_6 = \sim 0.5$ – $\sim 5$ ), depending on the heat-treatment temperature, organic precursor material and electrolyte. Such materials have been known since the late 1980’s, when several Japanese groups synthesized non-graphitic carbons with capacities of up to  $\sim 500 \text{ mAh}\cdot\text{g}^{-1}$ .<sup>259–261</sup> In some cases the capacity was dependent on the surface area, which was more than 100 times larger than that of graphite.<sup>259,260</sup>

---

\* The first Li-ion cell commercialized by Sony used these kinds of carbons.<sup>59,63,64</sup>

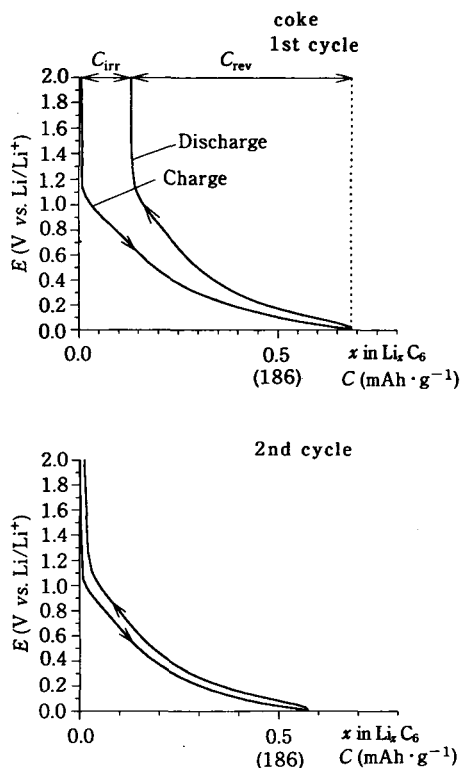


Fig. 6.11 Constant current charge/discharge of coke (Conoco) using  $\text{LiN}(\text{SO}_2\text{CF}_3)_2$  in EC/DMC as electrolyte.<sup>164</sup>  $C_{\text{irr}}$  denotes the irreversible capacity,  $C_{\text{rev}}$  the reversible capacity.

To rationalize the high “extra” lithium capacity, a variety of still controversial models and explanations have been suggested. The variety of employed organic precursors may account for the discrepancies in the models of the various investigators. Some models are of course more probable than others. This is discussed in Refs. 120, 122, 266, 267. Some examples are as follows: Sawai *et al.*<sup>121)</sup> assume that high capacity carbons offer a larger volume for lithium accommodation, so that only the gravimetric capacity is higher than that of graphite. Yazami *et al.*<sup>67,262–265)</sup> propose the formation of lithium multilayers on the graphene sheets. Peled *et al.*<sup>238,239)</sup> believe that the extra charge they reached by mild oxidation of graphite is attributed to accommodation of lithium in “zigzag and armchair faces between two adjacent crystallites and in the vicinity of defects and impurities.” Sato *et al.*<sup>268,269)</sup> suggest that lithium occupies nearest neighbor sites in intercalated carbons (Fig. 6.12a). Mabuchi *et al.*<sup>113,237,270,271,272)</sup> propose that extra lithium can be accommodated into nanoscopic cavities (Fig. 6.12b). Yata *et al.*<sup>273)</sup> discuss the principal possibility of the formation of  $\text{LiC}_2$  in carbons with high interlayer spacing of  $\sim 0.400$  nm (for comparison: graphite 0.335 nm, see Fig. 6.1) for their so-called “Polyacenic Semiconductor” material.<sup>273–276)</sup> Matsumura *et al.*<sup>277–280)</sup> assume that small particle-size carbons can store considerable amounts of lithium on graphite edges and surfaces in addition to the lithium

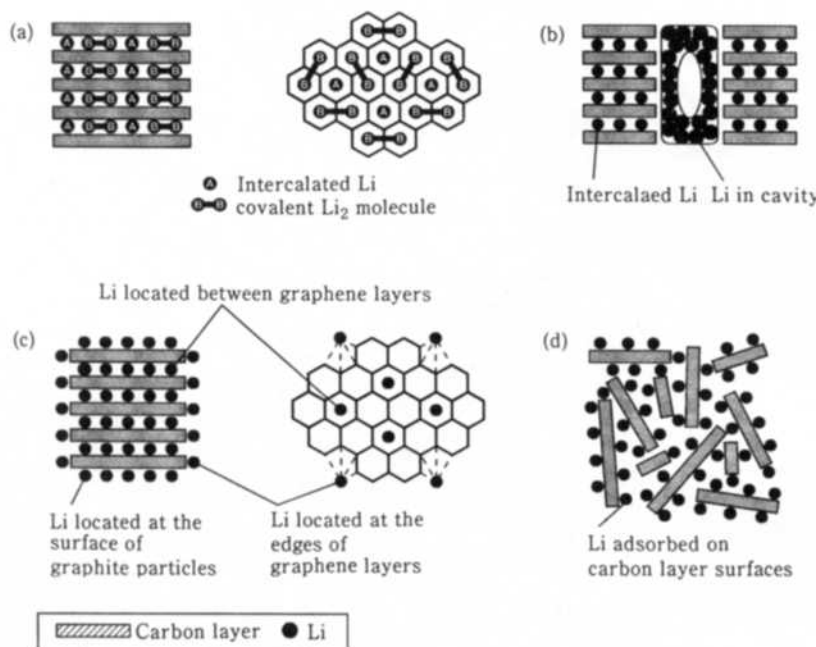


Fig. 6.12 Schematic drawing of some mechanisms for reversible lithium storage in high capacity carbonaceous materials as proposed (a) in Ref. 268, (b) in Ref. 113, (c) in Ref. 280 and (d) in Ref. 283.

which is located between the graphene layers (Fig. 6.12c). The existence of different “Li-doping sites” and cavities is discussed also by Mori *et al.*<sup>281,282</sup>

Dahn *et al.*<sup>120,122,284,291,294</sup> analyzed the high capacity carbons in detail. Both graphitizing (soft) and non-graphitizing (hard) carbons heated below approximately  $\sim 800^\circ\text{C}$  give large capacities (“ $x$ ” in  $\text{Li}_x\text{C}_6$  can approach 5), which exhibit hysteresis, *i.e.*, lithium insertion occurs near 0 V vs.  $\text{Li}/\text{Li}^+$  and removal at potentials near 1 V vs.  $\text{Li}/\text{Li}^+$  (*e.g.*, Fig. 6.13).<sup>120,122,273,291,294</sup> The “hysteresis capacity” is proportional to the hydrogen content of the carbon and it is believed that lithium is somehow bound near the hydrogen.\*

Hydrogen is removed with increasing temperature. The achieved capacities after removal of hydrogen depend on the resulting structure of the carbonaceous material, *i.e.*, whether it is a graphitizing or non-graphitizing carbon (Dahn *et al.*<sup>122,294</sup>) and *e.g.*, Refs. 117, 237, 270, 285–290).

At temperature  $> \sim 1000^\circ\text{C}$  the graphitizing (soft) carbons develop a structure like a “low-capacity” carbon.<sup>120,295</sup> Correspondingly relatively low capacities (“ $x$ ” in  $\text{Li}_x\text{C}_6 > \sim 0.5$ ) are observed. When graphitization proceeds at higher temperatures, the fraction of stacked layers with graphitic order increases, as does the capacity. For example, after heating to  $2800\text{--}3000^\circ\text{C}$ , a capacity corresponding to “ $x$ ” in  $\text{Li}_x\text{C}_6 = \sim 0.7$  can be achieved (*e.g.*, Refs. 289, 290).

By contrast, non-graphitizing (hard) carbons obtained at temperatures of  $\sim 1000^\circ\text{C}$  show

\* The influence of heteroatoms in the organic precursor material on properties of the resulting low-temperature carbon was mentioned as early as 1951 by Franklin.<sup>134</sup>

little hysteresis. However, they develop a capacity of several hundred  $\text{mAh} \cdot \text{g}^{-1}$  at a low potential of a few mV vs.  $\text{Li}/\text{Li}^+$ .<sup>283,293,294)</sup> In order to explain this behavior, Dahn *et al.*<sup>283,293,295)</sup> suggest that lithium is “adsorbed” on both sides of single layer sheets which are arranged like a “house of cards” (Fig. 6.12d; it should be noted that quite often the precursor and, at least to some extent, the preparation and assumed structure of these carbons resemble those of glassy carbon.).<sup>296–298)</sup> Further heat-treatment leads to drastically reduced capacities, *e.g.*, after heating to  $\sim 2900^\circ\text{C}$ , “ $x$ ” in  $\text{Li}_x\text{C}_6 = \sim 0.3$ .<sup>288)</sup>

Despite the fact that many of these high capacity carbons ultimately approach 2–6 times the capacity of graphite, one has to consider some major drawbacks: (i) In many cases extremely high irreversible capacity losses are observed (*e.g.*, Fig. 6.13, see also Refs. 115, 120, 122, 237, 274, 275, 281, 283, 299), occasionally even at higher cycle numbers.<sup>122,281,299,300)</sup> The irreversible capacities are explained in terms of film formation<sup>122,184,237,238,283,292)</sup> or irreversible lithium incorporation.<sup>184,281)</sup> (ii) Graphitizing carbons that exhibit hysteresis show an unstable discharge behavior over a potential region of *ca.* 2 V (for comparison, graphite: 0.25 V, see Fig. 6.5) and poor cycling performance (see *e.g.*, Fig. 6.13 and Refs. 113, 120, 122, 270–275, 283, 293, 295, 299, 300). (iii) The capacity of the non-graphitizing carbons showing no hysteresis (but a reversible capacity at low potentials) is almost

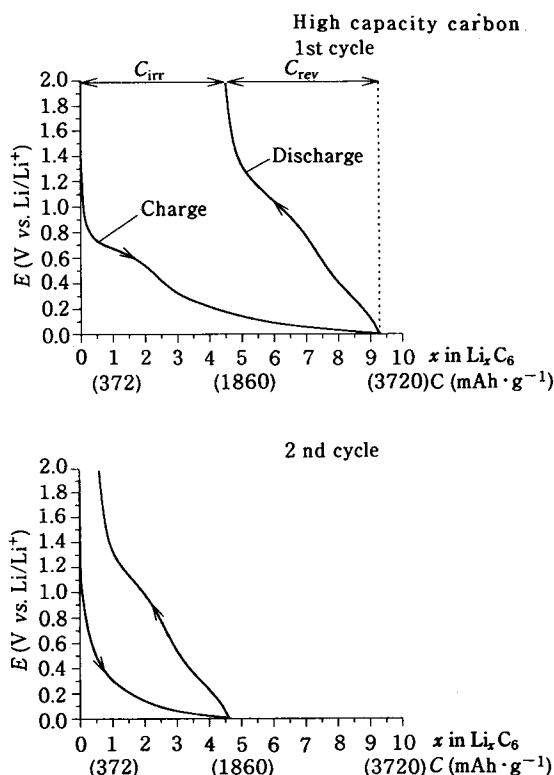


Fig. 6.13 Constant current charge/discharge of a high capacity carbonaceous material (poly-*p*-phenylene heat-treated at  $700^\circ\text{C}$ ) using  $\text{LiPF}_6$  in EC/DMC as electrolyte.<sup>164)</sup>  $C_{\text{irr}}$  denotes the irreversible capacity,  $C_{\text{rev}}$  the reversible capacity.

constant during cycling.<sup>293)</sup> However, to take advantage of the full capacity, the electrode must be charged to potentials below 0 V vs. Li/Li<sup>+</sup>, *i.e.*, lithium deposition with subsequent partial stripping takes place (see Refs. 122, 283, 293 and section 6.5). Therefore, there is a search for high-capacity carbons with graphite-like potential characteristics (*e.g.*, Ref. 301).

## 6.4 Special Carbonaceous Materials as Hosts for Lithium Intercalation

### 6.4.1 Fullerenes

Fullerenes have been evaluated by several groups, *e.g.*, Refs. 302–305. A maximum reversible capacity corresponding to the stoichiometry  $\sim \text{Li}_2\text{C}_{60}$  (“*x*” in  $\text{Li}_x\text{C}_6 = 0.2$ ) is not sufficient for the application in high energy density batteries.<sup>302,305)</sup>

### 6.4.2 Carbonaceous Materials Containing Heteroatoms

The carbonaceous materials discussed so far contain heteroatoms in addition to carbon atoms depending on the precursor and the heat-treatment temperature. Even highly crystalline graphite is saturated with heteroatoms at dislocations and at the edges of the graphene layers (prismatic surfaces, *e.g.*, Ref. 91). However, the intended substitution/addition of larger amounts of “foreign” elements for/to carbon to alter the electrochemical performance is of great interest and will be briefly reviewed in this chapter.

Substitutional boron is assumed to act as an electron acceptor in a carbon host and thus to cause a shift of the intercalation potential to more positive values and an increase of the reversible capacity due to more electronic sites.<sup>81,114,306–308)</sup> For the preparation and characterization of the materials, see Refs. 307–314. Substitutional nitrogen (materials aspects in Refs. 312, 314, 315) presumably functions as an electron donor and should therefore have the opposite effect on the reversible capacity and the intercalation potential.<sup>81,315)</sup> On the contrary, Ref. 316 discloses that nitrogen-containing carbons can also contain considerable high capacities of  $\sim 500 \text{ mAh} \cdot \text{g}^{-1}$ . Further substituted carbons, like *e.g.*, phosphorus doped carbons,<sup>317–320)</sup>  $\text{C}_x\text{S}^{316)}$  and mixed B/N-doped carbons<sup>314,321–327)</sup> have been discussed (see also reviews Refs. 81, 114, 328 and the references therein). Generally, the effects of the heteroatoms and their interactions with the respective carbon neighbors (prepared from various precursors) have not yet been clarified sufficiently to explain their electrochemical performance. This is also true for high-capacity lithium storage materials derived from silicon-containing polymer precursors. In addition to silicon and carbon these materials contain substantial hydrogen and oxygen (Wilson *et al.*<sup>329,330)</sup>). Thus, the effect of one heteroatom alone is difficult to evaluate.

In contrast to partly substituted carbons, composite carbon/silicon insertion materials exhibit high reversible capacities because of the high lithium alloying capacity of silicon<sup>65–69,331)</sup> in addition to the lithium incorporation in disordered carbon regions proceeding independently.<sup>332,333)</sup> Recently, Li-ion cells using new Ag/C composites for the negative electrode have been presented by Hitachi.<sup>334)</sup>



## 6.5 Technical Aspects

The application of any battery material is not only dependent on its intrinsic structural and chemical features, but also strongly affected by several material and manufacturing parameters. Considering the electrochemical properties of electrodes that contain carbonaceous materials as the electrochemically active component, it is desirable that the ratio of the reversible capacity to the irreversible capacity be sufficiently high. This means that the technical conception of the electrode must provide the maximum utilization of the reversible capacity while the irreversible capacity is kept as low as possible. An additional requirement is the high rate performance (= high specific power) of the lithium intercalation/deintercalation reaction, *i.e.*, the charge/discharge reaction, allows high current densities.

The high rate capability of a carbon electrode may be achieved by thin layer electrodes<sup>335–337</sup>) that are made up from small particle size graphite. However, many investigations proved that the particle surface area,<sup>19,177,320,338–341</sup>) particle size,<sup>123,320,340</sup>) shape<sup>60,118,236,320</sup>) and morphology<sup>115,236,320,342,343</sup>) also influence the capacity losses as, in the first approximation, the irreversible capacity due to film-formation is related with the surface area which is wetted by the electrolyte.

Particularly important for the preparation of electrodes consisting of small particle size carbon powders is the electrode thickness,<sup>211</sup>) the manufacture pressure<sup>84,339,344</sup>) and the resulting electrode porosity. Low manufacture pressure, *i.e.*, high porosity, causes poor contact between the carbon particles. Moreover, due to the formation of a passive film the contact resistance between the particles rises and electrical isolation of carbon particles can take place also. At high manufacture pressure, *i.e.*, low porosities, the electrode lacks inner pores and is therefore insufficiently wetted by the electrolyte.<sup>84,339,344</sup>) For optimum performance the electrode porosity must be precisely adjusted. Novák *et al.* demonstrated that the electrode porosity can be tailored by utilizing pore forming additives.<sup>344</sup>) The complex dependence of electrode performance on electrode and particle parameters is additionally influenced by the binder,<sup>57,102,320,339,344–349</sup>) which is usually added to support the compactness of an electrode consisting of small carbon particles. For example, the binder in the electrode on the one hand partly coats the electrochemically active surface area and therefore film formation, *i.e.*, irreversible capacity, is reduced.<sup>348</sup>) On the other hand, the rate capability is decreased because of the covered surface areas. In addition, it must be taken into consideration that the binder also reduces the gravimetric capacity because of the extra inactive binder mass.

In order to predict the interactive behavior of the different structural, chemical and technical parameters of the electrode preparation, several groups utilize (computational) “modeling.”<sup>350–358</sup>) As the behavior of practical electrodes is complex and in most cases not ideal, it is a fastidious attempt to design an electrode with particular electrochemical and technical properties on the basis of theoretical calculations.

A general problem to be considered is the fact that the charging potential of lithium/carbon electrodes and metallic lithium are located very close together. There is a potential gap of only approximately 0.1 V between the fully intercalated first stage GIC-LiC<sub>6</sub> and lithium deposition (Figs. 6.4 and 6.5). For the non-graphitic carbons, like coke (Fig. 6.11) or high-capacity carbons (Fig. 6.13), the situation is even worse, as the charging potential

slopes asymptotically to 0 V vs. Li/Li<sup>+</sup>.<sup>\*1</sup> Because the solid-state transport process for the insertion of lithium in carbons is slow,<sup>19,57,58,116,335,359,360</sup> even moderate charge currents yield considerable overpotentials and there is a high risk of (dendritic) lithium plating at the end of charging.<sup>\*2</sup> Therefore, the fast-charging of carbon electrodes affords relatively sophisticated charging under potential control.

In particular, in large size Li-ion cells one also has to be aware of the significant effects of unhomogeneous current density distributions, caused *e.g.*, by Ohmic drops in the electrode, differences in the morphology of the active material, variations of separator properties or the distance between the electrodes. Variations in current density are paralleled by variations in electrolyte concentration, which affects the potential of lithium intercalation or deposition, as the transference numbers of Li<sup>+</sup>-ions in liquid and polymer organic electrolytes are  $\ll 1$ . The potential measured at the terminal of the negative electrode of a Li-ion cell is a “mixed potential” resulting from the various superimposed electrode processes. The fact that the “mixed potential” of a lithium–carbon electrode is positive against Li/Li<sup>+</sup> does not necessarily exclude that on the electrode also some metallic lithium is present. Moreover, in a Li-ion cell the potential of the negative electrode is measured against the potential of the positive Li<sub>x</sub>MO<sub>n</sub> electrode, and *vice versa*. However, the potential measured at the terminal of the positive electrode is also subject to “mixed potential” effects and also strongly depends on the stoichiometric factor “*x*” in the charged state. Therefore, the “terminal voltage” of a Li-ion cell is of debatable merit with respect to sensing of undesired reactions like metallic lithium deposition.

## 6.6 Outlook

Carbonaceous materials as active materials for the negative electrode are the current state-of-the-art in commercialized “safe” rechargeable lithium batteries. Some problems, such as irreversible capacity losses and a charging potential close to lithium deposition are still unsolved, and many research groups and companies concentrate their research and development activities on the investigation and improvement of the active carbonaceous material, additional electrode components, and interactive characteristics with other cell components such as the positive electrode material and the electrolyte.

Some attention should also be devoted to alternative negative electrode materials, the gravimetric and in particular the volumetric capacities of some Li alloys, *e.g.*, Li<sub>21</sub>Sn<sub>5</sub> (Table 6.1), exceed by far the available capacities of carbonaceous materials. In a recent paper it was demonstrated that the capacity of advanced Li alloys is almost constant over several hundred cycles.<sup>70)</sup> A Li-ion cell with the product name STALION, recently introduced by Fujifilm Celltec uses an “amorphous tin-based composite oxide (ATCO)” for the negative electrode. The high specific capacity of  $\sim 650 \text{ mAh} \cdot \text{g}^{-1}$  is close to the alloying capacity of metallic tin. The estimated reactions of the composite material include the insertion of Li in metallic Sn, SnO, and SnB<sub>x</sub>P<sub>y</sub>O<sub>z</sub> ( $x \sim 0.5$ ,  $y \sim 0.5$ ,  $z \sim 3$ ) which yields Sn<sub>5</sub>Li<sub>22</sub>, Li<sub>5–6</sub>SnO, and Li<sub>7–8</sub>SnB<sub>x</sub>P<sub>y</sub>O<sub>z</sub>. Because SnB<sub>x</sub>P<sub>y</sub>O<sub>z</sub> has glass-forming properties, it is believed that it stabilizes the dimensional stability of the composite host.<sup>361)</sup> Further new

\*1 The flatter discharge curve of graphite is also advantageous for a more constant discharge voltage profile of the Li-ion cell.

\*2 In this respect, the shift of the useful capacity of boron-doped carbons to a more positive potential enables a more rapid charging process.

negative electrode materials containing dispersed Ag on a graphitic material take advantage of the high lithium storage capacity of metallic silver.<sup>334,362</sup> Finally, new lithium/metal nitrides with high, during cycling stable capacities have been proposed as negative electrode materials by several Japanese groups.<sup>363-366</sup>

## Acknowledgments

This work was partially supported by the Austrian "Fonds zur Foerderung der wissenschaftlichen Forschung (FWF)" in the "Electroactive Materials" special research program. Parts of this work were prepared at the Paul Scherrer Institute, Villigen, Switzerland.

## REFERENCES

- 1) K. Brandt, *Solid State Ionics*, **69**, 173 (1994).
- 2) S.B. Brummer, *Lithium Battery Technology* (Ed. by H.V. Ventakassetty), p. 159, John Wiley & Sons (1981).
- 3) D. Linden (Ed.), *Handbook of Batteries and Solar Cells*, McGraw-Hill (1984).
- 4) K. Wiesener, J. Garcke and W. Schneider, *Elektrochemische Stromquellen*, Akademie-Verlag (1981).
- 5) A. Kozawa and K.V. Kordesch, *Progress in Batteries & Solar Cells*, Vol. 2, JEC Press (1979).
- 6) A. Kozawa and K.V. Kordesch, *Progress in Batteries & Solar Cells*, Vol. 3, JEC Press (1979).
- 7) K.J. Euler, *Batterien und Brennstoffzellen-Aufbau, Verwendung, Chemie*, Springer-Verlag (1982).
- 8) H.P. Fritz and J.O. Besenhard, *Elektrochemische Energietechnik* (Ed. by BMFT), Mintzel-Druck (1981).
- 9) G. Eichinger and G. Semrau, *Chem. unserer Z.*, **24**, 32 (1990).
- 10) G. Eichinger and G. Semrau, *Chem. unserer Z.*, **24**, 90 (1990).
- 11) M. Hughes, N.A. Hampson and S.A.G.R. Karunatilaka, *J. Power Sources*, **12**, 83 (1984).
- 12) J.-P. Gabano (Ed.), *Lithium Batteries*, Academic Press (1983).
- 13) D. Linden (Ed.), *Handbook of Batteries*, McGraw-Hill (1995).
- 14) D. Devilliers and M. Vogler, *L'Actualité Chimique*, p. 21 (Janvier-Février, 1994).
- 15) M. Broussely, *L'Actualité Chimique*, p. 24 (Janvier-Février, 1994).
- 16) M.J.A. Trindade, I.M.M.B. Domingues and C.A.C. Sequeira, *Chemistry and Energy-I* (Ed. by C.A.C. Sequeira), p. 97, Elsevier (1991).
- 17) D. Eyre, *Chem. Ind.*, **3**, 74 (1 February, 1988).
- 18) C.D.S. Tuck (Ed.), *Modern Battery Technology*, Ellis Horwood Ltd. (1991).
- 19) S. Hossain, *Handbook of Batteries* (Ed. by D. Linden), Ch. 36, McGraw-Hill (1995).
- 20) V.S. Bagotzky and A.M. Skundin, *Russ. J. Electrochem.*, **31**, 308 (1995).
- 21) P. Dan, E. Mengeritsky, Y. Geronov and D. Aurbach, *J. Power Sources*, **54**, 143 (1995).
- 22) P. Dan, E. Mengeritsky, D. Aurbach, I. Weissman and E. Zinigrad, 8th Int. Meet. Lithium Batteries, Nagoya, Japan, June 1996, Ext. Abstr., p.352.
- 23) E. Mengeritsky, P. Dan, I. Weissman, A. Zaban and D. Aurbach, *J. Electrochem. Soc.*, **143**, 2110 (1996).
- 24) J.O. Besenhard, *Progress in Intercalation Research* (Eds. by W. Müller-Warmuth and R. Schöllhorn), p.457, Kluwer Academic Publishers (1994).
- 25) J.O. Besenhard, *Soft Chemistry Routes to New Materials* (Eds. by J. Rouxel, M. Tournoux and R. Brec), *Mater. Sci. Forum*, **152-153**, p.13, Trans-Tech Publications (1994).
- 26) E. Peled, *Lithium Batteries* (Ed. by J.-P. Gabano), Ch. 3, Academic Press (1983).
- 27) V.R. Koch, *J. Power Sources*, **6**, 357 (1981).
- 28) E. Peled, *J. Electrochem. Soc.*, **126**, 40 (1979).
- 29) J.O. Besenhard, P. Castella and J. Gürtler, *Bull. Electrochem.*, **6**, 53 (1990).
- 30) J.O. Besenhard, J. Gürtler, P. Komenda and A. Paxinos, *J. Power Sources*, **20**, 253 (1987).
- 31) C.D. Desjardins and G.K. MacLean, *Rechargeable Lithium Batteries* (Eds. by S. Subbarao, V.R. Koch, B.B. Owens and W.H. Smyrl), p. 108, The Electrochemical Society (1990).
- 32) S. Surampudi, D.H. Shen, C.-K. Huang, S.R. Narayanan, A. Attia and G. Halpert, *J. Power Sources*, **43-44**, 21 (1993).
- 33) M. Arakawa, S. Tobishima, Y. Nemoto, M. Ichimura and J. Yamaki, *J. Power Sources*, **43-44**, 27 (1993).

- 34) T. Osaka, T. Momma, K. Nishimura and T. Tajima, *J. Electrochem. Soc.*, **140**, 2745 (1993).
- 35) Y. Geronov, P. Zlatilova, B. Puresheva, M. Pasquali and G. Pistoia, *J. Power Sources*, **26**, 585 (1989).
- 36) N. Goldenfield, *J. Power Sources*, **26**, 121 (1989).
- 37) K. Kanamura, S. Shirashi and Z. Takehara, *J. Electrochem. Soc.*, **141**, L108 (1994).
- 38) J.O. Besenhard, J. Gürtler, P. Komenda and M. Josowicz, *Primary and Secondary Ambient Temperature Lithium Batteries* (Eds. by J.-P. Gabano and Z. Takehara), p. 618, The Electrochemical Society (1988).
- 39) S. Megahed and B. Scrosati, *Interface*, **4**, 34 (1995).
- 40) T. Matsui, K. Takeyama, *Electrochim. Acta*, **40**, 2165 (1995).
- 41) R. Selim and P. Bro, *J. Electrochem. Soc.*, **21**, 1467 (1974).
- 42) S.C. Levy and P. Bro, *Battery Hazards and Accident Prevention*, Plenum Press (1994).
- 43) U. von Sacken, E. Nodwell, A. Sundher and J.R. Dahn, *Solid State Ionics*, **69**, 284 (1994).
- 44) D. Fouchard, L. Xie, W. Ebner and S. Megahed, *Rechargeable Lithium and Lithium-Ion Batteries* (Eds. by S. Megahed, B. Barnett and L. Xie), p. 349, The Electrochemical Society (1995).
- 45) M. Armand, *Materials for Advanced Batteries* (Eds. by D.W. Murphy, J. Broadhead and B.C.H. Steele), p. 145, Plenum Press (1980).
- 46) S. Morzilli, B. Scrosati and F. Sgarlata, *Electrochim. Acta*, **30**, 1271 (1985).
- 47) B. Di Pietro, M. Patriarca and B. Scrosati, *J. Power Sources*, **8**, 289 (1982).
- 48) M. Lazzari and B. Scrosati, *J. Electrochem. Soc.*, **127**, 773 (1980).
- 49) B. Scrosati, *J. Electrochem. Soc.*, **139**, 2776 (1992).
- 50) B. Di Pietro, M. Patriarca and B. Scrosati, *Synth. Met.*, **5**, 1 (1982).
- 51) J.-F. Fauvarque, *L'Actualité Chimique*, p. 34 (Janvier-Février, 1994).
- 52) K. M. Abraham, *Electrochim. Acta*, **38**, 1233 (1993).
- 53) S. Subbarao, D.H. Shen, F. Deligiannis, C.-K. Huang and G. Halpert, *J. Power Sources*, **29**, 579 (1990).
- 54) D. Fauteux and R. Koksang, *J. Appl. Chem.*, **23**, 1 (1993).
- 55) G. Halpert, S. Surampudi, D. Shen, C.-K. Huang, S. Narayanan, E. Vamos and D. Perrone, *J. Power Sources*, **47**, 287 (1994).
- 56) Z. Takehara and K. Kanamura, *Electrochim. Acta*, **38**, 1169 (1993).
- 57) S. Megahed and B. Scrosati, *J. Power Sources*, **51**, 79 (1994).
- 58) B. Scrosati, *The Electrochemistry of Novel Materials* (Eds. by J. Lipkowski and P.N. Ross), p. 111, VCH, (1994).
- 59) K. Ozawa, *Solid State Ionics*, **69**, 212 (1994).
- 60) S. Megahed and W. Ebner, *J. Power Sources*, **54**, 155 (1995).
- 61) Y. Asami, K. Tsuchiya, H. Nose, S. Suzuki and K. Mizushima, *J. Power Sources*, **54**, 146 (1995).
- 62) K. Sekai, H. Azuma, A. Omaru, S. Fujita, H. Imoto, T. Endo, K. Yamaura, Y. Nishi, S. Mashiko and M. Yokogawa, *J. Power Sources*, **43-44**, 241 (1993).
- 63) T. Nagaura, *Progress in Batteries & Solar Cells*, **10**, 218 (1991).
- 64) T. Nagaura and K. Tozawa, *Progress in Batteries & Solar Cells*, **9**, 209 (1990).
- 65) R.A. Huggins, *Fast Ion Transport Solids* (Eds. by B. Scrosati, A. Magistris, C.M. Mari and G. Mariotto), p. 143, Kluwer Academic Publishers (1993).
- 66) R. Nesper, *Progress in Solid State Chem.*, **20**, 1 (1990).
- 67) R. Yazami and M.Z.A. Munshi, *Handbook of Solid State Batteries and Capacitors* (Ed. by M.Z.A. Munshi), p. 425, World Scientific (1995).
- 68) J.O. Besenhard and M. Winter, *2. Ulmer Elektrochemische Tage, Ladungsspeicherung in der Doppelschicht* (Ed. by W. Schmickler), p. 47, Universitätsverlag Ulm (1995).
- 69) R.A. Huggins, *J. Power Sources*, **26**, 109 (1989).
- 70) J.O. Besenhard, J. Yang and M. Winter, 8th Int. Meet. Lithium Batteries, Nagoya, Japan, June 1996, Ext. Abstr., p. 69.
- 71) J.J. Auborn and Y.L. Barberio, *J. Electrochem. Soc.*, **134**, 638 (1987).
- 72) M.S. Whittingham, *Progress in Solid State Chemistry*, **12**, 41 (1978).
- 73) T. Shodai, Y. Sakurai and S. Okada, *Rechargeable Lithium and Lithium-Ion Batteries* (Eds. by S. Megahed, B. Barnett and L. Xie), p. 224, The Electrochemical Society (1995).
- 74) E.J. Plichta and W.K. Behl, *J. Electrochem. Soc.*, **140**, 46 (1993).
- 75) E.J. Plichta, W.K. Behl, D. Vujic, W.H.S. Chang and D.M. Schleich, *J. Electrochem. Soc.*, **139**, 1509 (1992).
- 76) F. Croce, S. Passerini, B. Scrosati, E. Plichta, W. Behl and M. Salomon, *J. Power Sources*, **43-44**, 481 (1993).
- 77) P. Novak, K. Müller, K.S.V. Santhanam and O. Haas, *Chem. Rev.*, **97**, 207 (1997).
- 78) F. Croce, S. Panero, S. Passerini and B. Scrosati, *Electrochim. Acta*, **39**, 255 (1994).
- 79) K. Brandt, *J. Power Sources*, **54**, 151 (1995).
- 80) K. Brandt and F.J. Krüger, *Batteries International*, p. 24, (July 1993).
- 81) J.R. Dahn, A.K. Sleight, H. Shi, B.M. Way, W.J. Weydanz, J. N. Reimers, Q. Zhong and U. von Sacken, *Lithium Batteries, New Materials, Developments and Perspectives* (Ed. by G. Pistoia), p. 1, Elsevier (1994).
- 82) R. C. Weast (Ed.), *Handbook of Chemistry and Physics*, 68th Edition, CRC Press (1987).

- 83) D. Billaud, E. McRae and A. Hérold, *Mater. Res. Bull.*, **14**, 857 (1979).
- 84) V. Manev, I. Naidenov, B. Puresheva and G. Pistoia, *J. Power Sources*, **57**, 133 (1995).
- 85) M.S. Whittingham, *Intercalation Chemistry* (Eds. by M.S. Whittingham and A.J. Jacobsen), Ch. 1, Academic Press (1982).
- 86) M.S. Whittingham, *Fast Ion Transport Solids* (Eds. by B. Scrosati, A. Magistris, C.M. Mari and G. Mariotto), p. 69, Kluwer Academic Publishers (1993).
- 87) R. Schöllhorn, *Angew. Chem. Int. Ed. Engl.*, **19**, 983 (1980).
- 88) J.B. Goodenough, *Solid State Ionics*, **69**, 184 (1994).
- 89) W. Müller-Warmuth and R. Schöllhorn (Eds.), *Progress in Intercalation Research*, Kluwer Academic Publishers, Dordrecht (1994).
- 90) R. Schöllhorn, *Intercalation Chemistry* (Eds. by M.S. Whittingham and A.J. Jacobsen), Ch.10, Academic Press (1982).
- 91) J.O. Besenhard and H.P. Fritz, *Angew. Chem. Int. Ed. Engl.*, **95**, 950 (1983).
- 92) J. Barthel and H.-J. Gores, *Chemistry of Nonaqueous Solutions* (Eds. by G. Mamantov and A.I. Popov), p. 1, VCH (1994).
- 93) L.A. Dominey, *Lithium Batteries, New Materials, Developments and Perspectives* (Ed. by G. Pistoia), p. 137, Elsevier (1994).
- 94) M. Armand, *Solid State Ionics*, **69**, 309 (1994).
- 95) M. Alamgir and K. M. Abraham, *Lithium Batteries, New Materials, Developments and Perspectives* (Ed. by G. Pistoia), p. 49, Elsevier (1994).
- 96) A.S. Gozdz, J.-M. Tarascon, C.N. Schmutz, P.C. Warren, O.S. Gebizlioglu and F. Shokoohi, Proc. 10th Ann. Battery Conf. Appl. Advan., Long Beach, California, p. 301, January (1995).
- 97) M. Z. A. Munshi, *Handbook of Solid State Batteries and Capacitors* (Ed. by M. Z. A. Munshi), p. 393, World Scientific, Singapore (1995).
- 98) C.N. Schmutz, J.M. Tarascon, A.S. Gozdz, P.C. Warren and F.K. Shokoohi, *Rechargeable Lithium and Lithium-Ion Batteries* (Eds. by S. Megahed, B. Barnett and L. Xie), p. 330, The Electrochemical Society (1995).
- 99) A.S. Gozdz, J.M. Tarascon, O.S. Gebizlioglu, C.N. Schmutz, P.C. Warren and F.K. Shokoohi, *Rechargeable Lithium and Lithium-Ion Batteries* (Eds. by S. Megahed, B. Barnett and L. Xie), p. 400, The Electrochemical Society (1995).
- 100) R. Yazami and M. Deschamps, 8th Int. Meet. Lithium Batteries, Nagoya, Japan, June 1996, Ext. Abstr., p. 190.
- 101) K. Zaghib, Y. Chouquette, A. Guerfi, M. Simoneau, A. Belanger and M. Gauthier, 8th Int. Meet. Lithium Batteries, Nagoya, June 1996, Ext. Abstr., p. 298.
- 102) J.M. Tarascon, C. Schmutz, A.S. Gozdz, P.C. Warren and F. Shokoohi, *Solid State Ionics IV* (Eds. by G.-A. Nazri, J.-M. Tarascon and M. Schreiber), *Mater. Res. Soc. Symp. Proc.*, **369**, 595 (1995).
- 103) R. Yazami and Ph. Touzain, *J. Power Sources*, **9**, 365 (1983).
- 104) S. Lemont and D. Billaud, *J. Power Sources*, **54**, 340 (1995).
- 105) R. Yazami, *Lithium Batteries, New Materials, Developments and Perspectives* (Ed. by G. Pistoia), p. 49, Elsevier (1994).
- 106) C. Julien, *Lithium Batteries, New Materials, Developments and Perspectives* (Ed. by G. Pistoia), p. 167, Elsevier (1994).
- 107) N. Doddapaneni, G. Nagasubramanian and D. Ingersoll, *Handbook of Solid State Batteries and Capacitors* (Ed. by M.Z.A. Munshi), p. 371, World Scientific (1995).
- 108) J. O. Besenhard, M. Winter, J. Yang and W. Biberacher, *J. Power Sources*, **54**, 228 (1995).
- 109) A.P. Johnson and C.R. Schlaikjer, 8th Int. Meet. Lithium Batteries, Nagoya, Japan, June 1996, Ext. Abstr., p. 318.
- 110) R.T. Carlin and J.S. Wilkens, *Chemistry of Nonaqueous Solutions* (Eds. by G. Mamantov and A.I. Popov), p. 277, VCH (1994).
- 111) R.T. Carlin, J.F. Fuller and M. Hedenskoog, *J. Electrochem. Soc.*, **141**, L21 (1994).
- 112) M. Bagouin, D. Guerard and A. Herold, *C. R. Acad. Sci. (Paris)*, **262C**, 557 (1996).
- 113) A. Mabuchi, *Tanso*, **165**, 298 (1994).
- 114) J.R. Dahn, A.K. Sleight, H. Shi, J.N. Reimers, Q. Zhong and B.M. Way, *Electrochim. Acta*, **38**, 1179 (1993).
- 115) O. Yamamoto, Y. Takeda, N. Imanishi and R. Kanno, *New Sealed Rechargeable Batteries and Supercapacitors* (Eds. by B.M. Barnett, E. Dowgiallo, G. Halpert, Y. Matsuda and Z. Takehara), p. 302, The Electrochemical Society (1993).
- 116) N. Takami, A. Satoh, M. Hara and T. Ohsaki, *J. Electrochem. Soc.*, **142**, 371 (1995).
- 117) A. Satoh, N. Takami and T. Ohsaki, *Solid State Ionics*, **80**, 291 (1995).
- 118) M. Endo, J. Nakamura, A. Emori, Y. Sasabe, K. Takeuchi and M. Inagaki, *Mol. Cryst. Liq. Cryst.*, **245**, 171 (1994).
- 119) R. Yazami, K. Zaghib and M. Deschamps, *Mol. Cryst. Liq. Cryst.*, **245**, 165 (1994).

- 120) T. Zheng, J.S. Xue and J.R. Dahn, *Chem. Mater.*, **8**, 389 (1996).
- 121) K. Sawai, Y. Iwakoshi and T. Ohzuku, *Solid State Ionics*, **69**, 273 (1994).
- 122) T. Zheng, Y. Liu, E.W. Fuller, S. Tseng, U. v. Sacken and J.R. Dahn, *J. Electrochem. Soc.*, **142**, 2581 (1995).
- 123) O. Yamamoto, N. Imanishi, Y. Takeda and H. Kashiwagi, *J. Power Sources*, **54**, 72 (1995).
- 124) G. Li, R. Xue, L. Chen and Y. Huang, *J. Power Sources*, **54**, 271 (1995).
- 125) J. Yamaura, Y. Ohzaki, A. Morita and A. Ohta, *J. Power Sources*, **43-44**, 233 (1993).
- 126) G. Li, Z. Lu, B. Huang, H. Huang, R. Xue and L. Chen, *Solid State Ionics*, **81**, 15 (1995).
- 127) T.D. Tran, J.H. Feikert, X. Song and K. Kinoshita, *J. Electrochem. Soc.*, **142**, 3297 (1995).
- 128) H. Shi, J. Barker, M.Y. Saiidi, R. Koksang and L. Morris, 8th Int. Meet. Lithium Batteries, Nagoya, Japan, June 1996, Ext. Abstr. p. 240.
- 129) R.E. Winans and K.A. Carrado, *J. Power Sources*, **54**, 11 (1995).
- 130) G. Sandi, R.E. Winans and K.A. Carrado, *J. Electrochem. Soc.*, **143**, L95 (1996).
- 131) H.O. Pierson, *Handbook of Carbon, Graphite, Diamond and Fullerenes*, p. 43, Noyes Publications (1993).
- 132) B.E. Warren, *Phys. Rev.*, **59**, 693 (1941).
- 133) R.E. Franklin, *Acta Cryst.*, **4**, 253 (1951).
- 134) R.E. Franklin, *Proc. Roy. Soc. (Lond.)*, **A209**, 196 (1951).
- 135) K. Kinoshita, *Carbon, Electrochemical and Physicochemical Properties*, John Wiley & Sons (1987).
- 136) K. Inada, K. Ikeda, Y. Sato, A. Itsubo, M. Miyabashi and H. Yui, *Primary and Secondary Ambient Temperature Lithium Batteries* (Eds. by J.-P. Gabano, Z. Takehara and P. Bro), p. 530, The Electrochemical Society (1988).
- 137) O. Vohler, F. von Sturm, E. Wege, H. von Kienle, M. Voll and P. Kleinschmitt, *Ullmann's Encyclopedia of Industrial Chemistry* (Executive Ed. by W. Gerhartz), 5th Ed., Vol. 5A, p. 95, VCH (1986).
- 138) B.T. Kelly, *Physics of Graphite*, Applied Science Publishers (1981).
- 139) A. Hérold, *Chemical Physics of Intercalation, NATO ASI Ser.* (Eds. by A.P. Legrand and S. Flandrois), **B172** p. 3, Plenum Press (1987).
- 140) H. Selig and L.B. Ebert, *Advan. Inorg. Chem. Radiochem.*, **23**, 281 (1980).
- 141) R. Setton, *Synth. Met.*, **23**, 467 (1988).
- 142) M. Inagaki, *J. Mater. Res.*, **4**, 1560 (1989).
- 143) H. Touhara, F. Okino and S. Sugnuma, *Kino Zairyo*, **11**, 18 (1991); *Chem. Abstr.*, **116**, 258422f (1992).
- 144) D. Guerard, H. Fuzellier, *NATO ASI Ser.*, **B253**, 695 (1991).
- 145) T. Nakajima, *Seramikkusu*, **27**, 226 (1992); *Chem. Abstr.*, **117**, 38891p (1992).
- 146) T. Sugiura, *Kino Zairyo*, **12**, 22 (1992); *Chem. Abstr.*, **116**, 258426k (1992).
- 147) W. Rüdorff, *Advan. Inorg. Chem. Radiochem.* (Eds. by H.J. Eméleus and A.G. Sharpe), Vol. 1, p. 223, Academic Press (1959).
- 148) L.B. Ebert, *Ann. Rev. Mater. Sci.*, **6**, 181 (1976).
- 149) N. Bartlett and B.W. McQuillan, *Intercalation Chemistry* (Eds. by M.S. Whittingham and A. J. Jacobsen), p. 19, Academic Press (1982).
- 150) R. Moret, *Intercalation in Layered Materials, NATO ASI Ser.* (Ed. by M.S. Dresselhaus), **B148**, p. 185, Plenum Press (1986).
- 151) R. Schlögl, *Progress in Intercalation Research* (Eds. by W. Müller-Warmuth and R. Schöllhorn), p. 83, Kluwer Academic Publishers (1994).
- 152) R. Setton, *Synth. Met.*, **23**, 511 (1988).
- 153) R. Setton, *Synth. Met.*, **23**, 519 (1988).
- 154) K. Fredenhagen and G. Cadenbach, *Z. Anorg. Allg. Chem.*, **158**, 249 (1926).
- 155) W. Rüdorff and U. Hofmann, *Z. Anorg. Allg. Chem.*, **238**, 1 (1938).
- 156) A. Hérold, *Bull. Soc. Chim. France*, **187**, 999 (1955).
- 157) T. Tran and K. Kinoshita, *J. Electroanal. Chem.*, **386**, 221 (1995).
- 158) X.Y. Song, K. Kinoshita and T.D. Tran, *J. Electrochem. Soc.*, **143**, L120 (1996).
- 159) J. Rossat-Mignod, D. Fruchart, M.J. Moran, J.W. Milliken and J.E. Fisher, *Synth. Met.*, **2**, 143 (1980).
- 160) V.V. Avdev, V.A. Nalimova and K.N. Semenenko, *High Pressure Research*, **6**, 11 (1990).
- 161) D. Guerard and V. A. Nalimova, *Solid State Ionics IV* (Eds. by G.-A. Nazri, J.-M. Tarascon and M. Schreiber), *Mater. Res. Soc. Symp. Proc.*, **369**, 155 (1995).
- 162) V. A. Nalimova, G. Guerard, M. Lelaurain and O.V. Fateev, *Carbon*, **33**, 177 (1995).
- 163) V. A. Nalimova, C. Bindra and J.E. Fisher, *Solid State Commun.*, **97**, 583 (1996).
- 164) M. Winter, J.O. Besenhard, M.E. Spahr and P. Novak, in preparation.
- 165) N. Daumas and A. Hérold, *C. R. Acad. Sci. (Paris)*, **268C**, 373 (1969).
- 166) N. Daumas and A. Hérold, *Bull. Soc. Chim.*, **5**, 1598 (1971).
- 167) J.E. Fisher, *Chemical Physics of Intercalation, NATO ASI Ser.* (Eds. by A.P. Legrand and S. Flandrois), **B172**, p. 59, Plenum Press (1987).
- 168) J.R. Dahn, *Phys. Rev.*, **B44**, 9170 (1991).
- 169) D. Guerard and A. Hérold, *Carbon*, **13**, 337 (1975).

- 170) P. Pflüger, V. Geiser, S. Stolz and H.-J. Güntherodt, *Synth. Met.*, **3**, 27 (1981).
- 171) D. Billaud, F.X. Henry and P. Willmann, *Mater. Res. Bull.*, **28**, 477 (1993).
- 172) D. Billaud, F. Henry and P. Willmann, *Mol. Cryst. Liq. Cryst.*, **245**, 159 (1994).
- 173) M. Inaba, H. Yoshida, Z. Ogumi, T. Abe, Y. Mizutani and M. Asano, *J. Electrochem. Soc.*, **142**, 20 (1995).
- 174) A. J. Bard and L.R. Faulkner, *Electrochemical Methods*, John Wiley & Sons (1980).
- 175) J. O'M Bockris and A.K.N. Reddy, *Modern Electrochemistry*, Vol. 1, Plenum Press (1970).
- 176) J. O'M Bockris and A.K.N. Reddy, *Modern Electrochemistry*, Vol. 2, Plenum Press (1970).
- 177) R. Fong, U. v. Sacken and J.R. Dahn, *J. Electrochem. Soc.*, **137**, 2009 (1990).
- 178) K. Yokoyama and N. Nagawa, *New Sealed Rechargeable Batteries and Supercapacitors* (Eds. by B.M. Barnett, E. D'Agostino, G. Halpert, Y. Matsuda and Z. Takehara), p. 270, The Electrochemical Society (1993).
- 179) R. Kanno, Y. Kawamoto, Y. Takeda, S. Ohashi, N. Imanishi and O. Yamamoto, *J. Electrochem. Soc.*, **139**, 3397 (1992).
- 180) M. Arakawa and J. Yamaki, *J. Electroanal. Chem.*, **219**, 273 (1987).
- 181) R. Yazami, K. Zaghib and M. Deschamps, *J. Power Sources*, **52**, 55 (1994).
- 182) R. Bittihn, R. Herr and D. Hoge, *J. Power Sources*, **43-44**, 409 (1993).
- 183) T. Ohzuku, Y. Iwakoshi and K. Sawai, *J. Electrochem. Soc.*, **140**, 2490 (1993).
- 184) Y. Matsumura, S. Wang and J. Mondori, *J. Electrochem. Soc.*, **142**, 2914 (1995).
- 185) M. Kikuchi, Y. Ikezawa and T. Takamura, *J. Electroanal. Chem.*, **396**, 451 (1995).
- 186) T. Takamura, M. Kikuchi, J. Ebana, M. Nagashima and Y. Ikezawa, *New Sealed Rechargeable Batteries and Supercapacitors* (Eds. by B.M. Barnett, E. D'Agostino, G. Halpert, Y. Matsuda and Z. Takehara), p. 229, The Electrochemical Society (1993).
- 187) T. Takamura, M. Kikuchi and Y. Ikezawa, *Rechargeable Lithium and Lithium-Ion Batteries* (Eds. by S. Megahed, B. Barnett and L. Xie), p. 213, The Electrochemical Society (1995).
- 188) T. Takamura, H. Awano, T. Ura and M. Yashiro, 8th Int. Meet. Lithium Batteries, Nagoya, Japan, June 1996, Ext. Abstr., p. 111.
- 189) Y. Ein-Eli, B. Markovsky, D. Aurbach, Y. Carmeli, H. Yamin and S. Luski, *Electrochim. Acta*, **39**, 2559 (1994).
- 190) D. Aurbach, Y. Ein-Eli, B. Markovsky, A. Zaban and A. Schechter, *Rechargeable Lithium and Lithium-Ion Batteries* (Eds. by S. Megahed, B. M. Barnett and L. Xie), p. 26, The Electrochemical Society (1994).
- 191) D. Aurbach, Y. Ein-Eli, B. Markovsky, A. Zaban, S. Lusky, Y. Carmeli and H. Yamin, *J. Electrochem. Soc.*, **142**, 2882 (1995).
- 192) D. Aurbach, Y. Ein-Eli, O. Chusid, Y. Carmeli, M. Babai and H. Yamin, *J. Electrochem. Soc.*, **141**, 603 (1994).
- 193) D. Aurbach and Y. Ein-Eli, *J. Electrochem. Soc.*, **142**, 1746 (1995).
- 194) S. Mori, H. Asahina, H. Suzuki, A. Yonei and E. Yasukawa, 8th Int. Meet. Lithium Batteries, Nagoya, Japan, June 1996, Ext. Abstr., p. 40.
- 195) M. Winter, J.O. Besenhard and P. Novák, *GDCh-Monographie*, **3**, 438 (1996).
- 196) A.N. Dey and B.P. Sullivan, *J. Electrochem. Soc.*, **117**, 222 (1970).
- 197) J.O. Besenhard and H.P. Fritz, *J. Electroanal. Chem.*, **53**, 329 (1974).
- 198) J.O. Besenhard, *Carbon*, **14**, 111 (1976).
- 199) J.O. Besenhard, H. Möhwald and J.J. Nickl, *Carbon*, **18**, 399 (1980).
- 200) M. Rose, C. Nacchache and J. Golé, *C. R. Acad. Sci. (Paris)*, **266C**, 421 (1968).
- 201) Co-Minh-Duc, M. Rose and J.-P. Pascault, *C. R. Acad. Sci. (Paris)*, **270C**, 569 (1970).
- 202) F. Beguin, R. Setton, A. Hamwi and P. Touzain, *Mater. Sci. Eng.*, **40**, 167 (1979).
- 203) J. O. Besenhard, H. Witty and H.-F. Klein, *Carbon*, **22**, 98 (1984).
- 204) J. O. Besenhard, H.-F. Klein and H. Möhwald and J. J. Nickl, *Synth. Met.*, **4**, 51 (1981).
- 205) J. O. Besenhard, I. Kain, H.-F. Klein, H. Möhwald and H. Witty, *Intercalated Graphite* (Eds. by M. S. Dresselhaus, G. Dresselhaus, J.E. Fischer and M.J. Moran), p. 221, North-Holland (1983).
- 206) B. Marcus and P. Touzain, *J. Solid State Chem.*, **77**, 223 (1988).
- 207) P. Schoderböck and H.P. Boehm, *Synth. Met.*, **44**, 239 (1991).
- 208) A.N. Dey, *J. Electrochem. Soc.*, **117**, 222 (1970).
- 209) G. Eichinger, *J. Electroanal. Chem.*, **74**, 183 (1976).
- 210) M. Arakawa and J. Yamaki, *J. Electroanal. Chem.*, **219**, 273 (1987).
- 211) Z. X. Shu, R.S. McMillan and J. J. Murray, *J. Electrochem. Soc.*, **140**, 922 (1993).
- 212) Z. X. Shu, R.S. McMillan and J. J. Murray, *J. Electrochem. Soc.*, **140**, L101 (1993).
- 213) Z.X. Shu, R.S. McMillan and J.J. Murray, *New Sealed Rechargeable Batteries and Supercapacitors* (Eds. by B.M. Barnett, E. D'Agostino, G. Halpert, Y. Matsuda and Z. Takehara), p. 238, The Electrochemical Society (1993).
- 214) M. Jean, A. Tranchant and R. Messina, *J. Electrochem. Soc.*, **143**, 391 (1996).
- 215) M. Jean, A. Chausse and R. Messina, 8th Int. Meet. Lithium Batteries, Nagoya, Japan, June 1996, Ext.

- Abstr., p. 186.
- 216) E. Peled, *Rechargeable Lithium and Lithium-Ion Batteries* (Eds. by S. Megahed, B. Barnett and L. Xie), p. 1, The Electrochemical Society (1995).
  - 217) N.R. Avery and K.J. Black, 8th Int. Meet. Lithium Batteries, Nagoya, Japan, June 1996, Ext. Abstr., p. 163.
  - 218) D.P. Wilkinson and J.R. Dahn, US Patent 5,130,211 (1992).
  - 219) J.M. Tarascon, D. Guyomard and G.L. Baker, *J. Power Sources*, **43-44**, 689 (1993).
  - 220) D. Guyomard and J.M. Tarascon, *J. Electrochem. Soc.*, **140**, 3071 (1993).
  - 221) J.M. Tarascon and D. Guyomard, *Solid State Ionics*, **69**, 293 (1994).
  - 222) J.M. Tarascon and D. Guyomard, *Electrochim. Acta*, **38**, 1221 (1993).
  - 223) D. Guyomard and J.M. Tarascon, *J. Power Sources*, **54**, 92 (1995).
  - 224) D. Guyomard and J.M. Tarascon, *Solid State Ionics*, **69**, 222 (1994).
  - 225) D. Guyomard and J.M. Tarascon, US Patent 5,192,629 (1993).
  - 226) D. Aurbach, A. Zaban, A. Schechter, Y. Ein-Eli, E. Zinigrad and B. Markovsky, *J. Electrochem. Soc.*, **142**, 2873 (1995).
  - 227) A. Ohta, H. Koshina, H. Okuno and H. Murai, *J. Power Sources*, **54**, 6 (1995).
  - 228) I. Naidenov, B. Puresheva and V. Manev, 8th Int. Meet. Lithium Batteries, Nagoya, Japan, June 1996, Ext. Abstr., p. 159.
  - 229) S. T. Mayer, C. Bragg, H.C. Yoon and J.H. Lee, 8th Int. Meet. Lithium Batteries, Nagoya, Japan, June 1996, Ext. Abstr., p. 256.
  - 230) M. Inaba, Z. Siroma, A. Funabiki and Z. Ogumi, *Langmuir*, **12**, 1535 (1996).
  - 231) M. Inaba, Z. Siroma, Y. Kawadate, A. Funabiki and Z. Ogumi, 8th Int. Meet. Lithium Batteries, Nagoya, Japan, June 1996, Ext. Abstr., p. 181.
  - 232) Z. X. Shu, R.S. McMillan and J.J. Murray, *J. Electrochem. Soc.*, **142**, L161 (1995).
  - 233) Z. X. Shu, R.S. McMillan and J.J. Murray, in: *Rechargeable Lithium and Lithium-Ion Batteries* (Eds. by S. Megahed, B.M. Barnett and L. Xie), p. 431, The Electrochemical Society, Pennington, NJ (1994).
  - 234) Z. X. Shu, R.S. McMillan, J. J. Murray and I. J. Davidson, *J. Electrochem. Soc.*, **143**, 2231 (1996).
  - 235) D. Billaud, A. Naji and P. Willmann, *J. Chem. Soc., Chem. Commun.*, 1867 (1995).
  - 236) K. Takei, N. Terada, K. Kumai, T. Iwahori, T. Uwai and T. Miura, *J. Power Sources*, **55**, 191 (1995).
  - 237) H. Fujimoto, A. Mabuchi, K. Tokumitsu and T. Kasuh, *J. Power Sources*, **54**, 440 (1995).
  - 238) E. Peled, C. Menachem, D. Bar-Tow and A. Melman, *J. Electrochem. Soc.*, **143**, L4 (1996).
  - 239) C. Menachem, E. Peled, L. Burstein and Y. Rosenberg, 8th Int. Meet. Lithium Batteries, Nagoya, Japan, June 1996, Ext. Abstr., p. 224.
  - 240) T. Uchida, T. Morita, M. Nagayama, H. Ikuta and M. Wakihara, 8th Int. Meet. Lithium Batteries, Nagoya, Japan, June 1996, Ext. Abstr., p. 230.
  - 241) C. Liebenow, M.W. Wagner, K. Lühder, P. Lobitz and J.O. Besenhard, *J. Power Sources*, **54**, 369 (1995).
  - 242) J.O. Besenhard, P. Castella and M.W. Wagner, *Mater. Sci. Forum*, **91-93**, 647 (1992).
  - 243) B. Simon, J.P. Boeue and M. Broussely, *J. Power Sources*, **43-44**, 65 (1993).
  - 244) O. Chusid, Y. Ein-Ely and D. Aurbach, *J. Power Sources*, **43-44**, 47 (1993).
  - 245) J.O. Besenhard, M. Winter and J. Yang, Int. Workshop Advan. Batteries (Lithium Batteries), Osaka, Japan, p. 129 (1995).
  - 246) J.O. Besenhard, M.W. Wagner, M. Winter, A.D. Jannakoudakis, P.D. Jannakoudakis and E. Theodoridou, *J. Power Sources*, **43-44**, 413 (1993).
  - 247) M.W. Wagner, C. Liebenow and J.O. Besenhard, 8th Int. Meet. Lithium Batteries, Nagoya, Japan, June 1996, Ext. Abstr., p. 266.
  - 248) R. Yazami and D. Guérard, *J. Power Sources*, **43-44**, 39 (1993).
  - 249) T. Zheng and J.R. Dahn, *Synth. Met.*, **73**, 1 (1995).
  - 250) T. Zheng and J.R. Dahn, *Phys. Rev.*, **B53**, 3061 (1996).
  - 251) T. Zheng, J.N. Reimers and J.R. Dahn, *Phys. Rev.*, **B51**, 734 (1995).
  - 252) M. Jean, C. Desnoyer, A. Tranchant and R. Messina, *J. Electrochem. Soc.*, **142**, 2122 (1995).
  - 253) R.V. Moshtev, P. Zlatilova, B. Puresheva and V. Manev, *J. Power Sources*, **56**, 144 (1995).
  - 254) J.M. Chen, C.Y. Yao, C.H. Cheng, W.M. Hurng and T.H. Kao, *J. Power Sources*, **54**, 494 (1995).
  - 255) A.K. Sleight and U. v. Sacken, *Solid State Ionics*, **57**, 99 (1992).
  - 256) K. Takei, K. Kumai, Y. Kobayashi, H. Miyashiro, T. Iwahori, T. Uwai and T. Miura, *J. Power Sources*, **54**, 171 (1995).
  - 257) X. Shu, L.D. Schmidt and W.H. Smyrl, *Rechargeable Lithium and Lithium-Ion Batteries* (Eds. by S. Megahed, B. Barnett and L. Xie), p. 196, The Electrochemical Society (1995).
  - 258) I. Kuribayashi, M. Yokoyama and M. Yamashita, *J. Power Sources*, **54**, 1 (1995).
  - 259) R. Kanno, Y. Takeda, T. Ichikawa, K. Nakanishi and O. Yamamoto, *J. Power Sources*, **26**, 535 (1989).
  - 260) N. Imanishi, S. Ohashi, T. Ichikawa, Y. Takeda, O. Yamamoto and R. Kanno, *J. Power Sources*, **39**, 185 (1992).
  - 261) M. Mohri, N. Yanagisawa, Y. Tajima, H. Tanaka, T. Mitate, S. Nakajima, M. Yoshida, Y. Yoshimoto, T.



- Suzuki and H. Wada, *J. Power Sources*, **26**, 545 (1989).
- 262) R. Yazami and M. Deschamps, *Advances in Solid State Ionics IV* (Eds. by G.-A. Nazri, J.-M. Tarascon and M. Schreiber), *Mater. Res. Soc. Symp. Proc.*, **369**, 165 (1995).
  - 263) R. Yazami and M. Deschamps, *J. Power Sources*, **54**, 411 (1995).
  - 264) R. Yazami and M. Deschamps, *Rechargeable Lithium and Lithium-Ion Batteries* (Eds. by S. Megahed, B. Barnett and L. Xie), p. 183, The Electrochemical Society (1995).
  - 265) M. Deschamps and R. Yazami, 8th Int. Meet. Lithium Batteries, Nagoya, Japan, June 1996, Ext. Abstr., p. 188.
  - 266) L.B. Ebert, *Carbon*, **34**, 671 (1996).
  - 267) J.R. Dahn, T. Zheng, Y. Liu and J.S. Xue, *Science*, **270**, 590 (1995).
  - 268) K. Sato, M. Noguchi, A. Demachi, N. Oki and M. Endo, *Science*, **264**, 556 (1994).
  - 269) K. Sato, M. Noguchi, A. Demachi, N. Oki, M. Endo and Y. Sasabe, Int. Workshop Advan. Batteries (Lithium Batteries), Osaka, Japan, p. 219 (1995).
  - 270) K. Tokumitsu, A. Mabuchi, H. Fujimoto and T. Kasuh, *J. Power Sources*, **54**, 444 (1995).
  - 271) K. Tokumitsu, A. Mabuchi, H. Fujimoto and T. Kasuh, 8th Int. Meet. Lithium Batteries, Nagoya, Japan, June 1996, Ext. Abstr., p. 212.
  - 272) K. Tokumitsu, A. Mabuchi, H. Fujimoto and T. Kasuh, *J. Electrochem. Soc.*, **143**, 2235 (1996).
  - 273) S. Yata, K. Sakurai, T. Osaki, Y. Inoue and K. Yamaguchi, *Synth. Met.*, **33**, 177 (1990).
  - 274) S. Yata, H. Kinoshita, M. Komori, N. Ando, T. Kashiwamura, T. Harada, K. Tanaka and T. Yamabe, *Synth. Met.*, **62**, 153 (1994).
  - 275) S. Yata, Y. Hato, H. Kinoshita, N. Ando, A. Anekawa, T. Hashimoto, M. Yamaguchi, K. Tanaka and T. Yamabe, *Synth. Met.*, **73**, 273 (1995).
  - 276) S. Yata, Int. Workshop Advan. Batteries (Lithium Batteries), Osaka, Japan, p. 204 (1995).
  - 277) Y. Matsumura, S. Wang, T. Kasuh and T. Maeda, *Synth. Met.*, **71**, 1755 (1995).
  - 278) Y. Matsumura, S. Wang and J. Mondori, *Carbon*, **33**, 1457 (1995).
  - 279) Y. Matsumura, S. Wang, K. Shinohara and T. Maeda, *Synth. Met.*, **71**, 1757 (1995).
  - 280) S. Wang, Y. Matsumura and T. Maeda, *Synth. Met.*, **71**, 1759 (1995).
  - 281) Y. Mori, T. Iriyama, T. Hashimoto, S. Yamazaki, F. Kawakami, H. Shiroki and T. Yamabe, *J. Power Sources*, **56**, 205 (1995).
  - 282) Y. Mori, T. Iriyama, T. Hashimoto, S. Yamazaki, F. Kawakami and H. Shiroki, Int. Workshop Advan. Batteries (Lithium Batteries), Osaka, Japan, p. 199 (1995).
  - 283) J.S. Xue and J.R. Dahn, *J. Electrochem. Soc.*, **142**, 3668 (1995).
  - 284) J.R. Dahn, J.S. Xue, W. Xing, A.M. Wilson and A. Gibaud, 8th Int. Meet. Lithium Batteries, Nagoya, Japan, June 1996, Ext. Abstr., p. 89.
  - 285) A. Satoh, N. Takami, T. Ohsaki and M. Kanda, *Rechargeable Lithium and Lithium-Ion Batteries* (Eds. by S. Megahed, B. Barnett and L. Xie), p. 143, The Electrochemical Society (1995).
  - 286) K. Tatsumi, A. Mabuchi, N. Iwashita, H. Sakaebe, H. Shioyama, H. Fujimoto and S. Higuchi, Proc. Symp. Batteries Fuel Cells Stationary Elec. Vehicle Appl. (Eds. by A.R. Landgrebe and Z. Takehara), p. 64 (1993).
  - 287) A. Mabuchi, H. Fujimoto, K. Tokumitsu and T. Kasuh, *J. Electrochem. Soc.*, **142**, 3049 (1995).
  - 288) K. Tokumitsu, A. Mabuchi, H. Fujimoto and T. Kasuh, *Rechargeable Lithium and Lithium-Ion Batteries* (Eds. by S. Megahed, B. Barnett and L. Xie), p. 136, The Electrochemical Society (1995).
  - 289) K. Tatsumi, T. Akai, T. Imamura, K. Zaghbi, N. Iwashita, S. Higuchi and Y. Sawada, *J. Electrochem. Soc.*, **143**, 1923 (1996).
  - 290) K. Tatsumi, N. Iwashita, H. Sakaebe, H. Shioyama, S. Higuchi, A. Mabuchi and H. Fujimoto, *J. Electrochem. Soc.*, **142**, 716 (1995).
  - 291) T. Zheng and J.R. Dahn, 8th Int. Meet. Lithium Batteries, Nagoya, Japan, June 1996, Ext. Abstr., p. 166.
  - 292) H. Imoto, M. Nagamine and Y. Nishi, *Rechargeable Lithium and Lithium-Ion Batteries* (Eds. by S. Megahed, B. Barnett and L. Xie), p. 43, The Electrochemical Society (1995).
  - 293) T. Zheng, Q. Zhong and J.R. Dahn, *J. Electrochem. Soc.*, **142**, L211 (1995).
  - 294) T. Zheng, W.R. McKinnon and J.R. Dahn, *J. Electrochem. Soc.*, **143**, 2137 (1996).
  - 295) Y. Liu, J. S. Xue, T. Zheng and J.R. Dahn, *Carbon*, **34**, 193 (1996).
  - 296) G.M. Jenkins and K. Kawamura, *Polymeric Carbons, Carbon Fibre, Glass and Char*, Cambridge University Press (1976).
  - 297) K. Kinoshita, *Carbon, Electrochemical and Physicochemical Properties*, p. 13, John Wiley & Sons (1988).
  - 298) R. Dubgen and G. Popp, *Z. Werkstofftech.*, **15**, 331 (1984).
  - 299) M. Alamgir, Q. Zuo and K.M. Abraham, *J. Electrochem. Soc.*, **141**, L143 (1994).
  - 300) T. Iijima, K. Suzuki and Y. Matsuda, *Synth. Met.*, **73**, 9 (1995).
  - 301) T. Kasuh, A. Mabuchi, K. Tokumitsu and H. Fujimoto, 8th Int. Meet. Lithium Batteries, Nagoya, Japan, June 1996, Ext. Abstr., p. 97.
  - 302) S. Lemont, J. Ghanbaja and D. Billaud, *Mol. Cryst. Liq. Cryst.*, **244**, 203 (1994).
  - 303) L. Firlej, A. Zahab, F. Brocard and P. Bernier, *Synth. Met.*, **70**, 1373 (1995).

- 304) W. Zho, H. Huang, Y. Li, R. Xue, Y. Huang, Z. Zhao and L. Chen, 7th Int. Meet. Lithium Batteries, Boston, May 1994, Ext. Abstr., p. 278.
- 305) R. Yazami and A. Cherigui, 7th Int. Meet. Lithium Batteries, Boston, May 1994, Ext. Abstr., p. 255.
- 306) J.R. Dahn, J.N. Reimers, A.K. Sleight and T. Tiedje, *Phys. Rev.*, **B45**, 3773 (1992).
- 307) B.M. Way and J.R. Dahn, *J. Electrochem. Soc.*, **141**, 907 (1994).
- 308) T. Tamaki and M. Tamaki, 8th Int. Meet. Lithium Batteries, Nagoya, Japan, June 1996, Ext. Abstr., p. 216.
- 309) B.M. Way, J.R. Dahn, T. Tiedje, K. Myrtle and M. Kasrai, *Phys. Rev.*, **B46**, 1697 (1992).
- 310) W. Cermignani, T.E. Paulson, C. Onneby and C.G. Pantano, *Carbon*, **33**, 367 (1995).
- 311) M. Wörle, R. Nesper, G. Mair and H.G. v. Schnering, *Z. Anorg. Allg. Chem.*, **621**, 1153 (1995).
- 312) J. Kouvetakis, R.B. Kaner, M.L. Sattler and N. Bartlett, *J. Chem., Chem. Commun.*, 1758 (1986).
- 313) Y.-S. Lee and M. Kertesz, *J. Chem., Chem. Commun.*, 75 (1988).
- 314) J. Kouvetakis, T. Saski, C. Chen, R. Hagiwara, M. Lerner, K.M. Krishan and N. Bartlett, *Synth. Met.*, **34**, 1 (1989).
- 315) W. J. Weydanz, B.M. Way, T. van Buuren and J.R. Dahn, *J. Electrochem. Soc.*, **141**, 900 (1994).
- 316) S. Ito, T. Murata, M. Hasegawa, Y. Bito and Y. Toyoguchi, 8th Int. Meet. Lithium Batteries, Nagoya, Japan, June 1996, Ext. Abstr., p. 196.
- 317) H.H. Schönfelder, K. Kitoh and H. Nemoto, 8th Int. Meet. Lithium Batteries, Nagoya, Japan, June 1996, Ext. Abstr., p. 206.
- 318) T.D. Tran, S.T. Mayer and R.W. Pekala, *Advances in Porous Materials* (Eds. by S. Komarneni, D.M. Smith and J.S. Beck), *Mater. Res. Soc. Symp. Proc.*, **369**, 449 (1995).
- 319) Q. Zhong and U. V. Sacken, 8th Int. Meet. Lithium Batteries, Nagoya, Japan, June 1996, Ext. Abstr., p. 202.
- 320) T.D. Tran, J.H. Feikert, S.T. Mayer, X. Song and K. Kinoshita, *Rechargeable Lithium and Lithium-Ion Batteries* (Eds. by S. Megahed, B. Barnett and L. Xie), p. 110, The Electrochemical Society (1995).
- 321) Y. Matsuda, M. Ishikawa, T. Nakamura, M. Morita, S. Tsujioka and T. Kawashima, *Rechargeable Lithium and Lithium-Ion Batteries* (Eds. by S. Megahed, B. Barnett and L. Xie), p. 85, The Electrochemical Society (1995).
- 322) M. Morita, T. Hanada, H. Tsotsumi, Y. Matsuda and M. Kawaguchi, *J. Electrochem. Soc.*, **139**, 1227 (1992).
- 323) Y. Matsuda, M. Morita, T. Hanada and M. Kawaguchi, *J. Power Sources*, **43-44**, 75 (1993).
- 324) M. Ishikawa, T. Nakamura, M. Morita, Y. Matsuda, S. Tsujioka and T. Kawashima, *J. Power Sources*, **55**, 127 (1995).
- 325) R.B. Kaner, J. Kouvetatis, C.E. Kouvetatis, C.E. Warble, M. L. Sattler and N. Bartlett, *Mater. Res. Bull.*, **22**, 399 (1987).
- 326) M. Hubacek and T. Sato, *J. Solid State Chem.*, **114**, 258 (1995).
- 327) J. Bill, M. Friess and R. Riedel, *Eur. J. Solid State Inorg. Chem.*, **29**, 195 (1992).
- 328) R. Riedel, *Advan. Mater.*, **6**, 549 (1994).
- 329) A.M. Wilson, J.N. Reimers, E.W. Fuller and J.R. Dahn, *Solid State Ionics*, **74**, 249 (1995).
- 330) A.M. Wilson, G. Zank, K. Eguchi, W. Xing and J.R. Dahn, 8th Int. Meet. Lithium Batteries, Nagoya, Japan, June 1996, Ext. Abstr., p. 165.
- 331) A. Anani and S. Crough-Baker, *Proc. Electrochem. Soc.*, **87-1**, 365 (1987).
- 332) A.M. Wilson and J.R. Dahn, *J. Electrochem. Soc.*, **142**, 326 (1995).
- 333) A.M. Wilson and J.R. Dahn, *Rechargeable Lithium and Lithium-Ion Batteries* (Eds. by S. Megahed, B. Barnett and L. Xie), p. 158, The Electrochemical Society (1995).
- 334) J. Aragane, K. Matsui, H. Andoh, S. Suzuki, H. Fukada, H. Ikeya, K. Kitaba and R. Ishikawa, 8th Int. Meet. Lithium Batteries, Nagoya, Japan, June 1996, Ext. Abstr., p. 18.
- 335) R.B. Goldner, T. Liu and S. Slaven, *J. Electrochem. Soc.*, **143**, L129 (1996).
- 336) R.B. Goldner, S. Slaven, T.Y. Liu, T.E. Haas, F.O. Arntz and P. Zerigan, *Advances in Porous Materials* (Eds. by S. Komarneni, D.M. Smith and J.S. Beck), *Mater. Res. Soc. Symp. Proc.*, **369**, 137 (1995).
- 337) M. Hess, E. Lebraud and A. Levasseur, 8th Int. Meet. Lithium Batteries, Nagoya, Japan, June 1996, Ext. Abstr., p. 168.
- 338) M. Fujimoto, K. Ueno, T. Nohma, M. Takahashi, K. Nishio and T. Saito, *New Sealed Rechargeable Batteries and Supercapacitors* (Eds. by B. Barnett, G. Halpert, E. Dowgiallo, Y. Matsuda and Z. Takehara), p. 280, The Electrochemical Society (1993).
- 339) V. Manev, I. Naidenov, B. Puresheva and G. Pistoia, *J. Power Sources*, **57**, 211 (1995).
- 340) K. Zaghib, K. Tatsumi, H. Abe, T. Ohsaki, Y. Sawada and S. Higuchi, *Rechargeable Lithium and Lithium-Ion Batteries* (Eds. by S. Megahed, B. Barnett and L. Xie), p. 121, The Electrochemical Society (1995).
- 341) K. Tatsumi, K. Zaghib, H. Abe, S. Higuchi, T. Ohsaki and Y. Sawada, *J. Power Sources*, **54**, 425 (1995).
- 342) N. Imanishi, H. Kashiwagi, T. Ichikawa, Y. Takeda, O. Yamamoto and M. Inagaki, *J. Electrochem. Soc.*, **140**, 315 (1993).
- 343) D. Billaud, F.X. Henry and P. Willmann, *J. Power Sources*, **54**, 383 (1995).
- 344) P. Novák, W. Scheifele, M. Winter and O. Haas, 8th Int. Meet. Lithium Batteries, Nagoya, Japan, June 1996, Ext. Abstr., p. 214.

- 345) K. Zaghib, K. Tatsumi, H. Abe, T. Ohsaki, Y. Sawada and S. Higuchi, *J. Power Sources*, **54**, 435 (1995).
- 346) S. Passerini, J.M. Rosolen and B. Scrosati, *J. Power Sources*, **45**, 333 (1993).
- 347) C.E. Newnham, S. Rinne and N. Scholey, *J. Power Sources*, **54**, 516 (1995).
- 348) M. Terasaki, H. Yoshida, T. Fukunaga, H. Tukamoto, M. Mizutani and M. Yamachi, Int. Workshop Advan. Batteries (Lithium Batteries), Osaka, Japan, p.302 (1995).
- 349) W. Liu, G. Li, Z. Wang, H. Huang, Z. Lu, R. Xue, X. Huang and L. Chen, 8th Int. Meet. Lithium Batteries, Nagoya, Japan, June 1996, Ext. Abstr., p.278.
- 350) W. Lehnert, W. Schmickler and A. Bannerjee, *Chem. Phys.*, **163**, 331 (1992).
- 351) D.P. DiVincenzo and E.J. Mele, *Mater. Res. Soc. Symp. Proc.* (Eds. by M.S. Dresselhaus, G. Dresselhaus, J.E. Fischer and M.J. Moran), **20**, 123 (1989).
- 352) W. Lehnert, 2. *Ulmer Elektrochemische Tage, Ladungsspeicherung in der Doppelschicht* (Ed. by W. Schmickler), p. 33, Universitätsverlag Ulm (1995).
- 353) M. Posternak, A. Baldereschi, A.J. Freeman, E. Wimmer and M. Weiner, *Mater. Res. Soc. Symp. Proc.* (Eds. by M.S. Dresselhaus, G. Dresselhaus, J.E. Fischer and M.J. Moran), **20**, 177 (1989).
- 354) T.F. Fuller, M. Doyle and J. Newman, *J. Electrochem. Soc.*, **141**, 982 (1994).
- 355) T.F. Fuller, M. Doyle and J. Newman, *J. Electrochem. Soc.*, **141**, 1 (1994).
- 356) M. Doyle, J. Newman, A.S. Gozdz, C.N. Schmutz and J.M. Tarascon, *J. Electrochem. Soc.*, **143**, 1890 (1996).
- 357) T.F. Fuller, M. Doyle and J. Newman, Proc. Symp. Lithium Batteries (Eds. by N. Doddapaneni and A.R. Landgrebe), p. 25 (1994).
- 358) M.W. Verbrugge and B.J. Koch, *J. Electrochem. Soc.*, **143**, 600 (1996).
- 359) T. Uchida, Y. Morikawa, H. Ikuta and M. Wakihara, *New Sealed Rechargeable Batteries and Supercapacitors* (Eds. by B.M. Barnett, E. D'Agostino, G. Halpert, Y. Matsuda and Z. Takehara), p. 292, The Electrochemical Society (1993).
- 360) D. Guyomard and J. M. Tarascon, *J. Electrochem. Soc.*, **139**, 937 (1992).
- 361) Y. Idota, Fujifilm Celltech. Co. Ltd., personal communication, February 1997.
- 362) K. Nishimura, H. Hondo, S. Takeuchi, T. Horiba, Y. Muranaka, Y. Kozono and H. Miyadera, 8th Int. Meet. Lithium Batteries, Nagoya, Japan, June 1996, Ext. Abstr., p.338.
- 363) T. Shodai, S. Okada, S. Tobishima and J. Yamaki, 8th Int. Meet. Lithium Batteries, Nagoya, Japan, June 1996, Ext. Abstr., p.405.
- 364) M. Nishijima, T. Kagohashi, M. Imanishi, Y. Takeda, O. Yamamoto and S. Kondo, *Solid State Ionics*, **83**, 107 (1996).
- 365) O. Yamamoto, Y. Takeda and N. Imanishi, Int. Workshop Advan. Batteries (Lithium Batteries), Osaka, Japan, p.189 (1995).
- 366) M. Nishijima, T. Kagohashi, Y. Takeda, N. Imanishi and O. Yamamoto, 8th Int. Meet. Lithium Batteries, Nagoya, Japan, June 1996, Ext. Abstr., p.402.

## 7

## Organic Electrolytes for Rechargeable Lithium Ion Batteries

Masayuki Morita<sup>\*1</sup>, Masashi Ishikawa<sup>\*1</sup> and Yoshiharu Matsuda<sup>\*2</sup>

## 7.1 Introduction

The basic features of battery performance, *i.e.*, operating voltage, theoretical energy density, *etc.*, are essentially determined by the chemistry of the active materials used as the positive and negative electrodes. Therefore, despite being an indispensable component, the electrolyte has long been regarded as a subordinate technology in the development of an advanced battery system. Practically, however, the chemistry of the electrolyte often affects battery performance significantly. Thus, a wide variety of non-aqueous electrolyte systems have been proposed and examined for primary and secondary (rechargeable) lithium batteries.

It is very important to establish a criterion for designing electrolytes of rechargeable lithium batteries. At present, however, we have no general guide for obtaining the best choice of electrolyte for the battery in question. We have found only one combination of a negative electrode/non-aqueous electrolyte/positive electrode system for a rechargeable battery with high energy density. Examples of the non-aqueous (organic) electrolytes once used (or proposed) for primary and secondary lithium batteries are listed in Table 7.1. These do not seem to be optimized in the lithium battery system because each combination of the negative and positive electrodes employs a different electrolyte system. The main reason for this may be found in the technological history of the development of rechargeable lithium batteries. That is, practical researches aiming to develop a lithium battery system with higher performance have preceded fundamental studies based on the science of the battery.

This chapter deals with systems consisting of organic solvents dissolving lithium salts as the electrolytes of rechargeable lithium (ion) batteries. Other non-aqueous electrolytes, such as polymer electrolytes and inorganic solid electrolytes, will be referred to elsewhere in this monograph. In this chapter we will not review all of the organic electrolyte solutions so far proposed or examined for rechargeable lithium batteries. Rather the fundamental aspects of designing the organic electrolyte solutions of rechargeable batteries are presented. The basic concept of the organic electrolytes for rechargeable lithium ion batteries is first described. Relation between the composition of the electrolyte system and

<sup>\*1</sup> Department of Applied Chemistry and Chemical Engineering, Faculty of Engineering, Yamaguchi University, 2557 Tokiwadai, Ube 755, Japan

<sup>\*2</sup> Department of Applied Chemistry, Faculty of Engineering, Kansai University, 3-3-35 Yamate-cho, Suita 564, Japan

Table 7.1 Examples of practical lithium batteries and the electrolytes used in the batteries.

Primary battery	
Negative/Positive	Electrolyte (Salt/Solvent)
Li/MnO <sub>2</sub>	LiClO <sub>4</sub> /PC (propylene carbonate) + DME (1,2-dimethoxyethane)
Li/(CF) <sub>n</sub>	LiBF <sub>4</sub> /BL (γ-butyrolactone)
Li/CuO	LiClO <sub>4</sub> /DOL (1,3-dioxolane)
Li/SOCl <sub>2</sub>	LiAlCl <sub>4</sub> /SOCl <sub>2</sub>

Secondary (Rechargeable) battery		
Negative/Positive	Electrolyte (Salt/Solvent*)	Company or Institute
Li/MoS <sub>2</sub>	LiAsF <sub>6</sub> /PC + co-solvent	Moli Energy (Canada)
Li-Al/TiS <sub>2</sub>	LiPF <sub>6</sub> /MeDOL + DME + additive	Hitachi Maxell (Japan)
Li-alloy/C	LiClO <sub>4</sub> /PC	Matsushita Battery (Japan)
Li-Al/Polyaniline	LiClO <sub>4</sub> /PC	Bridgestone-Seiko (Japan)
Li-C/LiCoO <sub>2</sub>	LiPF <sub>6</sub> /PC + DEC	Sony Energytec (Japan)
Li-C/LiCoO <sub>2</sub>	LiBF <sub>4</sub> /PC + EC + BL	A&T Battery (Japan)
Li-C/LiCoO <sub>2</sub>	LiPF <sub>6</sub> /EC + DEC + co-solvent	Matsushita Battery (Japan)
Li-C/LiCoO <sub>2</sub>	LiPF <sub>6</sub> /EC + co-solvent	Sanyo (Japan)
Li-C/Li <sub>1+x</sub> Mn <sub>2</sub> O <sub>4</sub>	LiPF <sub>6</sub> /EC + DMC	Bellcore (USA)
Li-C/LiNiO <sub>2</sub>	(LiPF <sub>6</sub> or LiN(CF <sub>3</sub> SO <sub>2</sub> ) <sub>2</sub> /EC + co-solvent)	Rayovac (USA)
Li/Li <sub>x</sub> MnO <sub>2</sub>	(Organic electrolyte)	Tadiran (Israel)
Li/TiS <sub>2</sub>	LiI-Li <sub>3</sub> PO <sub>4</sub> -P <sub>2</sub> S <sub>2</sub>	Everready (USA)
Li/V <sub>6</sub> O <sub>13</sub>	LiX/PEO-based polymer	Valence Technology (USA)

\* MeDOL: 4-methyl-1,3-dioxolane, DEC: diethyl carbonate, EC: ethylene carbonate, DMC: dimethyl carbonate.

their physicochemical properties, mainly the ionic conductivity of the electrolyte solution, is discussed. Then, we demonstrate some organic electrolyte systems that influence the electrode characteristics of lithium ion batteries, especially of the carbonaceous negative electrodes, as an example of the importance of the electrolyte in the battery system.

## 7.2 The Basic Concept for Designing Organic Electrolytes for Lithium Batteries

The battery electrolytes are generally required to have the following fundamental properties: (1) high ionic conductance, (2) thermal and chemical stability, (3) wide potential window (electrochemical stability), (4) low reactivity toward other components in the battery, such as positive and negative electrodes, current collectors, separator, *etc.*, and (5) non-toxicity and safety. Of course, each constituent in a commercially available battery should be made of an abundant inexpensive material. These properties can be independently examined by themselves, except for number 4. In fact, there are some combinations of organic solvents and lithium salts that satisfy the most of these requirements. It should be pointed out that electrolytes for rechargeable batteries must not inhibit, but preferentially promote, the reversible electrode reactions in the battery system.

### 7.2.1 Organic Solvents

Numbers of organic solvents dissolving lithium salts have been examined as electrolyte

Table 7.2 Physical properties of solvents at 25 °C (unless otherwise noted).

Solvent (Abbreviation)	m.p. (°C, 1 atm)	b.p. (°C, 1 atm)	Relative permittivity	Viscosity (cP)	Dipole moment (Debye)	D.N. <sup>a)</sup>	A.N. <sup>a)</sup>
Acetonitrile (AN)	-45.72	81.77	38	0.345	3.94	14.1	18.9
$\gamma$ -Butyrolactone (BL)	-42	206	39.1	1.751	4.12	—	—
Diethylether (DEE)	-116.2	34.60	4.27	0.224	1.18	19.2	3.9
1,2-Dimethoxyethane (DME)	-58	84.7	7.20	0.455	1.07	24	—
Dimethylsulfoxide (DMSO)	18.42	189	46.45	1.991	3.96	29.8	19.3
1,3-Dioxolane (DOL)	-95	78	6.79 <sup>b)</sup>	0.58	—	—	—
Ethylene carbonate (EC)	39-40	248	89.6 <sup>c)</sup>	1.86 <sup>c)</sup>	4.80	16.4	—
Methylformate (MF)	-99	31.50	8.5 <sup>d)</sup>	0.330	1.77	—	—
2-Methyltetrahydrofuran (MeTHF)	—	80	6.24	0.457	—	—	—
3-Methyloxazolidin-2-on (MO)	15.9	—	77.5	2.450	—	—	—
Propylene carbonate (PC)	-49.2	241.7	64.4	2.530	5.21	15.1	18.3
Sulfolane (S)	28.86	287.3	42.5 <sup>b)</sup>	9.87 <sup>b)</sup>	4.7	14.8	19.3
Tetrahydrofuran (THF)	-108.5	65.0	7.25 <sup>b)</sup>	0.46 <sup>b)</sup>	1.71	20.0	8.0

<sup>a)</sup> D.N.: Donicity, A.N.: Acceptor Number, <sup>b)</sup> at 30 °C, <sup>c)</sup> at 40 °C, <sup>d)</sup> at 20 °C

solutions for rechargeable lithium batteries. Table 7.2 summarizes selected physico-chemical properties of major solvents so far proposed and examined.<sup>1,2)</sup> The solvents should be aprotic to be stable at fairly negative potentials (or not react with metallic lithium) and should have high polarity to dissolve lithium salts giving high ionic conductivity. Melting point (m.p.) and boiling point (b.p.) of the solvent, which relate directly to the operating temperature of the resulting battery system, are parameters that reflect the physical chemistry of the solvent such as molecular structure and inter molecular forces. Relative permittivity (dielectric constant) and viscosity of the solvent are the most important properties that determine the ionic conductance of the electrolyte solution.<sup>3,4)</sup> Donicity and acceptor number are measures of the solvent-cation and solvent-anion interactions, respectively.<sup>5)</sup>

As the conditions to obtain an excellent electrolyte solution, the solvent should have lower m.p., higher b.p., and lower vapor pressure, with respect to a wider operating temperature range. Further, higher permittivity and lower viscosity are desirable for the solvent to ensure higher ionic conductivity of the electrolyte solution. It is quite difficult to satisfy all of these conditions because some of the properties are inconsistent with each other in principle. Thus, we may select one of these according to the use or specification of the battery. Solvent mixing is also effective to obtain a system that makes up for the shortcomings of each component.<sup>3,4)</sup>

Alkyl carbonates have widely been used as excellent solvents in lithium batteries. Cyclic esters like propylene carbonate (PC) and ethylene carbonate (EC) have high permittivities attributable to their high polarity, but these are highly viscous due to strong intermolecular forces. On the other hand, linear esters like dimethyl carbonate (DMC) and diethyl carbonate (DEC) show lower viscosities and permittivities due to their molecular structures with increasing degree of freedom in rotation of the alkyl groups. These esters have higher electrochemical stabilities under highly anodic conditions than other low viscosity ethers, 1,2-dimethoxyethane (DME) and tetrahydrofuran (THF). This is a main reason for the mixed ester systems (PC+DEC, EC+DMC, *etc.*) employed now in commercially

available lithium ion batteries.

### 7.2.2 Lithium Salts

As shown in Table 7.1, several kinds of lithium salts have been used in commercial batteries. Lithium salts with monovalent anions are preferable for the battery electrolyte to maintain a higher degree of dissociation of the salt and higher mobility of the resulting ion. In this respect, anions of moderate size are suitable for practical battery systems. Lithium perchlorate ( $\text{LiClO}_4$ ) gives high conductivity in organic solutions, but is not sufficiently stable under anodic conditions. Thus, candidates among the salts have been restricted to  $\text{LiBF}_4$ ,  $\text{LiPF}_6$  and  $\text{LiAsF}_6$ .<sup>6)</sup> Recently, lithium salts with organic anions of larger size have been proposed and examined in a practical system. Salts with perfluoro-alkylsulfonates such as  $\text{LiCF}_3\text{SO}_3$  have wide potential windows and are anodically more stable than the perchlorate. Further, perfluoro-alkylsulfonimides such as  $\text{Li}(\text{CF}_3\text{SO}_2)_2\text{N}$  (and more recently,  $\text{Li}(\text{C}_2\text{F}_5\text{SO}_2)_2\text{N}$ ) and perfluoro-alkylsulfomethanides such as  $\text{Li}(\text{CF}_3\text{SO}_2)_3\text{C}$  have been also reported as the electrolytes of rechargeable batteries.

### 7.2.3 Ionic Conductivity

The ionic conductivity of the electrolyte is of practical importance because it determines the internal resistance and rate performance of the battery. Generally, the conductivity of organic electrolyte solutions based on aprotic solvents dissolving lithium salts is at most  $2 \times 10^{-2} \text{ S} \cdot \text{cm}^{-1}$ , which is much lower than that of aqueous electrolyte solutions ( $8 \times 10^{-1} \text{ S} \cdot$

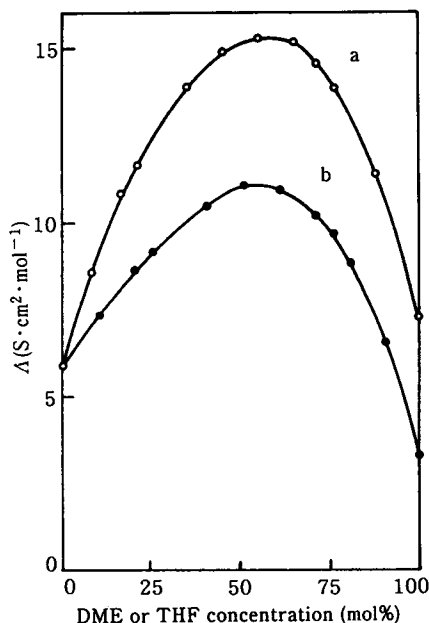


Fig. 7.1 Variations in the molar conductivity of 1 M  $\text{LiClO}_4$  with the solvent composition in mixed PC + ether systems at 30°C. (a) PC + DME, (b) PC + THF.

[Y. Matsuda *et al.*, *Bull. Chem. Soc. Jpn.*, **59**, 1970 (1986)]

$\text{cm}^{-1}$  of  $\text{H}_2\text{SO}_4$  for lead-acid batteries,  $5 \times 10^{-1} \text{ S} \cdot \text{cm}^{-1}$  of  $\text{KOH}$  for alkaline Ni-Cd batteries). Thus, much attention has been focused on efforts to obtain high ionic conductance for organic electrolyte solutions. On the other hand, the conductance behavior of the electrolyte directly reflects the ionic structure in the system. We can obtain a guiding principle for electrolyte design from the analytical results of the ionic behavior.

As shown in Table 7.1, many lithium batteries have used electrolyte solutions consisting of mixed solvent systems. This trend is due to the idea that the shortcomings of each solvent will be made up for by mixing the solvents with different characteristics. Fig. 7.1 shows a typical result of the variation in the molar conductivity of  $1 \text{ mol} \cdot \text{dm}^{-3} (\text{M})$   $\text{LiClO}_4$  with the solvent composition in PC mixed with DME (PC+DME) or with THF (PC+THF).<sup>7)</sup> The conductivity shows maximum values at about 50+50 mixing ratio (by volume) in these PC+ether mixed solvent systems, in which high permittivity of PC promotes the dissociation of the lithium salt and low viscosity of the ether contributes to high mobility of the dissociated ions.<sup>7,8)</sup> The molar conductivity in PC+DME is much higher than in PC+THF. Since THF has almost the same permittivity and viscosity as DME, the difference in conductivity between the two systems is attributable to differences in the microscopic structure of the solution. As expected from donorities of DME and THF which are higher than that of PC,  $\text{Li}^+$  in the mixed solvent systems forms specifically solvated ions. Analyses of spectroscopic data of concentrated solutions and conductance behavior in diluted systems suggest that the solvated ions are  $\text{Li}^+(\text{DME})_2$  and  $\text{Li}^+(\text{THF})_4$

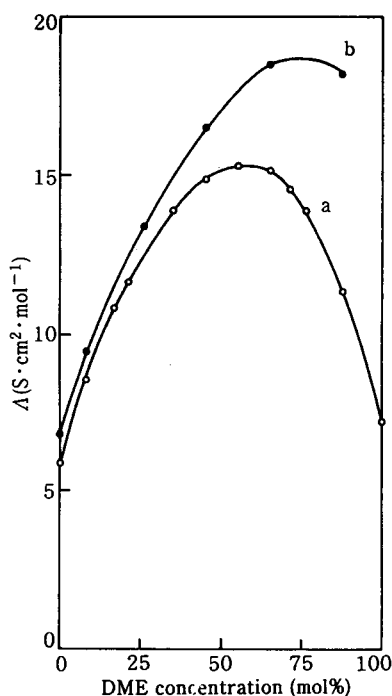


Fig. 7.2 Variations in the molar conductivity of 1 M  $\text{LiClO}_4$  (a) and  $\text{LiPF}_6$ , b) with the solvent composition in mixed PC+DME at 30 °C.

[Y. Matsuda *et al.*, *Bull. Chem. Soc. Jpn.*, **59**, 1971 (1986)]



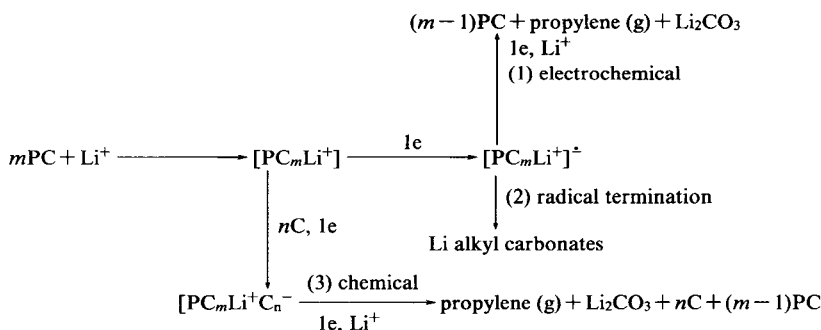
in PC + DME and PC + THF, respectively.<sup>4,9)</sup> The smaller size of  $\text{Li}^+(\text{DME})_2$  in PC + DME leads to higher conductivity than in PC + THF.

In practical batteries, rather high concentrations of lithium salts are used in organic solvents. Formation of ion-pairs and even ion-triplets may be taken into consideration in such concentrated electrolyte solutions. The size and the shape of anion also affect the conductance behavior through the mode of ion-pair formation. Fig. 7.2 shows an example of the effect of anions on the conductivity in PC + DME.<sup>7)</sup> The difference in the conductivity between  $\text{LiClO}_4$  and  $\text{LiPF}_6$ , especially in the high DME composition region (> 50 mol%), may be based on the difference in the mode of ion-pair formation. That is, in a lower permittivity region with a high concentration of DME,  $\text{LiPF}_6$  tends to be a "solvent-separated ion-pair," which contributes partly to the ionic conduction. On the other hand,  $\text{LiClO}_4$  have a tendency to form a "contact ion-pair," which does not serve the ionic conduction.<sup>7)</sup>

The electrolyte composition often affects the electrode reaction in battery. Therefore, it is very important to understand the ionic behavior and structure of the solution from the viewpoint of designing an electrolyte system for high performance batteries. Unfortunately, little is known about the physical chemistry of electrolyte solutions in practical battery systems. We need further information on the ionic behavior and structure of organic electrolyte solutions.

#### 7.2.4 Recent Studies on Organic Electrolytes for Rechargeable Lithium Ion Batteries

Much attention has been focused on the effects of electrolyte composition on the charge/discharge characteristics of various carbonaceous negative electrodes. Electrolyte solutions consisting of PC as the main solvent tend to decompose electrochemically on highly graphitized carbon electrodes during the cathodic polarization (charging process in the battery system).<sup>10)</sup> Thus, the current efficiency of the lithium intercalation is rather low in these electrolyte systems. There have been some reports on the reaction mechanism of



Scheme 7.1 A possible reaction mechanism for cathodic decomposition of propylene carbonate on a graphite electrode.

[Z.X. Shu *et al.*, *J. Electrochem. Soc.*, **140**, 925 (1993)]

the PC decomposition on graphite: one example is shown in Scheme 7.1.<sup>11)</sup>

According to Aurbach *et al.*,<sup>12–14)</sup> in solutions based on the carbonate solvents (PC and other carbonates), lithium alkyl carbonates ( $\text{ROCO}_2\text{Li}$ ) are produced as primary decomposition products. The resulting carbonates react immediately with trace water and other impurities in the system to precipitate as lithium carbonate ( $\text{Li}_2\text{CO}_3$ ) on the graphite surface. The chemical stability and the  $\text{Li}^+$  ion permeability of the precipitated film depends on the type of solvent; these are considered to be the determining factors for reversibility of the carbon electrode. It is generally understood that EC-based mixed solvent systems are more suitable for carbon materials with highly graphitized structures. Linear carbonates such as DMC, DEC and EMC (ethylmethyl carbonate) have been used as the low viscosity co-solvent. However, some research groups claim that the thermal and electrochemical stabilities of these electrolyte systems are insufficient.<sup>15–17)</sup> Typical conductivity data for some EC-based electrolyte solutions are listed in Table 7.3<sup>18)</sup> The conductivity of the solution based on a mixed carbonate solvent is generally about one half that of the solution with DME as the co-solvent, although this depends on the lithium salt which is dissolved in it.

Aurbach *et al.*<sup>14)</sup> have examined the effects of the solvent mixing ratio and the electrolytic salt on the discharge capacity of a graphite-based electrode in the EC + DEC system. They have also carried out Fourier transform infrared spectroscopy (FTIR) and ac impedance measurements, the results of which showed that the system of  $\text{LiAsF}_6$  dissolved in EC + DEC (3 : 1) to be the best of all those examined. Surface reactions on the graphite electrode are further discussed by other research groups.<sup>19,20)</sup> The effects of electrolyte composition on the charge/discharge characteristics of other carbon materials have also been examined extensively.<sup>18,21,22)</sup>

Recently, some new approaches to improving the properties of the interface between graphite-based electrode and organic electrolyte solution have been reported. Billaud *et al.*<sup>23)</sup> proved that reversible charge/discharge cycling is obtained even in a reactive solution of  $\text{LiClO}_4$  in PC, namely  $\text{LiClO}_4/\text{PC}$ , if the surface of the graphite has once been treated cathodically in  $\text{LiClO}_4/\text{EC}$  to form a stable protective film on the graphite surface. Shu *et*

Table 7.3 Conductivity of EC-based electrolytes  
(EC: co-solvent, 1:1 by vol.) (at 25 °C)

Electrolytic salt (1 mol·dm <sup>-3</sup> )	Co-solvent	Specific conductivity (mS·cm <sup>-1</sup> )
$\text{Li}(\text{CF}_3\text{SO}_2)_2\text{N}$	DME	13.3
	DMC	9.2
	DEC	6.5
	MP	10.8
$\text{LiCF}_3\text{SO}_3$	DME	8.3
	DMC	3.1
	DEC	2.1
	MP	3.7
$\text{LiPF}_6$	DME	16.6
	DMC	11.2
	DEC	7.8
	MP	13.3

*al.*<sup>24)</sup> reported the effects of a crown ether added to the  $\text{LiClO}_4/\text{PC} + \text{EC}$  electrolyte on the rechargeability of a graphite electrode. The addition of the crown ether improved the rechargeability of the graphite electrode in this electrolyte system. Chemical modification of solvents is also promising to improve the electrode characteristics of the graphite. Wakihara *et al.*<sup>25)</sup> demonstrated that PC modified with fluorine was difficult to decompose cathodically on a highly graphitized carbon electrode compared with conventional PC. We are very interested in the result that the reactivity of PC can be suppressed by the introduction of fluorine. A somewhat similar chemical modification has been examined for the solvent EC.<sup>26)</sup> That is, the solvent consisting of EC substituted by a chlorine atom, chloro-EC (4-chloro-1,3-dioxolane-2-one), mixed with reactive PC showed much lower reactivity for cathodic decomposition on graphite than that based on the conventional EC + PC mixed solvent system. These attempts encourage us to search for more improved electrolyte systems for high performance rechargeable lithium ion batteries.

Our recent studies on electrolyte systems affecting the electrode characteristics of some carbon-based electrodes are presented in the following sections.

### 7.3 Effects of the Electrolyte Composition on the Electrode Characteristics of Pitch-based Carbon Fiber with Graphite Structure

Numbers of carbonaceous materials have been examined for the negative electrode matrices of “rocking-chair” type lithium ion batteries.<sup>27,28)</sup> The electrode performance depends on the electrolyte system used in the battery as well as the type of carbon material.<sup>29)</sup> It is generally accepted that solvents with high reactivity, such as PC, are not suited for batteries using well-crystallized graphite electrodes.<sup>10,11,30)</sup> EC seems to be a better solvent for highly graphitized electrodes. In these cases, electrolytic solutions containing DEC or DMC as a co-solvent of EC show high discharge capability because of their surface chemistry in the electrolyte systems. However, the effects of the electrolyte composition on the electrochemical process on the carbon electrodes are at present insufficiently understood.

In this section, we demonstrate the effects of electrolyte salts and solvents on the cycling characteristics of carbon fiber with a highly graphitized structure. In particular, since there have been few studies on electrolyte systems containing  $\text{LiCF}_3\text{SO}_3$ , we focus mainly on a comparison of the systems containing  $\text{LiCF}_3\text{SO}_3$  with those consisting of  $\text{LiPF}_6$ , which is more conventionally used in practical lithium ion batteries.<sup>31)</sup> The fiber used here was prepared at Nippon Steel Co., Ltd. The diameter of the fiber was 10  $\mu\text{m}$ , and the size of the crystallite,  $L_c$ , was 18.4 nm. The interlayer spacing of the (002) plane,  $d_{(002)}$ , was 0.341 nm. A fagot of the fiber (10 mg) was used as the test electrode. All electrochemical measurements were carried out at room temperature (18–24°C) in a dry Ar atmosphere.

#### 7.3.1 Voltammetric Behavior in PC- and EC-based Solutions

The electrochemical stabilities of PC-based and EC-based solutions have been examined by cyclic voltammetry using a glassy carbon (GC) rod as the indicator electrode; this GC rod has the lowest electrocatalytic activity in general. Figs. 7.3 and 7.4 respectively show the voltammograms obtained in solutions with PC or EC as the main solvent. The results also include a comparison between  $\text{LiPF}_6$  and  $\text{LiCF}_3\text{SO}_3$  as the electrolyte salts. The current

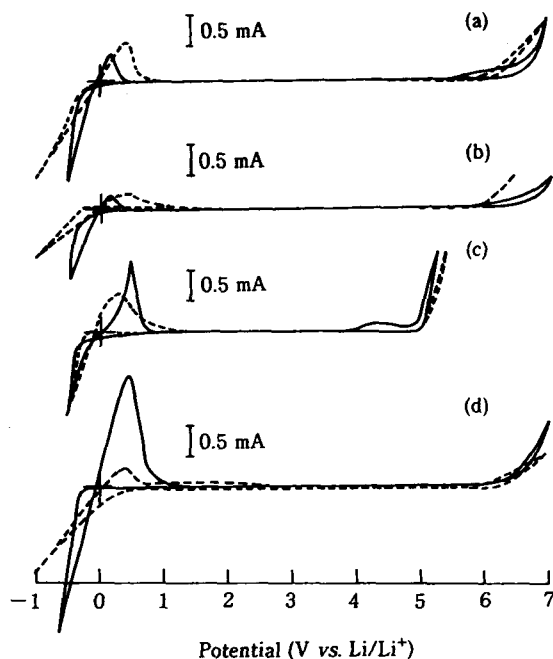


Fig. 7.3 Potential sweep voltammograms obtained at a GC electrode in PC-based solutions containing 1 M  $\text{LiCF}_3\text{SO}_3$  (broken lines) and  $\text{LiPF}_6$  (solid lines). (a) PC + DMC (50 + 50), (b) PC + DEC (50 + 50), (c) PC + DME (50 + 50), (d) PC, Sweep rate:  $0.02 \text{ V}\cdot\text{s}^{-1}$ .

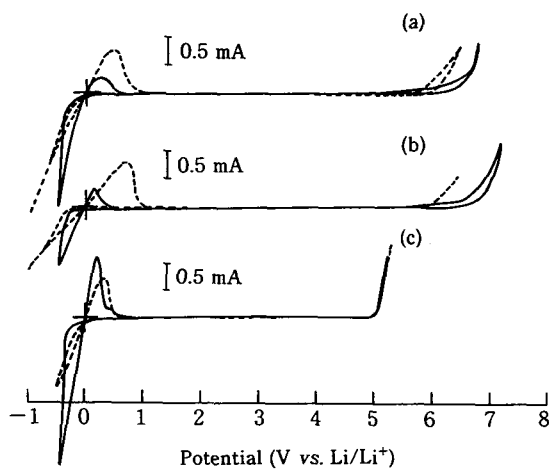


Fig. 7.4 Potential sweep voltammograms obtained at a GC electrode in EC-based solutions containing 1 M  $\text{LiCF}_3\text{SO}_3$  (broken lines) and  $\text{LiPF}_6$  (solid lines). (a) EC + DMC (50 + 50), (b) EC + DEC (50 + 50), (c) EC + DME (50 + 50), Sweep rate:  $0.02 \text{ V}\cdot\text{s}^{-1}$ .

responses around 0 V vs.  $\text{Li/Li}^+$  are based on the electrochemical deposition and dissolution of lithium on GC, which depend on the composition of the electrolyte solution. No intercalation nor de-intercalation of lithium occurs on GC under these experimental conditions. It is well known that the coulombic efficiency for the electrochemical deposition and dissolution of lithium varies with the electrolyte composition.<sup>32,33</sup> The anodic current increases at 5 V or above, indicating the oxidative decomposition of the electrolytes. The onset potential at which the anodic decomposition commences also depends on the electrolyte composition. The co-solvent DME lowers the anodic stability of the resulting solution although there is no significant difference in the onset potential among the base solvents PC and EC. With respect to the electrolyte salt,  $\text{LiCF}_3\text{SO}_3$  seems to be less stable than  $\text{LiPF}_6$  under anodically polarized conditions. In a practical sense it is preferable that the electrolyte has as a wide potential window as possible.

Figures 7.5–7.7 are voltammograms obtained at a pitch-based carbon fiber electrode with a graphitized structure.<sup>34</sup> In PC-based solutions (Fig. 7.5), increases in the cathodic current suggesting the electrochemical lithium intercalation are observed for the initial potential scan, and the corresponding anodic current peaks at around 0.5 V come from the

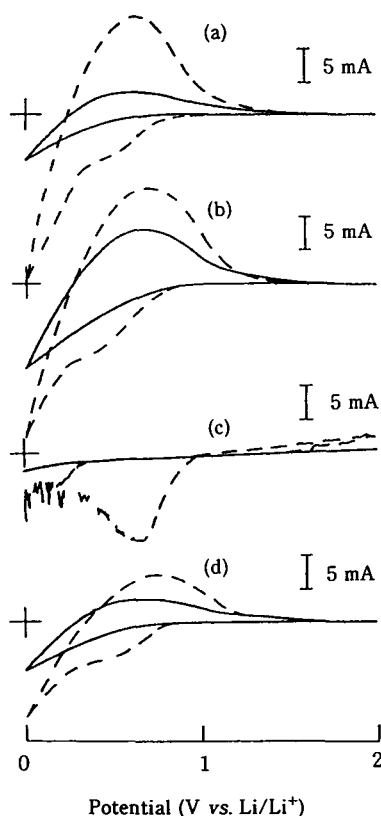


Fig. 7.5 Potential sweep voltammograms obtained at a carbon fiber electrode in PC-based solutions containing 1 M  $\text{LiPF}_6$ . (a) PC + DMC (50 + 50), (b) PC + DEC (50 + 50), (c) PC + DME (50 + 50), (d) PC. Broken lines: 1st cycle, Solid lines: 10th cycle, Sweep rate:  $0.01 \text{ V}\cdot\text{s}^{-1}$ .

deintercalation of lithium from the carbon fiber. The cathodic current increases are accompanied by small current shoulders at about 0.7 V, especially in the first potential scan. This is considered to be due to the cathodic reduction of the electrolyte to form a protective thin film at the carbon fiber surface. The cathodic current increase and the anodic current peak tend to decline with repeated potential cycling in the PC-based electrolytes. The degree of current decline, depending on the type of co-solvents (lower viscosity solvents), is lowest in the solution containing DEC (PC + DEC). No anodic current is observed in PC + DME.

In the solutions consisting of EC-based mixed solvents (Figs. 7.6 and 7.7), the degrees of current declines with repeated potential cycling are much less than those observed in the PC-based electrolytes. Among the solutions containing  $\text{LiPF}_6$ , the highest current response is observed for EC + DEC. On the other hand, the solution based on EC + DME gives the highest intercalation/deintercalation currents among the  $\text{LiCF}_3\text{SO}_3$  solutions. These results suggest that the cathodic reactions (lithium intercalation/deintercalation itself and electrolyte decomposition as a side reaction) on the carbon fiber electrode are much affected by not only the solvent composition but also the electrolyte salt (anion).

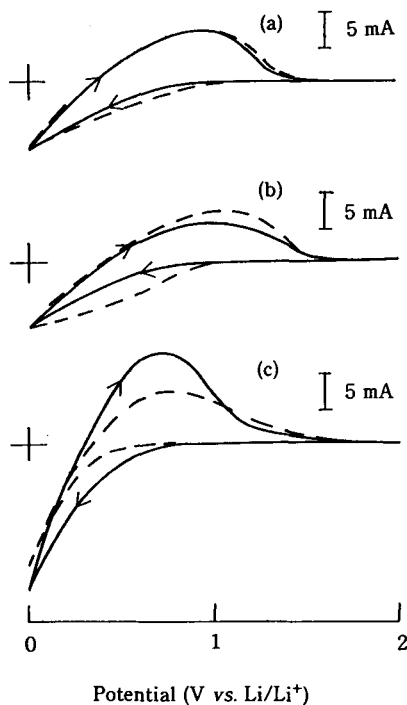


Fig. 7.6 Potential sweep voltammograms obtained at a carbon fiber electrode in EC-based solutions containing 1 M  $\text{LiCF}_3\text{SO}_3$ . (a) EC + DMC (50 + 50), (b) EC + DEC (50 + 50), (c) EC + DME (50 + 50), Broken lines: 1st cycle, Solid lines: 10th cycle, Sweep rate:  $0.01 \text{ V}\cdot\text{s}^{-1}$ . [M. Ishikawa *et al.*, *J. Electrochem. Soc.*, **141**, 1108 (1994)]

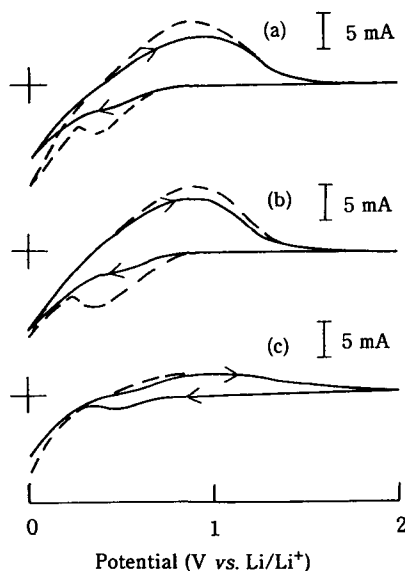


Fig. 7.7 Potential sweep voltammograms obtained at a carbon fiber electrode in EC-based solutions containing 1 M LiPF<sub>6</sub>. (a) EC + DMC (50 + 50), (b) EC + DEC (50 + 50), (c) EC + DME (50 + 50), Broken lines: 1st cycle, Solid lines: 10th cycle, Sweep rate: 0.01 V·s<sup>-1</sup>. [M. Ishikawa *et al.*, *J. Electrochem. Soc.*, **141**, 1108 (1994)]

### 7.3.2 Charge/Discharge Characteristics of the Carbon Fiber Electrode in LiCF<sub>3</sub>SO<sub>3</sub> Solutions

Figure 7.8 shows the potential–time curves during charge/discharge cycles of the carbon fiber electrode in PC-based electrolytes containing 1 M LiCF<sub>3</sub>SO<sub>3</sub>.<sup>34)</sup> The current density of the cycling was 20 mA·g<sup>-1</sup>. For the PC + DME system, a long plateau is observed at about 1.0 V to 0.8 V vs. Li/Li<sup>+</sup> in the first charging cycle, and then the potential gradually decreased to reach 0 V. On the other hand, for PC + DMC, PC + DEC and PC without co-solvents, a short plateau is present at about 0.8 V in the first charging, and then a long plateau is observed at about 0.1 V. It is known that a decomposition reaction of PC occurs at around 0.8 V on a graphite surface,<sup>30)</sup> and the lithium intercalation into the graphite structure proceeds at about 0.1 V or less positive potential. As the longer potential plateau during the charging process is characteristic of the PC + DME system, decomposition of co-solvent DME is also a possible reaction, as well as the exfoliation of the graphite structure,<sup>35)</sup> with a mechanism similar to that proposed for reactions in PC-based electrolytes.<sup>11,30)</sup>

The charge/discharge behavior in EC-based solutions containing 1 M LiCF<sub>3</sub>SO<sub>3</sub> is shown in Fig. 7.9.<sup>34)</sup> The charge/discharge profiles in these electrolytes are quite different from those obtained in PC-based electrolytes. That is, no potential plateau is observed at around 0.8 V during the charging process, and a long potential decay appears at which the lithium intercalation may occur. In the discharging process, even for the 20th cycle, the corresponding potential plateau is observed and a sufficiently long discharging period is obtained. These suggest that the reversibility of the carbon fiber electrode is excellent in

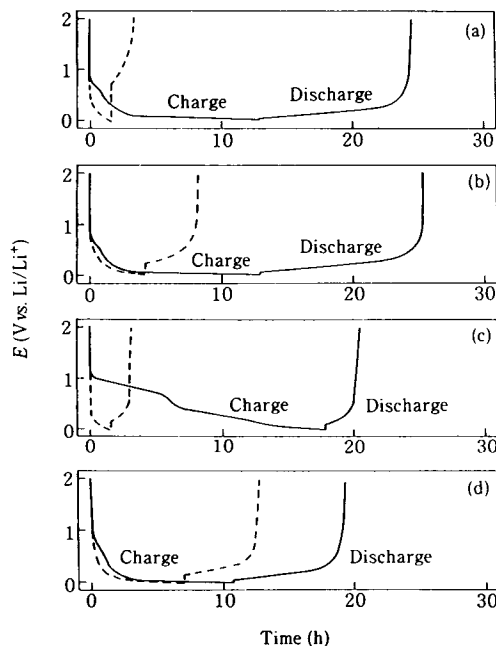


Fig. 7.8 Charge/discharge curves of a carbon fiber electrode in PC-based solutions containing 1 M  $\text{LiCF}_3\text{SO}_3$ ,  $i_{\text{ch}} = i_{\text{dis}} = 20 \text{ mA} \cdot \text{g}^{-1}$ . (a) PC + DMC (50 + 50), (b) PC + DEC (50 + 50), (c) PC + DME (50 + 50), (d) PC, Solid lines: 1st cycle, Broken lines: 10th cycle. [M. Ishikawa *et al.*, *J. Electrochem. Soc.*, **141**, 1107 (1994)]

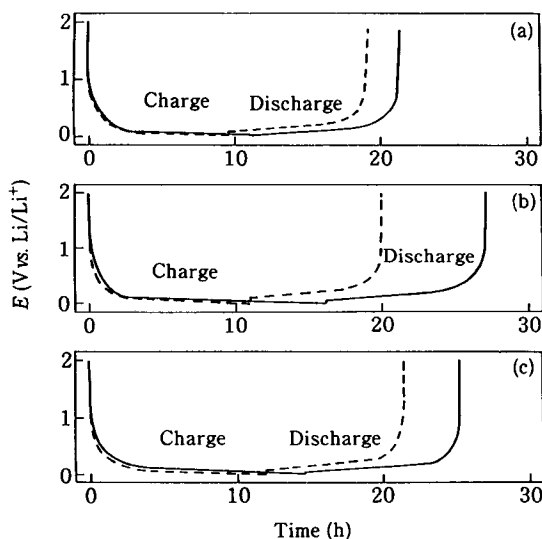


Fig. 7.9 Charge/discharge curves of a carbon fiber electrode in EC-based solutions containing 1 M  $\text{LiCF}_3\text{SO}_3$ ,  $i_{\text{ch}} = i_{\text{dis}} = 20 \text{ mA} \cdot \text{g}^{-1}$ . (a) EC + DMC (50 + 50), (b) EC + DEC (50 + 50), (c) EC + DME (50 + 50), Solid lines: 1st cycle, Broken lines: 20th cycle. [M. Ishikawa *et al.*, *J. Electrochem. Soc.*, **141**, 1107 (1994)]



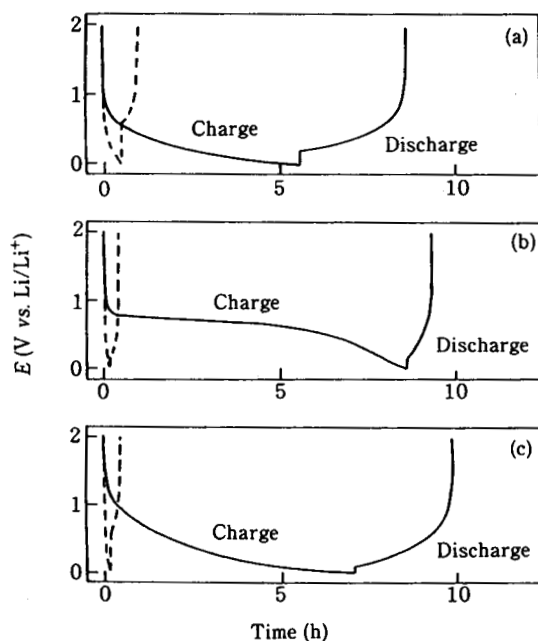


Fig. 7.10 Charge/discharge curves of a carbon fiber electrode in EC-based solutions containing 1 M  $\text{LiPF}_6$ ,  $i_{\text{ch}} = i_{\text{dis}} = 20 \text{ mA} \cdot \text{g}^{-1}$ . (a) EC + DMC (50 + 50), (b) EC + DEC (50 + 50), (c) EC + DME (50 + 50), Solid lines: 1st cycle, Broken lines: 5th cycle.  
[M. Ishikawa *et al.*, *J. Electrochem. Soc.*, **141**, 1107 (1994)]

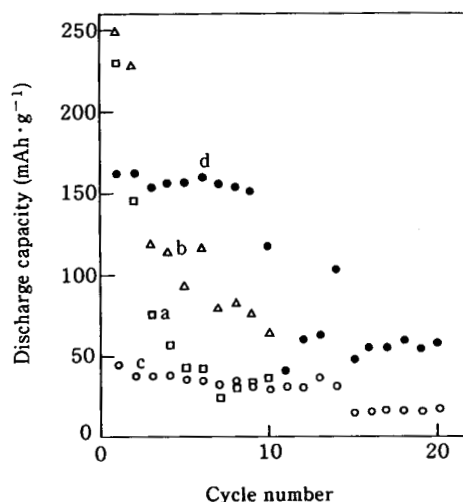


Fig. 7.11 Discharge capacity of a carbon fiber electrode for charge/discharge cycling in PC-based solutions containing 1 M  $\text{LiCF}_3\text{SO}_3$ .  $i_{\text{ch}} = i_{\text{dis}} = 20 \text{ mA} \cdot \text{g}^{-1}$ , Cut-off potential: 0–2.0 V vs.  $\text{Li/Li}^+$ , (a) PC + DMC (50 + 50), (b) PC + DEC (50 + 50), (c) PC + DME (50 + 50), (d) PC.  
[M. Ishikawa *et al.*, *J. Electrochem. Soc.*, **141**, 1107 (1994)]

the EC-based  $\text{LiCF}_3\text{SO}_3$  electrolyte system.

In EC-based solutions containing 1 M  $\text{LiPF}_6$ , however, the charging potential gradually decreases from about 1.0 V to 0 V, as shown in Fig. 7.10.<sup>34)</sup> Such a potential profile is quite different from that observed in EC-based solutions containing  $\text{LiCF}_3\text{SO}_3$ . Generally, the electrolytes consisting of  $\text{LiPF}_6$  are believed to be suitable for carbon-based negative electrodes.<sup>31)</sup> Under the present experimental conditions, however, the electrolyte solutions containing  $\text{LiCF}_3\text{SO}_3$  show better suitability, especially for the carbon fiber with a highly graphitized structure, than those containing  $\text{LiPF}_6$ .

Figure 7.11 shows the variations in the discharge capacity in PC-based solutions containing 1 M  $\text{LiCF}_3\text{SO}_3$  with the charge/discharge cycle.<sup>34)</sup> In every electrolyte system the capacity decreases with the cycle number, reaching a value of less than  $120 \text{ mAh} \cdot \text{g}^{-1}$  after the 10th cycle. The capacity loss may be caused by such side reactions as decomposition of the electrolyte and exfoliation of the graphite structure. On the other hand, the discharge capacities in EC-based  $\text{LiCF}_3\text{SO}_3$  solutions are high and stable with cycling, as shown in Fig. 7.12.<sup>34)</sup> The capacities at the first cycle are  $200 \text{ mA} \cdot \text{g}^{-1}$  or higher, corresponding to the composition of  $\text{Li}_{0.55-0.60}\text{C}_6$ . No significant degradation of the capacity is observed even after the 20th cycle.

With respect to the coulombic efficiency for cycling in EC-based electrolytes, about 98% of the efficiency is obtained in the EC + DMC system, where no degradation of the efficiency is shown after the repeated cycles (Fig. 7.12). In the systems of EC + DME and EC + DEC, the efficiencies are rather low, *ca.* 80%, but remain stable with cycling. For a comparison, the discharge capacities in  $\text{LiPF}_6$  solutions with EC-based solvents have also been examined. The efficiencies were about 60% or lower, even in the first cycle. After the 10th cycle, every system showed very low efficiency.<sup>34)</sup> These results are consistent with the discussion on voltammetric behavior (Figs. 7.5–7.7). In conclusion, the EC-based

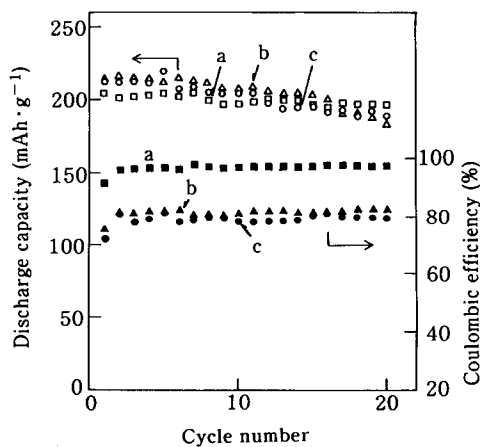


Fig. 7.12 Discharge capacity and coulombic efficiency of a carbon fiber electrode for charge/discharge cycling in EC-based solutions containing 1 M  $\text{LiCF}_3\text{SO}_3$ .  $i_{\text{ch}} = i_{\text{dis}} = 20 \text{ mA} \cdot \text{g}^{-1}$ , Cut-off potential: 0–2.0 V vs.  $\text{Li}/\text{Li}^+$ , (a) EC + DMC (50 + 50), (b) EC + DEC (50 + 50), (c) EC + DME (50 + 50), Open symbols: Discharge capacity, Closed symbols: Coulombic efficiency.

[M. Ishikawa *et al.*, *J. Electrochem. Soc.*, **141**, 1108 (1994)]

electrolyte systems dissolving  $\text{LiCF}_3\text{SO}_3$  are more compatible with the pitch-based carbon fiber negative electrode than the systems containing  $\text{LiPF}_6$  as the salt. The low viscosity solvent also affects the charge/discharge performance of the carbon fiber electrode to a considerable extent.

#### 7.4 Effects of the Electrolyte Composition on the Electrode Characteristics of Graphitized Mesocarbon Microbeads (MCMB)

In the previous section, we have described the  $\text{LiCF}_3\text{SO}_3$  solutions having excellent suitability for the pitch-based carbon fiber electrode with graphite structure. A shortcoming of this electrolyte system is low conductivity that is about one half that of the corresponding electrolyte system dissolving  $\text{LiPF}_6$ . This drawback may limit the extensive application of  $\text{LiCF}_3\text{SO}_3$  as the electrolytic salt in practical battery systems. Recently, considerable interest has been focused on lithium bis(trifluoromethanesulfonyl) imide [ $\text{Li}(\text{CF}_3\text{SO}_2)_2\text{N}$ : lithium imide salt] as an alternative salt for rechargeable lithium batteries. The electrolytic solutions of  $\text{Li}(\text{CF}_3\text{SO}_2)_2\text{N}$  show high ionic conductivity comparable to that of  $\text{LiPF}_6$  solutions, and has as good thermal stability as  $\text{LiCF}_3\text{SO}_3$ .<sup>36,37)</sup>

So far little has been published about the suitability of  $\text{Li}(\text{CF}_3\text{SO}_2)_2\text{N}$  for the carbon electrode with a highly graphitized structure,<sup>38)</sup> although there have been some reports on the fundamental properties of  $\text{Li}(\text{CF}_3\text{SO}_2)_2\text{N}$  and attempts to apply it to rechargeable battery systems with disordered carbon negative electrodes as well as lithium metal anodes.<sup>36-40)</sup> We describe herein the suitability of  $\text{Li}(\text{CF}_3\text{SO}_2)_2\text{N}$  for a mesocarbon microbead (MCMB) electrode with a highly graphitized structure. The experimental results<sup>41)</sup> of charge/discharge cycling tests and ac impedance measurements during the cathodic charge of the MCMB electrode are presented. The effects of the electrolyte composition on the electrochemistry of the carbon electrode/organic electrolyte interface are briefly discussed.

MCMB, produced from coal-tar pitch, were received from Osaka Gas Co., Ltd. Details of the preparation are described elsewhere.<sup>42-44)</sup> The average particle size is about 6  $\mu\text{m}$ , and the graphitized temperature (Heat Treatment Temperature, HTT) was 2800 °C. The crystallographic parameters of resulting MCMB were:  $d_{002}=0.337$  nm,  $a_0=0.246$  nm,  $L_c=46$  nm and  $L_a=61$  nm.<sup>44)</sup> The test electrode was made from a slurry consisting of a mixture of 95 wt% MCMB and 5 wt% poly(vinylidene fluoride) (PVDF) binder dispersed in 1-methyl-pyrrolidin-2-one (NMP). Average mass of MCMB on a copper substrate (0.95  $\text{cm}^2$ ) was about 15 mg. Electrochemical experiments were carried out at room temperature (18–24 °C) in a dry Ar atmosphere.

##### 7.4.1 Charge/Discharge Performance of MCMB in Electrolyte Solutions of Lithium Imide Salt

Figure 7.13 shows a typical result for the constant-current charge/discharge cycling test of a coin cell (2032 type) with MCMB test electrode and a lithium metal counter electrode.<sup>41)</sup> The electrolyte solutions are 1 M  $\text{Li}(\text{CF}_3\text{SO}_2)_2\text{N}$  in EC + DMC (Fig. 7.13a) and in EC + DEC (Fig. 7.13b). Since the surface area of the lithium metal counter electrode is much greater than that of the MCMB test electrode, the variation of the cell voltage is practically equivalent to that in the potential of the MCMB test electrode. At the first

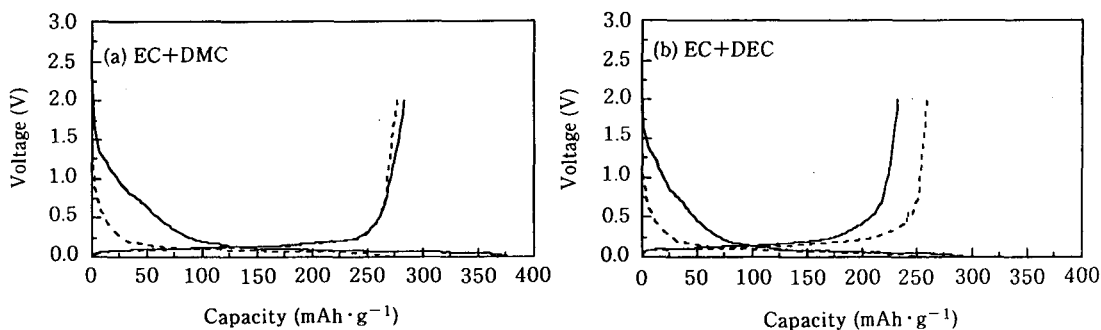


Fig. 7.13 Charge/discharge curves of a coin-type cell consisting of an MCMB working and a lithium metal counter electrodes, with 1 M  $\text{Li}(\text{CF}_3\text{SO}_2)_2\text{N}$  solutions. Electrolyte solvent: EC + DMC (a) and EC + DEC (b), Solid lines: 1st cycle, Broken lines: 5th cycle.

charging (cathodic polarization of MCMB), the cell voltage gradually decreases to about 0.25 V, and then a long plateau is observed in both cells using the EC + DMC and EC + DEC as the electrolyte solvent. At the fifth charging cycle the former high voltage region ( $>0.25$  V) becomes shorter and the voltage plateau to 0 V remains long. On the other hand, the discharge profiles observed at the first and fifth cycles in each system are essentially the same in long plateaus from 0 V to 0.25 V followed by steep increases to 2.0 V or above. For both electrolyte systems, a considerable capacity difference between the first charge and the first discharge, so-called retention, is observed. The retention disappears after the first cycle in both electrolytes. The retention at the first cycle as well as the above-mentioned potential profiles for the charging and discharging are typical for the electrodes consisting of highly graphitized carbon materials.<sup>42-46</sup> The retention phenomenon is generally ascribed to the decomposition of electrolyte components during the charging process and to the lithium remaining in the host carbon even after the

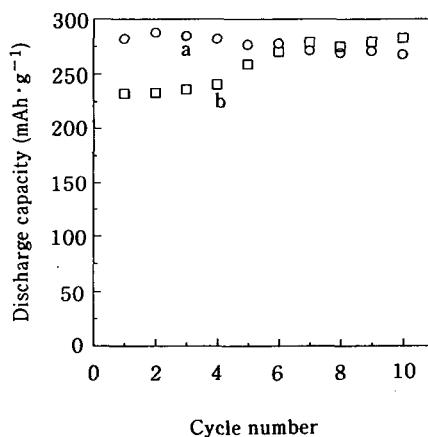


Fig. 7.14 Variations in the discharge capacity of an MCMB electrode with cycle number. Electrolyte solution: 1 M  $\text{Li}(\text{CF}_3\text{SO}_2)_2\text{N}$  in EC + DMC (a) and EC + DEC (b).

discharging process. However, if retention does not cause degradation of the charge/discharge capacities and cyclability after the first cycle, there will be no harm in the battery performance.<sup>47)</sup> The cathodic decomposition of the electrolyte during the charging process often forms a protective film at the electrode surface that inactivates the active sites inducing undesirable side reactions at the carbon surface.<sup>47)</sup>

Figure 7.14 shows the cycle dependence of the discharge capacity of the MCMB electrode examined using coin cells with EC+DMC and EC+DEC solutions containing  $\text{Li}(\text{CF}_3\text{SO}_2)_2\text{N}$ .<sup>41)</sup> The EC+DMC electrolyte system gives almost stable transition in the discharge capacity during repeated cycles. The discharge capacity of the cell with the EC+DEC system gradually increases until the sixth cycle to reach the same capacity as that obtained in the EC+DMC system ( $270\text{--}280\text{ mAh}\cdot\text{g}^{-1}$ ). The “maximum discharge capacity” of MCMB graphitized at  $2800^\circ\text{C}$  has been reported as  $282\text{ mAh}\cdot\text{g}^{-1}$ , taking into account a small amount of turbostratic structure contained in the bulk graphite structure.<sup>44)</sup> Therefore, the lithium imide salt,  $\text{Li}(\text{CF}_3\text{SO}_2)_2\text{N}$ , is regarded as one of the most attractive electrolytic salts for highly graphitized carbon electrodes such as MCMB treated at high temperatures because it guarantees a stable discharge capacity nearly equal to the “maximum capacity” even at repeated charge/discharge cycles. The coulombic efficiency for the charge/discharge cycle is practically 100% throughout the repeated cycles in both electrolyte systems except for the first cycle.

#### 7.4.2 Interfacial Characteristics between the MCMB Electrode and the Electrolyte Solutions Containing Lithium Imide Salt

In order to obtain information on the interface between the MCMB electrode and the electrolyte solution, ac impedance measurements have been carried out. Cole-Cole plots obtained before and during the cathodic charge are shown in Fig. 7.15, where the frequency is scanned from 65 kHz to 10 mHz.<sup>41)</sup> An arc observed in the high frequency region (the left part of the profiles) is probably due to the charge-transfer process between lithium ion and the host carbon as well as to the ohmic resistance of the bulk electrolyte. It is probably not due to the film derived from the decomposition of the electrolytes at the carbon surface because almost the same arc is observed even before the cathodic charging. There is no significant change in the shape of the arc in the high frequency region during the charging process in either electrolyte system. The arc observed in the EC+DEC system is somewhat larger than that in the EC+DMC system, suggesting that the interfacial resistance in the former electrolyte is slightly higher than that in the latter system. The difference in resistance between the two electrolyte systems at the first charge is related to the difference in the first discharge capacity between the corresponding systems, as shown in Figs. 7.13 and 7.14.

It is notable that the appearance of a new arc as well as an increase in the size of the original arc due to the film formation in the Cole-Cole plots can hardly be observed during the charging process to the negative potential. On the other hand, the film formation obviously detectable by the ac impedance analysis at the first charge (in this case, the film has high resistance) has been reported in most electrolyte systems containing  $\text{LiPF}_6$ . According to previous work, the film formation usually occurs at a potential below 1 V during the first charge on the surface of highly graphitized carbon electrodes.<sup>45–47)</sup> Even if the film is formed during the first charging process in the electrolyte solution containing the

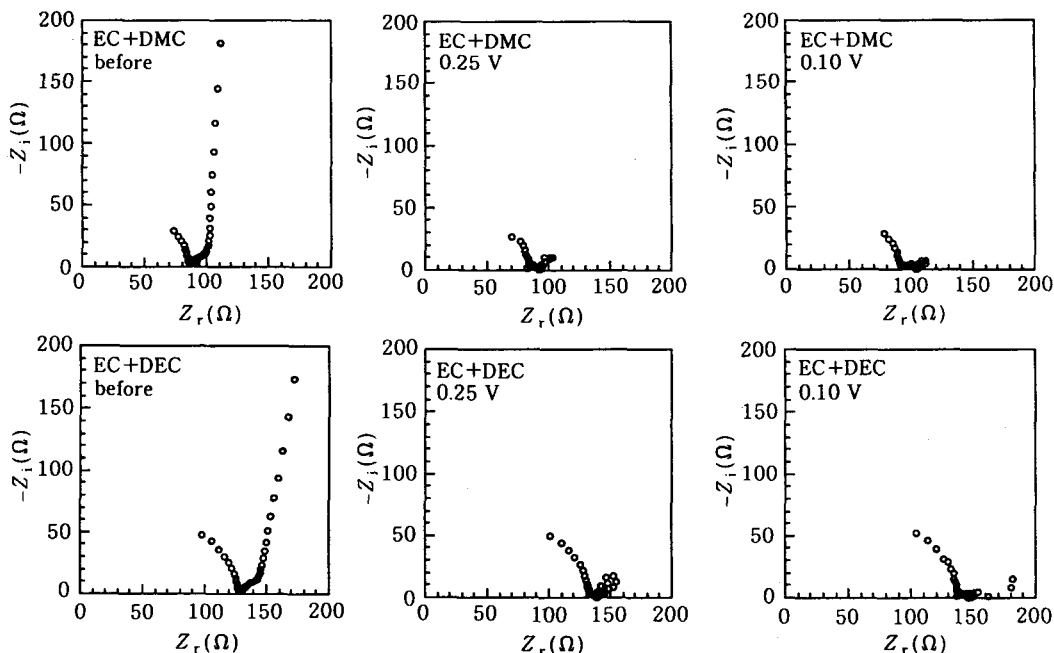


Fig. 7.15 Cole-Cole plots obtained for an MCMB electrode before and during the charge at each potential (0.25, 0.10 V vs.  $\text{Li}/\text{Li}^+$ ) in EC + DMC and EC + DEC containing 1 M  $\text{Li}(\text{CF}_3\text{SO}_2)_2\text{N}$ .

lithium imide salt,  $\text{Li}(\text{CF}_3\text{SO}_2)_2\text{N}$ , the film resistance should be rather low, judging from the ac impedance response observed in Fig. 7.15. Thus, the “retention” in the  $\text{Li}(\text{CF}_3\text{SO}_2)_2\text{N}$  solutions shown in Fig. 7.13 should not contribute to the film formation causing the degradation of the discharge capacity.

In conclusion, the lithium imide salt,  $\text{Li}(\text{CF}_3\text{SO}_2)_2\text{N}$ , provides a stable interface between the MCMB electrode and the organic electrolytes during the cathodic charge. This desirable property should lead to excellent stable charge/discharge performance of the MCMB electrode in EC-based electrolytes containing  $\text{Li}(\text{CF}_3\text{SO}_2)_2\text{N}$ .

## 7.5 Effects of Electrolyte Composition on the EQCM Response of Graphite during Cathodic Lithium Intercalation

As demonstrated above, the electrode performance of carbonaceous material depends on the electrolyte system used in the battery. The electrochemical stability of the solution and the chemistry at the electrode/electrolyte interface are considered to be major factors affecting the rechargeable capacity and cycling performance of the system. However, the effects of electrolyte composition on the electrochemical intercalation process itself are insufficiently understood at present.

In this section the influences of the co-solvent and the salt in EC-based electrolytes on the cathodic processes of a graphite electrode are discussed. We have applied an electrochemical quartz crystal microbalance (EQCM) technique to monitor the mass

changes in the electrodes during cathodic polarization. The utilization and effectiveness of the EQCM technique has already been reported for studies on the electrode processes in battery systems using organic electrolytes.<sup>48-51)</sup> To our knowledge, however, little has been published concerning mass changes for carbon-based negative electrodes during charge and discharge processes in organic electrolytes.<sup>52,53)</sup> We demonstrate here the usefulness of the EQCM technique for analyzing the cathodic processes of the carbon electrode in organic solutions containing lithium salts.

The electrode material used here was powdered artificial graphite (Lonza KS6, average particle size: *ca.* 6  $\mu\text{m}$ , BET surface area: *ca.* 20  $\text{m}^2\cdot\text{g}^{-1}$ ). Two types of test electrodes were prepared for X-ray diffraction (XRD) and EQCM measurements.<sup>52,53)</sup> (i) For the XRD experiments, graphite powder was mixed with fluoro-resin binder (14 wt%) and then molded on a nickel screen current collector to form a thin tablet (bulk electrode: 13 mm $\phi$ , about 0.5 mm thick). (ii) For the EQCM experiments, a thin graphite film was coated on a nickel-sputtered quartz crystal piece (AT-cut,  $f_0 = 6$  MHz) using a spin coating technique (film electrode). The coating solution was a graphite/cyclohexane slurry containing 2 wt% EPDM (ethylene propylene diene monomer) binder. The resulting quartz crystal is loaded with approximately 0.1  $\text{mg}\cdot\text{cm}^{-2}$  graphite powder. The electrolytes are mixed solvent systems based on EC with PC, DMC or DEC as the co-solvents (EC + PC, EC + DMC and EC + DEC; 50 + 50 by volume). Dehydrated  $\text{LiClO}_4$  or  $\text{Li}(\text{CF}_3\text{SO}_2)_2\text{N}$  as the electrolyte salt is dissolved in the mixed solvents to yield 1.0 M solutions. The EQCM experiments were carried out at room temperature (18–24  $^\circ\text{C}$ ) in a dry Ar atmosphere.

### 7.5.1 Effects of Solvent Composition on the First Charging Process

Figure 7.16 shows typical EQCM results obtained for a graphite (KS6) electrode in different electrolyte systems containing 1 M  $\text{LiClO}_4$  as the salt. The changes in the electrode potential and the resonance frequency are plotted against the charging capacity (quantity of electricity passed:  $Q$ ) under constant-current ( $30\ \mu\text{A}\cdot\text{cm}^{-2}$ ) polarization. The total charging capacity where the potential reaches 0 V vs.  $\text{Li}/\text{Li}^+$  depends on the electrolyte

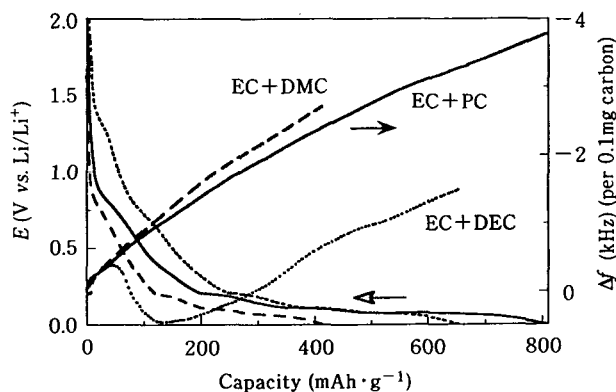


Fig. 7.16 Potential and frequency changes with charging capacity for graphite (KS6) in different electrolytes containing 1 M  $\text{LiClO}_4$ . Solid line: EC + PC, Dashed line: EC + DMC, Dotted line: EC + DEC.

composition. The frequency change ( $\Delta f = f - f_0$ ) decreases monotonously with the charging capacity for the polarization in EC + PC and EC + DMC, whereas the  $\Delta f$  in EC + DEC shows a rather complicated profile. If one assumes that the frequency change is simply caused by the mass change on the quartz crystal, the mass change per quantity of electricity passed ( $\Delta m \cdot \Delta Q^{-1}$ ) is evaluated from the frequency change using Sauerbrey's equation, Eq. (7.1),<sup>54)</sup>

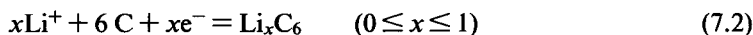
$$\Delta m = -k \cdot \Delta f \quad (7.1)$$

where  $k$  is a constant and consists of Eq. (7.1')

$$k = A \cdot (\rho_q \mu_q)^{1/2} \cdot (2f_0)^{-1} \quad (7.1')$$

where  $A$ ,  $\rho_q$  and  $\mu_q$  are geometric surface area of the electrode, density and a vibrating constant of quartz, respectively.

Figure 7.17 plots the mass changes obtained in EC + PC and EC + DMC containing 1 M LiClO<sub>4</sub> against the electrode potential. If the cathodic process consists of a simple lithium intercalation reaction, Eq. (7.2), the mass increase,  $\Delta m \cdot \Delta Q^{-1}$ , should be 6.94 g · F<sup>-1</sup> (F = 9.65 × 10<sup>4</sup> C).



In the potential region above 1.5 V vs. Li/Li<sup>+</sup>, very high values of  $\Delta m \cdot \Delta Q^{-1}$  were observed for both EC + PC and EC + DMC systems. The values of 27–35 g · F<sup>-1</sup> in the potential range of 0.5–0.8 V in EC + PC suggest that at least one other reaction proceeds in this potential region. For example, decomposition of the solvent PC yielding precipitation of Li<sub>2</sub>CO<sub>3</sub> on the surface of the graphite, Eq. (7.3), would lead to a mass increase of 36.9 g · F<sup>-1</sup>.

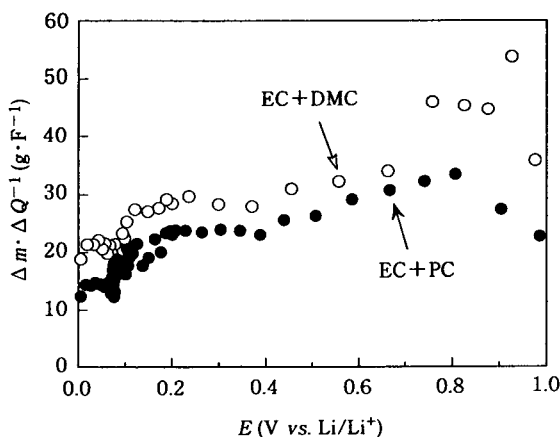
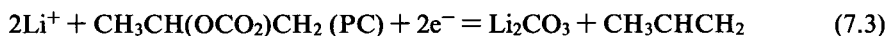


Fig. 7.17 Variations in  $\Delta m \cdot \Delta Q^{-1}$  with  $E$  for graphite (KS6) in different electrolytes containing 1 M LiClO<sub>4</sub>. Closed circles: EC + PC, Open circles: EC + DMC.



In PC-based solutions, Aurbach *et al.*<sup>55)</sup> detected some organic carbonates on a graphite surface by FTIR spectroscopy. In that case, the mass change should be higher than the value of  $36.9 \text{ g} \cdot \text{F}^{-1}$ . Thus, the observed mass change being lower than that expected from reaction (7.3) would be due to the conversion of the organic carbonate to lower molecular weight compounds such as  $\text{Li}_2\text{CO}_3$  which may occur through a reaction with trace water in the system, as shown in Eq. (7.4).<sup>51)</sup>



We assume that some competitive reactions occur on the graphite surface as well as Li incorporation in the graphite bulk under these polarization conditions. As  $\Delta m \cdot \Delta Q^{-1}$  decreases slightly with decrease in potential, the process probably depends on the electrode potential. A minimum  $\Delta m \cdot \Delta Q^{-1}$  value is observed at potentials below 0.1 V in EC + PC containing  $\text{LiClO}_4$ , but is still about 15. This means that, even at such less positive potentials, the cathodic lithium intercalation into graphite structure is accompanied by some side reactions such as Eqs. (7.3) and/or (7.4). No proof of the net solvent co-intercalation<sup>56,57)</sup> is present because the observed  $\Delta m \cdot \Delta Q^{-1}$  values are much lower than that expected from the molecular weight of the solvent.

The mass change observed in EC + DMC dissolving  $\text{LiClO}_4$  is apparently higher than that in EC + PC, especially in the lower potential region below 0.5 V. Yoshida *et al.* detected  $\text{CH}_3\text{OLi}$  as a cathodic decomposition product on the graphite surface in DMC-based electrolytes.<sup>17)</sup> The EQCM result may reflect such a difference in the decomposition product on the graphite surface depending on the organic solvent.

### 7.5.2 Effects on the Structure Changes of Graphite during the Charge/Discharge Process

Figures 7.18 and 7.19 shows a comparison of the XRD patterns obtained for the bulk graphite electrode before and after the constant-current charging and discharging in EC-based solutions containing 1 M  $\text{LiClO}_4$  as the salt. The XRD patterns showed the formation of graphite intercalation compounds (GICs) mainly with a stage-2 structure ( $\text{LiC}_{12}$ ) after the first charging process in the EC + PC electrolyte system (Fig. 7.18). The electrochemical intercalation/deintercalation process in this electrolyte system is generally reversible, as shown in the diffraction patterns after subsequent cycles. On the other hand, the charging in EC + DMC containing  $\text{LiClO}_4$  gives a rather complicated diffraction pattern (Fig. 7.19). The main peak at  $d = 0.368 \text{ nm}$  is not ascribed to any stage structures of Li-GICs. Another peak is also observed at a higher diffraction angle than that based on the stage-2 structure. However, the XRD pattern after discharging proves that the process is essentially reversible. We conclude that the electrochemical Li intercalation into graphite from EC + DMC dissolving  $\text{LiClO}_4$  may be accompanied by co-intercalation of either a solvent molecule or, more possibly, a fragment of the decomposed solvent.<sup>57)</sup>

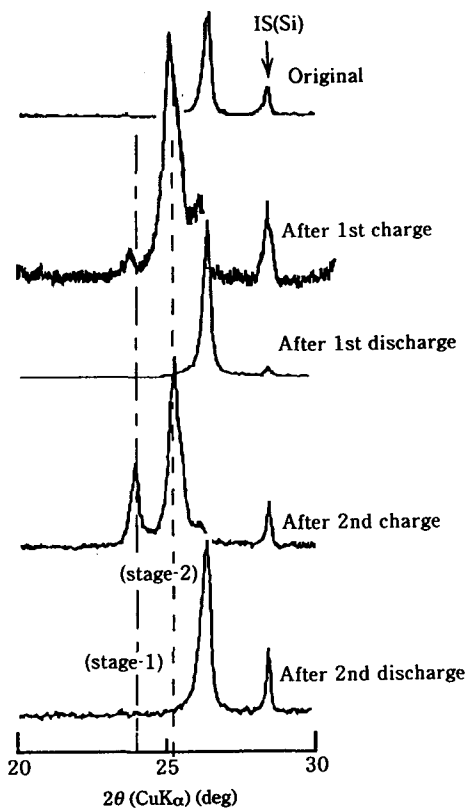


Fig. 7.18 XRD patterns for graphite (KS6) after charge and discharge cycles in 1 M LiClO<sub>4</sub>/EC+PC.

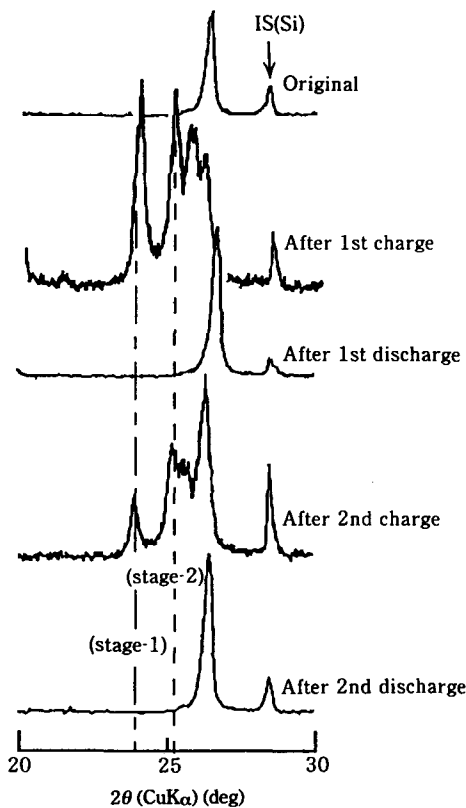


Fig. 7.19 XRD patterns for graphite (KS6) after charge and discharge cycles in 1 M LiClO<sub>4</sub>/EC+DMC.

### 7.5.3 Effects of the Electrolytic Salt on the EQCM Response of Graphite

The effects of the electrolyte salt are also observed on the EQCM response of the graphite film electrode. Typical results are shown in Fig. 7.20, where the mass change-electrode potential relations ( $\Delta m \cdot \Delta Q^{-1}$  vs.  $E$  plots) are compared between the electrolytic solutions containing LiClO<sub>4</sub> and Li(CF<sub>3</sub>SO<sub>2</sub>)<sub>2</sub>N. The mass changes ( $\Delta m \cdot \Delta Q^{-1}$ ) in the potential region below 0.1 V are about 7–15 in the solution of EC+DMC containing 1 M Li(CF<sub>3</sub>SO<sub>2</sub>)<sub>2</sub>N, whereas  $\Delta m \cdot \Delta Q^{-1}$  in the EC+DMC solution containing 1 M LiClO<sub>4</sub> varies in the range of 20–25. The lower value of the mass change in the Li(CF<sub>3</sub>SO<sub>2</sub>)<sub>2</sub>N solution seems to be related with higher coulombic capacities of the graphite-based negative electrode in Li(CF<sub>3</sub>SO<sub>2</sub>)<sub>2</sub>N solutions, as described in the previous section. Further experimental work should clarify in detail the effects of the salt on the charge-discharge performance of the graphite-based negative electrode.

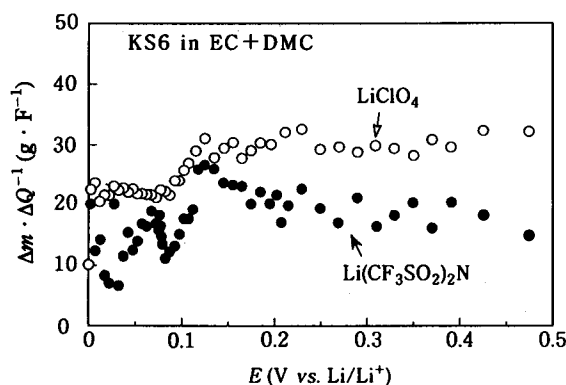


Fig. 7.20 Variations in  $\Delta m \cdot \Delta Q^{-1}$  with  $E$  for graphite (KS6) in 1 M  $\text{LiClO}_4/\text{EC} + \text{DMC}$  (open circles) and 1 M  $\text{Li}(\text{CF}_3\text{SO}_2)_2\text{N}/\text{EC} + \text{DMC}$  (closed circles).

## 7.6 Concluding Remarks

With respect to organic electrolyte solutions for rechargeable lithium (ion) batteries, the technology is still under investigation. New electrolyte systems have been proposed. For most of those new systems, however, we have no information even on the basic structures and properties. Recently, a newer approach has been proposed for a better understanding of the electrochemistry of organic electrolyte systems. Some research groups have applied theoretical calculations using computer chemistry to analyses of the ionic structure and behavior in organic solvent systems.<sup>58,59)</sup>

The development of rechargeable batteries with advanced performance will become a more important issue with growing public demand. Recent international meetings on battery technologies (e.g., 8th International Meeting on Lithium Batteries, Nagoya, Japan; *J. Power Sources*, **68** (1997)) have provided attractive results on the issue of the effects of the electrolyte on the battery performance. More researchers and scientists are expected to take part in this project, providing a variety of approaches.

## REFERENCES

- 1) G.E. Blomgren, *Lithium Batteries* (Ed. by J. P. Gabano), Ch. 2, Academic Press (1983).
- 2) Y. Matsuda, *Nippon Kagaku Kaishi (J. Chem. Soc. Jpn.)*, **1989**, 1 (1989).
- 3) Y. Matsuda and H. Satake, *J. Electrochem. Soc.*, **127**, 877 (1980).
- 4) Y. Matsuda, H. Nakashima, M. Morita and Y. Takasu, *J. Electrochem. Soc.*, **128**, 2552 (1981).
- 5) V. Gutmann, *The Donor-Acceptor Approach to Molecular Interactions*, Ch. 2, Plenum Press (1978).
- 6) K.M. Abraham and S.B. Brummer, *Lithium Batteries* (Ed. by J. P. Gabano), Ch. 14, Academic Press (1983).
- 7) Y. Matsuda, M. Morita and F. Tachihara, *Bull. Chem. Soc. Jpn.*, **59**, 1967 (1986).
- 8) Y. Matsuda, M. Morita and K. Kosaka, *J. Electrochem. Soc.*, **130**, 101 (1982).
- 9) R.A. Robinson and R.H. Stokes, *Electrolyte Solutions*, p. 124, Butterworths (1959).
- 10) M. Arakawa and J. Yamaki, *J. Electroanal. Chem.*, **219**, 273 (1987).
- 11) Z. X. Shu, R. S. McMillan and J.J. Murray, *J. Electrochem. Soc.*, **140**, 922 (1993).
- 12) Y. Ein-Eli, B. Markovsky, D. Aurbach, Y. Carmeli, H. Yamin and S. Luski, *Electrochim. Acta*, **39**, 2559 (1994).
- 13) D. Aurbach and Y. Ein-Eli, *J. Electrochem. Soc.*, **142**, 1746 (1995).

- 14) D. Aurbach, Y. Ein-Eli, B. Markovsky, A. Zaban, S. Luski, Y. Carmeli and H. Yamin, *J. Electrochem. Soc.*, **142**, 2882 (1995).
- 15) K. Shima, A. Kominato, K. Ida, E. Yasukawa and S. Mori, 36th Battery Symp. Jap., Kyoto, Japan, 1995, Ext. Abstr., 3C19, p. 321.
- 16) K. Yokoyama, 23rd Seminar Advan. Battery Technol., 1995, Ext. Abstr., No. 2, p. 11.
- 17) H. Yoshida, T. Fukunaga, T. Hazama, M. Terasaki, M. Mizutani and M. Yamaji, 36th Battery Symp. Jap., Kyoto, Japan, 1995, Ext. Abstr., 1B02, p. 101.
- 18) H. Kamohara, M. Ishikawa, M. Morita and Y. Matsuda, 36th Battery Symp. Jap., Kyoto, Japan, 1995, Ext. Abstr., 3C13, p. 309.
- 19) D.E. Irish, Z. Deng and M. Odziemkowski, *J. Power Sources*, **54**, 28 (1995).
- 20) P. Liu and H. Wu, *J. Power Sources*, **56**, 81 (1995).
- 21) T. Iijima, K. Suzuki and Y. Matsuda, *Syn. Met.*, **73**, 9 (1995).
- 22) A. Ohta, H. Koshina, H. Okuno and H. Murai, *J. Power Sources*, **54**, 6 (1995).
- 23) D. Billaud, A. Naji and P. Willman, *J. Chem. Soc., Chem. Commun.*, **1995**, 1867 (1995).
- 24) Z. X. Shu, R. S. McMillan and J. J. Murray, *J. Electrochem. Soc.*, **140**, L101 (1993).
- 25) M. Nagayama, H. Ikuta, T. Uchida and M. Wakihara, Fall Meet. Electrochem. Soc. Jap., 1995, Ext. Abstr. 1106, p. 162.
- 26) Z. X. Shu, R. S. McMillan, J. J. Murray and I. J. Davidson, *J. Electrochem. Soc.*, **142**, L161 (1995).
- 27) J.R. Dahn, A.K. Sleight, H. Shi, B.M. Way, W.J. Weydanz, J.N. Reimers, Q. Zhong and U.V. Sacken, *Lithium Batteries—New Materials, Developments and Perspectives* (Ed. by G. Pistoia), Ch. 1, Elsevier (1994).
- 28) R. Yazami, *Lithium Batteries—New Materials, Developments and Perspectives* (Ed. by G. Pistoia), Ch. 2, Elsevier (1994).
- 29) S. Megahed and B. Scrosati, *J. Power Sources*, **51**, 79 (1994).
- 30) A.N. Dey and B.P. Sullivan, *J. Electrochem. Soc.*, **117**, 222 (1970).
- 31) M. Nagamine, H. Kato and Y. Nishi, 33rd Battery Symp. Jap., 1992, Ext. Abstr., 1C11, p. 83.
- 32) S. Tobishima and T. Okada, *Electrochim. Acta*, **30**, 1715 (1985).
- 33) Y. Matsuda, M. Morita and K. Suetsugu, *Nippon Kagaku Kaishi (J. Chem. Soc. Jpn.)*, **1988**, 1459 (1988).
- 34) M. Ishikawa, M. Morita, M. Asao and Y. Matsuda, *J. Electrochem. Soc.*, **141**, 1105 (1994).
- 35) R. Fong, U. Sacken and J.R. Dahn, *J. Electrochem. Soc.*, **137**, 2009 (1990).
- 36) L. A. Dominey, J. L. Goldman, V.R. Koch and C. Nanjundiah, Proc. Symp. Rechargeable Lithium Batteries (Eds. by V. R. Koch *et al.*), Vol. 90-5, p. 56, The Electrochemical Society (1991).
- 37) A. Webber, *J. Electrochem. Soc.*, **138**, 2586 (1991).
- 38) T. D. Tran, J. H. Feikert, X. Song and K. Kinoshita, *J. Electrochem. Soc.*, **142**, 3297 (1995).
- 39) M. Odziemkowski and D.E. Irish, *J. Electrochem. Soc.*, **140**, 1546 (1993).
- 40) A.M. Wilson and J.R. Dahn, *J. Electrochem. Soc.*, **142**, 326 (1995).
- 41) M. Ishikawa, H. Kamohara, M. Morita and Y. Matsuda, *J. Power Sources*, **62**, 229 (1996).
- 42) K. Tatsumi, N. Iwashita, H. Sakaebe, H. Shioyama, S. Higuchi, A. Mabuchi and H. Fujimoto, *J. Electrochem. Soc.*, **142**, 716 (1995).
- 43) A. Mabuchi, K. Tokumitsu, H. Fujimoto and T. Kasuh, *J. Electrochem. Soc.*, **142**, 1041 (1995).
- 44) A. Mabuchi, H. Fujimoto, K. Tokumitsu and T. Kasuh, *J. Electrochem. Soc.*, **142**, 3049 (1995).
- 45) N. Takami, A. Satoh, M. Hara and T. Ohsaki, *J. Electrochem. Soc.*, **142**, 371 (1995).
- 46) N. Takami, A. Satoh, M. Hara and T. Ohsaki, *J. Electrochem. Soc.*, **142**, 2564 (1995).
- 47) D. Aurbach, Y. Ein-Eli, B. Markovsky, A. Zaban, S. Luski, Y. Carmeli and H. Yamin, *J. Electrochem. Soc.*, **142**, 2882 (1995).
- 48) H.-K. Park, K. Podolske, Z. Munshi, W.H. Smyrl and B.B. Owens, *J. Electrochem. Soc.*, **138**, 627 (1991).
- 49) H.-K. Park and W.H. Smyrl, *J. Electrochem. Soc.*, **141**, L25 (1994).
- 50) N. Yamamoto, H. Hirasawa, H. Ishida, T. Tatsuma and N. Oyama, *Bull. Chem. Soc. Jpn.*, **67**, 1296 (1994).
- 51) D. Aurbach and A. Zaban, *J. Electrochem. Soc.*, **142**, L108 (1995).
- 52) M. Morita, T. Ichimura, M. Ishikawa and Y. Matsuda, *J. Electrochem. Soc.*, **143**, L26 (1996).
- 53) M. Morita, T. Ichimura, M. Ishikawa and Y. Matsuda, 8th Int. Meet. Lithium Batteries, 1996, Ext. Abstr., 1A25, p. 204; *J. Power Sources*, **68** (1997).
- 54) G. Sauerbrey, *Z. Phys.*, **155**, 206 (1959).
- 55) D. Aurbach, Y. Ein-Eli, O. Chusid, Y. Carmeli, M. Babai and H. Yamin, *J. Electrochem. Soc.*, **141**, 603 (1994).
- 56) J.O. Besenhard, *Carbon*, **14**, 111 (1976).
- 57) J.O. Besenhard, M. Winter, J. Yang and W. Biberacher, *J. Power Sources*, **54**, 228 (1995).
- 58) M. Ue and S. Mori, *J. Electrochem. Soc.*, **142**, 2557 (1995).
- 59) L.G. Scanlon, Jr., W. Krawiec, A.T. Yeates and D.S. Dudis, *Electrochim. Acta*, **40**, 13 (1995).

## 8

# Performance of the First Lithium Ion Battery and Its Process Technology

Yoshio Nishi\*

### 8.1 Introduction

Since the beginning of the 1980's, portable electronic equipment has been designed to be smaller and smaller, increasing the demand for lighter, smaller and longer-lasting rechargeable batteries. While significant improvement in nickel-cadmium (Ni-Cd) batteries has been made to meet this need, energy characteristics have reached their technological limits. Moreover, cadmium has been the object of growing concern among environmentalists. These are reasons for the need to develop novel electrochemical cells.

Primary cells with metallic lithium anodes and non-aqueous electrolytes have been successfully introduced into the market. Their outstanding features in comparison with conventional dry cells with aqueous electrolytes are; (1) high voltage, (2) high energy density (both volumetric and gravimetric energy densities are very high), (3) low self-discharge rate, and (4) wide temperature range of operation.

Thus, rechargeable batteries with metallic lithium anodes have attracted much attention as a candidate for the battery of high energy density, and much effort has been made in developing secondary batteries with metallic lithium anodes.

Many practical problems, however, have been encountered in the development of rechargeable lithium batteries. Several among them are: (1) poor cycle performance, (2) the need for long charging time and (3) poor safety characteristics.

Almost all these problems are due to the dendritic formation of lithium during the charging process.

To overcome the weaknesses of the metallic lithium anode, some lithium-storing materials have been studied as anode materials, including aluminum, Wood's alloy and graphite.

Sony started its development of secondary lithium batteries with a metallic lithium anode in 1985<sup>1)</sup> and batteries with a carbonaceous anode in 1986.<sup>2)</sup> It succeeded in the development of novel rechargeable lithium batteries with carbon anodes (the name lithium ion secondary battery was given afterwards to this system) and introduced them into the market for the first time in the world in 1991.

The development of materials for lithium ion secondary batteries, their features, process technology and battery characteristics are described in this chapter.

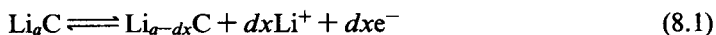
---

\* Sony Corporation  
6-7-35, Kitashinagawa, Shinagawa-ku, Tokyo 141, Japan

## 8.2 Anode Materials

Graphite has a layered structure and it is well known that graphite can be intercalated (or doped) with various atoms or atomic groups between its layers to form so-called graphite intercalation compounds (GIC), and lithium reacts with graphite to form lithium graphite intercalation compounds (Li-GIC) whose composition is  $\text{LiC}_6$ .

It has been confirmed that graphite is reduced by electrochemical intercalation (doping) with lithium in an aprotic organic electrolyte containing lithium salts to form a Li-GIC, and that a Li-GIC can be electrochemically oxidized by lithium deintercalation (undoping). This indicates that a Li-GIC can be charged and discharged as rechargeable anodes for nonaqueous cells according to Eq. (8.1).

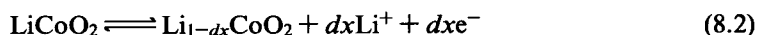


When the anode is discharged, lithium deintercalates from graphite and lithium ions dissolve into the electrolyte, and when the anode is charged, lithium intercalates between the layers of graphite.

Theoretically, a Li-GIC can be synthesized by chemical reaction of graphite with lithium or lithium compounds. Mass production of Li-GIC by chemical procedure, however, is not practical and from the battery manufacturing standpoint, pure graphite would be desirable as an anode material in place of Li-GIC. Graphite can be converted into Li-GIC inside cells through charging by utilizing lithium-containing compounds as cathode materials which can be electrochemically intercalated and deintercalated with lithium.

Goodenough *et al.*<sup>3)</sup> demonstrated that a lithium-containing cobalt compound called lithium cobaltite ( $\text{LiCoO}_2$ ) can be reversibly charged and discharged. When  $\text{LiCoO}_2$  is applied to a cathode in an electrochemical cell, lithium ions are extracted by electrochemical oxidation from the cathode compounds during charging and are inserted by electrochemical reduction during discharging. Their work stimulated further studies on this unique material,<sup>4-9)</sup> and it has been confirmed that pure graphite can be used as anode material in place of Li-GIC for rechargeable electrochemical devices when lithium cobaltite is used as the cathode material.

The composition of the  $\text{LiCoO}_2$  cathode reversibly changes during charging and discharging as indicated in Eq. (8.2).



In the lithium cobaltite cathode/graphite anode system, the overall cell reaction is that shown in Eq. (8.3)



The principle of the lithium ion secondary battery is shown in Fig. 8.1.

Several types of carbonaceous materials as well as graphite can be doped with lithium to form similar intercalation compounds. These we named carbon intercalation compounds (CICs).

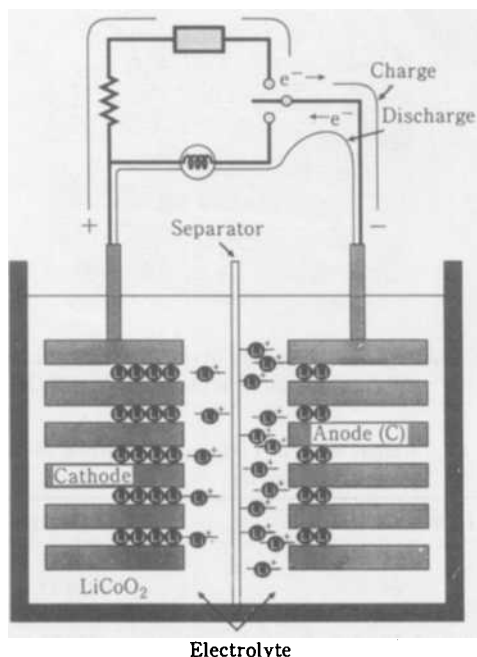


Fig. 8.1 Schematic diagram of the principles of lithium ion secondary batteries.  
[Y. Nishi, *Kiitekunorojii Denchi*, p. 73, Maruzen (1996) (in Japanese)]

There exist various classes of carbonaceous materials and it has been confirmed that certain carbonaceous materials are reduced by electrochemical lithium doping in aprotic organic electrolytes containing lithium salts to form Li-CIC's, and there is a possibility that some carbonaceous materials can be utilized as anodes of lithium ion rechargeable cells in place of graphite.

The carbon anode is a key component of the lithium ion secondary battery, and various carbon materials ranging from graphite to amorphous carbon have been proposed.

Although graphite is a passable material as an anode, several drawbacks have been observed, including poor cyclability, limitation of capacity, and anode bulging.

As discharge capacity of the cathode material is limited by the stoichiometry of lithium cobaltite ( $\text{LiCoO}_2$ ), the cell capacity depends significantly on the lithium doping capability of the anode when  $\text{LiCoO}_2$  is used as the cathode.

The lithium doping capacity of graphite, however, does not exceed  $372 \text{ mAh} \cdot \text{g}^{-1}$ , which is calculated from the stoichiometry of Li-GIC ( $\text{LiC}_6$ ).

Thus, in order to improve the energy density of the battery, it is indispensable to develop carbonaceous materials which can be doped with more lithium than the stoichiometric limitation of Li-GIC, and our efforts have focused on research of carbonaceous anodes whose lithium doping capacity is much greater than that of graphite.

Graphitizable carbon (soft carbon) and non-graphitizable carbon (hard carbon) have been chosen as candidates for the anode materials of lithium ion secondary cells in place of graphite.

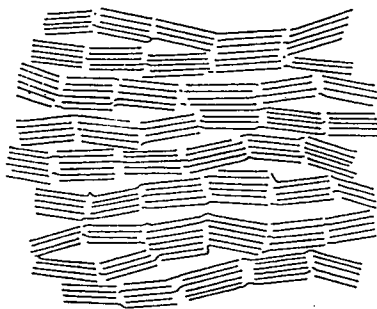


Fig. 8.2 Schematic diagram of structure of soft carbon.  
[R.E. Franklin, *Acta Cryst.*, 4, 235 (1951)]

Table 8.1 Knight shifts of Li-doped soft carbon in  $^7\text{Li}$  solid state NMR analysis.

Doping rate (%)	Knight shift (ppm)
45	-250.05
90	-239.19
100	-236.43
LiCl	-256.01

Metallic Li = 0 ppm

LiCl = reference for ionic lithium compound

Our initial efforts focused on soft carbon. This type of carbon has a considerably layered structure, as shown in Fig. 8.2. Soft carbon can be easily converted to graphite by calcination at around 3000 °C, whence the name graphitizable carbon.

We investigated the ionic state of lithium species doped into soft carbon layers by applying the  $^7\text{Li}$ -NMR technique. Knight shift of metallic lithium was taken as 0 ppm and Knight shifts of several samples of lithium doped soft carbon were determined. Lithium chloride, LiCl, was used as the reference compound for the ionic lithium compound.

The results are shown in Table 8.1. Lithium doping rates of the carbon were 45%, 90% and 100% and Knight shifts of these samples were -250.05, -239.19 and -236.43 ppm, respectively, being almost the same as that of LiCl (-256.01 ppm). It was concluded from this experiment that lithium doped into the carbon layers is in the ionic state and that no metallic lithium is present in the system.

To make a distinction from conventional secondary lithium batteries in which metallic lithium anodes are used, we have given the name "lithium ion secondary battery" to this battery system because a special ionic bond compound is used as the cathode and only lithium species in the ionic state are found in the anode.

Cokes prepared from petrochemical pitch were heat-treated at various temperatures and their charge/discharge capacities and  $d_{002}$  spacings were determined. The results are shown in Fig. 8.3 in which discharge capacities of the cokes studied in the electrolyte propylene carbonate (PC)/diethylcarbonate (DEC) with 1 M  $\text{LiPF}_6$  are plotted as functions of the cycle number,  $d_{002}$  and heat-treatment temperature (HTT). Fig. 8.3 indicates that the



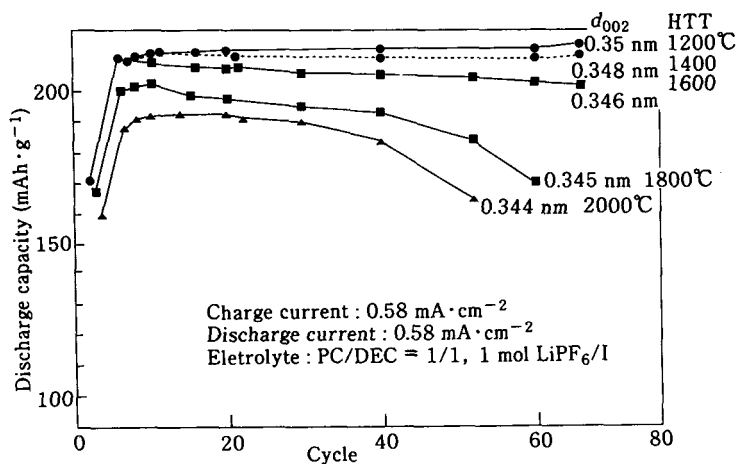


Fig. 8.3 Effects of HTT and resulting  $d_{002}$  of soft carbon on discharge capacities of cokes. Charged to 2 mV (vs. Li/Li<sup>+</sup>) Discharged to 1500 mV (vs. Li/Li<sup>+</sup>); for measuring method, see Ref. 15. [Y. Nishi, Richiumuon Nijidenchi no Hanashi, Shokabo (1997) (in Japanese)]

lower the HTT, the broader the resultant  $d_{002}$  and the higher the discharge capacity of the cokes in the temperature range investigated.

Dey and Sullivan<sup>10)</sup> investigated lithium insertion into graphite in the PC-based electrolyte and found that a decomposition reaction of the electrolyte occurs in preference to the lithium doping reaction. The results of Fig. 8.3 are likely to show that the morphology of soft carbon treated at higher temperatures approaches that of graphite and the electrolyte degrades simultaneously with lithium insertion, bringing about poorer lithium doping capability.

It is well known that  $d_{002}$  of graphite is 0.335 nm and when lithium intercalates between the layers of graphite,  $d_{002}$  spacings expand up to 0.372 nm, then shrink back to 0.335 nm again by deintercalation of lithium.

While soft carbon has slightly broader  $d_{002}$  spacings than graphite, as shown in Fig. 8.3, it is still significantly narrower than 0.372 nm and soft carbon cannot get rid of the expansion of the spacings due to lithium insertion. This was demonstrated by X-ray diffraction analysis of soft carbon doped with lithium (Fig. 8.4). The diffraction angle shifts toward the lower angle by lithium doping, indicating expansion of  $d_{002}$  spacings.

It was assumed from the results of Figs. 8.3 and 8.4 that carbonaceous materials with  $d_{002}$  spacings broader than 0.372 nm could be smoothly doped with lithium without expansion of the spacings and could be doped with much more lithium than graphite. Thus our interest focused on hard carbon with much broader spacings than graphite and soft carbon.

Hard carbon materials were prepared by carbonizing polyfurfuryl alcohol (PFA) resin at various temperatures, and charge/discharge capacity of resulting carbons were determined as well as  $d_{002}$  spacings. Discharge capacities of hard carbon (PFA carbon) prepared at various HTT's are shown in Table 8.2.

Comparison of Table 8.2 with Fig. 8.3 indicates that the discharge capacity of hard carbon is much higher than that of soft carbon. In Fig. 8.5  $d_{002}$  spacings of PFA carbon

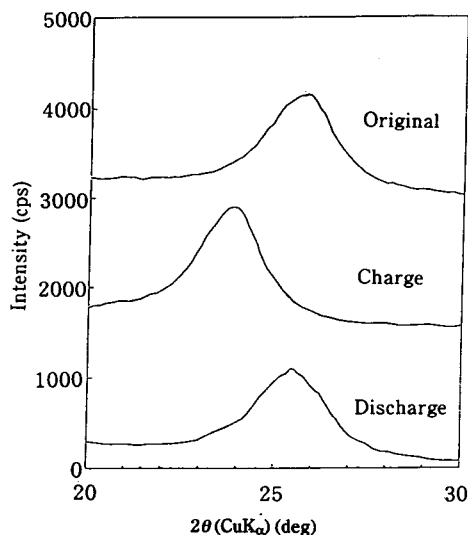


Fig. 8.4 Changes in XRD pattern of cokes with electrochemical dope/undope reaction with Li.

Table 8.2 Effects of HTT on discharge capacity of PFA carbon.

HTT (°C)	Discharge capacity (mAh·g <sup>-1</sup> )
800	264
1000	311
1100	319
1200	314
1300	312
1500	300

Charge: 0.58 mA·cm<sup>-2</sup>, to 2 mV (vs. Li/Li<sup>+</sup>)

Discharge: 0.58 mA·cm<sup>-2</sup>, to 1500 mV (vs. Li/Li<sup>+</sup>)

Electrolyte: PC/DEC (1/1), 1 mol LiPF<sub>6</sub>/L

(measuring method is described elsewhere<sup>15</sup> in detail)

are compared with soft carbon as a function of HTT and it is clearly seen from this figure that  $d_{002}$  spacings of this carbon, being over 0.372 nm at temperatures below 1500 °C, are considerably broader than those of soft carbon.

Hard carbon production from PFA is not industrially practical, and we found that petrochemical pitch crosslinked with oxygen is an excellent raw material from which hard carbon of the same morphology as PFA carbon can be prepared, and we have been using this (supplied by Kureha Chemical Co.) as the precursor of our hard carbon anode.

<sup>7</sup>Li-NMR analysis was applied to graphite and hard carbon doped with various amounts of lithium. The results are shown in Figs. 8.6 and 8.7. In these experiments Knight shift of metallic lithium was taken as 265.7 ppm (note that this is taken as 0 ppm in Table 8.1). In graphite (Fig. 8.6) doped with lithium equivalent to less than 372 mAh·g<sup>-1</sup>, a Knight shift

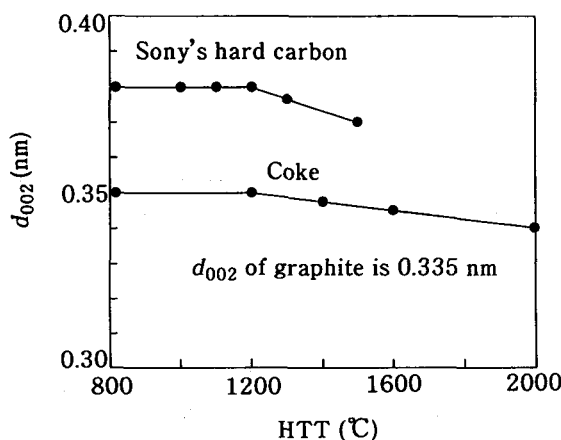


Fig. 8.5 HTT dependence of  $d_{002}$  spacings of hard carbon and soft carbon.  
[Y. Nishi, Richiumuion Nijidenchi no Hanashi, Shokabo (1997) (in Japanese)]

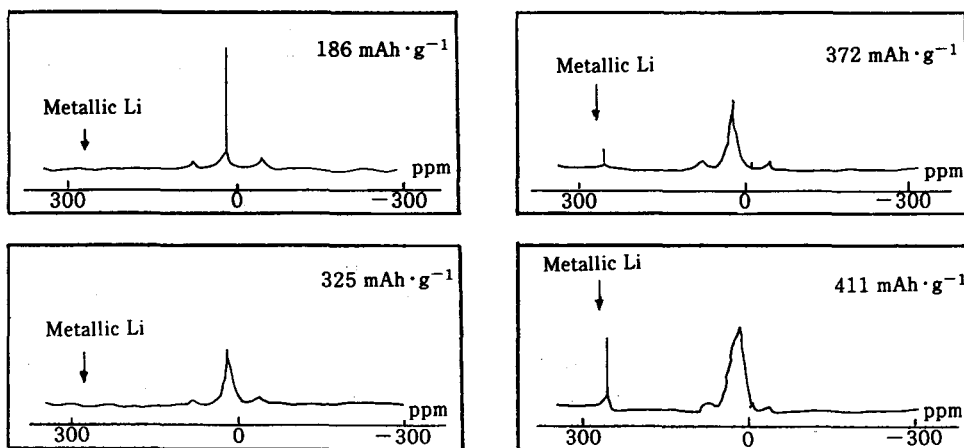


Fig. 8.6  $^7\text{Li}$  spectra of graphite doped with varying amounts of lithium.

peak corresponding to metallic lithium does not appear. A tiny peak of lithium metal is observed when lithium doping reaches  $372 \text{ mAh} \cdot \text{g}^{-1}$ , which is equivalent to the lithium content in  $\text{LiC}_6$ , and the height of the peak rises as the amount of doped lithium increases beyond the value of  $372 \text{ mAh} \cdot \text{g}^{-1}$ , which means that all the excess lithium deposits on the surface of graphite as metallic lithium.

On the other hand, in the case of hard carbon, lithium retention capability is much higher than that of graphite, as shown in  $^7\text{Li}$ -NMR data on hard carbon (Fig. 8.7). No peak of metallic lithium can be observed even when hard carbon is charged to  $450 \text{ mAh} \cdot \text{g}^{-1}$ . A small peak appears for the first time at  $500 \text{ mAh} \cdot \text{g}^{-1}$  charging (Figs. 8.6 and 8.7: courtesy of Kureha Chemical Co.).

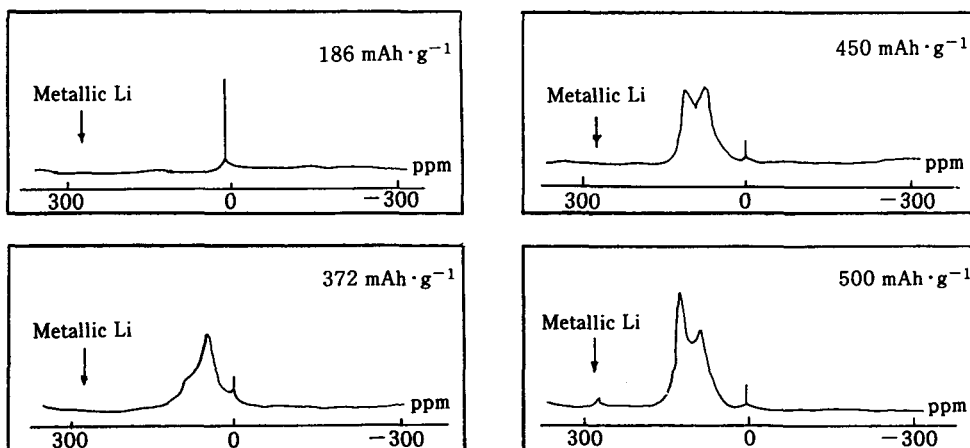


Fig. 8.7  $^7\text{Li}$  spectra of hard carbon doped with varying amounts of lithium.

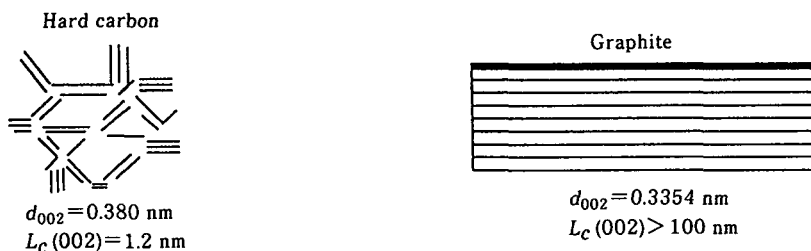


Fig. 8.8 Schematic diagrams of structures of hard carbon and graphite.

It is assumed that this outstanding feature of hard carbon is due to the morphological differences between graphite and hard carbon. Schematic diagrams of morphological structures of graphite and hard carbon are shown in Fig. 8.8.

Graphite has an orderly layered structure and lithium can intercalate only into the spacings between these layers to form  $\text{LiC}_6$ , and soft carbon, which has a slightly disordered structure, is assumed to behave like graphite.

On the other hand, hard carbon consists of randomly oriented small crystallites, as shown in Fig. 8.8, and this type of carbon cannot be converted to graphite by calcination even at  $3000^\circ\text{C}$ , which is the reason why hard carbon is called non-graphitizable carbon.

In the case of hard carbon, lithium can be electrochemically inserted into the ultramicropores (with diameter of about 0.7 to 0.8 nm) surrounded by these crystallites as well as the layers of crystallites themselves (Fig. 8.9). The ultramicropores are assumed to be able to trap lithium in clusters.

The lithium doping capacity of these crystallites is subject to the stoichiometry of  $\text{LiC}_6$  ( $372 \text{ mAh}\cdot\text{g}^{-1}$ ), but as lithium trapped in the ultramicropores can also be discharged, the stoichiometric capacity limitation of hard carbon as a whole can be eliminated. In fact, a charging capacity of around  $600 \text{ mAh}\cdot\text{g}^{-1}$  has been achieved in the hard carbon anode by optimizing the carbonizing conditions, and this value exceeds the stoichiometric limitation of GIC.

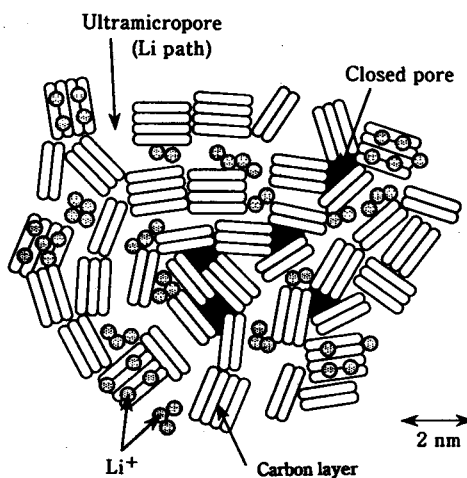


Fig. 8.9 Model of lithium trapping sites in hard carbon.  
[Y. Nishi, *Richiumuion Nijidenchi no Hanashi*, Shokabo (1997) (in Japanese)]

Overcharge of a cell exceeding the designed voltage limits may result in the undesirable formation of metallic lithium with high surface area on the negative electrode surface. Thus, the large lithium doping capability of hard carbon is favorable for safety because of the larger margin until lithium deposition on carbon.

Hard carbon is very stable during charge/discharge cycles. This stability is due to the broader spacings between layers. As described above, during charge and discharge cycles, graphite (and soft carbon) repeatedly expands and shrinks. The graphite structure is damaged by this repeated expanding and shrinking of spacings between layers, resulting in rapid capacity fade during cycles. Furthermore, this expansion during charge causes deformation of electrodes, as shown in Fig. 8.10. This figure is a cross-sectional view of a cell taken by CT scanner, a non-destructive inspection method. Although no deformation of the electrodes can be observed in the initial cycle, it is clear that significant deformation is caused by the expansion of the graphite spacings after 100 cycles. This deformation of the electrode results in poor cyclability.

While the spacings of hard carbon also decrease with the increase of HTT, they are broader than those of graphite or soft carbon (Fig. 8.5). Moreover,  $d_{002}$  spacings of hard carbon with heat-treatment at suitable temperatures (in the case of Fig. 8.5, below 1500 °C) are over 0.372 nm, so no expansion of  $d_{002}$  spacings due to Li insertion can be observed. This outstanding property prevents deformation of the anode even after 200 cycles, as shown in Fig. 8.11.

Figure 8.12 shows the cycle performance of the experimental lithium ion secondary cells with hard carbon and graphite anodes. When graphite cells are charged at 4.2 V, capacity retention at the 500th cycle is about 60%. In order to realize better cyclability, it is necessary for graphite cells to be charged at lower voltage, for example at 4.1 V. But this causes significant decrease in capacity. On the other hand, the cycle performance is by far better in hard carbon cells, and 60% capacity retention is observed even after the 1200th cycle.

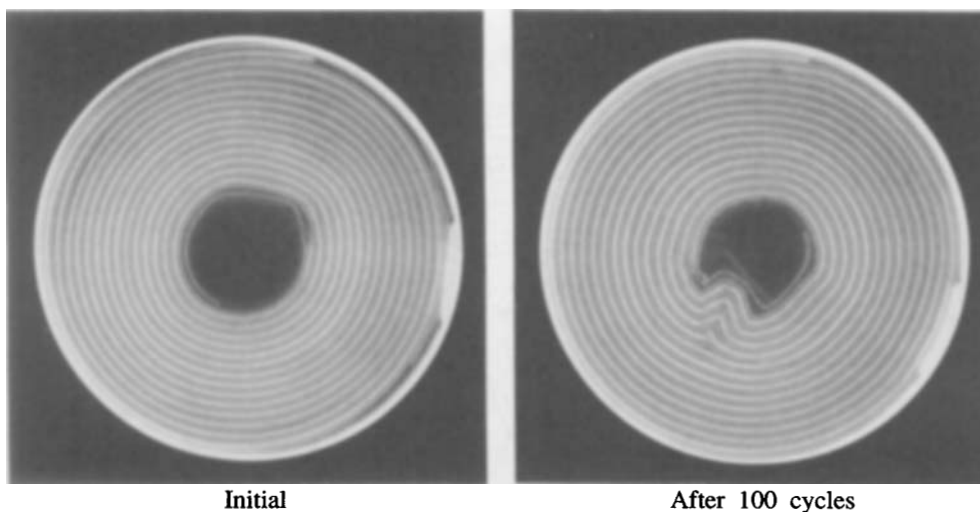


Fig. 8.10 Cross-sectional view of graphite anode cells taken by CT scanner.  
[Y. Nishi, Kiitekunorojii Denchi, p. 69, Maruzen (1996) (in Japanese)]

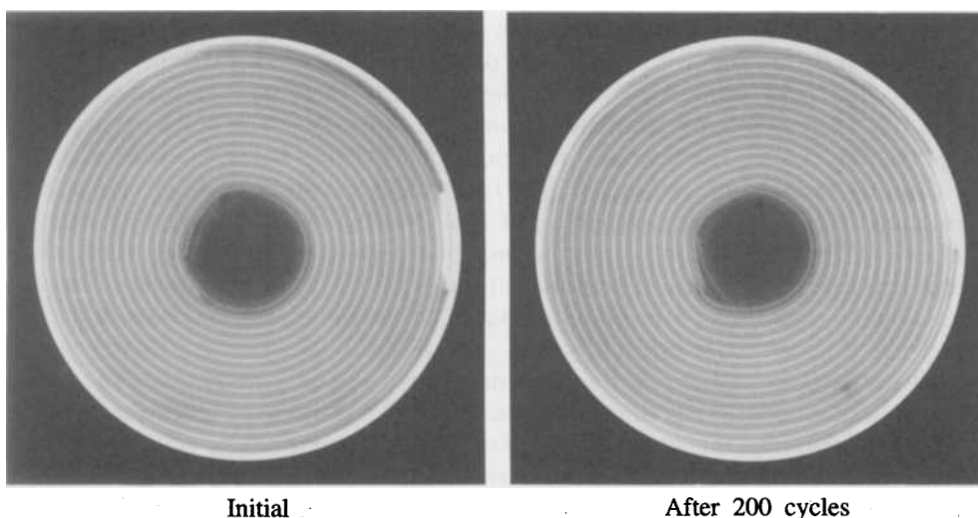


Fig. 8.11 Cross-sectional view of hard carbon anode cells taken by CT scanner.  
[Y. Nishi, Kiitekunorojii Denchi, p. 69, Maruzen (1996) (in Japanese)]

This excellent cyclability of the hard carbon cell is attributed to structural stability and no deformation of anodes during cycles.

Profiles of discharge curve of lithium ion secondary cells with graphite and hard carbon anodes are compared in Fig. 8.13. The profile of the graphite cell is rather flat while that of the hard carbon cell is sloping. This sloping profile is favorable for a state-of-charge

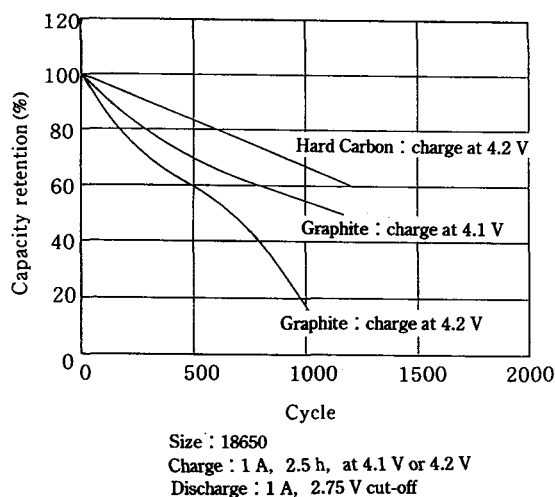


Fig. 8.12 Cycle performance of lithium ion secondary batteries with graphite and hard carbon anodes.  
 [Y. Nishi, Kiitekunorjii Denchi, p. 70, Maruzen (1996) (in Japanese)]

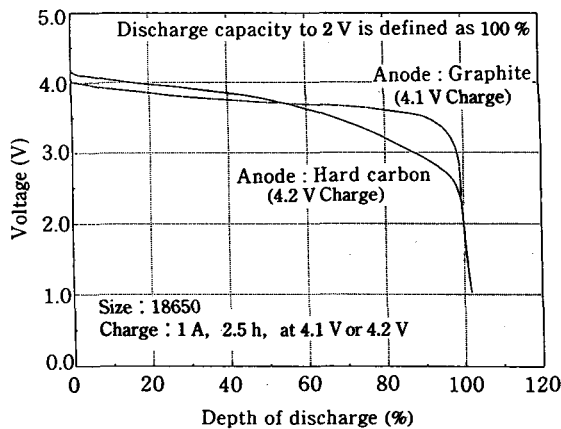


Fig. 8.13 Discharge curve profiles of graphite and hard carbon cells.  
 [Y. Nishi, Kiitekunorjii Denchi, p. 71, Maruzen (1996) (in Japanese)]

indicator, because open circuit voltages (OCV) correspond to remaining capacity and the state of charge or discharge can be easily determined by measuring the OCV of a cell.

### 8.3 Cathode Materials

To investigate candidates for cathode materials of lithium ion secondary batteries, we constructed cells with metallic lithium as anodes and three kinds of lithium-containing compounds,  $\text{LiCoO}_2$ ,  $\text{LiNiO}_2$  and  $\text{LiMn}_2\text{O}_4$ , as cathodes.

Charge and discharge curves of these cells are shown in Fig. 8.14. We made detailed comparisons of discharge capacity, charge and discharge efficiency (reversibility), discharge

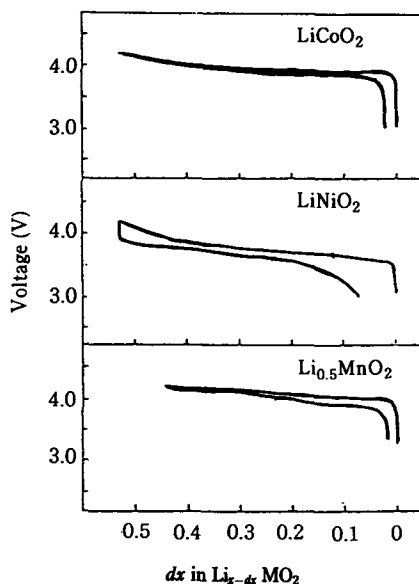


Fig. 8.14 Charge and discharge curves of  $\text{Li}/\text{Li}_x\text{MO}_2$  cells ( $\text{M} = \text{Co}, \text{Ni}, \text{Mn}$ ).  
 Charge:  $0.5 \text{ mA}\cdot\text{cm}^{-2}$ ,  $4.2 \text{ V}_{\text{max}}$   
 Discharge:  $0.5 \text{ mA}\cdot\text{cm}^{-2}$ ,  $3.3 \text{ V}$  cut-off  
 [T. Nagaura, *Progress in Batteries & Battery Materials*, 10, 218 (1991)]

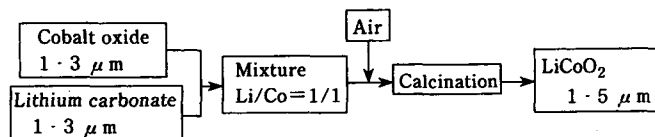


Fig. 8.15 Conventional method for synthesizing  $\text{LiCoO}_2$ .

curve profile and cyclability of three materials (the cyclability is not shown in the figure) and selected  $\text{LiCoO}_2$  as the cathode material.

We first prepared  $\text{LiCoO}_2$  by the conventional synthesis method indicated in Fig. 8.15. Tricobalt tetraoxide ( $\text{Co}_3\text{O}_4$ ) and lithium carbonate ( $\text{Li}_2\text{CO}_3$ ) were mixed well, followed by calcination in the air flow at a temperature of around  $950^\circ\text{C}$ . By this method, however, it was very difficult to prepare coarse particles of  $\text{LiCoO}_2$  and only fine particles with diameters of  $1\text{--}3 \mu\text{m}$  could be obtained. Fine active electrode materials are not desirable from the safety point of view. In the case of abuses such as external short circuit or crushing, fine particles with large specific surface area easily react at one time and all the cell energy is abruptly released with in a very short time with accompanying temperature rise. In the worst case, the cell can catch fire.

We have developed a novel process (Fig. 8.16) for synthesizing lithium cobaltite of larger particle size. Our methods feature two points.

The first point is that a small amount of PVA resin is added in the mixtures of raw materials ( $\text{Co}_3\text{O}_4$  and  $\text{Li}_2\text{CO}_3$ ) to form granular pellets with a granulator. By sintering the



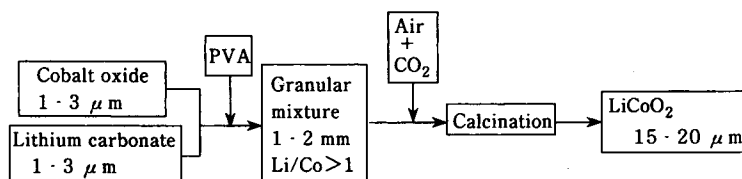


Fig. 8.16 Newly developed method for synthesizing  $\text{LiCoO}_2$ .

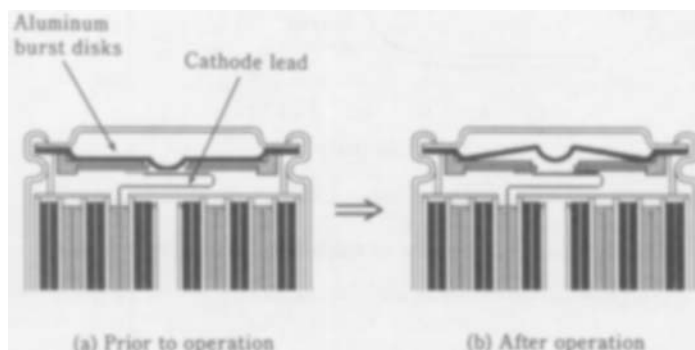


Fig. 8.17 Safety device which operates on internal pressure build-up in cells.  
[Y. Nishi, Kiitekunorogiji Denchi, p. 78, Maruzen (1996) (in Japanese)]

pellets in an air flow containing a suitable amount of  $\text{CO}_2$  gas, lithium cobaltite particles with an average diameter of  $20\text{ }\mu\text{m}$  are synthesized.

The second point is that we use a slightly excessive amount of lithium carbonate ( $\text{Li}_2\text{CO}_3$ ) in the raw materials, so the  $\text{Li/Co}$  atomic ratio in the raw materials is greater than one. This procedure is also favorable for obtaining coarse particles, and in addition, the resulting  $\text{LiCoO}_2$  contains a small amount of residual  $\text{Li}_2\text{CO}_3$ .

We have developed a safety vent in which this residual  $\text{Li}_2\text{CO}_3$  plays an important role.<sup>11)</sup> As shown in Fig. 8.17, the safety vent consists of a concave aluminum disk to which a cathode lead is welded. When a lithium ion secondary cell is overcharged to voltages higher than about  $4.8\text{ V}$ ,  $\text{Li}_2\text{CO}_3$  decomposes to evolve  $\text{CO}_2$  gas resulting in the build-up of the internal pressure of the cell. The aluminum disk is pushed upward in consequence of this pressure rise to disconnect the cathode lead and to stop the charging current. As shown in Fig. 8.19, this device prevents the cell from thermal runaway due to excessive overcharge.

If a cathode material is constructed with  $\text{LiCoO}_2$  without  $\text{Li}_2\text{CO}_3$ , internal pressure build-up is not sufficient to disconnect the cathode lead before thermal runaway begins (Fig. 8.18).

The residual  $\text{Li}_2\text{CO}_3$  in a cathode has been demonstrated not to cause adverse effect on cyclability of cells.<sup>11)</sup>

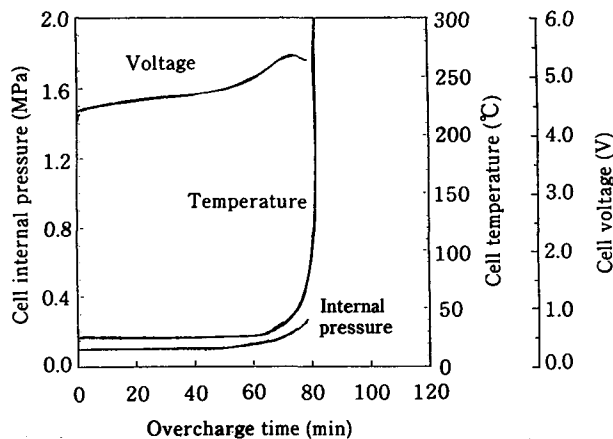


Fig. 8.18 Behavior of overcharged cells employing  $\text{LiCoO}_2$  without residual  $\text{Li}_2\text{CO}_3$ .  
Charge: 1 A, without voltage limit  
[Y. Nishi, Richiumuion Nijidenchi no Hanashi, Shokabo (1997) (in Japanese)]

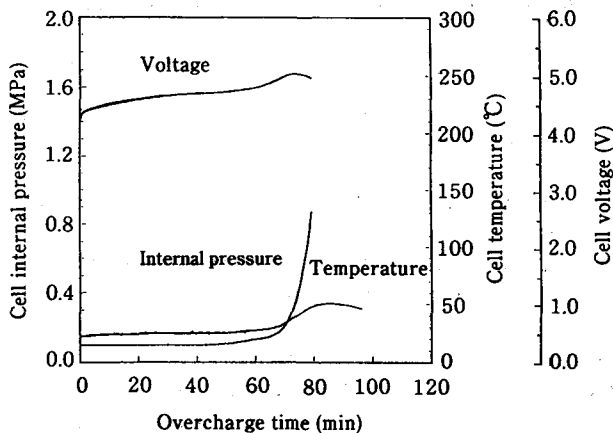


Fig. 8.19 Behavior of overcharged cells employing  $\text{LiCoO}_2$  with residual  $\text{Li}_2\text{CO}_3$ .  
Charge: 1 A, without voltage limit  
[Y. Nishi, Richiumuion Nijidenchi no Hanashi, Shokabo (1997) (in Japanese)]

## 8.4 Other Materials

### 8.4.1 Electrolyte

In general, non-aqueous electrolyte systems are formulated with solvents with high dielectric constants such as propylene carbonate (PC), ethylene carbonate (EC), dimethyl sulfoxide (DMSO), *etc.* in which lithium-containing sustaining salts like  $\text{LiPF}_6$ ,  $\text{LiBF}_4$ ,  $\text{LiClO}_4$ ,  $\text{LiAsF}_6$ , *etc.* are dissolved. Many lithium ions can be dissolved and solvated in these solvents.

Solvents with high dielectric constants, however, have generally very high viscosity even at room temperature, resulting in slow transfer of lithium ions, *i.e.*, low ionic conductivity in electrolytes.

Practically, solvents with low viscosity are mixed with the solvents described above in order to lower the viscosity of the electrolyte system and to increase ionic conductivity. Among these solvents are tetrahydrofuran, dimethoxyethane, diethyl carbonate (DEC), dimethyl carbonate (DMC) and methyl ethyl carbonate (MEC).

In lithium ion secondary batteries with graphite anodes, PC cannot be used as an electrolyte solvent because PC decomposes with coulombic efficiency of almost 100% upon lithium insertion.<sup>10)</sup> EC is significantly stabler during lithium doping than PC, and the mixture of EC and solvents with low viscosity are favorably utilized in place of PC in graphite anode cells. However, EC is solid at room temperature and those cells using the EC-based electrolyte system show poorer performance, especially at low temperatures, than cells with a PC-based electrolyte, due to higher viscosity.

Hard carbon does not cause decomposition of PC, and a PC-based electrolyte can be used successfully. We utilize a mixture of PC and linear organic carbonates such as DEC, DMC and MEC as electrolyte solvents in which  $\text{LiPF}_6$  is dissolved.

#### 8.4.2 Separator

Several kinds of separators are available, including uniaxially drawn polyethylene (PE) and polypropylene (PP) film, biaxially drawn PE film and multilayered film such as PP/PE/PP film.

We use biaxially drawn PE microporous film (25  $\mu\text{m}$  thick) as the separator.

The separator, in principle, separates the cathode and anode to prevent direct contact between the positive and negative electrodes while allowing ionic transport. Besides this, however, the separator plays an important role for safety characteristics in lithium ion secondary batteries. If a cell is overcharged in excess, for example, the temperature in the cell rises abnormally, which acts to soften the thermoplastic separator material and close the micropores of the separator (we call this phenomenon “shutdown” of the separator).

Once the pores of the separator have closed due to softening, the battery cannot continue to be charged or discharged, and thus thermal runaway is prevented. In rare cases, the cell temperature continues to rise due to thermal inertia even after “shutdown” of separator and the separator melts to break, causing direct contact between the positive and negative electrodes, which gives rise to vigorous heat generation (we call this behavior of separator “meltdown” or “breakdown”). It is desirable that the difference between “shutdown” and “meltdown” temperatures be as large as possible.

#### 8.4.3 PTC Devices

Figure 8.20 is a schematic drawing of a lithium ion secondary cell, and as shown in this figure a PTC (Positive Temperature Coefficient) element (called a Polyswitch) is installed inside the cell in order to arrest excessive charge or discharge currents.

Although PTC devices have low electric resistance under normal temperature conditions, resistance suddenly jumps to infinite value when the temperature of the Polyswitch exceeds a certain level (this temperature is called the “trip temperature” and its value is generally

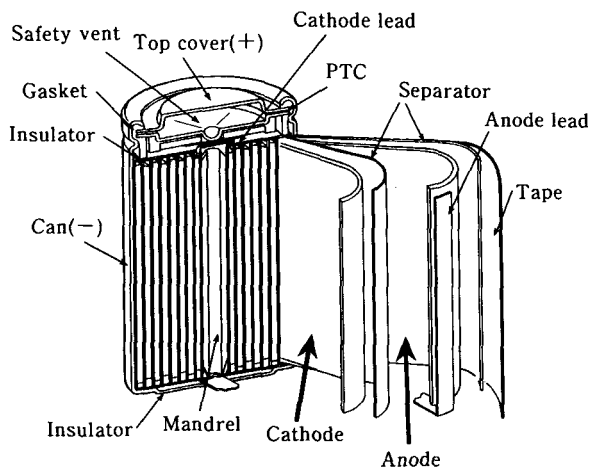


Fig. 8.20 Structure of lithium ion secondary battery.  
[Y. Nishi, Kiitekunorogiji Denchi, p. 79, Maruzen (1996) (in Japanese)]

around 100 °C). When a cell is externally shorted incidentally, for example, high currents flow in the PTC element and its temperature rises abruptly due to Joule heat within the element itself up to the trip temperature. As soon as the temperature reaches this point, short current is stopped due to infinite electric resistance, preventing thermal runaway of the cell.

## 8.5 Cell Structure

As shown in Fig. 8.20, copper foil (10  $\mu\text{m}$  thick) and aluminum foil (20  $\mu\text{m}$  thick) are used as anode and cathode current collectors, respectively.

Lithium cobaltite is mixed with a poly(vinylidene fluoride) (PVdF) binder in NMP solvent to formulate paint for cathode active material, and the paint is applied to both surfaces of the aluminum foil using a doctor blade to make positive electrodes. A small amount of graphite powder is added to the paint in order to improve electronic conductivity of the cathode.

In order to prepare anodes, on the other hand, paint consisting of PVdF resin, hard carbon powder and NMP solvent is coated on both surfaces of the copper foil in a similar way as for cathodes.

PVdF binder is thermally stable and lithium does not react with PVdF. PVdF swells significantly in PC-based electrolyte and this favors ionic transfer across the active material layers. Swelling, however, weakens adhesive strength of PVdF to current collector metals. Adhesive force was improved by the introduction of a carboxylic group to PVdF through graft copolymerization with carboxylic acid anhydride.

Microporous PE films are placed between the cathode and the anode, then spiral-wound together to form a cylindrical cell.

## 8.6 Performance of Lithium Ion Secondary Batteries

Cell construction of Sony's first generation (1991) lithium ion secondary batteries is shown below.

cathode	LiCoO <sub>2</sub>
anode	soft carbon (coke)
electrolyte	PC/DEC (1/1), 1 M LiPF <sub>6</sub>
separator	PP, 25 $\mu$ m
size	diameter 20 mm, height 50 mm

Cell performance was as follows.

charging voltage	4.1 V
average operating voltage	3.55 V
capacity	900 mAh
energy density	200 Wh·l <sup>-1</sup> , 80 Wh·kg <sup>-1</sup>
cycle life	500
charge:	4.1 V <sub>max</sub> , 1 A
discharge:	0.2 C, cut-off voltage 2.75 V

In order to improve the performance of the first generation cell, we used a hard carbon anode in place of a soft carbon anode, and several other modifications were also made as noted below.

cathode	LiCoO <sub>2</sub> with residual Li <sub>2</sub> CO <sub>3</sub>
anode	hard carbon
electrolyte	PC/DEC (1/1), 1 M LiPF <sub>6</sub>
separator	PE, 25 $\mu$ m
size	diameter 18 mm, height 65 mm

The characteristics and features of this second generation cell (1992) were as follows.

charging voltage	4.2 V
average operating voltage	3.6 V
capacity	950 mAh
energy density	220 Wh·l <sup>-1</sup> , 85 Wh·kg <sup>-1</sup>
cycle life	500
charge:	4.2 V <sub>max</sub> , 1 A
discharge:	0.2 C, cut-off voltage 2.75 V

Furthermore, characteristics of hard carbon for anodes have been improved by the proper selection of raw materials and optimization of heat-treatment conditions of carbon such as HTT and atmosphere. We are now using PVdF modified with a carboxylic group as binders for cathode and anode active materials in order to improve cyclability.

Performance of the cell of the latest generation (1995) is as follows.

charging voltage	4.2 V
average operating voltage	3.6 V
capacity	1350 mAh
energy density	295 Wh·l <sup>-1</sup> , 120 Wh·kg <sup>-1</sup>
cycle life	1000
charge:	4.2 V <sub>max</sub> , 1 A
discharge:	0.2 C, cut-off voltage 2.75 V

## 8.7 Possibility of Further Improvement

Much effort has been focusing on further improvement of cell energy density and price reduction of cell materials, particularly cathode active materials.

We have been engaged in the chemical modification of carbon and found that heat-treatment of carbon with addition of phosphorus is very effective to increase the lithium doping capability of carbon.<sup>12)</sup> Heat-treatment of carbon with boron was also found to be effective.<sup>13)</sup> This was later confirmed by Way and Dahn.<sup>14)</sup>

We also found that heat-treatment of carbon in vacuum improves anode capacity to a great extent. Thus, it is assumed that much room is left for improvement of lithium insertion capability of carbonaceous materials and energy density of lithium ion secondary batteries.

Cathode materials less expensive than LiCoO<sub>2</sub>, such as LiNiO<sub>2</sub> and LiMn<sub>2</sub>O<sub>4</sub>, have been investigated intensively and practical use seems close at hand.

These efforts will undoubtedly result in lithium ion secondary batteries with higher energy density and lower price.

## REFERENCES

- 1) T. Nagaura, *Progress in Batteries & Battery Materials*, **10**, 209 (1991).
- 2) T. Nagaura, *Progress in Batteries & Battery Materials*, **10**, 218 (1991).
- 3) K. Mizushima, P. C. Jones, P. J. Wiseman and J. B. Goodenough, *Solid State Ionics*, **3/4**, 171 (1981).
- 4) M.G.S.R. Thomas, P.G. Bruce and J.B. Goodenough, *Solid State Ionics*, **17**, 13 (1985).
- 5) J. J. Auborn and Y. L. Barberio, *J. Electrochem. Soc.*, **134**, 638 (1987).
- 6) E. Plichta, M. Salomon, S. Slane and M. Uchiyama, *J. Power Sources*, **21**, 25 (1987).
- 7) A. Mendiboure, C. Deimas and P. Hagenmuller, *Mater. Res. Bull.*, **19**, 1383 (1984).
- 8) M.G.S.R. Thomas, P.G. Bruce and J.B. Goodenough, *J. Electrochem. Soc.*, **132**, 1521 (1985).
- 9) E. Plichta, S. Slane, M. Uchiyama, M. Salomon, D. Chua, W. B. Ebner and H.W. Lin, *J. Electrochem. Soc.*, **136**, 1865 (1989).
- 10) A.N. Dey and B.P. Sullivan, *J. Electrochem. Soc.*, **117**, 222 (1970).
- 11) H. Kato, Y. Yamamoto and Y. Nishi, 184th ECS Fall Meet., 1993, Ext. Abstr. 93-2 No. 22.
- 12) A. Omaru, H. Azuma, M. Aoki, A. Kita and Y. Nishi, 182nd ECS Fall Meet., 1992, Ext. Abstr. **92-2**, No. 25.
- 13) A. Omaru, H. Azuma and Y. Nishi, Japanese Patent Kokai H3-245, 458 (1991).
- 14) B.M. Way and J.R. Dahn, *J. Electrochem. Soc.*, **141**, 907 (1994).
- 15) H. Azuma, H. Imoto and Y. Nishi, 182nd ECS Fall Meet., 1992, Ext. Abstr. **92-2**, No. 26.

## 9

## All Solid-State Lithium Secondary Battery with Highly Ion Conductive Glassy Electrolyte

Shigeo Kondo\*

## 9.1 Introduction

A battery consists of pair of positive and negative electrodes as well as an electrolyte and a separator between them. Lithium batteries are characterized by their nonaqueous electrolytes. Cell voltage of the batteries with aqueous electrolytes is thermodynamically limited to 1.23 V by the decomposition of  $\text{H}_2\text{O}$ . The absence of  $\text{H}^+$  ions and  $\text{OH}^-$  ions in nonaqueous electrolytes makes the cell voltage of lithium batteries higher than in batteries with aqueous electrolytes.

A lithium battery currently under enthusiastic development is so called "lithium ion battery." It consists of lithium cobalt oxide ( $\text{Li}_{1-x}\text{CoO}_2$ ) as the positive electrode (cathode) and carbon as the negative electrode (anode). The electrolyte is, for example, lithium hexafluorophosphate ( $\text{LiPF}_6$ ) dissolved in an organic solvent, *i.e.*, a mixture of propylene carbonate and dimethoxyethane. Before the development of the lithium ion battery anodes used in lithium batteries were lithium metal or lithium alloys. Dendritic formation of lithium during charging such kinds of batteries has been a big problem in the development of rechargeable lithium batteries. Application of carbon intercalation material as the anode effectively suppressed dendritic formation. It also made it possible to construct a lithium battery of large capacity. In addition, the equivalent potential of  $\text{Li}_{1-x}\text{CoO}_2$  is as high as 4.2 V vs. Li electrode and makes the cell voltage high. Large capacity and high voltage have made lithium ion batteries widely used as power sources of portable equipment, *e.g.*, video recorders and handheld phones.

However, the larger capacity and higher voltage have made safety considerations more serious<sup>1)</sup> because such batteries have flammable substances including an organic solvent used as an electrolyte. The fundamental solution to this problem is substituting the flammable organic electrolyte with nonflammable electrolytes, *i.e.*, inorganic solid electrolytes. Studies on solid electrolytes have therefore become much more extensive in order to improve the high reliability of lithium batteries.

To date, solid-state batteries have rarely been put into practical use. The only exception is a Li/ $\text{I}_2$ -complex primary battery for pacemakers.<sup>2)</sup> The battery has lithium iodide (LiI) as the solid electrolyte. The current drain is as small as *ca.*  $10 \mu\text{A} \cdot \text{cm}^{-2}$  due to the low ionic conductivity of  $5.5 \times 10^{-7} \text{ S} \cdot \text{cm}^{-1}$  of LiI.<sup>3)</sup> The reason why the battery is in practical use

\* Technology Laboratory, Matsushita Battery Industrial Co., Ltd., 1, Matsushita-cho, Moriguchi, Osaka 570, Japan

is reliability even though it is limited to special usage due to its small current drain. In other words, (1) it shows extremely small self discharge, (2) the solid electrolyte layer is formed as a product of an *in situ* reaction between the cathode and the anode just by contact between them. Therefore there is no possibility of an internal short circuit, and (3) of course, it is free from electrolyte leakage because the electrolyte is solid. The high reliability, which is of vital importance for heart pacemaker batteries, led to the battery's commercialization.

However, solid-state batteries are not widely used. In this chapter, lithium ion conductive solid electrolytes are briefly reviewed and the reason why solid-state batteries have not been widely used will be discussed. Next, details of a new lithium ion conductive solid electrolyte of lithium sulfide phosphate glass will be shown. New solid-state lithium batteries on Li/TiS<sub>2</sub> and In-Li<sub>x</sub>/Li<sub>1-x</sub>CoO<sub>2</sub> are reviewed in the following section.

## 9.2 Lithium Ion Conductive Solid Electrolytes

The main reason why solid-state batteries have not been widely used is because solid electrolytes have not completely satisfied the requirements for practical application.

Studies on lithium ion conductive solid electrolytes started with crystalline materials, such as lithium halides including LiI, lithium nitride (Li<sub>3</sub>N), their derivatives, oxysalts including LISICON<sup>4)</sup> and sulfides. However, very few solid electrolytes are suitable for application in solid-state lithium batteries.

Electrolytes must have high ionic conductivity as well as chemical and electrochemical stability. Ionic conductivity of lithium ion conductive solid electrolytes is generally lower than that of organic liquid electrolytes by a factor of 1/10–1/10<sup>5</sup>. Low ionic conductivity makes it difficult to obtain high current drains from solid-state batteries, limiting use of the batteries.

Chemical stability is an important factor for solid electrolytes. Potentials of anodes in solid-state lithium batteries are far less noble than potentials of hydrogen generation; the batteries must be kept in a dehydrated atmosphere. Therefore, stability against humidity is not indispensable to the solid electrolytes. Chemical stability against positive and negative electrode materials is a much more important factor for consideration.

Electrochemical windows of solid electrolytes with high ionic conductivity were not wide enough for the solid-state battery application. Li<sub>3</sub>N, for example, indicates a high ionic conductivity of 10<sup>-3</sup> S·cm<sup>-1</sup>.<sup>5)</sup> however, the decomposition potential is about 0.45 V. The low decomposition potential limits the cell voltage of the battery with a solid electrolyte.

Some oxysalts, *e.g.*, Li<sub>1+x</sub>M<sub>x</sub>Ti<sub>2-x</sub>(PO<sub>4</sub>)<sub>3</sub> (M = Al, Sc, Y, La),<sup>6)</sup> and Li<sub>0.5-3x</sub>TiO<sub>3</sub> (RE = La, Pr, Nd, Sm),<sup>7)</sup> also show ionic conductivity as high as 10<sup>-3</sup> S·cm<sup>-1</sup>. However, the transition metal elements are easily reduced electrochemically, because negative electrode materials in lithium batteries are strong reducing agents. The reduction, *i.e.*, injection of electrons to transition metal elements, creates free electrons, and the free electrons contribute to electronic conduction, which should never occur in electrolytes.

As described above, we have not found out any candidates for lithium ion conductive solid electrolytes among crystalline materials that satisfy the characteristics necessary for application to batteries. Glassy solid electrolytes have the following advantages compared with crystalline ones.



Glassy materials have greater variation in composition than crystalline materials. This is an advantage for achieving higher ionic conductivity.

In addition, glassy materials are essentially isotropic, and the ionic diffusion pathway is also isotropic. Therefore, connection of diffusion pathways across the grain boundary is easier than that in crystalline materials. For example,  $\text{Li}_3\text{N}$  has a two-dimensional structure with anisotropic conduction pathways.<sup>5)</sup> Therefore, a sintering process is necessary to connect diffusion pathway across the grain boundary, which allows high ionic conductivity.<sup>8)</sup> In contrast, resistance at the grain boundary is so small that the resistance of an electrolyte body made of glassy material is only influenced by its packing density besides the bulk impedance, as indicated by using  $\text{AgI-Ag}_2\text{O-P}_2\text{O}_5$  glass.<sup>9)</sup> Solid-state batteries using glassy electrolytes have the following advantages: small resistance at the grain boundary and no necessity for a sintering process, making it possible to fabricate batteries only by a pressing process.

Lithium ion conductive glasses are classified into two groups; oxides and sulfides. Oxide glasses are obtained from network forming oxides, *e.g.*,  $\text{SiO}_2$ ,  $\text{B}_2\text{O}_3$ ,  $\text{P}_2\text{O}_5$ , *etc.*, and a network modifier oxide, *i.e.*,  $\text{Li}_2\text{O}$ . Oxide ions are covalently bound to the glass network and are then immobile. Only  $\text{Li}^+$  ions are mobile. Increasing concentration of  $\text{Li}_2\text{O}$  tends to increase the ionic conductivity. On the contrary, concomitant increase in a given amount of nonbridging oxygen atom created by the large concentration of  $\text{Li}_2\text{O}$  probably decreases ionic conductivity despite an increasing amount of  $\text{Li}^+$  ion because the nonbridging oxygen acts as a trappingcenter for  $\text{Li}^+$  ions. Consequently, the ionic conductivity of the oxide glasses is around  $10^{-6} \text{ S} \cdot \text{cm}^{-1}$ .

Replacing oxide ions with sulfide ions improves ionic conductivity, because sulfide ion has larger polarizability than oxide ion. Ionic conductivities of various sulfide glasses are listed in Table 9.1. Doping lithium halide, especially  $\text{LiI}$ , to the sulfide glasses enhances conductivity. Among the  $\text{LiI}$ -doped sulfide glasses,  $\text{LiI-Li}_2\text{S-SiS}_2$  and  $\text{LiI-Li}_2\text{S-B}_2\text{S}_3$  have high ionic conductivities of  $1.8 \times 10^{-3} \text{ S} \cdot \text{cm}^{-1}$  and  $1.7 \times 10^{-3} \text{ S} \cdot \text{cm}^{-1}$ , respectively.

Both high ionic conductivity and chemical stability are necessary for solid electrolytes. Kennedy and Zhang investigated the stability of some sulfide glasses against  $\text{Li}$  metal.<sup>15)</sup> They constructed electrochemical cells in which the glasses were sandwiched between  $\text{Li}$  metal electrodes. Impedance of the cells increased with storage duration, and the  $\text{Li/glass}$  interface turned black. The formation of an interface layer with high impedance was assumed to be due to the decomposition of the solid electrolyte as a result of instability when in contact with  $\text{Li}$  metal.

When the authors started developing a new lithium ion conductive solid electrolyte, materials suitable for a solid-state battery had not been found even for glass materials.

Table 9.1 Lithium ion conductive glasses based on sulfides and their ionic conductivity.

Glass composition	Ionic conductivity ( $\text{S} \cdot \text{cm}^{-1}$ )	Reference
$0.66\text{Li}_2\text{S} \cdot 0.33\text{P}_2\text{S}_5$	$0.1 \times 10^{-3}$	10
$0.45\text{LiI} \cdot 0.37\text{Li}_2\text{S} \cdot 0.18\text{P}_2\text{S}_5$	$1 \times 10^{-3}$	10
$0.44\text{LiI} \cdot 0.30\text{Li}_2\text{S} \cdot 0.26\text{B}_2\text{S}_3$	$1.7 \times 10^{-3}$	11
$0.30\text{LiBr} \cdot 0.35\text{Li}_2\text{S} \cdot 0.35\text{SiS}_2$	$0.32 \times 10^{-3}$	12
$0.20\text{LiCl} \cdot 0.40\text{Li}_2\text{S} \cdot 0.40\text{SiS}_2$	$0.24 \times 10^{-3}$	13
$0.30\text{LiI} \cdot 0.42\text{Li}_2\text{S} \cdot 0.28\text{SiS}_2$	$1.8 \times 10^{-3}$	14

$\text{Li}_2\text{S}$ – $\text{SiS}_2$  glass was selected as the a base glass because it was relatively thermally stable with a glass transition temperature higher than  $300^\circ\text{C}$ , and  $\text{SiS}_2$  shows relatively low vapor pressure among sulfide glass formers including  $\text{P}_2\text{S}_5$ . Furthermore, the low vapor pressure is suitable for the large-scale preparation of the glass. A dopant that enhances its conductivity without spoiling its chemical and electrochemical stability was sought.

The doping of  $\text{Li}_3\text{PO}_4$  was finally found to enhance ionic conductivity of  $\text{Li}_2\text{S}$ – $\text{SiS}_2$  glass.<sup>16–18)</sup> The stabilitiy against Li metal and the electrochemical window are discussed in the following section.

### 9.3 $\text{Li}_3\text{PO}_4$ – $\text{Li}_2\text{S}$ – $\text{SiS}_2$ Glassy Electrolyte

#### 9.3.1 Synthesis and Glass-Forming Region

The glassy solid electrolyte was synthesized as follows. Appropriate amounts of  $\text{Li}_2\text{S}$  and  $\text{SiS}_2$  were mixed in an inert atmosphere. The mixture was put in a vitreous cabon crucible and heated at  $1000^\circ\text{C}$ . The molten mixture was quenched in liquid nitrogen and  $\text{Li}_2\text{S}$ – $\text{SiS}_2$  base glass was obtained. Next the base glass was ground and mixed with  $\text{Li}_3\text{PO}_4$ . The mixture was heated then quenched in liquid nitrogen.

In a separate procedure, glass was synthesized by twin-roller quenching. The higher cooling rate offered by the twin-roller quenching resulted in expansion of the glass-forming region, as indicated in Fig. 9.1. The figure shows the ionic conductivities of the glasses obtained by the two quenching methods. Maximum conductivity of the glass obtained by liquid nitrogen quenching was  $5.2 \times 10^{-4} \text{ S} \cdot \text{cm}^{-1}$  at a composition of  $0.61\text{Li}_2\text{S} \cdot 0.39\text{SiS}_2$ . Beyond the  $\text{Li}_2\text{S}$  composition, the sample was crystalline and the conductivity was very low. In contrast, the twin-roller quenching offered a glassy sample with a higher  $\text{Li}_2\text{S}$  composition of  $0.65\text{Li}_2\text{S} \cdot 0.35\text{SiS}_2$ , whose conductivity was  $7.6 \times 10^{-4} \text{ S} \cdot \text{cm}^{-1}$ .

Figure 9.2 shows the glass-forming region of  $\text{Li}_3\text{PO}_4$ – $\text{Li}_2\text{S}$ – $\text{SiS}_2$  obtained by the liquid

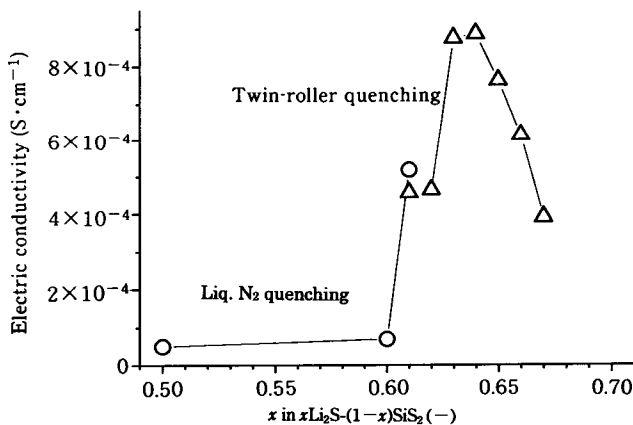


Fig. 9.1 Ionic conductivity of  $\text{Li}_3\text{PO}_4$ – $\text{Li}_2\text{S}$ – $\text{SiS}_2$  glass obtained by liquid nitrogen quenching (circles) and twin-roller quenching (triangles).

[N. Aotani *et al.*, *Solid-State Ionics*, **68**, 36 (1994)]

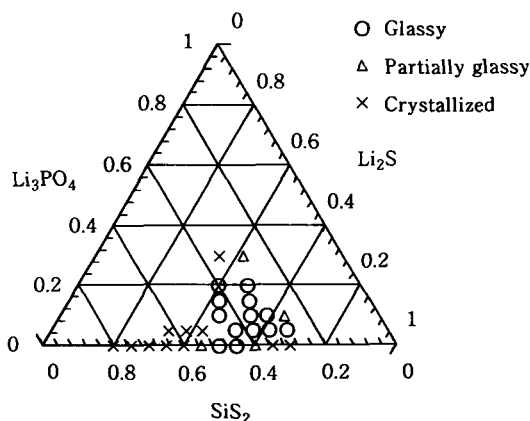


Fig. 9.2 Glass-forming region of  $\text{Li}_3\text{PO}_4\text{-Li}_2\text{S-SiS}_2$  glass obtained by liquid nitrogen quenching. [K. Takada *et al.*, *J. Power Sources*, 43-44, 136 (1993)]

nitrogen quenching. This indicates that the glass-forming region of  $\text{Li}_3\text{PO}_4\text{-Li}_2\text{S-SiS}_2$  was wider than that of  $\text{Li}_2\text{S-SiS}_2$ . A glassy sample of  $0.70\text{Li}_2\text{S} \cdot 0.30\text{SiS}_2$  was obtained by doping 5%  $\text{Li}_3\text{PO}_4$ , although the product was not glassy in the  $\text{Li}_2\text{S-SiS}_2$  system at such a high content of  $\text{Li}_2\text{S}$ . This suggests that  $\text{Li}_3\text{PO}_4$  doping stabilizes the glass-forming network.

In contrast,  $\text{LiI}$  is considered to be isolated in the glass network among  $\text{LiI}$ -doped sulfide glasses. Glass transition temperatures of  $\text{LiI-Li}_2\text{S-SiS}_2$  and  $\text{LiI-Li}_2\text{S-P}_2\text{S}_5$  decrease with increasing  $\text{LiI}$  content. For example, the glass transition temperature of  $0.67\text{Li}_2\text{S} \cdot 0.33\text{P}_2\text{S}_5$  decreased from  $200^\circ$  to  $120^\circ\text{C}$  by doping 40 mol%  $\text{LiI}$ ,<sup>10)</sup> and that of  $0.60\text{Li}_2\text{S} \cdot 0.40\text{SiS}_2$  decreased from  $334^\circ$  to  $306^\circ\text{C}$  by doping 30 mol%  $\text{LiI}$ .<sup>19)</sup> Raman spectroscopy<sup>10)</sup> and infrared spectroscopy<sup>20)</sup> revealed no structural changes in the glass-forming network with  $\text{LiI}$  doping. The insertion of macro-domains of  $\text{LiI}$  is considered to diminish the stiffness of the glass-forming network and decrease the glass transition temperature.

### 9.3.2 Ionic Conductivity and Structure of the Glass

Figure 9.3 shows relationship between the doping amounts of  $\text{Li}_3\text{PO}_4$  and conductivities of  $\text{Li}_3\text{PO}_4\text{-Li}_2\text{S-SiS}_2$  obtained by liquid nitrogen quenching. Conductivity was measured using pellets by pressing the ground glasses. The compositions of the base glasses were  $[\text{Li}_2\text{S}]/[\text{SiS}_2] = 50/50, 60/40, 61/39$  and  $65/35$ . Doping  $\text{Li}_3\text{PO}_4$  enhanced the conductivity of the glass with each base glass composition, and the highest conductivity of  $7.6 \times 10^{-4} \text{ S} \cdot \text{cm}^{-1}$  was observed at a composition of  $0.02\text{Li}_3\text{PO}_4 \cdot 0.60\text{Li}_2\text{S} \cdot 0.38\text{SiS}_2$ . A glassy sample with conductivity higher than  $10^{-4} \text{ S} \cdot \text{cm}^{-1}$  was achieved using a base glass with a composition of  $65/35$ . The glassy sample was not obtained at a composition of  $0.65\text{Li}_2\text{S} \cdot 0.35\text{SiS}_2$ , because of the high  $\text{Li}_2\text{S}$  concentration. Conductivity lower than  $10^{-6} \text{ S} \cdot \text{cm}^{-1}$  was due to crystallization. Despite crystallization of the base material, doping  $\text{Li}_3\text{PO}_4$  offered glassy samples with ionic conductivities higher than  $10^{-4} \text{ S} \cdot \text{cm}^{-1}$ . This phenomenon also suggests that  $\text{Li}_3\text{PO}_4$  doping is effective in not only enhancing conductivity but also in stabilizing its glass-forming network.

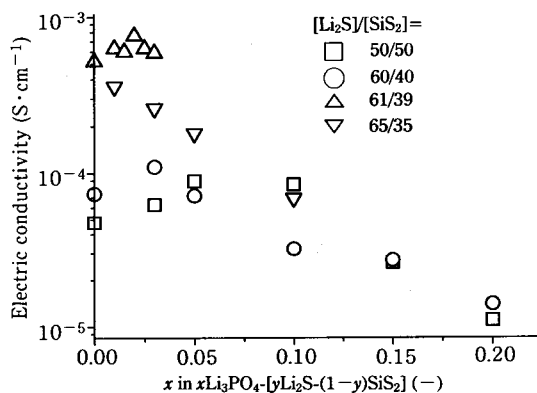


Fig. 9.3 Electric conductivity of  $\text{Li}_3\text{PO}_4\text{-Li}_2\text{S-SiS}_2$  glass obtained by liquid nitrogen quenching as a function of the  $\text{Li}_3\text{PO}_4$  composition.

[K. Takada *et al.*, *J. Power Sources*, **43-44**, 137 (1993)]

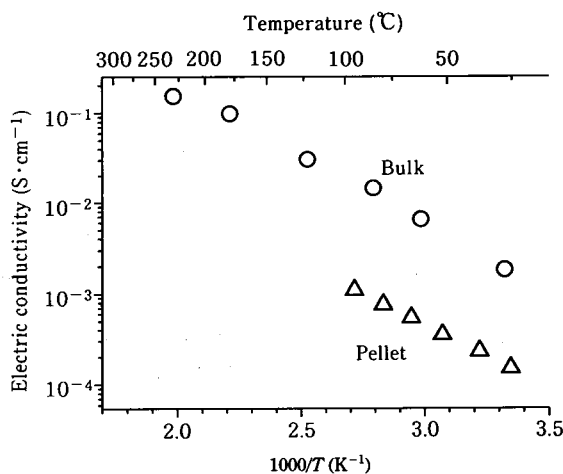


Fig. 9.4 Electric conductivity of  $\text{Li}_3\text{PO}_4\text{-Li}_2\text{S-SiS}_2$  glass obtained by liquid nitrogen quenching as a function of reciprocal temperature. Circles denote conductivity measured using a bulk of the glass, and triangles denote conductivity using a pressed pellet of the ground glass.

[N. Aotani *et al.*, *Solid-State Ionics*, **68**, 37 (1994)]

Twin roller quenching is a more promising method for achieving higher ionic conductivity, because glassy samples with higher concentrations of the glass network modifier, *i.e.*,  $\text{Li}_2\text{S}$ , can be obtained. The highest conductivity was observed at a composition of  $0.01\text{Li}_3\text{PO}_4 \cdot 0.63\text{Li}_2\text{S} \cdot 0.36\text{SiS}_2$ . Fig. 9.4 shown “bulk conductivity” as a function of reciprocal temperature. The conductivity was measured using a piece of quenched glass of ribbon shape. Carbon paste was used as electrodes. The conductivity of the glass obtained by this method was  $1.8 \times 10^{-3} \text{ S} \cdot \text{cm}^{-1}$  at ambient temperature and was higher than that prepared by liquid nitrogen quenching.

Figure 9.4 also shows conductivity measured by a pressed pellet of glass after being ground. The conductivity showed lower values in pressed pellet than in ribbon-shaped glass. Fig. 9.5 indicates dependency on pressure when fabricating a pellet and particle size of the ground glass of the conductivity. The conductivity increased with increasing pressure due to increasing packing density of the pellet. The pores in a pressed pellet result in a low value, as shown in Fig. 9.4. Despite the difference in conductivity, the activation energy for conduction ( $E_a$ ) is almost the same,  $E_a = 0.29$  eV for bulk glass and 0.27 eV for pressed pellet. The good agreement of the  $E_a$  indicates that the bulk impedance is a predominant factor in the impedance of the pressed pellet, and the resistance at the grain boundary in the pellet is very small. The small impedance at the grain boundary is suitable for the construction of a solid-state battery by the pressing process.

The structure of  $\text{Li}_2\text{S-SiS}_2$  glass is considerably different from that of its oxide counterpart. In  $\text{Li}_2\text{O-SiO}_2$  glass, silicon atoms can have all numbers from 0 to 4 bridging oxygen atoms.<sup>21)</sup> In contrast, it has been shown that only silicon atoms that have 0, 2, or 4 bridging sulfur atoms (presented as  $Q^{(n)}$ :  $n$  = number of bridging sulfur) are in  $\text{Li}_2\text{S-SiS}_2$  glass.<sup>22)</sup>  $\text{Li}^+$  ions are ionically bound to the nonbridging sulfur in the sulfide glass. Therefore high ionic conduction will be achieved in the glass with a large amount of nonbridging sulfur, which means that it has a large amount of silicon atoms with the structure presented as  $Q^{(0)}$ . Glass network is, however, difficult to form at such high  $\text{Li}_2\text{S}$  composition. As a result, ionic conductivity decreases due to crystallization. Therefore a sulfide glass with high ionic conductivity should contain a sufficient amount of silicon atoms with  $Q^{(2)}$  structure to form a glass structure in addition to as many silicon atoms with  $Q^{(0)}$  structure as possible.

On the other hand, the structure of  $\text{Li}_3\text{PO}_4\text{-Li}_2\text{S-SiS}_2$  glass is different from that of  $\text{Li}_2\text{S-SiS}_2$ . Nuclear magnetic resonance spectroscopy of the  $\text{Li}_3\text{PO}_4\text{-Li}_2\text{S-SiS}_2$  glass revealed that the silicon atom is not only coordinated by sulfur atoms but also by oxygen atoms, and the phosphorus atom is not only coordinated by oxygen atoms but also by sulfur atoms.<sup>23)</sup> This means that  $\text{Li}_3\text{PO}_4$  doping partially replaces sulfur with oxygen in the glass-forming of  $\text{Li}_2\text{S-SiS}_2$  network. The substitution of sulfur by oxygen is considered to enhance ionic

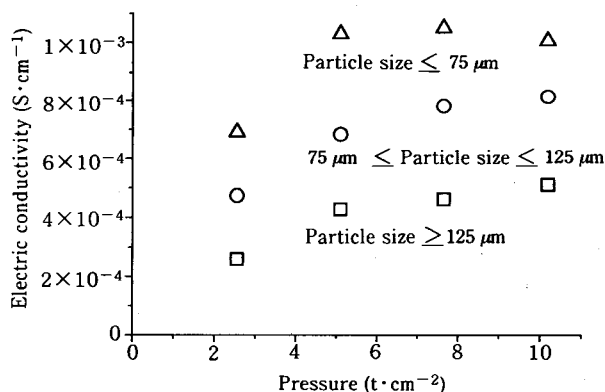


Fig. 9.5 Electric conductivity of  $\text{Li}_3\text{PO}_4\text{-Li}_2\text{S-SiS}_2$  glass measured using a pellet pressed at various pressures of ground glass of varying particle size.

[N. Aotani *et al.*, *Solid-State Ionics*, **68**, 37 (1994)]

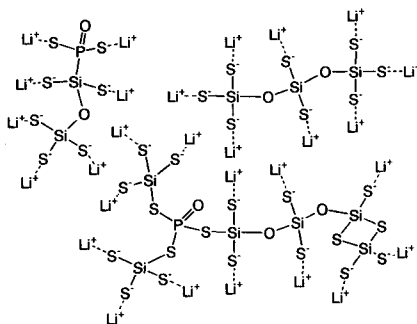


Fig. 9.6 Structural model of the  $\text{Li}_2\text{S-SiS}_2$  glass-doped with a small amount of  $\text{Li}_3\text{PO}_4$ .  
[K. Hirai *et al.*, *J. Am. Ceram. Soc.*, **79**, 349 (1996)]

conductivity and stabilize the glass structure for the following reasons. (1) Si–O bonding is formed by the substitution and allows silicon atoms with  $Q^{(1)}$  structure. It will make a glass-forming network at higher  $\text{Li}^+$  ion concentration, which is good for higher conductivity. (2) The oxygen atoms can selectively occupy the bridging sites in the glass-forming network, as shown in Fig. 9.6. It means that the nonbridging sites to which  $\text{Li}^+$  ions are bound are occupied by sulfur, which has greater polarizability than oxygen. Therefore attraction between  $\text{Li}^+$  ions and the glass-forming network will not increase by the substitution of sulfur atoms with oxygen atoms. On the other hand, oxygen atoms occupying the bridging sites will make the glass-network stronger, because chemical bonding between silicon and oxygen is stronger than that between silicon and sulfur. As a result,  $\text{Li}_3\text{PO}_4$  doping to  $\text{Li}_2\text{S-SiS}_2$  glass is effective not only in increasing ionic conductivity but also in stabilizing the glass structure.

### 9.3.3 Electrochemical Stability

Figure 9.7 shows a cyclic voltammogram of  $0.01\text{Li}_3\text{PO}_4 \cdot 0.63\text{Li}_2\text{S} \cdot 0.36\text{SiS}_2$ . The cyclic voltammogram was obtained using an electrochemical cell with a stainless steel plate as its working electrode and a Li foil as its counter electrode. The sweep rate was  $10 \text{ mV} \cdot \text{s}^{-1}$ . Cathodic current observed from 0 V vs. Li electrode in the cathodic sweep corresponds to the reduction reaction of  $\text{Li}^+$  ion in the electrolyte, *i.e.*, deposition reaction of Li metal onto the working electrode. Anodic current corresponding to ionization of lithium metal was also observed in the anodic sweep at the potential. However, no additional anodic current was observed in the potential range up to 10 V, indicating that the solid electrolyte is quite stable within a wide potential range.

The electrochemical stability was also evaluated by direct polarization. An electrochemical cell with the same construction as that above (the electrode area:  $0.785 \text{ cm}^2$ , the thickness of the electrolyte: 2.3 mm) was polarized at 100 V, and the current was recorded during polarization. The current decay curve of the cell is also shown in Fig. 9.7. The current decayed down to less than  $10^{-7} \text{ A} \cdot \text{cm}^{-2}$ . The small residual current indicates that the decomposition potential of the glass is extremely high.

As mentioned in a previous study<sup>15)</sup>, most of  $\text{LiI-Li}_2\text{S-SiS}_2$  glasses decompose when they come in contact with lithium metal. Fig. 9.8 shows the impedance of a cell with the

construction of  $\text{Li/Li}_3\text{PO}_4\text{-Li}_2\text{S-SiS}_2/\text{Li}$  as a function of storage duration. The cell was stored at  $60^\circ\text{C}$  and the impedance was measured at room temperature. The vertical axis indicates the electric conductivity of the glass calculated from the impedance. No change in conductivity was observed during storage. The chemical stability of the glass vs. Li

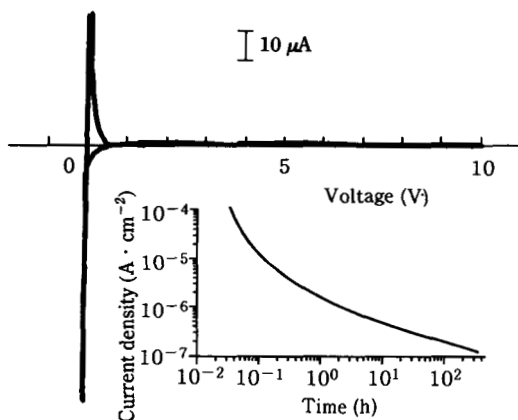


Fig. 9.7 A cyclic voltammogram of  $0.01\text{Li}_3\text{PO}_4 \cdot 0.63\text{Li}_2\text{S} \cdot 0.36\text{SiS}_2$  and a current decay curve of a cell,  $\text{Li}/\text{the glass}/\text{a stainless steel plate}$ , under polarization at 100 V. [K. Takada *et al.*, *Solid-State Ionics*, **86-88**, 879 (1966)]

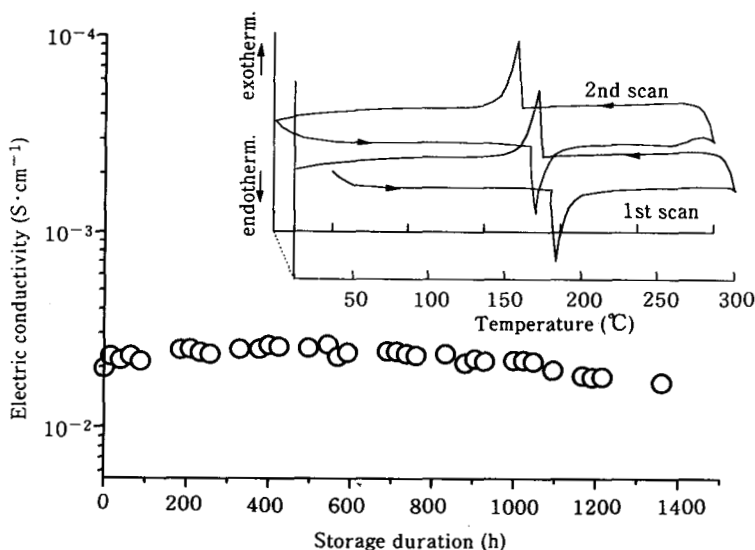


Fig. 9.8 Change in impedance of a cell with a construction of  $\text{Li}/0.01\text{Li}_3\text{PO}_4 \cdot 0.63\text{Li}_2\text{S} \cdot 0.36\text{SiS}_2/\text{Li}$ . DSC curves of a mixture of  $0.01\text{Li}_3\text{PO}_4 \cdot 0.63\text{Li}_2\text{S} \cdot 0.36\text{SiS}_2$  and Li metal are also shown. [K. Takada *et al.*, *Solid-State Ionics*, **86-88**, 879 (1996)]

metal was also investigated by thermal analysis. Fig. 9.8 also shows the result of differential scanning calorimetry carried out to a mixture of the glass and Li metal. Only two peaks were observed at around 180 °C in the temperature range in each scan. The endothermic peak corresponds to melting of Li, and the exothermic peak to solidification of Li. The peaks were reversible and reproducible so the glass is stable enough not to cause any reaction with Li metal. These results indicate that the glass is quite chemically stable against Li metal.

Figures 9.9a and 9.9b show the cyclic voltammograms of the  $\text{Li}_2\text{S}$ – $\text{SiS}_2$  based glasses obtained to investigate their stability against electrochemical reduction. The electrochemical cell has a Pt plate as the working electrode, Li foil as the counter electrode, and Ag wire embedded in the solid electrolyte layer as the reference electrode, which indicates *ca.* 2 V vs. Li electrode. The voltammogram in Fig. 9.9a was obtained for  $0.30\text{LiI} \cdot 0.43\text{Li}_2\text{S} \cdot 0.29\text{SiS}_2$ . The coulombic efficiency, or the ratio of the anodic electrical charge to the cathodic charge calculated from the voltammogram was 0.78. A large deviation from 1 means that irreversible electrochemical reactions occurs under polarization to the potential of Li metal. This irreversible reaction is considered to form a layer of the reaction product at the electrode/electrolyte interface, resulting in the increase of impedance of the Li/glass/Li cell reported in Ref. 15.

In contrast, the coulombic efficiency calculated from the voltammogram in Fig. 9.9b, which was obtained for  $0.02\text{Li}_3\text{PO}_4 \cdot 0.60\text{Li}_2\text{S} \cdot 0.38\text{SiS}_2$ , was almost 1, indicating that  $\text{Li}_3\text{PO}_4$ – $\text{Li}_2\text{S}$ – $\text{SiS}_2$  is very stable against electrochemical reduction.

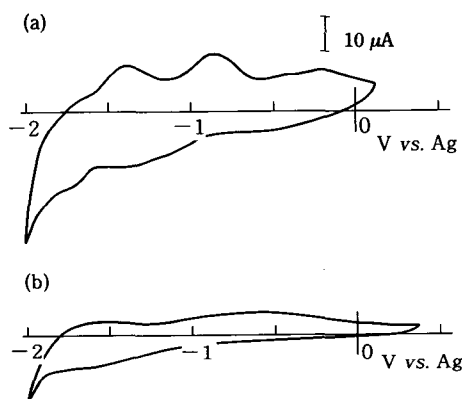


Fig. 9.9 Cyclic voltammograms of the lithium ion conductive glasses. (a):  $0.30\text{LiI} \cdot 0.43\text{Li}_2\text{S} \cdot 0.29\text{SiS}_2$ , (b):  $0.02\text{Li}_3\text{PO}_4 \cdot 0.60\text{Li}_2\text{S} \cdot 0.38\text{SiS}_2$ .

[K. Takada *et al.*, *J. Power Sources*, **43–44**, 139 (1993)]

## 9.4 Solid-State Lithium Batteries

### 9.4.1 Brief Review of Solid-State Lithium Batteries in Previous Studies

A bulk solid-state battery using a  $\text{LiI}$ – $\text{Li}_2\text{S}$ – $\text{P}_2\text{S}_5$  sulfide glass as the electrolyte, a Li–Al alloy as its negative electrode, and  $\text{TiS}_2$  or  $\text{Cu}_4\text{O}(\text{PO}_4)_2$  as its positive electrode was reported in 1983.<sup>24)</sup> The solid electrolyte,  $0.45\text{LiI} \cdot 0.55(0.6\text{Li}_2\text{S} \cdot 0.33\text{P}_2\text{S}_5)$ , had an ionic con-



ductivity of  $5 \times 10^{-4} \text{ S} \cdot \text{cm}^{-1}$ , and the current drain of the battery was about  $20 \mu\text{A} \cdot \text{cm}^{-2}$  at ambient temperature.

Thin film batteries fabricated by evaporation process have been studied extensively to make up for the low ionic conductivities of the solid electrolytes and reduce their internal resistance.

Kanehori *et al.* reported a thin film solid-state battery with a construction of  $\text{Li}/\text{Li}_{3.6}\text{Si}_{0.6}\text{P}_{0.4}\text{O}_4/\text{TiS}_2$ .<sup>25)</sup> The thin layer of the solid electrolyte with a thickness of  $10 \mu\text{m}$  made its short circuit current as high as  $1.3 \text{ mA} \cdot \text{cm}^{-2}$ . On the other hand, Jones and Akridge reported a thin film solid-state battery with a sulfide based solid electrolyte,  $\text{LiI}-\text{Li}_3\text{PO}_4-\text{P}_2\text{S}_5$ .<sup>26)</sup> The battery consists of  $\text{TiS}_2$  as its positive electrode (cathode) and lithium metal as its negative electrode (anode). The thin film battery consists of (1) a d.c. magnetron sputtered chromium contact, (2) an RF magnetron sputtered  $\text{TiS}_2$  layer, (3) an RF sputtered solid electrolyte layer, (4) a vacuum evaporated  $\text{LiI}$  film and (5) a vacuum evaporated  $\text{Li}$  metal layer. The thickness of the electrolyte enabled the battery to generate a current drain as large as  $2 \text{ mA} \cdot \text{cm}^{-2}$ .

Inorganic solid electrolytes are naturally ion selective. Only  $\text{Li}^+$  ion, no anions, can move in them. Therefore no ions except for  $\text{Li}^+$  ions take part in the electrode reactions. This means that side reactions rarely occur in the solid-state batteries. The thin film battery reported by Jones and Akridge showed a cycle life of more than 5000 cycles.

Although the thin film batteries showed excellent performance, they are no longer practical. Volume of energy storage, *i.e.*, volume of the electrodes in the thin film batteries, is too small compared to conventional batteries, and electric equipment requires batteries with large energies. Fabrication costs are too high because of the evaporation process to put them into practical use even if they could be commercialized when integrated with semiconductor components.

Solid-state batteries become truly practical when they are comparable in their performance and cost to conventional batteries. They should be "thick film" batteries or "bulky" ones fabricated by a conventional pressing process. The  $\text{Li}_3\text{PO}_4-\text{Li}_2\text{S}-\text{SiS}_2$  glass indicates a high ionic conductivity only by pressing. Thus it is promising for application to solid-state batteries, and solid-state batteries were constructed with constructions of  $\text{Li}/\text{Li}_x\text{TiS}_2$ <sup>27,28)</sup> and  $\text{In}-\text{Li}_x/\text{Li}_{1-x}\text{CoO}_2$ .<sup>29)</sup>

#### 9.4.2 Application of $\text{Li}_3\text{PO}_4-\text{Li}_2\text{S}-\text{SiS}_2$ Glass to the Solid-State Battery

##### A. $\text{Li}/\text{Li}_x\text{TiS}_2$ Battery

Many of the batteries in the previous studies have  $\text{TiS}_2$  as the positive electrode material. Electrode materials in which topochemical reactions occur, such as  $\text{TiS}_2$ , should be introduced to solid-state batteries for the following reasons.

In contrast to batteries with liquid electrolytes products of the charge-discharge reactions do not diffuse into the electrolyte in solid-state batteries because only  $\text{Li}^+$  ions diffuse in the electrolyte. Therefore the products covering the electrode surfaces probably interfere with electrode reactions. Furthermore, alternate formation and disappearance of the products often destroy the interface between the electrode and the electrolyte. On the other hand, topochemical reactions at the electrodes in lithium batteries are insertion and extraction of  $\text{Li}^+$  ions to the ion sites in the electrode materials. The reaction products are considered to be occupied sites in electrochemical reduction or vacant sites in electrochemical

oxidation. Because they diffuse into the electrode materials, the reaction products do not remain at the surface of the electrode and do not ruin the contact between electrode and electrolyte. Consequently electrode materials that show topochemical reactions should be introduced to solid-state batteries to prevent such problems.

The  $\text{Li}/\text{Li}_x\text{TiS}_2$  battery consists of a foil of Li metal as its negative electrode, and  $\text{TiS}_2$  was mixed with the ground solid electrolyte powder as its positive electrode to obtain a wide electrode area and to shorten the diffusion length of  $\text{Li}^+$  ions in  $\text{TiS}_2$ . The battery performance was changed largely depending on the particle size of the materials and the composition of the mixture.<sup>28)</sup> The ratio of  $\text{TiS}_2$ /the electrolyte should be large enough to connect with each other to ensure a conduction pathway for electrons from the  $\text{TiS}_2$  particles to the current collector. Some  $\text{TiS}_2$  particles are completely surrounded by the solid electrolyte when the content of  $\text{TiS}_2$  is too small. Electrons will not enter or exit from such particles because of the lack of a pathway of electrons connecting the particles to the current collector. The particles do not take part in the electrode reaction, therefore the utilization of  $\text{TiS}_2$  becomes low. However, the content of the solid electrolyte must be large enough to achieve high ionic conduction in the electrode. It must also be large enough to allow the surface of  $\text{TiS}_2$  particles in contact with the solid electrolyte particles to form sufficient electrode area. Therefore, the content of the electrolyte can not be too

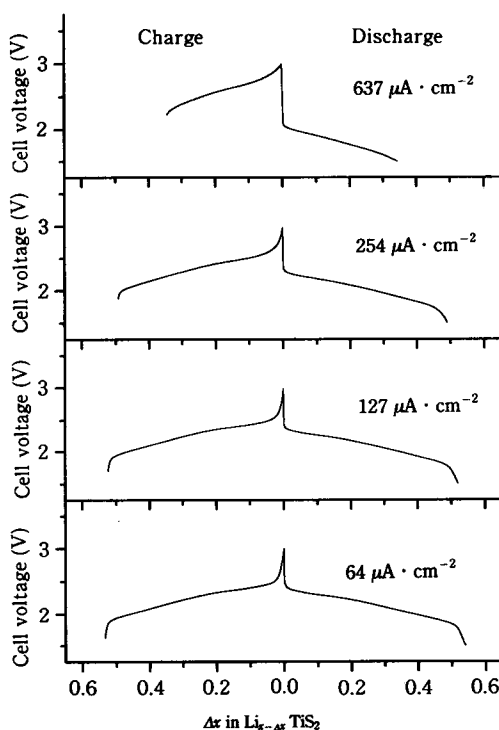


Fig. 9.10 Charge-discharge curves of the  $\text{Li}/\text{TiS}_2$  battery with  $0.01\text{Li}_3\text{PO}_4 \cdot 0.63\text{Li}_2\text{S} \cdot 0.36\text{SiS}_2$  at various current densities.

[K. Iwamoto *et al.*, *Denkikagaku*, 63, 27 (1995) (in Japanese)]

small. Particle size of the electrolyte must also be small enough for good contact between the  $\text{TiS}_2$  particles and the electrolyte particles.

Figure 9.10 shows charge–discharge curves of the battery at various current densities. The battery can be operated at a high current drain of several hundred of microamperes. The current drain was almost comparable to conventional batteries even though the battery was fabricated not by the evaporation method but solely by the pressing method.

### B. In– $\text{Li}_x/\text{Li}_{1-x}\text{CoO}_2$ Battery

Most of the solid-state lithium batteries in the previous studies contained  $\text{LiI}$ -doped glasses, because lithium ion conductive glasses showed high ionic conductivities only when they were composed of  $\text{LiI}$ . They have isolated  $\text{I}^-$  ions in their glass-forming networks. These isolated  $\text{I}^-$  ions are oxidized on contact with positive electrode materials with high equivalent potentials. Therefore, the cell voltages of the batteries in the previous studies were less than 3 V. Solid electrolytes without  $\text{LiI}$  should be used in order to construct solid-state batteries with positive electrode materials with high equivalent potentials, *e.g.*, some kinds of lithium transition metal oxides whose potentials exceed 4 V. Such thin film solid-state lithium batteries studied previously included, for example, a  $\text{Li}/\text{MnO}_2$  battery with  $\text{Li}_{3.4}\text{V}_{0.6}\text{Si}_{0.4}\text{O}_4$  as its electrolyte<sup>30)</sup> and a  $\text{Li}/\text{Li}_x\text{Mn}_2\text{O}_4$  battery with  $\text{Li}_{3.3}\text{PO}_{3.8}\text{N}_{0.22}$ .<sup>31)</sup> The absence of  $\text{I}^-$  ions in the electrolytes made their cell voltage from 3 V to 4 V. The current drain was, however, as small as  $10\text{--}30\ \mu\text{A}\cdot\text{cm}^{-2}$ , because ionic conductivities of the electrolytes were so low that even the thinness of the electrolyte layers could not make up for them.

On the contrary, the  $\text{Li}_3\text{PO}_4\text{--Li}_2\text{S--SiS}_2$  glass does not have isolated anions in it. The oxidation reaction will be oxidation of the glass-forming network consisting of covalent bonding, and a large energy will be necessary to oxidize it. Therefore the decomposition potential will be much higher than that of the electrolytes containing  $\text{LiI}$ . The high decomposition potential will enable us to use a positive electrode material with a high equivalent potential. The authors constructed a solid-state battery with  $\text{Li}_{1-x}\text{CoO}_2$ <sup>32)</sup> as its positive electrode material, making the cell voltage higher than the battery with  $\text{Li}_x\text{TiS}_2$ .

Diffusion of  $\text{Li}^+$  ions in  $\text{Li}_{1-x}\text{CoO}_2$  is reported to be faster than in  $\text{Li}_x\text{TiS}_2$ .<sup>33)</sup> The faster diffusion makes the current drain larger. It also enables the fabrication of a battery with a thicker electrode since the faster diffusion of  $\text{Li}^+$  ion can catch up with the operation current even in the thicker electrode. The increase in the volume of the electrode means the capacity of the battery becomes sufficiently large. On the other hand, deposition and dissolution of  $\text{Li}$  on the negative electrode during its charge–discharge cycle will become larger when  $\text{Li}$  metal is used as the negative electrode. It will more likely destroy the contact between the negative electrode and the solid electrolyte. As a result,  $\text{In--Li}_x$  alloy was used as its negative electrode material to solve this problem on contact.

The battery was fabricated with  $\text{LiCoO}_2$  as the positive electrode material and  $\text{In}$  metal as the negative electrode material.  $\text{Li}_{1-x}\text{CoO}_2$  and  $\text{In--Li}_x$  alloy are formed in the following battery reactions, *i.e.*,  $\text{Li}^+$  ions are deintercalated from among the layers of  $\text{LiCoO}_2$  and form  $\text{In--Li}_x$  alloy at the negative electrode when the battery is charged.



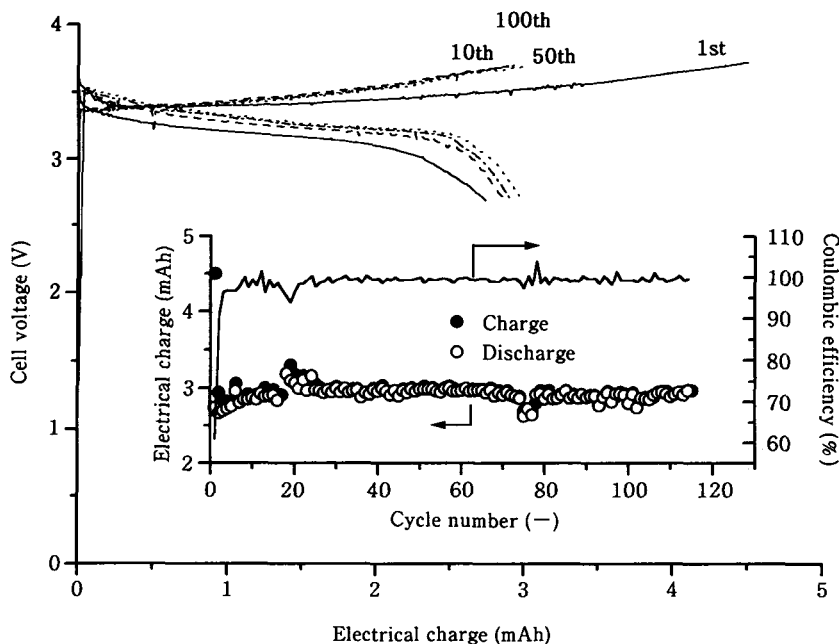


Fig. 9.11 Charge-discharge properties of the  $\text{In-Li}_x/\text{Li}_{1-x}\text{CoO}_2$  battery. [K. Iwamoto *et al.*, *Solid-State Ionics*, **79**, 289, 290 (1995)]

Total reactions



Figure 9.11 shows the cycling properties of the battery. The battery consists of a 91 mg mixture of  $\text{LiCoO}_2$  and the solid electrolyte in a weight ratio of 2:3 as the positive electrode and 60 mg In foil as the negative electrode. The battery was charged and discharged at a current density of  $127 \mu\text{A}\cdot\text{cm}^{-2}$  from 2.7 V to 3.7 V. There is no change in the charge-discharge curves during the cycle. The figure also shows the electrical charge for charge-discharge and coulombic efficiency. The charge-discharge efficiencies were almost 100% except for the first cycle, and no degradation was found after 100 cycles.

Figure 9.12 shows rate capability in discharging and charging of the battery. Fig. 9.12a shows discharge curves of the battery discharged at various current densities after charging up to 3.7 V at a current density of  $127 \mu\text{A}\cdot\text{cm}^{-2}$ . This indicates that the battery can be operated at a current density of up to nearly  $1 \text{ mA}\cdot\text{cm}^{-2}$ .

Figure 9.12b shows discharge curves at  $127 \mu\text{A}\cdot\text{cm}^{-2}$  after charging by an electrical charge of 3 mAh at various current densities. No change in discharged capacity according to change in the charged current density is observed. In conventional batteries with organic electrolytes, decomposition reactions of the electrolytes occur concurrently with the electrode reactions when the cell voltage becomes too high during high rate charging. The decomposition reactions cause a deviation of charge-discharge efficiency from 100%, because electrical charges that pass through the batteries are not completely stored in the batteries but also consumed by the decomposition reaction. However, in the battery under discussion, electrical charge passing during charging was completely discharged. This means there were no side reactions other than the charge reaction even when the cell voltage

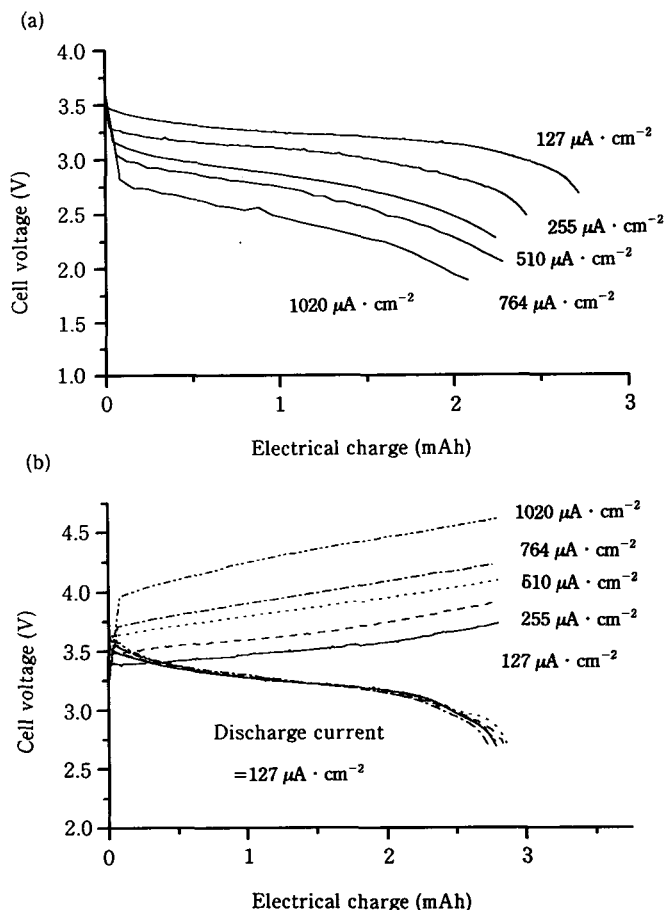


Fig. 9.12 High rate capability of the In-Li<sub>x</sub>/Li<sub>1-x</sub>CoO<sub>2</sub> battery. (a) Discharge curves of the battery after charging at 127  $\mu\text{A} \cdot \text{cm}^{-2}$  to 3.7 V. (b) Charge-discharge curves of the battery. The battery was charged at various current densities, then discharged at a certain current density. [K. Iwamoto *et al.*, *Solid-State Ionics*, 79, 290 (1995)]

exceeded 4.5 V during high rate charging.

Figure 9.13 shows a current decay curve during charging at a constant voltage of 3.7 V. The current decreased less than  $10^{-8} \text{ A} \cdot \text{cm}^{-2}$  at the end of the charging. The extremely small residual current proves that the battery is stable against overcharging at a constant voltage due to the absence of side reactions.

The high ionic conductivity of the glass made the current drain of the solid-state lithium battery as large as  $1 \text{ mA} \cdot \text{cm}^{-2}$ . The glass consisted of only anionic glass forming networks and mobile Li<sup>+</sup> ions. Therefore only the Li<sup>+</sup> ions took part in the electrode reactions, and there were no mobile substances in the glass to cause side reactions. The features of the glass gave excellent performance to the battery. The absence of side reactions result in excellent cycling property, high efficiency at high rate charging, and extremely small residual current.

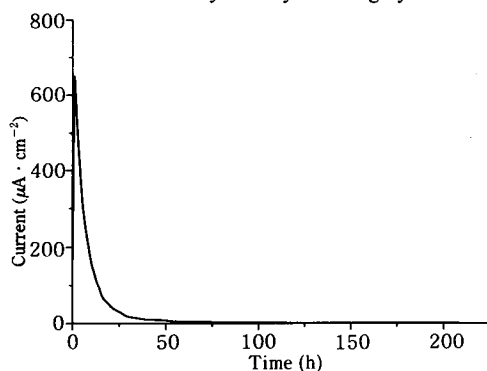


Fig. 9.13 Current decay curve of the In-Li<sub>x</sub>/Li<sub>1-x</sub>CoO<sub>2</sub> battery charged at a constant voltage of 3.7 V. [K. Iwamoto *et al.*, *Solid-State Ionics*, **79**, 291 (1995)]

Table 9.2 Comparison of battery performance between the solid-state battery and commercialized batteries.

Model No.		Cell voltage (V)	Capacity (mAh)	Operation current (μA)	Diameter (mm)	Thickness (mm)	Weight (g)	Energy (mWh·cm <sup>-3</sup> )	Density (mWh·g <sup>-1</sup> )
SSB	Secondary	3.5	15	>200	20	1.6	1.7	104.4	30.9
VL2020	Secondary	3.0	20	1-70	20	2.0	2.2	119.4	27.3
CL2020	Secondary	3.0	1	1-100	20	2.0	2.2	6.0	1.4
VN1616	Secondary	1.5	8		16	1.6	1.2	23.9	10.0
CR2016	Primary	3.0	90	100	20	1.6	1.7	537.1	158.8
BR2016	Primary	3.0	75	30	20	1.6	1.5	447.6	150.0

Table 9.2 lists battery performances of the solid-state battery (SSB) and conventional batteries. The performance of the solid-state battery was estimated from these data for the coin type battery constructed with dimensions of 20 mm in diameter and 1.6 mm in thickness. The performance of the conventional batteries is quoted from the General Catalogue of Batteries of Matsushita Electric Ind. Co., Ltd. The estimation reveals that the solid-state lithium battery has a comparable or higher energy density than commercialized secondary lithium batteries.

## 9.5 Prospects for Solid-State Lithium Batteries in the Future

In the beginning of the development of rechargeable lithium batteries, there were only coin type cells. After the development of the so called “lithium ion battery” or “rocking chair technology,” cylindrical type cells and prismatic type cells were commercialized. In the other words, it is a history of enlargement in inherent energy by increasing the volume of the battery and other technologies. The trend continues, and “large” lithium batteries for industrial use, *e.g.*, stationary lithium batteries, batteries for electric vehicles, *etc.*, are expected to be developed. This means that safety concerns become more important because of the use of much larger amounts of flammable substances, *e.g.*, organic electrolyte and inherent chemical energy. A lithium ion conductive solid electrolyte, which renders batteries nonflammable, will also become a more important key to a fundamental solution to the problem in development of “large” batteries.

Another problem in the development of such kind large lithium batteries is the difficulty

in stacking unit cells. The battery will be required to generate a high voltage of several tens to several hundreds of volts, so it will be a stacking cell. One of the problems in stacking is that the unit cell with the smallest capacity in the stacking cell will be charged at an extraordinary high voltage when there is a deviation in capacity in the unit cells. Besides the danger caused by charging at high voltage, the electrolyte in the cell will decompose, causing battery performance to deteriorate.

The most remarkable advantage of the solid-state lithium battery is its safety because of the absence of flammable substances. It is also promising for the stacking cell, because, as already mentioned in this chapter, no decomposition is expected due to the high decomposition potential of the  $\text{Li}_3\text{PO}_4\text{-Li}_2\text{S-SiS}_2$  glass when the battery with it is charged at high voltage.

A solid-state battery constructed with  $\text{Li}_{1-x}\text{CoO}_2$ , however, does not withstand overcharging at high voltage in spite of the high decomposition potential of the electrolyte for the following reason.  $\text{Li}_{1-x}\text{CoO}_2$  consists of  $\text{CoO}_2$  sheets and  $\text{Li}^+$  ions between them.  $\text{Li}^+$  ions bind the  $\text{CoO}_2$  sheets to each other by electrostatic attraction. Removal of  $\text{Li}^+$  ions results in decrease of binding force between the  $\text{CoO}_2$  sheets and in  $c$ -lattice expansion. Consequently deintercalation of  $\text{Li}^+$  ions of more than  $x = 0.5$  causes deterioration in the reversibility of the electrode reaction<sup>34)</sup> because of the structural instability. This means that batteries with  $\text{Li}_{1-x}\text{CoO}_2$  as the positive electrode material cannot withstand charging at high voltages.

Besides  $\text{Li}_{1-x}\text{CoO}_2$ , there are many recent studies on transition metal oxides, *e.g.*,  $\text{Li}_{1-x}\text{NiO}_2$ ,<sup>35)</sup>  $\text{Li}_{1-x}\text{Mn}_2\text{O}_4$ ,<sup>36)</sup> *etc.*, as positive electrode materials for lithium batteries. The common characteristics of these materials are not only their high equivalent potentials but also their structural and thermal instability against full deintercalation of  $\text{Li}^+$  ions.<sup>37)</sup> This means that the batteries with these materials will not withstand overcharging at high voltage. The lack of tolerance against overcharging is an obstacle to the development of a stacking cell.

The reason why we constructed a  $\text{Li/Li}_x\text{TiS}_2$  battery is not only that the system has been studied for a long time but also that it will solve the above problem of stacking.  $\text{Li}_x\text{TiS}_2$  is quite stable against full deintercalation of  $\text{Li}^+$  ions, and the battery is expected to be stable against charging at even extraordinarily high voltages. When the stacking cell is composed of the  $\text{Li/Li}_x\text{TiS}_2$  battery as one of the series of unit cells and the capacity of the  $\text{Li/Li}_x\text{TiS}_2$  battery is the smallest among the unit cells, the battery will be fully charged at first. After  $\text{Li}^+$  ions are completely deintercalated from  $\text{Li}_x\text{TiS}_2$ , there will be no side reactions including decomposition of the electrolyte in it. Therefore, no current will pass through the battery any more. The charging current passing through the series of unit cells will also be interrupted. Consequently, the  $\text{Li/TiS}_2$  battery will prevent the other unit cells from overcharging at high voltages.

As noted above, the chemical and electrochemical properties of the lithium ion conductive glass, *e.g.*, its nonflammability and high decomposition potential, are promising for the construction of "large" lithium batteries. However, its mechanical properties are not favorable for this purpose. It is a brittle substance like other inorganic solid electrolytes and lacks processibility. Although solid-state batteries are generally fabricated by a pressing process, this process is not appropriate for the fabrication of batteries with a large area. High processibility must be given to the electrolyte in order to open this large field of application to solid-state lithium batteries.

The authors proposed previously a flexible electrolyte sheet, a so-called "paper formed solid electrolyte" made from a copper ion conductive solid electrolyte and a synthetic rubber.<sup>38)</sup> The use of synthetic rubber made up for the difficulty in application of solid electrolytes to solid-state batteries. The obtained sheet was flexible and highly processible with a thickness of less than 100  $\mu\text{m}$ . Solid-state batteries can be constructed from solid electrolyte sheets and the electrode sheets obtained by composing the electrode material and the synthetic rubber.<sup>39)</sup> The sheets can be made to adhere to each other, for example, by roller pressing. The resultant batteries are also processible, and batteries with large areas can be constructed more easily by this process. A lithium ion conductive sheet can be obtained by the same method, enabling construction of large solid-state lithium batteries.

Another way to give flexibility to glass in order to make it processible is by forming it into fibers.<sup>40)</sup> Nonwoven fabrics were also obtained from lithium ion conductive fibers. Such technologies to improve the processibility of solid electrolytes will be very important to make solid-state lithium batteries practical.

## 9.6 Summary

Lithium ion conductive solid electrolytes and solid-state lithium batteries have been reviewed focusing mainly on research on conductive glasses and its application to solid-state batteries done by the authors' group, ionic conductivity of the glass,  $\text{Li}_3\text{PO}_4\text{-Li}_2\text{S-SiS}_2$ , is more than  $10^{-3} \text{ S}\cdot\text{cm}^{-1}$ , which is one of the highest ionic conductivities found among the lithium ion conductive solid electrolytes. This glass shows a wide electrochemical window and stability against lithium metal. These features are promising for its application to solid-state lithium batteries, as proved by the performance of the batteries constructed with the glass. The high ionic conductivity made the current drain as high as that of conventional lithium batteries with organic electrolytes. Its ion selective property resulted in excellent cycling properties and extremely small residual current superior to those of conventional batteries. These features will contribute to the realization of a solid-state battery of high reliability and safety.

## REFERENCES

- 1) D.H. Doughty and S.C. Levy, 36th Battery Symp. Jap., Kyoto, Japan, 1995, Ext. Abstr., p.1.
- 2) F. E. Kraus and A. A. Schneider, *Power Sources Symp. Proc.*, **27**, 144 (1976).
- 3) C.R. Schlaikjer and C.C. Liang, *J. Electrochem. Soc.*, **118**, 1447 (1971).
- 4) U. v. Alpen, M.F. Bell and W.F. Wichelhaus, *Electrochim. Acta*, **23**, 1395 (1978).
- 5) U. v. Alpen, A. Rabenau and G.H. Talat, *Appl. Phys. Letters*, **30**, 621 (1977).
- 6) H. Aono, E. Sugimoto, Y. Sadaoka, N. Imanaka and G. Adachi, *J. Electrochem. Soc.*, **136**, 590 (1989).
- 7) A.D. Robertson, S.G. Martin, A. Coats and A.R. West, *J. Mater. Chem.*, **5**, 1405 (1995).
- 8) R. A. Huggins, *Electrochim. Acta*, **22**, 773 (1977).
- 9) T. Minami, Y. Takuma and M. Tanaka, *J. Electrochem. Soc.*, **124**, 1659 (1977).
- 10) R. Mercier, J.P. Maugani, B. Fahys and G. Robert, *Solid-State Ionics*, **5**, 663 (1981).
- 11) H. Wada, M. Menetrier, A. Levasseur and P. Hagenmuller, *Mater. Res. Bull.*, **18**, 189 (1983).
- 12) S. Sahami, S.W. Shea and J.H. Kennedy, *J. Electrochem. Soc.*, **132**, 985 (1985).
- 13) J.H. Kennedy, S. Sahami, S.W. Shea and Z. Zhang, *Solid-State Ionics*, **18 & 19**, 368 (1986).
- 14) J.H. Kennedy and Y. Yang, *J. Electrochem. Soc.*, **133**, 2437 (1986).
- 15) J.H. Kennedy and Z. Zhang, *Solid-State Ionics*, **28-30**, 726 (1988).
- 16) S. Kondo, K. Takada and Y. Yamamura, *Solid-State Ionics*, **53-56**, 1183 (1992).
- 17) K. Takada, N. Aotani and S. Kondo, *J. Power Sources*, **43-44**, 135 (1993).



- 18) N. Aotani, K. Iwamoto, K. Takada and S. Kondo, *Solid-State Ionics*, **68**, 35 (1994).
- 19) A. Pradel and M. Ribes, *Solid-State Ionics*, **18 & 19**, 351 (1986).
- 20) J.H. Kennedy and Y. Yang, *J. Solid-State Chem.*, **69**, 252 (1987).
- 21) C.M. Schramm, B.H.W.S.d. Jong and V.E. Parziale, *J. Am. Chem. Soc.*, **106**, 4396 (1984).
- 22) H. Eckert, J.H. Kennedy, A. Pradel and M. Ribes, *J. Non-Cryst. Solids*, **113**, 287 (1989).
- 23) K. Hirai, M. Tatsumisago, M. Takahashi and T. Minami, *J. Am. Ceram. Soc.*, **79**, 349 (1996).
- 24) J.P. Malugani, B. Fahys, R. Mercier, G. Robert, J.P. Duchange, S. Baudry, M. Broussely and J.P. Gabano, *Solid-State Ionics*, **9 & 10**, 659 (1983).
- 25) K. Kanehori, K. Matsumoto, K. Miyauchi and T. Kudo, *Solid-State Ionics*, **9 & 10**, 1445 (1983).
- 26) S.D. Jones and J.R. Akridge, *J. Power Sources*, **43–44**, 505 (1993).
- 27) K. Iwamoto, N. Aotani, K. Takada and S. Kondo, *Solid-State Ionics*, **70/71**, 658 (1994).
- 28) K. Iwamoto, N. Aotani, K. Takada and S. Kondo, *Denki Kagaku*, **63**, 25 (1995).
- 29) K. Iwamoto, N. Aotani, K. Takada and S. Kondo, *Solid-State Ionics*, **79**, 288 (1995).
- 30) H. Ohtsuka, S. Okada and J. Yamaki, *Solid-State Ionics*, **40/41**, 964 (1990).
- 31) J. B. Bates, G. R. Gruzalski, N. J. Dudney, C. F. Luck and X. Yu, *Solid-State Ionics*, **70/71**, 619 (1994).
- 32) K. Mizushima, P. C. Jones, P. J. Wiseman and J. B. Goodenough, *Mater. Res. Bull.*, **15**, 783 (1980).
- 33) M.G.S.R. Thomas, P.G. Bruce and J.B. Goodenough, *Solid-State Ionics*, **18 & 19**, 794 (1986).
- 34) J.N. Reimers and J.R. Dahn, *J. Electrochem. Soc.*, **139**, 2091 (1992).
- 35) J. R. Dahn, U. v. Sacken and C. A. Michal, *Solid-State Ionics*, **44**, 87 (1990).
- 36) R. J. Gummow, A. d. Kock and M. M. Thackeray, *Solid-State Ionics*, **69**, 59 (1994).
- 37) J. R. Dahn, E.W. Fuller, M. Obrovac and U. v. Sacken, *Solid-State Ionics*, **69**, 265 (1994).
- 38) H. Hara, N. Yasuda, M. Nagata, S. Kondo and T. Sotomura, *Polymers for Advanced Technology*, **4**, 194 (1992).
- 39) T. Sotomura, S. Itoh, S. Kondo and T. Iwaki, *Denki Kagaku*, **59**, 129 (1991).
- 40) J. Ino, N. Sato, T. Yamagishi, K. Iwamoto, K. Takada and S. Kondo, 10th Int. Conf. Solid State Ionics., Singapore, 1995, Ext. Abstr., p.76.

# 10

## Lithium Ion Plastic Batteries

Bruno Scrosati\*

### 10.1 Introduction

As extensively described in this volume, the development of lithium ion batteries has been a very successful technological achievement. These batteries, which were conceived only few years ago, are now produced commercially in several millions of units per year.<sup>1)</sup> This continuous commercial growth is well represented in Fig. 10.1, which illustrates the evolution of production of rechargeable batteries in Japan. Indeed, Japanese manufacturers have established a commanding leadership in the field. However, North American and European companies are also and progressively entering into production. Lithium ion batteries today are produced in cylindrical and prismatic sizes and they are expected to compete soon with nickel–cadmium and nickel–metal hydride batteries in the consumer electronics market, which includes popular devices such as cellular phones, laptop computers and camcorders.

Although tremendous progress has been achieved in lithium ion technology, the continuous expansion of consumer electronics production and the stringent requirements for optimizing their power constantly call for improvements in battery structure and

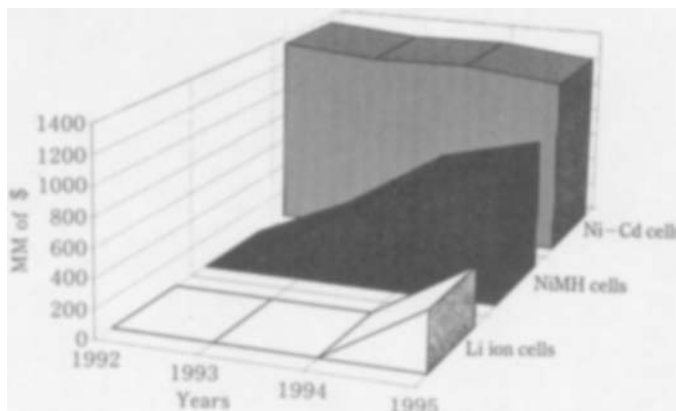


Fig. 10.1 Production of rechargeable batteries in Japan. Derived from Ref.2.

\* Dipartimento di Chimica, Università "La Sapienza", 00185 Rome, Italy

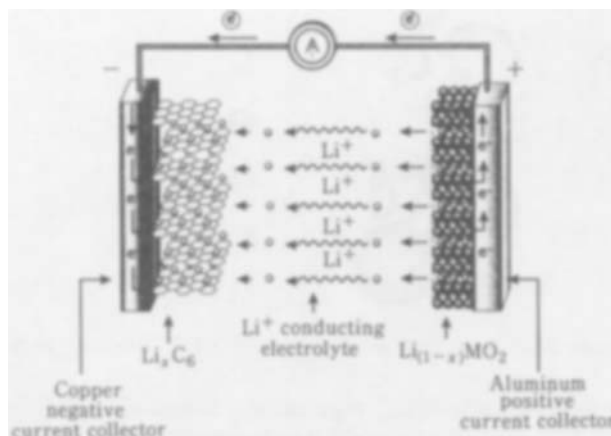


Fig. 10.2 Schematic illustration of a lithium ion rechargeable battery. Derived from Ref.1. (Reproduced with permission of The Electrochemical Society, Inc.)

performance. The basic structure of a lithium ion battery, which is schematically illustrated in Fig. 10.2,<sup>2)</sup> involves a carbon anode, a lithium metal oxide cathode and a lithium ion-conducting liquid electrolyte. Important progress may involve the replacement of the “conventional” liquid electrolyte with an advanced polymer electrolyte membrane for the fabrication of plastic lithium ion (PLI) batteries. This innovation may in fact lead to a very important result, namely that of combining high energy and long cycling performances, which are inherent to the lithium ion concept, with the reliability and the processability, which are typical of a full plastic structure.

Indeed, this new concept is very appealing for the battery industry since PLI batteries are expected to cost less and to be more easily scaled up than their liquid electrolyte counterparts. Also, the absence of free liquids implies that PLI batteries can be packaged in light-weight plastic containers, unlike conventional batteries which require metallic casing. Finally, since the electrolyte membrane and the associated plasticized electrodes may be formed as laminates, PLI can be fabricated in any desired shape and size, an important issue from the application point of view.

All these features make PLI batteries very attractive power sources for the consumer electronic market and accordingly, substantial work is in progress for the identification of the most suitable components of this new device, with particular concern on the most crucial, namely the electrolyte membrane.

## 10.2 Polymer Electrolyte Membranes

### 10.2.1 Types and Preparation Procedures

To be successfully used as an electrolyte separator, a polymer membrane must meet a list of requirements which mainly include: (i) high ionic conductivity (to assure a low  $iR$  drop through the battery); (ii) a lithium ion transport number approaching unity (to avoid concentration polarization); (iii) negligible electronic conductivity (to assure efficient

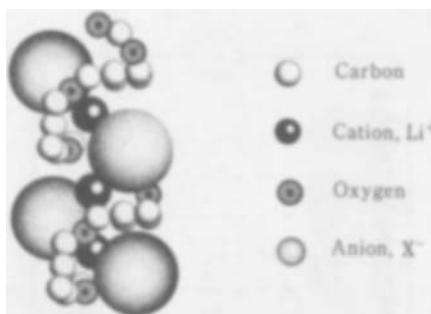


Fig. 10.3 Schematic illustration of the structure of a PEO-LiX complex. Derived from Ref.3.

separation between the electrodes); (iv) high chemical and electrochemical stability with respect to the electrode materials (to avoid decomposition phenomena); (v) low cost (to open to a wide market), and (vi) benign chemical composition (to assure compatibility with the ambient).

The initial development of polymer electrolytes membranes involved the preparation of complexes between lithium salt LiX (*e.g.*,  $\text{LiClO}_4$ ,  $\text{LiCF}_3\text{SO}_3$ ,  $\text{LiBF}_4$  or  $\text{LiN}(\text{CF}_3\text{SO}_2)_2$ ) and high molecular weight polymers containing  $\text{Li}^+$  coordinating atoms (*e.g.*, poly(ethylene oxide), PEO, where oxygen acts as the coordinating atom).<sup>3,4)</sup> The PEO-LiX membranes are conveniently obtained by a simple casting procedure which involves the dissolution of PEO and the lithium salt (in adequate reciprocal compositions) in a suitable solvent (*e.g.*, acetonitrile). The two solutions are then mixed and, after extended stirring, the solvent is slowly evaporated to finally obtain a thin film.<sup>5)</sup> By a proper control of the conditions of the synthesis, it is possible to obtain membranes of thickness of between 25 and 100  $\mu\text{m}$ . Many extensive reviews have been published to describe the properties of LiX-PEO electrolytes,<sup>3-8)</sup> to which the reader is referred for details. Here it will be mainly stressed that the formation of the electrolytes occurs *via* the coordination of the lithium ions by the oxygen atoms of the PEO polymer chains, with a basic structure involving the folding of the chains around the  $\text{Li}^+$  cations with their consequent separation from the anions (Fig. 10.3). Although the effective structure of the PEO-LiX systems may be much more complicated (involving ion pairs and ion clusters in addition to single ions) the simple scheme of Fig. 10.3 is representative for understanding the mechanism of the ionic conductivity, which may be basically described as a hopping transport of cations between equilibrium sites. Consequently, the cation mobility is regulated by ion-polymer interactions primarily due to cation-ether oxygen coordination bonds: the stronger the interaction the lower the cation mobility. Since the ionic transport is strongly related to the freedom of chain movements and to their rearrangements, it is clear how local relaxations and segmental motions of the polymer host chains become essential to confer high conductivity to the electrolyte. Such a favorable situation is obtained only at temperatures above the glass transition and particularly in the presence of a certain degree of amorphicity.

To obtain high ionic mobility one must necessarily consider alternative structures and configurations, and focus on “new generation” polymer-like ionics. Generally, the common and most successful concept has been that of trapping liquid solutions into polymer cages. The immobilizing procedure varies from case to case and includes UV

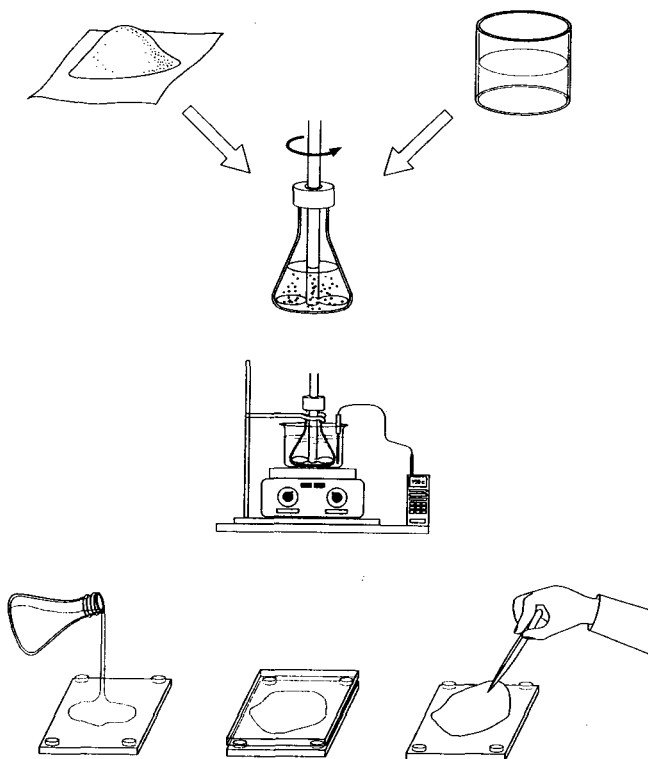


Fig. 10.4 Schematic process of preparation of laboratory samples of polymer electrolyte membranes.

crosslinking, gelification and casting. Particularly interesting are the electrolyte membranes obtained by the gelification of organic liquid solutions (*e.g.*, solutions of a lithium salt, LiX, in a mixture of propylene carbonate, PC and ethylene carbonate, EC or in  $\gamma$ -butyrolactone, BL) in polymer (*e.g.*, poly(acrylonitrile), PAN or poly(methyl methacrylate), PMMA or poly(vinylidene fluoride), PVDF) networks.

Historically, ionically conducting membranes formed by gelling liquid solutions into PAN or PMMA hosts were first proposed in 1975 by Feullade and Perche.<sup>9)</sup> However, the relevance of these gel membranes in the battery field has been fully recognized only recently following the work of Abraham and co-workers,<sup>10,11)</sup> Halpert and co-workers<sup>12)</sup> and Tarascon and co-workers.<sup>13)</sup> Also, a detailed investigation of the electrochemical properties of a large variety of these membranes has been carried out in our laboratory.<sup>14-16)</sup>

Generally, the laboratory synthesis of these membranes involves the dissolution of the lithium salt and of the selected polymer in an appropriate liquid organic solvent (or organic solvent mixtures), the homogenization of the resulting mixtures and finally, gelification by slowing cooling between glass plates to obtain the desired shape and thickness (see Fig. 10.4, which illustrates in scheme this laboratory procedure). This simple method may be easily scaled-up into industrial production by using suitable lamination machines.

For simplicity's sake, all the membranes are hereafter indicated by writing in sequence the selected lithium salt, the liquid solvent (or solvent mixture) and the immobilizing polymer.

Table 10.1 Composition of selected PMMA membranes.

Membrane	Composition (molar ratio)
LiClO <sub>4</sub> -EC-PC-PMMA	4.5:46.5:19:30
LiAsF <sub>6</sub> -EC-PC-PMMA	4.5:46.5:19:30
LiN(CF <sub>3</sub> SO <sub>2</sub> ) <sub>2</sub> -EC-PC-PMMA	4.5:46.5:19:30

For instance, the notation LiClO<sub>4</sub>-EC-PC-PMMA refers to a membrane formed by a solution of lithium perchlorate in an ethylene carbonate-propylene carbonate solvent mixture immobilized in a poly(methyl methacrylate) matrix.

Indeed, PMMA-based systems are typical examples of these new gel-type polymer electrolyte.<sup>14)</sup> Following the general preparation scheme, the synthesis of these polymer electrolytes involves the dissolution of all the components, namely the selected lithium salt and PMMA, in the EC-PC solvent mixture at temperatures ranging between 40 and 50 °C. The solution is then slowly heated to 70–80 °C to favor gelification and finally cast between glass sheets to obtain the desired solid membranes, generally having a transparent, elastomeric appearance.

Various samples can be prepared by varying the nature of the lithium salt, that of the liquid organic solvent and their reciprocal composition. Three representative examples are listed in Table 10.1.

The laboratory preparation of a new class of membranes originally developed in our laboratory<sup>17)</sup> and hereafter denoted with the acronym ALPE (advanced lithium polymer electrolyte) involves first the dissolution of a lithium salt (*e.g.*, LiN(SO<sub>2</sub>CF<sub>3</sub>)<sub>2</sub>) in a liquid poly(ethylene glycol-dimethylether), PEGDME and then the addition to this solution of a ceramic filler (*e.g.*,  $\gamma$ -LiAlO<sub>2</sub>). After reaching homogeneity by ultrasonic stirring, high molecular weight PEO is added and the mixture is slowly heated to 120–130 °C. The mixture is kept at this temperature under continuous stirring until it assumes a very viscous appearance. This viscous solution is then placed between two glass plates and slowly cooled to room temperature to finally obtain solid films of thickness ranging from 200 to 300  $\mu$ m, depending upon the spacers used between the glass plates.

By varying the reciprocal PEO-PEGDME composition, various ALPE samples can be prepared. In some cases variable amounts of plasticizers (*e.g.*, dimethyl carbonate (DMC), diethyl carbonate (DEC), ethylene carbonate (EC) or propylene carbonate (PC)) may be added to increase the amorphous fraction of the membranes. The characteristics of some selected examples are reported in Table 10.2.

Another class of membranes developed in our laboratory for specific use in PLI batteries and identified with the acronym LIMEs (lithium ion membrane electrolytes) involve a laboratory synthesis which includes the immobilization in a PMMA matrix of a solution of a LiN(CF<sub>3</sub>SO<sub>2</sub>)<sub>2</sub> lithium salt in an ethylene carbonate-dimethylcarbonate, EC-DMC mixture.<sup>18)</sup> The preferred LIMEs composition is (in molar ratio): LiN(CF<sub>3</sub>SO<sub>2</sub>)<sub>2</sub>:EC:DMC:PMMA, 5:50:20:25. The synthesis procedure, which closely resembles that of the general PMMA membranes, gives dimensionally stable membranes of typical thickness ranging between 50 and 100  $\mu$ m.

Finally, the types of polymer electrolyte separators specifically developed in our laboratory for PLI batteries also include a class of membranes based on poly(vinylidene

Table 10.2 Composition of selected ALPE membranes (all samples contain 10 weight percent addition of  $\gamma$ -LiAlO<sub>2</sub>).

Sample	Membrane	Composition (molar ratio)
ALPE 1	LiN(CF <sub>3</sub> SO <sub>2</sub> ) <sub>2</sub> -PEGDME-PEO	4.8-80.9-14.3
ALPE 2A-1	LiN(CF <sub>3</sub> SO <sub>2</sub> ) <sub>2</sub> -PEGDME-PEO-DEC	6.7-64.1-21.3-7.9
ALPE 2A-6	LiN(CF <sub>3</sub> SO <sub>2</sub> ) <sub>2</sub> -PEGDME-PEO-DEC	6.7-29.9-47.8-15.6
ALPE 3A-1	LiN(CF <sub>3</sub> SO <sub>2</sub> ) <sub>2</sub> -PEGDME-PEO-DMC	6.6-62.4-20.8-10.2
ALPE 4A-1	LiN(CF <sub>3</sub> SO <sub>2</sub> ) <sub>2</sub> -PEGDME-PEO-EC	6.6-56.0-18.7-18.7
ALPE 5A-1	LiN(CF <sub>3</sub> SO <sub>2</sub> ) <sub>2</sub> -PEGDME-PEO-PC	6.7-63.2-21.0-9.1

fluoride), PVDF. These membranes are synthesized by the gelification in PVDF of a solution of lithium methide, LiC(CF<sub>3</sub>SO<sub>2</sub>)<sub>3</sub>, in an ethylene carbonate-dibutyl phthalate, EC-DBP mixture. The synthesis first involves the careful mixing of DBP with PVDF to obtain a homogeneous paste. Part of EC is added to the paste to achieve complete dissolution. The methide salt is then dissolved in the remaining part of EC and the two solutions are mixed together and annealed to 60–70 °C. Finally, the resulting solution is cast on a glass plate to obtain the desired membrane having a preferred molar ratio composition of LiC(CF<sub>3</sub>SO<sub>2</sub>)<sub>3</sub> : EC : DBP : PVDF = 3.5 : 36.5 : 30 : 30.

Quite a successful achievement in this field has been obtained at the Bellcore Laboratories in the United States.<sup>19-21)</sup> In this case the PLI membrane is a copolymer of vinylidene fluoride and hexafluoropropylene (PVDF-HFP). This membrane is initially fabricated in the absence of a Li salt by conventional methods, such as solvent casting, extrusion or calendering.<sup>20)</sup> The electrolyte is then laminated in conjunction with the electrode films (see section 10.4) and the entire cell laminate is finally activated by the injection of a proper Li salt solution, *e.g.*, LiPF<sub>6</sub> in EC : DMC 2 : 1. The role of the HFP component is to decrease the high crystallinity of the PVDF copolymer and thus, to enhance its swelling in liquid electrolyte. In fact, it has been reported that by optimizing its composition, the PVDF-HFP membrane can adsorb a liquid electrolyte in the amount equal to *ca.* 200% of its solid volume, still retaining good mechanical properties.<sup>20)</sup> Effectively, the sole modification of PVDF by the addition of HFP is not sufficient to allow a level of swelling capable of assuring a high ionic conductivity. This goal is achieved by a further modification of the electrolyte membrane consisting of the addition of an extractable plasticizer and highly dispersed fillers.<sup>20,21)</sup> Indeed, this modification gives PVDF-HFP copolymers consisting of mixed amorphous and crystalline phases: while the crystalline regions hold large amounts of liquids to assure the high ionic conductivity, the crystalline domain provides the mechanical strength to assure processability.

### 10.2.2 Ionic Conductivity

The first important characteristic for a successful lithium battery electrolyte is a fast ionic transport. Accordingly, and most commonly, the preliminary screening test involves the determination of the conductivity of any given sample.

The test is generally performed by measuring the impedance response of cells formed by sandwiching the sample between two blocking (*i.e.*, non-lithium, *e.g.*, stainless steel) electrodes. Details on the technique are given in specialized textbooks.<sup>22)</sup> The results are

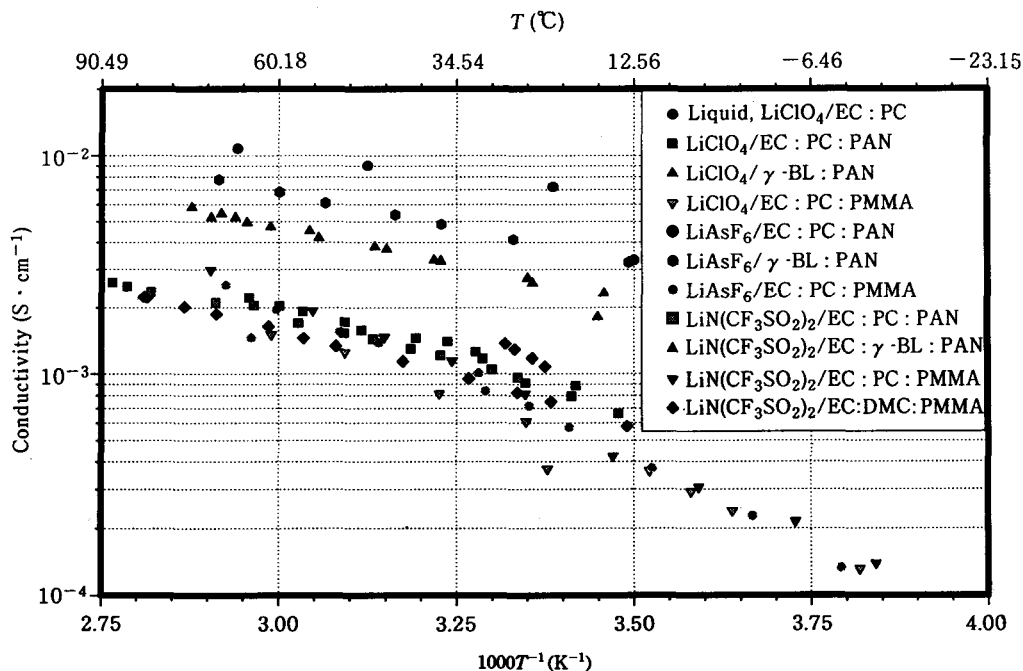


Fig. 10.5 Arrhenius plots of PAN- and PMMA-based membranes. From Refs.14–16.

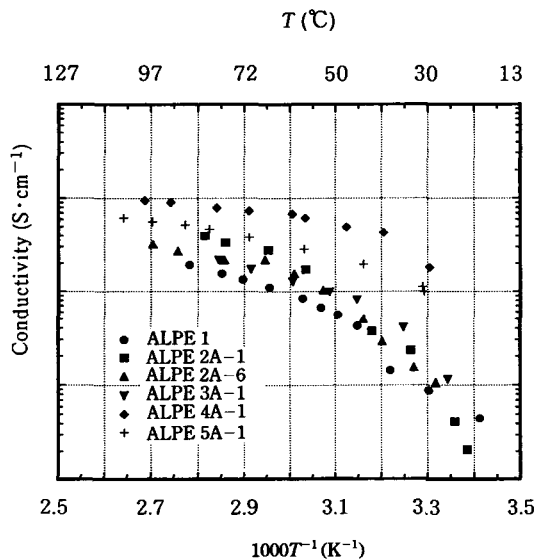


Fig. 10.6 Arrhenius plots of ALPE membranes.  
(Reproduced with permission of The Electrochemical Society, Inc.)



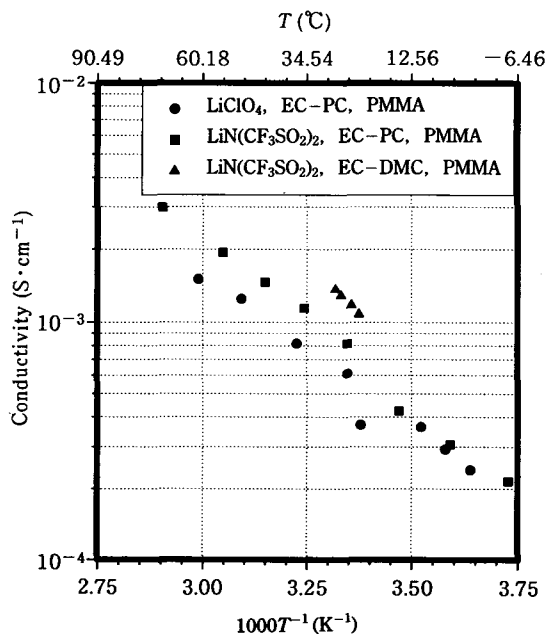


Fig. 10.7 Arrhenius plots of LIMEs membranes.  
(Reproduced with permission of Elsevier Science.)

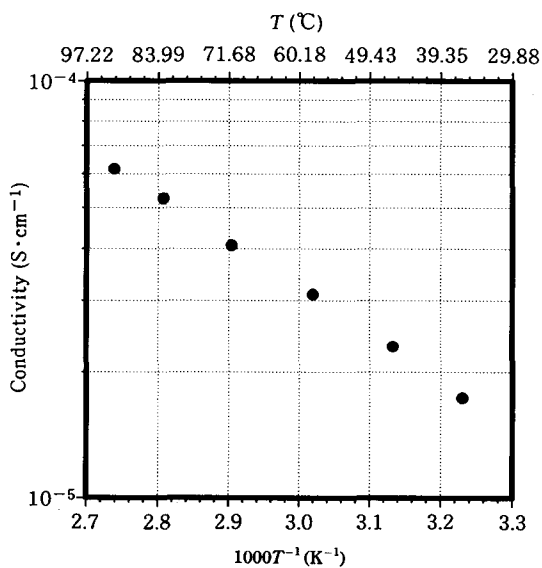


Fig. 10.8 Arrhenius plots of PVDF-based membranes.

generally reported in terms of Arrhenius plots of conductivity. Examples of these plots, specifically related to the membranes discussed in the previous paragraph, are illustrated in Figs. 10.5–10.8.

Table 10.3 Ionic conductivity at room temperature of various electrolyte membranes.

Membrane	Composition (molar ratio)	Conductivity ( $\text{S}\cdot\text{cm}^{-1}$ ) $\times 10^{-3}$
LiClO <sub>4</sub> -EC-PC-PAN	4.5-56.5-23.0-16.0	1.1
LiClO <sub>4</sub> - $\gamma$ BL-PAN	4.5-79.5-16.0	2.8
LiAsF <sub>6</sub> -EC-PC-PAN	4.5-56.5-23.0-16-0	0.9
LiAsF <sub>6</sub> - $\gamma$ BL-PAN	4.5-79.5-16.0	4.1
LiN(CF <sub>3</sub> SO <sub>2</sub> ) <sub>2</sub> -EC-PC-PAN	4.5-56.5-23.0-16.0	1.0
LiN(CF <sub>3</sub> SO <sub>2</sub> ) <sub>2</sub> -EC- $\gamma$ BL-PAN	4.5-56.5-23.0-16.0	2.6
LiClO <sub>4</sub> -EC-PC-PMMA	4.5-46.5-19.0-30.0	0.7
LiAsF <sub>6</sub> -EC-PC-PMMA	4.5-46.5-19.0-30.0	0.8
LiN(CF <sub>3</sub> SO <sub>2</sub> ) <sub>2</sub> -EC-PC-PMMA	4.5-46.5-19.0-30.0	0.7
LiN(CF <sub>3</sub> SO <sub>2</sub> ) <sub>2</sub> -EC-DMC-PMMA	5-50-20-25	1.1
LiC(CF <sub>3</sub> SO <sub>2</sub> ) <sub>2</sub> -EC-DBP-PVDF	3.5-36.5-30-30	$1.7 \times 10^{-2}$
LiN(CF <sub>3</sub> SO <sub>2</sub> ) <sub>2</sub> -PEGDME-PEO* (ALPE 1)	4.8-80.9-14.3	0.1
LiN(CF <sub>3</sub> SO <sub>2</sub> ) <sub>2</sub> -PEGDME-DEC-PEO* (ALPE 2A-1)	6.7-64.1-21.3-7.9	0.1
LiN(CF <sub>3</sub> SO <sub>2</sub> ) <sub>2</sub> -PEGDME-DEC-PEO* (ALPE 2A-6)	6.7-29.9-47.8-15.6	0.1
LiN(CF <sub>3</sub> SO <sub>2</sub> ) <sub>2</sub> -PEGDME-DMC-PEO* (ALPE 3A-1)	6.6-62.4-20.8-10.2	0.2
LiN(CF <sub>3</sub> SO <sub>2</sub> ) <sub>2</sub> -PEGDME-EC-PEO* (ALPE 4A-1)	6.6-56.0-18.7-18.7	1.9
LiN(CF <sub>3</sub> SO <sub>2</sub> ) <sub>2</sub> -PEGDME-PC-PEO* (ALPE 5A-1)	6.7-63.2-21.0-9.1	1.0

\* with addition of  $\gamma$ -LiAlO<sub>2</sub> (10 weight %)

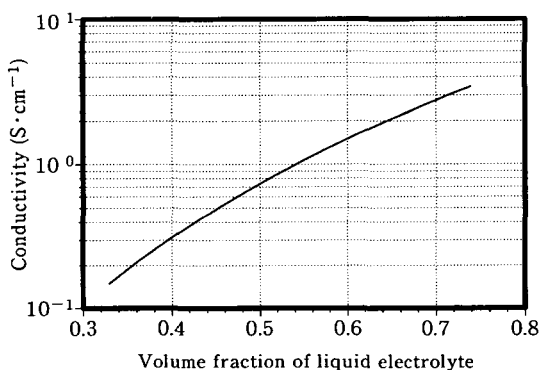


Fig. 10.9 Conductivity of a PVDF-HFP copolymer in function of the volume fraction of the adsorbed LiPF<sub>6</sub>-EC:DMC (2:1) electrolyte. Room temperature. Derived from Ref.20.

These plots evidence the high ionic conductivity of all the membranes here considered. One can clearly notice that the value of the conductivity is mostly influenced by the type of solvent and/or plasticizer used. However, in general all the samples have room conductivity values ranging between  $10^{-4}$  and  $10^{-3} \text{ S}\cdot\text{cm}^{-1}$ , even reaching in the most favorable cases the  $10^{-2} \text{ S}\cdot\text{cm}^{-1}$  range, thus approaching the conductivity of liquid solutions. Table 10.3, which lists the room temperature conductivity of various types of membranes, indeed demonstrates that high ionic conductivity is a specific feature of these new classes of polymer electrolytes.

In the case of the PVDF-HFP copolymer developed at the Bellcore Laboratories, the

ionic conductivity strongly depends on the content of the adsorbed liquid electrolyte. Fig. 10.9 illustrates this dependence in the case of absorption of a  $\text{LiPF}_6\text{-EC:DMC (2:1)}$  electrolyte.<sup>20)</sup>

### 10.2.3 Electrochemical Stability Window

The determination of the electrochemical stability of a given electrolyte is an important test for evaluating its compatibility with the high-voltage cathode materials which are typically used in lithium ion batteries, such as the lithium (transition) metal oxides, *e.g.*,  $\text{LiCoO}_2$ ,  $\text{LiNiO}_2$  and  $\text{LiMn}_2\text{O}_4$ . Traditionally, the stability range of an electrolyte is determined by running a sweep voltammetry of an “inert” electrode (*i.e.*, an electrode different from that which will actually be used in the battery) in the selected electrolyte. The onset of the current in the anodic high voltage range is then assumed to result from a decomposition process and thus the associated voltage is taken as the upper limit of the electrolyte stability range. Typical examples are shown in Figs. 10.10, 10.11 and 10.12, which illustrate the cases of the PAN-based, PMMA-based and ALPE membranes, respectively.

This method, however, gives only approximate values since it may be affected by the kinetics of the probing electrode. Therefore, attempts have been made in our laboratory to develop two new types of measuring methods.<sup>18)</sup> One again uses inert electrode cells which, however, are tested by a low a.c. voltage (10 mV) impedance analysis run at different applied bias voltages. A typical example, related to the response of a cell formed by sandwiching an ALPE-1 electrolyte (see Table 10.2 for composition) between two stainless steel electrodes, is shown in Fig. 10.13. As the bias voltage increases, the impedance response changes by passing from a linear spike to a semiarc trend. It is well known that a linear response in the middle-high frequency impedance plot is associated to an interfacial blocking condition while the appearance of an arc implies a charge-transfer process.<sup>23)</sup>

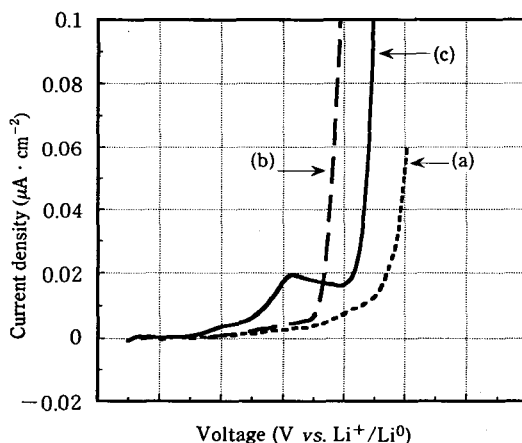


Fig. 10.10 Current-voltage response of an inert (*i.e.*, stainless steel) electrode in  $\text{LiX-PC-EC-PAN}$  electrolyte cells. Scan rate:  $1 \text{ mV} \cdot \text{s}^{-1}$ . Room temperature. (a)  $\text{X} = \text{ClO}_4$ ; (b)  $\text{X} = \text{AsF}_6$ ; (c)  $\text{X} = \text{N}(\text{SO}_2\text{CF}_3)_2$ . (Reproduced with permission by G. Dautzenberg *et al.*, *Chem. Mat.*, **6**, 538 (1994))

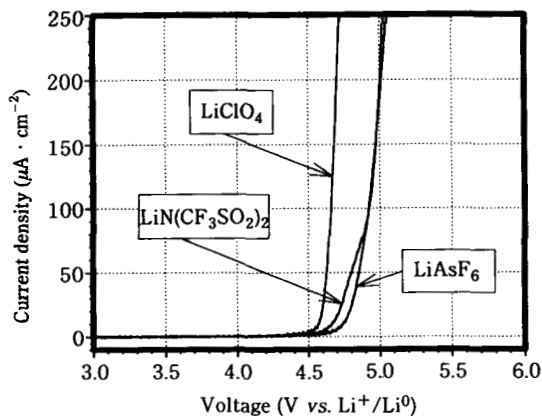


Fig. 10.11 Current-voltage response of an inert (*i.e.*, stainless steel) electrode in LiX-PC-EC-PMMA electrolyte cells. Scan rate:  $1 \text{ mV} \cdot \text{s}^{-1}$ . Room temperature. Derived from Ref. 14.

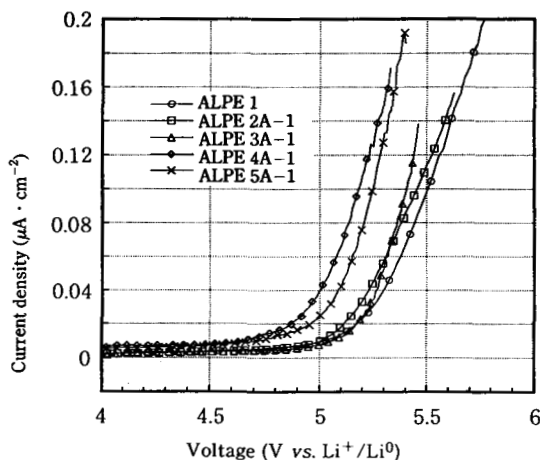


Fig. 10.12 Current-voltage response of an inert (*i.e.*, stainless steel) electrode in ALPE electrolyte cells. Scan rate:  $1 \text{ mV} \cdot \text{s}^{-1}$ . Room temperature. (Reproduced with permission of The Electrochemical Society, Inc.)

Considering the nature of the electrode used (*i.e.*, stainless steel), the latter process may only be associated with electrolyte decomposition. Therefore, the bias voltage at which the response approaches a well-defined arc may be taken as the anodic stability limit of the electrolyte.

The second method is again based on sweep voltammetry of cells using the electrolyte under test. However, the voltammetry is run at very low rates and the working electrode is not an “inert” material but rather a “real” electrode, namely of the same nature of the electrode which will eventually be used as cathode in a practical battery. A typical

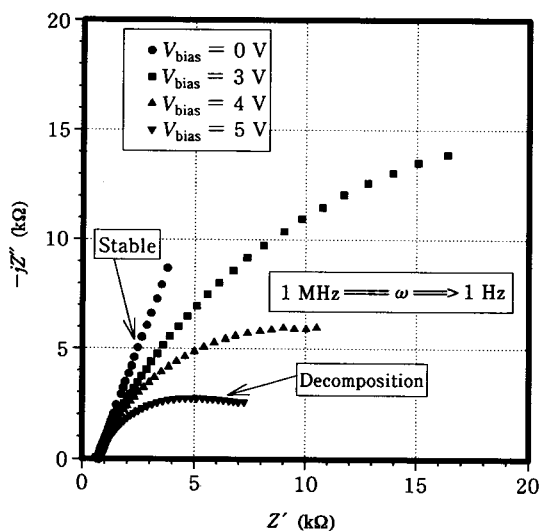


Fig. 10.13 Impedance spectra of a stainless steel/ALPE-1/stainless steel cell at room temperature and at different applied bias voltages. The curvature of the impedance response is taken as an indication of the electrolyte decomposition voltage. Frequency range : 1 Hz–1 MHz. (Reproduced with permission of Elsevier Science.)

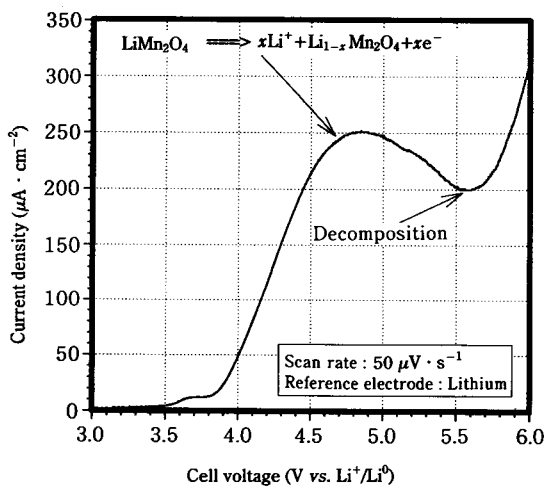


Fig. 10.14 Slow-scan ( $0.05 \text{ mV} \cdot \text{s}^{-1}$ ) voltammetry of an  $\text{LiMn}_2\text{O}_4$  electrode in an ALPE-1 cell at room temperature. Lithium counter and lithium reference. The evolution of the current–voltage trend shows that the electrolyte stability is sufficiently high to allow the completion of the electrochemical process. (Reproduced with permission of Elsevier Science.)

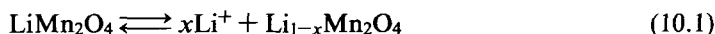
Table 10.4 Electrochemical properties of selected gelionic membranes at room temperature.

Gelionic membrane	Composition (molar ratio)	Conductivity (S·cm <sup>-1</sup> )×10 <sup>-3</sup>	Anodic stability (V) vs. Li <sup>+</sup> /Li	Li <sup>+</sup> Transfer number ( <i>TLi</i> <sup>+</sup> )
LiClO <sub>4</sub> -EC-PC-PAN	4.5-56.5-23.0-16.0	1.1	4.9	0.5
LiClO <sub>4</sub> -EC-PC-PMMA	4.5-46.5-19.0-30.0	0.7	4.6	0.4
LiN(CF <sub>3</sub> SO <sub>2</sub> ) <sub>2</sub> -EC-PC-PMMA	4.5-46.5-19.0-30.0	0.7	4.9	0.7
LiN(CF <sub>3</sub> SO <sub>2</sub> ) <sub>2</sub> -EC-DMC-PMMA	5 -50 -20 -25	1.1	4.8	0.4
LiN(CF <sub>3</sub> SO <sub>2</sub> ) <sub>2</sub> -PEGDME-PEO* (ALPE-1)	4.8-80.9-14.3	0.1	5.8	0.3
LiN(CF <sub>3</sub> SO <sub>2</sub> ) <sub>2</sub> -PEGDME-EC-PEO* (ALPE 4A-1)	6.6-56.0-18.7-18.7	1.9	4.9	0.3
LiC(CF <sub>3</sub> SO <sub>2</sub> ) <sub>3</sub> -EC-DBP-PVDF	3.5-36.5-30 -30	1.7×10 <sup>-2</sup>	—	—

PAN=poly(acrylonitrile); PMMA=poly(methylmethacrylate); PEO=poly(ethylene oxide); PVDF=poly(vinylidene fluoride); EC=ethylene carbonate; PC=propylene carbonate; PEGDME=poly(ethylene glycol-dimethylether); DMC=dimethylcarbonate; DBP=dibutyl phthalate.

\* with addition of  $\gamma$ -LiAlO<sub>2</sub> (10 weight %)

example, related to an ALPE-1 cell using LiMn<sub>2</sub>O<sub>4</sub> working electrode, is shown in Fig. 10.14. The current-voltage response clearly shows a peak centered at 4.75 V vs. Li, which is assumed to be associated with the electrochemical lithium deintercalation process of LiMn<sub>2</sub>O<sub>4</sub>:



The complete evolution of this peak confirms that the electrochemical process can indeed occur in the ALPE-1 electrolyte. In fact, a current rise, possibly related to decomposition phenomena, only occurs at a voltage far more positive than that of the electrochemical process.

In synthesis, results obtained with all the methods cited (Figs. 10.10–10.14) consist of confirming the wide electrochemical stability of the gelionics membranes, which typically extends up to 5 V vs. Li (see Table 10.4, which summarizes the electrochemical properties of some selected examples).

#### 10.2.4 Lithium Ion Transference Number

The determination of the fraction of ionic current transported by the lithium ion, *i.e.*, the determination of the lithium ion transport or more appropriately<sup>24)</sup> lithium transference number *TLi*<sup>+</sup>, is an important aspect in the development of electrolyte materials for lithium ion batteries. In fact, since these batteries are based on lithium intercalation processes, a high *TLi*<sup>+</sup> value, possibly approaching unity, is desired in order to avoid concentration polarization during battery operation.

As clearly evidenced by various authors,<sup>25)</sup> the practical determination of *TLi*<sup>+</sup> in polymer electrolyte cells is not an easy task. Different techniques may be adopted; however, the results obtained are always affected by a certain degree of uncertainty. Commonly used are the impedance method described by Bruce and Vincent<sup>25)</sup> and the so called “time-of-fly” method described by Watanabe *et al.*<sup>26)</sup> Basically, the first method consists of measuring by ac impedance the resistance of a symmetrical Li/electrolyte/Li

cell and by dc chronoamperometry the current across the same cell polarized by a dc voltage pulse,  $V$ . The measurements are taken at the initial time of the applied dc voltage pulse ( $t = t_0$ ,  $R = R_0$ ,  $I = I_0$ ) and under steady conditions ( $t = t_s$ ,  $R = R_s$ ,  $I = I_s$ ). By using these values, the  $T\text{Li}^+$  is given by the expression

$$T\text{Li}^+ = \frac{I_s(V - I_0 R_0)}{I_0(V - I_s R_s)} \quad (10.2)$$

where  $V$  is the value of the dc voltage pulse applied to the cell for the chronoamperometric analysis (typically,  $V = 10$  mV).

The Watanabe method<sup>26)</sup> consists of polarizing a “blocking” electrode cell, *e.g.*, an SS/electrolyte samples/SS (SS = stainless steel) cell for a reasonably long time (typically 1 h) in order to promote accumulation of charge at the interface, and then inverting the polarity of the applied voltage. The idea is to promote the separation of the ionic charge carriers during the initial long polarization period and then to monitor the current as a function of time during the reverse polarization in order to detect different peak times associated with the mobility of the ions migrating in opposite directions.

In fact, the mobility of a given ion,  $\mu_i$ , can be described by the expression

$$\mu_i = d^2 / (V \times \tau_i) \quad (10.3)$$

where  $d$  is the sample's thickness,  $V$  is the applied voltage pulse and  $\tau_i$  is the peak time. Accordingly, the lithium transference number may be evaluated by the expression

$$T\text{Li}^+ = \frac{\mu^+}{\mu^+ + \mu^-} = \frac{\tau^-}{\tau^+ + \tau^-} \quad (10.4)$$

Table 10.5 reports the lithium ion transference number values obtained for the various electrolyte membranes here considered and, for comparison purposes, the values for a common  $\text{LiClO}_4$ -PC liquid electrolyte organic and a PEO- $\text{LiClO}_4$  polymer electrolyte.

It is interesting to note from Table 10.5 that the electrolyte membranes seem on average to have  $\text{Li}^+$  transference numbers considerably higher than those usually obtained for the parent liquid and PEO-based polymer electrolytes. Therefore, it is possible to suppose that the gel membranes rather than being simple liquid-polymer, two-phase systems, could effectively be described as integrated systems where the polymer host (*i.e.*, PMMA, PAN or PVDF) can be more than just a passive component by interacting with the ions in the liquid solution, especially for compositions having a reduced content of organic solvent. Attempts to confirm the occurrence and, possibly, the extent of these inferred ion-polymer interactions have been undertaken employing spectroscopic techniques such as NMR and Raman spectroscopy. An NMR and dielectric study carried out on  $\text{NaClO}_4$ -EC-PC PAN membranes<sup>30)</sup> suggested that the polar nitrile group in the PAN chain may interact with the  $\text{Na}^+$  ion, leading the authors to conclude that the polymer, rather than simply acting as a rigid framework for regions of liquid electrolytes, also provides the stability of the gel network down to the immediate vicinity of the  $\text{Na}^+$  ions. However, results of a Raman spectroscopy study carried out on  $\text{LiX}$  ( $\text{X} = \text{ClO}_4$ ,  $\text{AsF}_6$ ,  $(\text{CF}_3\text{SO}_2)_2$ )-EC-PC-PMMA membranes<sup>31)</sup> did not provide the same evidence of interactions between the polymer and

Table 10.5 Lithium transport numbers at room temperature of polymer electrolyte membranes.

Electrolyte membrane	solvent/salt ratio	$T\text{Li}^{+ (a)}$	$T\text{Li}^{+ (b)}$
PC-LiClO <sub>4</sub>	liquid	0.4 <sup>(c)</sup>	0.25 <sup>(d)</sup>
PEO-LiClO <sub>4</sub>	polymer	0.2 <sup>(e)</sup>	—
LiClO <sub>4</sub> -EC-PC-PAN <sup>(f)</sup>	17:6:1	0.6	0.5
LiClO <sub>4</sub> - $\gamma$ BL-PAN	17:6:1	0.6	0.4
LiAsF <sub>6</sub> -EC-PC-PAN <sup>(e)</sup>	17:6:1	0.7	0.6
LiAsF <sub>6</sub> - $\gamma$ BL-PAN	17:6:1	0.7	0.6
LiN(CF <sub>3</sub> SO <sub>2</sub> ) <sub>2</sub> -EC-PC-PAN	17:6:1	0.8	0.7
LiN(CF <sub>3</sub> SO <sub>2</sub> ) <sub>2</sub> -EC- $\gamma$ BL-PAN	17:6:1	0.6	0.6
LiClO <sub>4</sub> -EC-PC-PMMA	14.6:1	0.1	0.4
LiAsF <sub>6</sub> -EC-PC-PMMA	14.6:1	—	0.6
LiN(CF <sub>3</sub> SO <sub>2</sub> ) <sub>2</sub> -EC-PC-PMMA	14.6:1	0.1	0.7
LiN(CF <sub>3</sub> SO <sub>2</sub> ) <sub>2</sub> -EC-DMC-PMMA	14.0:1	0.4	—
LiC(CF <sub>3</sub> SO <sub>2</sub> ) <sub>2</sub> -EC-DBP-PVDF	19.0:1	—	—
LiN(CF <sub>3</sub> SO <sub>2</sub> ) <sub>2</sub> -PEGDME-PEO* (ALPE 1)	16.8:1	0.3	0.3
LiN(CF <sub>3</sub> SO <sub>2</sub> ) <sub>2</sub> -PEGDME-DEC-PEO* (ALPE 2A-1)	10.7:1	0.2	0.2
LiN(CF <sub>3</sub> SO <sub>2</sub> ) <sub>2</sub> -PEGDME-DEC-PEO* (ALPE 2A-6)	6.8:1	—	—
LiN(CF <sub>3</sub> SO <sub>2</sub> ) <sub>2</sub> -PEGDME-DMC-PEO* (ALPE 3A-1)	11.0:1	0.4	0.4
LiN(CF <sub>3</sub> SO <sub>2</sub> ) <sub>2</sub> -PEGDME-EC-PEO* (ALPE 4A-1)	11.3:1	0.3	0.3
LiN(CF <sub>3</sub> SO <sub>2</sub> ) <sub>2</sub> -PEGDME-PC-PEO* (ALPE 5A-1)	10.8:1	—	—

\* with addition of  $\gamma$ -LiAlO<sub>2</sub> (10 weight %).

(a)=calculated using impedance technique<sup>25</sup>; (b)=calculated using pulse technique<sup>26</sup>; (c)= from Ref. 13;

(d)= from Ref. 14; (e)= from Ref. 11; (f)= from Ref. 1.

the electrolyte. Therefore, the experimental evidence available so far is contradictory and further work is certainly needed to reach a conclusive view of the structure of these complex systems. The lack of a precise idea on the effective structure of these membranes is reflected in the variety of names which have been used to describe them. These include hybrid,<sup>32</sup> wet-like<sup>33</sup> and gelionic<sup>14</sup> membranes.

### 10.3 Plasticized Electrodes

The successful production of an entirely plastic-like lithium ion battery requires the fulfillment of two very important practical requirements, namely (i) the fabrication of plasticized electrode films which can combine flexibility and high loading capacity with good adherence to the current collector and with low electronic resistance, and (ii) good compatibility between the electrode and the electrolyte film components. The former is essential in assuring high rate and high energy capabilities and the latter in assuring long cyclability and high capacity delivery.

The satisfactory accomplishment of the two combined requirements is not easy and still constitutes one of the major tasks in the development of PLI batteries. Indeed, very scarce open information is available in this area since the laboratories involved are very reluctant to disclose their results. The second requirement is the one which appears to be the most challenging. In fact, while the fabrication of high-loaded electrode films having good mechanical properties is now common in various industrial laboratories, a satisfactory interlayered contact between these electrodes and the electrolyte in a "real" solid-state cell configuration is not easily obtained, especially at the negative, carbon electrode side. The



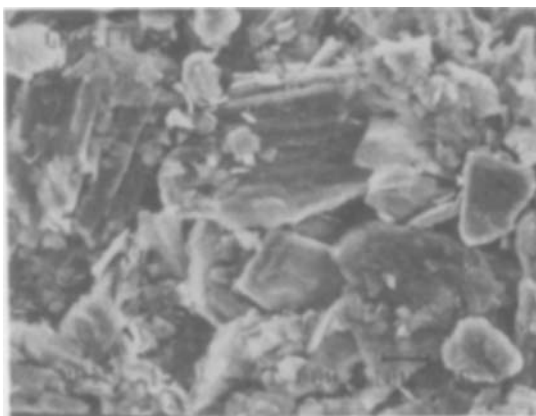


Fig. 10.15 Surface morphology of a carbon film electrode prepared by a spray technique. Bar: 10  $\mu\text{m}$ .

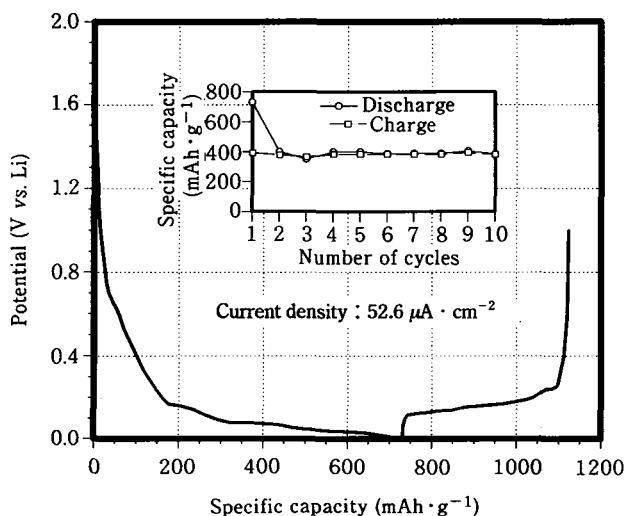


Fig. 10.16 Cycling response of a graphite thin ( $0.85 \text{ mg} \cdot \text{cm}^{-2}$ ) film electrode in a 1 M  $\text{LiClO}_4$  solution in an EC–DMC 2:1 mixture. Current rate:  $52.6 \mu\text{A} \cdot \text{cm}^{-2}$ .

major problem is to assure full wettability throughout the entire electrode mass, a process which is naturally achieved when the electrode is immersed into a liquid solution but which must be somewhat “activated” when the same electrolyte is trapped into a polymer matrix.

A clear demonstration of this crucial aspect is illustrated by the following example. A practically valuable carbon electrode may be constructed by a spray technique originally developed in our laboratory.<sup>34)</sup> This technique leads to very uniformly deposited, thin films formed by graphite (*e.g.*, Lonza KS 44) 93% in weight and a Teflon™ (5%)–PMMA (2%) binder (Fig. 10.15).

This electrode has excellent response when tested in a liquid electrolyte (*e.g.*, a 1 M  $\text{LiClO}_4$  solution in an EC–DC 2:1 mixture) cell. Fig. 10.16, which illustrates the first

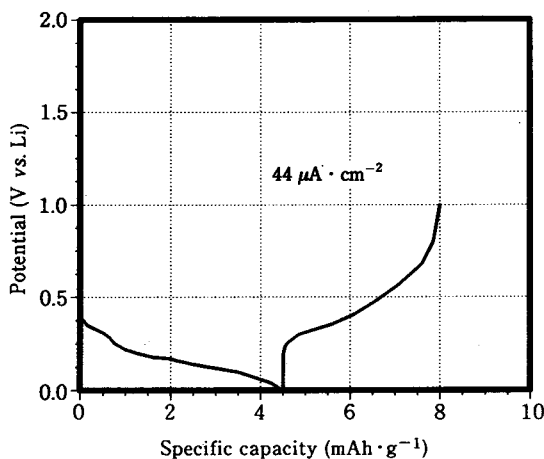


Fig. 10.17 Cycling response of a graphite thin ( $0.85 \text{ mg} \cdot \text{cm}^{-2}$ ) film electrode in an  $\text{LiClO}_4\text{-PC-EC-PMMA}$  electrolyte cell.

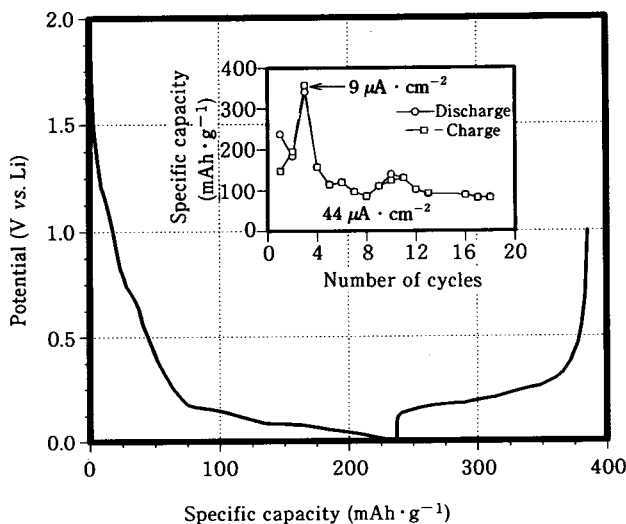


Fig. 10.18 Cycling response of a graphite thin ( $0.85 \text{ mg} \cdot \text{cm}^{-2}$ ) film electrode in a wetted  $\text{LiClO}_4\text{-PC-EC-PMMA}$  electrolyte cell.

charge (Li intercalation)–discharge (Li deintercalation) cycle and the specific capacity delivered upon subsequent cycling, demonstrates that the electrode achieves the expected theoretical behavior (e.g., reversible capacity of the order of  $370 \text{ mAh} \cdot \text{g}^{-1}$ ).

However, when the same electrode is merely placed in contact with a PMMA-based electrolyte membrane, very little cycling capacity can be obtained (see Fig. 10.17). The recovery of the electrode capacity requires a modification of the interface to facilitate the kinetics of the electrochemical process by promoting the full contact between the graphite

particles of the electrode and the lithium ions of the electrolyte. This sort of “activation” action may be obtained by, for instance, wetting the interface with few drops of the same liquid solution which constitutes the electrolyte membrane. As shown in Fig. 10.18 this procedure does restore part of the capacity and of the cyclability of the carbon electrode.

A somewhat similar approach, although modified and scaled-up to a commercially exploitable process, was adopted by the Bellcore Laboratory in the United States. In this case, the interfacial activation has been realized by a multi-stage process which involves first the lamination of the cell components by using a plasticizer-added electrolyte, then the removal of the plasticizer and finally the addition of a liquid electrolyte.<sup>19,20)</sup>

Although certainly successful and presently widely exploited, this process leads to a battery configuration which cannot be strictly defined as fully in the solid-state but which rather resembles that of the parent liquid electrolyte systems with the bonus of offering a final compact laminated structure. Undoubtedly, if this bonus could be achieved without undergoing a series of liquid extraction and liquid inclusion steps, a further important progress would be achieved in the area of PLI batteries. Accordingly, several academic and industrial laboratories are presently involved in various studies aimed to achieve this major goal.

## 10.4 Practical PLI Batteries

The Li-ion battery developed at Bellcore is today practically available. As already

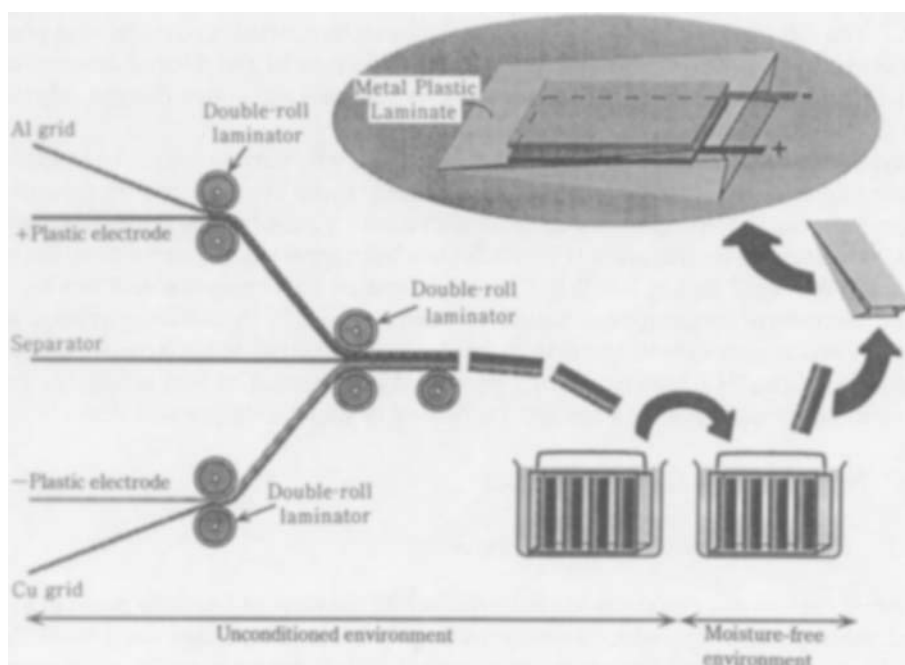


Fig. 10.19 Schematic processing of the Bellcore's process for the production of PLI batteries. Reproduced by courtesy of Bellcore (see Ref. 19).

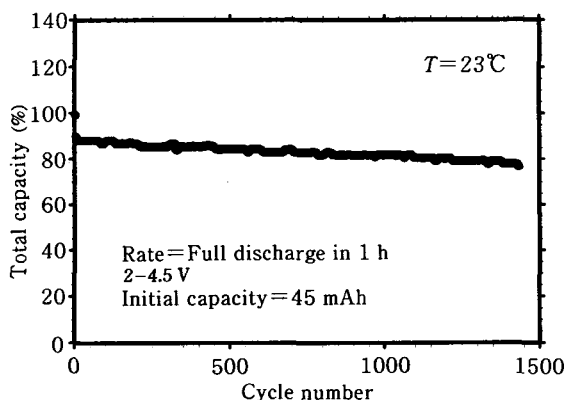


Fig. 10.20 Life cycle of Bellcore PLI batteries. Reproduced by courtesy of Bellcore (see Ref. 19).

mentioned, it involves a hybrid polymer electrolyte, an  $\text{LiMn}_2\text{O}_4$  cathode and a carbon anode. The specific relevance of Bellcore's plastic Li-ion battery technology is that it combines advantages of liquids and polymers, since it uses an inert polymer backbone to hold large amounts of liquids as well as to fuse the battery layers together in a continuous production process. The basic steps of this PLI battery preparation process are schematically illustrated in Fig. 10.19. Basically, a stack composed of the two electrode films separated by the plasticized electrolyte membrane is fused by lamination to form a unified cell package. Next, the plasticizer is removed by extraction with an organic solvent. The cell is then housed in a plastic aluminum bag, dried (under reduced pressure and/or at elevated temperature) and activated by injection of the desired amount of the selected Li salt solution. The thermal sealing of the package concludes the fabrication process.<sup>20)</sup>

This type of process ensures good interfacial contact, which in turn leads to low internal resistance and thus, to high rate capability and long cycle life. In papers presented in recent conferences,<sup>19,21)</sup> a cyclability up to 1500 cycles to a cut-off of 80% of initial capacity at the 1C rate at room temperature (Fig. 10.20) has been reported. Energy densities of the order of  $130 \text{ Wh} \cdot \text{kg}^{-1}$  and of  $300 \text{ Wh} \cdot \text{l}^{-1}$ , and estimated cost comparable if not less than the liquid electrolyte counterparts, have also been quoted.<sup>19)</sup> Specifically related to the preparation process are also the facts that, unlike liquid electrolyte batteries which require metallic casting, the PLI batteries, being produced and formed as thin laminates, can be packaged in lightweight plastic bags and fabricated in various shapes and sizes.

## 10.5 New Types of PLI Batteries

### 10.5.1 PLI Batteries with $\text{TiS}_2$ Anodes

The use of carbon coke as electrode material, while convenient from the point of view of cost and fabrication, may induce some problems in terms of voltage excursions during charge-discharge cycling. Variations in potential with concentrations (*e.g.*, of degree of lithium intercalation) are generally related to changes in the chemical potential of the lithium ions. In the case of  $\text{Li}_x\text{C}_6$  one can assume that these changes are associated with

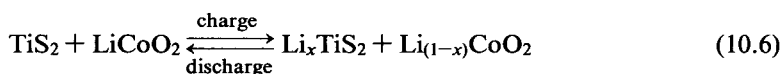
interactions between  $\text{Li}^+$  ions and the host structure. It would be then desirable to select electrode materials which experience small energy changes upon intercalation-deintercalation cycles. A possible example is  $\text{Li}_x\text{TiS}_2$  where the intercalation of the lithium ions within the Ti-S-Ti layers is accompanied by a modest free energy change and thus, by a limited voltage variation, *i.e.*, 0.7 V passing from  $x=0$  to  $x=1$ . Therefore, the replacement of carbon coke with titanium disulfide is expected to limit the cell voltage excursion of the “rocking chair” battery. To test this interesting concept, we have considered an “innovative” PLI battery structure involving a thin titanium disulfide film backed on a nickel or aluminum foil substrate as the negative electrode (anode) (in replacement of common lithiated carbon electrodes). Typical electrode thicknesses were about 5  $\mu\text{m}$ . The electrolyte was a thin PAN- or PMMA-based polymeric membrane and the positive electrode was a film of lithium metal oxide (*e.g.*,  $\text{LiCoO}_2$ ,  $\text{LiNiO}_2$  or  $\text{LiMn}_2\text{O}_4$ , respectively).<sup>35)</sup> The latter was prepared in the form of a thin, plastic-like membrane by casting a mixture of the selected lithium metal oxide, poly(vinylchloride) and acetylene black in tetrahydrofuran in the weight percent ratio of 75 : 20 : 5 on a glass substrate. The three powdered components were carefully mixed before adding the THF solvent. In order to avoid aggregates and discontinuities in the final membrane, the mixture was homogenized first by a mechanical stirrer for 30 min and then by an ultrasonic finger for 10 min. After complete solvent evaporation, the membrane was easily peeled off from the glass substrate. In this way, membranes with typical thickness ranging between 50 to 100  $\mu\text{m}$ , were obtained.<sup>35)</sup>

The  $\text{TiS}_2$ -LiMO (lithium metal oxide) PLI batteries were assembled by laminating the electrode and the electrolyte components to obtain a thin layer (typically 300  $\mu\text{m}$  thickness, 1  $\text{cm}^2$  surface) configuration. To prevent failure due to irreversible phase changes during cycling, the positive side contained an excess of the positive lithium metal oxide electrode.

One example of these PLI batteries is:



This cell, if assembled in the discharged state, has an open circuit voltage (OCV) of 0.3 V at room temperature. After charging, the cell assumes a voltage of 2.1 V. The cell may then be discharged to a voltage cut-off level of 0.5 V, and the cycling process:



where  $0 < x < 1$ , may be repeated several times with the typical trend illustrated in Fig. 10.21.

Similar results have been obtained with other types of PLI batteries, such as:



and



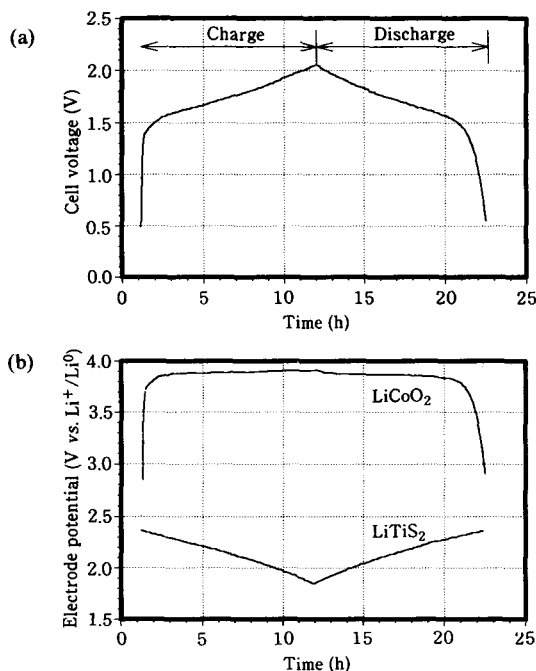
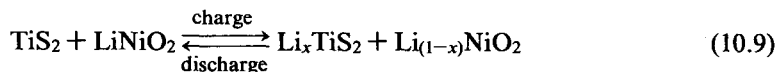
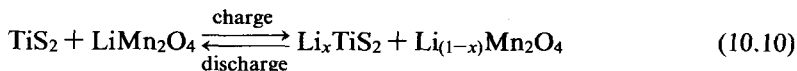


Fig. 10.21 Typical charge-discharge cycle (a) and single electrode polarization curves (b) of the thin-layer  $\text{Li}_x\text{TiS}_2/\text{LiClO}_4\text{-EC-PC-PAN/Li}_{(1-x)}\text{CoO}_2$  PLI cell. Room temperature. Lithium reference. Cycling current density:  $0.02 \text{ mA}\cdot\text{cm}^{-2}$ . (Reproduced with permission of The Electrochemical Society, Inc.)

The related cell charge-discharge reactions of these batteries are:



and



where  $0 < x < 1$ .

Typical charge-discharge curves are reported in Figs. 10.22 and 10.23, where the voltage acquired upon cycling by the single  $\text{Li}_x\text{TiS}_2$  and  $\text{LiMO}$  electrodes is also reported. The figures confirm that the cells have a relatively flat charge-discharge voltage profile (*i.e.*, varying from about 1.5 V for  $x=0$  to about 2.1 V for  $x=1$ ) and that complete utilization of the  $\text{TiS}_2$  is achieved.

This favorable behavior confirms the validity of the above stressed criteria for selecting alternative “rocking chair” battery electrodes, of which  $\text{Li}_x\text{TiS}_2$  is a possible example. Obviously, this electrode is far from being the final choice and it must be considered only

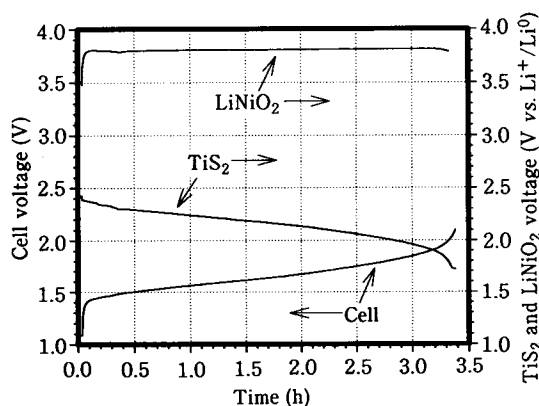


Fig. 10.22 Typical charge-cycle and single electrode ( $\text{Li}_x\text{TiS}_2$ , and  $\text{Li}_{(1-x)}\text{NiO}_2$ ) polarization curve of the  $\text{Li}_x\text{TiS}_2/\text{LiAsF}_6\text{-EC-DMC-PMMA}/\text{Li}_{(1-x)}\text{NiO}_2$  thin layer, PLI cell. Room temperature. Lithium reference. Cycling current density:  $0.02 \text{ mA}\cdot\text{cm}^{-2}$ . (Reproduced with permission of The Electrochemical Society, Inc.)

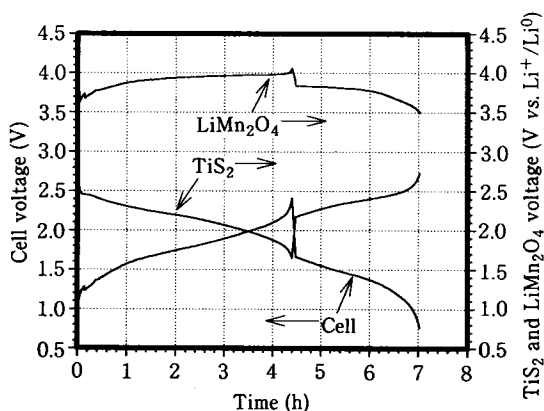


Fig. 10.23 Typical charge-cycle and single electrode ( $\text{Li}_x\text{TiS}_2$ , and  $\text{Li}_{(1-x)}\text{Mn}_2\text{O}_4$ ) polarization curve of the  $\text{Li}_x\text{TiS}_2/\text{LiAsF}_6\text{-EC-DMC-PMMA}/\text{Li}_{(1-x)}\text{Mn}_2\text{O}_4$  thin layer, PLI cell. Room temperature. Lithium reference. Cycling current density:  $0.02 \text{ mA}\cdot\text{cm}^{-2}$ . (Reproduced with permission of The Electrochemical Society, Inc.)

as a model system in view of the progress of the research of innovative but yet technologically competitive “rocking chair” electrodes. In fact, if from one side  $\text{Li}_x\text{TiS}_2$  offers acceptable voltage stability, from the other it exchanges lithium ions at a relatively high voltage range, namely from about 2.6 V ( $x=0$ ) to 1.9 V ( $x=1$ ) vs. Li (see Figs. 10.21–23). This is an obvious disadvantage which depresses the overall voltage of the entire  $\text{Li}_x\text{TiS}_2/\text{Li}_{(1-x)}\text{MO}$  cells. In fact these cells cycle around 1.5–2.1 V and this low voltage range reflects a relatively low energy content. The theoretical energy density of the cells is of the order of  $230 \text{ Wh}\cdot\text{kg}^{-1}$  (assuming an average voltage of 1.8 V) and the practical value is expected to fall to a more modest entity, especially considering that proper cell operation

requires an excess of the positive LiMO electrode.

### 10.5.2 The Dion Plastic Battery

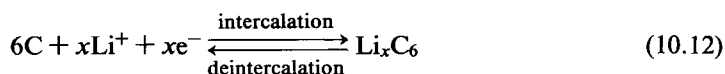
One possible drawback of "conventional" lithium ion batteries is in the limited choice of suitable cathode materials, which is presently restricted to three candidates only, *i.e.*, LiCoO<sub>2</sub>, LiNiO<sub>2</sub> and LiMn<sub>2</sub>O<sub>4</sub>.<sup>36)</sup> The reason is that these lithiated metal oxide, being unique in the capability of releasing lithium ions at high voltage levels, are the most convenient for assuring the electrochemical process to occur at a high energy level. However, these materials suffer from high cost (LiCoO<sub>2</sub>), temperature-dependent rate capability (LiNiO<sub>2</sub>) and difficult preparation procedure (LiMn<sub>2</sub>O<sub>4</sub>).

Therefore, the characterization of new lithium ion structures offering a wider choice of cathode materials would be highly welcome. A possible approach is the use of a very low cost family of cathode materials, *i.e.*, the family of heterocyclic polymers such as poly(pyrrole), pPy, poly(thiophene), pTh and their derivatives, for the fabrication of new types of lithium ion batteries.<sup>37)</sup> The cells, when fabricated in the discharge state, consist of a carbon-based anode (*e.g.*, a graphite anode), a lithium ion conducting membrane electrolyte and a polymer film cathode (*e.g.*, a pPy, (C<sub>4</sub>H<sub>3</sub>N)<sub>x</sub> cathode):

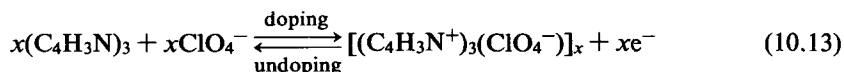


The pPy film electrodes may be prepared by electrochemical deposition on a metal (*e.g.*, stainless steel) net substrate from an appropriate solution (*e.g.*, a LiClO<sub>4</sub>, EC-DMC (2:1) solution) containing the pyrrole monomer and using lithium as the counter electrode.<sup>37,38)</sup> The graphite film electrodes may be obtained as described in section 10.3. For best performance, the pPy electrodes and, occasionally, the graphite electrodes must be electrochemically cleaned and preactivated by a few cycles *vs.* the lithium electrode before combining them in the cell structure. The C/pPy PLI battery prototypes may be assembled in a dry box in a prismatic configuration by folding the pPy film electrode around the C film electrode, using the electrolyte membrane as separators.<sup>37,38)</sup>

The electrochemical process of the C/pPy battery may be understood by considering the single electrode processes. For the graphite anode, the charge-discharge process evolves between 0.7 V and 0.05 V *vs.* Li with the intercalation-deintercalation of lithium ions:

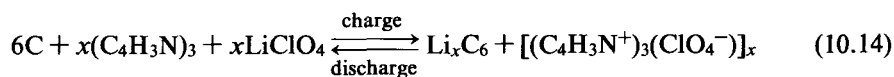


while the equivalent charge promotes the injection of ClO<sub>4</sub><sup>−</sup> ions in the cathode with a consequent *p*-doping-undoping process extending over three pPy monomeric units with an associated voltage range varying between 2.5 V and 3.5 V *vs.* Li<sup>39)</sup>:





Therefore, the C/pPy PLI cell operates around 3 V on the basis of the overall process:



By charging the cell,  $\text{Li}^+$  cations are intercalated into the graphite structure while the  $\text{ClO}_4^-$  counteranions are simultaneously injected into the pPy structure. The opposite process occurs in discharge.

This operation mechanism is indeed confirmed by Figs. 10.24 and 10.25, which show the trends of a charge–discharge cycle (Fig. 10.24) and the cyclability (Fig. 10.25) of the C/pPy prototype cell. Although not in an optimized configuration, the battery prototypes are

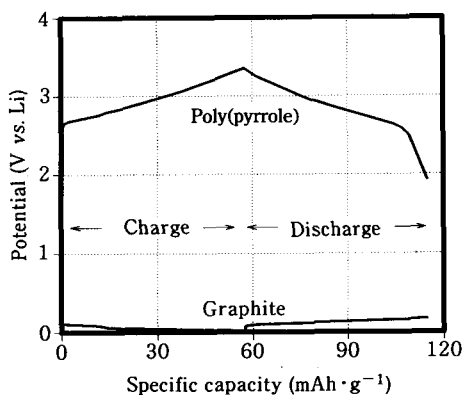


Fig. 10.24 Single electrodes voltage trends during the charge–discharge cycles of a C/LiClO<sub>4</sub>–EC–PC–PMMA/pPy plastic dion battery at room temperature. Electrodes preactivated. Electrode masses: pPy: 0.35 mg. Graphite 0.24 mg; Cycling rate: 22  $\mu\text{A}\cdot\text{cm}^{-2}$ . (Reproduced with permission of The Electrochemical Society, Inc.)

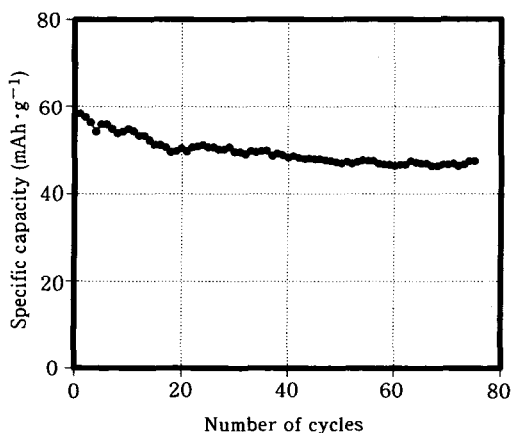


Fig. 10.25 Typical cycling response of a C/LiClO<sub>4</sub>–EC–PC–PMMA/pPy plastic dion battery at room temperature. Electrode masses: pPy: 0.35 mg. Graphite 0.24 mg; Cycling rate: 22  $\mu\text{A}\cdot\text{cm}^{-2}$ .

reported to show good cyclability and a theoretical energy density (calculated on the basis of the average values of discharge voltage and of the maximum theoretical capacity of both electrodes) of the order of  $300 \text{ Wh} \cdot \text{kg}^{-1}$ .<sup>37,38)</sup>

The difference between these new carbon/polymer PLI cells and the “conventional” carbon/lithiated metal oxide “lithium ion” cells is that in the latter only  $\text{Li}^+$  cations are cycled from the cathode to the graphite and *vice versa*, while in the former both the lithium cations and the counter anions are involved in the intercalating electrochemical process. Therefore, strictly speaking, neither the rocking chair nor the lithium ion terminology is adequate to describe this C/pPy cell. Possibly, one could more correctly refer to it as a dual-ion cell or “dion” cell.

The disadvantages of the dion cell over the usual lithium ion cells are in the lower voltage and the excess of electrolyte required for assuring both the electrochemical process and the low  $iR$  drop through the cell. Both factors act to reduce the specific energy value, which is expected to be lower than that of lithium ion batteries but possibly of the same order, if not higher, than that of Ni–Cd and Ni–MH batteries. This prevision is based on a comparison between the theoretical energy density of Ni–Cd ( $245 \text{ Wh} \cdot \text{kg}^{-1}$ ), Ni–MH ( $280 \text{ Wh} \cdot \text{kg}^{-1}$ ) and that of our C/pPy dion battery ( $300 \text{ Wh} \cdot \text{kg}^{-1}$ ).

These disadvantages, however, may be counterbalanced by the lower cost and the higher compatibility with the ambient. In fact, inexpensive, easily fabricated, heavy metal-free electrode materials are used in the dion cell. Therefore, the dion battery concept may have some relevance in lithium battery science and technology. Although having a modest energy density, the C/pPy batteries are expected to be of very low cost, environmentally friendly and easily produced in a full plastic configuration. These unique properties, combined with capabilities of high power density, can make the dion battery of particular interest for the advanced consumer electronic market.

## 10.6 Conclusions

The idea of replacing the conventional liquid electrolytes with polymer ionic membranes in advanced battery structures dates back to the eighties, as introduced by the pioneering work of Armand *et al.*,<sup>40)</sup> Hooper and North<sup>41)</sup> and Scrosati *et al.*<sup>42)</sup> However, the original concept was to use these membranes for the development of lithium metal polymer batteries. Performance tests soon demonstrated that the metal is attacked by the polymer electrolyte and that the related passivation phenomena may somewhat affect the cyclability and safety of the battery.<sup>43,44)</sup> Therefore, most of the recent work in polymer lithium batteries has been directed to the solution of the interfacial problems. One approach is that of improving the stability of the lithium interface, *e.g.*, by a high purification of the electrolyte<sup>45)</sup> and/or by the addition to the electrolyte of interfacial stabilizers.<sup>46)</sup> Obviously, a second approach is that of replacing the lithium metal by a lithiated carbon electrode to obtain the plastic lithium ion (PLI) battery structures described in this chapter. This second approach seems to be the closest to reaching practical success. In fact, while the PLI battery developed at Bellcore represents the state-of-the-art, many academic<sup>47)</sup> and industrial<sup>48,49)</sup> laboratories are presently involved in the fabrication and testing of other types of PLI systems of practical relevance. Due to all these successful achievements, PLI batteries are expected to be the power source of choice for the next generation of lightweight consumer electronics.

## Acknowledgments

The author thanks his co-workers, G.B. Appetecchi, F. Croce, G. Dautzenberg, F. Gerace, S. Panero, S. Passerini, F. Ronci and E. Spila, for their experimental work and help in producing this chapter. The New Energy and Industrial Technology Development Organization (NEDO) is acknowledged for the sponsorship of a part of the work reported in this chapter in the framework of an International Joint Research Programme titled "Pioneering development of high energy lithium batteries for the coming generation."

## REFERENCES

- 1) S. Megahed and B. Scrosati, *Interface*, **34** (1996).
- 2) A. Kozawa, T. Tagawa and A. Sato, 8th Int. Meet. Lithium Batteries, Nagoya, Japan, June 1996, Ext. Abstr., I-C-7.
- 3) C. A. Vincent, *Chemistry in Britain*, **391**, April 1981.
- 4) M. Armand, *Advan. Mater.*, **2**, 278 (1990).
- 5) B. Scrosati and R. Neat, *Applications of Electroactive Polymers* (Ed. by B. Scrosati), p. 182, Chapman & Hall (1993).
- 6) J. MacCallum and C. A. Vincent (Eds.), *Polymer Electrolyte Review I & II*, Elsevier Science (1987).
- 7) F. Gray, *Solid Polymer Electrolytes*, VCH (1991).
- 8) M. Armand, J.Y. Sanchez, M. Gauthier and Y. Coquette, *Electrochemistry of Novel Materials* (Eds. by J. Lopkowski and P.N. Ross), p. 65, VCH (1994).
- 9) G. Feullade and Ph. Perche, *J. Appl. Electrochem.*, **5**, 63 (1975).
- 10) K.M. Abraham and M. Alamgir, *J. Electrochem. Soc.*, **136**, 1657 (1990).
- 11) K.M. Abraham and M. Alamgir, *J. Power Sources*, **44**, 195 (1993).
- 12) G. Nagasubramanian, A.I. Attia and G. Halpert, *J. Appl. Electrochem.*, **24**, 298 (1994).
- 13) C. Schmutz, J.M. Tarascon, A.S. Gozdz, P.C. Warren and F.K. Shokoohi, Electrochem. Soc. Meet., Miami, FL, October 1994, Abstr., No. 109.
- 14) G.B. Appetecchi, F. Croce and B. Scrosati, *Electrochim. Acta*, **40**, 991 (1995).
- 15) G. Dautzenberg, F. Croce, S. Passerini and B. Scrosati, *Chem. Mater.*, **6**, 538 (1994).
- 16) G.B. Appetecchi, F. Croce and B. Scrosati, Proc. 36th Power Sources Conf., Cherry Hill, NJ, USA, p.233, June (1994).
- 17) G.B. Appetecchi, G. Dautzenberg and B. Scrosati, *J. Electrochem. Soc.*, **143**, 6 (1996).
- 18) G.B. Appetecchi, F. Croce and B. Scrosati, *J. Power Sources*, **66**, 77 (1997).
- 19) F.K. Shokoohi, J.M. Tarascon, A.S. Gozdz, P.C. Warren and G.G. Amatucci, 13th Int. Seminar Primary and Secondary Battery Technol. Appl., Boca Raton, FL, USA, March (1996).
- 20) J.M. Tarascon, G.G. Amatucci, C.N. Schmutz, A.S. Gozdz, P.C. Warren and F.K. Shokoohi, 8th Int. Meet. Lithium Battery, Nagoya, Japan, June 1996, Abstr., I-C-1.
- 21) F.K. Shokoohi, P.C. Warren, S. J. Greaney, J.M. Tarascon, A. Gozdz and G.G. Amatucci, Proc. 37th Power Sources Conf., Cherry Hill, NJ, USA, June (1996).
- 22) See for example, *Solid State Electrochemistry* (Ed. by P.G. Bruce), Cambridge Univ. Press (1995).
- 23) B. A. Boukamp, *Solid State Ionics*, **20**, 31 (1986).
- 24) P. Bruce, J. Evans and C. A. Vincent, *Solid State Ionics*, **28-30**, 918 (1988).
- 25) P. Bruce and C. A. Vincent, *J. Electroanal. Chem.*, **225**, 1 (1987).
- 26) M. Watanabe, K. Sanui and N. Ogata, *J. Appl. Phys.*, **57**, 123 (1985).
- 27) D. Fateux, J. Powell, A. Massucco, M. van Baren, M. Rona and B. Barnett, Proc. 10th Int. Symp. Primary and Secondary Battery Technol. Appl., Deerfield Beach, FL, USA (1993).
- 28) H.P. Fritz and A. Kuhun, *J. Power Sources*, **41**, 253 (1993).
- 29) G.B. Appetecchi, F. Gerace, F. Croce, G. Dautzenberg, S. Passerini and B. Scrosati, *Electrochim. Acta*, **39**, 2187 (1994).
- 30) P.E. Stallworth, J. Li, S.G. Greenbaum, F. Croce, S. Slane and M. Salomon, *Solid State Ionics*, **73**, 119 (1994).
- 31) E. Cazzanelli, G. Mariotto, G.B. Appetecchi, F. Croce and B. Scrosati, *Electrochim. Acta*, **40**, 13 (1995).

- 32) C. Arbizzani, M. Mastragostino, L. Meneghello, X. Andrieu and T. Vicedo, *Solid State Ionics III* (Eds. by G. A. Nazri, J.M. Tarascon, M. Armand), *Mater. Res. Soc. Symp. Proc.*, **293**, 169 (1993).
- 33) M. Armand, *Solid State Ionics*, **69**, 309 (1994).
- 34) F. Gerace, S. Panero, E. Spila and B. Scrosati, *J. Appl. Electrochem.*, in press.
- 35) F. Croce, S. Passerini and B. Scrosati, *J. Electrochem. Soc.*, **141**, 1405 (1994).
- 36) S. Megahed and B. Scrosati, *J. Power Sources*, **51**, 79 (1994).
- 37) S. Panero, E. Spila and B. Scrosati, *J. Electrochem. Soc.*, **143**, L29 (1996).
- 38) A. Clemente, S. Panero, E. Spila and B. Scrosati, *Solid State Ionics*, **85**, 273 (1996).
- 39) B. Scrosati, *Solid State Electrochemistry* (Ed. by P.G. Bruce), p. 229, Cambridge Univ. Press (1994).
- 40) M.B. Armand, J.M. Chabagno and M.J. Duclot, 2nd Int. Conf. Solid Electrolytes, St. Andrews, Scotland, 1978, paper 6.5.
- 41) A. Hooper and J.M. North, *Solid State Ionics*, **9 & 10**, 1161 (1983).
- 42) F. Bonino, F. Ottaviani, B. Scrosati and G. Pistoia, *J. Electrochem. Soc.*, **135**, 12 (1988).
- 43) F. Croce, F. Gerace and B. Scrosati, Proc. 35th Int. Power Sources Conf., p.267, IEEE Publication (1992).
- 44) B. Scrosati and R.J. Neat, *Applications of Electroactive Polymers* (Ed. by B. Scrosati), p. 182, Chapman & Hall, (1993).
- 45) M. Armand, J.Y. Sanchez, M. Gauthier and Y. Choquette, *Electrochemistry of Novel Materials* (Eds. by J. Lipkowski and P.N. Ross), p.65, VCH (1994).
- 46) B. Scrosati and F. Croce, *Polymers for Advanced Technology*, **4**, 198 (1993).
- 47) G.B. Appetecchi, F. Croce and B. Scrosati, Electrochem. Soc., Fall Meet., Paris, France, Aug.-Sept. 1997.
- 48) M. Alamgir and K.M. Abraham, *J. Power Sources*, **54**, 40 (1995).
- 49) L. Sun and K. Higuchi, 8th Int. Meet. Lithium Batteries, Nagoya, Japan, June 1996, Abstr., I-B-21.

## Index

### A

AA-stacking 110  
AB-stacking 111  
acceptor number 158  
ac impedance measurement 173  
additive 81  
additive in electrolyte 79  
aerogel 61, 63  
amorphous 84  
amorphous  $V_2O_5$  cathode 67  
anode 12  
anodic current 165, 206  
antifluorite 120  
antifluorite structure 120  
artificial graphite 175

### B

battery resistance 4, 6  
binding energy 40~42  
blocking electrode cell 231  
bonding site 112  
bond length 40  
Born-Harber's cycle 41  
breakdown 195  
bulk conductivity 204

### C

capacity loss 54  
capacity retention 53  
carbonaceous host material 129  
carbonaceous material 144, 182, 183, 185  
carbon black 131  
carbon fiber 117  
carbon film 131  
cathodic current 165, 206  
cathodic polarization 161  
chemical diffusion coefficient 42, 43, 52, 122  
chemical potential 4  
closed-circuit voltage 19  
close-packed oxygen array 14  
cluster compound 26  
coal-tar pitch 171  
co-intercalation 61  
cokes 100  
Cole-Cole plot 80, 173  
composite lithium anode 82  
concentric texture 117  
conductive diluent 58  
coulombic efficiency 102, 165, 173  
crown ether 163  
crush 92  
current-collector resistance 6  
current pulse relaxation technique (CPR) 42  
cyclic voltammetry 163

cyclic voltammogram 206  
cycling efficiency 69  
cycling performance 38

### D

dead lithium 71, 76  
dendritic 72  
dendritic formation 181, 199  
dendritic lithium 81  
dendritic structure 82  
dielectric constant 158  
differential scanning calorimetry 44  
disconnection 90  
donicity number 158  
doped spinel phase 34  
double core-shell texture 117  
dual-ion cell 243

### E

electrochemical lithiation 118  
electrochemical quartz crystal microbalance (EQCM) 72, 174, 175  
electrochemical reduction of graphitic carbon 135  
electrolyte 78  
electrolyte-electrode interface 5  
electrolyte resistance 4  
energy gap 3  
enthalpy of dissociation 41  
enthalpy of formation 41  
enthalpy of vaporization 41  
ester 158  
exfoliation of graphene sheet 114  
external short 91  
extrusion 77

### F

figure of merit for lithium cycling efficiency (FOM) 69, 70, 75, 79  
first-order transition 106  
forced discharge 91  
framework structure 12  
framework transition-metal oxide 11

### G

galvanostatic charge-discharge curve 34~36  
galvanostatic intermittent titration technique method 122  
gel-type polymer electrolyte 222  
glass-forming network 205  
glass-forming region 202  
glass transition temperature 203  
glassy carbon (GC) 99, 166  
glassy electrolyte 201  
glassy solid electrolyte 200, 202

granular 71  
 graphene layer 144  
 graphite 188, 189  
 graphite-coke composite anode 105  
 graphite intercalation compound (GIC) 131  
 graphitic carbon 129, 131  
 graphitizable carbon 183  
 graphitized carbon 161  
 graphitizing structure 165, 171  
 graphitizing (soft) carbon 140, 143

**H**

hard carbon 99, 102, 112, 118, 183, 185, 186, 188, 189  
 heat generation 86, 87, 89  
 high-capacity carbon 145  
 high capacity non-graphitic carbon 140  
 highly oriented pyrolytic graphite (HOPG) 115, 130  
 HOMO 3, 8, 13  
 hysteresis capacity 142

**I**

inert electrode 227  
 intercalation 127  
 internal resistance 3  
 internal short 90  
 ion-exchange 55  
 ionic conductivity 159  
 ion-pair formation 161  
 irreversible capacity 143  
 irreversible decomposition of electrolyte 116

**J, K**

Jahn-Teller distortion 7, 31

Knight shift 184, 186

**L**

layered dichalcogenide 50  
 layered manganate 56  
 layered manganese oxide 55  
 layered oxide 53, 58  
 layered transition-metal oxide 9  
 Li<sub>2</sub>CO<sub>3</sub> film 78  
 Li-doping site 142  
<sup>7</sup>Li-NMR analysis 186  
<sup>7</sup>Li-NMR technique 184  
 liquid electrolyte 2  
 lithium carbonate 192  
 lithium cobaltite 182, 192  
 lithium cycling efficiency 78  
 lithium deposition 73, 75  
 lithium diffusion 27  
 lithium imide salt 173  
 lithium ion plastic battery 218  
 lithium ion transference number 230  
 lithium metal anode cell 67  
 lithium salt 8, 158  
 lithium-storing material 181  
 lithium surface 82  
 lithium transference number 231

lithium whisker 73~75  
 low capacity carbon 142  
 low capacity non-graphitic carbon 140  
 LUMO 3, 8, 13

**M**

macro-domain 203  
 Madelung energy 14  
 meltdown 195  
 mesocarbon microbead (MCMB) 108, 171  
 mesophase pitch-based carbon 100  
 misfit 130  
 mixed conducting oxide 49  
 mixed conduction 129  
 mixed potential 146  
 Mn-O bond 55  
 monoclinic 18  
 Monte Carlo simulation 72  
 mossy 72  
 mossy lithium 72

**N**

$\alpha$ -NaFeO<sub>2</sub> 10  
 nail penetration 92  
 nail penetration test 90  
 NASICON 1  
 NASICON framework 18  
 natural graphite 100, 104, 105  
 nearest neighbor site 133  
 Nernst equation 6  
 nickel-cadmium battery 9  
 nitride 120  
 non-graphitic (disordered) carbon 128, 130, 140  
 non-graphitic (disordered) carbonaceous material 131  
 non-graphitizable carbon 183  
 non-graphitized carbon 111  
 non-graphitizing carbon 143

**O**

olivine 16  
 open-circuit voltage 3  
 organic electrolyte 157, 161  
 organic electrolyte solution 156  
 organic solvent 157  
 overcharge 91  
 overvoltage 6

**P**

PAN-based carbon fiber M46 102  
 petroleum coke 131  
 phase diagram of lithium-graphite system 106  
 phase transformation 33  
 pitch-based carbon fiber 163, 165  
 plasticized electrode 232  
 plasticizer 226  
 plastic lithium ion battery 219  
 plating efficiency 69  
 PLI battery 235, 236  
 PLI cell 242  
 PLI membrane 223

polyacrylonitrile 131  
 polyfurfuryl alcohol resin (PFA) 102, 103  
 polymer electrolyte membrane 219, 220  
 potential plateau 108  
 potential sweep voltammogram 167  
 power 3  
 pPy film electrode 240  
 protection film 67, 68, 81, 136, 162, 173  
 protonic conductivity 8  
 PTC device 195  
 PVDF-HFP copolymer 226  
 PVDF-HFP membrane 223  
 pyrocarbon 131  
 pyrolytic carbon 102  
 pyrolyzed PFA 118

## Q, R

QCM 72  
 quaternary spinel phase 34  
 radial with wedge 117  
 radial with zigzag layer 117  
 real electrode 228  
 real solid-state cell 232  
 rechargeable lithium battery 156, 181  
 redox energy 20  
 relative permittivity 158  
 retention 172, 174, 189  
 rhombohedral 18  
 RIETAN 46  
 Rietveld analysis 40  
 rutile structure 26

## S

safety 83  
 safety test 85, 86, 91  
 safety vent 193  
 Sauerbrey's equation 176  
 secondary lithium battery 13  
 self diffusion coefficient 51  
 separator 195  
 shear structure 26  
 shutdown 195  
 single-layer carbon 113  
 soft carbon 99, 100, 110, 111, 183~185, 189  
 soft chemistry 64  
 sol-gel process 61  
 solid electrolyte 2, 200  
 solid electrolyte interface (SEI) 118  
 solid electrolyte interphase (SEI) model 68  
 solid solution 58  
 solid-state battery 200, 209, 215  
 solid state lithium battery 200, 215  
 solvated ion 160  
 solvent-blocking effect 118  
 spin coating technique 175  
 spinel structure 27  
 spinel system 15  
 square pyramid 58, 59  
 stack pressure 81  
 stage-1 105

stage-4 105  
 stage-2 phase 105  
 stage-3 phase 105  
 staging phenomenon 133  
 standard Gibbs energy 31  
 standard potential 7  
 stripping current 77  
 sulfide glasses 201  
 synthetic metal 129

## T

terminal voltage 146  
 thermal decomposition 87, 88  
 thermal stability 92  
 thermal stability test 76  
 thin film battery 52, 209  
 thin film solid state battery 209  
 time-of-fly method 230  
 topotactic intercalation 132  
 transference number 2  
 transition metal nitride 120  
 transport number 2  
 tricobalt tetraoxide 192  
 trip temperature 195  
 tungsten bronze 49  
 turbostratic carbon 140  
 turbostratic disorder 130  
 turbostratic orientation 130  
 turbostratic structure 100, 108, 110  
 twin-roller quenching 202, 204

## U, V

ultramicropore 188  
 vacant interlayer distance of the natural graphite 107  
 vanadium bronze 49  
 vanadium oxide 58  
 vanadyl bond 62  
 van der Waals bonding 9  
 van der Waals layer 52  
 vapor grown carbon fiber 100  
 viscosity 158  
 voltage drop 3

## W, X

window 4  
 xerogel 61, 63